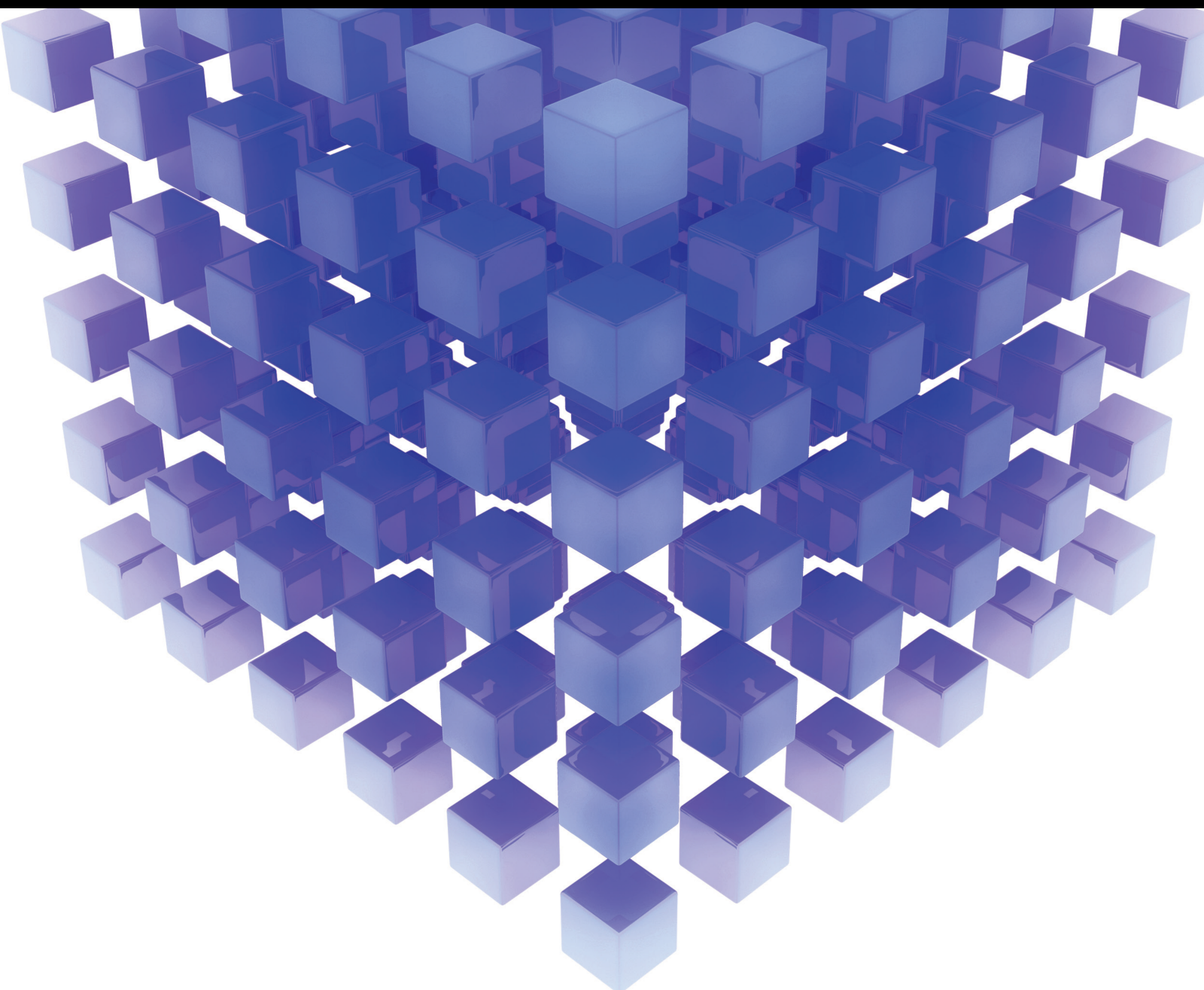


Mathematical Problems in Engineering

# Control of Networked Systems with Engineering Applications 2020

Lead Guest Editor: Hou-Sheng Su

Guest Editors: Michael Z. Q. Chen, Zhiwei Gao, Xiao Ling Wang, and Sahar Yazdani





---

**Control of Networked Systems with  
Engineering Applications 2020**

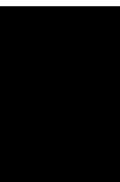
Mathematical Problems in Engineering

---

**Control of Networked Systems with  
Engineering Applications 2020**

Lead Guest Editor: Hou-Sheng Su

Guest Editors: Michael Z. Q. Chen, Zhiwei Gao,  
Xiao Ling Wang, and Sahar Yazdani




---

Copyright © 2020 Hindawi Limited. All rights reserved.

This is a special issue published in “Mathematical Problems in Engineering.” All articles are open access articles distributed under the Creative Commons Attribution License, which permits unrestricted use, distribution, and reproduction in any medium, provided the original work is properly cited.

# Chief Editor

Guangming Xie , China

## Academic Editors

Kumaravel A , India  
Waqas Abbasi, Pakistan  
Mohamed Abd El Aziz , Egypt  
Mahmoud Abdel-Aty , Egypt  
Mohammed S. Abdo, Yemen  
Mohammad Yaghoub Abdollahzadeh  
Jamalabadi , Republic of Korea  
Rahib Abiyev , Turkey  
Leonardo Acho , Spain  
Daniela Addessi , Italy  
Arooj Adeel , Pakistan  
Waleed Adel , Egypt  
Ramesh Agarwal , USA  
Francesco Aggogeri , Italy  
Ricardo Aguilar-Lopez , Mexico  
Afaq Ahmad , Pakistan  
Naveed Ahmed , Pakistan  
Elias Aifantis , USA  
Akif Akgul , Turkey  
Tareq Al-shami , Yemen  
Guido Ala, Italy  
Andrea Alaimo , Italy  
Reza Alam, USA  
Osamah Albahri , Malaysia  
Nicholas Alexander , United Kingdom  
Salvatore Alfonzetti, Italy  
Ghous Ali , Pakistan  
Nouman Ali , Pakistan  
Mohammad D. Aliyu , Canada  
Juan A. Almendral , Spain  
A.K. Alomari, Jordan  
José Domingo Álvarez , Spain  
Cláudio Alves , Portugal  
Juan P. Amezcua-Sanchez, Mexico  
Mukherjee Amitava, India  
Lionel Amodeo, France  
Sebastian Anita, Romania  
Costanza Arico , Italy  
Sabri Arik, Turkey  
Fausto Arpino , Italy  
Rashad Asharabi , Saudi Arabia  
Farhad Aslani , Australia  
Mohsen Asle Zaem , USA

Andrea Avanzini , Italy  
Richard I. Avery , USA  
Viktor Avrutin , Germany  
Mohammed A. Awadallah , Malaysia  
Francesco Aymerich , Italy  
Sajad Azizi , Belgium  
Michele Bacciocchi , Italy  
Seungik Baek , USA  
Khaled Bahlali, France  
M.V.A Raju Bahubalendruni, India  
Pedro Balaguer , Spain  
P. Balasubramaniam, India  
Stefan Balint , Romania  
Ines Tejado Balsera , Spain  
Alfonso Banos , Spain  
Jerzy Baranowski , Poland  
Tudor Barbu , Romania  
Andrzej Bartoszewicz , Poland  
Sergio Baselga , Spain  
S. Caglar Baslamisli , Turkey  
David Bassir , France  
Chiara Bedon , Italy  
Azeddine Beghdadi, France  
Andriette Bekker , South Africa  
Francisco Beltran-Carbajal , Mexico  
Abdellatif Ben Makhlof , Saudi Arabia  
Denis Benasciutti , Italy  
Ivano Benedetti , Italy  
Rosa M. Benito , Spain  
Elena Benvenuti , Italy  
Giovanni Berselli, Italy  
Michele Betti , Italy  
Pietro Bia , Italy  
Carlo Bianca , France  
Simone Bianco , Italy  
Vincenzo Bianco, Italy  
Vittorio Bianco, Italy  
David Bigaud , France  
Sardar Muhammad Bilal , Pakistan  
Antonio Bilotta , Italy  
Sylvio R. Bistafa, Brazil  
Chiara Boccaletti , Italy  
Rodolfo Bontempo , Italy  
Alberto Borboni , Italy  
Marco Bortolini, Italy

Paolo Boscariol, Italy  
Daniela Boso , Italy  
Guillermo Botella-Juan, Spain  
Abdesselem Boulkroune , Algeria  
Boulaïd Boulkroune, Belgium  
Fabio Bovenga , Italy  
Francesco Braghin , Italy  
Ricardo Branco, Portugal  
Julien Bruchon , France  
Matteo Bruggi , Italy  
Michele Brun , Italy  
Maria Elena Bruni, Italy  
Maria Angela Butturi , Italy  
Bartłomiej Błachowski , Poland  
Dhanamjayulu C , India  
Raquel Caballero-Águila , Spain  
Filippo Cacace , Italy  
Salvatore Caddemi , Italy  
Zuowei Cai , China  
Roberto Caldelli , Italy  
Francesco Cannizzaro , Italy  
Maosen Cao , China  
Ana Carpio, Spain  
Rodrigo Carvajal , Chile  
Caterina Casavola, Italy  
Sara Casciati, Italy  
Federica Caselli , Italy  
Carmen Castillo , Spain  
Inmaculada T. Castro , Spain  
Miguel Castro , Portugal  
Giuseppe Catalanotti , United Kingdom  
Alberto Cavallo , Italy  
Gabriele Cazzulani , Italy  
Fatih Vehbi Celebi, Turkey  
Miguel Cerrolaza , Venezuela  
Gregory Chagnon , France  
Ching-Ter Chang , Taiwan  
Kuei-Lun Chang , Taiwan  
Qing Chang , USA  
Xiaoheng Chang , China  
Prasenjit Chatterjee , Lithuania  
Kacem Chehdi, France  
Peter N. Cheimets, USA  
Chih-Chiang Chen , Taiwan  
He Chen , China

Kebing Chen , China  
Mengxin Chen , China  
Shyi-Ming Chen , Taiwan  
Xizhong Chen , Ireland  
Xue-Bo Chen , China  
Zhiwen Chen , China  
Qiang Cheng, USA  
Zeyang Cheng, China  
Luca Chiapponi , Italy  
Francisco Chicano , Spain  
Tirivanhu Chinyoka , South Africa  
Adrian Chmielewski , Poland  
Seongim Choi , USA  
Gautam Choubey , India  
Hung-Yuan Chung , Taiwan  
Yusheng Ci, China  
Simone Cinquemani , Italy  
Roberto G. Citarella , Italy  
Joaquim Ciurana , Spain  
John D. Clayton , USA  
Piero Colajanni , Italy  
Giuseppina Colicchio, Italy  
Vassilios Constantoudis , Greece  
Enrico Conte, Italy  
Alessandro Contento , USA  
Mario Cools , Belgium  
Gino Cortellessa, Italy  
Carlo Cosentino , Italy  
Paolo Crippa , Italy  
Erik Cuevas , Mexico  
Guozeng Cui , China  
Mehmet Cunkas , Turkey  
Giuseppe D'Aniello , Italy  
Peter Dabnichki, Australia  
Weizhong Dai , USA  
Zhifeng Dai , China  
Purushothaman Damodaran , USA  
Sergey Dashkovskiy, Germany  
Adiel T. De Almeida-Filho , Brazil  
Fabio De Angelis , Italy  
Samuele De Bartolo , Italy  
Stefano De Miranda , Italy  
Filippo De Monte , Italy

























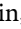

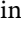
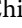
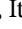

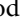

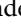

José António Fonseca De Oliveira  
Correia , Portugal  
Jose Renato De Sousa , Brazil  
Michael Defoort, France  
Alessandro Della Corte, Italy  
Laurent Dewasme , Belgium  
Sanku Dey , India  
Gianpaolo Di Bona , Italy  
Roberta Di Pace , Italy  
Francesca Di Puccio , Italy  
Ramón I. Diego , Spain  
Yannis Dimakopoulos , Greece  
Hasan Dinçer , Turkey  
José M. Domínguez , Spain  
Georgios Dounias, Greece  
Bo Du , China  
Emil Dumic, Croatia  
Madalina Dumitriu , United Kingdom  
Premraj Durairaj , India  
Saeed Eftekhari Azam, USA  
Said El Kafhali , Morocco  
Antonio Elipse , Spain  
R. Emre Erkmen, Canada  
John Escobar , Colombia  
Leandro F. F. Miguel , Brazil  
FRANCESCO FOTI , Italy  
Andrea L. Facci , Italy  
Shahla Faisal , Pakistan  
Giovanni Falsone , Italy  
Hua Fan, China  
Jianguang Fang, Australia  
Nicholas Fantuzzi , Italy  
Muhammad Shahid Farid , Pakistan  
Hamed Faruqi, Iran  
Yann Favennec, France  
Fiorenzo A. Fazzolari , United Kingdom  
Giuseppe Fedele , Italy  
Roberto Fedele , Italy  
Baowei Feng , China  
Mohammad Ferdows , Bangladesh  
Arturo J. Fernández , Spain  
Jesus M. Fernandez Oro, Spain  
Francesco Ferrise, Italy  
Eric Feulvarch , France  
Thierry Floquet, France

Eric Florentin , France  
Gerardo Flores, Mexico  
Antonio Forcina , Italy  
Alessandro Formisano, Italy  
Francesco Franco , Italy  
Elisa Francomano , Italy  
Juan Frausto-Solis, Mexico  
Shujun Fu , China  
Juan C. G. Prada , Spain  
HECTOR GOMEZ , Chile  
Matteo Gaeta , Italy  
Mauro Gaggero , Italy  
Zoran Gajic , USA  
Jaime Gallardo-Alvarado , Mexico  
Mosè Gallo , Italy  
Akemi Gálvez , Spain  
Maria L. Gandarias , Spain  
Hao Gao , Hong Kong  
Xingbao Gao , China  
Yan Gao , China  
Zhiwei Gao , United Kingdom  
Giovanni Garcea , Italy  
José García , Chile  
Harish Garg , India  
Alessandro Gasparetto , Italy  
Stylianos Georgantzinou, Greece  
Fotios Georgiades , India  
Parviz Ghadimi , Iran  
Ştefan Cristian Gherghina , Romania  
Georgios I. Giannopoulos , Greece  
Agathoklis Giaralis , United Kingdom  
Anna M. Gil-Lafuente , Spain  
Ivan Giorgio , Italy  
Gaetano Giunta , Luxembourg  
Jefferson L.M.A. Gomes , United Kingdom  
Emilio Gómez-Déniz , Spain  
Antonio M. Gonçalves de Lima , Brazil  
Qunxi Gong , China  
Chris Goodrich, USA  
Rama S. R. Gorla, USA  
Veena Goswami , India  
Xunjie Gou , Spain  
Jakub Grabski , Poland

Antoine Grall , France  
George A. Gravvanis , Greece  
Fabrizio Greco , Italy  
David Greiner , Spain  
Jason Gu , Canada  
Federico Guarracino , Italy  
Michele Guida , Italy  
Muhammet Gul , Turkey  
Dong-Sheng Guo , China  
Hu Guo , China  
Zhaoxia Guo, China  
Yusuf Gurefe, Turkey  
Salim HEDDAM , Algeria  
ABID HUSSANAN, China  
Quang Phuc Ha, Australia  
Li Haitao , China  
Petr Hájek , Czech Republic  
Mohamed Hamdy , Egypt  
Muhammad Hamid , United Kingdom  
Renke Han , United Kingdom  
Weimin Han , USA  
Xingsi Han, China  
Zhen-Lai Han , China  
Thomas Hanne , Switzerland  
Xinan Hao , China  
Mohammad A. Hariri-Ardebili , USA  
Khalid Hattaf , Morocco  
Defeng He , China  
Xiao-Qiao He, China  
Yanchao He, China  
Yu-Ling He , China  
Ramdane Hedjar , Saudi Arabia  
Jude Hemanth , India  
Reza Hemmati, Iran  
Nicolae Herisanu , Romania  
Alfredo G. Hernández-Díaz , Spain  
M.I. Herreros , Spain  
Eckhard Hitzer , Japan  
Paul Honeine , France  
Jaromir Horacek , Czech Republic  
Lei Hou , China  
Yingkun Hou , China  
Yu-Chen Hu , Taiwan  
Yunfeng Hu, China  
Can Huang , China  
Gordon Huang , Canada  
Linsheng Huo , China  
Sajid Hussain, Canada  
Asier Ibeas , Spain  
Orest V. Iftime , The Netherlands  
Przemyslaw Ignaciuk , Poland  
Giacomo Innocenti , Italy  
Emilio Insfran Pelozo , Spain  
Azeem Irshad, Pakistan  
Alessio Ishizaka, France  
Benjamin Ivorra , Spain  
Breno Jacob , Brazil  
Reema Jain , India  
Tushar Jain , India  
Amin Jajarmi , Iran  
Chiranjibe Jana , India  
Łukasz Jankowski , Poland  
Samuel N. Jator , USA  
Juan Carlos Jáuregui-Correa , Mexico  
Kandasamy Jayakrishna, India  
Reza Jazar, Australia  
Khalide Jbilou, France  
Isabel S. Jesus , Portugal  
Chao Ji , China  
Qing-Chao Jiang , China  
Peng-fei Jiao , China  
Ricardo Fabricio Escobar Jiménez , Mexico  
Emilio Jiménez Macías , Spain  
Maolin Jin, Republic of Korea  
Zhuo Jin, Australia  
Ramash Kumar K , India  
BHABEN KALITA , USA  
MOHAMMAD REZA KHEDMATI , Iran  
Viacheslav Kalashnikov , Mexico  
Mathiyalagan Kalidass , India  
Tamas Kalmar-Nagy , Hungary  
Rajesh Kaluri , India  
Jyotheeswara Reddy Kalvakurthi, India  
Zhao Kang , China  
Ramani Kannan , Malaysia  
Tomasz Kapitaniak , Poland  
Julius Kaplunov, United Kingdom  
Konstantinos Karamanos, Belgium  
Michal Kawulok, Poland



Irfan Kaymaz , Turkey  
Vahid Kayvanfar , Qatar  
Krzysztof Kecik , Poland  
Mohamed Khader , Egypt  
Chaudry M. Khalique , South Africa  
Mukhtaj Khan , Pakistan  
Shahid Khan , Pakistan  
Nam-Il Kim, Republic of Korea  
Philipp V. Kiryukhantsev-Korneev ,  
Russia  
P.V.V Kishore , India  
Jan Koci , Czech Republic  
Ioannis Kostavelis , Greece  
Sotiris B. Kotsiantis , Greece  
Frederic Kratz , France  
Vamsi Krishna , India  
Edyta Kucharska, Poland  
Krzysztof S. Kulpa , Poland  
Kamal Kumar, India  
Prof. Ashwani Kumar , India  
Michal Kunicki , Poland  
Cedrick A. K. Kwuimy , USA  
Kyandoghere Kyamakya, Austria  
Ivan Kyrchei , Ukraine  
Márcio J. Lacerda , Brazil  
Eduardo Lalla , The Netherlands  
Giovanni Lancioni , Italy  
Jaroslaw Latalski , Poland  
Hervé Laurent , France  
Agostino Lauria , Italy  
Aimé Lay-Ekuakille , Italy  
Nicolas J. Leconte , France  
Kun-Chou Lee , Taiwan  
Dimitri Lefebvre , France  
Eric Lefevre , France  
Marek Lefik, Poland  
Yaguo Lei , China  
Kauko Leiviskä , Finland  
Ervin Lenzi , Brazil  
ChenFeng Li , China  
Jian Li , USA  
Jun Li , China  
Yueyang Li , China  
Zhao Li , China































Zhen Li , China  
En-Qiang Lin, USA  
Jian Lin , China  
Qibin Lin, China  
Yao-Jin Lin, China  
Zhiyun Lin , China  
Bin Liu , China  
Bo Liu , China  
Heng Liu , China  
Jianxu Liu , Thailand  
Lei Liu , China  
Sixin Liu , China  
Wanquan Liu , China  
Yu Liu , China  
Yuanchang Liu , United Kingdom  
Bonifacio Llamazares , Spain  
Alessandro Lo Schiavo , Italy  
Jean Jacques Loiseau , France  
Francesco Lolli , Italy  
Paolo Lonetti , Italy  
António M. Lopes , Portugal  
Sebastian López, Spain  
Luis M. López-Ochoa , Spain  
Vassilios C. Loukopoulos, Greece  
Gabriele Maria Lozito , Italy  
Zhiguo Luo , China  
Gabriel Luque , Spain  
Valentin Lychagin, Norway  
YUE MEI, China  
Junwei Ma , China  
Xuanlong Ma , China  
Antonio Madeo , Italy  
Alessandro Magnani , Belgium  
Toqeer Mahmood , Pakistan  
Fazal M. Mahomed , South Africa  
Arunava Majumder , India  
Sarfranz Nawaz Malik, Pakistan  
Paolo Manfredi , Italy  
Adnan Maqsood , Pakistan  
Muazzam Maqsood, Pakistan  
Giuseppe Carlo Marano , Italy  
Damijan Markovic, France  
Filipe J. Marques , Portugal  
Luca Martinelli , Italy  
Denizar Cruz Martins, Brazil

Francisco J. Martos , Spain  
Elio Masciari , Italy  
Paolo Massioni , France  
Alessandro Mauro , Italy  
Jonathan Mayo-Maldonado , Mexico  
Pier Luigi Mazzeo , Italy  
Laura Mazzola, Italy  
Driss Mehdi , France  
Zahid Mehmood , Pakistan  
Roderick Melnik , Canada  
Xiangyu Meng , USA  
Jose Merodio , Spain  
Alessio Merola , Italy  
Mahmoud Mesbah , Iran  
Luciano Mescia , Italy  
Laurent Mevel , France  
Constantine Michailides , Cyprus  
Mariusz Michta , Poland  
Prankul Middha, Norway  
Aki Mikkola , Finland  
Giovanni Minafò , Italy  
Edmondo Minisci , United Kingdom  
Hiroyuki Mino , Japan  
Dimitrios Mitsotakis , New Zealand  
Ardashir Mohammadzadeh , Iran  
Francisco J. Montáns , Spain  
Francesco Montefusco , Italy  
Gisele Mophou , France  
Rafael Morales , Spain  
Marco Morandini , Italy  
Javier Moreno-Valenzuela , Mexico  
Simone Morganti , Italy  
Caroline Mota , Brazil  
Aziz Moukrim , France  
Shen Mouquan , China  
Dimitris Mourtzis , Greece  
Emiliano Mucchi , Italy  
Taseer Muhammad, Saudi Arabia  
Ghulam Muhiuddin, Saudi Arabia  
Amitava Mukherjee , India  
Josefa Mula , Spain  
Jose J. Muñoz , Spain  
Giuseppe Muscolino, Italy  
Marco Mussetta , Italy

Hariharan Muthusamy, India  
Alessandro Naddeo , Italy  
Raj Nandkeolyar, India  
Keivan Navaie , United Kingdom  
Soumya Nayak, India  
Adrian Neagu , USA  
Erivelton Geraldo Nepomuceno , Brazil  
AMA Neves, Portugal  
Ha Quang Thinh Ngo , Vietnam  
Nhon Nguyen-Thanh, Singapore  
Papakostas Nikolaos , Ireland  
Jelena Nikolic , Serbia  
Tatsushi Nishi, Japan  
Shanzhou Niu , China  
Ben T. Nohara , Japan  
Mohammed Nouari , France  
Mustapha Nourelfath, Canada  
Kazem Nouri , Iran  
Ciro Núñez-Gutiérrez , Mexico  
Włodzimierz Ogryczak, Poland  
Roger Ohayon, France  
Krzysztof Okarma , Poland  
Mitsuhiro Okayasu, Japan  
Murat Olgun , Turkey  
Diego Oliva, Mexico  
Alberto Olivares , Spain  
Enrique Onieva , Spain  
Calogero Orlando , Italy  
Susana Ortega-Cisneros , Mexico  
Sergio Ortobelli, Italy  
Naohisa Otsuka , Japan  
Sid Ahmed Ould Ahmed Mahmoud , Saudi Arabia  
Taoreed Owolabi , Nigeria  
EUGENIA PETROPOULOU , Greece  
Arturo Pagano, Italy  
Madhumangal Pal, India  
Pasquale Palumbo , Italy  
Dragan Pamučar, Serbia  
Weifeng Pan , China  
Chandan Pandey, India  
Rui Pang, United Kingdom  
Jürgen Pannek , Germany  
Elena Panteley, France  
Achille Paolone, Italy

George A. Papakostas , Greece  
Xosé M. Pardo , Spain  
You-Jin Park, Taiwan  
Manuel Pastor, Spain  
Pubudu N. Pathirana , Australia  
Surajit Kumar Paul , India  
Luis Payá , Spain  
Igor Pažanin , Croatia  
Libor Pekař , Czech Republic  
Francesco Pellicano , Italy  
Marcello Pellicciari , Italy  
Jian Peng , China  
Mingshu Peng, China  
Xiang Peng , China  
Xindong Peng, China  
Yuxing Peng, China  
Marzio Pennisi , Italy  
Maria Patrizia Pera , Italy  
Matjaz Perc , Slovenia  
A. M. Bastos Pereira , Portugal  
Wesley Peres, Brazil  
F. Javier Pérez-Pinal , Mexico  
Michele Perrella, Italy  
Francesco Pesavento , Italy  
Francesco Petrini , Italy  
Hoang Vu Phan, Republic of Korea  
Lukasz Pieczonka , Poland  
Dario Piga , Switzerland  
Marco Pizzarelli , Italy  
Javier Plaza , Spain  
Goutam Pohit , India  
Dragan Poljak , Croatia  
Jorge Pomares , Spain  
Hiram Ponce , Mexico  
Sébastien Poncet , Canada  
Volodymyr Ponomaryov , Mexico  
Jean-Christophe Ponsart , France  
Mauro Pontani , Italy  
Sivakumar Poruran, India  
Francesc Pozo , Spain  
Aditya Rio Prabowo , Indonesia  
Anchasa Pramuanjaroenkij , Thailand  
Leonardo Primavera , Italy  
B Rajanarayan Prusty, India

Krzysztof Puszynski , Poland  
Chuan Qin , China  
Dongdong Qin, China  
Jianlong Qiu , China  
Giuseppe Quaranta , Italy  
DR. RITU RAJ , India  
Vitomir Racic , Italy  
Carlo Rainieri , Italy  
Kumbakonam Ramamani Rajagopal, USA  
Ali Ramazani , USA  
Angel Manuel Ramos , Spain  
Higinio Ramos , Spain  
Muhammad Afzal Rana , Pakistan  
Muhammad Rashid, Saudi Arabia  
Manoj Rastogi, India  
Alessandro Rasulo , Italy  
S.S. Ravindran , USA  
Abdolrahman Razani , Iran  
Alessandro Reali , Italy  
Jose A. Reinoso , Spain  
Oscar Reinoso , Spain  
Haijun Ren , China  
Carlo Renno , Italy  
Fabrizio Renno , Italy  
Shahram Rezapour , Iran  
Ricardo Rianza , Spain  
Francesco Riganti-Fulginei , Italy  
Gerasimos Rigatos , Greece  
Francesco Ripamonti , Italy  
Jorge Rivera , Mexico  
Eugenio Roanes-Lozano , Spain  
Ana Maria A. C. Rocha , Portugal  
Luigi Rodino , Italy  
Francisco Rodríguez , Spain  
Rosana Rodríguez López, Spain  
Francisco Rossomando , Argentina  
Jose de Jesus Rubio , Mexico  
Weiguo Rui , China  
Rubén Ruiz , Spain  
Ivan D. Rukhlenko , Australia  
Dr. Eswaramoorthi S. , India  
Weichao SHI , United Kingdom  
Chaman Lal Sabharwal , USA  
Andrés Sáez , Spain

Bekir Sahin, Turkey  
Laxminarayan Sahoo , India  
John S. Sakellariou , Greece  
Michael Sakellariou , Greece  
Salvatore Salamone, USA  
Jose Vicente Salcedo , Spain  
Alejandro Salcido , Mexico  
Alejandro Salcido, Mexico  
Nunzio Salerno , Italy  
Rohit Salgotra , India  
Miguel A. Salido , Spain  
Sinan Salih , Iraq  
Alessandro Salvini , Italy  
Abdus Samad , India  
Sovan Samanta, India  
Nikolaos Samaras , Greece  
Ramon Sancibrian , Spain  
Giuseppe Sanfilippo , Italy  
Omar-Jacobo Santos, Mexico  
J Santos-Reyes , Mexico  
José A. Sanz-Herrera , Spain  
Musavarah Sarwar, Pakistan  
Shahzad Sarwar, Saudi Arabia  
Marcelo A. Savi , Brazil  
Andrey V. Savkin, Australia  
Tadeusz Sawik , Poland  
Roberta Sburlati, Italy  
Gustavo Scaglia , Argentina  
Thomas Schuster , Germany  
Hamid M. Sedighi , Iran  
Mijanur Rahaman Seikh, India  
Tapan Senapati , China  
Lotfi Senhadji , France  
Junwon Seo, USA  
Michele Serpilli, Italy  
Silvestar Šesnić , Croatia  
Gerardo Severino, Italy  
Ruben Sevilla , United Kingdom  
Stefano Sfarra , Italy  
Dr. Ismail Shah , Pakistan  
Leonid Shaikhet , Israel  
Vimal Shanmuganathan , India  
Prayas Sharma, India  
Bo Shen , Germany  
Hang Shen, China

Xin Pu Shen, China  
Dimitri O. Shepelsky, Ukraine  
Jian Shi , China  
Amin Shokrollahi, Australia  
Suzanne M. Shontz , USA  
Babak Shotorban , USA  
Zhan Shu , Canada  
Angelo Sifaleras , Greece  
Nuno Simões , Portugal  
Mehakpreet Singh , Ireland  
Piyush Pratap Singh , India  
Rajiv Singh, India  
Seralathan Sivamani , India  
S. Sivasankaran , Malaysia  
Christos H. Skiadas, Greece  
Konstantina Skouri , Greece  
Neale R. Smith , Mexico  
Bogdan Smolka, Poland  
Delfim Soares Jr. , Brazil  
Alba Sofi , Italy  
Francesco Soldovieri , Italy  
Raffaele Solimene , Italy  
Yang Song , Norway  
Jussi Sopanen , Finland  
Marco Spadini , Italy  
Paolo Spagnolo , Italy  
Ruben Specogna , Italy  
Vasilios Spitas , Greece  
Ivanka Stamova , USA  
Rafał Stanisławski , Poland  
Miladin Stefanović , Serbia  
Salvatore Strano , Italy  
Yakov Strelniker, Israel  
Kangkang Sun , China  
Qiuqin Sun , China  
Shuaishuai Sun, Australia  
Yanchao Sun , China  
Zong-Yao Sun , China  
Kumarasamy Suresh , India  
Sergey A. Suslov , Australia  
D.L. Suthar, Ethiopia  
D.L. Suthar , Ethiopia  
Andrzej Swierniak, Poland  
Andras Szekrenyes , Hungary  
Kumar K. Tamma, USA


Yong (Aaron) Tan, United Kingdom  
Marco Antonio Taneco-Hernández , Mexico  
Lu Tang , China  
Tianyou Tao, China  
Hafez Tari , USA  
Alessandro Tasora , Italy  
Sergio Teggi , Italy  
Adriana del Carmen Téllez-Anguiano , Mexico  
Ana C. Teodoro , Portugal  
Efstathios E. Theotokoglou , Greece  
Jing-Feng Tian, China  
Alexander Timokha , Norway  
Stefania Tomasiello , Italy  
Gisella Tomasini , Italy  
Isabella Torricollo , Italy  
Francesco Tornabene , Italy  
Mariano Torrisi , Italy  
Thang nguyen Trung, Vietnam  
George Tsiatas , Greece  
Le Anh Tuan , Vietnam  
Nerio Tullini , Italy  
Emilio Turco , Italy  
Ilhan Tuzcu , USA  
Efstratios Tzirtzilakis , Greece  
FRANCISCO UREÑA , Spain  
Filippo Ubertini , Italy  
Mohammad Uddin , Australia  
Mohammad Safi Ullah , Bangladesh  
Serdar Ulubeyli , Turkey  
Mati Ur Rahman , Pakistan  
Panayiotis Vafeas , Greece  
Giuseppe Vairo , Italy  
Jesus Valdez-Resendiz , Mexico  
Eusebio Valero, Spain  
Stefano Valvano , Italy  
Carlos-Renato Vázquez , Mexico  
Martin Velasco Villa , Mexico  
Franck J. Vernerey, USA  
Georgios Veronis , USA  
Vincenzo Vespri , Italy  
Renato Vidoni , Italy  
Venkatesh Vijayaraghavan, Australia

Anna Vila, Spain  
Francisco R. Villatoro , Spain  
Francesca Vipiana , Italy  
Stanislav Vitek , Czech Republic  
Jan Vorel , Czech Republic  
Michael Vynnycky , Sweden  
Mohammad W. Alomari, Jordan  
Roman Wan-Wendner , Austria  
Bingchang Wang, China  
C. H. Wang , Taiwan  
Dagang Wang, China  
Guoqiang Wang , China  
Huaiyu Wang, China  
Hui Wang , China  
J.G. Wang, China  
Ji Wang , China  
Kang-Jia Wang , China  
Lei Wang , China  
Qiang Wang, China  
Qingling Wang , China  
Weiwei Wang , China  
Xinyu Wang , China  
Yong Wang , China  
Yung-Chung Wang , Taiwan  
Zhenbo Wang , USA  
Zhibo Wang, China  
Waldemar T. Wójcik, Poland  
Chi Wu , Australia  
Qihong Wu, China  
Yuqiang Wu, China  
Zhibin Wu , China  
Zhizheng Wu , China  
Michalis Xenos , Greece  
Hao Xiao , China  
Xiao Ping Xie , China  
Qingzheng Xu , China  
Binghan Xue , China  
Yi Xue , China  
Joseph J. Yame , France  
Chuanliang Yan , China  
Xinggang Yan , United Kingdom  
Hongtai Yang , China  
Jixiang Yang , China  
Mijia Yang, USA  
Ray-Yeng Yang, Taiwan

Zaoli Yang , China  
Jun Ye , China  
Min Ye , China  
Luis J. Yebra , Spain  
Peng-Yeng Yin , Taiwan  
Muhammad Haroon Yousaf , Pakistan  
Yuan Yuan, United Kingdom  
Qin Yuming, China  
Elena Zaitseva , Slovakia  
Arkadiusz Zak , Poland  
Mohammad Zakwan , India  
Ernesto Zambrano-Serrano , Mexico  
Francesco Zammori , Italy  
Jessica Zangari , Italy  
Rafal Zdunek , Poland  
Ibrahim Zeid, USA  
Nianyin Zeng , China  
Junyong Zhai , China  
Hao Zhang , China  
Haopeng Zhang , USA  
Jian Zhang , China  
Kai Zhang, China  
Lingfan Zhang , China  
Mingjie Zhang , Norway  
Qian Zhang , China  
Tianwei Zhang , China  
Tongqian Zhang , China  
Wenyu Zhang , China  
Xianming Zhang , Australia  
Xuping Zhang , Denmark  
Yinyan Zhang, China  
Yifan Zhao , United Kingdom  
Debao Zhou, USA  
Heng Zhou , China  
Jian G. Zhou , United Kingdom  
Junyong Zhou , China  
Xueqian Zhou , United Kingdom  
Zhe Zhou , China  
Wu-Le Zhu, China  
Gaetano Zizzo , Italy  
Mingcheng Zuo, China

# Contents

## **Numerical Algorithms of the Discrete Coupled Algebraic Riccati Equation Arising in Optimal Control Systems**

Li Wang 



Research Article (8 pages), Article ID 1841582, Volume 2020 (2020)

## **Multirobot Collaborative Navigation Algorithms Based on Odometer/Vision Information Fusion**

Guohua Liu , Juan Guan, Haiying Liu, and Chenlin Wang




Research Article (16 pages), Article ID 5819409, Volume 2020 (2020)

## **Multiconsensus of Nonlinear Multiagent Systems with Intermittent Communication**

Jie Chen , Guang-Hui Xu , and Liang Geng



Research Article (8 pages), Article ID 1736706, Volume 2020 (2020)

## **An Efficient Nodes Failure Recovery Management Algorithm for Mobile Sensor Networks**

Rab Nawaz Jadoon , Adnan Anwar Awan, Muhammad Amir Khan , WuYang Zhou , and Aamir Shahzad

Research Article (14 pages), Article ID 1749467, Volume 2020 (2020)

## **Synchronization of Time Delay Coupled Neural Networks Based on Impulsive Control**

Jie Fang , Yin Zhang, Danying Xu, and Junwei Sun 

Research Article (8 pages), Article ID 5986018, Volume 2020 (2020)

## **Constant Frequency Control Strategy of Microgrids by Coordinating Energy Router and Energy Storage System**

Zheng Lan, Junzhang Wang , Jinhui Zeng , Dong He, Fan Xiao, and Fei Jiang

Research Article (8 pages), Article ID 4976529, Volume 2020 (2020)

## **Improving Fairness for Distributed Interactive Applications in Software-Defined Networks**

Ran Xu  and Weiqiang Zhang 

Research Article (10 pages), Article ID 5207105, Volume 2020 (2020)

## **Distributed Adaptive Output Consensus for High-Order Multiagent Systems with Input Saturation and Uncertain Nonlinear Dynamics**

Ming-Can Fan  and Wen Qin

Research Article (11 pages), Article ID 8098421, Volume 2020 (2020)

## **A Hybrid Event Trigger Mechanism and Time-Delay Partitioning Are Applied to Event-Driven Control Systems**

WanRu Wang , LianKun Sun, and BinBin Shen

Research Article (14 pages), Article ID 6724083, Volume 2020 (2020)

## **Decentralized Suboptimal State Feedback Integral Tracking Control Design for Coupled Linear Time-Varying Systems**

Mohamed Sadok Attia, Mohamed Karim Bouafoura , and Naceur Benhadj Braiek




Research Article (10 pages), Article ID 7519014, Volume 2020 (2020)

**A Model-Based Decoupling Method for Surge Speed and Heading Control in Vessel Path Following**

Xudong Wang, Jin Zhao , and Tao Geng


Research Article (11 pages), Article ID 4124027, Volume 2020 (2020)

**A New Method for Feature Extraction and Classification of Single-Stranded DNA Based on Collaborative Filter**

Bingyong Yan , Haixu Cui , Haitao Fu, Jiale Zhou, and Huifeng Wang 



Research Article (10 pages), Article ID 3876367, Volume 2020 (2020)

**A Time-Delay-Bounded Data Scheduling Algorithm for Delay Reduction in Distributed Networked Control Systems**

Zeming Fan, Xiaojun Yu , Hao Wan, Meilin Kang, Yuan Liu, Yuye He, and Gaoxi Xiao




Research Article (12 pages), Article ID 8290879, Volume 2020 (2020)

**Control of Multiple Viruses Interacting and Propagating in Multilayer Networks**

Xiao Tu , Guo-Ping Jiang , Yurong Song , and Xiaoling Wang

Research Article (14 pages), Article ID 9014353, Volume 2020 (2020)

**Sampled-Data-Based Adaptive Group Synchronization of Second-Order Nonlinear Complex Dynamical Networks with Time-Varying Delays**

Bo Liu , Jiahui Bai, Yue Zhao, Chao Liu , Xuemin Yan, and Hongtao Zhou 




Research Article (14 pages), Article ID 9819156, Volume 2020 (2020)

**Consensus Control of Nonlinear Multiagent Systems with Incremental Quadratic Constraints and Time Delays**

Dachao Wang , Fang Song , Wei Zhang , and Zhi Hu 



Research Article (11 pages), Article ID 6456190, Volume 2020 (2020)

**Epidemic Spreading Combined with Age and Region in Complex Networks**

Xu Zhang, Yurong Song , Haiyan Wang , and Guo-Ping Jiang 


Research Article (7 pages), Article ID 6753798, Volume 2020 (2020)

**Trajectory Planning and Tracking for Carrier Aircraft-Tractor System Based on Autonomous and Cooperative Movement**

Minghui Yu, Xue Gong , Guowei Fan, and Yu Zhang 




Research Article (24 pages), Article ID 6531984, Volume 2020 (2020)

**Distributed Optimal Control of Transient Stability for a Power Information Physical System**

Shiming Chen and Kaiqiang Li 

Research Article (11 pages), Article ID 1393216, Volume 2020 (2020)

**Multimotor Improved Relative Coupling Cooperative Control Based on Sliding-Mode Controller**

Changfan Zhang , Mingjie Xiao , and Jing He 


Research Article (10 pages), Article ID 5638462, Volume 2020 (2020)



# Contents

---

## **An Improved Iterative Method for Solving the Discrete Algebraic Riccati Equation**

Li Wang 





Research Article (6 pages), Article ID 3283157, Volume 2020 (2020)

## **Robust Fault Detection for Permanent-Magnet Synchronous Motor via Adaptive Sliding-Mode Observer**

Miaoying Zhang , Fan Xiao , Rui Shao , and Zhaojun Deng 

Research Article (6 pages), Article ID 9360939, Volume 2020 (2020)

## **On Zero Left Prime Factorizations for Matrices over Unique Factorization Domains**

Jinwang Liu , Tao Wu , Dongmei Li , and Jiancheng Guan 

Research Article (3 pages), Article ID 1684893, Volume 2020 (2020)

## **On Serre Reduction of Multidimensional Systems**

Dongmei Li , Jinwang Liu, and Licui Zheng 

Research Article (8 pages), Article ID 7435237, Volume 2020 (2020)

## **Improved Feature Learning: A Maximum-Average-Out Deep Neural Network for the Game Go**

Xiali Li , Zhengyu Lv , Bo Liu , Licheng Wu, and Zheng Wang

Research Article (6 pages), Article ID 1397948, Volume 2020 (2020)

## Research Article

# Numerical Algorithms of the Discrete Coupled Algebraic Riccati Equation Arising in Optimal Control Systems

Li Wang 

School of Mathematics and Computational Science, Hunan University of Science and Technology, Hunan 411201, China

Correspondence should be addressed to Li Wang; wanglileigh@163.com

Received 12 June 2020; Accepted 11 August 2020; Published 31 August 2020

Guest Editor: Hou-Sheng Su

Copyright © 2020 Li Wang. This is an open access article distributed under the Creative Commons Attribution License, which permits unrestricted use, distribution, and reproduction in any medium, provided the original work is properly cited.

The discrete coupled algebraic Riccati equation (DCARE) has wide applications in robust control, optimal control, and so on. In this paper, we present two iterative algorithms for solving the DCARE. The two iterative algorithms contain both the iterative solution in the last iterative step and the iterative solution in the current iterative step. And, for different initial value, the iterative sequences are increasing and bounded in one algorithm and decreasing and bounded in another. They are all monotonous and convergent. Numerical examples demonstrate the convergence effect of the presented algorithms.

## 1. Introduction and Preliminaries

The discrete coupled Riccati equation is usually encountered in optimal control and filter design problems in control theory [1–9], particularly in the jump-linear quadratic optimal control problem [10]. Consider the following jump-linear system:

$$\begin{cases} x_{k+1} = A(r_k)x_k + B(r_k)u_k, & 0 \leq k \leq N^+, \\ y_k = C(r_k)x_k, \end{cases} \quad (1)$$

with initial state  $x(0) = x_0$ ,  $r(0) = r_0$ , where  $x_k \in R^n$  is the plant state,  $u_k \in R^m$  is the control vector, and  $y_k \in R^q$  is the process output. Here,  $k$  is the time index,  $r_k$  is the form process taking values in the finite set  $S = \{1, 2, \dots, s\}$ , and  $r_k$  is a finite-state discrete-time Markov chain with transition probabilities.

$$\Pr\{r_{k+1} = j \mid r_k = i\} = \tilde{e}_{ij}, \quad 1 \leq i, j \leq s, \tilde{e}_{ii} > 0. \quad (2)$$

Minimizing the cost criterion of system (1) reduces to solving coupled algebraic Riccati-like equations. After some transformation, the coupled algebraic Riccati-like equations

turn the following discrete coupled algebraic Riccati equation (DCARE)

$$P_i = A_i^T F_i A_i - A_i^T F_i B_i (I + B_i^T F_i B_i)^{-1} B_i^T F_i A_i + Q_i, \quad (3)$$

where  $A_i \in R^{n \times n}$  is a constant matrix,  $B_i \in R^{n \times m}$ ,  $Q_i \in R^{n \times n}$  is a symmetric positive definite matrix,  $i \in S$ ,  $F_i = P_i + \sum_{j \neq i} e_{ij} P_j$  is the coupled term,  $e_{ij}$  are real non-negative constants defined as  $e_{ij} \equiv (\tilde{e}_{ij}/\tilde{e}_{ii})$  with the properties  $\tilde{e}_{ij} \in [0, 1]$ ,  $\tilde{e}_{ii} > 0$ , and  $\sum_{j \in S} \tilde{e}_{ij} = 1$ , and  $P_i \in R^{n \times n}$  denotes the symmetric positive definite solution of the DCARE. Applying Woodbury matrix equality

$$(A - BD^{-1}C)^{-1} = A^{-1} + A^{-1}B(D - CA^{-1}B)^{-1}CA^{-1}, \quad (4)$$

DCARE (3) turns to

$$P_i = A_i^T (F_i^{-1} + B_i B_i^T)^{-1} A_i + Q_i. \quad (5)$$

Because of the importance of Riccati equations in control theory and control engineering, a lot of research studies about Riccati equations have been devoted to this field, such

as solution bounds [11–15], trace and eigenvalue bounds [16–23], and the existence and uniqueness [24–26]. Besides these results, numerical solutions of Riccati equations are very important and have been studied by many scholars [27–34] because the numerical solutions of the Riccati equations are necessary in some practical engineering, such as finding the optimal state feedback controller in the optimal control system. Especially, for the DCARE, fixed point iterative algorithms are given in [24–26]. Stein iterations are presented in [35] which are based on the properties of a Stein equation. Among these results, we find less work has been done to discuss the numerical solution of the DCARE. Considering the importance and necessity of the numerical solutions of the DCARE, we propose two algorithms to discuss the numerical solution of the DCARE.

In this paper, we first propose an iterative algorithm with a parameter for solving the DCARE and prove its monotonically convergence. Second, we give an upper solution bound of the DCARE, by which another iterative algorithm is presented, and the proof of its monotonically convergence is given. For different initial values, the iterative sequences are increasing and bounded in one algorithm and decreasing and bounded in another. Last, numerical examples are given to illustrate the convergence effect of the two algorithms.

We first introduce some symbol conventions.  $R$  denotes the real number field.  $R^{n \times m}$  denotes the set of  $n \times m$  real matrices. For  $X = (x_{ij}) \in R^{n \times n}$ , let  $X^T$  and  $X^{-1}$  denote the transpose and inverse of the matrix  $X$ , respectively. The inequality  $X > (\geq) 0$  means  $X$  is a symmetric positive or semidefinite matrix, and the inequality  $X > (\geq) Y$  means  $X - Y$  is a symmetric positive (semi-) definite matrix. The

identity matrix with appropriate dimensions is represented by  $I$ .

**Lemma 1** (see [36]). *If  $A, B \in R^{n \times n}$  are symmetric positive definite matrices, then*

$$A \geq B, \quad \text{if and only if } B^{-1} \geq A^{-1}. \quad (6)$$

**Lemma 2** (see [22]). *Let matrices  $A, X, R, Y \in R^{n \times n}$  with  $X, Y > 0, R \geq 0$ , and  $X > (\geq) Y$ . Then,*

$$A^T(X^{-1} + R)^{-1}A > (\geq) A^T(Y^{-1} + R)^{-1}A, \quad (7)$$

with strict inequality if  $A$  is nonsingular, and  $X > Y$ .

## 2. Main Results

In [25, 26], the authors have derived several solution bounds by which iterative algorithms have been proposed, but there are many restrictions in these algorithms. In this part, we first present an iterative algorithm for DCARE (5) which do not have any restrictions.

*Algorithm 1*

Step 1: set  $P_i(0) = Q_i, F_i(0) = Q_i + \sum_{j \neq i} e_{ij} Q_j, 0 \leq \omega, i = 1, 2, \dots, s$ .

Step 2: compute

$$\begin{cases} P_i(k+1) = A_i^T [F_i^{-1}(k) + B_i B_i^T]^{-1} A_i + Q_i, \\ F_i(k+1) = P_i(k+1) + \sum_{j=1}^{i-1} e_{ij} [\omega P_j(k+1) + (1-\omega)P_j(k)] + \sum_{j=i+1}^s e_{ij} P_j(k+1), \quad k = 0, 1, 2, \dots \end{cases} \quad (8)$$

From Algorithm 1, we get an increasing and bounded iterative sequence, which is convergent to the positive definite solution of DCARE (5).

**Theorem 1.** *Let  $P_i(*)$  be the positive definite solution of DCARE (5) and  $Q_i > 0$ . The iterative sequences  $\{P_i(k)\}$  and  $\{F_i(k)\}$  are generated by the iterative (8) with  $0 \leq \omega \leq 1$ , and then*

$$\begin{aligned} P_i(0) \leq P_i(1) \leq P_i(2) \leq \dots, \quad \lim_{k \rightarrow \infty} P_i(k) = P_i(*), \\ F_i(0) \leq F_i(1) \leq F_i(2) \leq \dots, \quad F_i(k) \leq P_i(*) + \sum_{j \neq i} e_{ij} P_j(*). \end{aligned} \quad (9)$$

*Proof.* Since  $P_i(*)$  is positive definite solution of DCARE (5), then

$$P_i(*) = A_i^T \left\{ \left[ P_i(*) + \sum_{j \neq i} e_{ij} P_j(*) \right]^{-1} + B_i B_i^T \right\}^{-1} A_i + Q_i, \quad (10)$$

so  $P_i(*) \geq Q_i$ . Therefore,

$$\begin{aligned} P_i(1) &= A_i^T \{F_i^{-1}(0) + B_i B_i^T\}^{-1} A_i + Q_i \\ &= A_i^T \left\{ \left[ Q_i + \sum_{j \neq i} e_{ij} Q_j \right]^{-1} + B_i B_i^T \right\}^{-1} A_i + Q_i \\ &\leq A_i^T \left\{ \left[ P_i(*) + \sum_{j \neq i} e_{ij} P_j(*) \right]^{-1} + B_i B_i^T \right\}^{-1} A_i + Q_i = P_i(*), \end{aligned} \quad (11)$$

$$P_i(1) = A_i^T \{F_i^{-1}(0) + B_i B_i^T\}^{-1} A_i + Q_i \geq Q_i = P_i(0). \quad (12)$$

Since  $\omega - 1 \leq 0$  and (12), we get

$$\begin{aligned}
 F_i(0) &= Q_i + \sum_{j \neq i} e_{ij} Q_j = P_i(0) + \sum_{j=1}^{i-1} e_{ij} [\omega P_j(0) + (1 - \omega) P_j(0)] + \sum_{j=i+1}^s e_{ij} P_j(0) \\
 &\leq P_i(1) + \sum_{j=1}^{i-1} e_{ij} [\omega P_j(1) + (1 - \omega) P_j(0)] + \sum_{j=i+1}^s e_{ij} P_j(1) = F_i(1) \\
 &= P_i(1) + \sum_{j=1}^{i-1} e_{ij} [P_j(1) + (\omega - 1)(P_j(1) - P_j(0))] + \sum_{j=i+1}^s e_{ij} P_j(1) \\
 &\leq P_i(1) + \sum_{j=1}^{i-1} e_{ij} P_j(1) + \sum_{j=i+1}^s e_{ij} P_j(1) \leq P_i(*) + \sum_{j \neq i} e_{ij} P_j(*),
 \end{aligned} \tag{13}$$

that is,

$$\begin{aligned}
 F_i(0) \leq F_i(1) \leq P_i(*) + \sum_{j \neq i} e_{ij} P_j(*) & \tag{14} \\
 P_i(m-1) \leq P_i(m) \leq \dots \leq P_i(*) & \tag{15} \\
 F_i(m-1) \leq F_i(m) \leq P_i(*) + \sum_{j \neq i} e_{ij} P_j(*) & \tag{16}
 \end{aligned}$$

Suppose that

According to (16) and Lemma 2, we get

$$P_i(k+1) = A_i^T \{F_i^{-1}(k) + B_i B_i^T\}^{-1} A_i + Q_i \geq A_i^T \{F_i^{-1}(k-1) + B_i B_i^T\}^{-1} A_i + Q_i = P_i(k). \tag{17}$$

$$P_i(k+1) = A_i^T \{F_i^{-1}(k) + B_i B_i^T\}^{-1} A_i + Q_i \leq A_i^T \left\{ \left[ P_i(*) + \sum_{j \neq i} e_{ij} P_j(*) \right]^{-1} + B_i B_i^T \right\}^{-1} A_i + Q_i = P_i(*). \tag{18}$$

From (15), (17), (18), we get

$$\begin{aligned}
 F_i(k) &= P_i(k) + \sum_{j=1}^{i-1} e_{ij} [\omega P_j(k) + (1 - \omega) P_j(k-1)] + \sum_{j=i+1}^s e_{ij} P_j(k) \leq P_i(k+1) + \sum_{j=1}^{i-1} e_{ij} [\omega P_j(k+1) + (1 - \omega) P_j(k)] \\
 &+ \sum_{j=i+1}^s e_{ij} P_j(k+1) = F_i(k+1) \\
 &= P_i(k+1) + \sum_{j=1}^{i-1} e_{ij} [P_j(k+1) + (\omega - 1)(P_j(k+1) - P_j(k))] + \sum_{j=i+1}^s e_{ij} P_j(k+1) \leq P_i(k+1) + \sum_{j=1}^{i-1} e_{ij} P_j(k+1) \\
 &+ \sum_{j=i+1}^s e_{ij} P_j(k+1) \leq P_i(*) + \sum_{j \neq i} e_{ij} P_j(*).
 \end{aligned} \tag{19}$$

Thus, the proof of induction is completed. Because  $P_i(k)$  and  $F_i(k)$  are monotonically increasing and they are

bounded, then  $\lim_{k \rightarrow \infty} P_i(k)$  and  $\lim_{k \rightarrow \infty} F_i(k)$  exist. As  $k \rightarrow \infty$ , Algorithm 1 gives

$$\begin{aligned} P_i(\infty) &= A_i^T [F_i^{-1}(\infty) + B_i B_i^T]^{-1} A_i + Q_i \\ &= A_i^T \left\{ \left[ P_i(\infty) + \sum_{j=1}^{i-1} e_{ij} [\omega P_j(\infty) + (1-\omega)P_j(\infty)] + \sum_{j=i+1}^s e_{ij} P_j(\infty) \right]^{-1} + B_i B_i^T \right\}^{-1} A_i + Q_i \\ &= A_i^T \left\{ \left[ P_i(\infty) + \sum_{j \neq i} e_{ij} P_j(\infty) \right]^{-1} + B_i B_i^T \right\}^{-1} A_i + Q_i. \end{aligned} \quad (20)$$

Thus,  $\lim_{k \rightarrow \infty} P_i(k) = P_i(*)$ .  $\square$

**Theorem 2.** Let  $P_i$  be the positive definite solution of DCARE (5), then

$$P_i \leq A_i^T (B_i B_i^T)^{-1} A_i + Q_i. \quad (21)$$

*Proof.* If  $G > P_i + \sum_{j \neq i} e_{ij} P_j$ , then by Lemma 1, we get

$$\begin{aligned} P_i &= A_i^T \left\{ \left[ P_i + \sum_{j \neq i} e_{ij} P_j \right]^{-1} + B_i B_i^T \right\}^{-1} A_i + Q_i \\ &\leq A_i^T \{ G^{-1} + B_i B_i^T \}^{-1} A_i + Q_i. \end{aligned} \quad (22)$$

When  $\lambda_1(G) = \infty$ ,  $G^{-1} = \text{null matrix}$ ; therefore, (22) changes to (21) in this case.

We can choose (21) as starting value and get the following algorithm.  $\square$

*Algorithm 2*

Step 1: set  $P_i(0) = A_i^T (B_i B_i^T)^{-1} A_i + Q_i$ ,  $F_i(0) = P_i(0) + \sum_{j \neq i} e_{ij} P_j(0)$ ,  $0 \leq \omega$ ,  $i = 1, 2, \dots, s$ .

Step 2: compute

$$\begin{cases} P_i(k+1) = A_i^T [F_i^{-1}(k) + B_i B_i^T]^{-1} A_i + Q_i, \\ F_i(k+1) = P_i(k+1) + \sum_{j=1}^{i-1} e_{ij} [\omega P_j(k+1) + (1-\omega)P_j(k)] + \sum_{j=i+1}^s e_{ij} P_j(k+1), \quad k = 0, 1, 2, \dots \end{cases} \quad (23)$$

From Algorithm 2, we get a decreasing and bounded iterative sequences, which is convergent to the positive definite solution of DCARE (5).

**Theorem 3.** Let  $P_i(*)$  be the positive definite solution of DCARE (5) and  $Q_i > 0$ . The iterative sequences  $\{P_i(k)\}$  and  $\{F_i(k)\}$  are generated by iterative (23) with  $0 \leq \omega \leq 1$ , and then

$$P_i(0) \geq P_i(1) \geq P_i(2) \geq \dots, \quad \lim_{k \rightarrow \infty} P_i(k) = P_i(*),$$

$$F_i(0) \geq F_i(1) \geq F_i(2) \geq \dots, \quad F_i(k) \geq P_i(*) + \sum_{j \neq i} e_{ij} P_j(*).$$

(24)

*Proof.* According to (21) and (23), we have

$$\begin{aligned} P_i(1) &= A_i^T \{ F_i^{-1}(0) + B_i B_i^T \}^{-1} A_i + Q_i = A_i^T \left\{ \left[ A_i^T (B_i B_i^T)^{-1} A_i + Q_i + \sum_{j \neq i} e_{ij} (A_j^T (B_j B_j^T)^{-1} A_j + Q_j) \right]^{-1} + B_i B_i^T \right\}^{-1} A_i + Q_i \\ &\geq A_i^T \left\{ \left[ P_i(*) + \sum_{j \neq i} e_{ij} P_j(*) \right]^{-1} + B_i B_i^T \right\}^{-1} A_i + Q_i = P_i(*), \end{aligned} \quad (25)$$

$$P_i(1) = A_i^T \{ F_i^{-1}(0) + B_i B_i^T \}^{-1} A_i + Q_i \leq A_i^T (B_i B_i^T)^{-1} A_i + Q_i = P_i(0). \quad (26)$$

Since  $\omega - 1 \leq 0$ , with (25) and (26) we get

$$\begin{aligned}
 F_i(0) &= Q_i + \sum_{j \neq i} e_{ij} Q_j = P_i(0) + \sum_{j=1}^{i-1} e_{ij} [\omega P_j(0) + (1 - \omega) P_j(0)] \\
 &+ \sum_{j=i+1}^s e_{ij} P_j(0) \geq P_i(1) + \sum_{j=1}^{i-1} e_{ij} [\omega P_j(1) + (1 - \omega) P_j(0)] \\
 &+ \sum_{j=i+1}^s e_{ij} P_j(1) = F_i(1) \\
 &= P_i(1) + \sum_{j=1}^{i-1} e_{ij} [P_j(1) + (1 - \omega)(P_j(0) - P_j(1))] \\
 &+ \sum_{j=i+1}^s e_{ij} P_j(1) \geq P_i(1) + \sum_{j=1}^{i-1} e_{ij} P_j(1) \\
 &+ \sum_{j=i+1}^s e_{ij} P_j(1) \geq P_i(*) + \sum_{j \neq i} e_{ij} P_j(*),
 \end{aligned} \tag{27}$$

that is,

$$F_i(0) \geq F_i(1) \geq P_i(*) + \sum_{j \neq i} e_{ij} P_j(*) \tag{28}$$

Suppose that

---


$$\begin{aligned}
 F_i(k) &= P_i(k) + \sum_{j=1}^{i-1} e_{ij} [\omega P_j(k) + (1 - \omega) P_j(k - 1)] + \sum_{j=i+1}^s e_{ij} P_j(k) \geq P_i(k + 1) + \sum_{j=1}^{i-1} e_{ij} [\omega P_j(k + 1) + (1 - \omega) P_j(k)] \\
 &+ \sum_{j=i+1}^s e_{ij} P_j(k + 1) = F_i(k + 1) \\
 &= P_i(k + 1) + \sum_{j=1}^{i-1} e_{ij} [P_j(k + 1) + (1 - \omega)(P_j(k) - P_j(k + 1))] + \sum_{j=i+1}^s e_{ij} P_j(k + 1) \geq P_i(k + 1) + \sum_{j=1}^{i-1} e_{ij} P_j(k + 1) \\
 &+ \sum_{j=i+1}^s e_{ij} P_j(k + 1) \geq P_i(*) + \sum_{j \neq i} e_{ij} P_j(*).
 \end{aligned} \tag{33}$$

Thus, the proof of induction is completed. Because  $P_i(k)$  and  $F_i(k)$  are monotonically decreasing and they are bounded, then  $\lim_{k \rightarrow \infty} P_i(k)$  and  $\lim_{k \rightarrow \infty} F_i(k)$  exist. In a similar way as the proof of (20), as  $k \rightarrow \infty$ , Algorithm 2 gives  $\lim_{k \rightarrow \infty} P_i(k) = P_i(*)$ .  $\square$

*Remark 1.* In Algorithm 2, if  $B_i B_i^T$  is singular, we can choose a suitable  $G$  so that  $(G^{-1} + B_i B_i^T)^{-1}$  is nonsingular, as in Theorem 2.

*Remark 2.* In Algorithm 1, the sequence  $P_i(k)$  in (8) with the initial value  $P_i(0) = Q_i$  converges monotonically to a positive definite solution of DCARE (5), and so does the sequence  $P_i(k)$  in (23) with the initial value  $P_i(0) = A_i^T (B_i B_i^T)^{-1} A_i + Q_i$ . But the two positive definite solutions may be different. Whether the positive definite solution of DCARE (5) is unique or not, a problem needs to be discussed further.

$$P_i(m - 1) \geq P_i(m) \geq \dots \geq P_i(*), \tag{29}$$

$$F_i(m - 1) \geq F_i(m) \geq P_i(*) + \sum_{j \neq i} e_{ij} P_j(*), \quad m \leq k, k \geq 1. \tag{30}$$

According to (30) and Lemma 2, we get

$$\begin{aligned}
 P_i(k + 1) &= A_i^T \{F_i^{-1}(k) + B_i B_i^T\}^{-1} A_i + Q_i \\
 &\leq A_i^T \{F_i^{-1}(k - 1) + B_i B_i^T\}^{-1} A_i + Q_i = P_i(k),
 \end{aligned} \tag{31}$$

$$\begin{aligned}
 P_i(k + 1) &= A_i^T \{F_i^{-1}(k) + B_i B_i^T\}^{-1} A_i + Q_i \\
 &\geq A_i^T \left\{ \left[ P_i(*) + \sum_{j \neq i} e_{ij} P_j(*) \right]^{-1} + B_i B_i^T \right\}^{-1} \\
 &\cdot A_i + Q_i = P_i(*).
 \end{aligned} \tag{32}$$

From (29), (31), (32), we get

---

*Remark 3.* When  $e_{ij} = 0 (j \neq i)$ , DCARE (5) changes to the discrete algebraic Riccati equation. And iterative sequences (8) and (23), respectively, in Algorithm 1 and Algorithm 2, become the iterative (17) and iterative (28) in [22], which means that the algorithms of the DCARE in this paper are generalizations of the discrete algebraic Riccati equation. Moreover, when  $\omega = 1$ , the iterative (8) and (23) are extensions on the discrete coupled algebraic Riccati equation of the work of [22].

*Remark 4.* In this paper, we only prove Algorithms 1 and 2 are convergent under the condition  $0 \leq \omega \leq 1$ , but we can run the two algorithms with  $\omega > 1$  in practical computation. And, we have faster convergence speed if appropriate parameters are selected. We will illustrate it in the following examples.

### 3. Numerical Examples

In this section, the following numerical examples are presented to show the effectiveness of our results.

*Example 1* (see [26]). Consider DCARE (5) with

$$\begin{aligned}
 A_1 &= \begin{pmatrix} 0.25 & 0.15 \\ 0.25 & -0.1 \end{pmatrix}, \\
 A_2 &= \begin{pmatrix} -0.1 & 0.2 \\ 0.1 & -0.2 \end{pmatrix}, \\
 B_1 &= \begin{pmatrix} 0 \\ 1 \end{pmatrix}, \\
 B_2 &= \begin{pmatrix} 1 \\ 0 \end{pmatrix}, \\
 Q_1 &= \begin{pmatrix} 50 & -30 \\ -30 & 40 \end{pmatrix}, \\
 Q_2 &= \begin{pmatrix} 60 & -20 \\ -20 & 70 \end{pmatrix}, \\
 (\tilde{e}_{ij})_{i,j \in S} &= \begin{pmatrix} 0.6 & 0.4 \\ 0.2 & 0.8 \end{pmatrix}, \\
 S &= \{1, 2\}.
 \end{aligned} \tag{34}$$

Since there are two equations in the DCARE, the superiority of the  $\omega$  in Algorithm 1 is not obvious. So, we choose  $\omega = 1$  here. After 9 steps of iteration of (8), we obtain the solution  $P_i$  of DCARE (5).

$$\begin{aligned}
 P_1(9) &= \begin{pmatrix} 54.782858819173867 & -27.163728424128180 \\ -27.163728424128180 & 41.743512895466367 \end{pmatrix}, \\
 P_2(9) &= \begin{pmatrix} 60.745519196489681 & -21.491038392979359 \\ -21.491038392979359 & 72.982076785958711 \end{pmatrix},
 \end{aligned} \tag{35}$$

and the residual  $\|A_i^T \{ [P_i(9) + \sum_{j \neq i} e_{ij} P_j(9)]^{-1} + B_i B_i^T \}^{-1} A_i + Q_i - P_i(9)\|$  is  $8.246736626915663e - 009$ .

However, it needs 47 steps of iteration for the algorithm in [26] to get the iteration solution of DCARE (5).

*Example 2.* Consider DCARE (5) with

$$\begin{aligned}
 A_1 &= \begin{pmatrix} 0.8 & 0.07 \\ -0.13 & 2.1 \end{pmatrix}, \\
 A_2 &= \begin{pmatrix} 1.63 & 0.12 \\ -0.18 & 1.06 \end{pmatrix}, \\
 A_3 &= \begin{pmatrix} 0.65 & 0.13 \\ 0.14 & -1.08 \end{pmatrix}, \\
 Q_1 &= \begin{pmatrix} 40 & -2.5 \\ -2.5 & 1.1 \end{pmatrix}, \\
 Q_2 &= \begin{pmatrix} 6 & -1.5 \\ -1.5 & 0.4 \end{pmatrix}, \\
 Q_3 &= \begin{pmatrix} 0.48 & -1.4 \\ -1.4 & 48 \end{pmatrix},
 \end{aligned}$$

$$\begin{aligned}
 B_1 &= \begin{pmatrix} 0 \\ 1 \end{pmatrix}, \\
 B_2 &= \begin{pmatrix} 0 \\ 2 \end{pmatrix}, \\
 B_3 &= \begin{pmatrix} 0 \\ 3 \end{pmatrix}, \\
 (\tilde{e}_{ij})_{i,j \in S} &= \begin{pmatrix} 0.67 & 0.17 & 0.16 \\ 0.3 & 0.47 & 0.23 \\ 0.26 & 0.1 & 0.64 \end{pmatrix}, \\
 S &= \{1, 2, 3\}.
 \end{aligned} \tag{36}$$

Because the restrictions of the algorithms in [25, 26] are not met for this case, the algorithms in [25, 26] cannot work.

For Algorithm 1, the steps of iteration and the residual are presented in Table 1 with different parameter  $\omega$ . Although we only prove the convergence of Algorithm 1 with  $0 \leq \omega \leq 1$ , from Table 1, we find the convergence rapid is the fastest when  $\omega$  is 1.8. After 31 steps of iteration of (8) with  $\omega = 1.8$ , we obtain the solution  $P_i$  of DCARE (5).

$$\begin{aligned}
 P_1(31) &= \begin{pmatrix} 1103.165003916018 & 101.279835324595 \\ 101.279835324595 & 15.487684241437 \end{pmatrix}, \\
 P_2(31) &= \begin{pmatrix} 9664.052810636161 & 713.129010075344 \\ 713.129010075344 & 53.563508057380 \end{pmatrix}, \\
 P_3(31) &= \begin{pmatrix} 7325.056498352728 & 1445.922335403706 \\ 1445.922335403706 & 773.201080130236 \end{pmatrix},
 \end{aligned} \tag{37}$$

and the residual  $\|A_i^T \{ [P_i(31) + \sum_{j \neq i} e_{ij} P_j(31)]^{-1} + B_i B_i^T \}^{-1} A_i + Q_i - P_i(31)\|$  is  $8.307893040182535e - 009$ .

*Example 3* (see [26]). Consider the DCARE (5) with

$$\begin{aligned}
 A_1 &= \begin{pmatrix} 0 & 0.07 \\ -0.13 & 0.1 \end{pmatrix}, \\
 A_2 &= \begin{pmatrix} 0.03 & 0.12 \\ -0.18 & 0.06 \end{pmatrix}, \\
 A_3 &= \begin{pmatrix} 0.05 & 0.13 \\ 0.14 & -0.08 \end{pmatrix},
 \end{aligned} \tag{38}$$

$Q_1, Q_2, Q_3, B_1, B_2, B_3, (\tilde{e}_{ij})_{i,j \in S}$  and  $S$  are the same as Example 2.

For Algorithm 2, since  $B_i B_i^T$  is singular, by choosing  $G = I$ , then Algorithm 2 can work now. After 4 steps of iteration of (23) with  $\omega = 1$ , we obtain the solution  $P_i$  of DCARE (5):

TABLE 1: Numerical results.

$\omega$	Iterations	Residual	$\omega$	Iterations	Residual
0	46	$9.0841e-009$	1.8	31	$8.3079e-009$
0.4	44	$8.3616e-009$	2	32	$8.0616e-009$
0.8	42	$6.2660e-009$	4	41	$5.6463e-009$
1	41	$4.7366e-009$	6	49	$9.3612e-009$
1.4	37	$8.0066e-009$	8	58	$6.7581e-009$

$$\begin{aligned}
 P_1(4) &= \begin{pmatrix} 40.015697705014347 & -2.510023450561822 \\ -2.510023450561822 & 1.306818585337136 \end{pmatrix}, \\
 P_2(4) &= \begin{pmatrix} 6.030297717859115 & -1.387771050220626 \\ -1.387771050220626 & 0.850999482654777 \end{pmatrix}, \\
 P_3(4) &= \begin{pmatrix} 6.030297717859115 & -1.387771050220626 \\ -1.387771050220626 & 0.850999482654777 \end{pmatrix},
 \end{aligned} \tag{39}$$

and the residual  $\|A_i^T \{ [P_i(4) + \sum_{j \neq i} e_{ij} P_j(4)]^{-1} + B_i B_i^T \}^{-1} A_i + Q_i - P_i(4)\|$  is  $9.070366679964081e-011$ .

However, it needs 18 steps of iteration for the algorithm in [26] to get the iteration solution of DCARE (5).

## Data Availability

All data generated or analyzed during this study are included in this article.

## Conflicts of Interest

The authors declare that they have no conflicts of interest.

## Acknowledgments

The work was supported in part by the National Natural Science Foundation for Youths of China (11801164), National Natural Science Foundation of China (11971413), the Key Project of National Natural Science Foundation of China (91430213), the General Project of Hunan Provincial Natural Science Foundation of China (2015JJ2134), and the General Project of Hunan Provincial Education Department of China (15C1320).

## References

- [1] H. Abou-Kandil, G. Freiling, and G. Jank, "On the solution of discrete-time markovian jump linear quadratic control problems," *Automatica*, vol. 31, no. 5, pp. 765–768, 1995.
- [2] C. Xu, Y. Zhao, B. Qin, and H. Zhang, "Adaptive synchronization of coupled harmonic oscillators under switching topology," *Journal of the Franklin Institute*, vol. 356, no. 2, pp. 1067–1087, 2019.
- [3] H. Kwakernaak and R. Sivan, *Linear Optimal Control Systems*, Wiley, Hoboken, NJ, USA, 1972.
- [4] H. Su, H. Wu, X. Chen et al., "Positive edge consensus of complex networks," *IEEE Transactions on Systems Man & Cybernetics Systems*, vol. 48, no. 12, pp. 1–9, 2017.
- [5] C. Xu, H. Xu, H. Su, and C. Liu, "Disturbance-observer based consensus of linear multi-agent systems with exogenous disturbance under intermittent communication," *Neuro-computing*, vol. 404, pp. 26–33, 2020.
- [6] H. Su, J. Zhang, and X. Chen, "A stochastic sampling mechanism for time-varying formation of multiagent systems with multiple leaders and communication delays," *IEEE Transactions on Neural Networks and Learning Systems*, vol. 30, no. 12, pp. 3699–3707, 2019.
- [7] Q. Liu, X. Li, and Y. Yan, "Large time behavior of solutions for a class of time-dependent hamilton-jacobi equations," *Science China Mathematics*, vol. 59, no. 5, pp. 875–890, 2016.
- [8] Q. Liu, X. Li, and D. Qian, "An abstract theorem on the existence of periodic motions of non-autonomous lagrange systems," *Journal of Differential Equations*, vol. 261, no. 10, pp. 5784–5802, 2016.
- [9] M. A. Rami and L. E. Ghaoui, "LMI optimization for non-standard riccati equations arising in stochastic control," *IEEE Transactions on Automatic Control*, vol. 41, no. 11, pp. 1666–1671, 1996.
- [10] H. Abou-Kandil, G. Freiling, and G. Jank, "Solution and asymptotic behavior of coupled riccati equations in jump linear systems," *IEEE Transactions on Automatic Control*, vol. 39, no. 8, pp. 1631–1636, 1994.
- [11] R. Davies, P. Shi, and R. Wiltshire, "New upper solution bounds of the discrete algebraic riccati matrix equation," *Journal of Computational and Applied Mathematics*, vol. 213, no. 2, pp. 307–315, 2008a.
- [12] R. Davies, P. Shi, and R. Wiltshire, "Upper solution bounds of the continuous and discrete coupled algebraic riccati equations," *Automatica*, vol. 44, no. 4, pp. 1088–1096, 2008.
- [13] C.-H. Lee, "Matrix bounds of the solutions of the continuous and discrete riccati equations—a unified approach," *International Journal of Control*, vol. 76, no. 6, pp. 635–642, 2003.
- [14] Q. Liu, C. Wang, and Z. Wang, "On littlewood's boundedness problem for relativistic oscillators with anharmonic potentials," *Journal of Differential Equations*, vol. 257, no. 12, pp. 4542–4571, 2014.
- [15] H. H. Choi, "Upper matrix bounds for the discrete algebraic riccati matrix equation," *IEEE Transactions on Automatic Control*, vol. 46, no. 3, pp. 504–508, 2001.
- [16] J. Liu, J. Zhang, and Y. Liu, "Trace inequalities for matrix products and trace bounds for the solution of the algebraic riccati equations," *Journal of Inequalities & Applications*, vol. 2009, no. 1, pp. 171–174, 2009.
- [17] R. Huang and D. Chu, "Relative perturbation analysis for eigenvalues and singular values of totally nonpositive matrices," *Siam Journal on Matrix Analysis & Applications*, vol. 36, no. 2, pp. 476–495, 2015.
- [18] J. Liu and J. Zhang, "New upper and lower eigenvalue bounds for the solution of the continuous algebraic riccati equation," *Asian Journal of Control*, vol. 16, no. 1, pp. 284–291, 2014.
- [19] R. Huang, "A Periodic qd-Type Reduction for Computing Eigenvalues of Structured Matrix Products to High Relative Accuracy," *Journal of Scientific Computing*, vol. 75, no. 3, pp. 1229–1261, 2018.
- [20] J. Zhang, J. Liu, and Y. Zha, "The improved eigenvalue bounds for the solution of the discrete algebraic riccati equation," *IMA Journal of Mathematical Control and Information*, vol. 34, no. 3, pp. 851–870, 2016.
- [21] H. Dai and Z. Z. Bai, "On eigenvalue bounds and iteration methods for discrete algebraic riccati equations," *Journal of Computational Mathematics*, vol. 29, no. 3, pp. 341–366, 2011.
- [22] N. Komaroff, "Iterative matrix bounds and computational solutions to the discrete algebraic riccati equation," *IEEE*



- Transactions on Automatic Control*, vol. 39, no. 8, pp. 1676–1678, 1994.
- [23] J. Liu and L. Wang, “New solution bounds of the continuous algebraic riccati equation and their applications in redundant control input systems,” *Science China Information Sciences*, vol. 62, no. 10, pp. 69–85, 2019.
  - [24] J. Liu and J. Zhang, “The existence uniqueness and the fixed iterative algorithm of the solution for the discrete coupled algebraic riccati equation,” *International Journal of Control*, vol. 84, no. 8, pp. 1430–1441, 2011.
  - [25] J. Liu, L. Wang, and J. Zhang, “The solution bounds and fixed point iterative algorithm for the discrete coupled algebraic riccati equation applied to automatic control,” *IMA Journal of Mathematical Control and Information*, vol. 34, no. 4, pp. 1135–1156, 2016.
  - [26] J. Liu, L. Wang, and J. Zhang, “New matrix bounds and iterative algorithms for the discrete coupled algebraic riccati equation,” *International Journal of Control*, vol. 90, no. 11, pp. 2326–2337, 2017.
  - [27] A. Wu, Y. Zhang, and T. Jiang, “Iterative algorithms for discrete periodic riccati matrix equations,” *International Journal of Systems Science*, vol. 1, 2019.
  - [28] R. Huang, “A qd-type algorithm for computing the generalized singular values of BF matrices with sign regularity to high relative accuracy,” *Mathematics of Computation*, vol. 89, pp. 229–252, 2020.
  - [29] J. Guan, “Modified alternately linearized implicit iteration method for m-matrix algebraic riccati equations,” *Applied Mathematics and Computation*, vol. 347, pp. 442–448, 2019.
  - [30] R. Huang and D. Chu, “Computing singular value decompositions of parameterized matrices with total nonpositivity to high relative accuracy,” *Journal of Scientific Computing*, vol. 71, no. 2, pp. 682–711, 2017.
  - [31] R. Huang, J. Liu, and L. Zhu, “Accurate solutions of diagonally dominant tridiagonal linear systems,” *BIT Numerical Mathematics*, vol. 54, no. 3, pp. 711–727, 2014.
  - [32] R. Huang, “Factoring symmetric totally nonpositive matrices and inverses with a diagonal pivoting method,” *BIT Numerical Mathematics*, vol. 53, pp. 433–458, 2013.
  - [33] W.-W. Lin and S.-F. Xu, “Convergence analysis of structure-preserving doubling algorithms for riccati-type matrix equations,” *SIAM Journal on Matrix Analysis and Applications*, vol. 28, no. 1, pp. 26–39, 2006.
  - [34] T.-M. Hwang, E. K.-W. Chu, and W.-W. Lin, “A generalized structure-preserving doubling algorithm for generalized discrete-time algebraic riccati equations,” *International Journal of Control*, vol. 78, no. 14, pp. 1063–1075, 2005.
  - [35] I. G. Ivanov, “A method to solve the discrete-time coupled algebraic riccati equations,” *Applied Mathematics and Computation*, vol. 206, no. 1, pp. 34–41, 2008.
  - [36] R. A. Horn and C. R. Johnson, *Matrix Analysis*, Cambridge University Press, Cambridge, UK, 2012.

## Research Article

# Multirobot Collaborative Navigation Algorithms Based on Odometer/Vision Information Fusion

Guohua Liu <sup>1</sup>, Juan Guan,<sup>1</sup> Haiying Liu,<sup>2</sup> and Chenlin Wang<sup>3</sup>

<sup>1</sup>School of Mathematics, Southeast University, Nanjing 210096, China

<sup>2</sup>College of Astronautics, Nanjing University of Aeronautics and Astronautics, Nanjing 210016, China

<sup>3</sup>China COMAC Shanghai Aircraft Design and Research Institute, Shanghai 201210, China

Correspondence should be addressed to Guohua Liu; liuguohua@seu.edu.cn

Received 24 May 2020; Revised 15 June 2020; Accepted 11 July 2020; Published 27 August 2020

Guest Editor: Xiao Ling Wang

Copyright © 2020 Guohua Liu et al. This is an open access article distributed under the Creative Commons Attribution License, which permits unrestricted use, distribution, and reproduction in any medium, provided the original work is properly cited.

Collaborative navigation is the key technology for multimobile robot system. In order to improve the performance of collaborative navigation system, the collaborative navigation algorithms based on odometer/vision multisource information fusion are presented in this paper. Firstly, the multisource information fusion collaborative navigation system model is established, including mobile robot model, odometry measurement model, lidar relative measurement model, UWB relative measurement model, and the SLAM model based on lidar measurement. Secondly, the frameworks of centralized and decentralized collaborative navigation based on odometer/vision fusion are given, and the SLAM algorithms based on vision are presented. Then, the centralized and decentralized odometer/vision collaborative navigation algorithms are derived, including the time update, single node measurement update, relative measurement update between nodes, and covariance cross filtering algorithm. Finally, different simulation experiments are designed to verify the effectiveness of the algorithms. Two kinds of multirobot collaborative navigation experimental scenes, which are relative measurement aided odometer and odometer/SLAM fusion, are designed, respectively. The advantages and disadvantages of centralized versus decentralized collaborative navigation algorithms in different experimental scenes are analyzed.

## 1. Introduction

With the development of the age of intelligence, the application scenarios and task requirements of intelligent mobile robots are becoming more and more complex [1, 2]. A single robot has difficulty in meeting the needs of humans for highly automated robots. Therefore, the multirobot system, which fully embodies the group wisdom, has a broad prospect. The subject has attracted extensive attention of researchers [3–5]. The premise of robot collaborative navigation operation is that each robot needs to have a certain ability of navigation and localization. Therefore, it is very important for the research of robot collaborative navigation system [6].

The navigation accuracy of a single robot depends on its own navigation system, independent of other motion bodies.

This navigation method is relatively simple, but due to the computing power of its own processor, sensor quality, and sensor field of vision and other factors, it limits the working range of the navigation system to a certain extent in the process of navigation and positioning. It also affects the ability of the navigation system to suppress noise, reducing errors and adapting to the complex environment. The collaborative navigation system of robot can make up for the single robot navigation system. When there is relative measurement between each robot, the relative information can be fully used to correct the navigation results. It is also possible to establish links with each other to realize the sharing of navigation resources among robots and to obtain better navigation performance [7–9].

In the research of mobile robot navigation and location technology, the development of Simultaneous Localization

and Mapping (SLAM) technology provides a new thought for autonomous positioning of mobile robot under complex scenes [10]. At the same time, as a significant technical means to realize relative navigation, radio navigation and visual navigation are being paid much attention. It provides important technical support for further research on the collaborative navigation of multirobots [11–13]. However, the traditional combined navigation technology is far from meeting the growing demand for the high performance of collaborative navigation.

At present, most of the data fusion methods of multi-source heterogeneous sensors in integrated navigation system use centralized data fusion algorithm. This algorithm has some defects in collaborative navigation of mobile robots, high communication cost, and poor robustness. However, the current research on decentralized data fusion algorithm, which is suitable for collaborative navigation environment is not mature enough [14, 15].

Therefore, based on the information fusion of multi-source heterogeneous sensors and related SLAM data association algorithms, this paper puts forward a new concept, model, and solution of multisource heterogeneous sensor information fusion, which can significantly improve the performance of collaborative navigation, address some problems of cooperative navigation technology, explore the key technologies that need to be solved in the collaborative navigation process of multirobot platform, and provide theoretical basis and technical support for high performance of collaborative navigation application.

The structure of this paper is outlined as follows: in Section 2, in the multisource information fusion collaborative navigation system model, the principle of the module involved, and the source of error are analyzed. In Section 3, the framework of centralized and decentralized collaborative navigation framework based on odometer/vision red fusion is given, and the SLAM algorithms based on vision are presented. In Sections 4 and 5, the centralized and decentralized odometer/vision collaborative navigation algorithms are derived, respectively. In Section 6, different simulation experiments are designed to verify the effectiveness of the algorithms.

## 2. Multisource Information Fusion Collaborative Navigation System Model

**2.1. Motion Robot Model.** Suppose that the mobile robot moves according to the circular arc trajectory. Figure 1 shows the motion of a single mobile robot (see Figure 1).

**2.1.1. Odometry Measurement Model.** According to the principle of odometer motion calculation [16], it is assumed that the starting position of the mobile robot is  $(x, y, \theta)$ , after  $\Delta T$  of movement to the end. The end position is  $(x + \Delta x, y + \Delta y, \theta + \Delta\theta)$ , and the trajectory can be regarded as a circular arc  $\Delta S$  with radius  $R$ . In this case, the pose of the robot (in discrete time) is given by

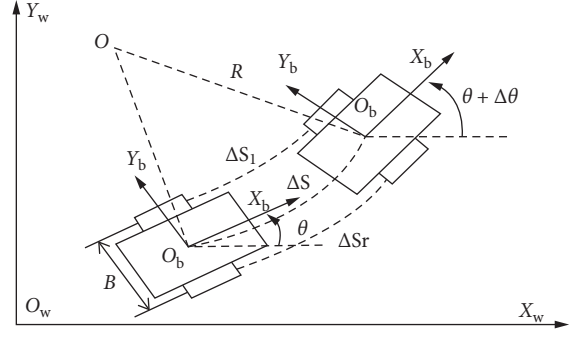


FIGURE 1: Motion model of a single mobile robot.

$$\begin{cases} \Delta S_l = \pi D \cdot \frac{\Delta N_L}{P} = \left(R - \frac{B}{2}\right) \Delta\theta, \\ \Delta S_r = \pi D \cdot \frac{\Delta N_R}{P} = \left(R + \frac{B}{2}\right) \Delta\theta, \end{cases} \quad (1)$$

where  $\Delta N_L, \Delta N_R$  are increment of pulse number of odometer left and right wheel encoder.  $(\Delta S_r, \Delta S_l)$  is the distance between the right wheel and the left wheel of a mobile robot.  $P$  are the resolution parameters of left and right wheel encoder. The pose increment of sampling period  $\Delta T$  is obtained by solving the above equations. The discrete motion equation of the mobile robot is further obtained by

$$\begin{cases} x_k \approx x_{k-1} + \Delta S_{k-1} \cos\left(\frac{\theta_{k-1} + \Delta\theta_{k-1}}{2}\right), \\ y_k \approx y_{k-1} + \Delta S_{k-1} \sin\left(\frac{\theta_{k-1} + \Delta\theta_{k-1}}{2}\right), \\ \theta_k = \theta_{k-1} + \Delta\theta_{k-1}. \end{cases} \quad (2)$$

**2.1.2. Odometer Error Model.** There are systematic errors and random errors in odometer based positioning [17]. In the simulation experiment, the influence of random error is mainly considered. The corresponding covariance matrix  $\Sigma_{\text{odom}}$  is given by

$$\Sigma_{\text{odom}} = \begin{bmatrix} k_r |\Delta S_r| & 0 \\ 0 & k_l |\Delta S_l| \end{bmatrix}. \quad (3)$$

**2.2. Lidar Environmental Detection Model.** As the main module to realize the SLAM, environment detection module mainly obtains the surrounding environment information through the external sensing sensor.

**2.2.1. Lidar Scanning Model.** The two-dimensional lidar outputs the point cloud data from the surrounding environment and contains the angular information. The scanning schematic of the two-dimensional lidar is shown in Figure 2 (see Figure 2).

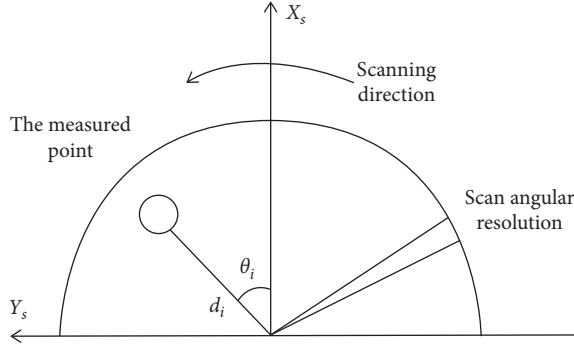


FIGURE 2: The scanning schematic diagram of the two-dimensional lidar.

As shown in Figure 2, the lidar is scanned in the sensor coordinate system along the scanning direction, with a fixed scanning angle resolution. The measured point is detected in the  $i$ th direction. Denote  $\theta_i$  as the angle between this direction and the positive direction of the  $X_s$ -axis, and  $\theta_i$  can be obtained by the resolution of the scanning angle with the inherent. A frame of point cloud data is obtained after a scan, which can be recorded as a set  $A = \{(d_i, \theta_i) | i = 1, \dots, n\}$ , where  $n$  is the number of scanned data points in this frame of data,  $(d_i, \theta_i)$  is the coordinate of the measured point in the polar coordinate system. And the final point cloud data set  $B = \{(x_i, y_i) | i = 1, \dots, n\}$  is obtained too.

**2.2.2. Lidar Error Model.** In the simulation experiment, the above error can be simplified to Gaussian white noise along the  $x$  and  $y$  directions in the carrier coordinate system of the mobile robot [18]. It is assumed that the positioning errors are in the two independent directions, so the corresponding covariance matrix is given by

$$\Sigma_{\text{rad}} = \begin{bmatrix} \sigma_x^b & 0 \\ 0 & \sigma_y^b \end{bmatrix}, \quad (4)$$

where  $\sigma_x^b$  and  $\sigma_y^b$  represent the variance along the  $x$  and  $y$  directions of the observation in the carrier coordinate system of the mobile robot, respectively.

**2.3. UWB Relative Measurement Model.** The relative measurement module is an important part of the cooperative navigation network in which nodes relate to the state information of the surrounding nodes. UWB (Ultra Wide Band) can measure relative distance and lidar can measure relative position which are selected as research objects in this paper. Because the scanning model of lidar has been described in the previous section, this section only establishes the corresponding ranging model and error model.

**2.3.1. UWB Ranging Model.** At present, there are two main ranging methods, that is, two-way ranging (TWR) method and symmetric double-sided two-way ranging (SDSTWR) method. SDSTWR method is greatly improved compared with TWR method in terms of ranging error caused by clock

synchronization. Therefore, SDSTWR method is often used for distance measurement [19] (see Figure 3).

The distance expression between transceiver A and transceiver B can be obtained from Figure 3:

$$d = c \frac{T_{A1}T_{B2} - T_{B1}T_{A2}}{T_{A1} + T_{A2} + T_{B1} + T_{B2}}, \quad (5)$$

where  $d$  is the distance between the two tested transceivers.  $T_{A1} = T_{a2} - T_{a1}$  is the time interval between the first signal and the received signal of transceiver A. We can get  $T_{A2}, T_{B1}, T_{B2}$  in the same way.

**2.3.2. UWB Error Model.** One of the main sources of error in UWB ranging is the error caused by the clock synchronization of the two transceivers [20]:

$$e_{\text{SDS}} = T_f c \left( 1 - \frac{k_A + k_B}{2} \right), \quad (6)$$

where  $k_A$  and  $k_B$  are the ratio of transceivers A and B between the actual and the expected frequency.

**2.4. SLAM Model Based on Lidar Measurement.** SLAM is widely used in the field of mobile robot navigation and positioning [21]. It is the key technology to solve the mapping problem at the same time, and it also provides a new idea for solving the path planning problem. SLAM technology mainly aims at the unknown location of the mobile robot. The environmental map is built in the form of an increasing perception of the surrounding strange environment according to the external sensor. At the same time, the state estimation of the mobile robot itself is obtained by using the built map information.

The SLAM localization technology is the key technology to realize the autonomous positioning of the mobile robot under the unknown environment. It is of great research value to realized more accurate navigation and localization under the condition of reducing the limitation of moving robot (such as no GPS) [22]. By applying the technology to the framework of the collaborative navigation system of the mobile robot, the navigation performance of the whole collaborative navigation system can be effectively improved (see Figure 4).

It can be seen from Figure 4 that a mobile robot's localization using a SLAM navigation system is essentially a process, which is continuous estimation to approximate the true value [23]. The triangle in the graph represents the mobile robot and the circle represents the observed landmark, where the grey circle represents the estimated landmark. The solid line connecting the triangle represents the real trajectory, and the dotted line is the estimated trajectory (see Figure 4).

### 3. Collaborative Navigation Framework Based on Odometer/Vision

When nodes in collaborative navigation network participate in collaborative navigation, different data fusion algorithms

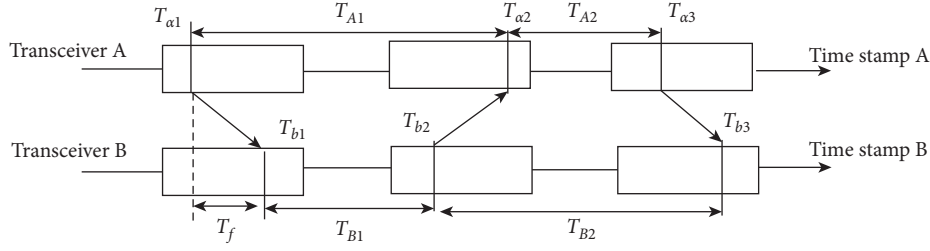


FIGURE 3: Principle of SDSTWR.

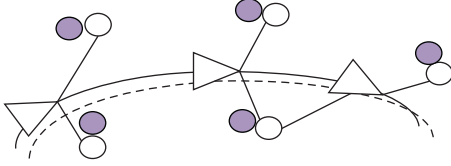


FIGURE 4: SLAM model diagram.

can be used for data fusion, which is obtained multisource heterogeneous sensors of different nodes. There are two data fusion algorithms generally used, centralized and decentralized data fusion algorithms [24].

**3.1. Framework of Collaborative Navigation Algorithm.** In this subsection, a corresponding data fusion framework of the centralized collaborative navigation algorithm is designed for the general odometer/vision model, and a data fusion framework of decentralized collaborative navigation algorithm is designed in the same way.

In the centralized collaborative navigation structure, the measured data obtained by each node are concentrated in a data fusion center for data fusion. In a distributed collaborative navigation structure, each node shares some information with other nodes while processing its own sensor data (see Figure 5).

According to the odometer/vision collaborative navigation model, we use the most common EKF algorithms to simulate centralized and decentralized cooperative navigation. A centralized location algorithm (CL) and a decentralized location algorithm (DCL) are designed.

As shown in Figure 6, in the CL algorithm corresponding to the centralized cooperative navigation structure, each node sends the information obtained by the sensor itself to the central server and realizes the data fusion through the EKF algorithm. Its state vector is a set of state vectors of each node, which is updated with the principle of track reckoning. After that, the measurement information obtained after data association in the SLAM process and the relative measurement information between nodes are selected. CL algorithm gathers the state and covariance information of all nodes, corrects them uniformly, and sends the corrected estimation results to each node. Because of participating in the joint measurement update process, the state information of each node is related to each other after the first update (see Figure 6).

This correlation is reasonably estimated based on the CL algorithm, and the task of data fusion is distributed to each node; then the DCL algorithm is proposed accordingly. Since the position of each node in the algorithm is equivalent, only one node needs to be discussed (see Figure 7). In order to avoid overoptimal estimation to the greatest extent, the DCL algorithm in this paper introduces the concept of separating covariance crossover filter. The covariance of each node is divided into correlation term and irrelevant term, and the time update process is basically consistent with the time update process of a single node. The measurement update process will take two steps. Firstly, according to the measurement information of the SLAM navigation system, the state estimation results are obtained by propagating the state and integrating the related information of the auxiliary navigation system. Then, the state information sent by the adjacent nodes and the relative measurement information between the nodes can obtain another state estimation of the node. Here, relevant state information sent to neighboring nodes is used to update local maps (see Figure 7).

### 3.2. SLAM Algorithms Based on Vision

**3.2.1. Landmark State Estimation Algorithm.** The key of SLAM navigation algorithm lies in the process of data association. The positioning process of this SLAM navigation system is essentially a process, which is continuous estimation to approximate the true value. This kind of probability estimation problem is usually solved by introducing appropriate filter. The most common is the EKF algorithm (see Figure 8).

Because of the high sampling frequency of the odometer selected in this paper, the lidar also has the advantages of high precision and high reliability; the EKF algorithm with better real-time performance is selected. The state estimation process of landmark information in SLAM based on EKF is described below. The observation equation of the feature information obtained by lidar is as follows:

$$z_k = h(X_{k,l}, X_{k,r}) + n_k = \begin{bmatrix} (x_{k,l} - x_{k,r}) \cos \theta_{k,r} + (y_{k,l} - y_{k,r}) \sin \theta_{k,r} \\ -(x_{k,l} - x_{k,r}) \sin \theta_{k,r} + (y_{k,l} - y_{k,r}) \cos \theta_{k,r} \end{bmatrix} + n_k, \quad (7)$$

where  $X_{k,l} = (x_{k,l}, y_{k,l})^T$  is state vector of landmark at  $k$  time and  $X_{k,r} = (x_{k,r}, y_{k,r}, \theta_{k,r})^T$  is state vector of mobile robot at

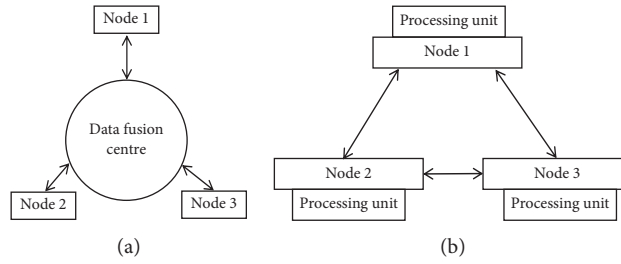


FIGURE 5: Collaborative navigation structure. (a) Centralized collaborative navigation. (b) Decentralized collaborative navigation.

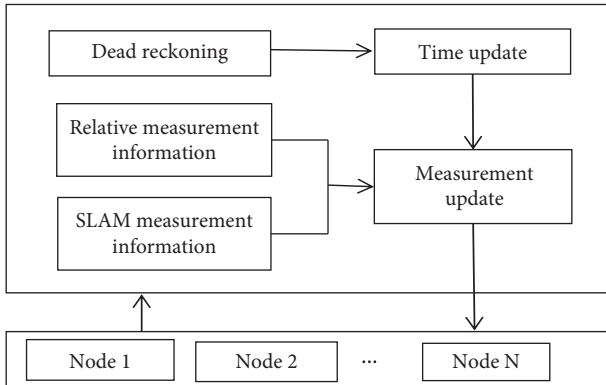


FIGURE 6: Data fusion framework of centralized collaborative navigation algorithm.

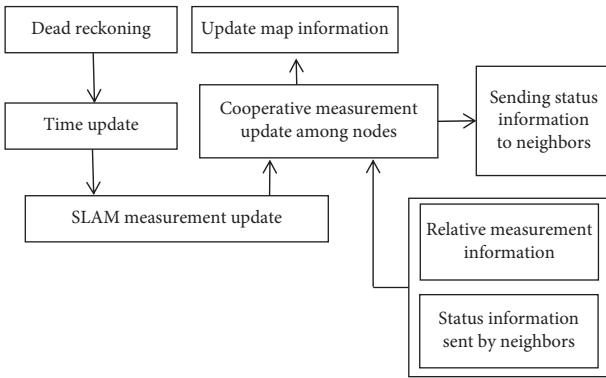


FIGURE 7: Data fusion framework of decentralized collaborative navigation algorithm.

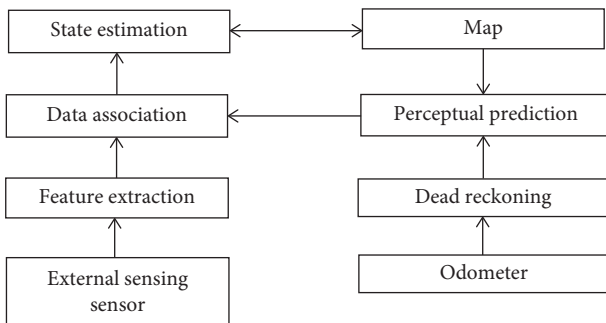


FIGURE 8: SLAM flow chart.

$k$  time.  $n_k$  is measurement noise. Its variance matrix is  $R_k$ , which can be denoted as  $n_k \sim N(0, R_k)$ . Since the landmarks are static, the state estimation of  $k - 1$  time landmark can be regarded as a priori estimation of  $k$  time landmark state. The measurement update process based on EKF is as follows:

Step 1: calculating the innovation and the filter gain:

$$\begin{aligned} v_k &= z_k - h(X_{k-1,l}, X_{k,r}^-), \\ K_k &= \Sigma_{k-1} H_k^T (H_k \Sigma_{k-1} H_k^T + R_k)^{-1}. \end{aligned} \quad (8)$$

Step 2: updating the state estimation and the corresponding covariance:

$$\begin{aligned} X_{k,l} &= X_{k-1,l} + K_k v_k, \\ \Sigma_k &= (I - K_k H_k) \Sigma_{k-1}, \end{aligned} \quad (9)$$

where  $\Sigma_k$  is the covariance matrix for state estimation of landmark at  $k$  time and  $H_k$  is the measurement matrix at  $k$  time.

*Remark 1.* Any observed landmark information can be position corrected by the above method, and it is noted that such position correction is limited to the landmark in the local map observed at the  $k$  time.

**3.2.2. Data Association Algorithm.** In a SLAM navigation system, the process of data association is an important prerequisite for state estimation. Incorrect data association is likely to lead to serious deviation of estimation results [25, 26].

At present, there are two data association algorithms commonly used in SLAM technology, that is, the nearest neighbor data association algorithm (NN, nearest neighbor) [27] and joint compatibility body & body data association algorithm (JCBB) [28]. The NN algorithm has less computation, but it is easy to form wrong data association when the density of feature information is large, which leads to the divergence of SLAM results, so it is only suitable for the environment where the density of feature information is small and the system error is small. JCBB is the improvement of the NN algorithm, which extends the association of single features in the NN to all observed feature information, which

is more binding and more reliable. The JCBB algorithm can obtain more credible association assumptions than the NN algorithm and exclude some wrong association assumptions. However, the computation amount is obviously increased, which to some extent affects the real-time performance of SLAM navigation system.

To ensure the accuracy of data association in the process of the SLAM, reduce the amount of computation as much as possible, and enhance the real-time performance of SLAM algorithm, this subsection describes an optimized data association algorithm. The classification method mentioned in [29] is used to divide the related feature information set; finally the appropriate feature information set in the local map and the preprocessed observation feature information set are selected to form the association space.

First, the collection of feature information in the local map is divided as follows:

$$\begin{cases} D[(x_m, y_m), (x_k, y_k)] \leq \Delta d, & (x_k, y_k) \in F_k, \\ D[(x_m, y_m), (x_k, y_k)] > \Delta d, & (x_k, y_k) \notin F_k, \end{cases} \quad (10)$$

where  $D[(x_m, y_m), (x_k, y_k)]$  is the relative distance between the feature information  $(x_k, y_k)$  of the local map and other feature information  $(x_m, y_m)$ .

Then, the observation feature information set is preprocessed and divided. In the actual navigation process, the observation feature information obtained by lidar contains noise information. The purpose of preprocessing is to filter out some noise information, improve the accuracy of data association, and reduce the amount of computation at the same time. The judgment process is as follows:

$$f(i, j) = \begin{cases} 1, & D[(x_i, y_j), (x_i, y_j)] < \Delta D, \\ 0, & D[(x_i, y_j), (x_i, y_j)] \geq \Delta D, \end{cases} \quad (11)$$

where  $\Delta D$  is the threshold, which is determined by the performance of the laser sensor. When the relative distance between the two observation feature information is less than the threshold, the observation feature information is considered to be the feature point; otherwise the noise point does not participate in the subsequent calculation.

When the set is divided, the set of observed feature information is sorted according to the order of observation. Based on the process of the local map feature information set above, the subset is divided in turn, and all points are not involved in the division repeatedly.

Finally, we select the appropriate association set to execute the data association algorithm. The subset of feature information of each local map and the subset of observed feature information at the current time are joint compatibility test, and the feature information with the best test results is selected to form a new subset as the data association object.

## 4. Centralized Collaborative Navigation Algorithm

**4.1. Time Update.** First of all, the state space model should be established. The state vector of a single mobile robot with three degrees of freedom contains position and heading angle information. Suppose the number of nodes is  $N$ , the state space of collaborative navigation system in centralized framework contains the state vectors of all mobile robots in the group, and the state vector of mobile robot  $i$  is  $X_k^i$  and the state of system is  $X_k$ . Then the state space equation of the system can be expressed as follows:

$$\begin{aligned} X_k &= \begin{bmatrix} X_k^1 \\ X_k^2 \\ \vdots \\ X_k^N \end{bmatrix} = \begin{bmatrix} f^1(X_{k-1}^1, u_{k-1}^1) \\ f^2(X_{k-1}^2, u_{k-1}^2) \\ \vdots \\ f^N(X_{k-1}^N, u_{k-1}^N) \end{bmatrix} + \begin{bmatrix} w_{k-1}^1 \\ w_{k-1}^2 \\ \vdots \\ w_{k-1}^N \end{bmatrix} \\ &\triangleq \Phi(X_{k-1}, u_{k-1}) + w_{k-1}, \end{aligned} \quad (12)$$

where the function  $f^i(X, u)$  describes the kinematic characteristics of the mobile robot,  $u_{k-1}^i = [\Delta S_{r,k-1} \ \Delta S_{l,k-1}]^T$  represents the input required by the mobile robot  $i$  to calculate the track at time  $k$ ,  $w_{k-1}^i$  is the system noise, and  $w_{k-1}^i \sim N(0, Q_{k-1}^i)$ .

It is assumed that the motion of any node is not affected by any other node, and each node moves independently without being controlled by other nodes. Therefore, the state transfer matrix for centralized collaborative positioning is given by

$$F_{k-1} = \begin{bmatrix} J_{X^{(k-1)}}^1 & 0 & \cdots & 0 \\ 0 & J_{X^{(k-1)}}^2 & \cdots & 0 \\ \vdots & \vdots & \ddots & \vdots \\ 0 & 0 & \cdots & J_{X^{(k-1)}}^N \end{bmatrix}, \quad (13)$$

where  $J_{u^{(k-1)}}^i$  and  $J_{X^{(k-1)}}^i$  are the Jacobian matrices of function  $f$  for state vectors and control inputs, respectively. The system noise variance matrix of collaborative navigation system in centralized framework is as follows:

$$Q_{k-1} = \begin{bmatrix} Q_{k-1}^1 & 0 & \cdots & 0 \\ 0 & Q_{k-1}^2 & \cdots & 0 \\ \vdots & \vdots & \ddots & \vdots \\ 0 & 0 & \cdots & Q_{k-1}^N \end{bmatrix}, \quad (14)$$

where  $Q_{k-1}^i = J_{u^{(k-1)}}^i \Sigma_u J_{u^{(k-1)}}^{iT}$  and  $\Sigma_u$  is the covariance matrix for controlling input. Then, the time update process of collaborative navigation system in centralized framework can be deduced:

$$X_k^- = \Phi(X_{k-1}^+, u_{k-1}),$$

$$P_k^- = F_{k-1}P_{k-1}F_{k-1}^T + Q_{k-1} \triangleq \begin{bmatrix} P_{11,k}^- & P_{12,k}^- & \cdots & P_{1N,k}^- \\ P_{21,k}^- & P_{22,k}^- & \cdots & P_{2N,k}^- \\ \vdots & \vdots & \ddots & \vdots \\ P_{N1,k}^- & P_{N2,k}^- & \cdots & P_{NN,k}^- \end{bmatrix}, \quad (15)$$

where

$$P_{ii,k}^- = J_{X(k-1)}^i P_{ii,k-1} J_{X(k-1)}^{iT} + Q_{k-1}^i, \quad (16)$$

$$P_{ij,k}^- = J_{X(k-1)}^i P_{ij,k-1} J_{X(k-1)}^{jT}.$$

**4.2. Single-Node Measurement Update.** In this section, the measurement updating process involving only one node in the centralized framework is described. The aided navigation system selected is SLAM navigation system, which integrates the landmark information of the surrounding environment measured by lidar. In this paper, a measurement model based on this navigation system is built, and the process of measurement updating based on EKF is described.

**4.2.1. Measurement Model Based on SLAM.** The measurement model based on SLAM is the measurement model after data association. In this paper, the position information of landmarks obtained by lidar is taken as the observation equation.

$$z_k^i = \begin{bmatrix} x_l^b \\ y_l^b \end{bmatrix}$$

$$= \begin{bmatrix} (x_l^w - x_k^i) \cos \theta_k^i + (y_l^w - y_k^i) \sin \theta_k^i \\ -(x_l^w - x_k^i) \sin \theta_k^i + (y_l^w - y_k^i) \cos \theta_k^i \end{bmatrix} + n_k^i, \quad (17)$$

where  $(x_l^b, y_l^b)$  is position information for landmarks obtained by lidar.  $(x_l^w, y_l^w, \theta_k^i)$  is the coordinates of landmarks in the world coordinate system.  $(x_k^i, y_k^i)$  is the state of the mobile robot at the time of  $k$ .  $n_k^i$  is the measurement noise and its variance matrix is  $R_k^i$ , which can be denoted as  $n_k^i \sim N(0, R_k^i)$ . After linearization and state extension, the observation equations of the whole system can be obtained:

$$z_k^i = H_k^i X_k + h^i(X_k^{i,-}) - \nabla h^i X_k^{i,-} + n_k^i, \quad (18)$$

where

$$H_k^i = [0 \cdots \nabla h^i \cdots 0]_{2 \times 3N}, \quad (19)$$

and  $\nabla h^i$  is Jacobian matrices of function  $h^i(X_k^i)$ .

**4.2.2. Measurement and Update Based on EKF.** Combined with the basic principle of Kalman filter, the measurement and update process of the aided navigation system for a single node can be obtained as follows:

Step 1: calculating the innovation and the filter gain:

$$v = z_k^i - h^i(X_k^{i,-}),$$

$$S^i = H_k^i P_k^- (H_k^i)^T + R_k^i, \quad (20)$$

$$S^i = H_k^i P_k^- (H_k^i)^T + R_k^i$$

Step 2: updating the state estimation and the corresponding covariance:

$$X_k^+ = X_k^- + K^i v, \quad (21)$$

$$P_k = P_k^- - P_k^- (H_k^i)^T (S^i)^{-1} H_k^i P_k^-.$$

**4.3. Relative Measurement Update among Nodes.** The standard observation model can be divided into two types: the measurement model based on the relative distance and the measurement model based on the relative position.

**4.3.1. Measurement Model Based on Relative Distance.** The observation of mobile robot  $i$  to mobile robot  $j$  at  $k$  time can be denoted by  $z_k^{ij}$ ; then the observation equation is given by

$$z_k^{ij} = h^{ij}(X_k^i, X_k^j) + n_k^{ij}$$

$$= \sqrt{(x_k^i - x_k^j)^2 + (y_k^i - y_k^j)^2} + n_k^{ij}, \quad (22)$$

where  $n_k^{ij}$  is the measurement noise, its variance matrix is  $R_k^{ij} = \sigma_{\text{UWB}}^2$ , which can be denoted as  $n_k^{ij} \sim N(0, R_k^{ij})$ , and  $\sigma_{\text{UWB}}$  is the variance for UWB ranging.

After linearization and state extension, the observation equations of the whole system can be obtained:

$$z_k^{ij} = H_k^{ij} X_k + h^{ij}(X_k^{i,-}, X_k^{j,-}) - \nabla h_i^{ij} X_k^{i,-} - \nabla h_j^{ij} X_k^{j,-} + n_k^{ij}, \quad (23)$$

where

$$H_k^{ij} = [0 \cdots \nabla h_i^{ij} \cdots \nabla h_j^{ij} \cdots 0]_{2 \times 3N}, \quad (24)$$

and  $\nabla h_i^{ij}$  and  $\nabla h_j^{ij}$  are Jacobian matrices of function  $h^{ij}(X^i, X^j)$ , respectively.

**4.3.2. Measurement Model Based on Relative Position.** Using lidar as the sensor to realize the relative observation among nodes can be divided into two kinds: direct method and indirect method. The direct method is to measure the relative position between the two nodes directly; the indirect method is to use lidar to observe the nearest landmark between the two nodes. The relative position between the two nodes is obtained by correlation calculation.

The state of mobile robot  $i$  is denoted by  $(x_k^i, y_k^i, \theta_k^i)$ , at time  $k$  and the state of mobile robot  $j$  is denoted by  $(x_k^j, y_k^j, \theta_k^j)$ . The coordinates of landmark  $L_1$  adjacent to



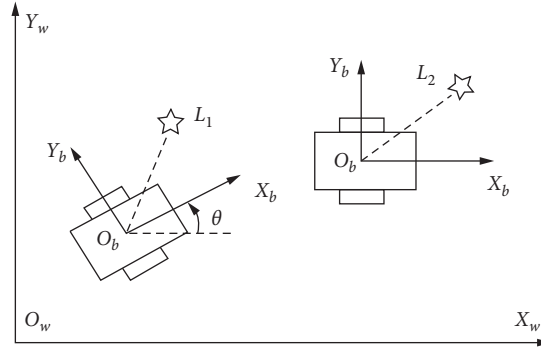


FIGURE 9: Indirect observation schematic diagram.

mobile robot  $i$  in the world coordinate system are  $(x_{l1}^w, y_{l1}^w)$ , the coordinates in the mobile robot  $i$  coordinate system are  $(x_{l1}^i, y_{l1}^i)$ , the coordinates of landmark  $L_2$  adjacent to mobile robot  $j$  in the world coordinate system are  $(x_{l2}^w, y_{l2}^w)$ , and the coordinates in the coordinate system of mobile robot  $j$  are  $(x_{l2}^j, y_{l2}^j)$ . The specific solution process of the indirect method is as follows (see Figure 9):

$$\begin{bmatrix} x_k^j - x_k^i \\ y_k^j - y_k^i \end{bmatrix} = \begin{bmatrix} x_{l2}^j \cos \theta_k^j - y_{l2}^j \sin \theta_k^j \\ x_{l2}^j \sin \theta_k^j + y_{l2}^j \cos \theta_k^j \end{bmatrix} - \begin{bmatrix} (x_{l1}^i \cos \theta_k^i - y_{l1}^i \sin \theta_k^i) + (x_{l1}^w - x_{l2}^w) \\ (x_{l1}^i \sin \theta_k^i + y_{l1}^i \cos \theta_k^i) + (y_{l1}^w - y_{l2}^w) \end{bmatrix}, \quad (25)$$

when mobile robot  $i$  observe mobile robot  $j$  at  $k$  time, the coordinates of mobile robot  $j$  in the mobile robot  $i$  coordinate system as the observation. The observation equations are as follows:

$$z_k^{ij} = \begin{bmatrix} x_k^{j,i} \\ y_k^{j,i} \end{bmatrix} = \begin{bmatrix} (x_k^j - x_k^i) \cos \theta_k^i + (y_k^j - y_k^i) \sin \theta_k^i \\ -(x_k^j - x_k^i) \sin \theta_k^i + (y_k^j - y_k^i) \cos \theta_k^i \end{bmatrix} + n_k^{ij}, \quad (26)$$

where  $n_k^{ij}$  is the measurement noise, its variance matrix is  $R_k^{ij}$ , which can be denoted as  $n_k^{ij} \sim N(0, R_k^{ij})$ , and  $(x_k^{j,i}, y_k^{j,i})$  is the coordinate of mobile robot  $j$  in the coordinate system of mobile robot  $i$  at  $k$  time.

**4.3.3. Measurement Update Based on EKF.** Similarly, we can finally get the measurement update process for the relative observation between nodes.

## 5. Decentralized Collaborative Navigation Algorithm

The state and covariance information of each node under the decentralized collaborative navigation algorithm is, respectively, calculated. In order to avoid overoptimal estimation to the maximum extent, the concept of the covariance intersection filter is introduced and the covariance of each node is divided into related and irrelevant items.

**5.1. Covariance Intersection Filter.** Given the state estimation vector  $X$  and corresponding covariance matrix  $P$ , assuming

that  $P^*$  is the covariance of the error between the state estimate  $X$  and the state real value  $X^*$ , it can be expressed as follows:

$$P^* = E[(X - X^*)(X - X^*)^T]. \quad (27)$$

Consistency is a characteristic of the covariance matrix of the estimation [30]. When the covariance matrix of the state estimation is not less than the real covariance, it is said that the estimation satisfies the consistency, that is, no overoptimal estimation is produced. Suppose two state estimates  $X_1$  and  $X_2$  are independent and satisfy the consistency, the corresponding covariances are  $P_1$  and  $P_2$ . If there is a correlation between the two estimates, the Kalman filter may produce inconsistent results; in other words, it leads to overoptimal estimation:

$$P_1 = \frac{P_{1d}}{w} + P_{1i}, \quad (28)$$

$$P_2 = \frac{P_{2d}}{w} + P_{2i}, \quad (29)$$

$$P^{-1} = P_1^{-1} + P_2^{-1}, \quad (30)$$

$$X = P(P_1^{-1}X_1 + P_2^{-1}X_2), \quad (31)$$

$$P_i = P(P_1^{-1}P_{1i}P_1^{-1} + P_2^{-1}P_{2i}P_2^{-1}), \quad (32)$$

$$P_d = P - P_i, \quad (33)$$

where the covariance corresponding to two state estimates  $X_1$  and  $X_2$  is  $P_{1d} + P_{1i}$  and  $P_{2d} + P_{2i}$ , respectively.  $P_{1d}$  and  $P_{2d}$  are the correlation covariance components corresponding to the maximum correlation between the two state estimates.  $P_{1i}$  and  $P_{2i}$  are independent covariance components corresponding to absolute independence of two state estimates,  $W$  within interval  $[0, 1]$ . It is an optimization parameter that minimizes the covariance after fusion, and the  $w$  in this interval can ensure the consistency of the fusion results.

**5.2. Time Update.** Before describing the time update process of DCL algorithm, it is necessary to decompose the state information of the system in the framework of centralized collaborative navigation, which can be expressed as

$$\begin{aligned} E_G &= \{X_G, P_G\} \\ &= \{\{X_1, P_1\}; \{X_2, P_2\} \cdots \{X_N, P_N\}\} \\ &= \{\{X_1, P_{1d} + P_{1i}\}; \{X_2, P_{2d} + P_{2i}\} \cdots \{X_N, P_{Nd} + P_{Ni}\}\}, \end{aligned} \quad (34)$$

where  $E_G$  is the set of states under the centralized collaborative navigation framework, and  $X_G$  and  $P_G$  are the state space and the corresponding covariance matrix under the centralized collaborative navigation framework, respectively.

The state propagation process under the decentralized collaborative navigation framework is the state propagation process of a single node, and the propagation process of covariance can be expressed as

$$\begin{aligned} P_k^{i-} &= J_{X(k-1)}^i P_{k-1}^i J_{X(k-1)}^{iT} + J_{u(k-1)}^i \Sigma_u J_{u(k-1)}^{iT}, \\ P_{k,i}^{i-} &= J_{X(k-1)}^i P_{k-1,i}^i J_{X(k-1)}^{iT} + J_{u(k-1)}^i \Sigma_u J_{u(k-1)}^{iT}, \end{aligned} \quad (35)$$

where  $P_k^{i-}$  is the one-step prediction covariance matrix of the mobile robot  $i$  at time  $k$  and  $P_{k,i}^{i-}$  is the covariance. The independent covariance components of the matrix,  $J_{X(k-1)}^i$  and  $J_{u(k-1)}^i$ , are Jacobian matrices of function  $f^i(X, u)$  for state vector and control input and  $\Sigma_u$  is the error matrix of the control input.

**5.3. Single Node Measurement Update.** The measurement and updating process of a single node only involves the aided navigation system of a single node, so there is no need to estimate the correlation, that is, the process of saving formulas (28) and (29). Similar to the single node measurement update process in centralized collaborative navigation, the single node measurement update process in distributed collaborative navigation can be expressed as

Step 1: calculate the innovation and the filtering gain:

$$\begin{aligned} v &= z_k^i - \nabla h^i X_k^{i-}, \\ S &= \nabla h^i P_k^{i-} (\nabla h^i)^T + R_k^i, \\ K &= P_k^{i-} (\nabla h^i)^T S^{-1}. \end{aligned} \quad (36)$$

Step 2: update the state estimation and the corresponding covariance:

$$\begin{aligned} X_k^{i+} &= X_k^{i-} + Kv, \\ P_k^i &= (I - K\nabla h^i) P_k^{i-}, \\ P_{k,i}^i &= (I - K\nabla h^i) P_{k,i}^{i-} (I - K\nabla h^i)^T + KR_k^i K^T, \\ P_{k,d}^i &= P_k^i - P_{k,i}^i. \end{aligned} \quad (37)$$

**5.4. Collaborative Measurement Update among Nodes.** In the framework of decentralized collaborative navigation, the state estimation results of a single node aided navigation system and the state estimation results based on information sharing among nodes are integrated in the process of internode collaborative measurement updating, and the corrected state information is derived.

For the decentralized collaborative navigation framework, any node can clearly estimate the state of other nodes. In order to save the communication cost and reduce the computation of a single mobile robot platform, this paper sets up that the information exchange among the mobile robots is only taking place between the two adjacent mobile robot nodes.

Assuming that the mobile robot  $i$  performs relative observations of the mobile robot  $j$  at the  $k$  time and shares its own state and covariance information with the mobile robot  $j$ , the state of the mobile robot  $j$  can be clearly expressed with information received state of the mobile robot  $i$  and the relative measurement information between the two nodes:

$$X_k^{\text{coj}} = \begin{bmatrix} x_k^{\text{coj}} \\ y_k^{\text{coj}} \end{bmatrix} = \begin{bmatrix} x_k^i + x_k^{j,i} \cos \theta_k^i - y_k^{j,i} \sin \theta_k^i \\ y_k^i + x_k^{j,i} \sin \theta_k^i + y_k^{j,i} \cos \theta_k^i \end{bmatrix}, \quad (38)$$

where  $(x_k^{\text{coj}}, y_k^{\text{coj}})$  is the partial state estimation of the mobile robot  $j$  obtained by the information sharing between the mobile robot  $i$  and the mobile robot  $j$  at  $k$  time,  $(x_k^i, x_k^{j,i}, \theta_k^i)$  is the state vector shared by the mobile robot  $j$  in the  $k$  direction of the mobile robot  $i$ , and  $u_{\text{rel}} = (x_k^{j,i}, y_k^{j,i})$  is the relative measurement information of the two nodes in the  $i$  coordinate system of the mobile robot.

If there is a direct relative observation between the two nodes, the relative measurement information can be obtained directly by the sensor that carries on the relative observation. If the relative observation between the two nodes is with the help of the indirect relative observation of the surrounding landmark information, then the relative measurement information needs to be solved to a certain extent, and the concrete solution method can be combined (25) and then converted into the mobile robot.

Finally, based on the principle of covariance intersection filter, the updating process of collaborative measurement among nodes in the framework of decentralized collaborative navigation can be obtained.

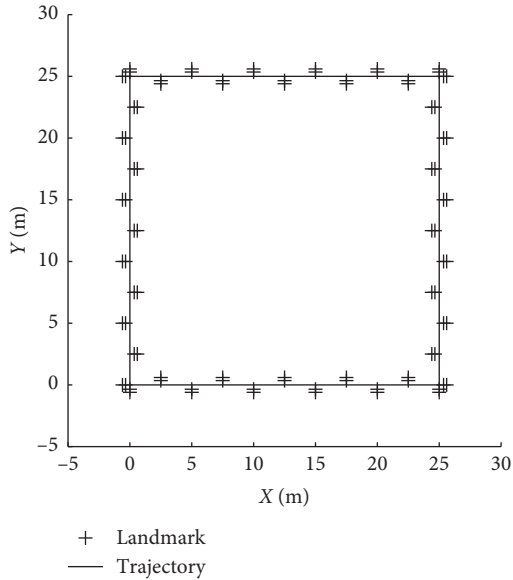


FIGURE 10: Simulation trajectory diagram.

## 6. Simulation Results

**6.1. Simulated Experimental Environment.** In this section, the nodes of the mobile robot network involved in collaborative navigation are 3. Assuming that the area of the moving 2D environment is  $25\text{ m} \times 25\text{ m}$  when the mobile robot population group works together, each node in the environment is assigned to an initial position, and each node can follow random trajectory motion in this area. Assuming that all nodes follow the same simulation trajectory, only the initial position is different. The maximum speed of the mobile robot in the straight line is  $0.3125\text{ m/s}$  and the angular velocity at the bend is  $0.1^\circ/\text{s}$ . It is assumed that the environment around the simulated trajectory of this rectangle can be extracted by lidar scanning to 88 landmarks (environmental feature points) for the SLAM-assisted navigation system (see Figure 10).

During this simulation, mobile robots as carriers can carry different types of sensors, including odometers, UWB, and lidar. Suitable sensors are selected according to the requirements of positioning accuracy, among which Time Domain P410 UWB sensors are used to measure the relative distance, and lidar is selected from LMS291 series 2D lidar produced by a German company. Based on the relevant parameters of these sensors, which are shown in Table 1, a simulation model for mobile robots carrying different types of sensors is built using MATLAB.

**6.2. Relative Measurement Aided Odometer Collaborative Navigation.** In the experiment, all three mobile robots are equipped with odometer capable of moving monitoring, UWB capable of measuring relative distance, or lidar capable of measuring relative position.

From Figure 11, it can be seen that the collaborative navigation system which realizes relative information sharing has significant advantages over the case of not

TABLE 1: Relevant parameters of sensors.

Type	Measure	Frequency (Hz)	Error
Odometer	Linear velocity of the two wheels	20	4 cm/s
UWB	Relative distance	10	3 cm
Lidar	Relative position of X direction	10	2 cm
	Relative position of Y direction	10	2 cm

sharing any information in positioning accuracy. Besides, the improvement of group navigation performance of mobile robots is affected by the type of shared relative information. When the relative position information is shared, the growth of the error can be effectively limited; relatively speaking, when the relative distance information is shared, the position error is still growing slowly, which only reduces the growth rate of the error (see Figure 11).

The analysis shows that the relative distance information is weakly constrained, so sharing this information cannot effectively realize the navigation and localization of mobile robots. In contrast, the sharing of relative position information includes the solution to mobile robot navigation and information. Information accuracy is significantly improved. It can even be increased by more than 60% at some time. This difference is more obvious in the angle error diagram (see Figure 11).

In this paper, two observation methods, direct relative measurement and indirect relative measurement, are mentioned in the description of the measurement model based on relative position. Based on this experimental scene, scenario I is three mobile robots to observe the relative position information directly through lidar. Scenario II is three mobile robots to extract the surrounding landmark information through lidar, and based on this solution, the relative position information is calculated. In the above experimental scenario, the centralized collaborative navigation algorithm is used to solve the navigation problem. The two relative position measurement methods are compared through the above simulation experimental scenarios. The comparison results are shown in Figure 12 (see Figure 12).

Through Figure 12, it is clear that the collaborative navigation and positioning accuracy of relative position measurement using the direct method are better than those of indirect method. However, cost calculation cannot be ignored while navigation performance is considered. The direct method requires that the measurement range of lidar includes the activity range of the whole mobile robot population group while the measurement range of lidar required by indirect method only needs to include the surrounding landmarks. This greatly reduces the cost calculation. Considering that the accuracy of collaborative navigation and positioning using the two relative position measurement methods is not much different, it is obvious that the indirect method is more suitable for practical application (see Figure 12).

The difference of the decentralized collaborative navigation framework compared with the centralized collaborative navigation framework is that the correlation among

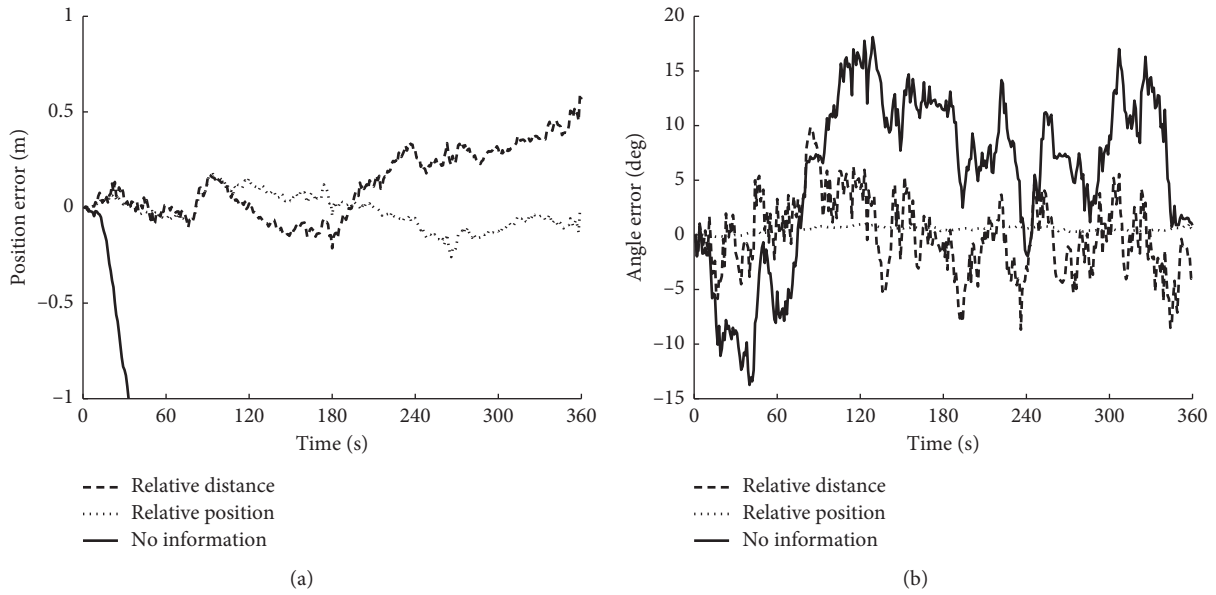


FIGURE 11: Comparative diagram of navigation error under the condition of sharing different relative information. (a) Position error. (b) Angle error.

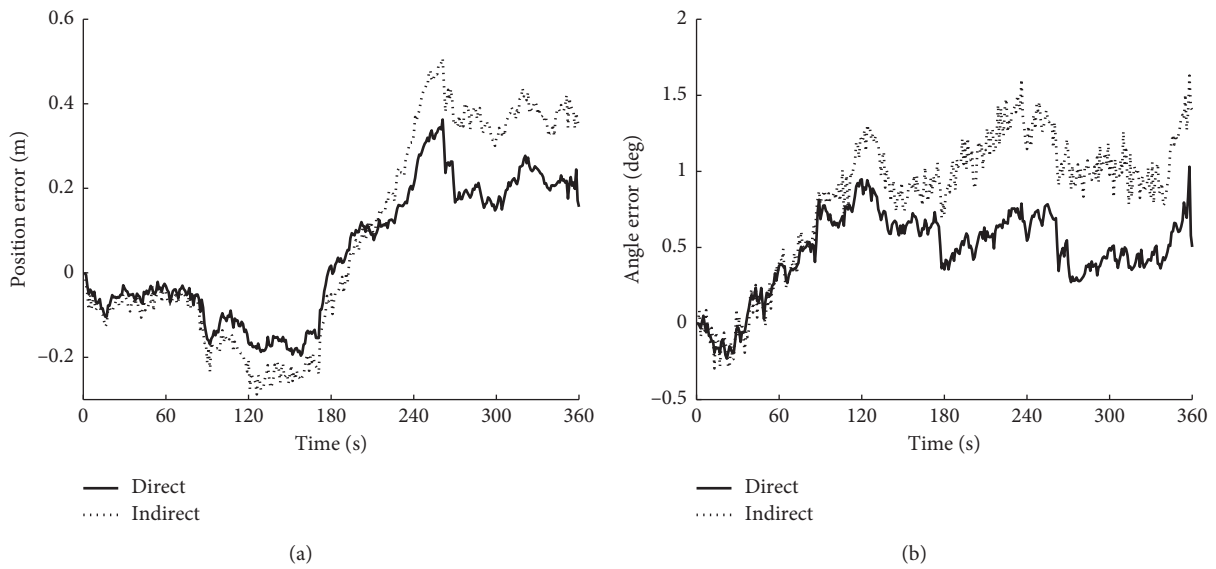


FIGURE 12: Comparison of navigation errors under different relative position measuring methods. (a) Position error. (b) Angle error.

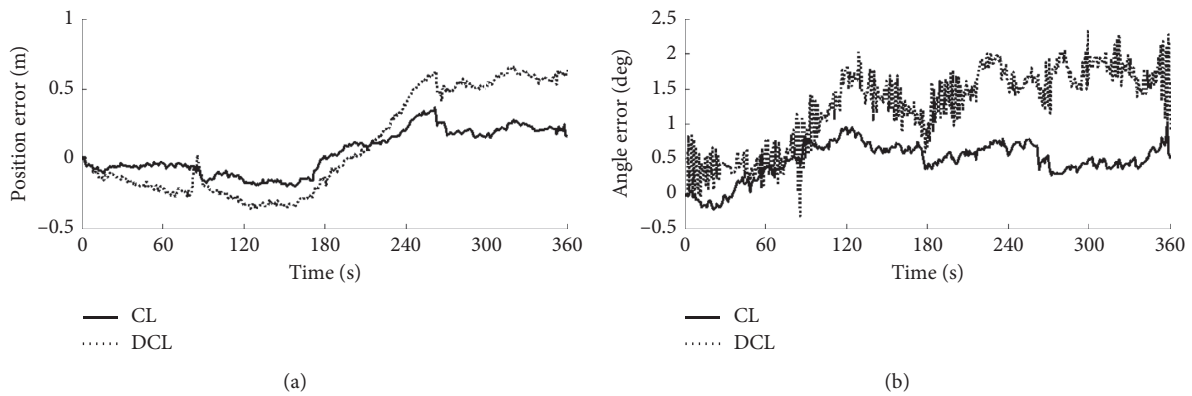


FIGURE 13: Comparison of navigation errors under different collaborative navigation algorithms. (a) Position error. (b) Angle error.

the different node states is accurately calculated in the centralized collaborative navigation framework, and this correlation cannot be used in the decentralized collaborative navigation framework. In order to better reflect the impact of this correlation, the navigation errors of the two collaborative navigation algorithms in the odometer collaborative navigation system are shown in Figure 13 (see Figure 13).

To compare the two algorithms, 20 experiments are carried out in this paper, and the root mean square error (RMS) and formulas of the two collaborative navigation algorithms are calculated as shown in the following formula:

$$\text{RMS} = \sqrt{\frac{1}{n} \sum_{i=1}^n (x_i - \bar{x}_i)^2}, \quad (39)$$

where  $n$  is the total number of samples,  $x_i$  is the actual value, and  $\bar{x}_i$  is the estimated value. RMS parameters for the odometer collaborative navigation are shown in Table 2.

As can be seen from Figure 13 and Table 2, the error of the centralized collaborative navigation algorithm is smaller than that of the decentralized collaborative navigation algorithm. This can be predicted because the correlation among node states in the centralized collaborative navigation algorithm can be calculated accurately, which is estimated in the decentralized collaborative navigation algorithm. However, the improved accuracy of the navigation is at the expense of high computing power and high quality data communication. Therefore, although the performance of centralized collaborative navigation framework is better than that of distributed collaborative navigation framework, the centralized collaborative navigation framework is not applicable in some practical scenarios (see Figure 13).

**6.3. Odometer/Vision SLAM Collaborative Navigation.** In the odometer/vision collaborative navigation model, scenario I is designed that all the mobile robots are equipped with an odometer which can monitor the motion. One of the mobile robots is equipped with SLAM-aided navigation system and can work properly.

Firstly, the mobile robot with SLAM-aided navigation system is studied, and it only runs its own integrated navigation algorithm without sharing the relative position information. Using the centralized collaborative navigation algorithm, the navigation error of nodes with SLAM-aided navigation system is shown in Figure 14 (see Figure 14).

Figure 14 fully verifies the correctness of a centralized collaborative navigation algorithm based on the odometer/vision collaborative navigation model. The SLAM-assisted navigation system is based on the relative observation. The position estimation of the node itself and the position estimation of the landmark have the error accumulation, but the association algorithm of the SLAM is combined, the centralized collaborative navigation algorithm makes the position estimation of the landmark closer to the real value while the positioning accuracy of the mobile robot is

TABLE 2: Odometer collaborative navigation RMS parameters.

Algorithm type	Position error (m)	Angle error (°)
CL	0.1629	0.74625
DCL	0.36342	1.3762

improved, the data association is more reliable, further correcting the state estimation of the mobile robot itself. Therefore, the algorithm is very obvious to improve the navigation accuracy of mobile robot (see Figure 14).

Then, the mobile robots without the SLAM-aided navigation system in the experiment are studied. In order to fully reflect the influence of the SLAM-aided navigation information on the navigation performance of other nodes, Scenario II is designed that all mobile robots are equipped with odometer which can monitor the motion, and two of them are equipped with SLAM-aided navigation system and can work properly. The navigation error of other nodes without SLAM-aided navigation system is shown in Figure 15 (see Figure 15).

As shown in Figure 15, the mobile robot with SLAM-aided navigation system performs loop-back detection in about 320 seconds and data associated with the local map created at the initial location, thus eliminating most of the accumulated errors. The unique superior performance of the SLAM-aided navigation system is transmitted to other nodes in the group through the process of information sharing in the process of collaborative navigation, so that it can also eliminate most of the accumulated errors in the vicinity of the time, which is an important advantage of the collaborative navigation system (see Figure 15).

To verify the NN algorithm, JBCC algorithm, and the optimized data association algorithm on the navigation performance of nodes without SLAM-aided navigation system, the experimental scene is designed that all mobile robots are equipped with odometer which can carry out motion monitoring. One of the mobile robots is equipped with SLAM-aided navigation system and can work normally, and the CL algorithm is run. The navigation error of nodes without SLAM-aided navigation system is shown in Figure 16 (see Figure 16).

The performance of the centralized collaborative navigation algorithm under the three SLAM data association algorithms is shown in Table 3.

From Figure 16 and Table 3, it can be seen that the navigation performance of nodes without SLAM-aided navigation system is affected by the SLAM data association algorithm used by nodes carrying SLAM-aided navigation system. Running the NN algorithm, the matching accuracy of feature information is not high, so that the navigation accuracy is poor. Running the JCBB algorithm, the correct rate of data association is the highest, but the operation time is the longest. Running optimization data association algorithm, the navigation accuracy is slightly reduced, but the operation time is less, which can meet the real-time requirements (see Figure 16).

In this subsection, to compare the performance of collaborative navigation systems in odometer/vision collaborative navigation systems under centralized and

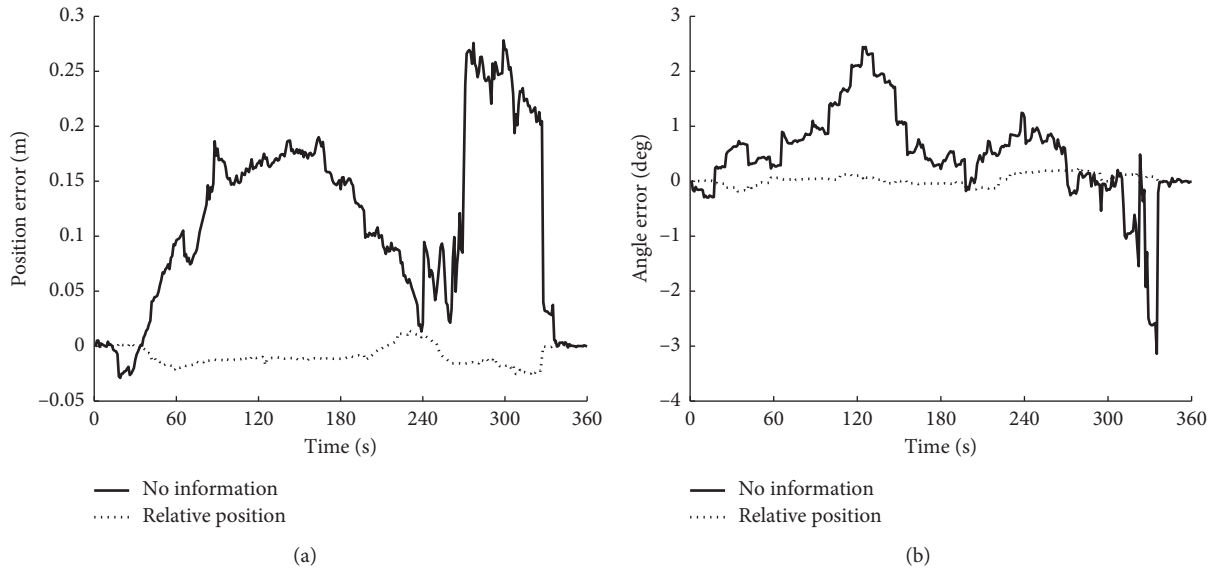


FIGURE 14: The navigation error map of the node with the SLAM-aided navigation system. (a) Position error. (b) Angle error.

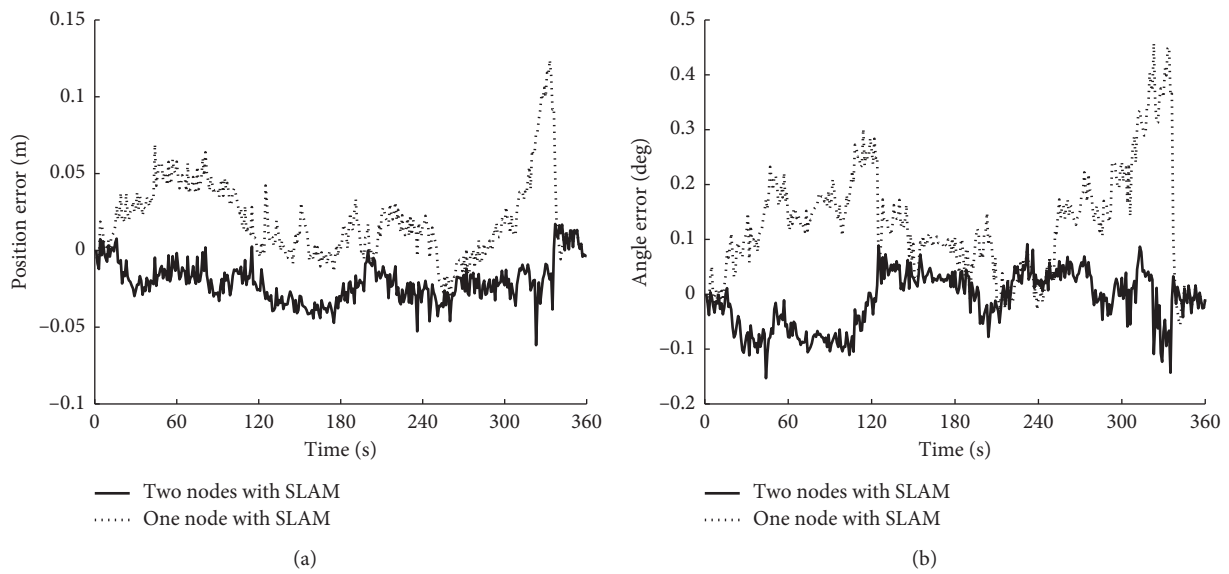


FIGURE 15: Some nodes are equipped with SLAM-aided navigation system. (a) Position error. (b) Angle error.

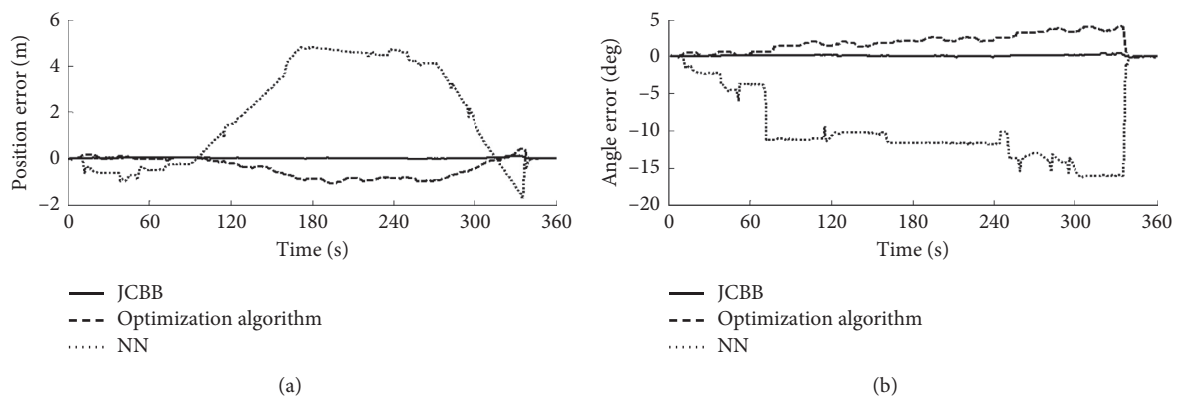


FIGURE 16: Comparison diagram of navigation error for fusion of single node SLAM information under different SLAM data association algorithms. (a) Position error. (b) Angle error.

TABLE 3: Performance comparison of centralized collaborative navigation algorithms under different SLAM data association algorithms.

Algorithm type	Position error (m)	Angle error (°)	Relative time
NN	2.8323	10.7919	4
JCBB	0.0322	0.1623	12
Optimization	0.5587	2.2476	1

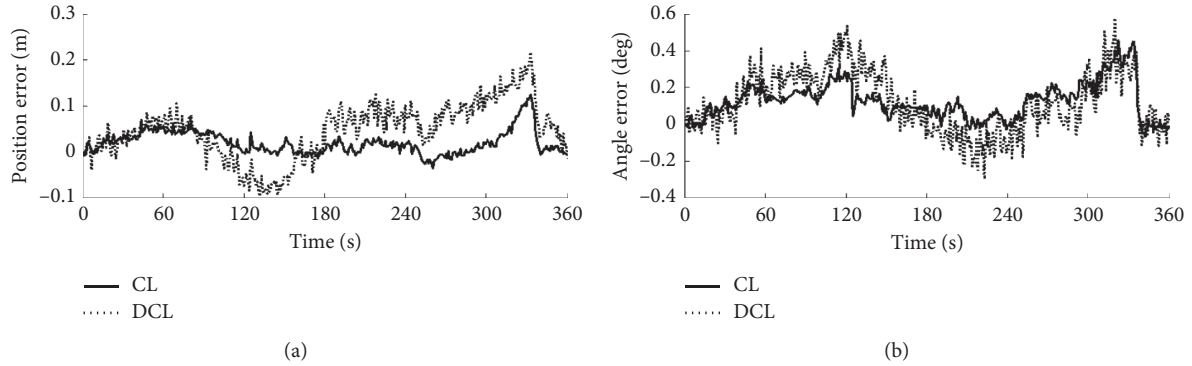


FIGURE 17: Comparative diagram of navigation error for fusion of single node SLAM information under different collaborative navigation algorithms. (a) Position error. (b) Angle error.

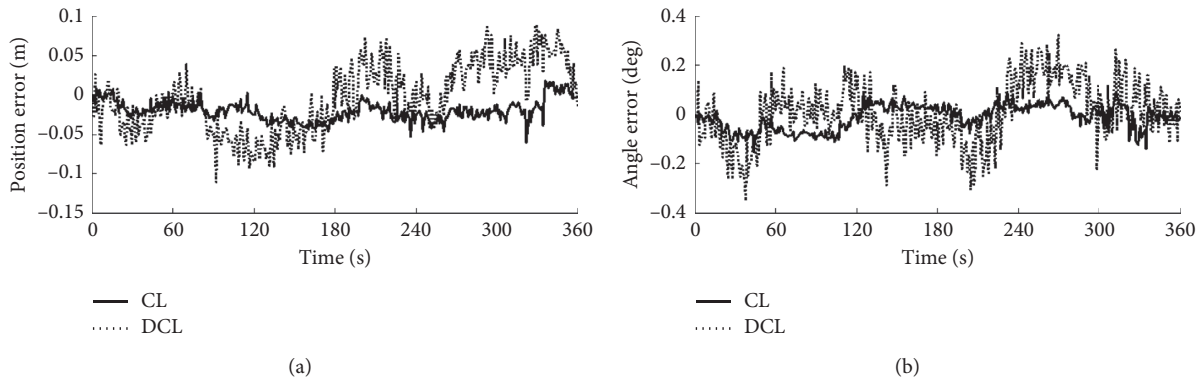


FIGURE 18: Comparison diagram of navigation error for fusion of multinode SLAM information under different collaborative navigation algorithms. (a) Position error. (b) Angle error.

TABLE 4: Collaborative navigation RMS parameters for fusion of single node SLAM information.

Algorithm type	Position error (m)	Angle error (°)
CL	0.0322	0.1623
DCL	0.0669	0.2094

decentralized collaborative navigation algorithms, we run the CL and DCL algorithms separately under the experimental scenario I. The navigation errors of the two collaborative navigation algorithms are compared as shown in Figure 17. Under the experimental scenario II of this subsection, we run the CL algorithm and the DCL algorithm, respectively. The navigation errors of the two collaborative navigation algorithms are compared as shown in Figure 18 (see Figures 17 and 18).

TABLE 5: Collaborative navigation RMS parameters for fusion of multinode SLAM information.

Algorithm type	Position error (m)	Angle error (°)
CL	0.0243	0.0524
DCL	0.0438	0.1265

After 20 experiments, the RMS parameters of collaborative navigation with single node SLAM information are shown in Table 4.

The RMS parameters of the coordinated navigation with the fused multinode SLAM information are shown in Table 5.

As can be seen from Figures 17 and 18 in conjunction with Tables 4 and 5, in the odometer/vision collaborative navigation system, the error of the centralized collaborative

navigation algorithm is less than the distributed collaborative navigation algorithm; after the landmark information collected by the single node or the multinode is fused, there is a small gap between the two algorithms. In other words, the distributed collaborative navigation algorithm based on the odometer/vision collaborative navigation model can well estimate the correlation of the internode information (see Figures 17 and 18).

Considering the high requirement of the centralized collaborative navigation algorithm to the computing power and the communication level, the application scenarios of the two algorithms are analyzed in combination with the abovementioned collaborative navigation experiment: the centralized collaborative navigation algorithm is suitable for the case that there are few nodes and the nodes are not equipped with additional aided navigation system, the decentralized collaborative navigation algorithm is suitable for the large number of nodes and the large amount of information shared, and some nodes are equipped with additional aided navigation systems, especially in the case of SLAM-aided navigation system.

## 7. Conclusion

In order to improve the performance of cooperative navigation system, a multirobot collaborative navigation algorithm based on odometer/vision multisource information fusion is studied. On the basis of establishing the multisource information fusion collaborative navigation system model, the centralized collaborative navigation of odometer/vision fusion, the decentralized collaborative navigation framework, and the vision-based SLAM are given, and the centralized and decentralized odometer/vision collaborative navigation algorithms are derived, respectively. The effectiveness of the proposed algorithm is verified by the simulation experiments, which has some theoretical value and application value in high performance collaborative navigation applications.

## Data Availability

The data used to support the findings of this study are available from the corresponding author upon request.

## Conflicts of Interest

The authors declare that they have no conflicts of interest.

## References

- [1] K. N. Olivier, D. E. Griffith, G. Eagle et al., "Randomized trial of liposomal amikacin for inhalation in nontuberculous mycobacterial lung disease," *American Journal of Respiratory and Critical Care Medicine*, vol. 195, no. 6, pp. 814–823, 2017.
- [2] M. Schwarz, M. Beul, D. Droeschel et al., "DRC team nimbro rescue: perception and control for centaur-like mobile manipulation robot momaro," *Springer Tracts in Advanced Robotics*, Springer, Berlin, Germany, pp. 145–190, 2018.
- [3] M. Long, H. Su, and B. Liu, "Group controllability of two-time-scale discrete-time multi-agent systems," *Journal of the Franklin Institute*, vol. 357, no. 6, pp. 3524–3540, 2020.
- [4] T. Fukuda, S. Nakagawa, Y. Kawauchi, and M. Buss, "Structure decision method for self organising robots based on cell structures-CEBOT," in *Proceedings of the 1989 International Conference on Robotics and Automation*, Scottsdale, AZ, USA, May 1989.
- [5] H. Asama, A. Matsumoto, and Y. Ishida, "Design of an autonomous and distributed robot system: actress," in *Proceedings of the IEEE/RSJ International Workshop on Intelligent Robots and Systems (IROS '89) the Autonomous Mobile Robots and its Applications*, September 1989.
- [6] J. Zhou, Y. Lv, G. Wen, X. Wu, and M. Cai, "Three-dimensional cooperative guidance law design for simultaneous attack with multiple missiles against a maneuvering target," in *Proceedings of the 2018 IEEE CSAA Guidance, Navigation and Control Conference (CGNCC)*, August 2018.
- [7] H. Su, J. Zhang, and Z. Zeng, "Formation-containment control of multi-robot systems under a stochastic sampling mechanism," *Science China Technological Sciences*, vol. 63, no. 6, pp. 1025–1034, 2020.
- [8] H. Park and S. Hutchinson, "A distributed robust convergence algorithm for multi-robot systems in the presence of faulty robots," in *Proceedings of the 2015 IEEE/RSJ International Conference on Intelligent Robots and Systems (IROS)*, pp. 2980–2985, IEEE, Hamburg, Germany, September–October 2015.
- [9] K. Petersen and R. Nagpal, "Complex design by simple robots: a collective embodied intelligence approach to construction," *Architectural Design*, vol. 87, no. 4, pp. 44–49, 2017.
- [10] L. Chaimowicz, T. Sugar, V. Kumar, and M. F. M. Campos, "An architecture for tightly coupled multi-robot cooperation," in *Proceedings 2001 ICRA. IEEE International Conference on Robotics and Automation (Cat. no. O1CH37164)*, vol. 3, pp. 2992–2997, IEEE, Seoul, Korea, May 2001.
- [11] H.-X. Hu, G. Chen, and G. Wen, "Event-triggered control on quasi-average consensus in the cooperation-competition network," in *Proceedings of the IECON 2018—44th Annual Conference of the IEEE Industrial Electronics Society*, October 2018.
- [12] A. Amanatiadis, K. Charalampous, I. Kostavelis et al., "The avert project: autonomous vehicle emergency recovery tool," in *Proceedings of the 2013 IEEE International Symposium on Safety, Security, and Rescue Robotics (SSRR)*, pp. 1–5, IEEE, Linköping, Sweden, October 2013.
- [13] R. Kurazume, S. Hirose, T. Iwasaki, S. Nagata, and N. Sashida, "Study on cooperative positioning system," in *Proceedings of the IEEE International Conference on Robotics and Automation*, Minneapolis, MN, USA, August 1996.
- [14] Z. Fu, Y. Zhao, and G. Wen, "Distributed continuous-time optimization in multi-agent networks with undirected topology," in *Proceedings of the 2019 IEEE 15th International Conference on Control and Automation (ICCA)*, November 2019.
- [15] Y. Zhao, Y. Liu, and G. Wen, "Finite-time average estimation for multiple double integrators with unknown bounded inputs," in *Proceedings of the 2018 33rd Youth Academic Annual Conference of Chinese Association of Automation (YAC)*, May 2018.
- [16] S. Mao, *Mobile robot localization in indoor environment*, Zhejiang University, Hangzhou, China, Ph.D. dissertation, 2016.
- [17] J. Yang, "Analysis approach to odometric non-systematic error uncertainty for mobile robots," *Chinese Journal of Mechanical Engineering*, vol. 44, no. 8, pp. 7–12, 2008.
- [18] J. Kang, F. Zhang, and X. Qu, *Angle Measuring Error Analysis of Coordinate Measuring System of Laser Radar*, vol. 40, no. 6, pp. 834–839, 2016.



- [19] J. Zhang, P. Orlik, Z. Sahinoglu, A. Molisch, and P. Kinney, "UWB systems for wireless sensor networks," *Proceedings of the IEEE*, vol. 97, no. 2, pp. 313–331.
- [20] D. Kaushal and T. Shanmuganatham, "Design of a compact and novel microstrip patch antenna for multiband satellite applications," *Materials Today: Proceedings*, vol. 5, no. 10, pp. 21 175–21 182, 2018.
- [21] J. Xiucui, *Data association problem for simultaneous localization and mapping of mobile robots*, National University of Defense Technology, Changsha, China, Ph.D. dissertation, 2008.
- [22] Z. Yuan, "Research of mobile robot's slam based on binocular vision," Master's thesis, Tianjin University of Technology, Tianjin, China, 2016.
- [23] F. Bellavia, M. Fanfani, F. Pazzaglia, and C. Colombo, "Robust selective stereo slam without loop closure and bundle adjustment," in *Proceedings of the International Conference on Image Analysis and Processing*, pp. 462–471, Springer, Naples, Italy, 2013.
- [24] H. Fourati, *Multisensor Data Fusion: From Algorithms and Architectural Design to Applications*, CRC Press, Boca Raton, FL, USA, 2015.
- [25] S. Jia, X. Yin, and X. Li, "Mobile robot parallel pf-slam based on openmp," in *Proceedings of the 2012 IEEE International Conference on Robotics and Biomimetics (ROBIO)*, pp. 508–513, IEEE, Guangzhou, China, December 2012.
- [26] W. Zhou, E. Shiju, Z. Cao, and Y. Dong, "Review of slam data association study," in *Proceedings of the 2016 International Conference on Sensor Network and Computer Engineering*, Atlantis Press, Shanghai, China, 2016.
- [27] R. Singer and R. Sea, "A new filter for optimal tracking in dense multitarget environments," in *Proceedings of the Annual Allerton Conference on Circuit and System Theory*, pp. 201–211, Monticello, MN, USA, 1972.
- [28] J. Neira and J. D. Tardós, "Data association in stochastic mapping using the joint compatibility test," *IEEE Transactions on Robotics and Automation*, vol. 17, no. 6, pp. 890–897, 2001.
- [29] L. Yanju, X. Yufeng, G. Song, H. Xi, and G. Zhengping, "Research on data association in slam based laser sensor," *Microcomputer & Its Application*, vol. 36, no. 2, pp. 78–82, 2017.
- [30] O. Hlinka, O. Slučiak, F. Hlawatsch, and M. Rupp, "Distributed data fusion using iterative covariance intersection," in *Proceedings of the 2014 IEEE International Conference on Acoustics, Speech and Signal Processing (ICASSP)*, pp. 1861–1865, IEEE, Florence, Italy, May 2014.

## Research Article

# Multiconsensus of Nonlinear Multiagent Systems with Intermittent Communication

Jie Chen <sup>1</sup>, Guang-Hui Xu <sup>2</sup>, and Liang Geng<sup>1</sup>

<sup>1</sup>Hubei University of Technology, School of Science, Wuhan 430068, China

<sup>2</sup>Hubei University of Technology, School of Electrical and Electronic Engineering, Wuhan 430068, China

Correspondence should be addressed to Guang-Hui Xu; [xuguanghui29@163.com](mailto:xuguanghui29@163.com)

Received 18 May 2020; Accepted 11 August 2020; Published 27 August 2020

Guest Editor: Hou-Sheng Su

Copyright © 2020 Jie Chen et al. This is an open access article distributed under the Creative Commons Attribution License, which permits unrestricted use, distribution, and reproduction in any medium, provided the original work is properly cited.

Compared with single consensus, the multiconsensus of multiagent systems with nonlinear dynamics can reflect some real-world cases. This paper proposes a novel distributed law based only on intermittent relative information to achieve the multiconsensus. By constructing an appropriate Lyapunov function, sufficient conditions on control parameters are derived to undertake the reliability of closed-loop dynamics. Ultimately, the availability of results is completely validated by these numerical examples.

## 1. Introduction

Multiagent systems have attracted much attention in the field as computer science, vehicle systems, unmanned aerial vehicles, or formation flight of spacecraft since 2009. In most of studies on consensus problem, researchers always adopt the same method that makes all agents finally reach the same value in systems [1–5]. Due to various parameters as sudden changes on environment or cooperative tasks in the reality, the purpose of our research also becomes multiple.

In [6], the consensus problem from asynchronous group of the discrete-time heterogeneous multiagent system under dynamic-change interaction topology is discussed and studied briefly. For different agents, two asynchronous consensus protocols are given in this paper. Based on fixed and switching topology, the multiconsensus of first-order multiagent system is discussed. And we assumed that interactions could reach balance between two subnetworks in [6, 7]. The relationship between multiconsensus ability and the underlying digraph topology is discussed in [8]. For fixed communication networks, the author proposes a consensus protocol which can be applied to two different second-order multiagent systems under the same assumption [9]. By using pinning control method in [10–12], we can obtain some criteria on multiconsensus of networks without assuming the balance of network

topology. For multiconsensus problem from discrete-time multiagent systems with stochastic and fixed topologies, the author performs a professional study in [13]. In [14], the author performs the research on multiconsensus control of switching-directed interaction and fixed topology in common linear multiagent systems, based on pinning control techniques, matrix analysis theory, and Lyapunov stability theory. The cluster consensus of multiagent dynamical systems with impulsive effects and coupling delays was investigated in [15], where interactions among agents were uncertain.

In other words, above conclusion on the consensus of multiagent system with nonlinear dynamics is mostly based on common assumption that information is transmitted continuously between all agents, which means that each single agent shares the information with its neighbors without any communication constraints. However, this is not the fact in reality. For instance, all agents can only get the information from their neighbors during certain disconnected time intervals, as a reason of communication restrictions. In [16–23], intermittent control has attracted more attention. For distributed consensus problem from intermittent control of a time-invariant undirected communication topology in the linear multiagent system, the author designs a type of distributed-observer protocols. In [24], the consensus problem on periodical-intermittent

control of second-order agent networks, which is based on matrix theory, Lyapunov control method, and algebraic graph theory, is discussed. Based on the above discussion and research, this paper mainly studies on some characteristics of the second-order multiagent system, such as multiconsensus. In the same subnet, nonlinear dynamics of all agents are the same, while all agents in different subnet have different dynamics. Multiconsensus indicates that all agents in every subgroup can be consistent. Between different groups, there is no consistent value. The research performed in this paper can be summarized as three points: firstly, the multiconsensus of the multiagent system with nonlinear dynamics is studied. Secondly, a novel multiconsensus law, which is devised through intermittent and relative state information, is more general than other second-order multiconsensus protocol. And, in such a protocol, all agents always need to communicate with their neighbors.

In Section 2 of this paper, the research model has been designed. In Section 3, we perform the study and discussion on the multiconsensus problem of second-order multiagent systems with nonlinear dynamics. In Section 4, two numerical examples are given to prove the effectiveness on the designed protocol. And the conclusion is summarized in Section 5.

## 2. Preliminary

**2.1. Algebraic Graph Theory.** In general, the communication topology between agents in a multiagent system is described by a directed graph. Let  $G = (V, \varepsilon, A)$  be a system communication topology diagram consisting of  $N$  nodes, the vertex set  $V = \{\nu_1, \nu_2, \dots, \nu_n\}$  is nonempty finite, the edge set  $\varepsilon \subseteq V \times V$ , and a nonsymmetric  $A = (a_{ij})_{n \times n}$  is nonnegative weighted adjacency matrix.  $A = (a_{ij})_{n \times n}$  is defined as  $a_{ij} \neq 0$  if  $\varepsilon_{ij} \in \varepsilon$  and  $a_{ij} = 0$  otherwise. There are no self-loops, i.e.,  $a_{ii} = 0$ . The set of neighbors of agent  $i$  is denoted by  $N_i = \{\nu_j \mid \varepsilon_{ij} \in \varepsilon\}$ . A directed path is a sequence of distinct vertices  $1, 2, \dots, r$  such that  $(\nu_i, \nu_j) \in \varepsilon$ ,  $i = 1, 2, \dots, r - 1$ .

**2.2. Problem Description.** Consider a multiagent system with  $n$  agents,  $\nu = \{1, 2, \dots, N\}$ . Suppose the multiagent system composed with  $p$  subgroup,  $\nu_p$  is a set of  $p$  subgroup. Note that the corresponding subtopology graph of each subgroup is  $\mathcal{G}_p$ , and the topology diagram of the whole system is  $G$ . The corresponding numbering sets for each subgroup are  $\nu_1 = \{1, \dots, l_1\}$ ,  $\nu_2 = \{l_1 + 1, \dots, l_1 + l_2\}$ ,  $\nu_p = \{l_1 + l_2 + \dots + l_{p-1} + 1, \dots, N\}$ , and  $l_1 + l_2 + \dots + l_{p-1} + l_p = N$ .  $\nu_i \neq \emptyset$ ,  $\cup_{i=1}^p \nu_i = \nu$ , and  $\nu_i \cap \nu_j \neq \emptyset$  for  $i \neq j$ . For  $i \in \nu$ , let  $\bar{i}$  denote the subscript of the subset to which the integer  $i$  belongs. It is assumed in what follows that each agent knows which cluster it belongs to.

The dynamics of systems is described as follows:

$$\ddot{q}_i(t) = f_{\bar{i}}(q_i, \dot{q}_i, t) + u_i(t), \quad (1)$$

where  $q_i(t) \in R^n$ ,  $\dot{q}_i(t) \in R^n$ , and  $u_i(t) \in R^n$  are the position, velocity, and control input of agent  $i$ , respectively. The function  $f_{\bar{i}}(q_i, \dot{q}_i, t) \in R^n$ , describing the intrinsic dynamics of agent  $i$ , is continuously differentiable.

In this work, the leader in each group is described by

$$\ddot{q}_{\bar{i}}(t) = f_{\bar{i}}(q_{\bar{i}}, \dot{q}_{\bar{i}}, t). \quad (2)$$

**Definition 1.** The multiconsensus control for second-order multiagent systems is said to be achieved if

$$\begin{aligned} \lim_{t \rightarrow \infty} \|q_i(t) - q_{\bar{i}}(t)\| &= 0, \\ \lim_{t \rightarrow \infty} \|\dot{q}_i(t) - \dot{q}_{\bar{i}}(t)\| &= 0. \end{aligned} \quad (3)$$

Firstly, some basic assumptions and lemmas are given as follows:

**Lemma 1.** *There is a constant  $\omega \in R$ , and  $P, Q, M, N$  are matrices with suitable dimensions. Then, the Kronecker product has the following properties:*

$$\begin{aligned} (1) (P \otimes Q)^T &= P^T \otimes Q^T, \\ (2) (\omega P) \otimes Q &= P \otimes (\omega Q), \\ (3) (P + Q) \otimes M &= P \otimes M + Q \otimes M, \\ (4) (P \otimes Q)(M \otimes N) &= (PM \otimes QN). \end{aligned} \quad (4)$$

**Lemma 2.** *The linear matrix inequality*

$$\begin{bmatrix} A(s) & B(s) \\ B^T(s) & C(s) \end{bmatrix} > 0, \quad (5)$$

where  $A(s) = A^T(s)$ ,  $C(s) = C^T(s)$ , and  $B(s)$  depend affinely on  $s$ , which is equivalent to  $C(s) > 0$ ,  $A(s) - B(s)C^{-1}(s)B^T(s) > 0$ .

**Lemma 3.** *Suppose that  $S \in R^{n \times n}$  is positive definite and  $D \in R^{n \times n}$  is symmetric. Then, for  $\forall x \in R^n$ , the following inequality holds:*

$$\lambda_{\min}(S^{-1}D)x^T Sx \leq x^T D x \leq \lambda_{\max}(S^{-1}D)x^T Sx. \quad (6)$$

**Assumption 1**

- (1)  $\sum_{j=N+1}^{N+M} a_{ij} = 0$  for all  $i \in l_1$ ,  $\sum_{j=1}^N a_{ij} = 0$  for all  $i \in l_2$
- (2) The subgraph  $G_1$  and  $G_2$  have a directed spanning tree, respectively

**Assumption 2.** There exist nonnegative constants  $p$  and  $q$  such that nonlinear function satisfies the following equality:

$$\|f_{\bar{i}}(x_i, v_i, t) - f_{\bar{i}}(y_i, z_i, t)\| \leq p_{\bar{i}} \|x_i - y_i\|^2 + q_{\bar{i}} \|v_i - z_i\|^2, \quad (7)$$

where  $x, y, v, z \in R^n$ ,  $\forall t \geq 0$ .

## 3. Main Results

In this section, the multiconsensus of multiagent system is analyzed.

The distributed feedback controller of agent  $i$  is designed as

$$\begin{cases} u_i(t) = \alpha \sum_{j=1}^N a_{ij} [(q_j - q_i) + (\dot{q}_j - \dot{q}_i)] \\ \quad - \alpha d_i [(q_i - q_{\bar{i}}) + (\dot{q}_i - \dot{q}_{\bar{i}})], \\ \quad t \in [kH, kH + \delta), \\ u_i(t) = 0, \quad t \in [kH + \delta, (k+1)H), \end{cases} \quad (8)$$

where  $H > 0$  is the control period and  $\delta > 0$  is called the control time width.

Let  $\tilde{q}_i(t) = q_i(t) - q_{\bar{i}}(t)$  and  $\tilde{\dot{q}}_i(t) = \dot{q}_i(t) - \dot{q}_{\bar{i}}(t)$  are the measurement error of position and velocity of the  $i$ th agent.

Note that if  $j \in V(G_k)$ , then  $\bar{j} = k$  and  $\tilde{q}_j(t) = q_j(t) - q_{\bar{k}}(t)$ . We then observe

$$\begin{aligned} & \sum_{j=1}^N a_{ij} (q_j(t) - q_i(t)) \\ &= - \sum_{k=1}^p \sum_{j \in V(G_k)} l_{ij} q_j(t) \\ &= - \sum_{k=1}^p \sum_{j \in V(G_k)} l_{ij} (q_j(t) - q_{\bar{k}}(t) + q_{\bar{k}}(t)) \\ &= - \sum_{j=1}^N l_{ij} \tilde{x}_j(t) - \sum_{k=1}^p \left( \sum_{j \in V(G_k)} l_{ij} \right) q_{\bar{k}}(t) \sum_{j=1}^N a_{ij} (\tilde{x}_j(t) - \tilde{q}_i(t)). \end{aligned} \quad (9)$$

Obviously,  $\sum_{j=1}^N a_{ij} ((\dot{q})_j(t) - \dot{q}_i(t)) = \sum_{j=1}^N a_{ij} (\tilde{\dot{q}}_j(t) - \tilde{\dot{q}}_i(t))$ , which in turn together (1) and (2) yields the conclusion

$$\begin{cases} \tilde{\dot{q}}_i(t) = f_i(q_i, \dot{q}_i, t) - f_i(q_{\bar{i}}, \dot{q}_{\bar{i}}, t), \\ -\alpha \sum_{j \in V} a_{ij} (\tilde{q}_j(t) - \tilde{q}_i(t) + \tilde{\dot{q}}_j(t) - \tilde{\dot{q}}_i(t)), \\ -\alpha d_i (\tilde{q}_i(t) + \tilde{\dot{q}}_i(t)), \quad t \in [kH, kH + \delta), \\ \tilde{\dot{q}}_i(t) = f_i(q_i, \dot{q}_i, t) - f_i(q_{\bar{i}}, \dot{q}_{\bar{i}}, t), \\ t \in [kH + \delta, (k+1)T). \end{cases} \quad (10)$$

Define  $\tilde{q}(t) = (\tilde{q}_1^T(t), \tilde{q}_2^T(t), \dots, \tilde{q}_N^T(t))^T$  and  $\tilde{\dot{q}}(t) = (\tilde{\dot{q}}_1^T(t), \tilde{\dot{q}}_2^T(t), \dots, \tilde{\dot{q}}_N^T(t))^T$ .

Then, system (10) can be rewritten as

$$\begin{cases} \tilde{\dot{q}}(t) = F_i(q(t), \dot{q}(t), t) - \tilde{F}_i(q_{\bar{i}}(t), \dot{q}_{\bar{i}}(t), t), \\ -\alpha(L + D) \otimes I_n (\tilde{q}(t) + \tilde{\dot{q}}(t)), \\ t \in [kH, kH + \delta), \\ \tilde{\dot{q}}_i(t) = F_i(q(t), \dot{q}(t), t) - \tilde{F}_i(q_{\bar{i}}(t), \dot{q}_{\bar{i}}(t), t), \\ t \in [kH + \delta, (k+1)T). \end{cases} \quad (11)$$

where  $F(q(t), \dot{q}(t), t) = (f_1^H(q_1(t), \dot{q}_1(t), t), \dots, f_N^H(q_N(t), \dot{q}_N(t), t))^H$ ,  $\tilde{F}(\tilde{q}(t), \tilde{\dot{q}}(t), t) = (f_{\bar{1}}^H(q_{\bar{1}}(t), \dot{q}_{\bar{1}}(t), t), \dots, f_{\bar{N}}^H(q_{\bar{N}}(t), \dot{q}_{\bar{N}}(t), t))^H$ ,  $D = \text{diag}\{d_1, \dots, d_N\}$ .

**Theorem 1.** Under Assumption 1 and Assumption 2, system (1) can reach the multiconsensus if the parameters meet the following conditions:

$$\rho I_N - \frac{\alpha}{2} \bar{L} - \alpha D < 0, \quad (12)$$

$$\delta > \frac{\gamma}{\gamma + \eta} T, \quad (13)$$

where  $\rho = \max\{p, q + 1\}$ ,  $p = \max\{p_i\}$ ,  $q = \max\{q_i\}$ ,  $\gamma = 2$

$$\begin{aligned} \lambda_{\max}(\Omega^{-1}M), \eta = (\lambda_{\min}(Q)/\lambda_{\max}(\Omega)), \Omega = \begin{bmatrix} \alpha \bar{L} + 2\alpha D & I_N \\ I_N & I_N \end{bmatrix}, \\ Q = \begin{bmatrix} \alpha(\bar{L}/2) + \alpha D - pI_N & 0_N \\ 0_N & \alpha(\bar{L}/2) + \alpha D - (q+1)I_N \end{bmatrix}, \quad M = \\ \begin{bmatrix} pI_N & (\alpha/2)\bar{L} + \alpha D \\ (\alpha/2)\bar{L} + \alpha D & (q+1)I_N \end{bmatrix}, \text{ and } \bar{L} = L + L^T. \end{aligned}$$

*Proof.* It follows from (12) that

$$\begin{aligned} \alpha \frac{\bar{L}}{2} + \alpha D - \rho I_N > 0, \\ \begin{bmatrix} \alpha \bar{L} + 2\alpha D & I_N \\ I_N & I_N \end{bmatrix} > 0. \end{aligned} \quad (14)$$

Define the Lyapunov function for system (12):

$$V(t) = \frac{1}{2} \tilde{y}^T(t) (\Omega \otimes I_n) \tilde{y}(t), \quad (15)$$

where  $\Omega = \begin{bmatrix} \alpha \bar{L} + 2\alpha D & I_N \\ I_N & I_N \end{bmatrix}$  and  $\tilde{y}(t) = (\tilde{q}^T(t), \tilde{\dot{q}}^T(t))^T$ .

In view of (8), we know that Lyapunov function (15) satisfies  $V(t) \geq 0$  and  $V(t) = 0$  if and only if  $\tilde{q}(t) = \tilde{\dot{q}}(t) = 0$ .

$$V(t) = \frac{1}{2} \tilde{q}^T [(\alpha \bar{L} + 2\alpha D) \otimes I_n] \tilde{q} + \tilde{q}^T \tilde{\dot{q}} + \frac{1}{2} \tilde{\dot{q}}^T \tilde{\dot{q}}. \quad (16)$$

For  $t \in [kH, t_0 + kH + \delta)$ , the time derivative of  $V(t)$  along the trajectories of system (11) gives

$$\begin{aligned} \dot{V}(t) &= \tilde{q}^T [(\alpha \bar{L} + 2\alpha D) \otimes I_n] \dot{\tilde{q}} + \dot{\tilde{q}}^T \tilde{\dot{q}} + \tilde{q}^T \dot{\tilde{\dot{q}}} + \tilde{\dot{q}}^T \dot{\tilde{\dot{q}}} \\ &= -\tilde{q}^T [(\alpha L + \alpha D) \otimes I_n] \tilde{q} + \tilde{q}^T [(I_N - \alpha L - \alpha D) \otimes I_n] \tilde{\dot{q}} \\ &\quad + (\tilde{q} + \tilde{\dot{q}}) (F_i(q(t), \dot{q}(t), t) - \tilde{F}_i(\tilde{q}(t), \tilde{\dot{q}}(t), t)). \end{aligned} \quad (17)$$

Then, by (A1), we get

$$\begin{aligned}
(\tilde{q}^T + \tilde{q}^T)(F_i(q(t), \dot{q}(t), t) - \tilde{F}_i(\bar{q}(t), \bar{q}(t), t)) &= \sum_{i=1}^N (\tilde{q}_i(t) + \tilde{q}_i(t))^T (f_i(q_i, \dot{q}_i, t) - f_i(\tilde{q}_i, \dot{\tilde{q}}_i, t)) \\
&= \sum_{i=1}^N (p_i \|\tilde{q}_i(t)\|^2 + q_i \|\tilde{q}_i(t)\|^2) \leq \tilde{q}^T (pI_N \otimes I_n) \tilde{q} + \tilde{q}^T (qI_N \otimes I_n) \tilde{q}.
\end{aligned} \tag{18}$$

It follows from (17) and (18) that

$$\begin{aligned}
\dot{V}(t) &\leq -\tilde{q}^T \left[ \left( \alpha \frac{\bar{L}}{2} + \alpha D \right) \otimes I_n \right] \tilde{q} + \tilde{q}^T (qI_N \otimes I_n) \tilde{q} \tilde{q}^T \left[ \left( I_N - \alpha \frac{\bar{L}}{2} - \alpha D \right) \otimes I_n \right] \tilde{q} + \tilde{q}^T (pI_N \otimes I_n) \tilde{q} \\
&= \tilde{q}^T \left[ \left( -\alpha \frac{\bar{L}}{2} - \alpha D + pI_N \right) \otimes I_n \right] \tilde{q} + \tilde{q}^T \left[ \left( -\alpha \frac{\bar{L}}{2} - \alpha D + (q+1)I_N \right) \otimes I_n \right] \tilde{q} = -\tilde{y}^T [Q \otimes I_n] \tilde{y},
\end{aligned} \tag{19}$$

where  $Q = \begin{pmatrix} \alpha(\bar{L}/2) + \alpha D - pI_N & 0_N \\ 0_N & \alpha(\bar{L}/2) + \alpha D - (q+1)I_N \end{pmatrix}$ .

In view of condition (12), we can get  $Q > 0$ . It is known that Lyapunov function satisfies that

$$\lambda_{\min}(\Omega) \|\tilde{y}(t)\|^2 \leq V(t) \leq \lambda_{\max}(\Omega) \|\tilde{y}(t)\|^2. \tag{20}$$

Thus, one has

$$\dot{V}(t) \leq -\frac{\lambda_{\min}(Q)}{\lambda_{\max}(\Omega)} V(t) = -\eta V(t), \tag{21}$$

where  $\eta = (\lambda_{\min}(Q)/\lambda_{\max}(\Omega))$ .

For  $t \in [kH + \delta, (k+1)T)$ , taking the time derivative of  $V(t)$  along the trajectories of system (11)

$$\dot{V}(t) = \tilde{q}^T [(\alpha \bar{L} + 2\alpha D) \otimes I_n] \dot{\tilde{q}} + \tilde{q}^T \dot{H} \tilde{q} + \tilde{q}^T \dot{\tilde{q}} + \tilde{q}^T \tilde{q} \leq \tilde{y}^T \left( \begin{pmatrix} pI_N & \alpha \bar{L} + \alpha D \\ \alpha \bar{L} + \alpha D & (q+1)I_N \end{pmatrix} \otimes I_n \right) \tilde{y} \tag{22}$$

$$\tilde{y} \leq \tilde{y}^T [M \otimes I_n] \tilde{y} \leq 2\lambda_{\max}(\Omega^{-1}M) V(t) = \gamma V(t),$$

where  $M = \begin{bmatrix} pI_N & (\alpha/2)\bar{L} + \alpha D \\ (\alpha/2)\bar{L} + \alpha D & (q+1)I_N \end{bmatrix}$  and  $\gamma = 2\lambda_{\max}(\Omega^{-1}M)$ .

Then, by the above differential inequality (21) and (22), we have the following results:

(1) For  $0 < t < \delta$ ,  $V(t) \leq V(0)e^{-\eta t}$  and  $V(\delta) \leq V(0)e^{-\eta \delta}$

(2) For  $\delta \leq t < H$ ,  $V(t) \leq V(\delta)e^{\gamma(t-\delta)} \leq V(0)e^{\gamma(t-\delta)-\eta\delta}$  and  $V(H) \leq V(0)e^{\gamma(H-\delta)-\eta\delta}$

(3)  $H \leq t < H + \delta$ ,  $V(t) \leq V(H)e^{-\eta(t-H)} \leq V(0)e^{\gamma(H-\delta)-\eta\delta-\eta(t-H)}$ , and  $V(H + \delta) \leq V(0)e^{\gamma(H-\delta)-2\eta\delta}$

(4)  $H + \delta \leq t < 2H$ ,  $V(t) \leq V(H + \delta)e^{\gamma(t-H-\delta)} \leq V(0)e^{\gamma(H-\delta)+\gamma(t-H-\delta)-2\eta\delta}$  and  $V(2H) \leq V(0)e^{\gamma(H-\delta)+\gamma(H-\delta)-2\eta\delta} = V(0)e^{2\gamma(H-\delta)-2\eta\delta}$

Thus, one has

For  $kH \leq t \leq kH + \delta$ ,

$$\begin{aligned}
V(t) &\leq V(kH)\exp(-\eta(t-kH)) \\
&\leq V(0)\exp(k\gamma(H-\delta) - k\eta\delta - \eta(t-kH)) \\
&\leq V(0)\exp\left(-\frac{\eta\delta - \gamma(H-\delta)}{H}(t-\delta)\right)\exp\left(\frac{H-\delta}{H}\gamma\delta\right) \\
&\leq V(0)\exp\left(-\frac{\eta\delta - \gamma(H-\delta)}{H}(t-\delta)\right)\exp(\gamma(H-\delta)).
\end{aligned} \tag{23}$$

For  $kH + \delta \leq t < (k+1)H$ ,

$$\begin{aligned}
V(t) &\leq V(kH + \delta)e^{\gamma(t-kH-\delta)} \\
&\leq V(0)\exp(k+1)\gamma((H-\delta-k+1)\eta\delta) \\
&\leq V(0)\exp\left(-\frac{\eta\delta - \gamma(H-\delta)}{H}(t-\delta)\right)\exp(\gamma(H-\delta)).
\end{aligned} \tag{24}$$

If  $\delta > (\gamma/\gamma + \eta)H$ , then defining  $\xi = (\eta\delta - (H - \delta)\gamma/H) > 0$ . Let  $K = V(0)\exp((\eta\delta - \gamma(H - \delta)/H)\delta)\exp(\gamma(H - \delta))$ , and from the above analysis, we can draw the following conclusions:

$$V(t) \leq Ke^{-(\eta\delta - \gamma(H - \delta)/H)t}. \quad (25)$$

Therefore, the multiconsensus can be achieved. The proof is completed.

*Remark 1.* Under the condition of Theorem 1, the multiconsensus of system (1) can be achieved globally exponentially with the presented law.

*Remark 2.* When each agent has the identical nonlinear function, all the agents have the same virtual leader. The dynamics of the virtual leader can be described as

$$\ddot{q}_r(t) = f(q_r, \dot{q}_r, t). \quad (26)$$

Under the intermittent control, system (1) can reach consensus.

**Theorem 2.** Under Assumption 1 and Assumption 2, system (1) can reach the multiconsensus if the parameter meets the following conditions:

$$\begin{cases} \ddot{\tilde{q}}_i(t) = -\alpha \sum_{j \in V} a_{ij}(\tilde{q}_j(t) - \tilde{q}_i(t) + \tilde{q}_j(t) - \tilde{q}_i(t)) - \alpha d_i(\tilde{q}_i(t) + \tilde{\dot{q}}_i(t)), & t \in [kH, kH + \delta), \\ \ddot{\tilde{q}}_i(t) = 0, & t \in [kH + \delta, (k + 1)H). \end{cases} \quad (29)$$

where  $i = 1, 2, \dots, N$ . System (29) can be rewritten as

$$\begin{cases} \ddot{\tilde{q}}(t) = -((\alpha(L + D) \otimes I_n)(\tilde{q}(t) + n\tilde{\dot{q}}(t))), & t \in [kH, kH + \delta), \\ \ddot{\tilde{q}}(t) = 0, & t \in (kH + \delta, (k + 1)H). \end{cases} \quad (30)$$

The proof of this part is similar to that of Theorem 1, which is omitted here.

#### 4. Numerical Simulations

In this part, the effectiveness of presented theoretical results has been proven by numerical examples. The multiconsensus of second-order agent systems has been studied. Actually, seven agents can form a second-order system which is split into two clusters  $\nu_1 = \{1, 2, 3\}$  and  $\nu_2 = \{4, 5, 6, 7\}$ . If  $i \in \nu_1$ , then  $\hat{i} = 1$ ; and if  $i \in \nu_2$ , then  $\hat{i} = 2$ .

The Laplacian matrix is given as follows:

$$\begin{aligned} (1) \quad I_N - \frac{\alpha}{2}\bar{L} - \alpha D &< 0, \\ (2) \quad \delta &> \frac{\gamma}{\gamma + \eta}T, \end{aligned} \quad (27)$$

where  $\rho = \max\{\rho_1, \rho_2 + 1\}$ ,  $\gamma = 2\lambda_{\max}(\Omega^{-1}M)$ ,  $\eta = (\lambda_{\min}(Q)/\lambda_{\max}(\Omega))$ ,  $\bar{L} = L + L^T$ ,  $\Omega = \begin{bmatrix} \alpha\bar{L} + 2\alpha D & I_N \\ I_N & I_N \end{bmatrix}$ ,  $Q = \begin{bmatrix} \alpha(\bar{L}/2) + \alpha D & 0_N \\ 0_N & \alpha(\bar{L}/2) + \alpha D - I_N \end{bmatrix}$ , and  $M = \begin{bmatrix} 0 & (\alpha/2)\bar{L} + \alpha D \\ (\alpha/2)\bar{L} + \alpha D & I_N \end{bmatrix}$ .

When  $f(q_i, \dot{q}_i, t) = 0$ , the dynamics of the  $i$ th agent can be described as follows:

$$\ddot{q}_i(t) = u_i(t). \quad (28)$$

Then, (28) shows that the velocity of virtual leader is constant. Under protocol (8), let  $\tilde{q}_i(t) = q_i(t) - q_i^*(t)$ ,  $\tilde{\dot{q}}_i(t) = \dot{q}_i(t) - \dot{q}_i^*(t)$ , then the closed-loop system (28) becomes:

$$L = \begin{bmatrix} 3 & -3 & 0 & 1 & 0 & 0 & -1 \\ -2 & 3 & -1 & -1 & 0 & 0 & 1 \\ -1 & 0 & 1 & 0 & 0 & 0 & 0 \\ 1 & -1 & 0 & 2 & 0 & 0 & -2 \\ 0 & 0 & 0 & -1 & 1 & 0 & 0 \\ 0 & 0 & 0 & 0 & -1 & 1 & 0 \\ -1 & 1 & 0 & -2 & 0 & -1 & 3 \end{bmatrix}, \quad (31)$$

$$D = \text{diag}\{3, 0, 0, 3, 0, 0, 0\}.$$

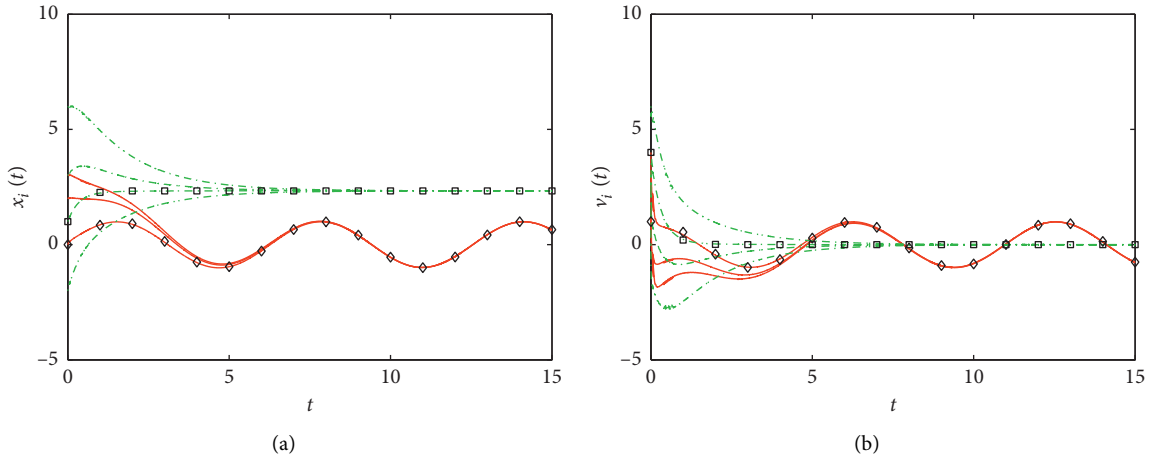


FIGURE 1: The trajectories of the agents.

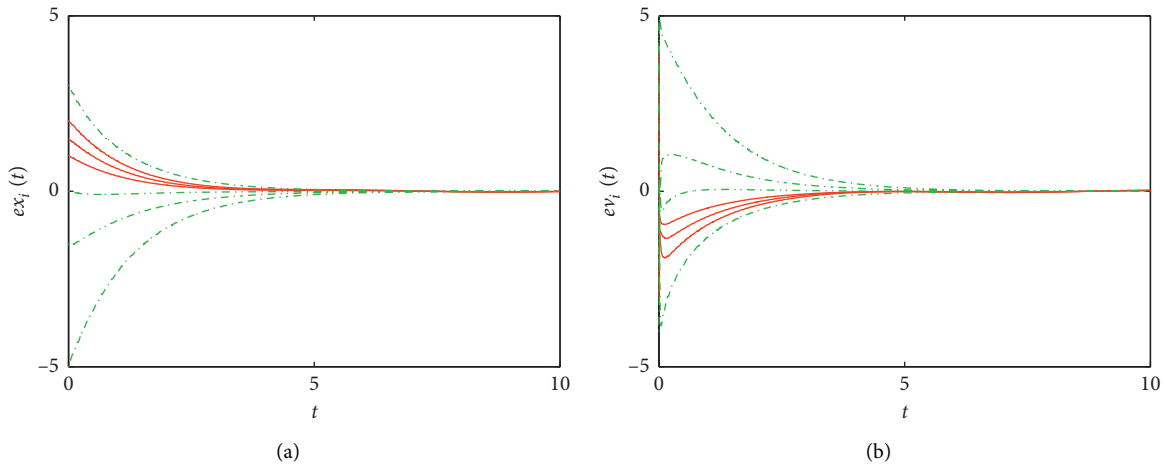


FIGURE 2: The error trajectories of the agents.

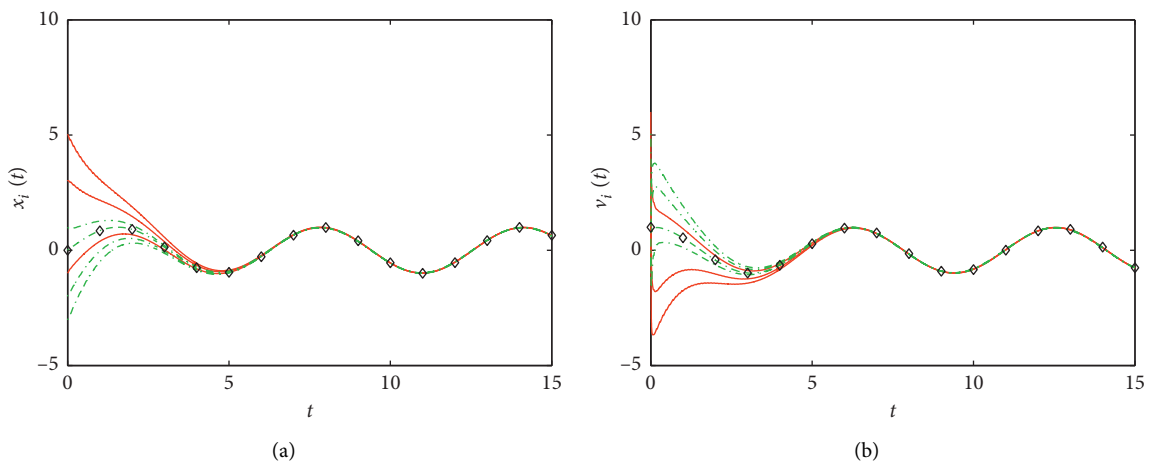


FIGURE 3: The trajectories of the agents.

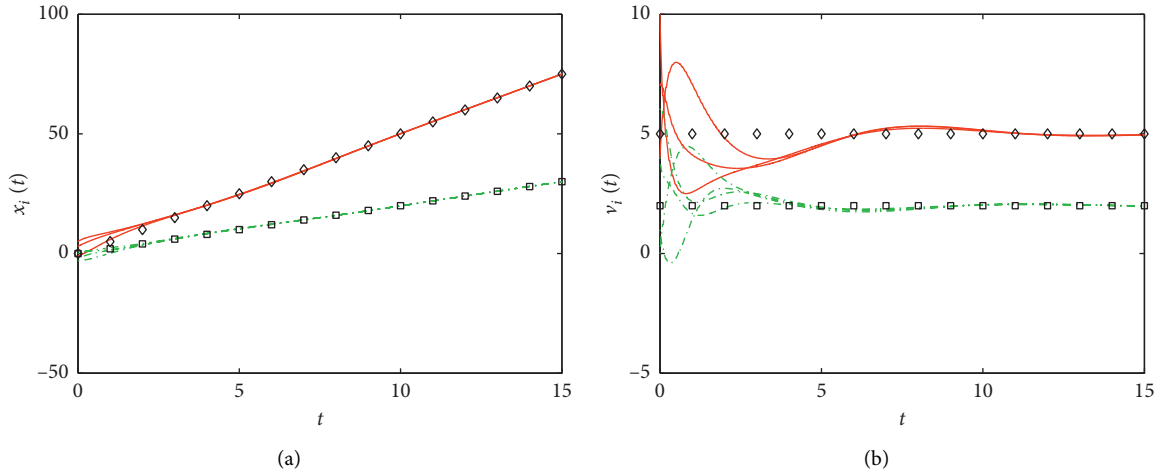


FIGURE 4: The trajectories of the agents.

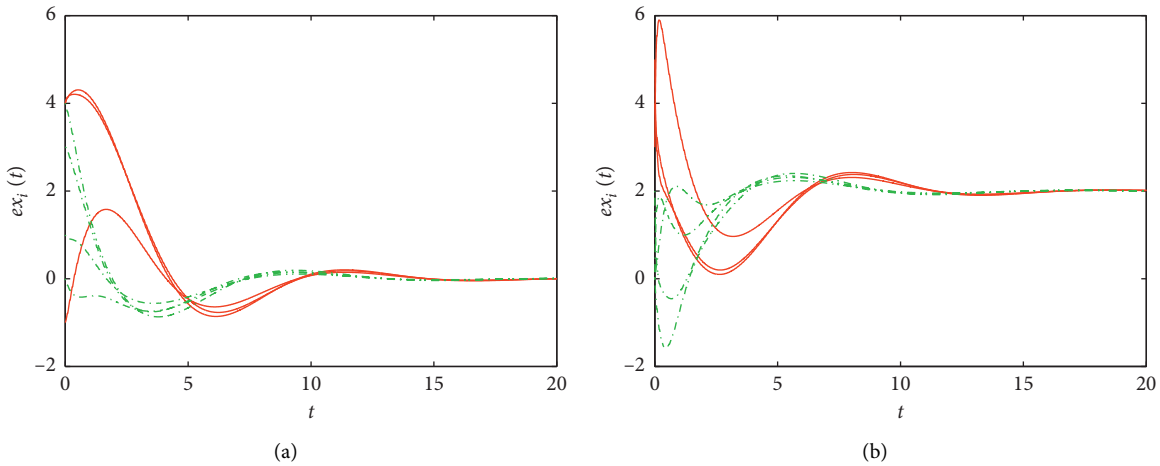


FIGURE 5: The error trajectories of the agents.

*Case 1.* Set  $f_1(x_i, v_i, t) = -x_i$  and  $f_2(x_i, v_i, t) = -3v_i$ . By Assumption 2,  $p_1 = 1, q_1 = 0$ , and  $p_2 = 0, q_2 = 3$ . Then,  $\rho = 4$ . In view of condition (12), we can choose  $\alpha = 15$ . By condition (13), we choose  $\delta = 0.08$ . The initial position and velocity of the virtual leader are given as follows:

$$\begin{aligned} (q_1(0), \dot{q}_1(0)) &= (0, 1), \\ (q_2(0), \dot{q}_2(0)) &= (1, 4). \end{aligned} \quad (32)$$

Figure 1 shows the states and velocity of the virtual leaders and followers. It is easy to see that the multiconsensus of systems (1) can be received. The error tracks of the agents are depicted in Figure 2.

When  $f_1(x_i, v_i, t) = f_2(x_i, v_i, t) = -x_i$ , as shown in Figure 3, the consensus problem of system (1) is indeed solved.

*Case 2.* Let  $f_1(x_i, v_i, t) = 0$  and  $f_2(x_i, v_i, t) = 0$ . The initial velocity of the virtual leader are given as follows:  $v_1(0) = 2$  and  $v_2(0) = 5$ . The multiconsensus of the

systems can be achieved. As a special case, when the initial velocity of the virtual leader is same, the system reaches consensus. The simulation result is shown in Figures 4 and 5, which show that the multiconsensus can be achieved.

## 5. Conclusion

In this paper, we have studied on multiconsensus of second-order multiagent systems with nonlinear dynamics. For the realization of multiconsensus, a distributed protocol based on intermittent relative information has been proposed. Some of sufficient conditions have been given to ensure that the states of all agents could reach more consistent values. In this paper, two simulation examples are given and applied to the effectiveness of theoretical results.

## Data Availability

All data included in this study are available upon request by contact with the corresponding author.



## Conflicts of Interest

The authors declare no potential conflicts of interest with respect to the research, authorship, and/or publication of this article.

## Acknowledgments

This work was supported in part by the Natural Science Foundation of Hubei Province (2016CFB514) and the Research Fund for the Doctoral Program of Hubei University of Technology (nos. BSQD2015044, BSQD2015024, BSQD2019050).

## References

- [1] X.-W. Jiang, X.-Y. Chen, T.-W. Huang, and H.-C. Yan, "Output tracking control of single-input multi-output systems over an erasure channel," *IEEE Transactions on Cybernetics*, pp. 1–9, 2020.
- [2] H. Su, H. Wu, and J. Lam, "Positive edge-consensus for nodal networks via output feedback," *IEEE Transactions on Automatic Control*, vol. 64, no. 3, pp. 1244–1249, 2019.
- [3] J.-W. Sun, G.-Y. Han, Z. Zeng, and Y.-F. Wang, "Memristor-based neural network circuit of full-function pavlov associative memory with time delay and variable learning rate," *IEEE Transactions on Cybernetics*, pp. 1–11, 2019.
- [4] J. Sun, Y. Wu, G. Cui, and Y. Wang, "Finite-time real combination synchronization of three complex-variable chaotic systems with unknown parameters via sliding mode control," *Nonlinear Dynamics*, vol. 88, no. 3, pp. 1677–1690, 2017.
- [5] G.-H. Xu, F. Qi, Q. Lai, and H. Ho-Ching Iu, "Fixed time synchronization control for bilateral teleoperation mobile manipulator with nonholonomic constraint and time delay," *IEEE Transactions on Circuits and Systems II: Express Briefs*, p. 1, 2020.
- [6] J. Yu and L. Wang, "Group consensus in multi-agent systems with switching topologies and communication delays," *Systems & Control Letters*, vol. 59, no. 6, pp. 340–348, 2010.
- [7] J. Yu and L. Wang, "Group consensus of multi-agent systems with directed information exchange," *International Journal of Systems Science*, vol. 43, no. 2, pp. 334–348, 2012.
- [8] S. Monaco and L. Ricciardi Celsi, "On multi-consensus and almost equitable graph partitions," *Automatica*, vol. 103, pp. 53–61, 2019.
- [9] Y. Feng, S. Xu, and B. Zhang, "Group consensus control for double-integrator dynamic multiagent systems with fixed communication topology," *International Journal of Robust and Nonlinear Control*, vol. 24, no. 3, pp. 532–547, 2014.
- [10] X.-Q. Lu, A. Francis, and S.-H. Chen, "Cluster consensus of nonlinearly coupled multi-agent systems in directed graphs," *Chinese Physics Letters*, vol. 27, no. 5, pp. 1089–1095, 2010.
- [11] X.-Q. Lu, F. Austin, and S.-H. Chen, "Cluster consensus of second-order multi-agent systems via pinning control," *Chinese Physics B*, vol. 19, no. 12, pp. 1–7, Article ID 120506, 2010.
- [12] X. Liao and L. Ji, "On pinning group consensus for dynamical multi-agent networks with general connected topology," *Neurocomputing*, vol. 135, pp. 262–267, 2014.
- [13] H. Zhao and J. H. Park, "Group consensus of discrete-time multi-agent systems with fixed and stochastic switching topologies," *Nonlinear Dynamics*, vol. 77, no. 4, pp. 1297–1307, 2014.
- [14] J. Qin and C. Yu, "Cluster consensus control of generic linear multi-agent systems under directed topology with acyclic partition," *Automatica*, vol. 49, no. 9, pp. 2898–2905, 2013.
- [15] G. Wang and Y. Shen, "Second-order cluster consensus of multi-agent dynamical systems with impulsive effects," *Communications in Nonlinear Science and Numerical Simulation*, vol. 19, no. 9, pp. 3220–3228, 2014.
- [16] G. Wen, Z. Li, Z. Duan, and G. Chen, "Distributed consensus control for linear multi-agent systems with discontinuous observations," *International Journal of Control*, vol. 86, no. 1, pp. 95–106, 2013.
- [17] L. Xiao and X. Liao, "Periodic intermittent consensus of second-order agents networks with nonlinear dynamics," *International Journal of Control, Automation and Systems*, vol. 12, no. 1, pp. 23–28, 2014.
- [18] Y. Gao and L. Wang, "Consensus of multiple double-integrator agents with intermittent measurement," *International Journal of Robust and Nonlinear Control*, vol. 20, pp. 1140–1155, 2010.
- [19] G. Wen, Z. Duan, W. Yu, and G. Chen, "Consensus of second-order multi-agent systems with delayed nonlinear dynamics and intermittent communications," *International Journal of Control*, vol. 86, no. 2, pp. 322–331, 2013.
- [20] A. Hu, J. Cao, and M. Hu, "Consensus of leader-following multi-agent systems in time-varying networks via intermittent control," *International Journal of Control, Automation and Systems*, vol. 12, no. 5, pp. 969–976, 2014.
- [21] G.-H. Xu, M. Xu, M.-F. Ge, T.-F. Ding, F. Qi, and M. Li, "Distributed event-based control of hierarchical leader-follower networks with time-varying layer-to-layer delays," *Energies*, vol. 13, no. 7, p. 1808, 2020.
- [22] Z. Peng, D. Wang, G. Sun, and H. Wang, "Distributed cooperative stabilisation of continuous-time uncertain nonlinear multi-agent systems," *International Journal of Systems Science*, vol. 45, no. 10, pp. 2031–2041, 2014.
- [23] H. Su, G. Jia, and M. Z. Q. Chen, "Semi-global containment control of multi-agent systems with intermittent input saturation," *Journal of The Franklin Institute*, vol. 352, no. 9, pp. 3504–3525, 2015.
- [24] G. Wen, Z. Peng, A. Rahmani, and Y. Yu, "Distributed leader-following consensus for second-order multi-agent systems with nonlinear inherent dynamics," *International Journal of Systems Science*, vol. 45, no. 9, pp. 1892–1901, 2014.

## Research Article

# An Efficient Nodes Failure Recovery Management Algorithm for Mobile Sensor Networks

Rab Nawaz Jadoon <sup>1,2</sup>, Adnan Anwar Awan,<sup>3</sup> Muhammad Amir Khan <sup>3</sup>,  
WuYang Zhou <sup>1</sup> and Aamir Shahzad<sup>3</sup>

<sup>1</sup>Key Laboratory of Wireless-Optical Communication, University of Science and Technology China, Hefei 230027, China

<sup>2</sup>Department of Computer Science, COMSATS University, Islamabad, Abbottabad Campus 22060, Pakistan

<sup>3</sup>Department of Electrical and Computer Engineering, COMSATS University, Islamabad, Abbottabad Campus, Pakistan

Correspondence should be addressed to Rab Nawaz Jadoon; [rabnawaz@mail.ustc.edu.cn](mailto:rabnawaz@mail.ustc.edu.cn) and WuYang Zhou; [wyzhou@ustc.edu.cn](mailto:wyzhou@ustc.edu.cn)

Received 17 March 2020; Revised 25 June 2020; Accepted 3 August 2020; Published 19 August 2020

Guest Editor: Hou-Sheng Su

Copyright © 2020 Rab Nawaz Jadoon et al. This is an open access article distributed under the Creative Commons Attribution License, which permits unrestricted use, distribution, and reproduction in any medium, provided the original work is properly cited.

Wireless sensor networks are not prone to harsh environments and may fail due to various reasons. Failure of sensor nodes causes partitioning of network into various small segments and restricts the communication of nodes. Due to the significant importance of restoration mechanisms, many approaches have been proposed in the literature so far. However, these approaches do not focus on uniform distribution of sensor nodes before the occurrence of failure. This paper fulfills the shortcoming in the literature by proposing a Uniform Distribution and Recovery Algorithm (UDRA) in two parts. The first part (prefailure algorithm) focuses on preparing the mobile sensor nodes to be ready for the failure beforehand by maintaining half of their communication distance between them. Also, it uses a novel method of directional matrix based on one-hop information. By using this method, each mobile node declares itself as cut-vertex (CV), intermediate node, or leaf node. The second part of the algorithm (postfailure algorithm) gives complete recovery procedure in the network by its recovery nodes. The extensive simulations prove that the proposed algorithm supersedes the existing approaches.

## 1. Introduction

Wireless sensor networks (WSNs) are an active area of interest for the researchers and engineering communities. A WSN is typically a network of distributed sensor nodes collecting data from the environment to monitor the physical conditions of that environment. The distributed nodes are of two types, namely, stationary nodes and mobile nodes. Stationary nodes remain stationary and perform sensing activities, routing of data, or act as sink nodes, whereas mobile nodes move around the network to perform sensing and different tasks like replacing failed nodes and may be equipped with different equipment such as fire extinguisher and guns to shoot enemies. These mobile nodes are known as actor nodes and such type of network is called Wireless Sensor and Actor Networks (WSANs). Actors have many capabilities, such as processing of sensed data,

decision making, and performing suitable actions as mentioned above. Robotic Mule [1] is an example of such an actor designed for military use for detection of mines in a battlefield. These distributed nodes are connected to a sink node, which is further connected to the wired world for the usage of the data.

The data provided by the sensor nodes may be used for monitoring the area to make suitable decisions and strategies. For example, in agriculture, this data may be used to make strategies for controlling temperature for different crops or in military decisions this data may be used to make movements of troops and other military equipment according to the enemy strength along the border. These kinds of networks are most suitable for harsh environments in which awareness of the surroundings is critical without compromising human lives. WSNs are very effective for many applications in important domains such as security

systems, surveillance, battlefield reconnaissance, space exploration, search and rescue, and deep sea exploration [2]. The performance of WSNs totally depends upon the fact that the sensor nodes remain connected to the sink node for sending data, as there may be some nodes which are positioned far away from the sink node and need many hops through their neighboring nodes to transmit their data [3, 4] to sink node. Another important fact is that the sensor nodes must cover maximum part of the monitored area for the maximum awareness of the environment.

Achieving connectivity and coverage in an integrated manner is practically a challenging task. One of the challenges is the design of sensor nodes as sensor nodes are small, having limited resources for processing and storage. In order to maintain WSN, mainly batteries are used as the central source of power for these sensor nodes [5], as the batteries used have limited power and get drained with the passage of time resulting in failure of nodes. Another challenging issue is that, in harsh environment such as a battlefield, the sensor nodes may be destroyed by the explosives. Failure of a node or multiple nodes may affect the connectivity and may cause partitioning of the network into multiple disjoint segments, which restricts many nodes from transmitting their data to the sink node. This may also cause connectivity and coverage holes in the area, which compromises monitoring process of the environment. Ineffective monitoring of the environment may cause harm to the entire network or fail to achieve objectives of monitoring because an unattended danger might be present in the coverage hole. Hence, restoration of connectivity and coverage for the network is of utmost importance.

A solution to this problem is to deploy fresh nodes replacing the dead ones which is a costly and sometimes infeasible process. The restoration process must be self-healing, self-organized, and fault tolerant [6] which makes sensor nodes useful in scenarios with minimum or no human interaction. Generally, sensor nodes are deployed in a random manner which creates a highly connected network in some areas and leaves the other areas partially connected. As coverage area may be compromised in such situations, sensor nodes must be capable of adjusting themselves in such a way that their distribution in the area becomes uniform and maximum coverage is attained. Usually, the distribution is supervised by the sink node which can process data and make decisions, but this method increases the overall communication overhead as the decisions must pass the entire network in form of messages and incur delay. Therefore, it is highly recommended that nodes must arrange themselves to decrease the overall messages in the network.

Uniform distribution of actor nodes has already been discussed in [7], but this approach does not give the exact distance by which each node must separate itself from the neighboring nodes, which results in two possible scenarios. First is the isolation of a single node or multiple actor nodes from the entire network. The second situation is the isolation of a network or multiple networks from the rest of network. These two scenarios are not suitable for mission critical networks in a harsh environment like a battlefield and can

cause disconnection of many nodes. To avoid these two scenarios, nodes must be cognizant of the exact distance by which they have to be separated from their neighbor nodes to achieve uniform distribution of nodes in the entire network. Based on our experimentation, we suggest that the distance should be half of the transmission range and nodes must be aware of this fact that they should maintain half of the distance of their communication range. For experimentation, we assume that all nodes have the same sensing and communication range. It is also assumed that transmission range and sensing ranges are also equal. All nodes are deployed in a random manner. Physical constraints are also taken into account in this paper, which are often not considered in many techniques in the literature so far. This paper proposes a new mechanism for the nodes to declare themselves as cut-vertex, intermediate, or leaf node by calculating point-to-point coverage area in all directions, i.e., east, west, north, south, north-east, north-west, south-east, and south-west; details are given later in this paper. After declaration, neighboring nodes are declared as recovery nodes, which are responsible for connectivity in case of failure. The main contributions of this paper are as follows:

- (1) UDRA focuses on proactive approach and stresses more on the pre-failure operations rather than post-failure operations and is most suitable for mission critical applications which need very less time for connectivity and coverage restoration.
- (2) UDRA also considers the physical constraints, which are often not taken into account, hence giving a practical solution.
- (3) UDRA gives the exact distance between two nodes for distribution in area and all nodes try to maintain this distance. This gives advantage that these nodes stay connected in case of failure of any node without movement of such nodes as described earlier.
- (4) UDRA also gives the complete recovery plan, in case of a failure of single node, if some nodes or multiple nodes cannot maintain a distance  $R_c/2$  between their neighbors due to physical constraints.
- (5) UDRA also gives a very simple solution to find cut-vertexes, intermediate, and leaf node by one hop information by node itself.

The rest of the paper is organized as follows. Section 2 gives the comparison of the proposed algorithm with the related work done in the past. Section 3 has the details of the proposed algorithm along with the pseudocode. Validation of results is reported in Section 4, and Section 5 concludes the paper.

## 2. Related Work

Preserving connectivity while maintaining overall coverage intact by using limited number of mobile nodes is a difficult task, especially when a single or multiple nodes fail. It is the problem of utmost importance which has been studied in the literature in recent years. Various solutions have been proposed regarding this issue. There are two kinds of

solutions. The first kind of solutions depends upon relocation on demand, whereas the second kind of solutions is based on postdeployment relocation. In general, sensor nodes are deployed randomly by aerial deployment. This kind of deployment may cause nonuniform distribution of mobile nodes in the AOI; i.e., some areas may have higher density and some areas may have lower density of mobile nodes. Therefore, relocation is desired in this situation so that the connectivity is assured between mobile nodes and the end user to maximize the coverage area. Connectivity issue has been targeted in the literature and many solutions have been provided in this regard [7–13]. To solve connectivity issue, coverage holes must be avoided in some areas. Therefore, a balance between connectivity and coverage restoration is important to keep both intact. Several approaches have been used in recent years.

In [8], the authors proposed a distributed algorithm for the network connectivity restoration, when a node is failed. For the restoration of network connectivity and improvement of coverage, the technique uses mobile nodes at the time of failure. A concept of 2-connected network was introduced in [13]. This means that among each pair of nodes there must exist at least two connected pathways in the network. This approach has 2-degree connectivity and requires 2-hop information for each node. In [7], coverage-aware and connectivity constrained actor positioning (C2AP) algorithm is proposed. In this approach, post-deployment of nodes is discussed. In [14], a cascade movement of nodes was given as a solution when some nodes fail. According to this technique, the neighboring node of the failed node replaces it. Then, such node is replaced by another node and replacements continue until being replaced by redundant node.

In [9], there is an algorithm known as Recovery by Invert Motion (RIM). In RIM, the recovery of the failed node was done by its neighboring nodes by invert movement towards the failed node. The main idea is that, through missing of HEART BEAT message, neighbors will know about the node failure. Therefore, neighbors make inward movements to the failed node for restoration of the network connectivity.

Prefailure cut-vertex nodes determination is done by Partition Detection and Recovery Algorithm (PADRA), which is presented in [10]. Failure of cut-vertex nodes causes disjoints in the network. The suitable neighbor is selected for each cut-vertex node to handle its failure. Hence, in this way, prefailure connectivity and coverage are restored. The connectivity restoration process involves relocations of all the involved neighboring nodes, which causes cascaded movements of such neighbors.

In [11], coverage-aware connectivity restoration (C3R) in mobile sensor networks technique gives the solution by replacing the failed nodes by their neighboring nodes. The solution suggests the to and fro movement of the neighboring nodes between the position of failed nodes and their original position. The schedule of changing turns of these nodes was made by the node which reaches the failed node first.

To restore the connectivity of the network, an algorithm known as Volunteer-instigated Connectivity Restoration

(VCR) is proposed in [12]. In this algorithm only, the immediate neighbors of the failed actor node take part. The selection criterion of the neighboring nodes is based on nearness. The cascaded movement is limited in this algorithm.

A provision of connected path planned by controlling a robot is described in [13]. Minimizing distance with minimal number of hops counts for mobile robots in such a way that connectivity remains intact which is the supreme goal of this algorithm. The proposed approach contains two algorithms. For allocation of a robot to an event location, the nearest robot to the event is identified by the first algorithm. Then, the nearest nonconnected robot is searched by this algorithm. The nearest robot is then directed to bring itself forward to connect to any of the joined section with allocated robot. This procedure is performed until the network becomes completely connected. For minimization of the hop count between the base station and the event area, the second algorithm is used. It optimally provides such locations where there are minimum numbers of hops.

However, a Backbone Polygon (BP) is built around the center of the disjoint network area in Connectivity Restoration with Assured Fault Tolerance (CRAFT) algorithm presented in [14]. To connect each outer partition to the BP, by two nonoverlapping paths, Relay Nodes (RNs) are positioned in the targeted area having low cost, resulting in the restoration of the connectivity of the network.

In [15], the authors give an exceptional connectivity restoration technique called Geometric Skeleton based Reconnection (GSR). GSR uses a geometrical skeleton based approach to partition network logically into different segments. A geometrical skeleton backbone consists of a group of nodes that have the maximum connectivity with other nodes. Each segment has record of all the skeletal backbone nodes, so, in case of network partitioning, each segment attempts to join the geometrical skeleton backbone. In this way, connectivity can be restored.

To observe the influence of realistic terrain, hybrid recovery strategy based on random terrain (HRSRT) is proposed in [16]. The Area of Interest (AOI) is divided into a grid of cells. All cells have equal size. Mapping of these cells is used to plan the terrain. The weight " $\omega(c)$ " represents each cell  $c$ . The weight of each cell " $\omega(c)$ " can be calculated by the summation of weight of each path " $\omega(P)$ ." A complete graph  $K_n$  is created by considering the minimum weights of paths between segments. A tour " $T$ " for MDCs (mobile data collectors) is done by a random terrain-based path planning algorithm, which is established on  $K_n$  for initialization of connectivity restoration. The weight of tour " $\omega(T)$ " is directly proportional to the cost of data collection and aggregation. There may be one or more than one MDCs. This results in different relay nodes deployment approaches. So, for connectivity restoration, an "optimized relay node deployment" and "relay nodes deployment" are responsible. Minimal energy and cost for data aggregation and collection are the goals of these algorithms.

In [17], Survivability-Aware Connectivity Restoration (SACR) is given. Data load levels of disjoint parts are considered for connection of the partitioned segments

between different disconnected segments. A set of moveable nodes are located in the proper location of these inaccessible segments. A relay partition is generated for every isolated segment, immediately after isolated segments are traced. This causes restoration of connectivity from the AOI to the base station.

Another technique for calculating cut-vertex is presented in [18]. For this purpose, this technique uses two localized and distributed algorithms. For the detection of cut-vertex and noncut-vertex nodes, a local subgraph having two hops with connected dominating set (CDS) knowledge is used in the first algorithm. The second proposed algorithm depends entirely on the first one. For unrecognized parts of the network, a limited distributed depth-first search algorithm is used without searching the whole network. This algorithm discovers the states of all nodes by comprehensive test bed experiments with the presence of a CDS. Cut-vertex nodes are detected with lower energy consumption. Simulations results are the witness of this fact.

A method for maintaining confidentiality of location of roaming position-based services (PBSs) users using machine learning techniques is suggested in [19]. For roaming PBS users, the authors suggest a triphase process. It identifies user position by merging decision trees and  $k$ -nearest neighbor and estimates user destination using hidden Markov models along with position track sequence. In addition, the proposed model follows a mobile edge computing service strategy which will ensure the timely delivery of PBSs. The advantages of a mobile edge service policy offer confidentiality of position and low latency through networking and computing services in the vicinity of roaming users.

In [20], an energy-conscious green adversary paradigm for its use in intelligent industrial environments by maintaining confidentiality is proposed. Although the hardware and software parts of cyber physical systems can be mutually improved to reduce their energy consumption, this paper focuses on aspects of position conservation and confidentiality of the information. Based on the literature findings (assumptions, adversary targets, and capabilities), the authors include some testimonials to support cyber physical security practitioners and researchers. The proposed model is running on real-time, anticipatory position-based query scheduling to reduce the cost of communication and computation for each query, thereby encouraging minimization of energy consumption. In addition, to avoid degrading slots, we measure the transfer/acceptance slots that are needed for each question. The experimental findings indicate that, in comparison with current methods, the proposed solution will reduce energy consumption by up to five times.

The key objective explained in [21] is to extend the lifespan of the network by extending the lifespan of the working sensors as well as moving the collected data from the super node into the sink. Bat Algorithm (BA) is used in this article to pick the optimal monitoring sensor node and corresponding direction to minimize energy consumption. Results of simulation and comparison with other algorithms suggest the superiority of the algorithm proposed. The simulation results of the proposed algorithm show that the

proposed algorithm was able to reduce the network's power consumption and increase the network's service life. The proposed algorithm may also outperform the comparable algorithms by 27 per cent on average.

In [22], the whale optimization algorithm (WOA) is used in this paper to solve the resource allocation (RA) problem in Internet of things (IoT) with the goal of optimum RA and to reduce the overall cost of communication between resources and gateways. There is a comparison of the proposed algorithm with other current algorithms. Results suggest that the proposed algorithm works properly. The proposed process, based on different metrics, is better than others in terms of "absolute cost of communication."

The solution to this problem has three optimization objectives. They are as follows:

- (a) Coverage restoration
- (b) Connectivity restoration
- (c) Both coverage and connectivity in an integrated manner

In order to achieve the above optimization objectives, three approaches are used.

- (a) Reactive approach: in this approach, a recovery mechanism is developed after the occurrence of failure. References [9–11] are the examples of such approach.
- (b) Proactive approach: in this approach, recovery mechanism is established before the occurrence of failure. It means that sensor nodes are prepared well before the failure. References [7, 18, 23] are the examples of such approach.
- (c) Hybrid approach: in this approach, both reactive and proactive approaches are used. This approach is used according to the requirement. Yihanli, Shivendra, 2006 [10, 24], etc. are the examples of such approach.

Table 1 shows optimization objective and nodes' mobility and either algorithm is reactive, proactive, or hybrid and shortcomings of the techniques presented in the literature since 2007.

The proposed (UDRA) gives the solution to achieve connectivity restoration objective by using hybrid approach. The extensive simulations show that the proposed algorithm outperforms its baseline algorithms. Table 2 gives the details of optimization objectives, approach, and strengths of the proposed algorithm.

### 3. Details of the Proposed Algorithm

**3.1. The Scenario and Assumptions of UDRA.** The proposed algorithm considers all sensor nodes as mobile sensor nodes, deployed randomly in an Area of Interest (AOI). It is assumed that all nodes have capability of sensing the environment to find the physical constraints. This gives them the knowledge of their capability for the decision of maintaining  $R_c/2$  distance with the neighbors. This can be useful for their availability to become recovery node for failure later. It is also assumed that, at the time of startup, all nodes discover

TABLE 1: Overview of related work algorithms.

Reference	Optimization objective	Nodes' mobility	Proactive, reactive, or hybrid	Shortcomings
C2AP [7]	Connectivity and coverage restoration	Actor nodes	Proactive	No exact distance b/w sensor nodes for maintaining coverage and connectivity is given
DCRA [8]	Connectivity restoration	Actor nodes	Hybrid	Cut-vertexes are determined by depth-first search trees (DFS) and CDS which are time consuming
RIM [9]	Connectivity restoration	Mobile sensors	Reactive	Cascade movements of sensor nodes consume a lot of energy
PADRA [10]	Connectivity restoration	Actor nodes	Hybrid	Exact distance of distribution is not given
C3R [11]	Connectivity and coverage restoration	Mobile sensors	Reactive	This requires a lot of movements of the nodes, which reduces network lifetime
VCR [12]	Connectivity restoration	Robots	Reactive	This takes a lot of time for convergence
DEEHC [13]	Connectivity restoration	Robots	Proactive	There is lack of multirobot communication and cooperation
CRAFT [14]	Connectivity restoration	Mobile sensors	Reactive	Detection of orphan nodes in multimode failure is not addressed
GSR [15]	Connectivity restoration	Mobile sensors	Reactive	The assumptions made in this technique are not practical which can increase overhead of network
HSRT [16]	Connectivity restoration	No mobility (replacement by relay nodes)	Reactive	No solution for coverage replacement of relay nodes may not be feasible in hostile environment
SACR [17]	Connectivity restoration and network lifetime	Mobile sensors	Hybrid	There is no solution for multinodes and simultaneous nodes failures
CDS [25]	Connectivity restoration	No mobility	Proactive	This does not present any plan of recovery in case of node failure
DCHS-WS [26]	Coverage restoration	Mobile sensors	Reactive	Particle swarm algorithm (PSA) is used which takes a lot of time
MMLPP [27]	Connectivity restoration	Mobile vehicles	Proactive	Path query algorithm needs a lot of time
AUR [24]	Connectivity restoration	Mobile sensors	Hybrid	CDS is complex to implement
TEEN [23]	Scalability and network lifetime	Mobile sensors	Proactive	There is no solution for coverage and connectivity

TABLE 2: Overview of the proposed algorithm.

The proposed technique	Optimization objective	Nodes mobility	Proactive, reactive, or hybrid	Strengths
UDRA	Connectivity restoration	Mobile sensors	Hybrid	(i) Having less time for connectivity restoration. (ii) Giving the exact distance between two nodes for distribution in area. (iii) Giving complete recovery plan. (iv) Giving very simple solution to determine cut-vertex, intermediate, and leaf nodes.

each other to form a network [8]. The proposed algorithm assumes that mobile nodes can determine their location relevant to their neighbors [9]. Each mobile node makes a list of its first hop neighbors, which reduces the messaging overhead in the network as compared to having two-hop neighbor information. This paper mainly focuses on proactive approach for the mobile nodes in such a way that it maintains connectivity as well as coverage. If the mobile nodes are not prepared before the failure, it will take some time to react, hence sacrificing the connectivity and coverage for a certain amount of time. URDA gives permanent

relocation of mobile nodes in case of failure which assures both connectivity and coverage without wasting a lot of time.

*3.2. Maintaining  $R_c/2$  Distance Distribution.* As mentioned in Section 1, the mobile nodes are deployed in random manner in some AOI. This may lead to a situation when there might be an abundance of mobile nodes in one area and shortage of mobile nodes in some other areas. Therefore, all mobile nodes must be uniformly distributed throughout AOI. To maintain uniform distribution, this paper suggests

that these mobile nodes should try to maintain  $R_c/2$  distance between them. If all the neighbors of a mobile node succeed in maintaining  $R_c/2$  distance, then there are two advantages of this distance. The first is that all the mobile nodes will be uniformly distributed in AOI, as mentioned earlier. The second advantage is that, in case of some node failure, there is no need for the neighbors of the failure node to move towards that failure node and restore coverage and connectivity. The reason is that neighbors will stay connected to the immediate neighboring nodes of the failed node. The first advantage is obvious, as all nodes have the same distance between them, so the mobile nodes will be distributed in uniform manner. However, the second advantage can be explained by the example depicted in Figure 1. In the example shown in Figure 1, mobile nodes A, B, C, D, E, F, and G are successful to maintain  $R_c/2$  distance between them. Half of the distance is taken by bisecting the distance between them by using dashed line segments just in case of failure of nodes D or F. Their neighboring nodes C and A will be stayed connected with nodes E and G, respectively. Their overlap coverage area, shown by shaded areas, remains intact. So, there is no need of movement for mobile nodes C and A for the restoration of connectivity and coverage. This saves extra movement in case of failure, hence saving extra energy spending on such movements, as the distance between the mobile nodes is well known by the localization methods as given in [9, 10]. The relationship between coverage area and distance is inversely proportional; i.e., the coverage area will be more when the distance between the nodes is less. The coverage area will increase with the decrease in distance. In Figure 2, it is depicted that there is the overlap area between nodes N1 and N2.  $R_c$  is their communication range, whereas  $\alpha$  and  $\beta$  are the angles, which helps in solving the area under arc "pq" with centers N1 and N2. So, the area of the arc "pq" when center is N1 can be calculated by the equations given in [15]

$$\text{area} = \left(\frac{\beta}{\pi} R_c^2\right) - \left(\frac{d}{2} R_c\right) \times \left(\sin\left(\frac{\beta}{2}\right)\right). \quad (1)$$

Equation (1) can also be used to find out the area under the same arc "pq" with the center N2. Hence, the overall coverage area can be found by the equation [15]

$$\text{overlap} = 2 \times \frac{\text{area}}{\pi R_c^2}. \quad (2)$$

**3.3. Determining Cut-Vortex, Intermediate, and Leaf Nodes.** For determining cut-vortex (CV), intermediate node (IN), and leaf node (LN), each mobile node is in a network. A novel method of directional matrix is proposed. All of the mobile nodes try to maintain  $R_c/2$  distance between them. If all nodes maintain such a distance, then there will be no cut-vertexes. But still there is a chance that there might be some nodes which cannot maintain  $R_c/2$  distance due to some physical constraints. In this case, the concerned node maintains a matrix showing the directions of its neighbors by their relative positions and the compass mounted on each

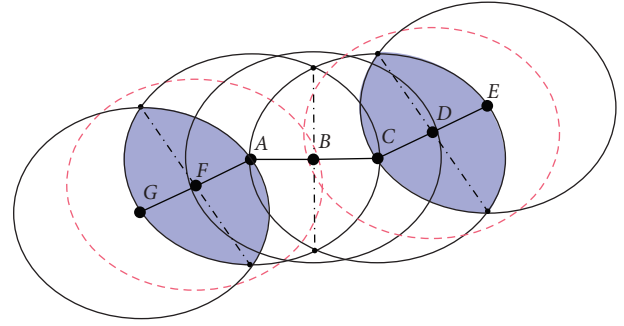


FIGURE 1: A and E will be still connected with G and C, respectively, if F or D fails.

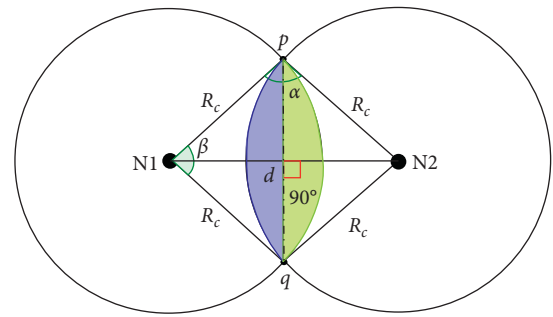


FIGURE 2: Overlap area between N1 and N2.

node. By this matrix, a node declares itself as cut-vertex, immediate, or leaf node. This matrix is based on consisting of three rows and three columns as shown in

$$A = \begin{bmatrix} a11 & a21 & a31 \\ a21 & a22 & a23 \\ a31 & a32 & a33 \end{bmatrix}. \quad (3)$$

Here, in this matrix, the position of the concerned node is in the middle of the matrix and is given by element a22, whereas the element a23 shows number of one-hop nodes in east direction. The element a21 shows number of one-hop nodes in west direction. The element a21 shows number of one-hop nodes in north direction. The element a32 shows number of one-hop nodes in south direction. The element a11 shows number of one-hop nodes in north-west direction. The element a31 shows number of one-hop nodes north-east direction. The element a31 shows number of one-hop nodes in south-west direction and the element a33 shows number of one-hop nodes in south-east direction. Directions are mapped on matrix according to directions shown in Figure 3.

$$A = \begin{bmatrix} nw & N & ne \\ W & 1 & E \\ sw & S & se \end{bmatrix}. \quad (4)$$

Initially, matrix A has the following values:

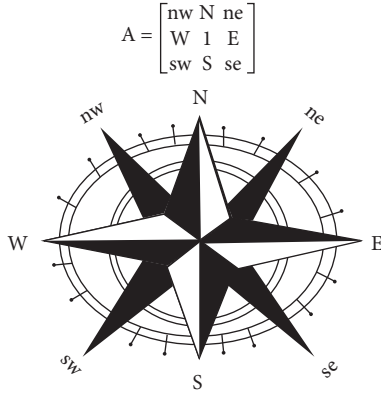


FIGURE 3: Directions of mobile nodes.

$$A = \begin{bmatrix} 0 & 0 & 0 \\ 0 & 1 & 0 \\ 0 & 0 & 0 \end{bmatrix}, \quad (5)$$

i.e., 1 for the position of the concerned node and 0 for all other directions. As far as the concerned node finds its neighbors by overlap area, it finds their direction by its navigational compass and by their relative positions. The concerned node increments the number of first hop nodes in their respective directions. The cases of determining cut-vertex, intermediate, and leaf node can be best explained with the help of Figure 4. In Figure 4, consider node A; it has a node let's say K, which cannot maintain the distance of  $R_c/2$  with A. Node A has B in east, K in north, E at south, F at south east, and C at south west, so the directional matrix for A will be

$$A = \begin{bmatrix} 0 & 1 & 0 \\ 1 & 1 & 1 \\ 0 & 1 & 1 \end{bmatrix}. \quad (6)$$

Node A will broadcast the message with the IDs of its neighbors that it has B, C, E, F, and K with it at its first hop. Do they have any of these connected with them? So, all of the neighbors receive this message, and answer back to A with "NO CONNECTION" message, if none of them are connected to each other. So, A makes its value 0 in the matrix and checks for connections of its neighbors:

$$A = \begin{bmatrix} 0 & 1 & 0 \\ 0 & 0 & 1 \\ 0 & 1 & 1 \end{bmatrix}. \quad (7)$$

It will find that none is connected without it, so it declares itself as cut-vertex and nominates its neighbors as its recovery nodes for the time of failure. Similarly, K has A node which cannot maintain  $R_c/2$  with K, so the K directional matrix will be

$$K = \begin{bmatrix} 2 & 0 & 2 \\ 0 & 1 & 0 \\ 0 & 1 & 0 \end{bmatrix}. \quad (8)$$

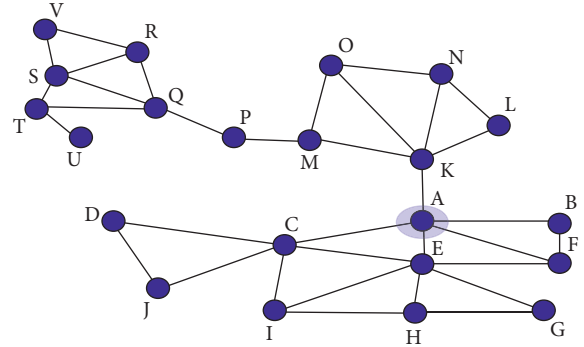


FIGURE 4: Scenario for determining CV, IN, and LF.

As K has two nodes in north-east, i.e., N and L and two nodes in north-west, O and M. So, node K checks its neighbor connections by setting its value to zero:

$$K = \begin{bmatrix} 2 & 0 & 2 \\ 0 & 0 & 0 \\ 0 & 1 & 0 \end{bmatrix}. \quad (9)$$

As N relates to L and O and O is connected with M and there is node A which lacks the connection with these four nodes, so node K declares itself as cut-vertex. Similarly, node E will make directional matrix as

$$E = \begin{bmatrix} 0 & 1 & 0 \\ 0 & 1 & 1 \\ 0 & 1 & 1 \end{bmatrix}. \quad (10)$$

As there is connection between H to G and F to A, so, E will declare itself as intermediate node. For the leaf node, examples are nodes D, V, N, and O. Leaf nodes can be found if there is triangle of zeros above, below, or both in directional matrices:

$$\begin{aligned} D &= \begin{bmatrix} 0 & 0 & 0 \\ 0 & 1 & 0 \\ 0 & 0 & 2 \end{bmatrix}, \\ V &= \begin{bmatrix} 0 & 0 & 0 \\ 0 & 1 & 0 \\ 0 & 0 & 2 \end{bmatrix}, \\ N &= \begin{bmatrix} 0 & 0 & 0 \\ 2 & 1 & 0 \\ 0 & 1 & 1 \end{bmatrix}, \\ Q &= \begin{bmatrix} 0 & 0 & 0 \\ 0 & 1 & 1 \\ 1 & 0 & 1 \end{bmatrix}. \end{aligned} \quad (11)$$

Similarly, all the nodes in the networks declare themselves as CV, IN, or LF. There might be a chance that there will be an IN and it declares itself as CV. After declaration,



the concerned nodes assign their neighbors as recovery nodes and are prepared for the node failure situation.

### 3.4. UDR Algorithm

**3.4.1. Prefailure UDR Algorithm.** As mentioned in Section 1, nodes are deployed in random manner. So, there is a chance of profusion of nodes in one area and lack of nodes in the other. This rises to a coverage problem as all the area is not attended in uniform manner. Uniform distribution of nodes can be done by the sink node, taking instructions from the end user. But this type of strategy is not suitable as overall messaging overhead of the network increases, because sink node must transmit its messages to all the network nodes and must wait for their acknowledgment. So, nodes must rearrange themselves, without adding extra messaging overhead to the network. So, first, a node after deployment tries to find its neighbors by coverage overlap of their  $R_c$ . Then, each node looks around its environment to find out any physical constraints. If it finds any unavoidable obstacle, it just sets CM (cannot move) flag, by sending message to its neighbors along with its ID. Then, that node calculates directional matrix to find out either it is cut-vertex (CV), intermediate node (IN), or leaf node (LF) which is already discussed in detail in previous section. The neighbors update their neighboring list by putting CM and CV or IN or LF with that node's ID. If there are no unavoidable obstacles, then a node compares its ID with neighboring node IDs. If its ID is greater than all other IDs, it sends message "distribution admin" (DA) along with its ID. After this, DA calculates each neighboring node distance, which may be less than, equal to, or more than  $R_c/2$ . If all neighboring distances are equal to the required distance, then prefailure algorithm ends. So, there is no need to move to the failed node's location. If all distances are less than  $R_c/2$ , then DA asks its neighbors to move away from the DA to maintain the mandatory distance in all directions. If all distances are greater than the required distance, then DA asks its neighbors to move towards the DA to maintain such distance. There may a situation. When some nodes may be at distance equal to  $R_c/2$ , some nodes may be at distance less than  $R_c/2$ , and some have distance more than  $R_c/2$  from DA, so, in such situation, DA broadcasts a single message having three parts: the first part of the message starts with "start," then node IDs of those which have distances equal to  $R_c/2$ , and ends at "Eq." Then, the second part of message starts with IDs of those nodes having distance less than  $R_c/2$  and ends with "less" and the third part contains IDs of those nodes which have distance with DA more than  $R_c/2$ . After this, there is a footer of "more" and its ends with "end" which means end of a message. This message is broadcast by DA and all neighboring nodes read this message looking for their ID and responding as accordingly. If a node has distance equal to  $R_c/2$ , then it stays there and simply discards the message. If node falls in the category of having distance less than  $R_c/2$ , so it moves away from DA to make it  $R_c/2$  and sends "done" message to DA. If distance from DA is greater than  $R_c/2$ , then that node calculates possible movement

distance towards the distribution admin (DA) node by calculating overlap coverage area and how much it can move towards admin node by finding the least coverage area with its neighbors. After calculating possible to move distance, the node moves to that possible distance and sends "done" message to DA. When all the neighbors adjust their distances, DA updates distance list and finds DM for node failure situation. However, there might be a chance of a node having more than one DA, so such node will find possible distance with the DA. It selects the DA with lesser possible distance with itself. There might be another situation that there are two or more admins in the neighborhood in this situation; none of DAs moves towards each other, as their other neighboring nodes require moving towards them. Detailed steps are explained in the proposed prefailure pseudocode in Algorithm 1.

**3.4.2. The Proposed Postfailure Algorithm.** Mobile nodes in a network become uniformly distributed in AOI with the help of prefailure algorithm, to guarantee connectivity and coverage. There might be some nodes which cannot maintain  $R_c/2$  with their neighbors, so recovery nodes are assigned to them. Now, for such nodes, which cannot maintain  $R_c/2$ , a problem occurs when some nodes fail in the network creating connectivity and coverage hole behind. To resolve this issue, a proposed node failure algorithm is presented in this paper. When a node finds one of its neighboring nodes has failed, for example, consider a scenario given in Figure 4. Suppose that node A finds node F which has failed. Node A will have the status of failed node F in its list that either F is a cut-vertex (CV), intermediate node (IN), or leaf node (LN). So, node A will react to this situation according to the status of failed node F. If failed node F is CV, then it has at least four recovery nodes. If it has four or two recovery nodes, then all of them move their possible movement distance to restore connectivity. If they still not find each other, then they will increase their communication range and send message to sink node for redundant node as there is no other possibility to restore both coverage and connectivity. If there is only one node for as recovery node for CV, then it will move its possible distance to restore connectivity; if recovery nodes still do not find any node to restore connectivity, then they increase their range and send message to sink node for redundant node. If failed node F is IN or LN, then the same procedure will be adopted; for IN, two recovery nodes or only one recovery node will move their possible distance or increase their range. For LN, only one recovery node will follow the above procedure. Pseudocode of this is given in Algorithm 2.

**3.5. Energy Model.** An energy model which we have used in this paper is illustrated in [25]. Equations (12) and (13) show the relationship of required energy for transmitting and receiving a B-bit data packet. Energy per bit consumption of receiver circuitry is given by (13). For more details, the readers are recommended to read details in [25]

Input: AOI and  $R_c$

- (1) Begin
- (2) Find ( $N_i$ )// $i = 1, 2, 3, \dots$  number of neighbors
- (3) Check for PC = physical constraint
- (4) If PC = true
- (5) Send (owned ID, CM)//CM = cannot move
- (6) Go to (step 48)
- (7) End if
- (8) If receive (some IDs, CM)
- (9) Update (some IDs, CM)//in neighbor's list
- (10) End if
- (11) If PC = false
- (12) Compare (owned ID with  $N_i$ 's IDs)
- (13) End if
- (14) If owned ID > all  $N_i$ 's IDs
- (15) Send (owned ID, distribution admin) to rest of neighbors
- (16) Calculate (distance with each neighbor)
- (17) If all neighbors' distances =  $R_c/2$
- (18) End if
- (19) If distance <  $R_c/2$
- (20) Send (move away)//to maintain  $R_c/2$  distance
- (21) End if
- (22) End if
- (23) Else
- (24) Send (calculate possible movement distance)//to those neighbors whose distance is >  $R_c/2$
- (25) Wait
- (26) Receive (possible movement distances of all neighboring nodes)
- (27) Calculate (actual distance—possible distance to move)//to find out which node can maintain  $R_c/2$
- (28) Send (adjust, distance to move)
- (29) End if
- (30) If receive (move away)
- (31) Move//to maintain  $R_c/2$
- (32) Else if receive (calculate possible movement distance)
- (33) If distribution admin > 1
- (34) Send (CM)//to distribution admins
- (35) Else
- (36) Calculate (possible movement distance)//keeping in mind  $d \leq 2 \times R_c$  and by averaging possible movement distance of each neighboring node
- (37) Send (adjustable distance)//to distribution admin
- (38) End if
- (39) End
- (40) Else if receive (adjust, distance to move)
- (41) Move//to adjust that  $R_c/2$
- (42) End if
- (43) Update all neighboring node distances ( $d_i$ )
- (44) If all  $d_i \neq R_c/2$
- (45) Go to (step 36)
- (46) End if
- (47) Else if all  $d_i = R_c/2$
- (48) Determine directional matrix = DM
- (49) End if
- (50) End
- (51) Determine DM
- (52) If DM = LN//leaf node
- (53) Go to (step 66)
- (54) Else if DM = IN//intermediate node
- (55) Go to (step 64)
- (56) Else if DM = CV//CV = cut-vertex
- (57) Check availability of four recovery nodes
- (58) If availability = false
- (59) Go to (step 64)

```

(60) If availability = true
(61) Set at least four neighboring nodes as recovery nodes
(62) End if
(63) End
(64) Set at least two neighboring nodes as recovery nodes
(65) If availability of two nodes = false
(66) Set at least one neighboring node as recovery node
(67) End if
(68) End

```

ALGORITHM 1: Prefailure algorithm.

```

Input: DM = CV or DM = IN or DM = LF
(1) If (node A detects, node F has failed)
(2) If distance =  $R_c/2$ 
(3) Find (new neighbors)
(4) If (new node found)
(5) Restore (connectivity)
(6) Else if (new node not found)
(7) Move (possible movement distance)
(8) Else if (new node not found)
(9) Go to (step 39)
(10) Restore (connectivity)
(11) Else if distance  $\neq R_c/2$ 
(12) Go to (step 18)
(13) End if
(14) End if
(15) End if
(16) End
(17) Else
(18) If DM = CV
(19) Move (towards node F by possible movement distance)
(20) Find (other recovery nodes)
(21) If new node found
(22) Restore (connectivity)
(23) Else if (new node not found)
(24) Go to (step 39)
(25) End if
(26) Else if DM = IN
(27) Move (towards node F by possible movement distance)
(28) Find (other recovery nodes)
(29) If new node found
(30) Restore (connectivity)
(31) Else if new node not found
(32) Go to (step 39)
(33) End if
(34) Else if DM = LF
(35) Move (towards node F by possible movement distance)
(36) Find (new node)
(37) Restore (connectivity)
(38) If new node not found
(39) Increase  $R_c$ 
(40) Send (redundant node)//to sink node
(41) End if
(42) End

```

ALGORITHM 2: Postfailure algorithm.

$$E_{Tx}(B, d) = \begin{cases} (E_{elec} + \varepsilon_{fs}d^2)B, & d < d_0, \\ (E_{elec} + \varepsilon_{mp}d^4)B, & d \geq d_0, \end{cases} \quad (12)$$

$$E_{Rx}(B) = E_{Rx-elec}B, \quad (13)$$

$$E_{reng}(n) = E_{max} - E_{Tx}(B, d) - E_{Rx}(B). \quad (14)$$

Different terms used in this model are explained in Table 3.

#### 4. Experimentation and Results Discussion

In order to validate the effectiveness and better performance of UDRA, UDRA is compared with other baseline approaches already present in the literature. The protocols of geometric skeleton based reconnection (GSR) approach [15], autonomous repair (AUR) [24], and UDRA have been simulated in OMNET++ platform. For the comparison of these three protocols, the performance parameters of total distance covered after relocation, average number of nodes moving during relocation, percentage reduction in field coverage, and number of packets exchanged have been set in the simulation for protocol evaluation.

**4.1. Simulation Setting.** This section discusses the simulation setup, performance metrics, and results of the simulations. All the simulation parameters are summarized in Table 4.

UDRA and other protocols of the category have been implemented and evaluated in OMNET++, INET simulation framework. Simulation parameters and their values are defined in Table 4.

Simulations for each algorithm are conducted in OMNET++ separately and simulation logs are imported in MATLAB for result presentation. All the simulation results are taken within 10% of simple mean, whereas the confidence analysis interval is taken as 90% for all simulations. To evaluate the performance of the proposed algorithm against baseline algorithms, the following metrics are used:

Total distance moved reports the total distance collectively travelled by the nodes involved during recovery. This may be envisaged as a network-wide assessment of the efficacy of the recovery schemes applied.

Number of nodes relocated records the number of mobile nodes moved during recovery. This metric measures the breadth of the network connection restoration process.

Number of messages exchanged tracks the total number of messages exchanged between nodes. This measure measures the overhead relating to contact imposed by the recovery process.

range of communication ( $R_c$ ), all experiment nodes have the same range of communication. Initial WSN topology is affected by the value of  $r$ . While small  $r$  creates a sparse topology, and a large  $R_c$  boosts network connectivity overall, very few nodes need to be involved

in the cascaded movement in a highly connected WSN and the restoration process will converge rapidly with little overhead; a large value of  $R_c$  would increase the number of neighbors of a failed node and thus increase the overhead incurred by these neighbors.

Figure 5 presents the total distance by movement for relocation versus increase in number of nodes. From the results, UDRA performs well in comparison to the other baseline algorithms because during its operation, only recovery nodes are moved. Hence, the cascaded relocations are minimized. As a result, the average distance moved for UDRA is less as compared to the other considered algorithms. UDRA performs consistently well as compared to other considered algorithms as the number of nodes in the network has increased. The major reason behind this is that the movements of the nodes which cause further partitioning of the network are restricted by UDRA. One fascinating thing to note from the above figure is that the performance of GSR, unlike other algorithms, improves with increase in number of nodes. The major reason behind increase in performance is the working methodology of GSR. As the number of nodes increases, the backbone of the network becomes stronger and stronger, resulting in making recovery mechanism be more proficient and stable and causing improved performance. Besides this, the assumptions taken by GSR are unrealistic and, in case of topology change, they cause enormous overhead in terms of packet exchanges. It can still be seen from Figure 5 that our protocol still performs reasonably well as compared to GSR.

The average number of nodes moved versus increase in the total number of nodes is present in Figure 6. A smaller number of nodes moved as compared to AUR and GSR algorithms can be observed from the figure. The avoidance of continuous cascaded relocations of nodes is the main reason behind this phenomenon. Furthermore, it can also be observed from Figure 6 that, as the number of nodes increases, number of nodes moved in UDRA increases less than other considered algorithms. This shows that UDRA is more scalable, when compared to other considered protocols.

The effect of recovery process on the coverage is shown in Figure 7. As the nodes are relocated because of failure of nodes, a reduction in the coverage area is observed. For all the considered protocols, it can be realized from Figure 7 that when there is decrease in the percentage field coverage, the communication range increases. However, percentage reduction in the field coverage of UDRA is least as compared to the GSR and AUR protocols. It is obvious from Figure 7, that the field coverage reduction under UDRA is much lesser as compared to the baseline algorithms. Among the considered protocols, GSR results in the most field coverage reduction. Cascaded relocation of nodes is the main reason behind this increase of field coverage reduction. Similarly, for the other considered algorithms, cascaded relocation is the main reason for more reduction in field coverage. In UDRA, more appropriate recovery nodes are chosen to take part in recovery process. These nodes have not moved at all or moved a smaller distance, resulting in higher overlapped coverage of these recovery nodes.

TABLE 3: Meaning of different terms in the energy model.

Term	Definition
$E_{Tx}$	Energy consumed to transmit data
$E_{Rx}$	Energy consumed to receive data
$E_{reng}$	Residual energy
$E_{elec}$	Energy consumed per bit by the transmitter circuitry
$E_{max}$	Initial energy of sensor nodes
$E_{Rx-elec}$	Energy consumed per bit of a receiver
$\epsilon_{fs}$	Energy required by radio frequency (RF) amplifier in free space
$\epsilon_{mp}$	Energy required by radio frequency (RF) amplifier in multipath
$d_0$	Threshold distance

TABLE 4: Simulation parameters.

Simulation parameters	Values
Area of simulation	1000 × 1000 m <sup>2</sup>
No. of nodes	50–250
Size of data packet	900 bits
$E_{elec}$	70 nanojoules/bits
$E_{max}$	25 J
$\epsilon_{fs}$	15 picojoules/bits/m <sup>2</sup>
$\epsilon_{mp}$	0.0012 picojoules/bits/m <sup>2</sup>
$d_0$	70 m
$R_c$	25–150 m
Simulation tool	OMNET++

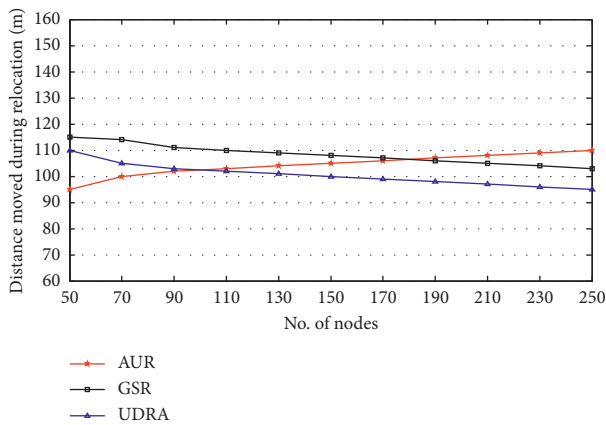


FIGURE 5: No. of nodes versus distance moved.

In Figure 8, the average number of packets exchanged during the procedure of connectivity restoration is shown. UDRA results in the minimum number of packets exchanged, while the maximum number of packets is exchanged by GSR. The major reason behind this is that, in UDRA, the emphasis is on minimizing the number of neighbors involved during the recovery process, which results in reduction of cascaded movement of nodes, hence reducing the total number of messages exchanged. On the other hand, due to excessive movement of nodes, GSR results in the maximum number of packets exchanged. So, it can be concluded that UDRA is more energy efficient as compared to AUR and GSR algorithms. Another important feature is the scalability associated with the reduction of the

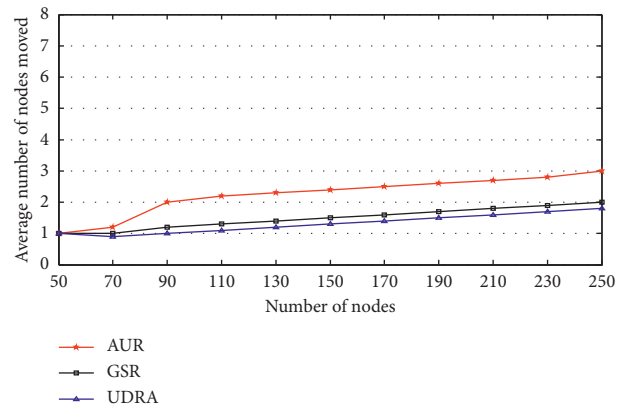


FIGURE 6: Average no. of nodes moved during recovery.

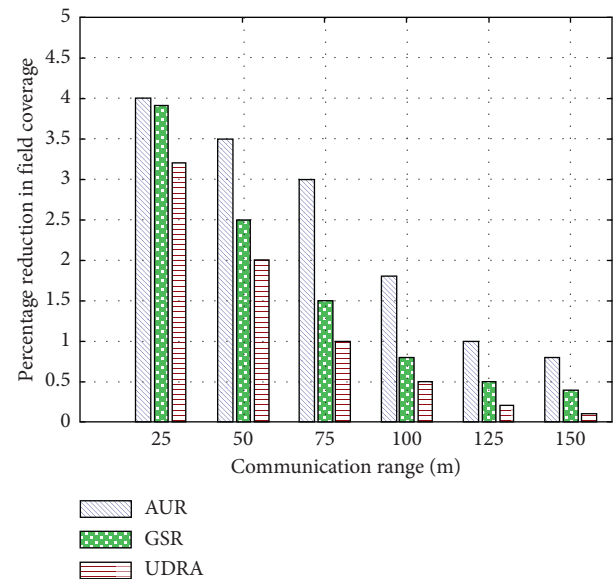


FIGURE 7: Percentage reduction in field coverage.

transmission/receiving of messages. Due to least number of messages exchanged by UDRA, it proves to be more scalable as compared to AUR and GSR protocols. In sensor networks, connectivity restoration is of immense importance and a technique must be capable of restoring the connectivity. During this work, our major emphasis was to design a

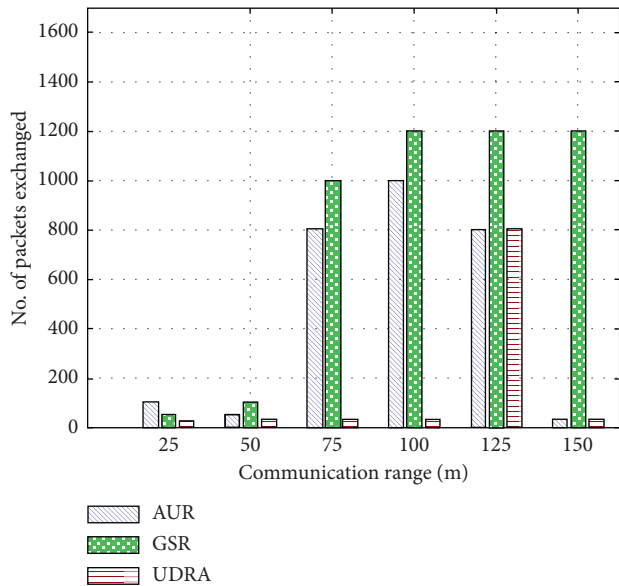


FIGURE 8: Total number of exchanged packets.

TABLE 5: Results summary.

Comparison of protocols for 250 nodes	Average distance travelled (m)	No. of messages exchanged (average)	No. of nodes relocated (average)	Age reduction in field coverage % (average)
UDRA	3000	700	70	03
RIR	13000	3000	200	10
AUR	15000	5500	700	15

prefailure and postfailure connectivity restoration protocol capable of achieving effective connectivity restoration by relying on minimal node mobility, minimal reduction in field coverage, and consuming minimal energy of nodes by reducing the overall number of exchanged messages. The solution proposed by UDRA achieves all the above goals. The performance of the UDRA was evaluated by using extensive simulations and by comparing its performance with AUR and a GSR technique; its effectiveness is proven.

### 5. Conclusions and Future Work

A novel algorithm “Uniform Distribution and Recovery Algorithm (UDRA)” is proposed in this paper. This algorithm provides both connectivity and coverage restoration solution for wireless sensor networks in an integrated manner. In Table 5, it is clear that average distance travelled by the sensor nodes is only 3000 meters. This distance is very less than 13000 meters and 15000 meters. So, having less average distance travelled proves that the proposed algorithm is an energy efficient solution. Most of the energy stored in batteries is consumed by travelling. If an algorithm is not energy efficient, then batteries of nodes will be drained off with the passage of time. This makes the problem worst and decreases the network lifetime. Furthermore, these results show that the number of messages exchanged by the

proposed algorithm is very less as compared to RIR and AUR. This decreases the message overhead in the network. Greater message overhead causes delay in recovery process as it takes a lot of time by communication messages. Another finding from Table 5 is that in the proposed technique only 70 nodes are relocated; this gives an upper hand to the proposed algorithm over RIR and AUR as more relocation of nodes needs more energy used. The other advantage of a smaller number of relocated nodes is that relocation of nodes can cause coverage loss. So, the lesser relocated nodes are, the lesser the coverage loss will be. The last most important finding of Table 5 is the percentage reduction in the field coverage. In UDRA, the percentage in field coverage reduction is only 3% after recovery process. This shows that UDRA outperforms its competitor baseline algorithm. Less percentage in field coverage reduction ensures that most of the network or AOI is monitored and less information from AOI is lost. The cost of these advantages would be that increased number of nodes is required to cover certain AOI, which is still affordable for mission critical applications. The detailed analysis would be done in the future.

### Data Availability

No data were used to support this study. We have conducted the simulations to evaluate the performance of the proposed protocol. However, any query about the research conducted in this paper is highly appreciated and can be asked from the principal authors (Rab Nawaz Jadoon (rabnawaz@mail.ustc.edu.cn) and Muhammad Amir Khan (amirkhan@cuiatd.edu.pk)) upon request.

### Conflicts of Interest

The authors declare that there are no conflicts of interest.

### Acknowledgments

Dr. Rab Nawaz Jadoon personally thanks COMSATS University, Islamabad, Abbottabad Campus, and School of Information Science and technology, USTC Hefei, China, that extended their full support by providing all key resources during the implementation and all afterward phases of this project. Also, special thanks are due to Prof. WuYang Zhou, because of his continuous encouragement and massive support academically, financially, and socially during this research work. This work was financially supported by the National Natural Science Foundation of China (Grant no. 61631018).

### References

- [1] R. N. Jadoon, W. Zhou, I. A. Khan, M. A. Khan, and W. Jadoon, “EEHRT: energy efficient technique for handling redundant traffic in zone-based routing for wireless sensor networks,” *Wireless Communications and Mobile Computing*, vol. 2019, Article ID 7502140, 12 pages, 2019.
- [2] S. Lee, M. Younis, and M. Lee, “Connectivity restoration in a partitioned wireless sensor network with assured fault tolerance,” *Ad Hoc Networks*, vol. 24, pp. 1–19, 2015.

- [3] V. Ranga, M. Dave, and A. K. Verma, "Node stability aware energy efficient single node failure recovery approach for WSANs," *Malaysian Journal of Computer Science*, vol. 29, no. 2, pp. 106–123, 2016.
- [4] C. Zhu, C. Zheng, L. Shu, and G. Han, "A survey on coverage and connectivity issues in wireless sensor networks," *Journal of Network and Computer Applications*, vol. 35, no. 2, pp. 619–632, 2012.
- [5] R. Jadoon, W. Zhou, W. Jadoon, and I. Ahmed Khan, "RARZ: ring-zone based routing protocol for wireless sensor networks," *Applied Sciences*, vol. 8, no. 7, p. 1023, 2018.
- [6] R. N. Jadoon, W. Zhou, I. Ahmed Khan, M. Amir Khan, S. Akhtar Abid, and N. Ali Khan, "Performance evaluation of zone-based routing with hierarchical routing in wireless sensor networks," *Wireless Communications and Mobile Computing*, vol. 2019, Article ID 7152858, 10 pages, 2019.
- [7] K. Akkaya and M. Younis, "C2AP: coverage-aware and connectivity-constrained actor positioning in wireless sensor and actor networks," in *Proceedings of the 2007 IEEE International Performance, Computing, and Communications Conference*, pp. 281–288, IEEE, New Orleans, LA, USA, April 2007.
- [8] A. Abbasi, K. Akkaya, and M. Younis, "A distributed connectivity restoration algorithm in wireless sensor and actor networks," in *Proceedings of the 32nd Conference on Local Computer Networks*, Dublin, Ireland, October 2007.
- [9] M. Younis, S. Lee, S. Gupta, and K. Fisher, "A localized self-healing algorithm for networks of moveable sensor nodes," in *Proceedings of the IEEE Global Telecommunications Conference (GLOBECOM'08)*, New Orleans, LA, USA, November 2008.
- [10] K. Akkaya, A. Thimrnapuram, F. Senel, and S. Uludag, "Distributed recovery of actor failures in wireless sensor and actor networks," in *Proceedings of the IEEE 2008 IEEE Wireless Communications and Networking Conference*, pp. 2480–2485, Las Vegas, NV, USA, April 2008.
- [11] N. Tamboli and M. Younis, "Coverage-aware connectivity restoration in mobile sensor networks," *Journal of Network and Computer Applications*, vol. 33, no. 4, pp. 363–374, 2010.
- [12] M. Imran, M. Younis, A. Md Said, and H. Hasbullah, "Volunteer-instigated connectivity restoration algorithm for wireless sensor and actor networks," in *Proceedings of the 2010 IEEE International Conference on Wireless Communications, Networking and Information Security (WCNIS)*, pp. 679–683, Beijing, China, June 2010.
- [13] P. Chanak, I. Banerjee, and R. S. Sherratt, "Energy-aware distributed routing algorithm to tolerate network failure in wireless sensor networks," *Ad Hoc Networks*, vol. 56, pp. 158–172, 2017.
- [14] Y. K. Joshi and M. Younis, "Exploiting skeletonization to restore connectivity in a wireless sensor network," *Computer Communications*, vol. 75, pp. 97–107, 2016.
- [15] X. Wang, L. Xu, S. Zhou, and W. Wu, "Hybrid recovery strategy based on random terrain in wireless sensor networks," *Scientific Programming*, vol. 2017, Article ID 5807289, 19 pages, 2017.
- [16] X. Liu, "Survivability-aware connectivity restoration for partitioned wireless sensor networks," *IEEE Communications Letters*, vol. 21, no. 11, pp. 2444–2447, 2017.
- [17] A. Wichmann, T. Korkmaz, and A. S. Tosun, "Robot control strategies for task allocation with connectivity constraints in wireless sensor and robot networks," *IEEE Transactions on Mobile Computing*, vol. 17, no. 6, pp. 1429–1441, 2018.
- [18] O. Dagdeviren, V. K. Akram, and B. Tavli, "Design and evaluation of algorithms for energy efficient and complete determination of critical nodes for wireless sensor network reliability," *IEEE Transactions on Reliability*, vol. 68, no. 1, pp. 280–290, 2019.
- [19] Y. Zeng, C. J. Sreenan, N. Xiong, L. T. Yang, and J. H. Park, "Connectivity and coverage maintenance in wireless sensor networks," *The Journal of Supercomputing*, vol. 52, no. 1, pp. 23–46, 2010.
- [20] A. K. Sangaiah, D. V. Medhane, T. Han, M. S. Hossain, and G. Muhammad, "Enforcing position-based confidentiality with machine learning paradigm through mobile edge computing in real-time industrial informatics," *IEEE Transactions on Industrial Informatics*, vol. 15, no. 7, pp. 4189–4196, 2019.
- [21] A. K. Sangaiah, D. Vishwasrao Medhane, G.-B. Bian, G. Ahmed, M. Alrashoud, and M. Shamim Hossain, "Energy-aware green adversary model for cyberphysical security in industrial system," *IEEE Transactions on Industrial Informatics*, vol. 16, no. 5, pp. 3322–3329, 2020.
- [22] A. K. Sangaiah, M. Sadeghilalimi, A. A. R. Hosseinabadi, and W. Zhang, "Energy consumption in point-coverage wireless sensor networks via bat algorithm," *IEEE Access*, vol. 7, pp. 180258–180269, 2019.
- [23] A. Abro, Z. Deng, K. Ali Memon et al., "Minimizing energy expenditures using genetic algorithm for scalability and longevity of multi hop sensor networks," in *Proceedings of the 2019 IEEE 9th International Conference on Electronics Information and Emergency Communication (ICEIEC)*, pp. 183–187, IEEE, Beijing, China, July 2019.
- [24] Y. Zhang, J. Wang, and H. Guan, "An autonomous connectivity restoration algorithm based on finite state machine for wireless sensor-actor networks," *Sensors*, vol. 18, no. 1, p. 153, 2018.
- [25] H. Essam, M. Younis, and E. Shaaban, "Minimum cost flow solution for tolerating multiple node failures in wireless sensor networks," in *Proceedings of the 2015 IEEE International Conference on Communications (ICC)*, pp. 6475–6480, London, UK, June 2015.
- [26] O. Moh'd Alia, "Dynamic relocation of mobile base station in wireless sensor networks using a cluster-based harmony search algorithm," *Information Sciences*, vol. 385–386, pp. 76–95, 2017.
- [27] Q. A. Arain, I. Memon, Z. Deng, M. H. Memon, F. A. Mangi, and A. Zubedi, "Location monitoring approach: multiple mix-zones with location privacy protection based on traffic flow over road networks," *Multimedia Tools and Applications*, vol. 77, no. 5, pp. 5563–5607, 2018.

## Research Article

# Synchronization of Time Delay Coupled Neural Networks Based on Impulsive Control

Jie Fang <sup>1,2</sup>, Yin Zhang,<sup>1</sup> Danying Xu,<sup>1</sup> and Junwei Sun <sup>1,2</sup>

<sup>1</sup>College of Electric and Message Engineering, Zhengzhou University of Light Industry, Zhengzhou 450002, China

<sup>2</sup>Henan Key Lab of Information-Based Electrical Appliances, Zhengzhou 450002, China

Correspondence should be addressed to Junwei Sun; [junweisun@yeah.net](mailto:junweisun@yeah.net)

Received 25 June 2020; Accepted 30 July 2020; Published 18 August 2020

Guest Editor: Hou-Sheng Su

Copyright © 2020 Jie Fang et al. This is an open access article distributed under the Creative Commons Attribution License, which permits unrestricted use, distribution, and reproduction in any medium, provided the original work is properly cited.

This paper investigates the impulsive synchronization of time delay coupled neural networks. Based on the Lyapunov stability theory and impulsive control method, a distributed delayed impulsive controller is designed to realize synchronization of the coupled neural networks. A new impulsive delayed inequality is proposed, where the control effect of distributed delayed impulses is fully considered. In addition, a suitable Lyapunov-like function is established to prove the stability of the synchronization system. Numerical simulation examples are introduced to illustrate the effectiveness and feasibility of the main results.

## 1. Introduction

Neural networks are a type of mathematical model that simulates the thinking patterns of the human brain, which is used to imitate the structure and thinking mode of neural network in the human brain [1–6]. The neural network learning is to abstract and simplify the human brain from the microscopic structure and function. It is one of the ways to realize artificial intelligence. Since 1980s, the research of neural network has made great progress [7–10]. Neural network synchronization research is one of the most important research directions of the neural network. Until now, various synchronization control schemes have been proposed, such as impulsive control [11, 12], adaptive control [13, 14], sliding mode control [15, 16], switching control [17–19], and pinning control [20].

Compared with continuous control, the structure of impulsive control is simpler. The small intermittent control input can achieve the expected control performance [21–24]. The key idea of impulse control is to convert the state of a continuous dynamic system into discontinuous forms through a discrete control input. Since impulsive control allows the system to admit discrete inputs and effectively save network bandwidth resources, it has been studied by many scholars. Liu et al. [25] realized the uniform

synchronization of chaotic dynamics system by designing three levels of event-triggered impulsive control. He et al. [26] realized the secure synchronization of multiagent systems under attacks through impulsive control. Qian et al. [27] realized the synchronization of multiagent systems through impulsive control. What is more, there always exists time delay in most practical systems, which should not be ignored in the study of neural network synchronization. For the time delay coupled neural network, the synchronization problem was first discussed in reference [28]. Xu et al. [29] realized the time delay synchronization of the chaotic neural networks based on impulsive control. Xie et al. [30] investigated the synchronization of time-varying delays coupled reaction-diffusion neural networks with pinning impulsive control. Wei et al. [31] realized synchronization of the coupled reaction-diffusion neural networks with time-varying delay by impulsive control. Li et al. [32] investigated the master-slave exponential synchronization of the neural networks with time-varying delays via discontinuous impulsive control. Until now, there are many control methods to realize the synchronization of neural networks. Among them, the research on time-delay impulsive control mainly concentrated on a single neural network system, while the research on the synchronization of coupled neural network with time-delay impulsive control is relatively rare.



In this paper, the problem of synchronization of delay coupled neural networks under distributed delay impulsive control is studied. Firstly, a time delay coupled neural networks model with  $N$  identical nodes is constructed. Secondly, based on the impulsive control method, a distributed delay impulsive controller is designed to achieve synchronization between the drive and response system. Thirdly, through the designed impulsive controller and impulsive delayed inequality, the stability of the synchronization system is analyzed. Finally, numerical examples are given to illustrate the effectiveness of the developed method.

The rest of this paper is organized as follows. In Section 2, synchronization problem of the time delay coupled neural networks and some premises are proposed. Section 3 presents the main results with proof. A simulation example is provided in Section 4 to illustrate the main results. The summary of this paper is given in Section 5.

## 2. Problem Statement

Considering a neural networks array consisting of  $N$  identical nodes, in which the dynamics of the  $i$ -th ( $1 < i < N$ ) node is described by the following neural networks:

$$\begin{cases} \dot{x}_i(t) = -Cx_i(t) + Af(x_i(t)) + Bf(x_i(t-\tau)) + \vartheta \sum_{j=1}^n d_{ij}\Gamma x_j(t) + J, & t \geq t_0, \\ x_i(s) = \varphi_i(s), & s \in [t_0 - \tau, t_0], \end{cases} \quad (1)$$

where  $x_i(t) = [x_{i1}(t), x_{i2}(t), \dots, x_{in}(t)]^T \in \mathbf{R}^n$  denotes the neuron state vector of the  $i$ -th dynamical node,  $i = 1, 2, 3, \dots, N$ ;  $C = \text{diag}(c_1, \dots, c_n) \in \mathbf{R}^{n \times n}$  denotes the positive definite diagonal matrix;  $A \in \mathbf{R}^{n \times n}$ ,  $B \in \mathbf{R}^{n \times n}$  represent the connection weight matrix and the delayed connection weight matrix, respectively;  $f(x_i(t)) = [f_1(x_{i1}(t)), f_2(x_{i2}(t)), \dots, f_n(x_{in}(t))]^T \in \mathbf{R}^n$  represents the neuron activation function satisfying

$|f_j(x_1) - f_j(x_2)| \leq l_j |x_1 - x_2|$  for all  $x_1, x_2 \in \mathbf{R}$ ,  $j = 1, 2, \dots, n$ , where  $l_j > 0$  are Lipschitz constants;  $D = (d_{ij})_{N \times N} \in \mathbf{R}^{N \times N}$  is the constant coupling matrix;  $\Gamma$  is the inner coupling matrix;  $\vartheta > 0$  represents coupling strength;  $\varphi_i(s)$  is the initial condition;  $\tau$  denotes the time delay occurring in transmission process;  $J$  is an external input.

Let (1) be the drive system and the response system is constructed as follows:

$$\begin{cases} \dot{y}_i(t) = -Cy_i(t) + Af(y_i(t)) + Bf(y_i(t-\tau)) + \vartheta \sum_{j=1}^n d_{ij}\Gamma y_j(t) + u_i(t) + J, & t \geq t_0, \\ y_i(s) = \psi_i(s), & s \in [t_0 - \tau, t_0], \end{cases} \quad (2)$$

where  $y_i(t) = [y_{i1}(t), y_{i2}(t), \dots, y_{in}(t)]^T \in \mathbf{R}^n$  denotes the neuron state vector of the  $i$ -th dynamical node,  $i = 1, 2, 3, \dots, N$ ;  $u_i(t)$  is the impulsive control input;  $\psi_i(s)$  is the initial condition.

Then, we will design a delayed impulse input to synchronize drive system (1) and response system (2). The impulsive controller is designed by

$$u_i(t) = \sum_{n=1}^{\infty} \left( K \int_{t-r_n}^t e_i(s) ds \right) \delta(t - t_n), \quad (3)$$

where  $e(t) = y(t) - x(t)$ ;  $K \in \mathbf{R}^{n \times n}$  is a gain matrix to be designed;  $r_n$  denote the distributed time delays in impulse input;  $\delta(t - t_n)$  is the Delta function.

When  $t \neq t_n$  and the controller  $u_i(t) = 0$ , the error derivative is

$$\dot{e}_i(t) = -Ce_i(t) + Ag(e_i(t)) + Bg(e_i(t-\tau)) + \vartheta \sum_{j=1}^n d_{ij}\Gamma e_j(t). \quad (4)$$

When  $t = t_n$ , the error derivative is

$$\begin{aligned} \dot{e}_i(t) = & -Ce_i(t) + Ag(e_i(t)) + Bg(e_i(t-\tau)) \\ & + \vartheta \sum_{j=1}^n d_{ij}\Gamma e_j(t) + K \int_{t-r_n}^t e_i(s) ds, \end{aligned} \quad (5)$$

where  $g(e_i(\cdot)) = f(e_i(\cdot) - x_i(\cdot)) - f(x_i(\cdot))$ . The above dynamical networks can be rewritten as the following Kronecker product form:

$$\begin{cases} \dot{e}(t) = -(I_N \otimes C)e(t) + (I_N \otimes A)g(e(t)) + (I_N \otimes B)g(e(t - \tau)) + \vartheta(D \otimes \Gamma)e(t), & t \neq t_n, \\ \dot{e}(t) = -(I_N \otimes C)e(t) + (I_N \otimes A)g(e(t)) + (I_N \otimes B)g(e(t - \tau)) + \vartheta(D \otimes \Gamma)e(t) + (I_N \otimes K) \int_{t-r_n}^t e(s)ds, & t = t_n, \end{cases} \quad (6)$$

where  $\otimes$  denotes the Kronecker product.

*Definition 1* (see [33]). The exponential convergence criterion of the distributed delayed impulsive inequality is given:

$$e(t) \leq \mu_n \int_{t-r_n}^t e(s)ds, \quad n \in Z_+, \quad (7)$$

where  $s \in [t - \tau, t]$ ,  $\mu_n > 0$ ,  $n \in Z_+$  are constants. Distributed delays  $r_n$  satisfy  $0 < r_n < r$ , where  $r$  is a real constant.

**Lemma 1** (see [34]). For the same dimension matrices  $H, M$  and the constant  $a > 0$ , then

$$2H^T M \leq a^{-1} H^T H + a M^T M. \quad (8)$$

*Assumption 1.* There exist positive constants  $\zeta > 0$ ,  $n \times n$  matrix  $P > 0$ , and  $n \times n$  diagonal matrices  $W_1 > 0, W_2 > 0$ , the following conditions hold:

$$\begin{pmatrix} Y & I_N \otimes PA & I_N \otimes PB \\ * & -W_1 \otimes I_N & 0 \\ * & * & -W_2 \otimes I_N \end{pmatrix} < 0, \quad (9)$$

$$\begin{pmatrix} \frac{1}{\zeta} I_N & PK \\ * & -P \end{pmatrix} < 0, \quad (10)$$

where  $L = \text{diag}(l_1, l_2, \dots, l_n)$ ,  $Y = -I_N \otimes PC + (1/2)W_1 \otimes L^T L + (1/2)W_2 \otimes L^T L + \vartheta D \otimes \Gamma$ .

### 3. Synchronization Analysis

In this part, we use the Lyapunov stability method and impulsive delayed inequality (7) to derive our main results.

**Theorem 1.** System (2) can achieve the impulsive synchronization with system (1) under delayed impulsive controller (3), if Assumption 1 holds.

*Proof 1.* Consider the Lyapunov-like function:

$$V(t) = \frac{1}{2} e^T(t) (I_N \otimes P) e(t) + \frac{1}{2} \int_{t-\tau}^t e^{-\alpha(t-s)} e^T(s) (W_2 \otimes L^T L) e(s) ds. \quad (11)$$

When  $t \neq t_n$ , the derivative of  $V(t)$  along the trajectory of system (6) can be calculated as follows:

$$\begin{aligned} \dot{V}(t) &= e^T(t) (I_N \otimes P) [-(I_N \otimes C)e(t) + (I_N \otimes A)g(e(t)) \\ &\quad + (I_N \otimes B)g(e(t - \tau)) + \vartheta(D \otimes \Gamma)e(t)] \\ &\quad - \frac{\alpha}{2} \int_{t-\tau}^t e^{-\alpha(t-s)} e^T(s) (W_2 \otimes L^T L) e(s) ds \\ &\quad + \frac{1}{2} e^T(t) (W_2 \otimes L^T L) e(t) - \frac{1}{2} e^{-\alpha\tau} e^T(t - \tau) \\ &\quad \cdot (W_2 \otimes L^T L) e(t - \tau). \end{aligned} \quad (12)$$

Based on Lemma 1, the inequality  $2A^T B \leq a^{-1} A^T A + a B^T B$ ,  $A, B \in R^n, a > 0$ , we can perform the following calculation:

$$\begin{aligned} e^T(t) (I_N \otimes P) (I_N \otimes A) g(e(t)) &= \sum_{i=1}^N e_i^T(t) P A g(e_i(t)) \\ &\leq \sum_{i=1}^N \frac{1}{2} w_{1i}^{-1} e_i^T(t) P A A^T P^T e_i(t) + \sum_{i=1}^N \frac{1}{2} w_{1i} g^T(e_i(t)) g(e_i(t)) \\ &\leq \sum_{i=1}^N \frac{1}{2} w_{1i}^{-1} e_i^T(t) P A A^T P^T e_i(t) + \sum_{i=1}^N \frac{1}{2} w_{1i} e_i^T(t) L^T L e_i(t). \end{aligned} \quad (13)$$

Changing formula (13) to Kronecker product, we can get

$$\begin{aligned} e^T(t) (I_N \otimes P) (I_N \otimes A) g(e(t)) \\ + \frac{1}{2} e^T(t) (W_1 \otimes L^T L) e(t). \end{aligned} \quad (14)$$

Similarly, it gives that

$$\begin{aligned} e^T(t) (I_N \otimes P) (I_N \otimes B) g(e(t - \tau)) \\ \leq \frac{1}{2} e^T(t) (W_2^{-1} \otimes (P B B^T P^T)) e(t) + \frac{1}{2} e^T(t - \tau) (W_2 \otimes L^T L) e(t - \tau). \end{aligned} \quad (15)$$

From formulas (14) and (15), formula (9) can be changed to

$$\begin{aligned}
\dot{V}(t) &= e^T(t)(I_N \otimes P)[-(I_N \otimes C)e(t) + (I_N \otimes A)g(e(t)) + (I_N \otimes B)g(e(t-\tau)) + \vartheta(D \otimes \Gamma)e(t)] \\
&\quad - \frac{\alpha}{2} \int_{t-\tau}^t e^{-\alpha(t-s)} e^T(s)(W_2 \otimes L^T L)e(s)ds + \frac{1}{2} e^T(t)(W_2 \otimes L^T L)e(t) - \frac{1}{2} e^{-\alpha\tau} e^T(t-\tau)(W_2 \otimes L^T L)e(t-\tau) \\
&\leq e^T(t) \left[ -I_N \otimes PC + \frac{1}{2} (W_1^{-1} \otimes (PAA^T P^T) + W_1 \otimes L^T L + W_2^{-1} \otimes (PBB^T P^T) + W_2 \otimes L^T L) + \vartheta(D \otimes P\Gamma) \right] e(t) \\
&\quad + \frac{1}{2} (1 - e^{-\alpha\tau}) e^T(t-\tau)(W_2 \otimes L^T L)e(t-\tau) - \frac{\alpha}{2} \int_{t-\tau}^t e^{-\alpha(t-s)} e^T(s)(W_2 \otimes L^T L)e(s)ds,
\end{aligned} \tag{16}$$

where  $e^{-\alpha\tau} < 1$ ; the following conditions are established:

$$\dot{V}(t) < 0. \tag{17}$$

When  $t = t_n$ , the derivative of  $V(t)$  along the trajectory of system (6) can be calculated as follows:

$$\begin{aligned}
\dot{V}(t) &= e^T(t)(I_N \otimes P) \left[ -(I_N \otimes C)e(t) + (I_N \otimes A)g(e(t)) + (I_N \otimes B)g(e(t-\tau)) + \vartheta(D \otimes \Gamma)e(t) + (I_N \otimes K) \int_{t-r_n}^t e(s)ds \right] \\
&\quad - \frac{\alpha}{2} \int_{t-\tau}^t e^{-\alpha(t-s)} e^T(s)(W_2 \otimes L^T L)e(s)ds + \frac{1}{2} e^T(t)(W_2 \otimes L^T L)e(t) - \frac{1}{2} e^{-\alpha\tau} e^T(t-\tau)(W_2 \otimes L^T L)e(t-\tau).
\end{aligned} \tag{18}$$

From (14) and (15), we have

$$\begin{aligned}
\dot{V}(t) &\leq e^T(t) \left[ -I_N \otimes PC + \frac{1}{2} (W_1^{-1} \otimes (PAA^T P^T) + W_1 \otimes L^T L + W_2^{-1} \otimes (PBB^T P^T) + W_2 \otimes L^T L) + \vartheta(D \otimes P\Gamma) \right] e(t) \\
&\quad + \frac{1}{2} (1 - e^{-\alpha\tau}) e^T(t-\tau)(W_2 \otimes L^T L)e(t-\tau) + e^T(t)(I_N \otimes P)(I_N \otimes K) \int_{t-r_n}^t e(s)ds.
\end{aligned} \tag{19}$$

Based on Lemma 1, we can perform the following calculation:

$$\begin{aligned}
&e^T(t)(I_N \otimes P)(I_N \otimes K) \int_{t-r_n}^t e(s)ds \\
&= e^T(t)(I_N \otimes PK) \int_{t-r_n}^t e(s)ds \\
&= \sum_{i=1}^N e_i^T(t)PK \int_{t-r_n}^t e_i(s)ds \\
&\leq \frac{1}{2} \sum_{i=1}^N \left( e_i^T(t)e_i(t) + \left( \int_{t-r_n}^t e_i(s)ds \right)^T K^T P^T PK \int_{t-r_n}^t e_i(s)ds \right).
\end{aligned} \tag{20}$$

It follows from (10) that there exists an inequality such that  $-(1/\zeta)P - PK(PK)^T < 0$ , which together with (20) implies that

$$\begin{aligned}
&e^T(t)(I_N \otimes P)(I_N \otimes K) \int_{t-r_n}^t e(s)ds \\
&\leq \frac{1}{2} \sum_{i=1}^N \left( e_i^T(t)Pe_i(t) - \left( \frac{1}{\zeta} \int_{t-r_n}^t e_i^T(s)Pe_i(s)ds \right) \right) \\
&\leq \frac{1}{2} \left( e^T(I_N \otimes P)e - \frac{1}{\zeta} \int_{t-r_n}^t e^T(s)(I_N \otimes P)e(s)ds \right) \\
&\leq \frac{1}{2} \left( V(t) - \frac{1}{\zeta} \int_{t-r_n}^t V(s)ds \right),
\end{aligned} \tag{21}$$

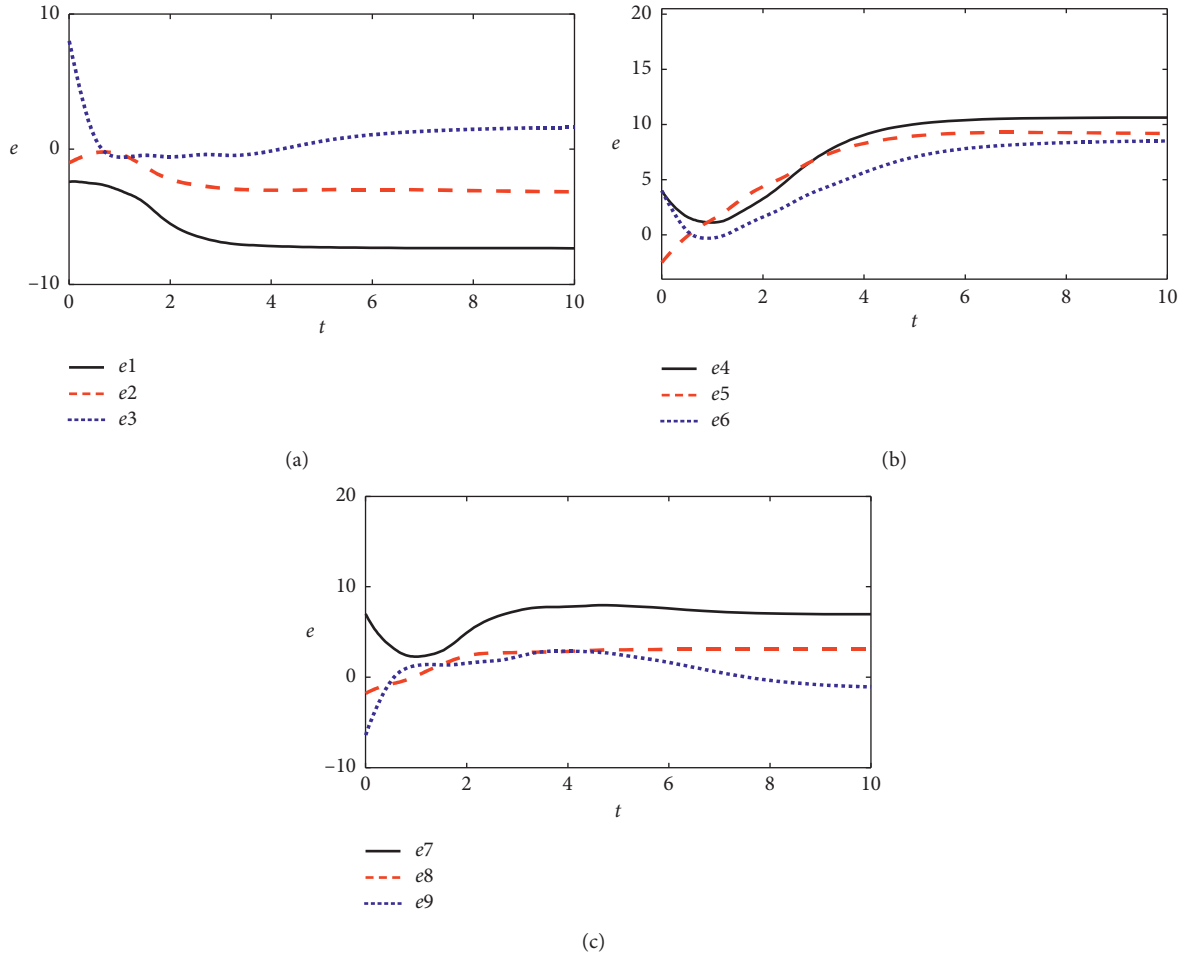


FIGURE 1: The error trajectories without impulsive control.

where  $\zeta = (1/\mu_n^2)$ . Then, it can be deduced that  $V(t) \leq \mu_n^2 \int_{t-r_n}^t V(s) ds$ . According to formulas (9) and (21), we can derive that

$$\dot{V}(t) < 0. \tag{22}$$

According to the Lyapunov stability theory, we can obtain  $e_i(t) \rightarrow 0$  as  $t \rightarrow \infty$ , which means that system (2) can achieve the impulsive synchronization with system (1) under impulsive controller (3). This completes the proof.

#### 4. Numerical Simulation

In the simulation, we studied the synchronization problem of the coupled neural network with three nodes, namely,  $N=3$ . The activation functions are chosen as  $f(x_i) = \tanh(x_i)$ .

Consider the following neural networks:

$$\begin{cases} \dot{x}_i(t) = -Cx_i(t) + Af(x_i(t)) + Bf(x_i(t-\tau)) + \vartheta_1 \sum_{j=1}^n d_{ij} \Gamma x_j(t), & t \geq t_0, \\ x_i(s) = \varphi_i(s), & s \in [t_0 - \tau, t_0]. \end{cases} \tag{23}$$

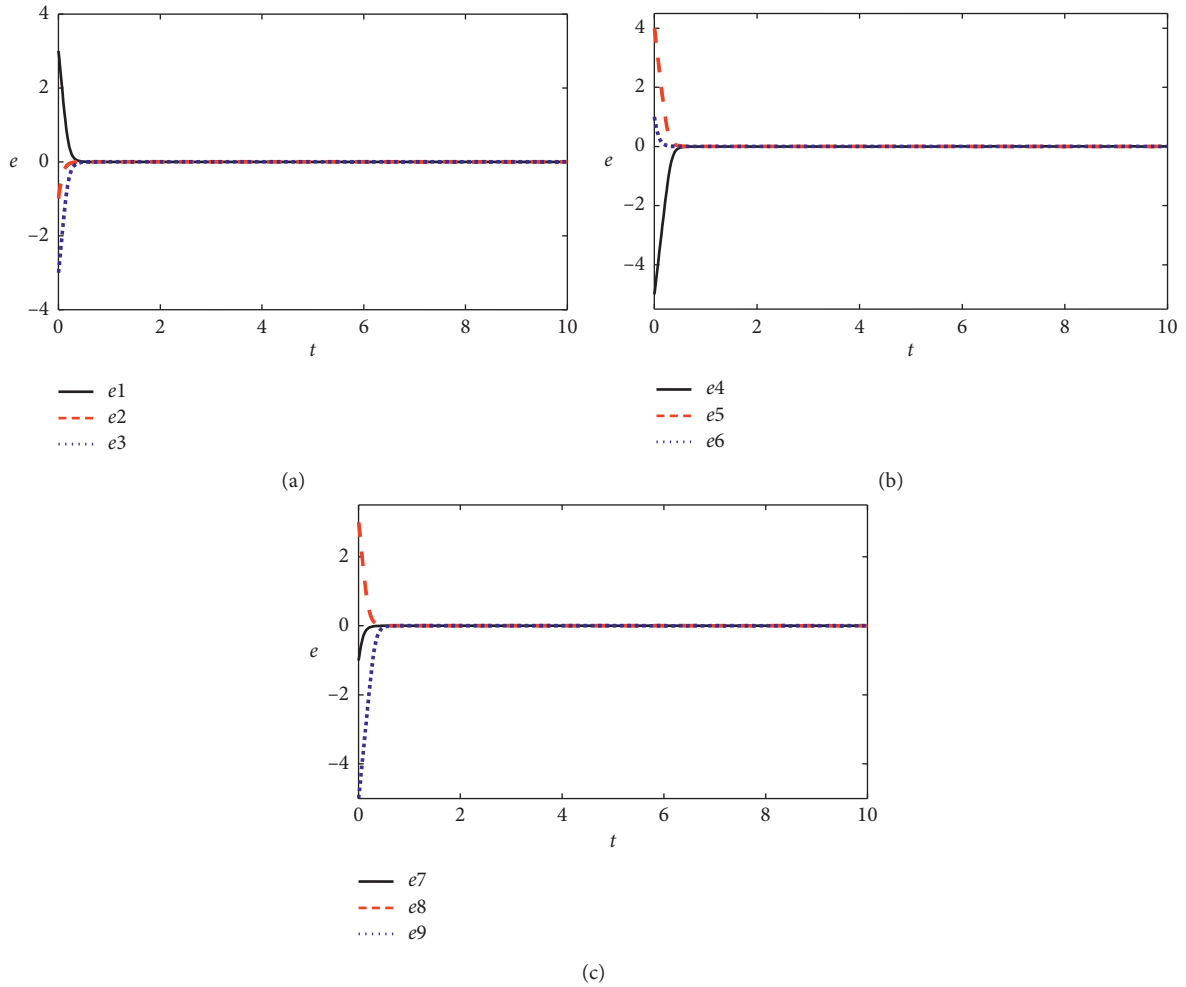


FIGURE 2: The error trajectories with impulsive control.

Consider the following response system:

$$\begin{cases} \dot{y}_i(t) = -Cy_i(t) + Af(y_i(t)) + Bf(y_i(t - \tau)) + \vartheta_2 \sum_{j=1}^n d_{ij}\Gamma y_j(t) + u_i(t), & t \geq t_0, \\ y_i(s) = \psi_i(s), & s \in [t_0 - \tau, t_0], \end{cases} \quad (24)$$

where  $\tau = 1$ ,  $i = 1, 2, 3$ ,  $j = 1, 2, 3$ ,  $\vartheta_1 = 0.5$ ,  $\vartheta_2 = 5$ , initial condition  $\varphi_1(s) = [0.5, 0.6, 0.7]^T$ ,  $\varphi_2(s) = [0.6, 0.7, 0.8]^T$ ,  $\varphi_3(s) = [0.7, 1, 1.5]^T$ ,  $\psi_1(s) = [1, 1.5, 2]^T$ ,  $\psi_2(s) = [1.4,$

$1.6, 1.5]^T$ ,  $\psi_3(s) = [1.6, 1.7, 1.8]^T$ , and  $s \in [-1, 0]$ , and the parameter matrices  $C, A, B, D$ , and  $\Gamma$  are given by

$$\begin{aligned}
 C_1 &= \begin{bmatrix} 1 & 0 & 0 \\ 0 & 1 & 0 \\ 0 & 0 & 1 \end{bmatrix}, & K &= \begin{bmatrix} 0.3756 & -0.1417 & 0.0184 \\ -0.1417 & -0.3321 & -0.0200 \\ 0.0184 & -0.0200 & 0.5108 \end{bmatrix}. & (27) \\
 C_2 &= \begin{bmatrix} 2 & 0 & 0 \\ 0 & 1 & 0 \\ 0 & 0 & 1 \end{bmatrix}, \\
 A_1 &= \begin{bmatrix} 1 & 3 & 2 \\ -0.1 & 2 & 0.5 \\ 3 & 1 & -3 \end{bmatrix}, \\
 A_2 &= \begin{bmatrix} 1 & 0.6 & -1 \\ -1 & 2 & 0.1 \\ 3 & 0.5 & -3 \end{bmatrix}, \\
 B_1 &= \begin{bmatrix} 0.2 & 1 & 0.5 \\ 3 & 0.4 & 0.1 \\ 0.4 & 0.6 & 2 \end{bmatrix}, \\
 B_2 &= \begin{bmatrix} 1 & 0.3 & 2 \\ 0.5 & 1 & 0.6 \\ 3 & 1 & 0.4 \end{bmatrix}, \\
 D_1 = D_2 &= \begin{bmatrix} -1 & 1 & 0 \\ 0 & -1 & 1 \\ 1 & 0 & -1 \end{bmatrix}, \\
 \Gamma_1 = \Gamma_2 &= \begin{bmatrix} 1 & 0 & 0 \\ 0 & 1 & 0 \\ 0 & 0 & 1 \end{bmatrix}. & (25)
 \end{aligned}$$

When there is no control input (i.e.,  $u(t) = 0$ ), system (24) cannot be synchronized with system (23), see Figure 1. Next, we consider distributed delayed impulsive control to achieve the synchronization between system (23) and system (24). The control input  $u(t)$  is given by (3) with  $r_n = 1.2$ . Choose  $\zeta = 0.05$ , using the MATLAB LMI toolbox, and the following feasible solutions can be derived:

$$\begin{aligned}
 P &= \begin{bmatrix} 0.7025 & -0.4528 & -0.0353 \\ -0.4528 & 0.8421 & -0.0435 \\ -0.0353 & -0.0435 & 0.2865 \end{bmatrix}, \\
 W_1 &= \begin{bmatrix} 0.3272 & 0 & 0 \\ 0 & 0.4158 & 0 \\ 0 & 0 & 0.4191 \end{bmatrix}, \\
 W_2 &= \begin{bmatrix} 0.4930 & 0 & 0 \\ 0 & 0.3724 & 0 \\ 0 & 0 & 0.3405 \end{bmatrix}. & (26)
 \end{aligned}$$

Thus, the gain matrix  $K$  is derived as follows:

For simulation, if we take  $t_n = 0.07n$ ,  $n \in Z$ , then the synchronization error is shown in Figure 2.

### 5. Conclusion

In this paper, the synchronization of coupled neural networks is studied by distributed delayed impulsive control. Based on the impulsive control theory and Lyapunov stability theory, a distributed delayed impulsive controller is proposed. The proposed inequality fully considers the synchronization of the response system and the drive system under different time conditions. The numerical simulation proves the feasibility and effectiveness of our proposed scheme. In the future, we will deal with finite time synchronization of coupled neural networks through distributed delayed impulsive control.

### Data Availability

The data used to support the findings of this study are available from the corresponding author upon request.

### Conflicts of Interest

The authors declare that they have no conflicts of interest.

### Acknowledgments

The work was supported by the National Natural Science Foundation of China (Grant no. 61775198), Science and Technology Project of Henan Province (Grant nos. 192102210083 and 202102210317), Key Scientific Research Projects of Universities in Henan Province (Grant no. 20A413012), and Science and Technology Innovation Team Project of Henan Province (Grant no. 19IRTSTHN013).

### References

- [1] S. Arik, "An analysis of exponential stability of delayed neural networks with time varying delays," *Neural Networks*, vol. 17, no. 7, pp. 1027–1031, 2004.
- [2] X. Ye, J. Mou, C. Luo, and Z. Wang, "Dynamics analysis of Wien-bridge hyperchaotic memristive circuit system," *Non-linear Dynamics*, vol. 92, no. 3, pp. 923–933, 2018.
- [3] L. O. Chua and L. Yang, "Cellular neural networks: applications," *IEEE Transactions on Circuits and Systems*, vol. 35, no. 10, pp. 1273–1290, 1998.
- [4] J. W. Sun, G. Y. Han, Z. G. Zeng, and Y. F. Wang, "Memristor-based neural network circuit of full-function pavlov associative memory with time delay and variable learning rate," *IEEE Transactions on Cybernetics*, vol. 10, p. 1109, 2019.
- [5] X. Liu, X. Shen, Y. Zhang, and Q. Wang, "Stability criteria for impulsive systems with time delay and unstable system

- matrices," *IEEE Transactions on Circuits and Systems I: Regular Papers*, vol. 54, no. 10, pp. 2288–2298, 2007.
- [6] H. Su, Y. Sun, and Z. Zeng, "Semiglobal observer-based non-negative edge consensus of networked systems with actuator saturation," *IEEE Transactions on Cybernetics*, vol. 50, no. 6, pp. 2827–2836, 2020.
  - [7] U. Fory and M. Bodnar, "Time delays in proliferation process for solid avascular tumour," *Math and Computer Modelling*, vol. 37, no. 11, pp. 1201–1209, 2003.
  - [8] W. Yu, J. Cao, and G. Chen, "Stability and Hopf bifurcation of a general delayed recurrent neural network," *IEEE Transactions on Neural Networks*, vol. 19, no. 5, pp. 845–854, 2008.
  - [9] H. Su, J. Zhang, and Z. Zeng, "Formation-containment control of multi-robot systems under a stochastic sampling mechanism," *Science China Technological Sciences*, vol. 63, no. 6, pp. 1025–1034, 2020.
  - [10] F. F. Yang, J. Mou, J. Liu, C. G. Ma, and H. Z. Yan, "Characteristic analysis of the fractional-order hyperchaotic complex system and its image encryption application," *Signal Processing*, vol. 169, 2020.
  - [11] Q. Zhang, J. Lu, and J. Zhao, "Impulsive synchronization of general continuous and discrete-time complex dynamical networks," *Communications in Nonlinear Science and Numerical Simulation*, vol. 15, no. 10, pp. 1063–1070, 2010.
  - [12] J. Zhou, L. Xiang, and Z. Liu, "Synchronization in complex delayed dynamical networks via impulsive control," *Physica A: Statistical Mechanics and Its Applications*, vol. 384, no. 2, pp. 684–692, 2007.
  - [13] W. Xu, S. Zhu, X. Fang, and W. Wang, "Adaptive synchronization of memristor-based complex-valued neural networks with time delays," *Neurocomputing*, vol. 364, no. 28, pp. 119–128, 2019.
  - [14] Q. Wang and J. L. Wu, "Finite-time output synchronization of undirected and directed coupled neural networks with output coupling," *IEEE Transactions on Neural Networks and Learning Systems*, vol. 10, p. 1109, 2020.
  - [15] M. P. Aghababa, K. Sohrab, and G. Alizadeh, "Finite-time synchronization of two different chaotic systems with unknown parameters via sliding mode technique," *Applied Mathematical Modelling*, vol. 35, no. 10, pp. 3080–3091, 2011.
  - [16] J. Sun, Y. Wu, G. Cui, and Y. Wang, "Finite-time real combination synchronization of three complex-variable chaotic systems with unknown parameters via sliding mode control," *Nonlinear Dynamics*, vol. 88, no. 3, pp. 1677–1690, 2017.
  - [17] P. Selvaraj, R. Sakthivel, and O. M. Kwon, "Finite-time synchronization of stochastic coupled neural networks subject to Markovian switching and input saturation," *Neural Networks*, vol. 105, pp. 154–165, 2018.
  - [18] D. Zhang, J. Cheng, J. Cao, and D. Zhang, "Finite-time synchronization control for semi-Markov jump neural networks with mode-dependent stochastic parametric uncertainties," *Applied Mathematics and Computation*, vol. 344–345, no. 1, pp. 230–242, 2019.
  - [19] Y. Wu, J. Cao, Q. Li, A. Alsaedi, and F. E. Alsaadi, "Finite-time synchronization of uncertain coupled switched neural networks under asynchronous switching," *Neural Networks*, vol. 85, pp. 128–139, 2017.
  - [20] Q. Song, J. Cao, and F. Liu, "Pinning synchronization of linearly coupled delayed neural networks," *Mathematics and Computers in Simulation*, vol. 86, pp. 39–51, 2012.
  - [21] W.-H. Chen and W. X. Zheng, "Exponential stability of nonlinear time-delay systems with delayed impulse effects," *Automatica*, vol. 47, no. 5, pp. 1075–1083, 2011.
  - [22] Z.-H. Guan, G.-S. Han, J. Li, D.-X. He, and G. Feng, "Impulsive multiconsensus of second-order multiagent networks using sampled position data," *IEEE Transactions on Neural Networks and Learning Systems*, vol. 26, no. 11, pp. 2678–2688, 2015.
  - [23] Z. Huang, J. Cao, J. Li, and H. Bin, "Quasi-synchronization of neural networks with parameter mismatches and delayed impulsive controller on time scales," *Nonlinear Analysis: Hybrid Systems*, vol. 33, pp. 104–115, 2019.
  - [24] X. Yang, X. Li, X. Li, Q. Xi, and P. Duan, "Review of stability and stabilization for impulsive delayed systems," *Mathematical Biosciences & Engineering*, vol. 15, no. 6, pp. 1495–1515, 2018.
  - [25] B. Liu, Z. Sun, Y. Luo, and Y. Zhong, "Uniform synchronization for chaotic dynamical systems via event-triggered impulsive control," *Physica A: Statistical Mechanics and Its Applications*, vol. 531, no. 1, p. 121725, 2019.
  - [26] W. He, X. Gao, W. Zhong, and F. Qian, "Secure impulsive synchronization control of multi-agent systems under deception attacks," *Information Sciences*, vol. 459, pp. 354–368, 2018.
  - [27] T. Qian, T. Yu, and B. Cui, "Adaptive synchronization of multi-agent systems via variable impulsive control," *Journal of the Franklin Institute*, vol. 355, no. 15, pp. 7490–7508, 2018.
  - [28] W. Lu and T. Chen, "Synchronization of coupled connected neural networks with delays," *IEEE Transactions on Circuits and Systems I: Regular Papers*, vol. 51, no. 12, pp. 2491–2503, 2004.
  - [29] Z. Xu, D. Peng, and X. Li, "Synchronization of chaotic neural networks with time delay via distributed delayed impulsive control," *Neural Networks*, vol. 118, pp. 332–337, 2019.
  - [30] X. Xie, X. Liu, H. Xu, X. Luo, and G. Liu, "Synchronization of coupled reaction-diffusion neural networks: delay-dependent pinning impulsive control," *Communications in Nonlinear Science and Numerical Simulation*, vol. 79, Article ID 104905, 2019.
  - [31] P.-C. Wei, J.-L. Wang, Y.-L. Huang, B.-B. Xu, and S.-Y. Ren, "Impulsive control for the synchronization of coupled neural networks with reaction-diffusion terms," *Neurocomputing*, vol. 207, no. 26, pp. 539–547, 2016.
  - [32] X. Li, J.-a. Fang, and H. Li, "Master-slave exponential synchronization of delayed complex-valued memristor-based neural networks via impulsive control," *Neural Networks*, vol. 93, pp. 165–175, 2017.
  - [33] Y. Kan, J. Lu, J. Qiu, and J. Kurths, "Exponential synchronization of time-varying delayed complex-valued neural networks under hybrid impulsive controllers," *Neural Networks*, vol. 114, pp. 157–163, 2019.
  - [34] S. Boyd, L. E. Ghaoui, E. Feron, and V. Balakrishnan, *Linear Matrix Inequality in Systems and Control Theory*, SIAM, Philadelphia, PA, USA, 1994.

## Research Article

# Constant Frequency Control Strategy of Microgrids by Coordinating Energy Router and Energy Storage System

Zheng Lan,<sup>1</sup> Junzhang Wang ,<sup>1</sup> Jinhui Zeng ,<sup>1</sup> Dong He,<sup>1</sup> Fan Xiao,<sup>2</sup> and Fei Jiang<sup>3</sup>

<sup>1</sup>College of Electrical and Information Engineering, Hunan University of Technology, Zhuzhou, Hunan, China

<sup>2</sup>College of Electrical and Information Engineering, Hunan University, Changsha, Hunan, China

<sup>3</sup>College of Electrical and Information Engineering, Changsha University of Science & Technology, Changsha, Hunan, China

Correspondence should be addressed to Jinhui Zeng; [zjh@hut.edu.cn](mailto:zjh@hut.edu.cn)

Received 19 May 2020; Accepted 15 July 2020; Published 14 August 2020

Guest Editor: Hou-Sheng Su

Copyright © 2020 Zheng Lan et al. This is an open access article distributed under the Creative Commons Attribution License, which permits unrestricted use, distribution, and reproduction in any medium, provided the original work is properly cited.

In this paper, a constant frequency control strategy of a microgrid by coordinating energy router (ER) and energy storage system is proposed to solve the frequency fluctuation problem of microgrid, in which ER is the core of the energy management system. The interface converter of ER connected to the microgrid adopts the virtual synchronous generator (VSG) control, which adjusts the mechanical reference power in real time according to the state of charge (SOC) of the energy storage. The energy storage system adopts constant voltage and constant frequency (V/F) control to maintain the frequency and voltage stability of microgrid. The energy storage system with fast charge and discharge responds to the power fluctuation of the microgrid. ER maintains the stability of the energy storage capacity through bidirectional power regulation. When the energy storage system fails, the frequency and voltage droop characteristics of ER controlled by VSG will play a role in maintaining the stable operation of the microgrid. By the coordinating control strategy, the maximum efficiency of intermittent distributed energy can be guaranteed, and the stability, reliability, and grid-connection friendliness of the microgrid operation can be improved. Simulation results prove the effectiveness of the proposed control strategy.

## 1. Introduction

In recent years, due to the rapid development of distributed power generation technology, a large number of distributed new energy grid-connection requirements have emerged. However, due to the intermittent and fluctuating characteristics of new energy sources such as photovoltaics, a large number of new energy sources directly incorporated into the grid will bring severe challenges to the stability of traditional power systems. The microgrid has become one of the effective ways to dissipate distributed energy sources (DER) [1, 2]. Among them, microgrids with ER as the core have been proposed successively [3–5].

In this kind of microgrid, DER, local loads, and battery energy storage system (BESS) are usually connected to the main grid through the low-voltage AC interface provided by the ER. The ER transmits and manages the surplus and deficit power of distributed power after local absorption and

completes the functions of initiative adjustment of electric energy and adjustment of electric power quality.

To control the frequency stability of the microgrid, we need an effective control strategy. The load in the microgrid is uncontrollable. At the same time, to avoid wind and light abandonment, distributed power generation units often use maximum power point tracking (MPPT) control [6, 7]. Therefore, neither load nodes nor distributed generation nodes can participate in frequency regulation without the use of deloading control. To improve the operational performance of the microgrid, we used the energy storage system as an energy buffer device to suppress power fluctuations. At the same time, the energy storage system is jointly powered with ER and DER [8–10]. Therefore, the microgrid with the ER as the core needs to control the energy storage unit node and the ER node to achieve the frequency stability of the microgrid. How to coordinate and control ER, distributed energy, and



related energy storage devices has become an urgent problem to be solved.

In the current research, there are two main research approaches to ensure the stable operation of the microgrid in the complex network connected with many distributed power sources. One is to make the output voltage and frequency of each distributed network node be the same. Many scholars have proposed the edge consensus algorithms [11, 12], which ensure that the network system can still maintain the consistency of output voltage and frequency of each node under various disturbances; to improve the stability of the system, many scholars put forward the global robust control algorithm of the network system [13]. The other is by coordinating the power of the units in the microgrid. The authors in [14, 15] propose to combine the energy storage system with wind turbines and other DER to reduce the power fluctuation of the microgrid. This scheme can make the wind turbine and other DER output at maximum power, and the energy storage system quickly absorbs or releases the surplus and deficiency power of the microgrid, which can avoid the frequency instability of microgrid caused by the power fluctuation of DER. The authors in [16] propose a master-slave control strategy, which controls the output of the ER as a constant voltage and constant frequency voltage source and the BESS control as a current source with controllable power. Under this control strategy, the microgrid can keep the frequency constant. However, because there is no local frequency variable as the judgment index of ER and BESS outputs, power allocation can only be implemented through the upper energy management system, the control is complex and transitionally dependent on communication, and the reliability is not high. Also, to solve the problem that the network system can still achieve synchronization in the case of coupling resonance or disturbance, the authors in [17, 18] propose adaptive synchronization algorithms, respectively. Lv et al. [19] introduced the VSG control technology into the control of the ER interface, which enhanced the inertial damping of the system and reduced the impact of the wind-wave output on the main grid. However, the coordinated operation of the ER and energy storage was not involved in the paper. However, the coordinated operation of the ER and the energy storage system was not involved in this paper.

Based on the above analysis, this paper proposes a constant frequency control strategy of the microgrid by coordinating the ER and the energy storage system. We can refer to the method of virtual reactance to limit fault current in [20] and introduce VSG control into the low-voltage AC output interface of ER to increase the inertia of the microgrid system and reduce the large frequency fluctuations caused by the load disturbance. The ER adjusts the SOC of the energy storage based on weak communication. The BESS adopts constant voltage and frequency (V/F) control to provide constant voltage and frequency for the microgrid. On the one hand, the proposed control strategy can solve the problem of frequency fluctuation of microgrid and, at the same time, avoid overcharging or overdischarging of the energy storage system. On the other hand, when ER or RSS fails, there is no need to switch control strategies, ensuring

the smooth operation of the microgrid. Finally, the operation results of the proposed control strategy are verified by simulation.

## 2. Description of the Microgrid System

The typical microgrid structure with the ER as the core is shown in Figure 1(a).

DC loads such as charging pile need to be extracted through AC/DC converter, and AC load such as the AC motor can be directly connected with a bus. The DER such as wind power and photovoltaic power is connected to an AC bus through DC/AC and AC/DC/AC converters, respectively, and the BESS is connected to microgrid through DC/AC converters to jointly supply power for the local loads. As an energy hub, ER connects the main grid and the microgrid, and its structure is shown in Figure 1(b). ER consists of three parts: the input stage, isolation stage, and output stage. The input stage is cascade-connected by the H-bridge AC/DC rectifier, which can realize different levels of voltage access of the main grid. The isolation stage is composed of a bidirectional active full-bridge DC/DC converter in parallel, which plays the role of bidirectional power transmission, changing voltage, and isolating the main grid and microgrid. The output stage is a three-phase bridge inverter structure that provides a low-voltage AC interface to connect to the AC bus of the microgrid.

*2.1. Principle of System Coordination Operation.* In the overall control of ER, the input stage mainly controls the voltage stability of the capacitance  $C_{HN}$  at the high voltage side, which plays a rectifying role; the isolation stage controls the voltage stability of the capacitance  $C_L$  at the low-voltage side, which plays a role of voltage level exchange, bidirectional energy flow, and isolation between the input stage and the output stage [21]; the output stage inverts the direct current into three-phase AC output. As the control strategy of this paper is mainly realized by the ER output stage, the following research on the analysis of the coordinated operation principle is mainly carried out in the output stage. In the whole microgrid topology, the MPPT control is used to ensure the maximum power output of distributed generation. When both ER and BESS are working properly, the BESS is used as the balance node to provide voltage and frequency support and respond to the unbalanced power of DER and load quickly. ER, as the PQ node, adjusts the power output according to the SOC of BESS in real time to ensure that the SOC of the BESS is always in the normal range. We can take Figure 2 as an example to analyze the coordination process of ER and BESS.

Suppose there is a mismatch between DER output and load demand at some time, such as a sudden increase in load or a sudden decrease in DER output, and a power deficit  $P_{eq}$  will occur in the microgrid:

$$P_{eq} = \sum_{i \in S_L} P_{Li} - \sum_{i \in S_{RS}} P_{RSi}, \quad (1)$$

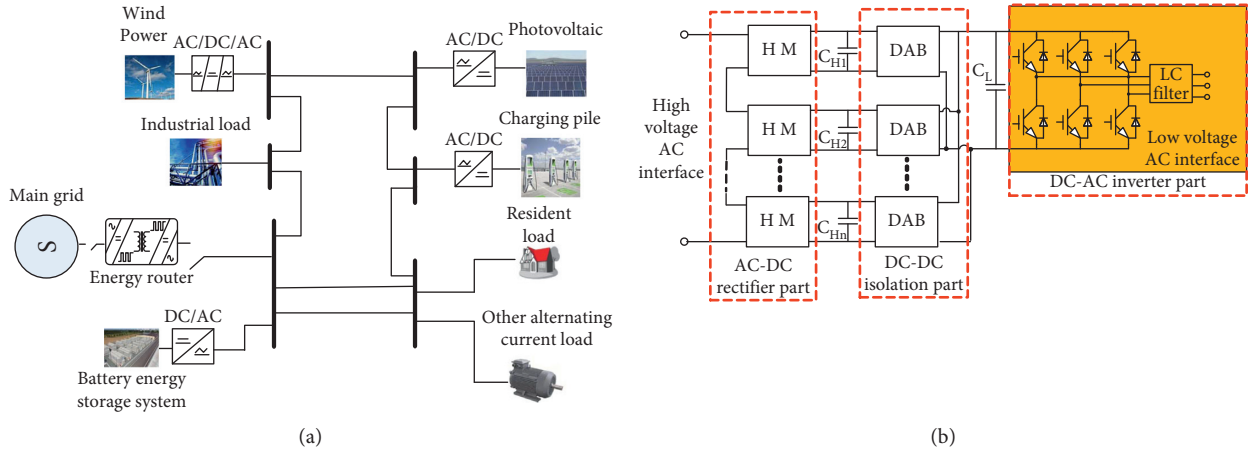


FIGURE 1: System structure of the microgrid and topology of the energy router: (a) microgrid system structure; (b) topology of energy router.

where  $P_{eq}$  is the net load of microgrid,  $P_{Li}$  is each load in the system,  $P_{RSi}$  is the power output of various renewable energy sources,  $S_L$  is the system load collection, and  $S_{RS}$  is the collection of renewable energy sources within the system.

If sufficient power is not replenished quickly, the frequency of the microgrid will fluctuate. When the power vacancy is too large, the frequency will drop sharply and even affect the stability of the microgrid. At this time, BESS rapidly releases the electric energy to ensure the active power balance. As the output power of BESS causes its SOC to be lower than the reference value, to maintain the stability of the energy storage capacity, ER reflects virtual inertia and slowly increases its active power output to share the power gap and charges the energy storage system. Through the adjustment of the ER, the electric energy released by BESS gradually reduces to zero and then absorbs the power to make its capacity recover. When the SOC returns to the reference value, the BESS output is zero, and the power gap is finally borne by the ER. Similarly, when DER output increases or load decreases, resulting in the power surplus of the microgrid, BESS quickly absorbs the surplus power, while ER slowly adjusts the SOC of the energy storage and finally transmits the surplus power to the main grid.

When the BESS fails and stops working, ER is naturally switched to a balance node and simulates the droop characteristics of synchronous generators to support the basic operation of the microgrid.

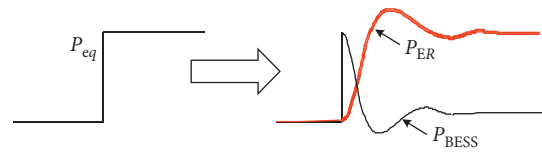


FIGURE 2: Schematic diagram of the coordinated control.

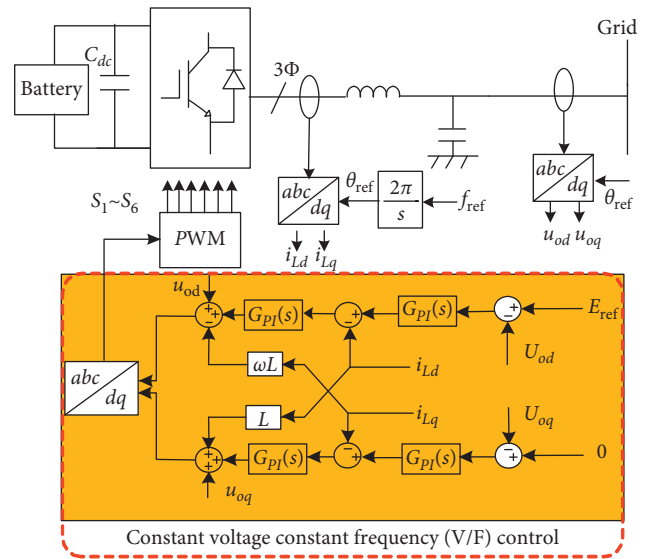


FIGURE 3: Control scheme of the BESS.

## 2.2. Coordination Control Strategy between the ER and the BESS

**2.2.1. Control of the BESS.** The BESS is composed of a battery, interface inverter, and LC filter. The output interface is connected with the AC bus of the microgrid. The purpose of BESS control is to provide stable voltage and frequency support for the microgrid and rapidly output according to the fluctuating power of DER or load. Its interface converter adopts constant voltage and constant frequency (V/F) control based on voltage and current double closed-loop [22]. The control block diagram is shown in Figure 3.

In Figure 3,  $i_{Labc}$  is the filtering inductance current,  $u_{oabc}$  is the output voltage of the interface converter, and  $E_{ref}$  and  $f_{ref}$  are the given voltage amplitude and frequency reference values, respectively. The phase angle  $\theta_{ref}$  needed for the coordinate transformation is obtained by integrating the reference frequency. After the  $abc/dq$  coordinate transformation of the output voltage, the  $u_{od}$  and  $u_{oq}$  components are obtained, which are compared with the voltage reference  $E_{ref}$  and 0, respectively, and the error is controlled by PI, so as to obtain the reference signals of the inner ring,  $i_{dref}$ , and  $i_{qref}$ . Voltage modulating signal  $u_{ref}$  was obtained through PI control, current loop, and  $dq/abc$  transformation of inner

loop current reference signal ( $i_{Ld}$ ) and filter inductance current component ( $i_{Lq}$ ).

**2.2.2. Control of the ER.** The objective of the input stage control of the ER is to stabilize the voltage of the capacitor on the high voltage side. To improve the control accuracy, the double closed-loop control is adopted. The voltage of the measured capacitor is compared with the voltage of the given capacitor to form a voltage outer loop to stabilize the voltage of the capacitor on the high side. The current inner loop can control the AC side current waveform, realize the control of the power factor of the input stage, and at the same time, can improve the control accuracy and response speed. The isolation stage adopts phase shift control [23] to realize the two-way flow of power.

The output stage of the ER adopts VSG control [19, 24, 25]. The VSG introduces the rotor motion equation and electromagnetic transient equation of the synchronous machine into the control of the output stage. It can make the inverter output of the output stage of ER equivalent to a voltage source with controllable power angle and voltage amplitude and make its output characteristics to simulate synchronous generator so that the inverter of the output stage of ER also has inertia, which can adjust voltage and frequency automatically. Since there are many studies on VSG at present, only the control block diagram (Figure 4) is given here, and the specific principle will not be detailed.

**2.3. Coordination Control between the ER and the BESS.** The BESS provides constant voltage and frequency for the system in the whole microgrid, and its fast charging and discharging capacity can also quickly respond to the power fluctuations of DER. However, BESS can neither maintain its SOC nor provide frequency droop characteristics for the system. To overcome this problem, the coordinated operation of the ER and BESS is realized by designing the mechanical reference power in VSG control. The specific control block diagram is shown in Figure 5.

When BESS is in normal operation, the switch is connected to point a. Since BESS provides a stable frequency for the microgrid at this time, the VSG power-frequency ( $P-f$ ) regulation characteristic does not work. ER outputs power according to the mechanical reference power  $P_{\text{ref}}$  and adjusts the energy storage capacity, and the  $P_{\text{ref}}$  expression is

$$P_{\text{ref}} = P_o + \Delta P, \quad (2)$$

where  $P_o$  is the base point of the running power command, which is estimated by the difference between the predicted value of the DER average output and the load and  $\Delta P$  is the adjusted power that the ER needs to output to maintain the stability of the energy storage capacity. Since the SOC can represent the remaining capacity of the battery, if the instantaneous value of the state of charge of the battery can track its reference value  $\text{SOC}_{\text{ref}}$ , the stability of the BESS capacity can be achieved. Therefore, closed-loop control is performed on the SOC. The acquired SOC instantaneous value is transmitted to the controller of the ER to form

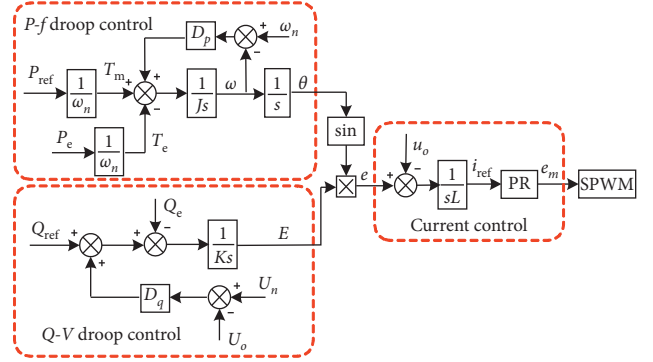


FIGURE 4: Control scheme of the VSG for the output stage of the ER.

closed-loop feedback with the  $\text{SOC}_{\text{ref}}$ . After the PI controller controls the feedback output, the adjusted power  $\Delta P$  can be obtained:

$$\Delta P = \left( K_p + \frac{K_i}{s} \right) (\text{SOC}_{\text{ref}} - \text{SOC}), \quad (3)$$

where  $K_p$  and  $K_i$  are the proportional coefficients and integral coefficient of PI controller, respectively.

In order to prevent the transmission power of the ER from exceeding the rated range in extreme cases,  $\text{SOC}_{\text{ref}}$  in this paper needs to be a reference value that can be dynamically adjusted. By changing  $\text{SOC}_{\text{ref}}$ , ER can control the active power output of BESS. For example, when faced with extreme weather without wind and light, the DER stops generating power, resulting in an imbalance between microgrid supply and demand. To prevent ER transmission power from exceeding the rated range, we can reduce the  $\text{SOC}_{\text{ref}}$  so that BESS can release part of the electric energy and share the transmission power of the ER.

As you can see from Figure 5, you can adjust the  $P_{\text{BESS,ref}}$  parameter to achieve the adjustment of  $\text{SOC}_{\text{ref}}$ .  $\text{SOC}_i$  is the initial value of the state of charge, which is determined by the initial state of BESS, so  $\text{SOC}_i$  cannot be adjusted. Adjusting the parameter of  $P_{\text{BESS,ref}}$  is essentially adjusting the slope of  $\text{SOC}_{\text{ref}}$ . This can be explained by the following equation. According to the relationship between the active power output of the battery and its state of charge [26, 27],

$$\text{SOC} = \text{SOC}_i - \int \frac{I_{dc}}{Q} dt, \quad (4)$$

$$I_{dc} = \frac{P_{\text{BESS}}}{V_{dc}}, \quad (5)$$

$$Q = \frac{I_{dc,\text{rate}} C_{\text{BESS,rate}}}{P_{\text{BESS,rate}}}, \quad (6)$$

where  $\text{SOC}_i$  is the initial value of the state of charge,  $I_{dc}$  is the output current of the DC side of the BESS,  $V_{dc}$  is the DC side voltage of the BESS,  $P_{\text{BESS}}$  is the active power output of the BESS,  $I_{dc,\text{rate}}$  is the rated value of the output DC,  $C_{\text{BESS,rate}}$  is the rated capacity of the BESS, and  $P_{\text{BESS,rate}}$  is the rated active power of the BESS. Substituting equations (5) and (6) into equation (4), we can get

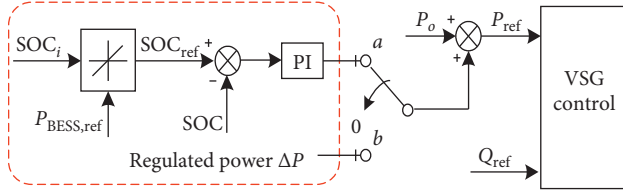


FIGURE 5: Power control scheme between ER and BESS.

$$\text{SOC} = \text{SOC}_i - \int \frac{P_{\text{BESS,rate}} P_{\text{BESS}}}{V_{dc} I_{dc,rate} C_{\text{BESS,rate}}} dt. \quad (7)$$

Differentiating both sides of equation (7), we get

$$\frac{d\text{SOC}}{dt} = -K_c P_{\text{BESS}}, \quad (8)$$

where  $K_c = P_{\text{BESS,rate}}/V_{dc} I_{dc,rate} \cdot C_{\text{BESS}}$ , rate because the  $V_{dc}$  is approximately constant, and  $K_c$  can be equivalent to constant. It is not difficult to find from equation (8) that BESS's active power output value  $P_{\text{BESS}}$  can be controlled by changing the slope  $d\text{SOC}/dt$ . Corresponding to the control in Figure 5,  $P_{\text{BESS,ref}}$  is the active power that ER wants BESS to share. Change the slope of  $\text{SOC}_{\text{ref}}$  by setting  $P_{\text{BESS}}$ , and then, change the value of  $\text{SOC}_{\text{ref}}$  dynamically. In this way, the active output of the ER can be adjusted to control the BESS to share the desired active power  $P_{\text{BESS,ref}}$ .

Since the frequency of the microgrid is only supported by the BESS, the stability of the microgrid will be greatly threatened when the BESS fails. To solve this problem, the switch design is carried out in the coordinated control strategy of ER and BESS. When BESS faults, the ER will receive the fault information transmitted from BESS through weak communication, and the switch will be connected to the point *b*. The BESS no longer provides frequency and voltage support for the microgrid. ER based on VSG control will adjust the frequency and voltage of the microgrid according to the active power-frequency droop characteristic and the reactive power-voltage droop characteristic and provide certain inertia for the system to enhance the frequency stability of the system. From the active frequency control loop in Figure 4, the frequency droop coefficient  $D_p$  can be expressed by

$$D_p = \frac{\Delta T}{\Delta \omega} = \frac{\Delta P}{\omega_n \Delta \omega} = \frac{\Delta P}{4\pi^2 f_n \Delta f}. \quad (9)$$

In the above formula,  $\Delta f$  is the variation range of the frequency offset of the microgrid,  $f_n$  is the rated value of the microgrid frequency (50 Hz), and  $\Delta P$  is the active power variation of the corresponding output of the ER.

### 3. Simulation Results

To verify the correctness and effectiveness of the proposed control strategy, we built a microgrid simulation model under the MATLAB/Simulink platform and set different working conditions for simulation verification. The DER in the model includes wind turbines and photovoltaics, and the

energy storage system uses currently widely used lead-acid batteries. When the rated frequency of the microgrid is 50 Hz, the rated capacity of ER is 100 kW, and the frequency variation range is  $\pm 0.5$  Hz, From equation (9), we can calculate that the frequency droop coefficient is 50.67 Nm/s/rad. The other main parameters of the simulation are shown in Table 1.

**3.1. Working Condition 1: Random Fluctuation of Wind and Solar.** As shown in Figure 6(a), the wind power fluctuation ranges from 47 kW to 83 kW, and the photovoltaic power fluctuation ranges from 18 kW to 33 kW. The total load demand is 100 kW. The output active power and SOC waveform of BESS and ER are shown in Figures 6(b)–6(d), respectively. It can be seen that when the output power of wind energy and photovoltaic light fluctuates, BESS can quickly respond to the unbalanced power of wind and light to ensure the balance of supply and demand in the microgrid, while ER reflects the virtual inertia to slowly adjust the output power according to SOC, support BESS operation, and maintain its SOC stability. Due to fluctuations in the output power of wind and photovoltaic, the SOC of BESS fluctuates. As can be seen from Figure 6(c), the frequency of the microgrid is stable at 50 Hz and hardly affected by the fluctuation of the landscape.

**3.2. Working Condition 2: Sudden Change in the Load.** To avoid disturbance of operation effect, the wind and sunlight output is constant with average output. At 3 s, the load of microgrid decreases sharply from 100 kW to 90 kW. At 3 s, due to sudden load reduction, 10 kW of surplus power appeared in the microgrid. At this time, BESS quickly absorbed the 10 kW of surplus power, and ER slowly reduced the power output. Finally, the output power of both BESS and ER tends to zero, as shown in Figure 7(a). At this time, all the loads in the microgrid are provided by wind power and photovoltaic. As can be seen from Figure 7(b), the SOC is gradually higher than the reference value at 3 s as BESS begins to absorb electricity energy.

The dynamic process of sudden changes in load can be seen more clearly that BESS has a fast output power, which can well suppress the frequency fluctuation caused by a sudden decrease in load, as shown in Figure 7(c). The ER output power waveform is smooth and slow, which effectively alleviates the influence of large power fluctuations on the main grid.

**3.3. Working Condition 3: BESS Failure and ER Runs Independently.** To simulate the actual situation, wind energy and photovoltaic energy still fluctuate by the law in working condition 1. When set at 8 s, the operation stopped due to the failure of the BESS. In the coordinated control between ER and BESS, when the ER receives the fault information transmitted from BESS through weak communication, the switch is connected from point *a* to point *b* (as shown in

TABLE 1: Key parameters of the simulation.

Parameter	Value/unit
Maximum fluctuation of the active power of the photovoltaic	33 kW
Maximum fluctuation of the active power of the wind power	83 kW
Average active power output of the photovoltaic	25 kW
Average active power output of the wind power	65 kW
The capacity of the battery energy storage system	5 Ah
Load	0–100 kW
Rated power of the ER	100 kW
$K_{PI}$ of the PI controller	110
$I_{PI}$ of the PI controller	210
Rated frequency of the microgrid	50 Hz
Rated line voltage	380 V
Droop control coefficient	50.67 Nm/s/rad

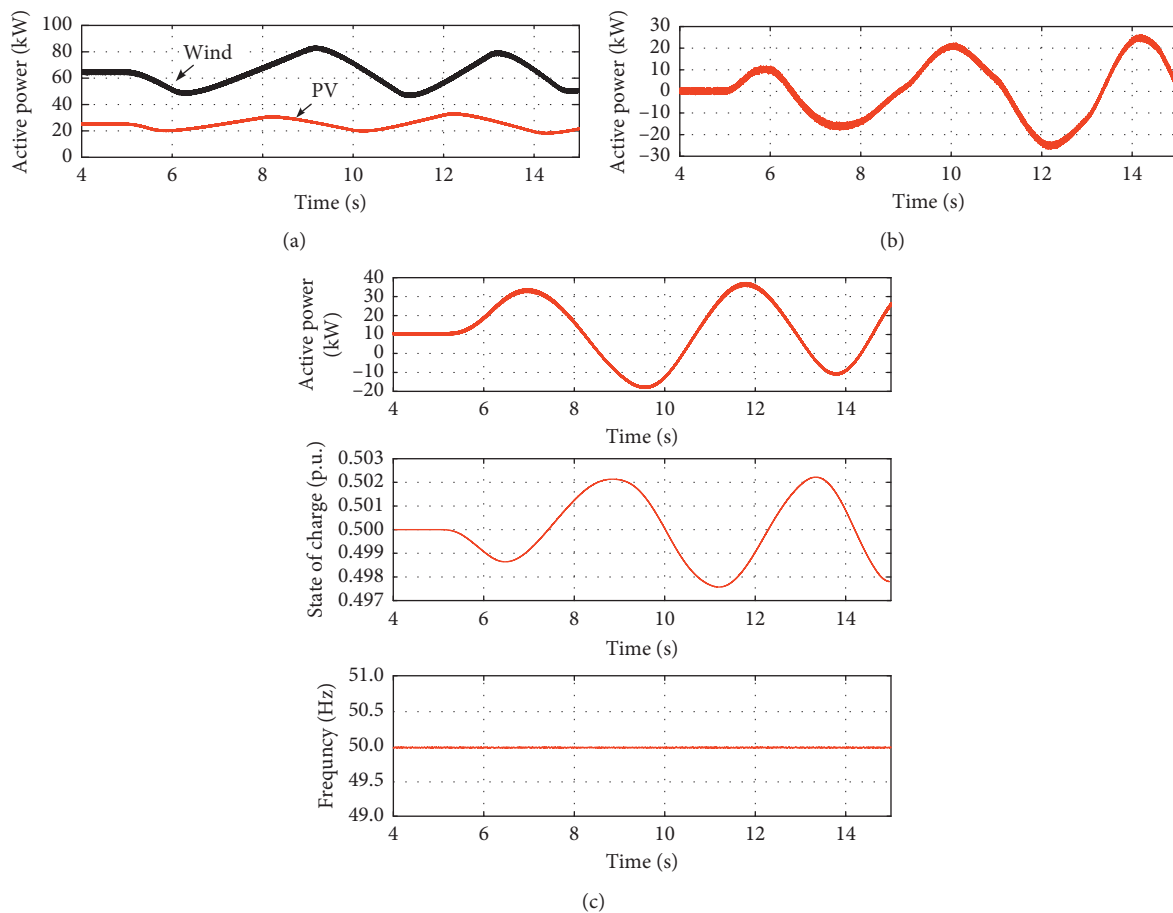


FIGURE 6: Simulation waveforms for wind and photovoltaic fluctuations: (a) active power of wind and photovoltaic; (b) active power of BESS; (c) frequency of microgrid.

Figure 5), switching to the independent operation mode of ER.

As can be seen from Figures 8(a) and 8(b), initially the BESS responded quickly to the wind and light fluctuations, and the system frequency fluctuations were small. At 8 s, the BESS fails, and its output power is zero. At this time, the ER controlled by VSG responds to the fluctuation of wind and light and adjusts the frequency of the microgrid according to

the characteristics of the droop frequency. Figure 8(c) is the waveform of the SOC of BESS. Since the BESS output power is zero at 8 s, the SOC will not change after 8 s. Figure 8(d) shows the voltage waveform of the AC bus of the microgrid. We can see that the voltage waveform is smooth and the amplitude is stable during the switching process, which realizes the smooth operation of the microgrid during the BESS fault.

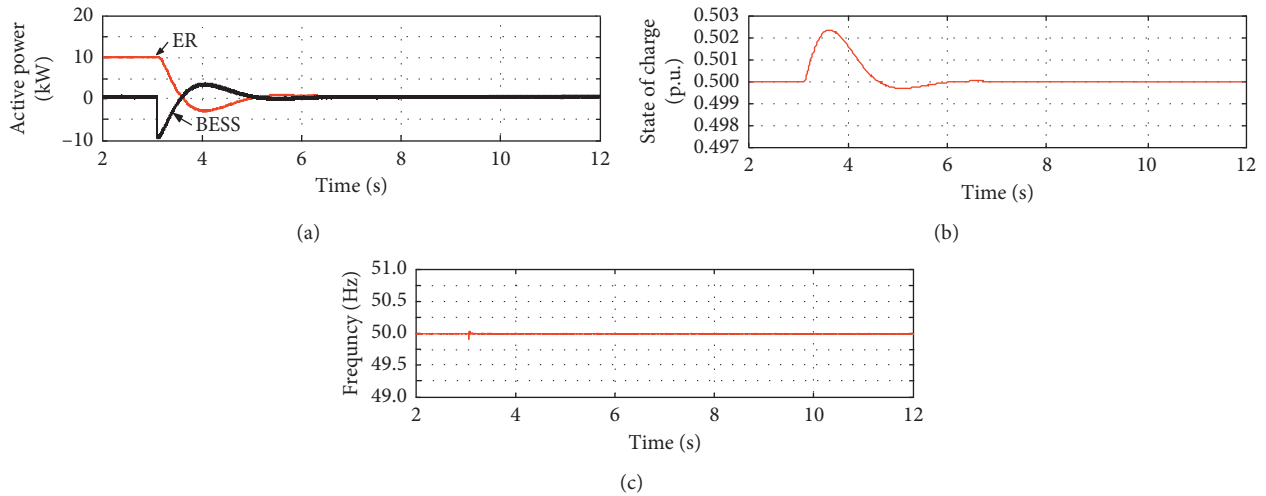


FIGURE 7: Simulation waveforms under load decrease: (a) active power of ER and BESS; (b) state of charge; (c) frequency of microgrid.

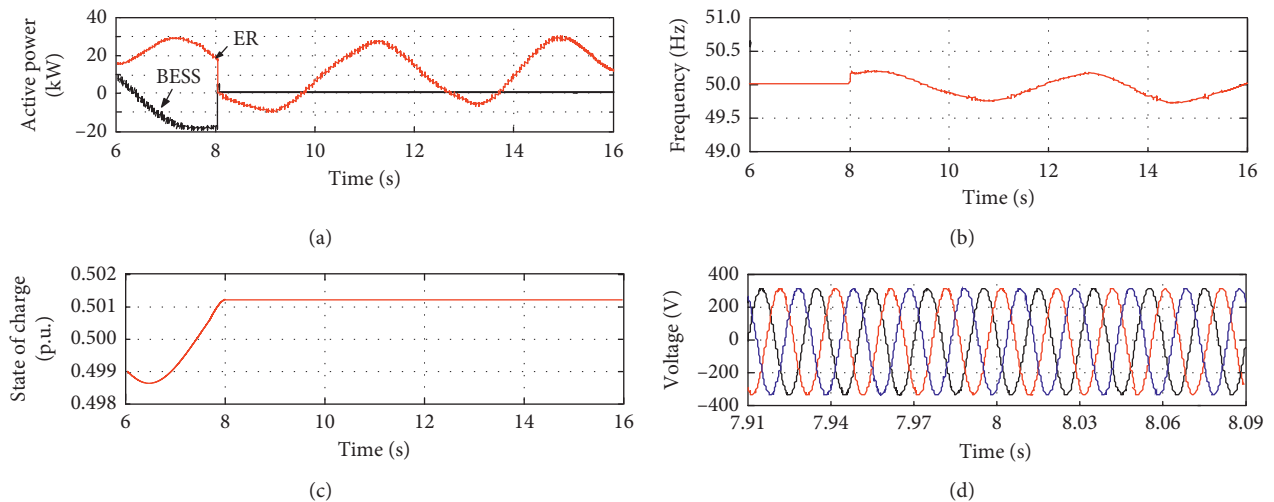


FIGURE 8: Simulation waveform when BESS fails: (a) active power of ER and BESS; (b) frequency of microgrid; (c) state of charge; (d) voltage of microgrid AC bus.

#### 4. Conclusion

To control the frequency of the microgrid with the ER as the core, we propose a constant frequency control strategy coordinated by the ER and BESS. The principle of coordinated operation of ER and BESS under the microgrid system structure has been described and analyzed; meanwhile, the specific coordinated control strategy of ER and BESS has been given. Finally, MATLAB/Simulink was used to build a simulation model and conduct simulation verification. We can get the following conclusions:

- (1) BESS uses constant voltage and constant frequency control to stabilize the frequency at the rated value and can quickly respond to power fluctuations to ensure the active balance of the microgrid.
- (2) ER maintains the stability of energy storage capacity and controls the output power of BESS by adjusting

the reference value of SOC. The virtual synchronous motor control makes the interface of the ER have the virtual inertia of the synchronous motor, which ensures the smooth exchange of power between the microgrid and the main grid.

- (3) When the BESS fails, the microgrid can switch smoothly to the fault operation state, which improves the reliability of the system operation.

#### Data Availability

The data used to support the findings of this study are included within the article.

#### Disclosure

This paper is an expanded version of a conference paper [28] previously published at 2<sup>nd</sup> International Conference on

Information Technologies and Electrical Engineering, Zhuzhou, Hunan, China, December 2019.

### Conflicts of Interest

The authors declare that there are no conflicts of interest regarding the publication of this article.

### Acknowledgments

This study was funded by the National Natural Science Foundation of China (51807058) and the Natural Science Foundation of Hunan Province of China (2018JJ3129).

### References

- [1] W.-S. Tan, M. Y. Hassan, M. S. Majid, and H. Abdul Rahman, "Optimal distributed renewable generation planning: a review of different approaches," *Renewable and Sustainable Energy Reviews*, vol. 18, no. 2, pp. 626–645, 2013.
- [2] H. Jiayi, J. Chuanwen, and X. Rong, "A review on distributed energy resources and microgrid," *Renewable and Sustainable Energy Reviews*, vol. 12, no. 9, pp. 2472–2483, 2008.
- [3] Q. Huang, M. L. Crow, G. T. Heydt, J. P. Zheng, and S. J. Dale, "The future renewable electric energy delivery and management (freedm) system: the energy internet," *Proceedings of the IEEE*, vol. 99, no. 1, pp. 133–148, 2011.
- [4] Y. Liu, Y. Li, H. Liang, J. He, and H. Cui, "Energy routing control strategy for integrated microgrids including photovoltaic, battery-energy storage and electric vehicles," *Energies*, vol. 12, no. 2, 2019.
- [5] S. Bifaretti, P. Zanchetta, A. Watson, L. Tarisciotti, and J. C. Clare, "Advanced power electronic conversion and control system for universal and flexible power management," *IEEE Transactions on Smart Grid*, vol. 2, no. 2, pp. 231–243, 2011.
- [6] T. Esmar and P. L. Chapman, "Comparison of photovoltaic array maximum power point tracking techniques," *IEEE Transactions on Energy Conversion*, vol. 22, no. 2, pp. 439–449, 2007.
- [7] E. Koutroulis and K. Kalaitzakis, "Design of a maximum power tracking system for wind-energy-conversion applications," *IEEE Transactions on Industrial Electronics*, vol. 53, no. 2, pp. 486–494, 2006.
- [8] S. Teleke, M. E. Baran, A. Q. Huang, S. Bhattacharya, and L. Anderson, "Control strategies for battery energy storage for wind farm dispatching," *IEEE Transactions on Energy Conversion*, vol. 24, no. 3, pp. 725–732, 2009.
- [9] G. Delille, B. François, and G. Malarange, "Dynamic frequency control support by energy storage to reduce the impact of wind and solar generation on isolated power system's inertia," *IEEE Transactions on Sustainable Energy*, vol. 3, no. 4, pp. 931–939, 2012.
- [10] J.-Y. Kim, J.-H. Jeon, S.-K. Kim et al., "Cooperative control strategy of energy storage system and microsourses for stabilizing the microgrid during islanded operation," *IEEE Transactions on Power Electronics*, vol. 25, no. 12, pp. 3037–3048, 2010.
- [11] H. Su, Y. Ye, Y. Qiu, Y. Cao, and M. Z. Q. Chen, "Semi-global output consensus for discrete-time switching networked systems subject to input saturation and external disturbances," *IEEE Transactions on Cybernetics*, vol. 49, no. 11, pp. 3934–3945, 2019.
- [12] H. Su, H. Wu, and J. Lam, "Positive edge-consensus for nodal networks via output feedback," *IEEE Transactions on Automatic Control*, vol. 64, no. 3, pp. 1244–1249, 2019.
- [13] X. Wang, G. Jiang, H. Su, and X. Wang, "Robust global coordination of networked systems with input saturation and external disturbances," *IEEE Transactions on Systems, Man, and Cybernetics: Systems*, pp. 1–13, 2020.
- [14] T. L. Tiang, D. Ishak, and D. Ishak, "Novel MPPT control in permanent magnet synchronous generator system for battery energy storage," *Applied Mechanics and Materials*, vol. 110–116, pp. 5179–5183, 2011.
- [15] S. Adhikari and F. Li, "Coordinated V-f and P-Q control of solar photovoltaic generators with MPPT and battery storage in microgrids," *IEEE Transactions on Smart Grid*, vol. 5, no. 3, pp. 1270–1281, 2014.
- [16] A. Q. Huang and J. Baliga, "FREEDM system: role of power electronics and power semiconductors in developing an energy internet," in *Proceedings of the 21st International Symposium on Power Semiconductor Devices & IC's (ISPSD)*, pp. 9–12, IEEE, Barcelona, Spain, 2009.
- [17] C. Xu, Y. Zhao, B. Qin, and H. Zhang, "Adaptive synchronization of coupled harmonic oscillators under switching topology," *Journal of the Franklin Institute*, vol. 356, no. 2, pp. 1067–1087, 2019.
- [18] C. Xu, H. Su, and C. Liu, "Robust adaptive synchronization of complex network with bounded disturbances," *Advances in Difference Equations*, vol. 2019, no. 1, p. 483, 2019.
- [19] Z. Lv, L. M. Wu, Z. H. Liu, L. Liu, Z. Song, and L. Sun, "Energy router with virtual inertia control schemes and concurrency operation," *Concurrency and Computation: Practice and Experience*, vol. 31, no. 9, p. e4715, 2018.
- [20] F. Jiang, Y. Li, C. Tu, Q. Guo, and H. Li, "A review of series voltage source converter with fault current limiting function," *Chinese Journal of Electrical Engineering*, vol. 4, no. 1, pp. 36–44, 2018.
- [21] H. Liu, *Research on Control Strategy of Electronic Power transformer*, Huazhong University of Science & Technology, Wuhan, China, 2009.
- [22] H. Long, J. L. Li, and K. F. He, "Research on double-closed-loop control for the frequency converters in parallel operation," *Advanced Materials Research*, vol. 722, pp. 503–506, 2013.
- [23] D. Segaran, B. P. McGrath, D. G. Holmes et al., "Adaptive dynamic control of a bi-directional DC-DC converter," in *Proceedings of the 2010 IEEE Energy Conversion Congress and Exposition*, pp. 1442–1449, Atlanta, GA, USA, September 2010.
- [24] J. Chen and T. O'Donnell, "Parameter constraints for virtual synchronous generator considering stability," *IEEE Transactions on Power Systems*, vol. 34, no. 3, pp. 2479–2481, 2019.
- [25] J. Chen, M. Liu, F. Milano, and T. O'Donnell, "Placement of virtual synchronous generator controlled electric storage combined with renewable generation," in *Proceedings of the 2019 IEEE Milan PowerTech*, Milano, Italy, June 2019.
- [26] L. Gao, S. Liu, and R. A. Dougal, "Dynamic lithium-ion battery model for system simulation," *IEEE Transactions on Components & Packaging Technologies*, vol. 25, no. 3, pp. 495–505, 2002.
- [27] U. Tamrakar, D. Galipeau, R. Tonkoski, and I. Tamrakar, "Improving transient stability of photovoltaic-hydro microgrids using virtual synchronous machines," in *Proceedings of the IEEE Eindhoven PowerTech*, pp. 1–6, Eindhoven, Netherlands, July 2015.
- [28] L. Zheng, J. Wang, and J. Zeng, "Cooperative control strategy of energy router and energy storage system in microgrid," in *Proceedings of the 2nd International Conference on Information Technologies and Electrical Engineering (ICITEE-2019)*, pp. 1–7, Changsha, China, December 2019.

## Research Article

# Improving Fairness for Distributed Interactive Applications in Software-Defined Networks

Ran Xu <sup>1</sup> and Weiqiang Zhang <sup>2</sup>

<sup>1</sup>State Key Laboratory of Networking and Switching Technology, Beijing University of Posts and Telecommunications, Beijing 100876, China

<sup>2</sup>Industrial Robot Training Center, Tangshan Vocational and Technical College, Tangshan, China

Correspondence should be addressed to Weiqiang Zhang; [weiqiangzhang@yeah.net](mailto:weiqiangzhang@yeah.net)

Received 9 March 2020; Revised 4 July 2020; Accepted 28 July 2020; Published 12 August 2020

Guest Editor: Hou-Sheng Su

Copyright © 2020 Ran Xu and Weiqiang Zhang. This is an open access article distributed under the Creative Commons Attribution License, which permits unrestricted use, distribution, and reproduction in any medium, provided the original work is properly cited.

With the popularization of distributed interactive applications (DIAs), for getting good interactive experience among participants, efficient and fair allocation of network resource should be considered. In software-defined networks, the presence of central controllers provides novel solution to deploy customizable routing for interactive applications, which allows fine-grained resource allocation for DIAs to achieve fairness among participants. But opportunities always come with challenges, the wide spread user locations often require distribution of controllers to meet the requirements of applications. Hence, the latency involved among participants is directly affected by the processing time of controllers. In this context, we address the DIAs' fair resource provisioning problems on computing and links load with the objective of balancing the achievable request rate and fairness among multiple flows in SDN networks. We firstly formulate the problems as a combination of controller loading and routing optimization. Then, we propose proactive assignment controller algorithm based on deep learning and fairness path allocation algorithm to share the bottleneck links. Compared with the state-of-the-art greedy assignment algorithm and priority order allocating algorithm, the final result is proven to get better fairness on controller and link load among DIAs' participants by trace driven simulation.

## 1. Introduction

In recent years, smart devices have emerged, and a variety of distributed interactive applications (e.g., multiparty network gaming, online video conference, teleconferencing, online trading, and multiperson augmented/virtual reality) are provided on smart devices. More and more applications require cooperation. One example of real-world most popular games with over 300,000 daily players can be found in [1], which has been released as a mobile game in China. As time goes on, we will see the previously distributed research (e.g., distributed live music concerts [2], shared whiteboard, shared workspaces on collaborative design [3], web-based e-learning, and interactive desktop applications on distributed infrastructures [4]), which will be or has been already used on diverse devices [5], which makes good user experience become more and more important.

In the network, different styles of DIAs (e.g., game) have different thresholds for maximum tolerable delays [6, 7], and resource allocation subject to the varying bandwidth capacities of different links. The networks with a single bottleneck resource, where congestion is signaled by the buildup of a queue at the bottleneck's buffer and where propagation delays are significant [8, 9], show that the network does not converge to an efficient and fair equilibrium in networks with multiple bottleneck nodes. Hence, excessive unfairness for on-demand resource provisioning can severely degrade the participants quality of experience. The fairness problems of flows include the propagation delay as well as the sharing of bottleneck links to multipath communication. For example, when playing a game over a network where quality of service is not guaranteed, the positions of an object at different players' terminals may be disturbed owing to the network delay [10], and latency



differences between players can lead to unfairness in fast-paced First Person Shooter games or 3D virtual space on haptic interface devices [10, 11]. Moreover, upon reaching such an allocation, the same weight priority for the requests 10 Gb/s and 2 Gb/s of bandwidth may drop sharply to the first service. To solve these problems, cloud computing and other techniques enable users to process their applications on the server-side [12]; for instance, the effort in [13] provided mechanisms and methods for facilitating tiered service model-based fair allocation of resources for application servers in multitenant environments. However, server-side latency compensation causes CPU processing power and memory overhead, which will restrain the total number of customers on the application servers. In addition, the efforts of previous works in [10, 14, 15] have proven that one of the contributing factors to the inconsistencies experienced is network, server-side estimation, which is usually deduced from application behaviors that are not always concerned to network issues, and the network in communication remains as a major barrier to achieve high quality interaction experience even if there is no limitation on the availability of server capacities [5, 10, 12, 16].

In recent years, a new paradigm that is known as Software Defined Networks (SDN) emerged [17]. SDN gives possibilities principled solution to manage the networks behavior at runtime for interactive online applications [18]. The basic concept of SDN is controller to run on servers and the network devices forward traffic based on installed flexible rules. Interactive applications can utilize this state information to obtain estimates of available bandwidth and latency that are current and more accurate than what can be obtained, since they are measured in real-time by the SDN controller [19]. Therefore, rerouting and reconfiguration are potentially fast and efficient in SDN [20]. This enables traffic to be steered in real-time. Whereas many interactive applications (e.g., smart homes, IoT applications, and edge computing) are widely distributed in different geographical areas, for better utilization of controller resources, it requires distribution of controllers process effectively. And the controller long processing time may not be significant for elephant flows; however, when the (1) new flow arrives, (2) logical topology changes, and (3) link failures and the intermediate switches can not resolve the data package; they will intercept the data flow and forward Packet-In message to the SDN controller [21]. The control requests are one of the major contributors of messages received by the controller [22]. Even if the forwarding path has been established, usually the network requests are frequent and rule storage space is limited; it still has the possibility of sending requests to the controller [21]. In terms of geographical distribution of the sources of demand, long processing time will fundamentally limit the network's ability to quickly react to events such as link congestion or failures [23, 24]. Hence, as part of the network, when we address the distributed interactive network applications (DIAs) fair allocation resources between various flows, the controllers' high processing time must be prevented.

Based on the blueprint of the software-defined network innovation, in this work, we investigate the flows fair

allocation problem combined with the problem of control processing and routing in SDN. Due to the latency involved in the interaction, in the distributed SDN architecture, in order to achieve fairness allocation for user flows, a runtime scheduler is needed to answer the following questions: (1) How to dynamically map requests to the controllers? (2) Which routes shall be used to interconnect the communication, and how to allocate the multiple paths and share the limit bandwidth capacity fairly?

Specifically, the summaries of our contributions are listed as follows:

- (1) We present a fair resource allocation for distributed interactive applications in Software-Defined Networks, in which the structural controller is introduced. It can be viewed as the flows fair sharing processing and routing resources.
- (2) We solve controller assignment problem proactively based on deep learning and the adjustment based on water filling process. From the view of routing and bandwidth allocation, we consider the multipath and bottleneck to fairly distribute links.
- (3) We choose some representative data sets to conduct some experiments. The experimental results show that the schemes get better fairness, while achieving better performance in terms of reaction time, etc.

The rest of this paper is organized as follows. In Section 2, we describe the problems in detail and model the problem. In Section 3, proactive controller assignment algorithm and routing and bandwidth's fair path allocation algorithm with the example are given. In Section 4, we choose some commonly used data sets to test the presented algorithms' performance. Moreover, we also compare performance of algorithms with others. In the final section, we give some conclusions.

## 2. Problems Description and Modeling

*2.1. Processing and Routing.* The typical unfairness of DIAs among participants is illustrated in Figure 1. Assuming there is an application for user 1 and user 2, both of them need to send real-time packets to the interactive application server, and the objective is to fairly allocate path delay between them. Most of the traditional routing protocols prefer to adopt the low latency paths to deliver applications traffic to destinations. Generally, the classic shortest path routing protocols (e.g., OSPF) are always used as the autonomous system routing protocol in previous network, even if, regardless of links bandwidth capacity limitations and controllers processing, in Figure 1, we suppose that users need to transfer one unit size of information and use the link propagation delays as the OSPF weights: (a) if the default paths for user 1 and user 2 are routing based on OSPF weights, there are user 1  $\rightarrow$  S1  $\rightarrow$  S2  $\rightarrow$  S8  $\rightarrow$  S10 and user 2  $\rightarrow$  S4  $\rightarrow$  S7  $\rightarrow$  S9  $\rightarrow$  S10, and the latency difference is 4; (b) if it is based on the paths that are denoted by the arrow lines in the picture, the latency difference will be 0; thus, the equalizing application delays between user 1 and

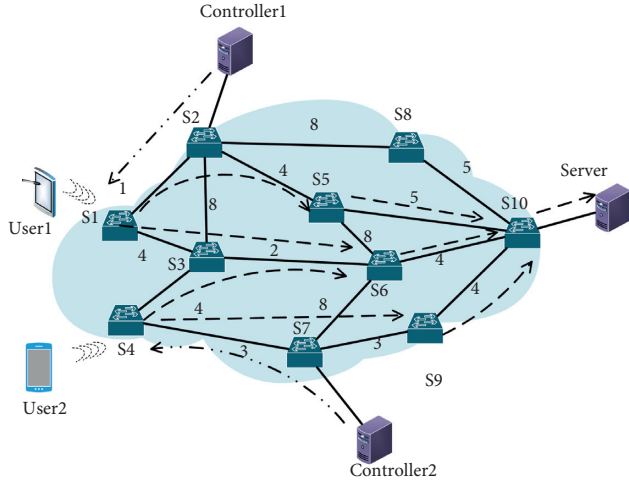


FIGURE 1: Illustration of allocation in SDN network.

user 2 are unfair in the shortest path routing way. In addition, different styles of DIAs have independently accounted for bandwidth, latency, and loss, and interaction process occupies the scarce bandwidth resources; how to adjust weights or priorities to flexibly allocate shared bottleneck links? For example, we may want to give a high priority user a weight of 10.0, which has been allocated 1 Gb/s, and a weight of 1.0 to another, which is allocated 2 Gb/s, when they share the bottleneck link.

Moreover, for distributed interactive applications in SDN, the customers carry on mutual interactions among themselves. The interaction includes not only the network latencies from the customers to server but the latencies between the customers and the controllers. Figures 2(a) and 2(b) show the structure and the interactive process in SDN network. In the figures, we refer to the request process as control and interaction. When issuing an operation, the DIA clients send action to the switch, which detects the DIA event, its relays are assigned a controller for further processing, the controller will compute and synchronize the state, and the participants will communicate through the fabric network. Thus, the controller's performance is based on the control traffic overhead, which will influence all users. In principle, SDN is possibly principled to provide customized service; therefore, it is feasible to associate a controller such that the processing time influencing fairness and consistency for all users is minimum.

**2.2. Problem Formulation.** The first thing we model the network as an undirected graph  $G = (V, E)$ , where  $E$  states the set of links with link bandwidth  $b_e$  per link  $e$ , and  $V$  represents the set of nodes containing the switches, servers, and the controllers. We use  $N$  to denote the number of controllers, and  $c_j$  represents the processing capacity of controller  $j$ . There is an interval of time slot  $t \in \{1, 2, \dots, T\}$  with a set  $F$  of flows and  $d$  denotes the delay between source user to its associated destination server, and corresponding flow  $f_i \in F$  starts from source node and finally reaches

destination node. The main symbols used throughout this paper are listed in Table 1.

We consider a discrete slot system model where the switch requests can be recorded and the controller provisioning decisions can be updated. At time slot  $t$ , function  $a_i(t)$  denotes the traffic rate at switch  $i$ , and the requests are aggregated at the processing queue of the connected controllers. The controller can be modeled as an M/M/1 queue. Here, we use the weighted average of controller response time, which evaluates the performance of controller relative to the proportional of its load, which has been proven in [25] and described below. The load of controller  $j$  is denoted as

$$l_j(t) = \sum_{i=1}^{|V|} w_i a_i(t) x_{ij}(t), \quad (1)$$

where  $x_{ij}(t)$  is denoted as whether switch  $i$  is connected to controller  $j$ . Symbol  $w_i$  represents the weight of traffic to requests. By applying the Little's law, the average processing time of the controller  $j$  can be represented as

$$p_j(t) = \frac{1}{c_j - l_j(t)} O(|V|^2). \quad (2)$$

So the overall controller response time can be calculated as

$$R(t) = \frac{\sum_{j=1}^N l_j(t) p_j(t)}{\sum_{j=1}^N l_j(t)}. \quad (3)$$

Since multiple DIAs user groups request the bandwidth and they share the same physical network, the bandwidth consumption may not exhaust the available link bandwidth. For the realistic network conditions, and the distributed interactive applications (DIAs) such as the bandwidth-intensive tasks (e.g., streaming game screens to clients) in [5], to avoid unfairness to use the resources, we need to ensure that service is distributed among users in a fair manner. In the most basic form, each network flow is associated with a utility as a function of its rate, various notions of fairness can be expressed simply by changing the shape of the utility functions [26]. According to [9], the utility function of interaction flow is defined as

$$u_{f_i}(r_{f_i}) = \frac{r_{f_i}^{1-\alpha}}{1-\alpha}, \quad (4)$$

so the overall utility can be calculated as

$$U = \sum_{f_i \in F} u_{f_i}(r_{f_i}), \quad (5)$$

An operator enables to express different preferences on the fairness/efficiency trade-off curve by varying  $\alpha$ ; when  $\alpha = 2$ , it translates to the minimum potential delay fairness, which can be interpreted as the delay of user transferring a file of unit size with the rate allocated of  $r_{f_i}$  going through allocated path  $p_{f_i}$ , eventually converging to the egalitarian max-min fair allocation as  $\alpha \rightarrow \infty$ , and  $\alpha \approx 5$  is sufficient for very good approximation in [26]. Thus, the object of optimization can be expressed as

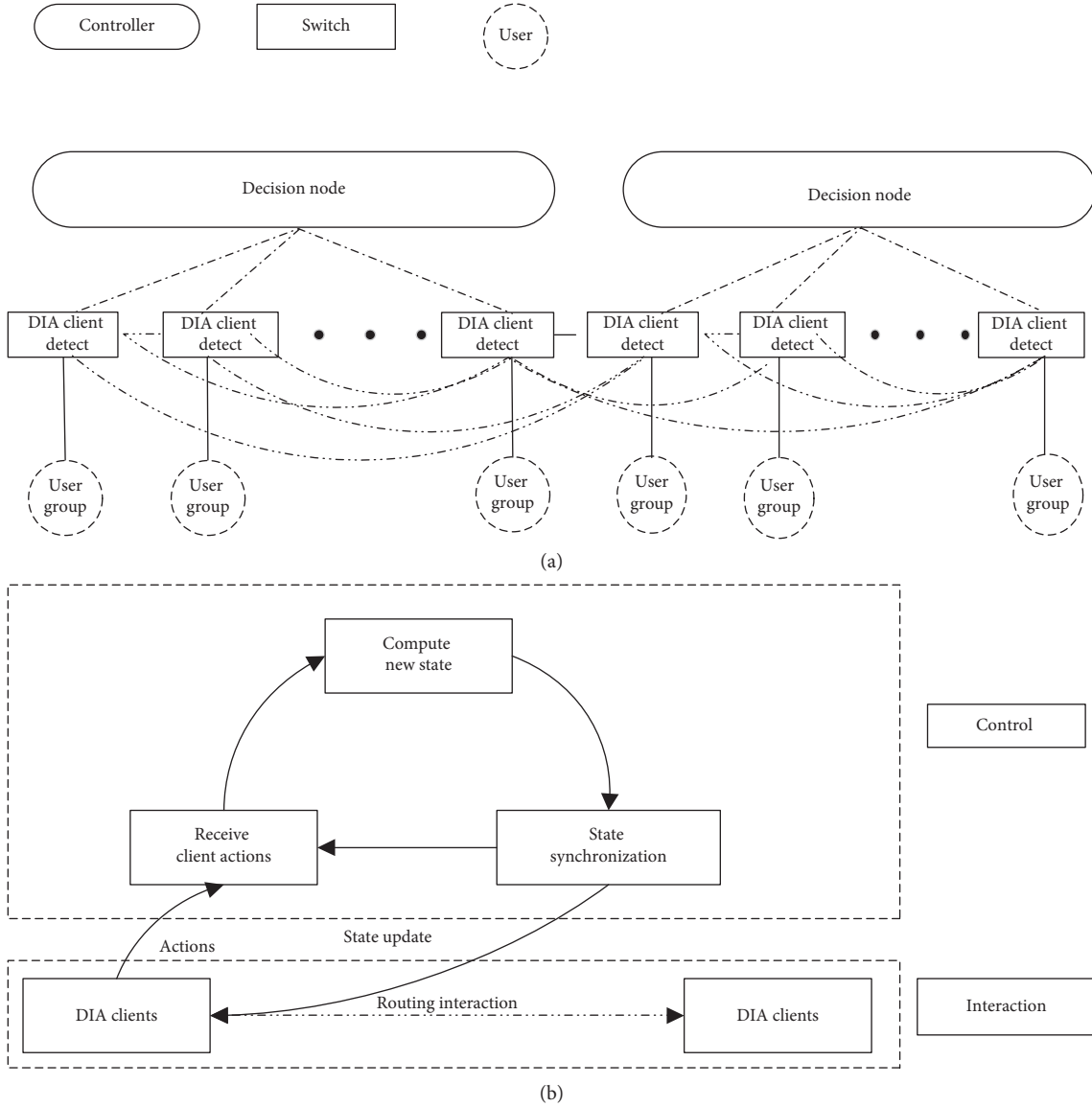


FIGURE 2: The structure and the interactive process in SDN network.

TABLE 1: Key symbol.

Symbol	Definitions or descriptions
$G = (V, E)$	The graph representing the network
$N$	The number of controllers
$c_j$	The processing capacity of controller $j$
$t$	The time slot
$a_i(t)$	The traffic rate at switch $i$
$l_j(t)$	The load of controller $j$ in time slot $t$
$p_j(t)$	The processing time of the controller $j$ in time slot $t$
$\alpha$	A nonnegative variable constant
$x_{ij}(t)$	A binary variable indicating whether switch $i$ is connected to controller $j$
$x_{ihj}$	A binary variable indicating the switch $h$ is included in the path $p_{ij}$ between source node $i$ and destination $j$

$$\begin{aligned}
 \min \delta &= \sum_{t=1}^T (R(t) - U(t)) \\
 &\sum_{f_i \in F, e \in p_{f_i}} r_{f_i} \leq b_e, \quad \forall e \in E \quad (1) \\
 \text{s.t.} \quad &(2) l_j \leq c_j, \quad \forall j, t \quad (2) \\
 &d_{f_i}(t) < d_i^m, \quad \forall f_i \in F, t \quad (3) \\
 &x_{ihj} \leq 1, \quad \forall p_{ij} \in P_f, f \in F \quad (4),
 \end{aligned} \tag{6}$$

where equation (1) reflects the amount of routing allocation flow that can not exceed the link capacity. Constraint (2) specifies that no controller is overloaded and constraint (3) denotes that any assigned path delay should be less than the maximum tolerable delays  $d_i^m$ . We define  $x_{ihj}$  to represent

that the switch  $h$  is included in the path  $p_{ij}$  between source node  $i$  and destination  $j$ , and constraint (4) guarantees loop-freedom when a switch is only used once per path.

### 3. Allocation Algorithm

**3.1. Proactive Controller Assignment Algorithm.** In this section, we firstly use controller and switch to examine and identify controller impacts. We randomly generated 60 groups of users; in every group, there are five pairs of users that communicate with each other for 2 seconds. For test 1 and test 2, the demands of bandwidth are 1 Mb and 2 Mb, respectively. When users contact with each other in SDN, Table 2 displays the number of packages, which shows that communication with controllers is inevitable, and the controller will bring extra processing latency to the interaction, and the request rate is monotonically increasing with the number of requests. Although the cost function of the response time can take any form to model a provider's specific delay cost factors [25], here, we only require to be monotonically increasing with the number of requests.

For faster controller response and better utilization of controller resources, we can dynamically allocate the control domain, and then, when requests vary, the switches are dynamically mapped to controllers. Hence, to figure out the controller assignment problem, the method such as DCAP in [25] can be used for data center, or scheme in [16, 27] used for large scale network, but we seek a proactive approach ahead of time. Therefore, we use the deep learning to estimate requests for user group based on their historical usage; the details of deep learning can be seen in our previous research [28]. Moreover, inspired by [27], but different from adjusting the facility location, we estimate the aggregate demand and adjust the control domain with the fixed number and location of controllers.

As shown in Algorithm 1, first, the method SM in [25] is used to generate a stable matching between switches and controllers. Second, since all requests that already have a promised value from the previous time-step, to reduce the computational overhead and improve response time, we examine the solution from the current time-step and future time-steps. Our algorithm conducts the increasing loading heuristic in which the highest loading values are decreased to the lowest loading values similar to a water filling process. The demands used in algorithm are based on peak historical usage, and different flow groups can peak at different times. Besides, these schemes plan for the time-step can be set to several minutes similar to Google [29] and Microsoft [30].

**3.2. Routing and Bandwidth Allocation Algorithm.** One of the challenges is the sources determining the paths of traffic flows based on the aggregate propagation delay along path, and the optimization for bandwidth allocation to individual flows. Here, we present a fairness objective scheme for user groups, which share the bottleneck links for multipath communication. As shown in Algorithm 2, traffic is spread across multiple paths and ensures that users fairly share the

TABLE 2: Formal context.

Name	Total	Controller
Test 1	104076	21828
Test 2	154389	21621

requests served that enable the network to run at higher levels of utilization.

Since different styles of DIAs have different thresholds for maximum tolerable delays, these thresholds influence the user rating, which can be further adjusted according to the user demand sensitivity or operating experience [31], even if we consider user-defined fair allocation of spare bandwidth, while still ensuring minimum bandwidth guarantees for each client [32]. In the algorithm, first, we use an adaptation of the gradient descent algorithm for flows to determine the paths, and the appropriate fraction on each path, so as to achieve weighted fairness for different service-level demands. In other words, we now try to maximize  $\sum_{f_i \in F} U_{f_i}(r_{f_i}) - \sum_{i \in P, D} (d_i^s / |L(i)|)$ . Here,  $|L(i)|$  denotes the number of links in flow  $i$ 's path, and  $P, D$  is the set of flow paths in the same group. The latter part of the equation is a "penalty" function, which penalizes the latency difference path, since the  $d_i^s$  and  $|L(i)|$  are integers, and the  $d_i^s \geq 1$  in each link. We estimate flow group demand by usage history  $x_i$ , which can predict the rate by the deep learning. Hence, the optimal value of weight  $w_i$  is given by  $w_i = x_i U'_i(x_i)$ . Since the weight is proportional to the bid, the ratio of  $w_i$  to  $x_i$  is similar to the price per unit. This has an intuitive interpretation: it sets the fraction of each path, such that the latency difference cost is equal to the overall sum of delay of the links on flow path, the weight of which is equal to the marginal utility as far as the price of per unit resource. If the values are at the optimal values, this calculation gives the optimal rates, but generally, the calculated values are not optimal rates for incorrect demand. After that, we execute a second optimization that uses an adaptation of MPFA [33] algorithm to find the bottleneck and seek the global max-min fairness by allocating all of the unused capacity in the current time-step. Here, using the algorithm has a crucial advantage: it finds a feasible and efficient allocation approximately, even if the estimated rates are not optimal.

An example is used to help illustrate the algorithm comprehension. Figure 3 is a simple network with three links,  $e_1$ ,  $e_2$ , and  $e_3$ , with bandwidth numbers capacity 10, 11, and 2, respectively. Assume that there are three flows: the source-destination pairs of  $f_1$  and  $f_2$  are from node 1 to 3, and  $f_3$  is from node 1 to 2. For simplicity of calculation, each link has a delay value of 1, and all flows have demand of 13. First of all,  $f_2$  is more sensitive on path delay than  $f_1$  (e.g., the first person shooter and role playing game); in other words, pay more than  $f_2$ ; the flows  $f_1$ ,  $f_2$  and  $f_3$  have weights of 1, 2, and 3, respectively, denoting the flow of relative priority. Hence, calculated by algorithm, the paths for  $f_1$  are  $e_2$  and  $e_1 \rightarrow e_3$  (the fractions of multipath are 0.67 and 0.33, respectively),  $f_2$  is  $e_2$ , and  $f_3$  is  $e_1$ . After determining the paths and fraction of flows, the algorithm

```

(1) Require:  $c_j$ : processing capacity of each controller;
(2) Ensure: mapping between switches and controllers  $x_{ij}(t)$ 
(3) Initialize: initial Stable Matching
(4) for  $t = 1, 2, \dots, T$  do
(5)   estimated request arrival rate  $a_i(t+1)$ ;
(6)   sort the nodes in  $V$  to decreasing order  $C_s$  according
(7)   to traffic overhead of current time-step  $t$  and next
(8)   time-step  $t+1$ ;
(9)   Temporarily holds the proposal, each switch builds list
(10)   $w_s$  according to the worst response time;
(11)  for  $i = 1, 2, \dots, \lfloor |V|/2 \rfloor$  do;
(12)    Find the lowest loading node  $v$  of  $u$ 's neighbors
(13)    here  $u$  is the first node in the ordered list  $C_s$ ;
(14)    mapping the smallest switch  $j \in w_s \subset v$  to  $v$ ;
(15)  end for
(16) end for

```

ALGORITHM 1: Proactive assignment algorithm.

```

(1) Input:  $c_j$ : Request flow  $f_i \in F$ ; allocable bandwidth
(2) capacities and delay for link  $\forall e_k, \forall d_k$ ;
(3) Output: Allocated fair share for  $\forall f_i$ 
(4) for each  $f_i$  in the user group do
(5)   Find the paths and available multipath  $P_i D$ 
(6)   with the links  $\min \sum_{i \in P_i D} (d_i^s / |L(i)|)$  on the flow paths  $p_i \in P_i$ 
(7)   within the maximum tolerable delays  $d_i^m$ ;
(8)   Calculate  $w_i = x_i U_i'(x_i)$ , the sum of
(9)   multipath's weight  $sw = \sum_{p_i \in P_i D} \min_{i \in S(i)} w_i$ ,  $S(i)$  is the set
(10)  of flows incident on link  $i$ , fraction  $(i) = (w_i / sw)$ 
(11) end for
(12) while  $\exists f_i$  do
(13)   for each link  $e_i$  do
(14)    Calculate the allocation function by  $A_{e_k} = b_k$ 
(15)    Calculate the fair share results of  $(s_1, \dots, s_i)$ 
(16)    Sort the result and find the bottleneck
(17)     $e_j, j \in \min(s_1, \dots, s_i)$ 
(18)    Upgrade the equation  $A_{e_k} = b_k$  by  $\min(s_1, \dots, s_i)$ 
(19)   end for
(20)   Fair share allocation  $af(f_i) = s_i \text{weight}_i$ 
(21) end while

```

ALGORITHM 2: Fairness path allocation algorithm.

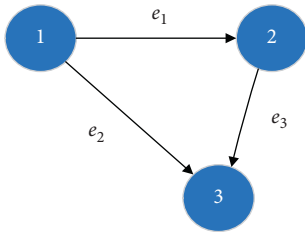


FIGURE 3: A simple example with three links.

executes a global allocation to fair share the bandwidth capacity. Based on the paths and fraction, the process is as follows:

First, find the bottleneck for each link, and the weighted bandwidth allocation function for links as

$$\begin{aligned}
 A_{e_1} &= 0.33 (\min(13, s)) + \min(13, 3s), \\
 A_{e_2} &= 0.67 (\min(13, s)) + \min(13, 2s), \\
 A_{e_3} &= 0.33 (\min(13, s)),
 \end{aligned} \tag{7}$$

Calculated by  $A_{e_k} = b_k$ , the fair share results of  $s_{e_1}$ ,  $s_{e_2}$  and  $s_{e_3}$  roughly equal 3, 4.12, and 6, respectively. So, the  $e_1$  is the bottleneck and  $f_1, f_3$  fairly share the bottleneck of 3. And then, for equation  $A_{e_k} = b_k$ , the interval of  $s$  is based on the new values. The results of  $s_{e_2}$  roughly equal 4.5 and  $s_{e_3}$  is huge. Hence,  $e_2$  is the bottleneck and  $f_2$  shares fairly 4.5, and

the corresponding bandwidth allocation of  $(f_1, f_2, f_3)$  is  $(3, 9, 9)$ .

We now give a brief complexity analysis for algorithms presented above. For Algorithm 1, sorting the switches needs  $O(N \log_2(V))$  computation. One-slot computation needs to calculate  $N$  different numbers of active controllers. Thus, in  $|N|$  mapping iteration, one controller accepts its most preferred switch. Therefore, the time complexity of Algorithm 1 is  $O(|N|V \log_2(V))$ . Since the length of the whole time frame  $T$  and the complexity of calculating is  $O(|T||N|V \log_2(V))$ , the  $|N|$  and  $|T|$  are settable constants. For Algorithm 2, the complexity of calculating multipath path is  $O(|E|)^2$ , which records after the calculation and does not participate in the algorithm run any further. From the controllers' perspective, the complexity comes from searching for bottleneck fair share, and in each round, the search space is  $O(\log_2(E))$ , and the complexity of calculating is  $O(E \log_2(E))$ . Thus, the hierarchical two-phase algorithm's computation complexity is  $O(|E|)^2 + O(|T|E \log_2(E))$ .

## 4. Experimental Evaluation

**4.1. Simulation Settings.** In our simulations, we demonstrate the rationale and advantages of the proposed mechanism by case study. The service demands are derived from the Skype traces [34], which contain timestamp, source, and destination pair and other information from real users, and we use the large topology with 115 nodes and 153 links obtained from [35]. We have extracted 290, 148 network flows from the dataset and used TensorFlow to implement the models, and the python package scikit-learn to calculate performance metrics. The detail of deep learning can be seen in our previous research [28]. Same as the setting of [36], here, we set the capacity of each controller as 1800 k flows/s. We use OpenDaylight and Mininet to test and identify controller impacts. All the simulations are carried out with six 2.2 GHz CPU cores and NVIDIA GeForce GTX 1060 GPU and 24 GB memories and Matlab 2015b. In each time slot, we regard the packets that have the same source and destination IP as a flow. The flow rate is calculated by dividing the total traffic size of the records in the flow by the interval of a time slot. We use the same  $\alpha$  for each flow. The statistical result of service demands is about 10,000 flows per minute. Each link exhibits the same bandwidth resource capacity 150. We set a mean arrival rate 100. We set each flow's max packet arrival rate, and the number of arrival packets at each time slot is uniformly and randomly distributed with  $[0, 200]$ . First, we test the availability of the proactive approach, and then we use the greedy state-of-the-art algorithm from [36], which is designed for controller to be compared with the proactive assignment algorithm (PAA). Second, we evaluate our fairness path allocation algorithm (FPAA) through numerical simulations, and each flow's delay tolerance is set as a linear function with the type of different DIA task.

**4.2. Effectiveness of PAA.** In this section, we conduct simulations of different algorithms to test the strategy of request assign to controller. Although it is impractical that requests

are triggered by each flow arrival event, the study in [25] has demonstrated the monotonically increasing relationship between the request number and the response time. Hence, in order to focus on evaluating the different algorithms strategy, here, we run with 5 controllers and evaluate the request arrival rates as load conditions.

To detect the availability of the proactive approach, we first examine the effectiveness of the request prediction. In Figure 4, to predict the 200 requests, we replace the source-destination requests pair with numbers, and the results show that deep learning achieves good accuracy on predicting the real request demands. Even though inaccurate prediction is inevitable, IP is usually segmented in different areas; therefore, the prediction error within a certain range is acceptable.

Then, we study the impact of different algorithms strategy for controller assignment. In each experiment, we simulate groups of DIA clients to communicate with each other. We compare the PAA algorithm against dynamic controller provisioning with greedy knapsack (DCP-gk) and nearest controller selection (NS) algorithm. Figure 5 shows single time slot to evaluate the load balancing and response time reduction among controllers. In this setting, we run all algorithms with sum of 5500 to 6500 k request rates to follow real-world data, which can be viewed as individual runs with different input requests in discrete time slots. The well-known Jain's index [37] is used to quantify the fairness between flows. Figure 6 shows the result of fairness for customers in the number of 20 time slots. We can observe that NS is sensitive to traffic variations due to lack of adjustment strategy, and DCP-gk uses the greedy algorithm to achieve a more balanced distribution. But compared with them, PAA predicts the request rates of flows that adopts an adaptive loading strategy by embracing the learning algorithms ahead of time, which achieves a good response time and fairness.

**4.3. Effectiveness of FPAA.** Next, in this section, we evaluate our path allocation algorithm for fair allocation and high utilization. We set each link the same bandwidth resource capacity, and each flow's delay tolerance related to the type of different DIA task (for example, game video encoding is less sensitive than streaming the game screens to clients). Our simulation spans over a few of 5-minute time slots. At each time slot, the demands of flows create a severe bottleneck that shows bandwidth resource competition among the flows. Obviously, different types of DIAs have varied bandwidth demands. Here, we compare with prior work that usually corresponds to greedy allocation, such as [38] that ensures allocating demands in priority order. The priority order setting is based on the sensitive of delay. In addition, for comparison, we use a single path (SP) method that meets the demands as much as possible. Figure 7 denotes the result of fairness, and the allocation is extremely fair across all flows (source-destination pairs). The flow-level fairness is a direct consequence of sharing a bottleneck link to multipath cluster-to-cluster communication, and the performance of FPAA

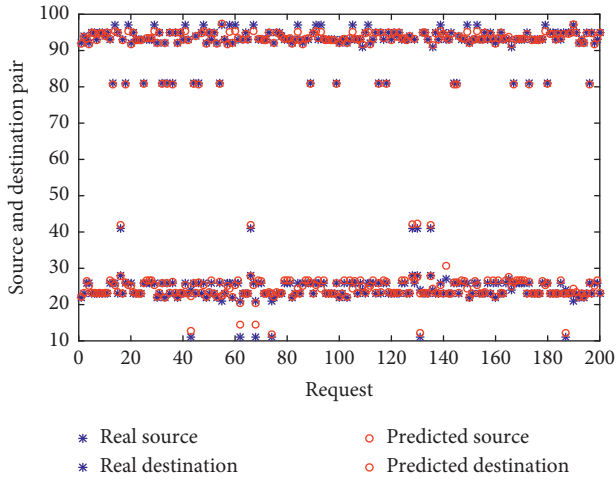


FIGURE 4: Performance of the proactive request.

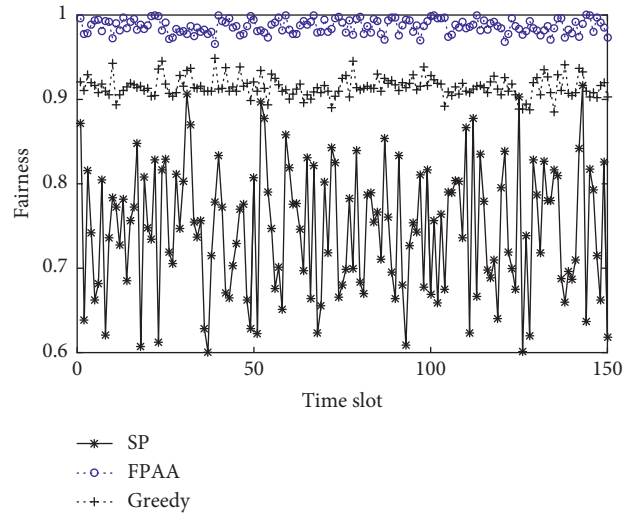


FIGURE 7: Fairness.

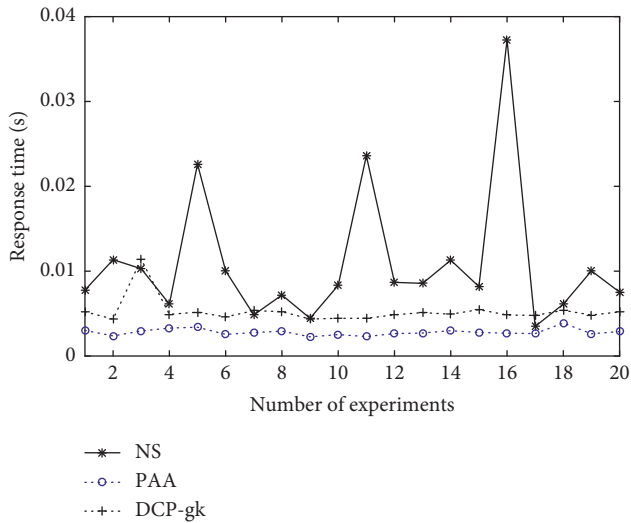


FIGURE 5: Response time.

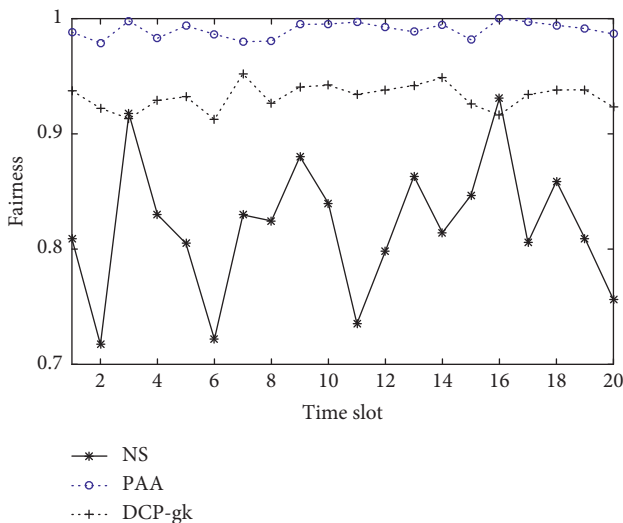


FIGURE 6: Fairness.

on routing allocation and fairness is significantly better on fairness of fair share.

## 5. Related Work

For distributed control plane across a cluster of controllers, the static mapping between switches and controllers improves robustness and scalability. Nevertheless, that may cause hot spots, which motivates several dynamic controller assignment works [25, 36, 39]. The work [39] firstly proposes a live switch migration protocol while introducing little overhead to the network. And work [36] presents an algorithm for dynamically and efficiently provision controllers in a WAN by periodically reassigning switches to controllers. However, they do not consider the processing time on controllers, which is a major cost in flow setup time [39]. The proposed heuristic is time-consuming and not partitioning application states and exploring the dependency between switches and applications. Work in [25] introduces the maintenance cost of the controller cluster and formulates the controller assignment problem as a long-term online cost minimization, which does not consider allocating bandwidth among users. Recent effort such as SWAN [38] is closely related but focuses on the network and routing infrastructure to effectively scale and utilize employing Software Defined Networking [33]. Previous studies have leveraged SDN capabilities for optimal bandwidth allocation in applications such as stream analytics [40]. However, the fairness considerations of SDN controller assignment and allocating bandwidth among users are not included.

A single controller is a single point of failure, and hence the distributed controller platform of the control plane has a fault-tolerant SDN controller that includes synchronization mechanisms, which is a well addressed. In several previous works, one of the first and most relevant proposals is ONIX [41], which provides a general framework where several important open issues have been identified, such as the trade-off between consistency, durability, and scalability. Other widely used distributed fault-tolerant controller

proposals are Hyperflow and ONOS [42, 43]. On the other hand, in the literature of fault-tolerant SDN controllers, Master-Slave controllers are a subclass that address the problem, where the central unit (the master) is in charge of taking the decisions, for example, [44, 45], where active and passive replication methods are proposed to provide fault tolerance. In the future, we need to make improvements based on previous achievements, but this is not in this work's scope.

In this work, we include fairness considerations as the state of the art of SDN controller assignment and allocating bandwidth among users in emerging DIAs environments. We generalize these concepts to the case of the problem. Building on related efforts of utility functions, weighted fair sharing, and controller-based control, we extend the problem for multipath routing and hierarchical fairness. This provides an elastic framework for resource sharing, with a significant degree of flexibility in balancing network bandwidth and controller processing power resources.

## 6. Conclusion and Future Work

The SDN architecture provides a pathway for networks to support scalable and adjustable multiparty interactive applications. In this paper, we have investigated the control and path unfairness problem to enhance the quality of the interactivity performance of DIAs. We have formulated the problem as a combinatorial optimization problem under SDN setting. The heuristic algorithms have been proposed to solve the problems, and real data is used to experimentally evaluate their performance. The results have shown that our scheme can achieve good performance. We further speculate that scheme can support different optimization policies that include reacting to failures and redirecting the control traffic.

## Data Availability

The data used to support the findings of this study are included within the article.

## Conflicts of Interest

The authors declare that they have no conflicts of interest.

## References

- [1] V. R. Carvalho, M. Lease, and E. Yilmaz, "Crowdsourcing for search evaluation," *ACM SIGIR Forum*, vol. 44, no. 2, pp. 17–22, 2011.
- [2] A. Kapur, G. Wang, P. Davidson, and P. R. Cook, "Interactive network performance: a dream worth dreaming?" *Organised Sound*, vol. 10, no. 3, pp. 209–219, 2005.
- [3] F. Liu, S. Xia, H. Shen, and C. Sun, "CoMaya: incorporating advanced collaboration capabilities into 3d digital media design tools," in *Proceedings of the 2008 ACM Conference on Computer Supported Cooperative Work ACM*, pp. 5–8, San Diego, CA, USA, November 2008.
- [4] T. Fu and G. Manglik, "Apparatus, systems and methods for deployment of interactive desktop applications on distributed infrastructures," US Patent 10003672, 2018.
- [5] H. Wang, T. Li, R. Shea et al., "Toward cloud-based distributed interactive applications: measurement, modeling, and analysis," *IEEE/ACM Transactions on Networking*, vol. 26, no. 1, pp. 3–16, 2018.
- [6] R. Shea, J. Liu, E. C.-H. Ngai, and Y. Cui, "Cloud gaming: architecture and performance," *IEEE Network*, vol. 27, no. 4, pp. 16–21, 2013.
- [7] K.-T. Chen, Y.-C. Chang, H.-J. Hsu, D.-Y. Chen, C.-Y. Huang, and C.-H. Hsu, "On the quality of service of cloud gaming systems," *IEEE Transactions on Multimedia*, vol. 16, no. 2, pp. 480–495, 2014.
- [8] F. P. Kelly, A. K. Maulloo, and D. K. H. Tan, "Rate control for communication networks: shadow prices, proportional fairness and stability," *The Journal of the Operational Research Society*, vol. 49, no. 3, pp. 237–252, 1998.
- [9] J. Mo and J. Walrand, "Fair end-to-end window-based congestion control," *IEEE/ACM Transactions on Networking*, vol. 8, no. 5, pp. 556–567, 2000.
- [10] M. Sithu, Y. Ishibashi, P. Huang, and N. Fukushima, "Influences of network delay on quality of experience for soft objects in networked real-time game with haptic sense," *International Journal of Communications, Network and System Sciences*, vol. 8, no. 11, pp. 440–445, 2015.
- [11] S. Zander, I. Leeder, and G. Armitage, "Achieving fairness in multiplayer network games through automated latency balancing," in *Proceedings of the 2005 ACM SIGCHI International Conference on Advances in Computer Entertainment Technology*, ACM, Valencia, Spain, pp. 117–124, June 2005.
- [12] H. Zheng and X. Tang, "Analysis of server provisioning for distributed interactive applications," *IEEE Transactions on Computers*, vol. 64, no. 10, pp. 2752–2766, 2015.
- [13] X. Wang, "Facilitating tiered service model-based fair allocation of resources for application servers in multi-tenant environments," US Patent 10169090, 2019.
- [14] M. Yu, M. Thottan, and L. Li, "Latency equalization as a new network service primitive," *IEEE/ACM Transactions on Networking*, vol. 20, no. 1, pp. 125–138, 2012.
- [15] M. Dick, O. Wellnitz, and L. Wolf, "Analysis of factors affecting players' performance and perception in multiplayer games," in *Proceedings of the 4th ACM SIGCOMM Workshop on Network and System Support for Games*, ACM, Hawthorne, NY, USA, pp. 1–7, October 2005.
- [16] L. Zhang and X. Tang, "Optimizing client assignment for enhancing interactivity in distributed interactive applications," *IEEE/ACM Transactions on Networking*, vol. 20, no. 6, pp. 1707–1720, 2012.
- [17] C. Lin, J. Hu, G. Li, and L. Cui, "A review on the architecture of software defined network," *Chinese Journal of Electronics*, vol. 27, no. 6, pp. 1111–1117, 2018.
- [18] S. Gorlatch and T. Humernbrum, "Enabling high-level QOS metrics for interactive online applications using SDN," in *Proceedings of the 2015 International Conference on Computing, Networking and Communications (ICNC)*, pp. 707–711, IEEE, Garden Grove, CA, USA, February 2015.
- [19] A. T. Naman, Y. Wang, H. H. Gharakheili, V. Sivaraman, and D. Taubman, "Responsive high throughput congestion control for interactive applications over SDN-enabled networks," *Computer Networks*, vol. 134, pp. 152–166, 2018.
- [20] K. Nguyen, Q. T. Minh, and S. Yamada, "A software-defined networking approach for disaster-resilient WANs," in *Proceedings of the 2013 22nd International Conference on Computer Communication and Networks (ICCCN)*, pp. 1–5, IEEE, Nassau, Bahamas, July 2013.



- [21] M. Canini, D. Venzano, P. Peresini et al., "A nice way to test openflow applications," in *Proceedings of the 9th USENIX Symposium on Networked Systems Design and Implementation (NSDI)*, San Jose, CA, USA, April 2012.
- [22] K. S. Sahoo, M. Tiwary, B. Sahoo, R. Dash, and K. Naik, "DSSDN: demand-supply based load balancing in software defined wide area networks," *International Journal of Network Management*, vol. 28, no. 4, Article ID e2022, 2018.
- [23] R. Govindan, I. Minei, M. Kallahalla, B. Koley, and A. Vahdat, "Evolve or die: high-availability design principles drawn from googles network infrastructure," in *Proceedings of the ACM SIGCOMM*, pp. 58–72, New York, NY, USA, August 2016.
- [24] H. H. Liu, S. Kandula, R. Mahajan, M. Zhang, and D. Gelernter, "Traffic engineering with forward fault correction," in *Proceedings of the ACM SIGCOMM*, pp. 527–538, Chicago, IL, USA, August 2014.
- [25] T. Wang, F. Liu, and H. Xu, "An efficient online algorithm for dynamic SDN controller assignment in data center networks," *IEEE/ACM Transactions on Networking*, vol. 25, no. 5, pp. 2788–2801, 2017.
- [26] K. Nagaraj, D. Bharadia, H. Mao et al., "Numfabric: fast and flexible bandwidth allocation in datacenters," in *Proceedings of the 2016 ACM SIGCOMM Conference*, ACM, Florianopolis, Brazil, pp. 188–201, August 2016.
- [27] N. Laoutaris, G. Smaragdakis, K. Oikonomou, I. Stavrakakis, and A. Bestavros, "Distributed placement of service facilities in large-scale networks," in *Proceedings of the 2007–26th IEEE International Conference on Computer Communications*, pp. 2144–2152, IEEE, Barcelona, Spain, May 2007.
- [28] R. Xu, "Proactive VNF scaling with heterogeneous cloud resources: fusing long short-term memory prediction and cooperative allocation," *Mathematical Problems in Engineering*, vol. 2020, Article ID 4371056, 10 pages, 2020.
- [29] C. Y. Hong, S. Mandal, M. Al-Fares et al., "B4 and after: managing hierarchy, partitioning, and asymmetry for availability and scale in google's software-defined WAN," in *Proceedings of the 2018 Conference of the ACM Special Interest Group on Data Communication*, ACM, Budapest, Hungary, pp. 74–87, August 2018.
- [30] S. Kandula, I. Menache, R. Schwartz et al., "Calendar for wide area networks," in *Proceedings of the 2014 ACM conference on SIGCOMM—SIGCOMM'14*, vol. 44, no. 4, pp. 515–526, ACM, Chicago, IL, USA, August 2014.
- [31] M. Jarschel, D. Schlosser, S. Scheuring, and T. Hofeld, "An evaluation of QoE in cloud gaming based on subjective tests," in *Proceedings of the Innovative Mobile and Internet Services in Ubiquitous Computing*, pp. 330–335, Seoul, South Korea, June 2011.
- [32] M. Elahi, J. van Egmond, M. Wang, C. Williamson, and J.-F. Amiot, "Fair and efficient dynamic bandwidth allocation with OpenFlow," in *Proceedings of the Companion of the ACM/SPEC International Conference on Performance Engineering*, pp. 36–37, Edmonton, Canada, April 2020.
- [33] A. Kumar, S. Jain, U. Naik et al., "BwE," *ACM SIGCOMM Computer Communication Review*, vol. 45, no. 4, pp. 1–14, 2015.
- [34] TCP STatistic and Analysis Tool: Skype Traces, <http://tstat.polito.it/traces-skype.shtml>.
- [35] R. Mahajan, N. Spring, D. Wetherall, and T. Anderson, "Inferring link weights using end-to-end measurements," in *Proceedings of the 2nd ACM SIGCOMM Workshop on Internet Measurment*, ACM, New York, NY, USA, pp. 231–236, November 2002.
- [36] M. F. Bari, X. Wang, and M. Huang, "Dynamic controller provisioning in software defined networks," in *Proceedings of the IEEE CNSM*, pp. 18–25, Zurich, Switzerland, October 2013.
- [37] R. K. Jain, D. M. W. Chiu, and W. R. Hawe, *A Quantitative Measure of Fairness and Discrimination*, Eastern Research Laboratory, Digital Equipment Corporation, Hudson, MA, USA, 1984.
- [38] C.-Y. Hong, S. Kandula, R. Mahajan et al., "Achieving high utilization with software-driven WAN," *ACM SIGCOMM Computer Communication Review*, vol. 43, no. 4, pp. 15–26, 2013.
- [39] A. Dixit, F. Hao, S. Mukherjee et al., "Towards an elastic distributed SDN controller," in *Proceedings of the Second ACM SIGCOMM Workshop on Hot Topics in Software Defined Networking*, pp. 7–12, Hong Kong, China, August 2013.
- [40] W. Aljoby, X. Wang, T. Fu, and R. Ma, "On SDN-enabled online and dynamic bandwidth allocation for stream analytics," in *Proceedings of the 2018 IEEE 26th International Conference on Network Protocols (ICNP)*, pp. 209–219, Cambridge, UK, September 2018.
- [41] T. Koponen, M. Casado, N. Gude et al., "ONIX: a distributed control platform for large-scale production networks," in *Proceedings of the OSDI*, vol. 10, Vancouver, Canada, October 2010.
- [42] A. Tootoonchian and Y. Ganjali, "HyperFlow: a distributed control plane for OpenFlow," in *Proceedings of the 2010 Internet Network Management Conference on Research on Enterprise Networking*, San Jose, CA, USA, April 2010.
- [43] P. Berde, M. Gerola, J. Hart et al., "ONOS: towards an open, distributed SDN OS," in *Proceedings of the Third Workshop on Hot Topics in Software Defined Networking*, ACM, Chicago, IL, USA, ACM, Chicago, IL, USA, August 2014.
- [44] P. Fonseca, R. Bennesby, E. Mota, and A. Passito, "Resilience of SDNs based on active and passive replication mechanisms," in *Proceedings of the 2013 IEEE Global Communications Conference (GLOBECOM)*, pp. 2188–2193, IEEE, Atlanta, GA, USA, December 2013.
- [45] N. Katta, H. Zhang, M. Freedman, and J. R. Ravana, "Controller fault-tolerance in software-defined networking," in *Proceedings of the SOSR*, Santa Clara, CA, USA, June 2015.

## Research Article

# Distributed Adaptive Output Consensus for High-Order Multiagent Systems with Input Saturation and Uncertain Nonlinear Dynamics

Ming-Can Fan <sup>1</sup> and Wen Qin<sup>2</sup>

<sup>1</sup>*School of Mathematics and Statistics, Huizhou University, Huizhou 516007, Guangdong, China*

<sup>2</sup>*College of Electrical Engineering and Control Science, Nanjing Tech University, Nanjing 211816, Jiangsu, China*

Correspondence should be addressed to Ming-Can Fan; [mingcan\\_fan@163.com](mailto:mingcan_fan@163.com)

Received 16 June 2020; Accepted 21 July 2020; Published 12 August 2020

Guest Editor: Xiao Ling Wang

Copyright © 2020 Ming-Can Fan and Wen Qin. This is an open access article distributed under the Creative Commons Attribution License, which permits unrestricted use, distribution, and reproduction in any medium, provided the original work is properly cited.

This paper deals with the leader-following output consensus problem for a class of high-order affine nonlinear strict-feedback multiagent systems with unknown control gains and input saturation under a general directed graph. Nussbaum gain function technique is used to handle the unknown control gains, and the uncertain nonlinear dynamics of each agent is approximated by radial basis function neural networks. Distributed adaptive controllers are designed via the backstepping technique as well as the dynamic surface control approach. It is proved that the closed-loop multiagent systems are semiglobally uniformly ultimately bounded, and the output consensus error can converge to a small region around the origin. Finally, the theoretical results are supported by a numerical simulation.

## 1. Introduction

Consensus control of multiagent systems (MAS) has drawn considerable attention in the past two decades due to its broad applications in multiple ground-moving robots [1], unmanned aerial vehicles (UAVs) [2], unmanned surface vessels [3], sensor networks [4], smart grids [5], and synchronization and flocking models [6–8], for instance. The investigation on this topic has been carried out from different perspectives, to mention a few, such as single-integrator or double-integrator MAS [9, 10], general linear MAS [11–13], nonlinear MAS [14–16], fractional-order MAS [17, 18], and high-order MAS [19, 20].

Consensus problems of MAS with unknown control gains, including unknown amplitudes of control gains or unknown signs of control gains (the so-called control directions), are gaining researchers' increasing attention in recent years. It is necessary and beneficial to study this topic since the control gains are often unknown in many

practical control systems, such as the autopilot design of time-varying ships and unmanned sailboat heading control. There are many results of consensus control for MAS with unknown control gains, for instance, [21–26]. In [21], Nussbaum function-based adaptive control was developed to handle the consensus problem for a first-order MAS provided that the communication digraph was balanced and weakly connected. By using a Nussbaum-like switching function, the authors in [22] also addressed the first-order consensus problem under a strongly connected communication digraph. In [23], using a novel Nussbaum gain function, consensus for a second-order linearly parameterized MAS was realized under the assumption that the control directions were the same and the communication graph was undirected and connected. Some progress has been made with respect to high-order MAS. In [24], adaptive backstepping-based controllers were designed to guarantee the consensus for high-order MAS under an undirected and connected communication graph. In [25], the authors investigated high-order

linearly parameterized MAS, while external disturbances were not considered. In [26], high-order MAS with nonlinear dynamics and partially unknown nonidentical time-varying control directions, as well as bounded external disturbances, was considered, where the communication digraph was assumed to be strongly connected. Note that most of the existing works including those mentioned above did not take input saturation into account, which is often encountered in practical applications due to physical limitations of actuators and may cause the instability or damage the control systems' performance [27–31].

Motivated by the limitation of the existing literatures, this paper studies the leader-following output consensus problem for a class of high-order nonlinear MAS subject to input saturation and bounded external disturbances. Moreover, the control gains are assumed to be time varying and unknown for the controller design. This issue has not been mentioned in any existing references to the best of the authors knowledge. Based on the backstepping technique combined with the dynamic surface control (DSC) method, and under the assumption that the communication digraph has a spanning tree, a distributed adaptive neural controller is proposed with the aid of the well-known Nussbaum gain function. It is proved that the closed-loop MAS is semiglobally uniformly ultimately bounded (SUUB), and the output consensus error can converge to a small region around the origin.

Compared with the existing results, the primary contributions of this paper can be summarized as follows. (1) First, the high-order MAS model discussed in this paper is a class of affine nonlinear systems in the strict-feedback form with external disturbances, which is more general than most existing systems regarding output consensus control with unknown control gains [26, 32, 33], where the system dynamics was described with the Brunovsky form or the input saturation was not considered. Hence, the consensus schemes in these references could not be applied. (2) Second, unlike some existing results where the signs of control gains were assumed to be known in advance and the derivative of each control gain function was assumed to be bounded [34] or the unknown nonlinear dynamics satisfied global Lipschitz conditions [35, 36], the control gains (including their amplitudes and signs) and the nonlinear dynamics in this paper are completely unknown.

The rest of this paper is organized as follows. In Section 2, some preliminaries are introduced and the problem of this paper is formulated. Then, a backstepping-based control algorithm is proposed in Section 3, and the closed-loop stability is proved in Section 4. In Section 5, a simulation example is given to verify the proposed control algorithm. Finally, some remarks of this paper are concluded in Section 6.

## 2. Preliminaries and Problem Statement

In this paper, a class of high-order affine nonlinear MAS with  $N$  followers is considered. The dynamics of each follower is described as follows:

$$\begin{aligned}\dot{x}_{i,j} &= h_{i,j}(\bar{x}_{i,j}) + \ell_{i,j}(\bar{x}_{i,j})x_{i,j+1} + d_{i,j}(t), \\ \dot{x}_{i,n_i} &= h_{i,n_i}(\bar{x}_{i,n_i}) + \ell_{i,n_i}(\bar{x}_{i,n_i})\sigma(v_i) + \bar{d}_{i,n_i}(t), \\ y_i &= x_{i,1}, \quad j = 1, 2, \dots, n_i - 1,\end{aligned}\quad (1)$$

where  $\bar{x}_{i,j} = [x_{i,1}, x_{i,2}, \dots, x_{i,j}]^T \in \mathbb{R}^j$ ,  $v_i \in \mathbb{R}$ , and  $y_i \in \mathbb{R}$  are the state vectors, actual controllers, and outputs of the MAS, respectively,  $i = 1, 2, \dots, N$ ,  $d_{i,j}(t)$  are the unknown bounded time-varying external disturbances, the unknown continuous function  $h_{i,j}(\cdot)$  represents the uncertain nonlinear dynamics,  $\ell_{i,j}(\cdot)$  represents a continuous and unknown time-varying control gain function, and  $\sigma(\cdot): \mathbb{R} \rightarrow \mathbb{R}$  is a standard saturation function defined as  $\sigma(x) = \text{sgn}(x)\min\{|x|, v^*\}$ , where  $v^* > 0$  is a saturation level constant. The output of the leader is  $y_0(t)$ , which satisfies the following assumption.

*Assumption 1.*  $y_0(t)$ ,  $\dot{y}_0(t)$ , and  $\ddot{y}_0(t)$  are bounded for  $t \geq 0$ .

*Remark 1.* The dynamics of the uncertain MAS (1) is affine nonlinear in the strict-feedback form with external disturbances, which cannot be converted to the Brunovsky form studied in most existing literatures [26, 32, 33] due to the unknown control gains. Hence, the MAS is more general, and the controller design is more challenging.

*Remark 2.* The strict-feedback nonlinear MAS (1) may have great potential for practical applications since it can describe many dynamical behaviors, such as robotic systems, flight systems, and biochemical process [37].

In order to use the backstepping technique, the discontinuous saturation nonlinearity  $\sigma(\cdot)$  is replaced by a smooth function [38]:  $\sigma(x) = v^* \times \text{erf}(px)$ , where  $p = \sqrt{\pi}/(2v^*)$  and  $\text{erf}(x) = (2/\sqrt{\pi}) \int_0^x e^{-t^2} dt$  is a Gaussian error function, which is a real-valued and continuous differentiable function. Defining  $\eta(v_i) = v^* \times \text{erf}(pv_i) - qv_i$ ,  $q > 0$ , and then we have  $\sigma(v_i) = qv_i + \eta(v_i)$ .

The purpose of this paper is to present an adaptive neural output consensus controller for MAS (1) such that the semiglobal uniform ultimate boundedness for all the signals in the closed-loop system is ensured, and each follower's output  $y_i$  ( $i = 1, 2, \dots, N$ ) synchronically tracks the leader's output  $y_0$ . Moreover, the output consensus error can converge to a small region around the origin. To this end, the following assumptions and preliminaries are required.

*Assumption 2.* There exist constants  $\bar{\eta}$ ,  $q$ ,  $\bar{q}$ , and  $\bar{d}_{i,j}$ , such that  $|\eta(v_i)| \leq \bar{\eta}$ ,  $q \in [q, \bar{q}]$ , and  $d_{i,j}(t) \leq \bar{d}_{i,j}$ , respectively,  $i = 1, 2, \dots, N$  and  $j = 1, 2, \dots, n_i$ .

*Assumption 3.* There exist positive constants  $\underline{\ell}_{i,j}$  and  $\bar{\ell}_{i,j}$  such that the unknown control gains  $\ell_{i,j}(\bar{x}_{i,j})$  satisfy  $\underline{\ell}_{i,j} \leq |\ell_{i,j}(\bar{x}_{i,j})| \leq \bar{\ell}_{i,j}$ ,  $\forall \bar{x}_{i,j} \in \Omega \subset \mathbb{R}^j$ .

*Definition 1* (see [39]). A continuous function  $N(\cdot): \mathbb{R} \rightarrow \mathbb{R}$  is called a Nussbaum gain function if it satisfies

$$\lim_{s \rightarrow +\infty} \sup \frac{1}{s} \int_0^s N(\kappa) d\kappa = +\infty, \quad (2)$$

$$\lim_{s \rightarrow +\infty} \inf \frac{1}{s} \int_0^s N(\kappa) d\kappa = -\infty.$$

In this paper, a Nussbaum gain function  $\kappa^2 \cos((\pi/2)\kappa)$  is chosen.

**Lemma 1** (see [40]). *Let  $\Gamma(t)$  and  $\kappa_i(t)$  be smooth functions defined on  $[0, T]$  with  $\Gamma(t) \geq 0, \forall t \in [0, T]$ , and  $N(\cdot)$  be an even smooth Nussbaum gain function. If the following inequality holds:*

$$\Gamma(t) \leq A + e^{-Bt} \sum_{i=1}^N \int_0^t [\ell_i(s)N(\kappa_i(s)) + 1] \dot{\kappa}_i(s) e^{Bs} ds, \quad (3)$$

where  $A$  represents some suitable constant,  $B > 0$  is a positive constant, and the value of the time-varying parameter  $\ell_i(\cdot)$  is located in the unknown intervals  $I = [L^-, L^+]$  with  $0 \notin I$ , then  $\Gamma(t)$ ,  $\kappa_i(t)$ , and  $\sum_{i=1}^N \int_0^t [\ell_i(s)N(\kappa_i(s)) + 1] \dot{\kappa}_i(s) ds$  are bounded on  $[0, T]$ .

The communication topology in MAS (1) with  $N$  followers is expressed via a digraph  $\mathcal{G} = (\mathcal{V}, \mathcal{E}, \mathcal{A})$ , where  $N$  followers are denoted by a node set  $\mathcal{V} = \{1, 2, \dots, N\}$ ,  $\mathcal{E} \subset \mathcal{V} \times \mathcal{V}$  is an edge set, and  $\mathcal{A} = [a_{ij}] \in \mathbb{R}^{N \times N}$  is an adjacency matrix.  $a_{ij} > 0$  if the  $i$ -th follower can receive information from the  $j$ -th follower, otherwise  $a_{ij} = 0$ . Self-loop is not considered, i.e.,  $a_{ii} = 0$ .  $D = \text{diag}(d_1, d_2, \dots, d_N)$  is defined as an in-degree matrix with  $d_i = \sum_{j=1}^N a_{ij}$  being the in-degree of the  $i$ -th follower. The Laplacian matrix of  $\mathcal{G}$  is denoted by  $\mathcal{L} = D - A = [l_{ij}] \in \mathbb{R}^{N \times N}$ . A digraph contains a spanning tree provided that there exists a directed path from one node (called root node) to every other node in the graph. A leader adjacency matrix  $\mathcal{R} = \text{diag}(r_1, r_2, \dots, r_N)$  is used to demonstrate the communication between the leader and the follower, where  $r_i > 0$  represents that the leader is a neighbor of the  $i$ -th follower, and  $r_i = 0$  otherwise.

**Assumption 4.** The communication digraph  $\mathcal{G}$  among the  $N$  followers contains a spanning tree, and the leader is a neighbor of the root node.

Since the uncertain nonlinear dynamics of MAS (1) is unknown and continuous, many function approximators can be used, such as neural networks, spline functions, polynomials, and fuzzy systems. Gaussian radial basis function neural network (RBFNN) approach is easy to implement due to its small number of control parameters; therefore, it is widely used in nonlinear function approximation. In this paper, we employ an RBFNN to approximate the unknown function  $\Psi(Z): \mathbb{R}^m \rightarrow \mathbb{R}$  on a prescribed compact set  $\Omega \subset \mathbb{R}^m$ , i.e.,

$$\Psi(Z) = \varrho^{*T} \vartheta(Z) + \varpi(Z), \quad Z \in \Omega, \quad (4)$$

where  $Z = [z_1, z_2, \dots, z_m]^T$  is the input vector,  $\varrho^* = [\varrho_1^*, \varrho_2^*, \dots, \varrho_s^*]^T \in \mathbb{R}^s$  is the ideal weight vector with  $s > 1$  being the number of neurons,  $\vartheta(Z) = [\vartheta_1(Z), \vartheta_2(Z), \dots, \vartheta_s(Z)]^T \in \mathbb{R}^s$  is the Gaussian basis function vector with  $\vartheta_i(Z) = \exp[-\|Z - c_i\|^2 / (2w_i^2)]$ ,

where  $c_i$  and  $w_i$  are the center and the width of the Gaussian function, respectively,  $i = 1, 2, \dots, s$ , and  $\varpi(Z)$  denotes the approximation error. It is known that given any positive constant  $\varepsilon$ , if  $s$  is large enough, there exist suitable vectors  $\varrho^*$  and  $\vartheta(Z)$  such that  $|\varpi(Z)| \leq \varepsilon$ .

### 3. Consensus Controller Design

The distributed adaptive output consensus controller design procedure consists of  $n_i$  steps using the backstepping technique. To begin with, the following error surfaces for the  $j$ -th follower are defined:

$$e_{i,1} = \sum_{j=1}^N a_{ij} (y_i - y_j) + r_i (y_i - y_0), \quad (5)$$

$$e_{i,j} = x_{i,j} - \bar{\gamma}_{i,j}, \quad j = 2, \dots, n_i, \quad (6)$$

where  $\bar{\gamma}_{i,j}$  is the filtered virtual controller, which is acquired through a first-order filter with the virtual controller  $\gamma_{i,j}$  as the input. The boundary layer error between  $\bar{\gamma}_{i,j}$  and  $\gamma_{i,j}$  is defined as  $\tilde{\gamma}_{i,j} = \bar{\gamma}_{i,j} - \gamma_{i,j}$ .

*Step 1.* The time derivative of  $e_{i,1}$  in equation (5) is obtained as

$$\begin{aligned} \dot{e}_{i,1} &= (r_i + d_i) [h_{i,1}(x_{i,1}) + \ell_{i,1}(x_{i,1})x_{i,2} + d_{i,1}] \\ &\quad - \sum_{j=1}^N a_{ij} [h_{j,1}(x_{j,1}) + \ell_{j,1}(x_{j,1})x_{j,2} + d_{j,1}] - r_i \dot{y}_0. \end{aligned} \quad (7)$$

Define  $\Psi_{i,1}(\zeta_{i,1}) := h_{i,1}(x_{i,1}) - (1/(r_i + d_i)) [\sum_{j=1}^N a_{ij} [h_{j,1}(x_{j,1}) + \ell_{j,1}(x_{j,1})x_{j,2}] - r_i \dot{y}_0]$ ,  $\zeta_{i,1} = [x_{i,1}, x_{j,1}, x_{j,2}, \dot{y}_0]^T$ . Throughout this paper, let  $\hat{x}$  be the estimates of  $x^*$ , and the corresponding estimation error be  $\tilde{x} = \hat{x} - x^*$ .

Then, the unknown smooth function  $\Psi_{i,1}(\zeta_{i,1})$  can be approximated by an RBFNN as

$$\Psi_{i,1}(\zeta_{i,1}) = \varrho_{i,1}^{*T} \vartheta_{i,1} + \varpi_{i,1} = \hat{\varrho}_{i,1}^T \vartheta_{i,1} - \tilde{\varrho}_{i,1}^T \vartheta_{i,1} + \varpi_{i,1}, \quad |\varpi_{i,1}| \leq \varepsilon_{i,1}. \quad (8)$$

Then, we have

$$\begin{aligned} \dot{e}_{i,1} &= (r_i + d_i) [\ell_{i,1}(x_{i,1})x_{i,2} + \hat{\varrho}_{i,1}^T \vartheta_{i,1} - \tilde{\varrho}_{i,1}^T \vartheta_{i,1} + \varpi_{i,1} + d_{i,1}] \\ &\quad - \sum_{j=1}^N a_{ij} d_{j,1}. \end{aligned} \quad (9)$$

The virtual controllers  $\gamma_{i,2}$  and adaptation laws  $\kappa_{i,1}$  and  $\hat{\varrho}_{i,1}$  are designed as follows:

$$\gamma_{i,2} = N(\kappa_{i,1}) (\alpha_{i,1} e_{i,1} + \hat{\varrho}_{i,1}^T \vartheta_{i,1}), \quad (10)$$

$$\dot{\kappa}_{i,1} = \alpha_{i,1} e_{i,1}^2 + e_{i,1} \hat{\varrho}_{i,1}^T \vartheta_{i,1}, \quad (11)$$

$$\dot{\hat{\varrho}}_{i,1} = \Lambda_{i,1} (\vartheta_{i,1} e_{i,1} - \beta_{i,1} \hat{\varrho}_{i,1}), \quad (12)$$

where  $\Lambda_{i,1}$  is a positive-definite matrix,  $\alpha_{i,1} > 0$  and  $\beta_{i,1} > 0$  are the design parameters. Adjusting the value of  $\alpha_{i,1}$  properly will make the error  $e_{i,1}$  converge to a small neighborhood of the origin.  $\beta_{i,1}\widehat{q}_{i,1}$  is a modification term with  $\beta_{i,1}$  being a small positive constant, such that  $\widehat{q}_{i,1}$  will not drift to very large values.

Under Assumption 4, we have  $r_i + d_i > 0 \forall i \in \mathcal{V}$ . Hence, we can construct the Lyapunov function candidate  $Y_{i,1} = 1/[2(r_i + d_i)]e_{i,1}^2$ . Note that  $\bar{\gamma}_{i,2} = \tilde{\gamma}_{i,2} + \gamma_{i,2}$ , and then we have

$$\begin{aligned} \dot{Y}_{i,1} &= \frac{1}{r_i + d_i} e_{i,1} \dot{e}_{i,1} = e_{i,1} \left[ \ell_{i,1} (e_{i,2} + \tilde{\gamma}_{i,2} + \gamma_{i,2}) + \widehat{Q}_{i,1}^T \vartheta_{i,1} - \widetilde{Q}_{i,1}^T \vartheta_{i,1} + \omega_{i,1} + d_{i,1} - \frac{1}{r_i + d_i} \sum_{j=1}^N a_{ij} d_{j,1} \right] \\ &= e_{i,1} \left[ \ell_{i,1} (e_{i,2} + \tilde{\gamma}_{i,2} + N(\kappa_{i,1})(\alpha_{i,1} e_{i,1} + \widehat{Q}_{i,1}^T \vartheta_{i,1})) + \widehat{Q}_{i,1}^T \vartheta_{i,1} - \widetilde{Q}_{i,1}^T \vartheta_{i,1} + \omega_{i,1} + d_{i,1} - \frac{1}{r_i + d_i} \sum_{j=1}^N a_{ij} d_{j,1} \right] \\ &= -\alpha_{i,1} e_{i,1}^2 + [\ell_{i,1} N(\kappa_{i,1}) + 1] \dot{\kappa}_{i,1} + \ell_{i,1} e_{i,1} e_{i,2} + \ell_{i,1} e_{i,1} \tilde{\gamma}_{i,2} - e_{i,1} \widetilde{Q}_{i,1}^T \vartheta_{i,1} + e_{i,1} \left[ \omega_{i,1} + d_{i,1} - \frac{1}{r_i + d_i} \sum_{j=1}^N a_{ij} d_{j,1} \right] \\ &\leq -\alpha_{i,1} e_{i,1}^2 + [\ell_{i,1} N(\kappa_{i,1}) + 1] \dot{\kappa}_{i,1} + \ell_{i,1} e_{i,1} e_{i,2} + \ell_{i,1} e_{i,1} \tilde{\gamma}_{i,2} + \xi_{i,1} |e_{i,1}| - e_{i,1} \widetilde{Q}_{i,1}^T \vartheta_{i,1}, \end{aligned} \quad (13)$$

where  $\xi_{i,1} = \varepsilon_{i,1} + \bar{d}_{i,1} + (1/(r_i + d_i)) \sum_{j=1}^N a_{ij} \bar{d}_{j,1} > 0$ . Using Young's inequality [41], the following inequalities hold:

$$\ell_{i,1} e_{i,1} e_{i,2} \leq e_{i,1}^2 + \frac{\ell_{i,1}^2 e_{i,2}^2}{4}, \quad (14)$$

$$\ell_{i,1} e_{i,1} \tilde{\gamma}_{i,2} \leq e_{i,1}^2 + \frac{\ell_{i,1}^2 \tilde{\gamma}_{i,2}^2}{4}, \quad (15)$$

$$\xi_{i,1} |e_{i,1}| \leq e_{i,1}^2 + \frac{\xi_{i,1}^2}{4}. \quad (16)$$

Substituting (14)–(16) into (13), one has

$$\begin{aligned} \dot{Y}_{i,1} &\leq -(\alpha_{i,1} - 3)e_{i,1}^2 + [\ell_{i,1} N(\kappa_{i,1}) + 1] \dot{\kappa}_{i,1} + \frac{1}{4} \ell_{i,1}^2 e_{i,2}^2 \\ &\quad + \frac{1}{4} \ell_{i,1}^2 \tilde{\gamma}_{i,2}^2 + \frac{1}{4} \xi_{i,1}^2 - e_{i,1} \widetilde{Q}_{i,1}^T \vartheta_{i,1}. \end{aligned} \quad (17)$$

In order to avoid differentiating  $\gamma_{i,2}$ , the so-call explosion of the complexity problem is inherent in the backstepping technique, and let  $\gamma_{i,2}$  pass through a first-order filter such that a filtered virtual controller  $\bar{\gamma}_{i,2}$  is acquired:

$$\begin{aligned} \tau_{i,2} \dot{\bar{\gamma}}_{i,2} + \bar{\gamma}_{i,2} &= \gamma_{i,2}, \\ \bar{\gamma}_{i,2}(0) &= \gamma_{i,2}(0), \end{aligned} \quad (18)$$

where  $\tau_{i,2} > 0$  is a small time constant.

A Lyapunov function candidate  $\Gamma_{i,1}(t)$  is given as

$$\Gamma_{i,1}(t) = Y_{i,1} + \frac{1}{2} \bar{\gamma}_{i,2}^2 + \frac{1}{2} \widetilde{Q}_{i,1}^T \Lambda_{i,1}^{-1} \widetilde{Q}_{i,1}. \quad (19)$$

Using (18), we have  $\dot{\bar{\gamma}}_{i,2} = \dot{\gamma}_{i,2} - \dot{\gamma}_{i,2} = -(\tilde{\gamma}_{i,2}/\tau_{i,2}) + B_{i,2}$ , where  $B_{i,2} = -(\partial\gamma_{i,2}/\partial\kappa_{i,1})\dot{\kappa}_{i,1} - (\partial\gamma_{i,2}/\partial e_{i,1})\dot{e}_{i,1} - (\partial\gamma_{i,2}/\partial\widehat{q}_{i,1})\dot{\widehat{q}}_{i,1}$  is a continuous function. Since for any  $B_0 > 0$  and  $Q > 0$ , the sets

$\Pi := \{(y_0, \dot{y}_0, \ddot{y}_0): y_0^2 + \dot{y}_0^2 + \ddot{y}_0^2 \leq B_0\}$  and  $\Pi_i := \{\sum_{j=1}^i 1/(r_j + d_j) e_{j,1}^2 + \sum_{j=1}^i \gamma_{j,2}^2 + \sum_{j=1}^i \widetilde{Q}_{j,1}^T \Lambda_{j,1}^{-1} \widetilde{Q}_{j,1} \leq 2Q\}$ ,  $i = 1, 2, \dots, N$ , are compact in  $R^3$  and  $R^{3i}$ , respectively, and  $\Pi \times \Pi_i$  is also compact in  $R^{3i+3}$ . Therefore,  $|B_{i,2}|$  has a maximum  $\bar{B}_{i,2}$  on  $\Pi \times \Pi_i$ , i.e.,  $|B_{i,2}| \leq \bar{B}_{i,2}$ . Similar analysis can be found in [42]. Hence, we have

$$\tilde{\gamma}_{i,2} \dot{\bar{\gamma}}_{i,2} \leq -\frac{\tilde{\gamma}_{i,2}^2}{\tau_{i,2}} + |\tilde{\gamma}_{i,2}| \bar{B}_{i,2} \leq -\frac{\tilde{\gamma}_{i,2}^2}{\tau_{i,2}} + \tilde{\gamma}_{i,2}^2 + \frac{1}{4} \bar{B}_{i,2}^2. \quad (20)$$

By taking the time derivative of  $\Gamma_{i,1}$ , one has

$$\begin{aligned} \dot{\Gamma}_{i,1}(t) &= \dot{Y}_{i,1} + \tilde{\gamma}_{i,2} \dot{\bar{\gamma}}_{i,2} + \widetilde{Q}_{i,1}^T \Lambda_{i,1}^{-1} \dot{\widetilde{Q}}_{i,1} \\ &\leq -(\alpha_{i,1} - 3)e_{i,1}^2 + [\ell_{i,1} N(\kappa_{i,1}) + 1] \dot{\kappa}_{i,1} + \frac{1}{4} \ell_{i,1}^2 e_{i,2}^2 \\ &\quad + \left( \frac{\ell_{i,1}^2}{4} - \frac{1}{\tau_{i,2}} + 1 \right) \tilde{\gamma}_{i,2}^2 + \frac{1}{4} \omega_{i,1}^2 - \beta_{i,1} \widetilde{Q}_{i,1}^T \widehat{Q}_{i,1}, \end{aligned} \quad (21)$$

where  $\omega_{i,1}^2 = \xi_{i,1}^2 + \bar{B}_{i,2}^2$ . Note that

$$\begin{aligned} -\widetilde{Q}_{i,1}^T \widehat{Q}_{i,1} &= -\widetilde{Q}_{i,1}^T (\widetilde{Q}_{i,1} + Q_{i,1}^*) \\ &\leq -\|\widetilde{Q}_{i,1}\|^2 + \|\widetilde{Q}_{i,1}\| \cdot \|Q_{i,1}^*\| \\ &\leq -\left(\frac{1}{2}\right) \|\widetilde{Q}_{i,1}\|^2 + \left(\frac{1}{2}\right) \|Q_{i,1}^*\|^2, \end{aligned} \quad (22)$$

then we have

$$\begin{aligned} \dot{\Gamma}_{i,1}(t) &\leq -(\alpha_{i,1} - 3)e_{i,1}^2 - \left( \frac{1}{\tau_{i,2}} - \frac{\ell_{i,1}^2}{4} - 1 \right) \tilde{\gamma}_{i,2}^2 - \frac{\beta_{i,1}}{2} \|\widetilde{Q}_{i,1}\|^2 \\ &\quad + [\ell_{i,1} N(\kappa_{i,1}) + 1] \dot{\kappa}_{i,1} + \frac{\beta_{i,1}}{2} \|Q_{i,1}^*\|^2 + \frac{1}{4} \omega_{i,1}^2 + \frac{1}{4} \ell_{i,1}^2 e_{i,2}^2. \end{aligned} \quad (23)$$

Step  $j$  ( $2 \leq j \leq n_i - 1$ ). The derivative of the error surface  $e_{i,j} = x_{i,j} - \bar{y}_{i,j+1}$  in (6) is obtained as

$$\dot{e}_{i,j} = h_{i,j}(\bar{x}_{i,j}) + \ell_{i,j}x_{i,j+1} + d_{i,j} - \dot{\bar{y}}_{i,j+1}. \quad (24)$$

Define  $\Psi_{i,j}(\zeta_{i,j}) := h_{i,j}(\bar{x}_{i,j}) - \dot{\bar{y}}_{i,j+1}$ ,  $\zeta_{i,j} = [\bar{x}_{i,j}, \bar{y}_{i,j}]^T \in \mathbb{R}^{j+1}$ . This unknown smooth function  $\Psi_{i,j}(\zeta_{i,j})$  can be approximated by an RBFNN as

$$\Psi_{i,j}(\zeta_{i,j}) = \varrho_{i,j}^{*T} \vartheta_{i,j} + \omega_{i,j} = \tilde{\varrho}_{i,j}^T \vartheta_{i,j} - \tilde{\varrho}_{i,j}^T \vartheta_{i,j} + \omega_{i,j}, \quad |\omega_{i,j}| \leq \varepsilon_{i,j}. \quad (25)$$

The virtual controllers  $\gamma_{i,j+1}$ ,  $j = 2, \dots, n_i - 1$ , and adaptation laws  $\kappa_{i,j}$  and  $\tilde{\varrho}_{i,j}$  are designed as follows:

$$\gamma_{i,j+1} = N(\kappa_{i,j})(\alpha_{i,j}e_{i,j} + \tilde{\varrho}_{i,j}^T \vartheta_{i,j}), \quad (26)$$

$$\dot{\kappa}_{i,j} = \alpha_{i,j}e_{i,j}^2 + e_{i,j}\tilde{\varrho}_{i,j}^T \vartheta_{i,j}, \quad (27)$$

$$\dot{\tilde{\varrho}}_{i,j} = \Lambda_{i,j}(\vartheta_{i,j}e_{i,j} - \beta_{i,j}\tilde{\varrho}_{i,j}), \quad (28)$$

where  $\Lambda_{i,j}$  is a positive-definite matrix,  $\alpha_{i,j} > 0$  and  $\beta_{i,j} > 0$  are the design parameters.

Applying the Lyapunov function  $Y_{i,j} = (1/2)e_{i,j}^2$  and noting that  $\bar{y}_{i,j+1} = \tilde{y}_{i,j+1} + \gamma_{i,j+1}$ , we have

$$\begin{aligned} \dot{Y}_{i,j} &= e_{i,j}\dot{e}_{i,j} = e_{i,j}[\ell_{i,j}(e_{i,j+1} + \tilde{y}_{i,j+1} + \gamma_{i,j+1}) + \tilde{\varrho}_{i,j}^T \vartheta_{i,j} - \tilde{\varrho}_{i,j}^T \vartheta_{i,j} + \omega_{i,j} + d_{i,j}] \\ &= -\alpha_{i,j}e_{i,j}^2 + [\ell_{i,j}N(\kappa_{i,j}) + 1]\dot{\kappa}_{i,j} + \ell_{i,j}e_{i,j}e_{i,j+1} + \ell_{i,j}e_{i,j}\tilde{y}_{i,j+1} - e_{i,j}\tilde{\varrho}_{i,j}^T \vartheta_{i,j} + e_{i,j}(\omega_{i,j} + d_{i,j}) \\ &\leq -\alpha_{i,j}e_{i,j}^2 + [\ell_{i,j}N(\kappa_{i,j}) + 1]\dot{\kappa}_{i,j} + \ell_{i,j}e_{i,j}e_{i,j+1} + \ell_{i,j}e_{i,j}\tilde{y}_{i,j+1} + e_{i,j}|\xi_{i,j}| - e_{i,j}\tilde{\varrho}_{i,j}^T \vartheta_{i,j}, \end{aligned} \quad (29)$$

where  $\xi_{i,j} = \omega_{i,j} + \bar{d}_{i,j}$ . Using Young's inequality, we have

$$\begin{aligned} \ell_{i,j}e_{i,j}e_{i,j+1} &\leq e_{i,j}^2 + \ell_{i,j}^2 \frac{e_{i,j+1}^2}{4}, \\ \ell_{i,j}e_{i,j}\tilde{y}_{i,j+1} &\leq e_{i,j}^2 + \ell_{i,j}^2 \frac{\tilde{y}_{i,j+1}^2}{4}, \\ e_{i,j}|\xi_{i,j}| &\leq e_{i,j}^2 + \frac{\xi_{i,j}^2}{4}. \end{aligned} \quad (30)$$

Substituting the above equations into (29) gives

$$\begin{aligned} \dot{Y}_{i,j} &\leq -(\alpha_{i,j} - 3)e_{i,j}^2 + [\ell_{i,j}N(\kappa_{i,j}) + 1]\dot{\kappa}_{i,j} + \frac{1}{4}\ell_{i,j}^2 e_{i,j+1}^2 \\ &\quad + \frac{1}{4}\ell_{i,j}^2 \tilde{y}_{i,j+1}^2 + \frac{1}{4}\xi_{i,j}^2 - e_{i,j}\tilde{\varrho}_{i,j}^T \vartheta_{i,j}. \end{aligned} \quad (31)$$

Let  $\gamma_{i,j+1}$  pass through a first-order filter with a small time constant  $\tau_{i,j+1} > 0$  to acquire  $\bar{\gamma}_{i,j+1}$ ,  $j = 2, \dots, n_i - 1$ :

$$\begin{aligned} \tau_{i,j+1}\dot{\bar{\gamma}}_{i,j+1} + \bar{\gamma}_{i,j+1} &= \gamma_{i,j+1}, \\ \bar{\gamma}_{i,j+1}(0) &= \gamma_{i,j+1}(0). \end{aligned} \quad (32)$$

From (32), we have

$$\dot{\bar{\gamma}}_{i,j+1} = \frac{\tilde{\gamma}_{i,j+1}}{\tau_{i,j+1}} + B_{i,j+1} \leq -\frac{\tilde{\gamma}_{i,j+1}}{\tau_{i,j+1}} + \tilde{\gamma}_{i,j+1}^2 + \frac{1}{4}B_{i,j+1}^2, \quad (33)$$

where  $B_{i,j+1} = (\partial\gamma_{i,j+1}/\partial\kappa_{i,j})\dot{\kappa}_{i,j} + (\partial\gamma_{i,j+1}/\partial e_{i,j})\dot{e}_{i,j} + (\partial\gamma_{i,j+1}/\partial\tilde{\varrho}_{i,j})\dot{\tilde{\varrho}}_{i,j}$  is a continuous and bounded function satisfying  $|B_{i,j+1}| \leq \bar{B}_{i,j+1}$ .

Applying the Lyapunov function,

$$\Gamma_{i,j}(t) = Y_{i,j} + \frac{1}{2}\tilde{y}_{i,j+1}^2 + \frac{1}{2}\tilde{\varrho}_{i,j}^T \Lambda_{i,j}^{-1} \tilde{\varrho}_{i,j}. \quad (34)$$

Similar to the previous step, we have

$$\begin{aligned} \dot{\Gamma}_{i,j}(t) &= \dot{Y}_{i,j} + \tilde{y}_{i,j+1}\dot{\tilde{y}}_{i,j+1} + \tilde{\varrho}_{i,j}^T \Lambda_{i,j}^{-1} \dot{\tilde{\varrho}}_{i,j} \\ &\leq -(\alpha_{i,j} - 3)e_{i,j}^2 + [\ell_{i,j}N(\kappa_{i,j}) + 1]\dot{\kappa}_{i,j} + \frac{1}{4}\ell_{i,j}^2 e_{i,j+1}^2 \\ &\quad + \left(\frac{\bar{\varrho}_{i,j}^2}{4} - \frac{1}{\tau_{i,j+1}} + 1\right)\tilde{y}_{i,j+1}^2 + \frac{1}{4}\omega_{i,j}^2 - \beta_{i,j}\tilde{\varrho}_{i,j}^T \tilde{\varrho}_{i,j}, \end{aligned} \quad (35)$$

where  $\omega_{i,j}^2 = \xi_{i,j}^2 + \bar{B}_{i,j+1}^2$ . Similar to (22), one has

$$-e_{i,j}\tilde{\varrho}_{i,j}^T \tilde{\varrho}_{i,j} \leq -\frac{1}{2}\|\tilde{\varrho}_{i,j}\|^2 + \frac{1}{2}\|\varrho_{i,j}^*\|^2, \quad (36)$$

then we have

$$\begin{aligned} \dot{\Gamma}_{i,j}(t) &\leq -(\alpha_{i,j} - 3)e_{i,j}^2 - \left(\frac{1}{\tau_{i,j+1}} - \frac{\bar{\varrho}_{i,j}^2}{4} - 1\right)\tilde{y}_{i,j+1}^2 - \frac{\beta_{i,j}}{2}\|\tilde{\varrho}_{i,j}\|^2 \\ &\quad + [\ell_{i,j}N(\kappa_{i,j}) + 1]\dot{\kappa}_{i,j} \\ &\quad + \frac{\beta_{i,j}}{2}\|\varrho_{i,j}^*\|^2 + \frac{1}{4}\omega_{i,j}^2 + \frac{1}{4}\ell_{i,j}^2 e_{i,j+1}^2. \end{aligned} \quad (37)$$

Step  $n_i$ . At this final step, the actual controller  $v_i(t)$  is designed. The derivative of the error surface  $e_{i,n_i} = x_{i,n_i} - \bar{y}_{i,n_i}$  is obtained as

$$\dot{e}_{i,n_i} = h_{i,n_i}(\bar{x}_{i,n_i}) + \ell_{i,n_i}(\bar{x}_{i,n_i})[c(v_i) + \eta(v_i)] + d_{i,n_i} - \dot{\bar{y}}_{i,n_i}. \quad (38)$$

Define  $\Psi_{i,n_i}(\zeta_{i,n_i}) = h_{i,n_i}(\bar{x}_{i,n_i}) - \dot{\bar{y}}_{i,n_i}$ ,  $\zeta_{i,n_i} = [\bar{x}_{i,n_i}, \dot{\bar{y}}_{i,n_i}]^T \in \mathbb{R}^{n_i+1}$ . This unknown smooth function  $\Psi_{i,n_i}(\zeta_{i,n_i})$  can be approximated by an RBFNN as

$$\begin{aligned} \Psi_{i,n_i}(\zeta_{i,n_i}) &= \varrho_{i,n_i}^{*T} \vartheta_{i,n_i} + \omega_{i,n_i} \\ &= \tilde{\varrho}_{i,n_i}^T \vartheta_{i,n_i}(\zeta_{i,n_i}) - \tilde{\varrho}_{i,n_i}^T \vartheta_{i,n_i}(\zeta_{i,n_i}) + \omega_{i,n_i}, \quad |\omega_{i,n_i}| \leq \varepsilon_{i,n_i}. \end{aligned} \quad (39)$$

The actual controllers  $v_i$  and adaptation laws  $\kappa_{i,n_i}$  and  $\hat{\varrho}_{i,n_i}$  are designed as follows:

$$v_i = N(\kappa_{i,n_i}) [\alpha_{i,n_i} e_{i,n_i} + \hat{\varrho}_{i,n_i}^T \vartheta_{i,n_i}], \quad (40)$$

$$\dot{\kappa}_{i,n_i} = \alpha_{i,n_i} e_{i,n_i}^2 + e_{i,n_i} \hat{\varrho}_{i,n_i}^T \vartheta_{i,n_i}, \quad (41)$$

$$\dot{\hat{\varrho}}_{i,n_i} = \Lambda_{i,n_i} [\vartheta_{i,n_i} e_{i,n_i} - \beta_{i,n_i} \hat{\varrho}_{i,n_i}], \quad (42)$$

where  $\Lambda_{i,n_i}$  is a positive-definite matrix,  $\alpha_{i,n_i} > 0$  and  $\beta_{i,n_i} > 0$  are the design parameters.

Applying the Lyapunov function  $\Gamma_{i,n_i}(t) = (1/2)e_{i,n_i}^2 + (1/2)\tilde{\varrho}_{i,n_i}^T \Lambda_{i,n_i}^{-1} \tilde{\varrho}_{i,n_i}$ ; similar to the aforementioned step, we have

$$\begin{aligned} \dot{\Gamma}_{i,n_i}(t) &= e_{i,n_i} [\hat{\varrho}_{i,n_i}^T \vartheta_{i,n_i}(\zeta_{i,n_i}) - \tilde{\varrho}_{i,n_i}^T \vartheta_{i,n_i}(\zeta_{i,n_i}) + \omega_{i,n_i} \\ &\quad + \ell_{i,n_i} [c(v_i) + \eta(v_i)] + d_{i,n_i} - \dot{\bar{y}}_{i,n_i}] \\ &\leq -(\alpha_i n_i - 1)e_{i,n_i}^2 + [\ell_{i,n_i} cN(\kappa_{i,n_i}) + 1] \dot{\kappa}_{i,n_i} \\ &\quad - \frac{\beta_{i,n_i}}{2} \|\tilde{\varrho}_{i,n_i}\|^2 + \frac{\beta_{i,n_i}}{2} \|\varrho_{i,n_i}^*\|^2 + \frac{1}{4} \omega_{i,n_i}^2, \end{aligned} \quad (43)$$

where  $\omega_{i,n_i} = \bar{\ell}_{i,n_i} \bar{\eta} + \bar{d}_{i,n_i} + \varepsilon_{i,n_i}$ .

#### 4. Stability Analysis

**Theorem 1.** Suppose that the initial conditions are bounded and the design parameters fulfill the following inequalities (44), then the output consensus problem for MAS (1) can be addressed by the controllers (10), (26), and (40) combining with adaptation laws (11), (12), (9), (28), (41), and (42), as well as the filters (18) and (32) under Assumptions 1–4. Moreover, all signals in the closed-loop MAS are SUUB, and the output consensus error can converge to a small region around the origin provided that the design parameters are appropriately selected:

$$\left\{ \begin{array}{l} \alpha_{i,1} > 3, \\ \alpha_{i,j+1} > \frac{\bar{\ell}_{i,j}^2}{4} + 3, \quad j = 1, 2, \dots, n_i - 2, \\ \alpha_{i,n_i} > 1, \\ \frac{1}{\tau_{i,j+1}} > \frac{\bar{\ell}_{i,j}^2}{4} + 1, \quad j = 1, 2, \dots, n_i - 1. \end{array} \right. \quad (44)$$

*Proof.* Select the following constants  $\mu_{i,1} > 0$  and  $\nu_{i,1} > 0$  as

$$\begin{aligned} \mu_{i,1} &= \min \left\{ 2(r_i + d_i)(\alpha_{i,1} - 3), \frac{\beta_{i,1}}{\lambda_{\max}(\Lambda_{i,1}^{-1})}, 2 \left( \frac{1}{\tau_{i,2}} - \frac{\bar{\ell}_{i,1}^2}{4} - 1 \right) \right\}, \\ \nu_{i,1} &= \frac{\beta_{i,1} \|\varrho_{i,j}^*\|^2}{2} + \frac{\omega_{i,1}^2}{4}. \end{aligned} \quad (45)$$

From (23), one has

$$\dot{\Gamma}_{i,1}(t) \leq -\mu_{i,1} \Gamma_{i,1}(t) + [\ell_{i,1} N(\kappa_{i,1}) + 1] \dot{\kappa}_{i,1} + \nu_{i,1} + \frac{1}{4} \ell_{i,1}^2 e_{i,2}^2. \quad (46)$$

Multiplying (46) by  $e^{\mu_{i,1}t}$  and then integrating it with respect to  $t$  over  $[0, t]$ , one has

$$\begin{aligned} \Gamma_{i,1}(t) &\leq \frac{\nu_{i,1}}{\mu_{i,1}} + \Gamma_{i,1}(0) + e^{-\mu_{i,1}t} \int_0^t [\ell_{i,1} N(\kappa_{i,1}) + 1] \dot{\kappa}_{i,1} e^{\mu_{i,1}s} ds \\ &\quad + \frac{1}{4} e^{-\mu_{i,1}t} \int_0^t \ell_{i,1}^2 e_{i,2}^2 e^{\mu_{i,1}s} ds. \end{aligned} \quad (47)$$

Since  $e^{-\mu_{i,1}t} \int_0^t \ell_{i,1}^2 e_{i,2}^2 e^{\mu_{i,1}s} ds \leq (1/\mu_{i,1}) \bar{\ell}_{i,1}^2 \sup_{s \in [0,t]} [e_{i,2}^2(s)]$ , we have

$$\Gamma_{i,1}(t) \leq \rho_{i,1} + e^{-\mu_{i,1}t} \int_0^t [\ell_{i,1} N(\kappa_{i,1}) + 1] \dot{\kappa}_{i,1} e^{\mu_{i,1}s} ds, \quad (48)$$

where

$\rho_{i,1} = (\nu_{i,1}/\mu_{i,1}) + \Gamma_{i,1}(0) + (1/4\mu_{i,1}) \bar{\ell}_{i,1}^2 \sup_{s \in [0,t]} [e_{i,2}^2(s)]$ . Then, according to Lemma 1, we can conclude that  $\Gamma_{i,1}(t)$ ,  $e_{i,1}(t)$ ,  $\kappa_{i,1}(t)$ ,  $\tilde{\varrho}_{i,1}(t)$ , and  $\int_0^t [\ell_{i,1} N(\kappa_{i,1}) + 1] \dot{\kappa}_{i,1} ds$  are all SUUB on  $[0, T)$ . Let  $\varsigma_{i,1} > 0$  be the upper bound of  $\int_0^t [\ell_{i,1} N(\kappa_{i,1}) + 1] \dot{\kappa}_{i,1} ds$ , i.e.,  $|\int_0^t [\ell_{i,1} N(\kappa_{i,1}) + 1] \dot{\kappa}_{i,1} ds| \leq \varsigma_{i,1}$ . For  $j = 2, \dots, n_i - 1$ , select the following constants  $\mu_{i,j} > 0$  and  $\nu_{i,j} > 0$  as

$$\begin{aligned} \mu_{i,j} &= \min \left\{ 2(\alpha_{i,j} - 3), \frac{\beta_{i,j}}{\lambda_{\max}(\Lambda_{i,j}^{-1})}, 2 \left( \frac{1}{\tau_{i,j+1}} - \frac{\bar{\ell}_{i,j}^2}{4} - 1 \right) \right\}, \\ \nu_{i,j} &= \frac{\beta_{i,j} \|\varrho_{i,j}^*\|^2}{2} + \frac{\omega_{i,j}^2}{4}. \end{aligned} \quad (49)$$

From (37), we have

$$\dot{\Gamma}_{i,j}(t) \leq -\mu_{i,j} \Gamma_{i,j}(t) + [\ell_{i,j} N(\kappa_{i,j}) + 1] \dot{\kappa}_{i,j} + \nu_{i,j} + \frac{1}{4} \ell_{i,j}^2 e_{i,j+1}^2. \quad (50)$$

Similar to (48), one has

$$\Gamma_{i,j}(t) \leq \rho_{i,j} + e^{-\mu_{i,j}t} \int_0^t [\ell_{i,j} N(\kappa_{i,j}) + 1] \dot{\kappa}_{i,j} e^{\mu_{i,j}s} ds, \quad (51)$$

where  $\rho_{i,j} = (v_{i,j}/\mu_{i,j}) + \Gamma_{i,j}(0) + (1/(4\mu_{i,j}))\bar{\ell}_{i,j}^2 \sup_{s \in [0,t]} [e_{i,j+1}^2(s)]$ . Then, according to Lemma 1, one can conclude that  $\Gamma_{i,j}(t)$ ,  $e_{i,j}(t)$ ,  $\kappa_{i,j}(t)$ ,  $\tilde{\varrho}_{i,j}(t)$ , and  $\int_0^t [\ell_{i,j}N(\kappa_{i,j}) + 1]\dot{\kappa}_{i,j}ds$  are all SUUB. Let  $\varsigma_{i,j} > 0$  be the upper bound of  $\int_0^t [\ell_{i,j}N(\kappa_{i,j}) + 1]\dot{\kappa}_{i,j}ds$ , i.e.,  $|\int_0^t [\ell_{i,j}N(\kappa_{i,j}) + 1]\dot{\kappa}_{i,j}ds| \leq \varsigma_{i,j}$ . Finally, applying the Lyapunov function,

$$\begin{aligned} \Gamma(t) &= \sum_{i=1}^N \sum_{j=1}^{n_i} \Gamma_{i,j}(t) = \sum_{i=1}^N \left[ \frac{1}{2(r_i + d_i)} e_{i,1}^2 + \frac{1}{2} \sum_{j=2}^{n_i} e_{i,j}^2 \right. \\ &\quad \left. + \frac{1}{2} \sum_{j=1}^{n_i-1} \tilde{\gamma}_{i,j+1}^2 + \frac{1}{2} \sum_{j=1}^{n_i} \tilde{\varrho}_{i,j}^T \Lambda_{i,j}^{-1} \tilde{\varrho}_{i,j} \right]. \end{aligned} \quad (52)$$

Denote

$$\begin{aligned} 0 < \delta \leq \min_{\substack{i=1,2,\dots,N \\ j=1,2,\dots,n_i-1}} \left\{ \mu_{i,j}, 2 \left( \alpha_{i,j+1} - 3 - \frac{\bar{\ell}_{i,j}^2}{4} \right), 2(\alpha_{i,n_i} - 1) \right. \\ &\quad \left. \frac{\beta_{i,n_i}}{\lambda_{\max}(\Lambda_{i,n_i}^{-1})} \right\}, \\ \chi &= \sum_{i=1}^N \sum_{j=1}^{n_i} \frac{\beta_{i,j}}{2} \|\varrho_{i,j}^*\|^2 + \frac{1}{4} \sum_{i=1}^N \sum_{j=1}^{n_i} \omega_{i,j}^2, \\ \hat{\ell}_{i,j} &= \begin{cases} \ell_{i,j}, & j = 1, 2, \dots, n_i - 1, \\ c\ell_{i,n_i}, & j = n_i, \end{cases} \end{aligned} \quad (53)$$

then substitute (23), (37), and (43) into the time derivative of (52), and based on (44), we have

$$\begin{aligned} \dot{\Gamma}(t) &= - \sum_{i=1}^N (\alpha_{i,1} - 3) e_{i,1}^2 - \sum_{i=1}^N \sum_{j=2}^{n_i-1} \left( \alpha_{i,j} - 3 - \frac{\bar{\ell}_{i,j-1}^2}{4} \right) e_{i,j}^2 - \sum_{i=1}^N (\alpha_{i,n_i} - 1) e_{i,n_i}^2 \\ &\quad - \sum_{i=1}^N \sum_{j=1}^{n_i-1} \left( \frac{1}{\tau_{i,j+1}} - \sum_{i=1}^N \frac{\bar{\ell}_{i,j}^2}{4} - 1 \right) \tilde{\gamma}_{i,j+1}^2 - \sum_{i=1}^N \sum_{j=1}^{n_i} \frac{\beta_{i,j}}{2} \|\tilde{\varrho}_{i,j}\|^2 \\ &\quad + \sum_{i=1}^N \sum_{j=1}^{n_i} [\hat{\ell}_{i,j}N(\kappa_{i,j}) + 1] \dot{\kappa}_{i,j} + \sum_{i=1}^N \sum_{j=1}^{n_i} \frac{\beta_{i,j}}{2} \|\varrho_{i,j}^*\|^2 + \frac{1}{4} \sum_{i=1}^N \sum_{j=1}^{n_i} \omega_{i,j}^2 \\ &\leq -\delta \Gamma(t) + \sum_{i=1}^N \sum_{j=1}^{n_i} [\hat{\ell}_{i,j}N(\kappa_{i,j}) + 1] \dot{\kappa}_{i,j} + \chi. \end{aligned} \quad (54)$$

Multiplying the above inequality by  $e^{\delta t}$  and then integrating it with respect to  $t$  over  $[0, t]$ , we have

$$\begin{aligned} \Gamma(t) &\leq \frac{\chi}{\delta} + e^{-\delta t} \left[ \Gamma(0) - \frac{\chi}{\delta} \right] + e^{-\delta t} \sum_{i=1}^N \sum_{j=1}^{n_i} \int_0^t [\hat{\ell}_{i,j}N(\kappa_{i,j}) + 1] \\ &\quad \times \dot{\kappa}_{i,j} e^{\delta s} ds, \end{aligned} \quad (55)$$

$$\leq \frac{\chi}{\delta} + \Gamma(0) + \sum_{i=1}^N \sum_{j=1}^{n_i} \int_0^t [\hat{\ell}_{i,j}N(\kappa_{i,j}) + 1] \dot{\kappa}_{i,j} e^{-\delta(t-s)} ds, \quad (56)$$

$$\begin{aligned} &\leq \frac{\chi}{\delta} + \Gamma(0) + \sum_{i=1}^N \sum_{j=1}^{n_i-1} \varsigma_{i,j} + e^{-\delta t} \sum_{i=1}^N \int_0^t [\hat{\ell}_{i,n_i}N(\kappa_{i,n_i}) + 1] \\ &\quad \times \dot{\kappa}_{i,n_i} e^{\delta s} ds. \end{aligned} \quad (57)$$

By Lemma 1, it can be concluded that  $\Gamma(t)$ ,  $e_{i,n_i}(t)$ ,  $\kappa_{i,n_i}(t)$ ,  $\tilde{\varrho}_{i,n_i}(t)$ , and  $\sum_{i=1}^N \int_0^t [\hat{\ell}_{i,n_i}N(\kappa_{i,n_i}) + 1] \dot{\kappa}_{i,n_i} ds$  are all

SUUB; i.e., all the signals in the closed-loop system are SUUB. Besides, from (52) and (55), one has

$$\begin{aligned} \sum_{i=1}^N \frac{1}{2(r_i + d_i)} e_{i,1}^2 \leq \Gamma(t) \leq \frac{\chi}{\delta} + e^{-\delta t} \left[ \Gamma(0) - \frac{\chi}{\delta} \right] \\ + e^{-\delta t} \sum_{i=1}^N [\hat{\ell}_{i,j}N(\kappa_{i,j}) + 1] \dot{\kappa}_{i,j} e^{\delta s} ds. \end{aligned} \quad (58)$$

Since the matrix  $\mathcal{L} + \mathcal{R}$  is nonsingular under Assumption 4, denote its minimum singular value as  $\sigma$ , which is a positive constant [10]. Define  $M = \max_i \{r_i + d_i\}$  and  $z_1 = [z_{1,1}, z_{2,1}, \dots, z_{N,1}]^T = (\mathcal{L} + \mathcal{R})(y - y_0 \mathbf{1})$  with  $y = [y_1, y_2, \dots, y_N]^T$  and  $\mathbf{1} = [1, 1, \dots, 1]^T \in \mathbb{R}^N$ . Then, we have

$$\lim_{t \rightarrow \infty} \|y - y_0 \mathbf{1}\| \leq \sqrt{\frac{2M\chi}{\sigma\delta}}. \quad (59)$$

Hence, the output consensus error can converge to a small region around the origin provided that the design parameters  $\alpha_{i,j}$ ,  $\beta_{i,j}$ , and  $\tau_{i,j+1}$  are appropriately selected.  $\square$



## 5. Numerical Simulation

To test the availability of the proposed control algorithm, consider the following uncertain MAS with 3 followers:

$$\begin{cases} \dot{x}_{i1} = h_{i1}(x_{i1}) + \ell_{i1}(x_{i1})x_{i2} + d_{i1}(t), \\ \dot{x}_{i2} = h_{i2}(\bar{x}_{i2}) + \ell_{i2}(\bar{x}_{i2})\sigma(v_i) + d_{i2}(t), \\ y_i = x_{i1}, \\ i = 1, 2, 3, \end{cases} \quad (60)$$

where  $h_{11}(x_{11}) = -2x_{11} + x_{11}^2$ ,  $\ell_{11}(x_{11}) = -[3 + 2 \sin(x_{11}^2)]$ ,  $h_{12}(\bar{x}_{12}) = x_{11}x_{12}^2$ ,  $\ell_{12}(\bar{x}_{12}) = -[4 + 2 \cos(x_{11}x_{12}^2)]$ ,  $h_{21}(x_{21}) = -x_{21} + \sin(x_{21})$ ,  $\ell_{21}(x_{21}) = 5 - 3 \cos(x_{21})$ ,  $h_{22}(\bar{x}_{22}) = -\cos(x_{21})x_{22}$ ,  $\ell_{22}(\bar{x}_{22}) = -[2 - \sin(x_{21}x_{22}^3)]$ ,  $h_{31}(x_{31}) = -x_{31} \cos(x_{31})$ ,  $\ell_{31}(x_{31}) = 2 + \sin(x_{31}^2)$ ,  $h_{32}(\bar{x}_{32}) = -0.5x_{31}x_{32}$ , and  $\ell_{32}(\bar{x}_{32}) = -[2 + \cos(x_{31}x_{32})]$  are the unknown continuous functions and  $d_{11}(t) = d_{21}(t) = -0.01 \sin(t)$ ,  $d_{12}(t) = d_{22}(t) = 0.02 \cos(t)$ ,  $d_{31}(t) = -0.02 \cos(t)$ , and  $d_{32}(t) = 0.01 \sin(t)$  are the unknown disturbances. The leader's output is given by  $y_0(t) = 0.4 \sin(t)$ . It is easy to verify that the conditions in Assumptions 1–3 are all satisfied. Figure 1 depicts the communication digraph of the leader and the 3 followers.

In simulation, RBFNNs  $\varrho_{i,1} T \vartheta_{i,1}(\zeta_{i,1})$  and  $\varrho_{i,2} T \vartheta_{i,2}(\zeta_{i,2})$ , which contain 11 neurons with centers spaced evenly in  $[-1, 1]$  and widths being equal to  $w_1 = 0.5$  and  $w_2 = 5$ , respectively, are used to approximate the unknown continuous functions  $h_{i1}(x_{i1})$  and  $h_{i2}(\bar{x}_{i2})$ ,  $i = 1, 2, 3$ . The initial conditions are chosen as

$$\begin{aligned} & [x_{11}(0), x_{12}(0), x_{21}(0), x_{22}(0), x_{31}(0), x_{32}(0)]^T \\ & = [0.3, 0.01, 0.2, 0.01, 0.1, 0.01]^T, \\ & v^* = 5, \\ & \alpha_{i,1} = 20, \\ & \alpha_{i,2} = 10, \\ & \Lambda_{i,j} = 0.1I, \\ & \tau_{i,j} = 0.01, \\ & \beta_{i,j} = 0.01, \\ & \kappa_{i,j}(0) = 0, \\ & \hat{Q}_{i,j}(0) = 0, \\ & i = 1, 2, 3; j = 1, 2. \end{aligned} \quad (61)$$

Figures 2–4 display the evolution of the output trajectories of the 3 followers and the leader, the corresponding output consensus errors, and the actual controllers  $v_i$ , respectively. One can see that the outputs of the 3 followers can track the leader's output since the output consensus error converges to a small neighborhood of zero. Additionally, it can be seen that there exist large differences between  $v_i$  and the saturation level constant  $v^*$ , which indicates the significant saturation effect. The simulation results illustrate that the proposed control algorithm is effective.

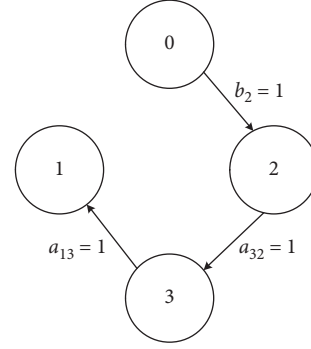


FIGURE 1: Communication graph, where 0 denotes the leader and 1–3 denote the 3 followers, respectively.

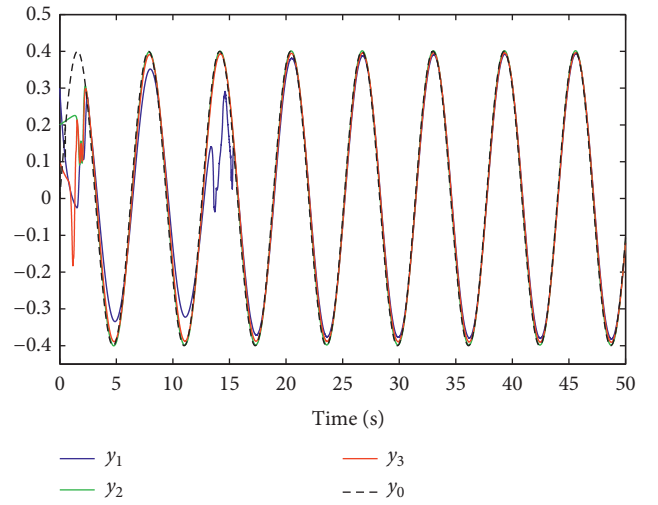


FIGURE 2: Evolution of the output trajectories.

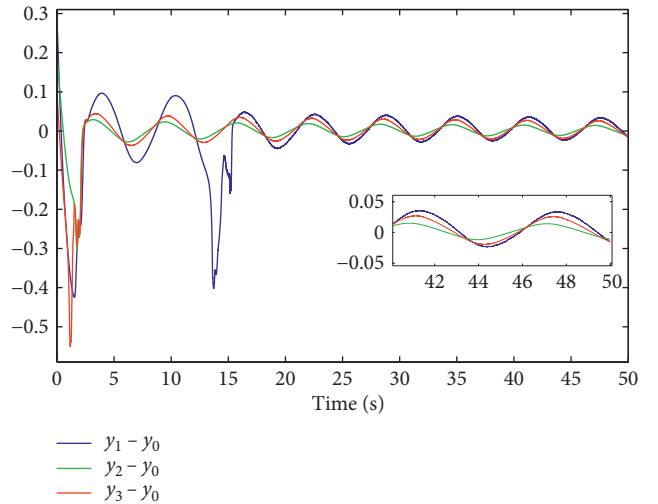


FIGURE 3: Evolution of the output consensus errors.

*Remark 3.* The reason that why there exist large fluctuations in the output trajectories of  $y_i$  lies in the large fluctuations of the actual controllers  $v_i$  (see Figure 4). Because the Nussbaum gain function  $N(\kappa_{i,2}) = \kappa_{i,2}^2 \cos((\pi/2)\kappa_{i,2})$  will be very

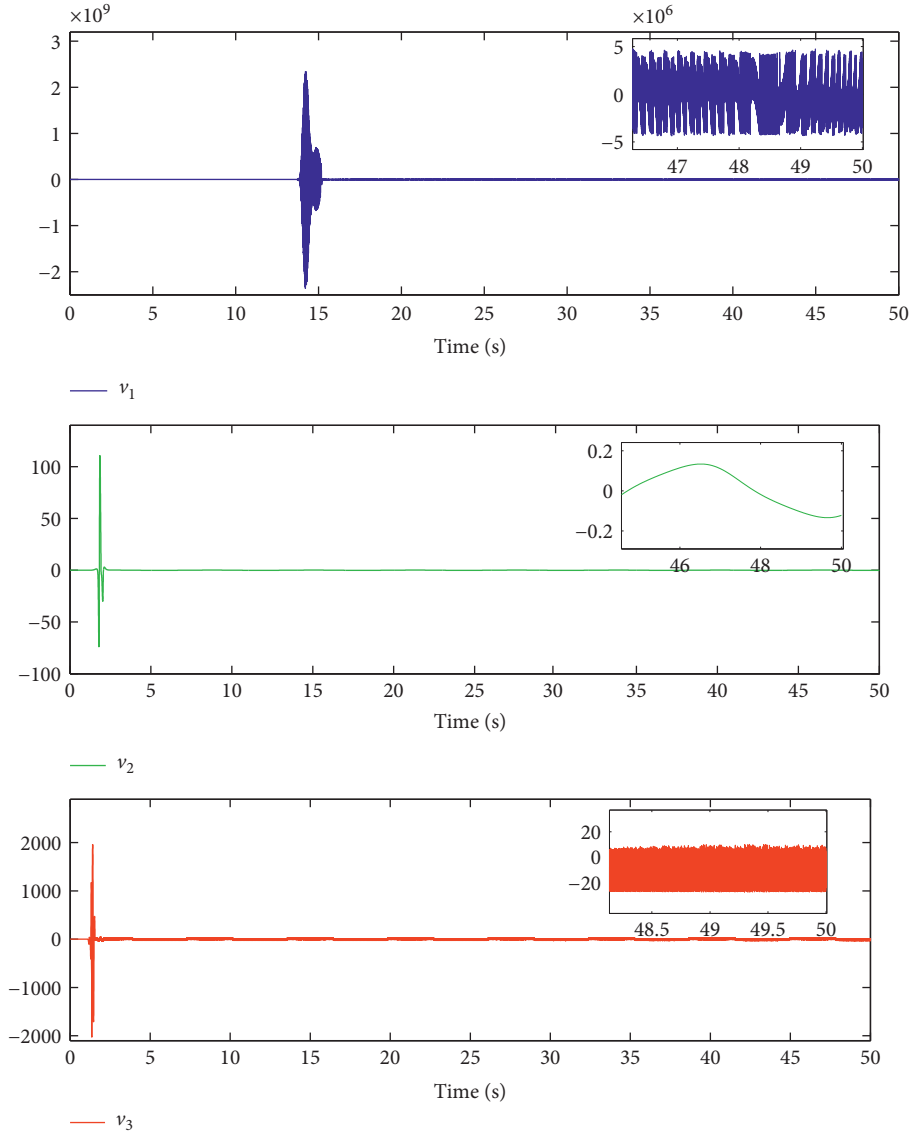


FIGURE 4: Evolution of the actual controllers  $v_i$ .

large (positively or negatively) if  $\kappa_{i,2}$  becomes very large, correspondingly the actual controllers  $v_i$  will be very large according to equation (40). To reduce the values of  $\kappa_{i,2}$ , the design parameters  $\alpha_{i,2}$  should be turned smaller. However, from the proof of Theorem 1, we know that smaller  $\alpha_{i,2}$  may lead to a smaller value of  $\delta$  and thereby causes a larger output consensus error (see equation (59)). In a word, there is a tradeoff between smaller output consensus errors and smooth output trajectories. This is another problem worthy to explore, which may be our future work.

## 6. Conclusion

In this paper, an output consensus scheme for a class of high-order affine nonlinear MAS with unknown control gains and input saturation under a directed communication graph is proposed. Combining the adaptive RBFNN approximation and the DSC methodology, consensus control laws are developed to

guarantee the semiglobal uniform ultimate boundedness for all signals in the closed-loop system. Moreover, the output consensus error can converge to a small region around the origin provided that the design parameters are appropriately selected. The effectiveness of the proposed control algorithm is revealed by a numerical simulation.

## Data Availability

No data were used to support this study.

## Conflicts of Interest

The authors declare that they have no conflicts of interest.

## Acknowledgments

This research was partially supported by the National Natural Science Foundation of China (Grant nos. 61703175

and 11626111), the Natural Science Foundation of Huizhou University (Grant no. hzu201806), the Natural Science Foundation of Jiangsu Province, China (Grant no. BK20171019), and the Research Fund for the Doctoral Program of Huizhou University (Grant no. 2015JB020).

## References

- [1] H. Zhang, Z. Chen, and M. Fan, "Collaborative control of multivehicle systems in diverse motion patterns," *IEEE Transactions on Control Systems Technology*, vol. 24, no. 4, pp. 1488–1494, 2016.
- [2] T. Han, M. Chi, Z.-H. Guan, B. Hu, J.-W. Xiao, and Y. Huang, "Distributed three-dimensional formation containment control of multiple unmanned aerial vehicle systems," *Asian Journal of Control*, vol. 19, no. 3, pp. 1103–1113, 2017.
- [3] B. Liu, H. Zhang, H. Meng, D. Fu, and H. Su, "Scanning-chain formation control for multiple unmanned surface vessels to pass through water channels," *IEEE Transactions on Cybernetics*, 2020.
- [4] Y. Zhang and Y.-P. Tian, "A fully distributed weight design approach to consensus kalman filtering for sensor networks," *Automatica*, vol. 104, pp. 34–40, 2019.
- [5] G. Wen, X. Yu, Z. W. Liu, and W. Yu, "Adaptive consensus-based robust strategy for economic dispatch of smart grids subject to communication uncertainties," *IEEE Transactions on Industrial Informatics*, vol. 14, no. 6, pp. 2484–2496, 2018.
- [6] H. Zhang, M. Fan, Y. Wu et al., "Ultrafast synchronization via local observation," *New Journal of Physics*, vol. 21, no. 1, Article ID 013040, 2019.
- [7] D. Chen, M. Kang, and W. Yu, "Probabilistic causal inference for coordinated movement of pigeon flocks," *EPL*, vol. 130, p. 28004, 2020.
- [8] D. Chen, W. Li, X. Li, W. Yu, and Y. Sun, "Effects of measurement noise on flocking dynamics of cucker-smale systems," *IEEE Transactions on Circuits and Systems II: Express Briefs*, 2019.
- [9] X. Xu, L. Liu, and G. Feng, "Consensus of single integrator multi-agent systems with directed topology and communication delays," *Control Theory and Technology*, vol. 14, no. 1, pp. 21–27, 2016.
- [10] W. Ren, "On consensus algorithms for double-integrator dynamics," *IEEE Transactions on Automatic Control*, vol. 53, no. 6, pp. 1503–1509, 2008.
- [11] G. Wen, H.-T. Zhang, W. Yu, Z. Zuo, and Y. Zhao, "Coordination tracking of multi-agent dynamical systems with general linear node dynamics," *International Journal of Robust and Nonlinear Control*, vol. 27, no. 9, pp. 1526–1546, 2017.
- [12] X. Wang, H. Su, M. Z. Q. Chen, X. F. Wang, and G. Chen, "Reaching non-negative edge consensus of networked dynamical systems," *IEEE Transactions on Cybernetics*, vol. 48, no. 9, pp. 2712–2722, 2018.
- [13] H. Ji, H. Zhang, Z. Ye, H. Zhang, B. Xu, and G. Chen, "Stochastic consensus control of second-order nonlinear multiagent systems with external disturbances," *IEEE Transactions on Control of Network Systems*, vol. 5, no. 4, pp. 1585–1596, 2018.
- [14] M. Fan, Z. Chen, and H.-T. Zhang, "Semi-global consensus of nonlinear second-order multi-agent systems with measurement output feedback," *IEEE Transactions on Automatic Control*, vol. 59, no. 8, pp. 2222–2227, 2014.
- [15] W. Qin, Z.-X. Liu, and Z. Chen, "Observer-based consensus for nonlinear multi-agent systems with intermittent communication," *Neurocomputing*, vol. 154, pp. 230–238, 2015.
- [16] H. Meng, Z. Chen, L. Zhu, and R. Middleton, "Consensus of a class of second-order nonlinear heterogeneous multi-agent systems with uncertainty and communication delay," *International Journal of Robust and Nonlinear Control*, vol. 26, no. 15, pp. 3311–3329, 2016.
- [17] X. Yin, H. Su, and D. Yue, "Consensus of fractional-order heterogeneous multi-agent systems," *IET Control Theory & Applications*, vol. 7, no. 2, pp. 314–322, 2013.
- [18] L. Chen, Y. W. Wang, W. Yang, and J. W. Xiao, "Robust consensus of fractional-order multi-agent systems with input saturation and external disturbances," *Neurocomputing*, vol. 303, pp. 11–19, 2018.
- [19] Y. Xie and Z. Lin, "Global optimal consensus for higher-order multi-agent systems with bounded controls," *Automatica*, vol. 99, pp. 301–307, 2019.
- [20] C. C. Hua, K. Li, and X. P. Guan, "Leader-following output consensus for high-order nonlinear multiagent systems," *IEEE Transactions on Automatic Control*, vol. 64, no. 3, pp. 1156–1161, 2019.
- [21] J. Peng and X. Ye, "Cooperative control of multiple heterogeneous agents with unknown high-frequency-gain signs," *Systems & Control Letters*, vol. 68, pp. 51–56, 2014.
- [22] M. Radenkovic and M. Tadi, "Multi-agent adaptive consensus of networked systems on directed graphs," *International Journal of Adaptive Control and Signal Processing*, vol. 30, no. 1, pp. 46–59, 2016.
- [23] W. Chen, X. Li, W. Ren, and C. Chen, "Adaptive consensus of multi-agent systems with unknown identical control directions based on a novel nussbaum-type function," *IEEE Transactions on Automatic Control*, vol. 59, no. 7, pp. 1887–1892, 2014.
- [24] Q. Ma, "Cooperative control of multi-agent systems with unknown control directions," *Applied Mathematics and Computation*, vol. 292, pp. 240–252, 2017.
- [25] J. Huang, Y. Song, W. Wang, C. Wen, and G. Li, "Fully distributed adaptive consensus control of a class of high-order nonlinear systems with a directed topology and unknown control directions," *IEEE Transactions on Cybernetics*, vol. 48, no. 8, pp. 2349–2356, 2018.
- [26] C. Chen, C. Wen, Z. Liu, K. Xie, Y. Zhang, and C. P. Chen, "Adaptive consensus of nonlinear multi-agent systems with non-identical partially unknown control directions and bounded modelling errors," *IEEE Transactions on Automatic Control*, vol. 62, no. 9, pp. 4654–4659, 2016.
- [27] M. Fan, H.-T. Zhang, and Z. Lin, "Distributed semiglobal consensus with relative output feedback and input saturation under directed switching networks," *IEEE Transactions on Circuits and Systems II: Express Briefs*, vol. 62, no. 8, pp. 796–800, 2015.
- [28] M. Fan and M. Wang, "Second-order consensus for a class of uncertain multi-agent systems subject to input saturation," *Transactions of the Institute of Measurement and Control*, vol. 41, no. 7, pp. 1957–1964, 2019.
- [29] X. Wang, H. Su, M. Z. Q. Chen, and X. F. Wang, "Observer-based robust coordinated control of multiagent systems with input saturation," *IEEE Transactions on Neural Networks and Learning Systems*, vol. 29, no. 5, pp. 1933–1946, 2018.
- [30] X. Liu, J.-W. Xiao, D. Chen, and Y.-W. Wang, "Dynamic consensus of nonlinear time-delay multi-agent systems with input saturation: an impulsive control algorithm," *Nonlinear Dynamics*, vol. 97, no. 2, pp. 1699–1710, 2019.

- [31] D. Chen, T. Lu, X. Liu, and W. Yu, "Finite-time consensus of multiagent systems with input saturation and disturbance," *International Journal of Robust and Nonlinear Control*, 2020.
- [32] H. Zhang and F. L. Lewis, "Adaptive cooperative tracking control of higher-order nonlinear systems with unknown dynamics," *Automatica*, vol. 48, no. 7, pp. 1432–1439, 2012.
- [33] G. Wang, "Distributed control of higher-order nonlinear multi-agent systems with unknown non-identical control directions under general directed graphs," *Automatica*, vol. 110, Article ID 108559, 2019.
- [34] M. Shahriari-kahkeshi and M. Taj, "Distributed adaptive consensus tracking control for uncertain non-linear multi-agent systems with input saturation," *IET Control Theory & Applications*, vol. 14, no. 13, pp. 2153–2162, 2019.
- [35] W. Wang, D. Wang, Z. Peng, and H. Wang, "Cooperative adaptive fuzzy output feedback control for synchronization of nonlinear multi-agent systems in the presence of input saturation," *Asian Journal of Control*, vol. 18, no. 2, pp. 619–630, 2016.
- [36] M. Fan and Y. Wu, "Global leader-following consensus of nonlinear multi-agent systems with unknown control directions and unknown external disturbances," *Applied Mathematics and Computation*, vol. 331, pp. 274–286, 2018.
- [37] M. Krstic, I. Kanellakopoulos, and P. Kokotovic, *Nonlinear and Adaptive Control Design*, Wiley-Interscience, Hoboken, NJ, USA, 1995.
- [38] Z. Zheng, C. Jin, M. Zhu, and K. Sun, "Trajectory tracking control for a marine surface vessel with asymmetric saturation actuators," *Robotics and Autonomous Systems*, vol. 97, pp. 83–91, 2017.
- [39] X. Ye and J. Jiang, "Adaptive nonlinear design without a priori knowledge of control directions," *IEEE Transactions on Automatic Control*, vol. 43, no. 11, pp. 1617–1621, 1998.
- [40] S. S. Ge, F. Hong, and T. H. Lee, "Adaptive neural control of nonlinear time-delay systems with unknown virtual control coefficients," *IEEE Transactions on Systems, Man and Cybernetics, Part B (Cybernetics)*, vol. 34, no. 1, pp. 499–516, 2004.
- [41] J. J. E. Slotine and W. Li, *Applied Nonlinear Control*, Prentice-Hall, Upper Saddle River, NJ, USA, 1991.
- [42] D. Wang and J. Huang, "Neural network-based adaptive dynamic surface control for a class of uncertain nonlinear systems in strict-feedback form," *IEEE Transactions on Neural Networks*, vol. 16, no. 1, pp. 195–202, 2005.

## Research Article

# A Hybrid Event Trigger Mechanism and Time-Delay Partitioning Are Applied to Event-Driven Control Systems

WanRu Wang <sup>1,2</sup>, LianKun Sun,<sup>1,2</sup> and BinBin Shen<sup>1</sup>

<sup>1</sup>School of Computer Science and Technology Engineering, Tiangong University, Tianjin 300387, China

<sup>2</sup>Tianjin Key Laboratory of Autonomous Intelligence Technology and Systems, Tianjin 300387, China

Correspondence should be addressed to WanRu Wang; [tjpuwrr@126.com](mailto:tjpuwrr@126.com)

Received 8 April 2020; Accepted 22 June 2020; Published 1 August 2020

Guest Editor: Sahar Yazdani

Copyright © 2020 WanRu Wang et al. This is an open access article distributed under the Creative Commons Attribution License, which permits unrestricted use, distribution, and reproduction in any medium, provided the original work is properly cited.

This paper proposes an idea of using time-delay partitioning to construct a Lyapunov–Krasovskii functional (LKF) to analyse event-driven network control systems (NCSs) with the  $H_\infty$  performance. Firstly, select a mixed event-driven mechanism, in which an adjustable absolute trigger mechanism is added to the trigger condition. Trigger term can be indicated to use a delay model. Secondly, a suitable LKF is created, which makes use of time-delay partitioning. Based on Wirtinger inequality and linear matrix inequalities (LMI), the close system with  $H_\infty$  performance index level is global uniform ultimate bounded. Finally, a numerical simulation example proves the effectiveness of the proposed method.

## 1. Introduction

With the rapid development of computer and networked technologies, data transmission via communication networks has received considerable research attentions [1–10]. Due to the advantages of the NCSs such as data sharing, low cost, and easy maintenance, it has been widely used in the field of process control, electricity system, aircraft control systems, automobile controlling systems, etc. The traditional control system is based on time-driven, but for the NCSs with limited resources, if the control tasks are executed periodically based on fixed time points, this not only wastes limited computing and bandwidth resources but also may cause network-induced phenomena such as network congestion, data transmission delay, and data loss. As a non-uniform scheduling mechanism, event-driven can effectively solve the abovementioned problems, so it has become a hot research topic at present.

In event-driven control, only when the system reaches the trigger threshold set in advance can the control instruction be executed or the information be transmitted. Therefore, event-driven control can achieve similar or better control performance and reduce data transmission rate, thus saving the limited network bandwidth, computation, energy,

and other resources in the system. As such, fruitful results based on different event-driven schemes are made in [11–20]. The triggering threshold has a great effect on the implementation of control task [11, 12]; however, because the threshold of the static triggering mechanism is fixed, it is difficult to adjust for external interference and environmental changes. In order to overcome the above drawbacks, a dynamic event-triggered scheme has been addressed in [13–15]. Besides that, a  $H_\infty$  controller is designed in [21], in which Markov jump systems are studied based on event-triggered considering finite time. Rahnama et al. [22] consider the effects of network-induced time delays, signal quantization, and data loss and show L-2-stability and robustness for the control design. Gu et al. [23] consider an adaptive  $H_\infty$  filter, which is based on event triggered to solve the problem of decentralize in NCSs. Furthermore, in [24], observer-based fuzzy controller is proposed to stabilize the NCSs under event-triggered mechanism in [25]; the stabilization problem for nonlinear NCSs with a two-terminal event-triggered mechanism is concerned. It is worth noting that the LKF method is mainly used in the above research, which will bring certain conservativeness to the conclusion due to the different treatment methods for cross items.

In order to reduce the conservativeness of the conclusion, the investigators bring forward two different research directions. One way is to choose a suitable LKF, and the other is to select a better scaling method in the process of dealing with the integral terms. Rich investigative achievements have been achieved by LKF picking [26–30]. In the early years, a simple LKF for fixed-delay systems was adopted. In order to make the LKF contain more system information, fixed time delay and variable delay are added to the system status in LKF [26]. Come up with the opinion of using time-delay partitioning to establish LKF [27]. More explore consequences have been generated in dealing with integral items. Use Jensen inequality to process integral items in event-driven NCSs [31]. Seuret and Gouaisbaut [32] put forward cinequality to deal with the integral terms in the study of NCSs stability, which can introduce additional system integral terms to bring more system information. This method not only includes the information in the Jensen inequality but also adds some integral terms of the state to the system.

Motivated by the above discussions, in this paper, we focus on the  $H_\infty$  performance analysis of network control system based on event trigger mechanism. The main contributions of this paper are summarized as follows. (i) Using mixed trigger mechanism to reduce network burden, that is, an adjustable parameter is added on the basis of the dynamic trigger mechanism, so as to avoid Zeno phenomenon and long-term nonsampling phenomenon. (ii) The LKF is constructed with the idea of time-delay partitioning, and a new method is used to remove the coupling between the input matrix and the output matrix. On this basis, Wirtinger inequality is used to scale down and reduce the conservativeness of the conclusion.

*1.1. Notation.* In this paper,  $Y > 0$  ( $Y < 0$ ) denotes that the symmetric matrix  $Y$  is positive (or negative).  $\mathbb{R}^n$  is defined as  $n$ -dimensional Euclidean space.  $\mathbb{R}^{n \times m}$  is defined as a set of  $n \times m$  real matrix,  $X^T$  refers to the transpose of  $X$ ,  $*$  denotes a symmetric term of a symmetric matrix, and  $\|\cdot\|$  refers to the Euclidean norm. Followed by  $M + M^T$ , which is defined as  $\text{He}(M)$ .  $I_n$  refers to the  $n$ -dimensional unit matrix;  $0_{n \times m}$  refers to the  $n \times m$  dimension block matrix. The rest of the paper is adapted to the needs of the text of the adaptive dimension matrix.

## 2. Problem Formulation

Consider the following kind of linear time invariant system as follows:

$$\begin{cases} \dot{x}(t) = Ax(t) + B_1u(t) + C_1\omega(t), \\ z(t) = D_1x(t) + B_2u(t) + C_2\omega(t), \\ y(t) = D_2x(t), \end{cases} \quad (1)$$

where  $x(t) \in \mathbb{R}^m$  is the state vector,  $u(t) \in \mathbb{R}^n$  is the control input,  $y(t) \in \mathbb{R}^p$  is the control output,  $z(t) \in \mathbb{R}^q$  is the control regulated output,  $\omega(t) \in L_2[0, \infty]$  is the square integrable disturbance input,  $A, B_1, B_2, C_1, C_2, D_1$ , and  $D_2$

are any matrices with adaptive dimensions. The event-triggered communication mechanism can be described by

$$\begin{aligned} t_{k+1}h &= t_kh + \min_l \{ |lh| \{ e^T(i_kh)\Phi e(i_kh) \\ &\geq \delta y^T(t_kh)\Phi y(t_kh) + \vartheta(t) \} \}, \end{aligned} \quad (2)$$

where  $\vartheta(t) = \beta e^{-\alpha t}$ ,  $e(i_kh) = y(i_kh) - y(t_kh)$  is the error between the output at the current sampling time  $i_kh = t_kh + lh$  ( $l \in \mathbb{N}$ ) and the output at the latest triggered time  $t_kh$ ;  $\Phi$  is a symmetric positive matrix;  $h$  is the time sampling period; and  $\delta \in [0, 0.5]$  and  $\beta \in [0, 0.5]$  are given scalar. If  $\delta = 0$ , the system trigger threshold is the absolute trigger mechanism. If  $\beta = 0$ , the system trigger threshold is the relative trigger mechanism. If  $\delta > 0$  and  $\beta > 0$ , the system trigger threshold is the mixed trigger mechanism.

Divide  $\Omega$  into subsets  $\Omega_1 = [i_kh + d_{i_k}, i_kh + h + d_{i_{k+1}})$ , i.e.,  $\Omega = \cup \Omega_1$ , where  $i_kh = t_kh + lh$ ,  $l = 0, \dots, t_{k+1} - t_k - 1$ ;  $i_kh$  and  $t_kh$  represent the current sampling time and triggering time, respectively. For  $l = t_{k+1} - t_k - 1$ , then  $d_{i_{k+1}} = d_{i_{k+1}}$ ; otherwise,  $d_{i_k} = d_{t_k}$ . Define  $d(t) \triangleq t - i_kh$ . Note that  $h_1 \leq d(t) \leq h_2$ ,  $h_1 = d_m$ ,  $h_2 = d_M$ , and  $h_m = (h_1 + h_2)/2$ .  $h_1$  and  $h_2$  represent the lower and upper bounds of the time delay ( $h_1 < h_m < h_2$ ):

$$\begin{cases} \dot{x}(t) = Ax(t) + B_1KD_2x(t - d(t)) - B_1Ke(i_kh) + C_1\omega(t), \\ z(t) = D_1x(t) + B_2KD_2x(t - d(t)) - B_2Ke(i_kh) + C_2\omega(t), \\ u(t) = Kx(t_kh), \quad t \in \Omega, \end{cases} \quad (3)$$

where  $u(t)$  is the controller law and control gain  $K$ .

**Lemma 1** (see [12]). *Given matrices  $D, E(t)$ , and  $F$  of appropriate dimensions with  $E(t)$  satisfying  $E^T(t)E(t) \leq I$ , for any  $\varepsilon > 0$ , the following inequality holds:*

$$DE(t)F + F^TE^T(t)D^T \leq \varepsilon DD^T + \varepsilon^{-1}F^TF. \quad (4)$$

**Lemma 2** (see [12]). *The following two inequalities are equivalent:*

(a) *There exists a symmetric and positive-definite matrix  $P$  satisfying*

$$\begin{bmatrix} -P & A^T \\ A & -P^{-1} \end{bmatrix} < 0. \quad (5)$$

(b) *There exists a symmetric and positive-definite matrix  $P$  and matrix  $Y$  satisfying*

$$\begin{bmatrix} -P & (YA)^T \\ YA & \text{He}(-Y) + P \end{bmatrix} < 0. \quad (6)$$

**Lemma 3** (see [12]). *For a given matrix  $R > 0$ , the following inequality holds for all continuously differentiable function  $w$  in  $[a, b] \rightarrow \mathbb{R}^p$ :*

$$\int_a^b \omega^T(u)R\omega(u)du \geq \frac{1}{b-a} ((\omega(b) - \omega(a))^T R (\omega(b) - \omega(a))) + \frac{3}{b-a} \mathfrak{S}^T R \mathfrak{S}, \tag{7}$$

where  $\mathfrak{S} = \omega(b) + \omega(a) - 2/b - a \int_a^b \omega(u) du$ .

### 3. Main Results

*Definition 1* (see [33]). The state  $x(t)$  of the continuous-time system is GUUB, if for every  $x(0) \in \mathbb{R}^n$ , there exists a positive constant  $\varepsilon$  and a time  $\bar{t}$  satisfying  $x(t) \in \{x : \|x\| \leq \varepsilon\}, \forall t \geq \bar{t}$ . Moreover, the continuous-time system is ultimately bounded or stable if its state  $x(t)$  is GUUB

The objective of this section is to explore system (3) meeting the following requirements:

- (i) System (3) is globally uniformly ultimately bounded (GUUB) stability and eventually exponentially converges to the bounded region by LMI.

- (ii) System (3) guarantees, under zero-initial conditions,  $\|z(t)\| < \gamma \|\omega(t)\|_2$  for all nonzero  $\omega \in L_2[0, \infty)$  and a given proper positive constant scalar  $\gamma$ .

**Theorem 1.** Consider the closed-loop system (3) and parameters driving mechanism (2) with  $\delta, \beta, h_1 > 0, h_2 > 0, h_m > 0$ . Given a scalar  $\gamma > 0$ , the close system (2) meets  $H_\infty$  application if there exist matrices  $P > 0, H_1 > 0, H_2 > 0, H_3 > 0, \Phi > 0, R_1 > 0, R_2 > 0, R_3 > 0, J$  and  $U_i (i = 1, 2, 3, 4)$ , matrices  $Z$  and  $S$ , with appropriate dimensions such that

$$\begin{bmatrix} \Gamma_{11} + J & \Gamma_{12} & 0 & 0 \\ * & \Gamma_{22} & \Gamma_{23} & 0 \\ * & * & He(-B_1^T B_1 Z) & \Gamma_{34} \\ * & * & * & -J \end{bmatrix} < 0, \tag{8}$$

where

$$\begin{aligned} \Gamma_{11} &= \begin{bmatrix} W_{11} & h_1(R_1 A)^T & a_2(R_2 A)^T & a_3(R_3 A)^T & D_1^T & 6R_1 & 0 & 0 & 0 \\ * & -R_1 & 0 & 0 & 0 & 0 & 0 & 0 & 0 \\ * & * & -R_2 & 0 & 0 & 0 & 0 & 0 & 0 \\ * & * & * & -R_3 & 0 & 0 & 0 & 0 & 0 \\ * & * & * & * & -I & 0 & 0 & 0 & 0 \\ * & * & * & * & * & -12R_1 & 0 & 0 & 0 \\ * & * & * & * & * & * & -12R_2 & 0 & 0 \\ * & * & * & * & * & * & * & -12R_2 & 0 \\ * & * & * & * & * & * & * & * & -12R_3 \end{bmatrix}, \\ \Gamma_{12} &= \begin{bmatrix} -B_1 S & PC_1 & B_1 S D_2 & -2R_1 & 0 & 0 \\ -h_1 B_1 S & h_1 R_1 C_1 & h_1 B_1 S D_2 & 0 & 0 & 0 \\ -a_2 B_1 S & a_2 R_2 C_1 & a_2 B_1 S D_2 & 0 & 0 & 0 \\ -a_3 B_1 S & a_3 R_3 C_1 & a_3 B_1 S D_2 & 0 & 0 & 0 \\ -B_2 S & C_2 & B_2 S D_2 & 0 & 0 & 0 \\ 0 & 0 & 0 & 6R_1^T & 0 & 0 \\ 0 & 0 & -F_{27}^T & 6R_2^T & -F_{47}^T & 0 \\ 0 & 0 & -F_{28}^T & -F_{38}^T & 6R_2^T & 0 \\ 0 & 0 & 0 & 0 & 6R_3^T & 6R_3^T \end{bmatrix}, \\ \Gamma_{22} &= \begin{bmatrix} (\delta - 1)\Phi & 0 & -\delta \Phi D_2 & 0 & 0 & 0 \\ * & -\gamma^2 I & 0 & 0 & 0 & 0 \\ * & * & W_{22} & -F_{23} & -F_{24} & 0 \\ * & * & * & W_{33} & -F_{34} & 0 \\ * & * & * & * & W_{44} & -2R_3 \\ * & * & * & * & * & W_{55} \end{bmatrix}, \\ \Gamma_{23} &= \begin{bmatrix} -(B_1^T B_1 S)^T \\ 0 \\ (B_1^T B_1 S D_2)^T \\ 0 \\ 0 \\ 0 \end{bmatrix}, \end{aligned} \tag{9}$$

$$\begin{aligned}
\Gamma_{34} &= \left[ (PB_1 - B_1Z)^T \quad h_1(R_1B_1 - B_1Z)^T \quad a_2(R_2B_1 - B_1Z)^T \quad a_3(R_3B_1 - B_1Z)^T \quad (B_2 - B_2Z)^T \quad 0 \quad 0 \quad 0 \quad 0 \right], \\
\eta^T(t) &= \left[ x^T(t) \quad x^T(t-d(t)) \quad x^T(t-h_1) \quad x^T(t-h_m) \quad x^T(t-h_2) \quad Q_1 \quad Q_2 \quad Q_3 \quad Q_4 \quad e^T(i_k h) \quad \omega^T(t) \right], \\
Q_1 &= \frac{1}{h_1} \int_{t-h_1}^t x^T(s) ds, \\
Q_2 &= \frac{1}{h_1-d(t)} \int_{t-d(t)}^{t-h_1} x^T(s) ds, \\
Q_3 &= \frac{1}{h_m-d(t)} \int_{t-h_m}^{t-d(t)} x^T(s) ds, \\
Q_4 &= \frac{1}{h_2-h_m} \int_{t-h_2}^{t-h_m} x^T(s) ds, \\
W_{11} &= H_1 + H_2 + H_3 + \text{He}(PA) - 4R_1, \\
W_{22} &= \delta D_2^T V D_2 - 8R_2 - \text{He}(-U_1 - U_2 + U_3 + U_4), \\
W_{33} &= -H_1 - 4R_1 - 4R_2, \\
W_{44} &= -H_2 - 4R_2, \\
W_{55} &= -H_3 - 4R_3, \\
F_{23} &= 2R_2 + U_1^T + U_2^T + U_3^T + U_4^T, \\
F_{24} &= 2R_2 + U_1 - U_2 - U_3 + U_4, \\
F_{27} &= -6R_2 - 2(U_3^T + U_4^T), \\
F_{34} &= -U_1 + U_2 - U_3 + U_4, \\
F_{38} &= -2(U_2 + U_4), \\
F_{47} &= 2(U_3^T - U_4^T).
\end{aligned} \tag{10}$$

Then, the closed-loop system (3) based on the mixed event trigger mechanism (2) achieves GUUB. When  $t \rightarrow \infty$ , the system state  $\xi(t)$  exponentially converges to the bounded area:

$$\bar{\mathfrak{B}} = \begin{cases} x(t) \in \left\{ x : \|x(t)\| \leq \sqrt{\frac{\beta}{\delta \lambda_{\min}(P)}} \right\}, & \beta > 0, \quad \alpha = 0, \\ 0, & \text{otherwise.} \end{cases} \tag{11}$$

*Proof.* Using the delay partitioning method to construct a suitable LKF for the paper,

$$\begin{aligned}
V(t) &= x^T(t)Px(t) + \int_{t-h_1}^t x^T(s)H_1x(s)ds + \int_{t-h_m}^t x^T(s)H_2x(s)ds + \int_{t-h_2}^t x^T(s)H_3x(s)ds \\
&\quad + h_1 \int_{-h_1}^0 \int_{t+s}^t \dot{x}^T(v)R_1\dot{x}(v)dv ds + a_2 \int_{-h_m}^{-h_1} \int_{t+s}^t \dot{x}^T(v)R_2\dot{x}(v)dv ds \\
&\quad + a_3 \int_{-h_2}^{-h_m} \int_{t+s}^t \dot{x}^T(v)R_3\dot{x}(v)dv ds,
\end{aligned} \tag{12}$$

where  $a_2 = d(t) - h_1$  and  $a_3 = h_m - d(t)$ .

Taking the time derivative of (12) yields



$$\begin{aligned} \dot{V}(t) &= 2x^T(t)Px(t) + x^T(t)(H_1 + H_2 + H_3)\dot{x}(t) - x^T(t - h_1)H_1x(t - h_1) - x^T(t - h_m)H_2x(t - h_m), \\ &\quad - x^T(t - h_2)H_3x(t - h_2) + h_1^2\dot{x}^T(t)R_1\dot{x}(t) + a_2^2\dot{x}^T(t)R_2\dot{x}(t) + a_3^2\dot{x}^T(t)R_3\dot{x}(t), \\ &\quad - h_1 \int_{t-h_1}^t \dot{x}^T(s)R\dot{x}(s) ds - a_2 \int_{t-h_m}^{t-h_1} \dot{x}^T(s)R\dot{x}(s) ds - a_3 \int_{t-h_2}^{t-h_m} \dot{x}^T(s)R\dot{x}(s) ds + \rho^T(i_k h)\Phi\rho(i_k h) \\ &\quad - \rho^T(i_k h)\Phi\rho(i_k h) + \gamma^2 I\omega^T(t)\omega(t) - \gamma^2 I\omega^T(t)\omega(t) - z^T(t)z(t) + z^T(t)z(t), \\ &\leq \eta^T(t) \left( \Xi_1 - \Xi_2 - \Xi_3 + \bar{\Omega}^T R^{-1} \bar{\Omega} + \zeta^T \varsigma \right) \eta(t) - z^T(t)z(t) + \gamma^2 I\omega^T(t)\omega(t) + \vartheta(t). \end{aligned} \tag{13}$$

$d(t) \in [h_1, h_2]$  can be divided into  $d(t) \in [h_1, h_m]$  and  $d(t) \in [h_m, h_2]$ . We only discuss  $d(t) \in [h_1, h_m]$  in this paper. The process of  $d(t) \in [h_m, h_2]$  is similar to that of  $h_2$  and  $d(t) \in [h_1, h_m]$ . Based on Lemma 3,

$-(h_m - h_1) \int_{t-h_m}^{t-h_1} \dot{x}^T(s)R_2\dot{x}(s) ds$  can be transformed as follows:

$$\begin{aligned} -(h_m - h_1) \int_{t-h_m}^{t-h_1} \dot{x}^T(s)R_2\dot{x}(s) ds &= -(h_m - h_1) \int_{t-d(t)}^{t-h_1} \dot{x}^T(s)R_2\dot{x}(s) ds - (h_m - h_1) \int_{t-h_m}^{t-d(t)} \dot{x}^T(s)R_2\dot{x}(s) ds \\ &\leq -\frac{(h_m - h_1)}{d(t) - h_1} \eta^T(t) \begin{bmatrix} e_1^T & e_2^T \end{bmatrix} \begin{bmatrix} R_2 & 0 \\ 0 & 3R_2 \end{bmatrix} \begin{bmatrix} e_1 \\ e_2 \end{bmatrix} \eta(t) \\ &\quad - \frac{(h_m - h_1)}{h_m - d(t)} \eta^T(t) \begin{bmatrix} e_3^T & e_4^T \end{bmatrix} \begin{bmatrix} R_2 & 0 \\ 0 & 3R_2 \end{bmatrix} \begin{bmatrix} e_3 \\ e_4 \end{bmatrix} \eta(t) \leq -\eta^T(t)\Xi_2\eta(t). \end{aligned} \tag{14}$$

According to Lemma 3, the integral term  $-(h_1) \int_{t-h_1}^t \dot{x}^T(s)R_1\dot{x}(s) ds$  and  $-(h_2 - h_m) \int_{t-h_2}^{t-h_m} \dot{x}^T(s)R_3\dot{x}(s) ds$  can be transformed as follows:

$$\begin{aligned} -h_1 \int_{t-h_1}^t \dot{x}^T(s)R_1\dot{x}(s) ds &\leq 4x^T(t)R_1x(t) + 4x^T(t - h_1)R_1x(t) + 2x^T(t)R_1x(t - h_1) + 2x^T(t - h_1)R_1x(t) \\ &\quad - \frac{6}{h_1} x^T(t)R_1 \int_{t-h_1}^t \dot{x}(s) ds - \frac{6}{h_1} \int_{t-h_1}^t \dot{x}^T(s) ds R_1x(t) - \frac{6}{h_1} x^T(t - h_1)R_1t \int_{t-h_1}^t \dot{x}(s) ds \\ &\quad - \frac{6}{h_1} \int_{t-h_1}^t \dot{x}^T(s) ds R_1x(t - h_1) - a_3 \int_{t-h_2}^{t-h_m} \dot{x}^T(s)R_3\dot{x}(s) ds \\ &\leq 4x^T(t - h_m)R_3x(t - h_m) + 4x^T(t - h_2)R_3x(t - h_2) + 2x^T(t - h_m)R_3x(t - h_2) \\ &\quad + 2x^T(t - h_2)R_3x(t - h_m) - \frac{6}{a_3} x^T(t - h_m)R_3 \int_{t-h_2}^{t-h_m} \dot{x}(s) ds - \frac{6}{a_3} \int_{t-h_2}^{t-h_m} \dot{x}^T(s) ds R_3x(t - h_m) \\ &\quad - \frac{6}{a_3} x^T(t - h_2)R_3 \int_{t-h_2}^{t-h_m} \dot{x}(s) ds - \frac{6}{a_3} \int_{t-h_2}^{t-h_m} \dot{x}^T(s) ds R_3x(t - h_2). \end{aligned} \tag{15}$$

So,  $-h_1 \int_{t-h_1}^t \dot{x}^T(s)R_1\dot{x}(s) ds - h_1 \int_{t-h_1}^t \dot{x}^T(s)R_1\dot{x}(s) ds \leq -\eta^T(t)\Xi_3\eta(t)$ , where  $Q_{11} = H_1 + H_2 + H_3 + \text{He}(PA)$ :

$$\begin{aligned}
\Xi_1 = & \begin{bmatrix} Q_{11} & PB_1KD_2 & 0 & 0 & 0 & 0 & 0 & 0 & 0 & 0 & -PB_1K & PC_1 \\ * & \delta D_2^T \Phi D_2 & 0 & 0 & 0 & 0 & 0 & 0 & 0 & 0 & -\delta D_2^T V & 0 \\ * & * & -H_1 & 0 & 0 & 0 & 0 & 0 & 0 & 0 & 0 & 0 \\ * & * & * & -H_2 & 0 & 0 & 0 & 0 & 0 & 0 & 0 & 0 \\ * & * & * & * & -H_3 & 0 & 0 & 0 & 0 & 0 & 0 & 0 \\ * & * & * & * & * & -12R_1 & 0 & 0 & 0 & 0 & 0 & 0 \\ * & * & * & * & * & * & -12R_2 & 0 & 0 & 0 & 0 & 0 \\ * & * & * & * & * & * & * & -12R_2 & 0 & 0 & 0 & 0 \\ * & * & * & * & * & * & * & * & -12R_3 & 0 & 0 & 0 \\ * & * & * & * & * & * & * & * & * & (\delta - 1)\Phi & 0 & 0 \\ * & * & * & * & * & * & * & * & * & * & * & -\gamma^2 I \end{bmatrix}, \\
\Xi_2 = & \begin{bmatrix} 0 & 0 & 0 & 0 & 0 & 0 & 0 & 0 & 0 & 0 & 0 & 0 \\ * & F_{22} & F_{23} & F_{24} & 0 & 0 & F_{27} & F_{28} & 0 & 0 & 0 & 0 \\ * & * & 4R_2 & F_{34} & 0 & 0 & -6R_2 & F_{38} & 0 & 0 & 0 & 0 \\ * & * & * & 4R_2 & 0 & 0 & F_{47} & -6R_2 & 0 & 0 & 0 & 0 \\ * & * & * & * & 0 & 0 & 0 & 0 & 0 & 0 & 0 & 0 \\ * & * & * & * & * & 0 & 0 & 0 & 0 & 0 & 0 & 0 \\ * & * & * & * & * & * & 12R_2 & 0 & 0 & 0 & 0 & 0 \\ * & * & * & * & * & * & * & 12R_2 & 0 & 0 & 0 & 0 \\ * & * & * & * & * & * & * & * & 0 & 0 & 0 & 0 \\ * & * & * & * & * & * & * & * & * & 0 & 0 & 0 \\ * & * & * & * & * & * & * & * & * & * & 0 & 0 \end{bmatrix}, \\
\Xi_3 = & \begin{bmatrix} 4R_1 & 0 & 2R_1 & 0 & 0 & -6R_1 & 0 & 0 & 0 & 0 & 0 & 0 \\ * & 0 & 0 & 0 & 0 & 0 & 0 & 0 & 0 & 0 & 0 & 0 \\ * & * & 4R_1 & 0 & 0 & -6R_1 & 0 & 0 & 0 & 0 & 0 & 0 \\ * & * & * & 4R_3 & 2R_3 & 0 & 0 & 0 & -6R_3 & 0 & 0 & 0 \\ * & * & * & * & 4R_3 & 0 & 0 & 0 & -6R_3 & 0 & 0 & 0 \\ * & * & * & * & * & 12R_1 & 0 & 0 & 0 & 0 & 0 & 0 \\ * & * & * & * & * & * & 0 & 0 & 0 & 0 & 0 & 0 \\ * & * & * & * & * & * & * & 0 & 0 & 0 & 0 & 0 \\ * & * & * & * & * & * & * & * & 12R_3 & 0 & 0 & 0 \\ * & * & * & * & * & * & * & * & * & * & 0 & 0 \\ * & * & * & * & * & * & * & * & * & * & * & 0 \end{bmatrix},
\end{aligned} \tag{16}$$

$$\begin{aligned}
\bar{\Omega}_1 &= [h_1 R_1 A \quad h_1 R_1 B_1 K D_2 \quad 0 \quad 0 \quad 0 \quad 0 \quad 0 \quad 0 \quad 0 \quad -h_1 R_1 B_1 K \quad h_1 R_1 C_1], \\
\bar{\Omega}_2 &= [a_2 R_2 A \quad a_2 R_2 B_1 K D_2 \quad 0 \quad 0 \quad 0 \quad 0 \quad 0 \quad 0 \quad 0 \quad -a_2 R_2 B_1 K \quad a_2 R_2 C_1], \\
\bar{\Omega}_3 &= [a_3 R_3 A \quad a_3 R_3 B_1 K D_2 \quad 0 \quad 0 \quad 0 \quad 0 \quad 0 \quad 0 \quad 0 \quad -a_3 R_3 B_1 K \quad a_2 R_3 C_1], \\
\varsigma &= [D_1^T \quad B_2 K D_2 \quad 0 \quad 0 \quad 0 \quad 0 \quad 0 \quad 0 \quad 0 \quad -B_2 K \quad C_2].
\end{aligned} \tag{17}$$

To make closed-loop system (3) meet the  $H\infty$  applications, we can conclude

$$\begin{aligned} \Xi_1 - \Xi_2 - \Xi_3 + \overline{\Omega}_1^T R_1^{-1} \overline{\Omega}_1 + \overline{\Omega}_2^T R_2^{-1} \overline{\Omega}_2 + \overline{\Omega}_3^T R_3^{-1} \overline{\Omega}_3 + \zeta^T, \\ \zeta < 0. \end{aligned} \tag{18}$$

Through Schur supplement for (18), we can obtain

$$\left[ \begin{array}{cccccccc} W_{11} & PB_1KD_2 & 0 & 0 & 0 & 0 & 0 & 0 \\ * & \delta D_2^TVD_2 & 0 & 0 & 0 & 0 & 0 & 0 \\ * & * & -H_1 & 0 & 0 & 0 & 0 & 0 \\ * & * & * & -H_2 & 0 & 0 & 0 & 0 \\ * & * & * & * & -H_3 & 0 & 0 & 0 \\ * & * & * & * & * & 0 & 0 & 0 \\ * & * & * & * & * & * & 0 & 0 \\ * & * & * & * & * & * & * & 0 \\ * & * & * & * & * & * & * & * \\ * & * & * & * & * & * & * & * \\ * & * & * & * & * & * & * & * \\ * & * & * & * & * & * & * & * \\ * & * & * & * & * & * & * & * \\ * & * & * & * & * & * & * & * \\ * & * & * & * & * & * & * & * \\ * & * & * & * & * & * & * & * \\ * & * & * & * & * & * & * & * \end{array} \right] \tag{19}$$
  

$$\left[ \begin{array}{cccccc} -PB_1K & PC_1 & h_1(R_1A)^T & a_2(R_2A)^T & a_3(R_3A)^T & D_1^T \\ -\delta D_2^TV & 0 & h_1(R_1B_1KD_2)^T & a_2(R_2B_1KD_2)^T & a_3(R_3B_1KD_2)^T & (B_2KD_2)^T \\ 0 & 0 & 0 & 0 & 0 & 0 \\ 0 & 0 & 0 & 0 & 0 & 0 \\ 0 & 0 & 0 & 0 & 0 & 0 \\ 0 & 0 & 0 & 0 & 0 & 0 \\ 0 & 0 & 0 & 0 & 0 & 0 \\ 0 & 0 & 0 & 0 & 0 & 0 \\ 0 & 0 & 0 & 0 & 0 & 0 \\ 0 & 0 & 0 & 0 & 0 & 0 \\ (\delta - 1)\Phi & 0 & -h_1(R_1B_1K)^T & -a_2(R_2B_1K)^T & -a_3(R_3B_1K)^T & -(B_2K)^T \\ * & -\gamma^2I & h_1(R_1C_1)^T & a_2(R_1C_1)^T & a_3(R_3C_1)^T & C_1^T \\ * & * & -R_1 & 0 & 0 & 0 \\ * & * & * & -R_2 & 0 & 0 \\ * & * & * & * & -R_3 & 0 \\ * & * & * & * & * & -I \end{array} \right] < 0.$$

Multiplying left by  $\Lambda$  and right by  $\Lambda^T$ , we have

$$\begin{aligned}
 & \left[ \begin{array}{cccccccccc}
 W_{11} & h_1(R_1A)^T & a_2(R_2A)^T & a_3(R_2A)^T & D_1^T & 6R_1 & 0 & 0 & 0 \\
 * & -R_1 & 0 & 0 & 0 & 0 & 0 & 0 & 0 \\
 * & * & -R_2 & 0 & 0 & 0 & 0 & 0 & 0 \\
 * & * & * & -R_3 & 0 & 0 & 0 & 0 & 0 \\
 * & * & * & * & -I & 0 & 0 & 0 & 0 \\
 * & * & * & * & * & -12R_1 & 0 & 0 & 0 \\
 * & * & * & * & * & * & -12R_2 & 0 & 0 \\
 * & * & * & * & * & * & * & -12R_2 & 0 \\
 * & * & * & * & * & * & * & * & -12R_3 \\
 * & * & * & * & * & * & * & * & * \\
 * & * & * & * & * & * & * & * & * \\
 * & * & * & * & * & * & * & * & * \\
 * & * & * & * & * & * & * & * & * \\
 * & * & * & * & * & * & * & * & * \\
 * & * & * & * & * & * & * & * & * \\
 * & * & * & * & * & * & * & * & * \\
 * & * & * & * & * & * & * & * & *
 \end{array} \right] & \quad (20)
 \end{aligned}$$

$$\begin{aligned}
 & \left[ \begin{array}{cccccc}
 -PB_1K & PC_1 & PB_1KD_2 & -2R_1 & 0 & 0 \\
 -h_1PB_1K & h_1(R_1C_1) & h_1PB_1KD_2 & 0 & 0 & 0 \\
 -a_2PB_1K & a_2(R_2C_1) & a_2PB_1KD_2 & 0 & 0 & 0 \\
 -a_3PB_1K & a_3(R_3C_1) & a_3PB_1KD_2 & 0 & 0 & 0 \\
 -B_2S & C_2 & B_2SD_2 & 0 & 0 & 0 \\
 0 & 0 & 0 & 6R_1^T & 0 & 0 \\
 0 & 0 & -F_{27}^T & 6R_2^T & -F_{47}^T & 0 \\
 0 & 0 & -F_{28}^T & -F_{38}^T & 6R_2^T & 0 \\
 0 & 0 & 0 & 0 & 6R_3^T & 6R_3^T \\
 (\delta - 1)V & 0 & -\delta VD_2 & 0 & 0 & 0 \\
 * & -\gamma^2 I & 0 & 0 & 0 & 0 \\
 * & * & W_{22} & -F_{23} & -F_{24} & 0 \\
 * & * & * & W_{33} & -F_{34} & 0 \\
 * & * & * & * & W_{44} & -2R_3 \\
 * & * & * & * & * & W_{55}
 \end{array} \right] < 0,
 \end{aligned}$$

where

$$\Lambda = \begin{bmatrix} I & 0 & 0 & 0 & 0 & 0 & 0 & 0 & 0 & 0 & 0 & 0 & 0 & 0 & 0 & 0 & 0 & 0 & 0 & 0 \\ 0 & 0 & 0 & 0 & 0 & 0 & 0 & 0 & 0 & 0 & 0 & 0 & I & 0 & 0 & 0 & 0 & 0 & 0 & 0 \\ 0 & 0 & 0 & 0 & 0 & 0 & 0 & 0 & 0 & 0 & 0 & 0 & I & 0 & 0 & 0 & 0 & 0 & 0 & 0 \\ 0 & 0 & 0 & 0 & 0 & 0 & 0 & 0 & 0 & 0 & 0 & 0 & 0 & 0 & 0 & 0 & 0 & 0 & 0 & I \\ 0 & 0 & 0 & 0 & 0 & 0 & 0 & 0 & 0 & 0 & 0 & 0 & 0 & 0 & 0 & 0 & 0 & 0 & 0 & I \\ 0 & 0 & 0 & 0 & 0 & I & 0 & 0 & 0 & 0 & 0 & 0 & 0 & 0 & 0 & 0 & 0 & 0 & 0 & 0 \\ 0 & 0 & 0 & 0 & 0 & 0 & I & 0 & 0 & 0 & 0 & 0 & 0 & 0 & 0 & 0 & 0 & 0 & 0 & 0 \\ 0 & 0 & 0 & 0 & 0 & 0 & 0 & I & 0 & 0 & 0 & 0 & 0 & 0 & 0 & 0 & 0 & 0 & 0 & 0 \\ 0 & 0 & 0 & 0 & 0 & 0 & 0 & 0 & I & 0 & 0 & 0 & 0 & 0 & 0 & 0 & 0 & 0 & 0 & 0 \\ 0 & I & 0 & 0 & 0 & 0 & 0 & 0 & 0 & 0 & 0 & 0 & 0 & 0 & 0 & 0 & 0 & 0 & 0 & 0 \\ 0 & 0 & I & 0 & 0 & 0 & 0 & 0 & 0 & 0 & 0 & 0 & 0 & 0 & 0 & 0 & 0 & 0 & 0 & 0 \\ 0 & 0 & 0 & I & 0 & 0 & 0 & 0 & 0 & 0 & 0 & 0 & 0 & 0 & 0 & 0 & 0 & 0 & 0 & 0 \\ 0 & 0 & 0 & 0 & I & 0 & 0 & 0 & 0 & 0 & 0 & 0 & 0 & 0 & 0 & 0 & 0 & 0 & 0 & 0 \end{bmatrix}. \quad (21)$$

Let  $K = Z^{-1}S$ , and (18) can be rewritten as follows:

$$\begin{bmatrix} \Gamma_{11} & \Gamma_{12} \\ * & \Gamma_{22} \end{bmatrix} + \text{He} \begin{bmatrix} I_9 \\ 0_{6 \times 9} \end{bmatrix} \begin{bmatrix} PB_1 - B_1Z \\ h_1(R_1B_1 - B_1Z) \\ a_2(R_2B_1 - B_1Z) \\ a_3(R_3B_1 - B_1Z) \\ B_2 - B_2Z \\ 0 \\ 0 \\ 0 \\ 0 \end{bmatrix} \begin{bmatrix} -Z^{-1}S & 0 & -Z^{-1}SD_2 & 0 & 0 & 0 \\ 0_{6 \times 9} & I_6 \end{bmatrix} < 0. \quad (22)$$

Applying Lemma 1, we can obtain

$$\begin{aligned} & \text{He} \begin{bmatrix} I_9 \\ 0_{6 \times 9} \end{bmatrix} H = \begin{bmatrix} PB_1 - B_1Z \\ h_1(R_1B_1 - B_1Z) \\ a_2(R_2B_1 - B_1Z) \\ a_3(R_3B_1 - B_1Z) \\ B_2 - B_2Z \\ 0 \\ 0 \\ 0 \\ 0 \end{bmatrix} \begin{bmatrix} -Z^{-1}S & 0 & -Z^{-1}SD_2 & 0 & 0 & 0 \\ 0_{6 \times 9} & I_6 \end{bmatrix} \\ & \leq \begin{bmatrix} 0_{6 \times 9} \\ I_9 \end{bmatrix} \begin{bmatrix} -Z^{-1}S & 0 & -Z^{-1}SD_2 & 0 & 0 & 0 \end{bmatrix}^T \times \begin{bmatrix} PB_1 - B_1Z \\ h_1(R_1B_1 - B_1Z) \\ a_2(R_2B_1 - B_1Z) \\ a_3(R_3B_1 - B_1Z) \\ B_2 - B_2Z \\ 0 \\ 0 \\ 0 \\ 0 \end{bmatrix}^T J^{-1} \begin{bmatrix} PB_1 - B_1Z \\ h_1(R_1B_1 - B_1Z) \\ a_2(R_2B_1 - B_1Z) \\ a_3(R_3B_1 - B_1Z) \\ B_2 - B_2Z \\ 0 \\ 0 \\ 0 \\ 0 \end{bmatrix}. \end{aligned} \quad (23)$$

Combining (20) and (22) can lead to

$$\begin{bmatrix} \Gamma_{11} & \Gamma_{12} & 0 \\ * & \Gamma_{22} & E^T \\ * & * & H^T J^{-1} H \end{bmatrix} < 0, \quad (24)$$

where

$$E = [-Z^{-1}S \ 0 \ -Z^{-1}SD_2 \ 0 \ 0],$$

$$H = \begin{bmatrix} PB_1 - B_1Z \\ \sqrt{h_1} (R_1B_1 - B_1Z) \\ \sqrt{a_2} (R_2B_1 - B_1Z) \\ \sqrt{a_3} (R_3B_1 - B_1Z) \\ B_2 - B_2Z \\ 0 \\ 0 \\ 0 \\ 0 \end{bmatrix}. \quad (25)$$

Through Lemma 2 and Schur complement to (24), we can obtain

$$\begin{bmatrix} \Gamma_{11} + J & \Gamma_{12} & 0 & 0 \\ * & \Gamma_{22} & E^T G^T B_1^T B_1 & 0 \\ * & * & He(-B_1^T B_1 G) & \Gamma_{34} \\ * & * & * & -J \end{bmatrix} < 0. \quad (26)$$

So, we can obtain that

$$\eta^T(t) (\Xi_1 - \Xi_2 - \Xi_3 + \bar{\Omega}_1^T R_1^{-1} \bar{\Omega}_1 + \bar{\Omega}_2^T R_2^{-1} \bar{\Omega}_2 + \bar{\Omega}_3^T R_3^{-1} \bar{\Omega}_3 + \zeta^T \zeta),$$

$$\eta(t) < 0, \quad (27)$$

and we can conclude

$$\begin{aligned} \dot{V}(t) + \delta V(t) &\leq \eta^T(t) (\Xi_1 - \Xi_2 - \Xi_3 + \bar{\Omega}_1^T R_1^{-1} \bar{\Omega}_1 + \bar{\Omega}_2^T R_2^{-1} \bar{\Omega}_2 \\ &\quad + \bar{\Omega}_3^T R_3^{-1} \bar{\Omega}_3 + \zeta^T \zeta) \eta(t) \eta(t) - z^T(t) z(t) \\ &\quad + \gamma^2 \|\omega(t)\|_2 + \vartheta(t) \leq \gamma^2 \|\omega(t)\|_2 + \vartheta(t). \end{aligned} \quad (28)$$

Applying comparison lemma [34] to (26),

$$V(t) \leq e^{-\delta t} V(0) + \psi(t) \frac{\gamma}{\delta} (1 - e^{-\delta t}) \|\omega(t)\|_2, \quad (29)$$

where  $\psi(t) = \int_0^t e^{-\delta(t-s)} (\beta \varepsilon^{-\alpha s}) ds$ .

We consider the following situations by category.

(i) If  $\beta = 0$ , we can conclude  $\psi(t) = 0$ :

$$V(t) \leq e^{-\delta t} \left( V(0) - \frac{\gamma}{\delta} \|\omega(t)\|_2 \right) + \frac{\gamma}{\delta} \|\omega(t)\|_2. \quad (30)$$

(ii) If  $\beta > 0, \alpha = 0$ , we can conclude  $\psi(t) = \gamma/\delta(1 - e^{-\delta t})$ :

$$V(t) \leq e^{-\delta t} \left( V(0) - \frac{\gamma}{\delta} \|\omega(t)\|_2 - \frac{\gamma}{\delta} \right) + \frac{\gamma}{\delta} \|\omega(t)\|_2 + \frac{\gamma}{\delta}. \quad (31)$$

(iii) If  $\beta > 0, \alpha > 0, \delta - \alpha \ln \varepsilon = 0$ , we can conclude  $\psi(t) = \beta t e^{-\alpha t}$ :

$$V(t) \leq e^{-\delta t} \left( V(0) - \frac{\gamma}{\delta} \|\omega(t)\|_2 + \beta t \right) + \frac{\gamma}{\delta} \|\omega(t)\|_2. \quad (32)$$

(iv) If  $\beta > 0, \alpha > 0, \delta - \alpha \ln \varepsilon > 0$ , we can conclude  $\psi(t) = \beta/\delta - \alpha \ln \varepsilon (\varepsilon^{-\alpha t} - e^{-\delta t})$ :

$$\begin{aligned} V(t) &\leq e^{-\delta t} \left( V(0) - \frac{\gamma}{\delta} \|\omega(t)\|_2 + \beta t - \frac{\beta}{\delta - \alpha \ln \varepsilon} \right) + \frac{\gamma}{\delta} \|\omega(t)\|_2 \\ &\quad + \frac{\beta}{\delta - \alpha \ln \varepsilon} e^{-\alpha t}. \end{aligned} \quad (33)$$

Define  $\psi_{\max} = \max \psi(t)$  and union (30)–(33) can lead:

$$\psi_{\max} = \begin{cases} 0, & \beta = 0, \\ \frac{\beta}{\delta}, & \beta > 0, \alpha > 0, \\ \frac{\beta \varepsilon^{\alpha h_2}}{\delta e}, & \beta > 0, \alpha > 0, \delta - \alpha \ln \varepsilon = 0, \\ \frac{\beta \varepsilon^{\alpha h_2}}{|\delta - \alpha \ln \varepsilon|}, & \beta > 0, \alpha > 0, \delta - \alpha \ln \varepsilon \neq 0. \end{cases} \quad (34)$$

Accordingly, LKF can lead  $x^T(t)Px(t) \leq V(t)$ . If  $\omega(t) = 0$ , we can obtain

$$x^T(t)Px(t) \leq V(t) \leq V(0) + \psi_{\max}, \quad (35)$$

and we delimit

$$\mathfrak{F} = \sqrt{\frac{V(0)\psi_{\max}}{\lambda_{\min}}(P)}. \quad (36)$$

Accordingly, (34) and (35) can lead:

$$x(t) \in \{x : \|x(t)\| \leq \mathfrak{F}\}, \quad t > 0. \quad (37)$$

Meanwhile, if  $\omega(t) = 0$ , accordingly, (36) can lead:

$$\lim_{t \rightarrow \infty} V(t) \leq \begin{cases} \frac{\beta}{\delta} & \beta > 0, \alpha = 0, \\ 0, & \text{otherwise,} \end{cases} \quad (38)$$

when  $t \rightarrow \infty$ , (12) exponentially converges to the bounded region:

$$\bar{\mathfrak{S}} = \begin{cases} x(t) \in \left\{ x : \|x(t)\| \leq \sqrt{\frac{\beta}{\delta \lambda_{\min}(P)}} \right\}, & \beta > 0, \alpha = 0, \\ 0, & \text{otherwise.} \end{cases} \quad (39)$$

Then, we can get the closed-loop system (3) is GUUB when  $t \rightarrow \infty$ ,  $\omega(t) = 0$  the system state exponentially converges to the bounded area. At the same time,  $\|z(t)\| < \gamma \|\omega(t)\|_2$  at the zero-initial conditions is obtained.  $\square$

*Remark 1.* Compared with [15], this paper has three different characteristics. (1) A mixed event triggering mechanism, in which absolute trigger mechanism is added to the relative to the trigger term. (2) The concept of the time-delay partitions was applied to build a LKF. (3) The external disturbance is added to the original system and  $H_\infty$  performance index can be obtained. The purpose of the three improved views is to make the system robust.

*Remark 2.* Another class of method is reducing the conservatism of simple LKF. The augmented LKF is established,

$$\xi_1(t) = \begin{bmatrix} x^T(t) & x^T(t-h_1) & x^T(t-h_2) & \int_{t-h_1}^t x^T(s) ds & \int_{t-h_2}^t x^T(s) ds \end{bmatrix} \quad \xi_2(t) = \begin{bmatrix} x^T(t) & \dot{x}^T(t) \end{bmatrix}. \quad (41)$$

## 4. Simulation

This section provides two numerical simulation examples. The first example shows that the proposed method is effective. The second example shows the dynamic response of the system in the event-driven mode.

*Example 1.* Given the following parameters,

$$\begin{aligned} A &= \begin{bmatrix} -0.2 & -0.1 \\ 0.2 & -0.5 \end{bmatrix}, \\ B_1 &= \begin{bmatrix} 1 \\ 1 \end{bmatrix}, \\ C_1 &= [0 \ 1], \\ D_1 &= [0.3 \ 1], \\ D_2 &= [1 \ 0], \\ B_2 &= 0.1. \end{aligned} \quad (42)$$

Apply Theorem 1 with  $h = 0.01$  s,  $d_M = 0.5$ , and  $\gamma = 50$ . With the change of  $\delta$ , the corresponding controller gain  $K$  and event-driven matrix  $\Phi$  are listed in Table 1.

TABLE 1: The controller gain  $K$  and the weight matrix  $\Phi$ .

$\delta$	0.1	0.2	0.3
$K$	-0.0684	-0.0130	-0.0114
$\Phi$	163	58.7500	27.7632

in which it contains not only the state vector but also the derivative of the state. Meanwhile, the free-weight matrix inequality is raised in the study of integral inequalities. The free-weight matrix inequality adds some freedoms to the system based on the Wirtinger inequality. Constructing a suitable LKF by combining the two methods above, the function can be selected as

$$\begin{aligned} V(t) &= \xi_1^T(t) P \xi_1(t) + \int_{t-h_1}^t \xi_2^T(s) H_1 \xi_2(s) ds \\ &+ \int_{t-h_2}^t \xi_2^T(s) H_2 \xi_2(s) ds \\ &+ \int_{-h_1}^0 \int_{t+s}^t \dot{x}^T(v) R_1 \dot{x}(v) dv ds \\ &+ \int_{-h_2}^{-h_1} \int_{t+s}^t \dot{x}^T(v) R_2 \dot{x}(v) dv ds, \end{aligned} \quad (40)$$

where

$$\delta = 0.2, \alpha_1 = 0, \beta = 0.1, \alpha = 0.5, \varepsilon = e, \text{ and } \varepsilon_0 = 0.01$$

*Example 2.* Given  $\delta = 0.1$ ,  $h_1 = 0.01$ ,  $h_2 = 0.15$ ,  $h_m = 0.1$ , controller gain  $K = -0.00684$ , weight matrix  $\Phi = 2921.3$ ,  $h = 0.01$ , and  $\gamma = 50$ , according to the above conditions, system (1) is stable in the event-driven mode.  $x$  initial conditions are  $x(0) = \begin{bmatrix} 1 \\ -1 \end{bmatrix}$ ,  $\omega(t) = 0.09 * \sin 0.2 * t$ .

If  $\delta = 0.1$ ,  $\beta = 0$  result is shown in following figures. According to the above set parameters in the paper, some simulation results are shown in Figure 1.

From Figure 1, we can find that the system actually works under the relative trigger mechanism. When the output error reaches a certain threshold, the system state updates and then presents a periodic update state. The length of update interval will depend on the setting of  $\delta$  value.

If  $\delta = 0$ ,  $\beta = 0.3$  result is shown in Figure 2.

From Figure 2, we can find that the actual operation of the system is under the absolute trigger mechanism, and the trigger threshold is independent of the system state. Depending on the setting of  $\beta$  value, it is obvious that the update time of the system is earlier and the update interval is denser.

If  $\delta = 0.1$ ,  $\beta = 0.3$  result is shown in Figure 3.

From Figure 3, we can find that the system actually works under the mixed trigger mechanism. The trigger

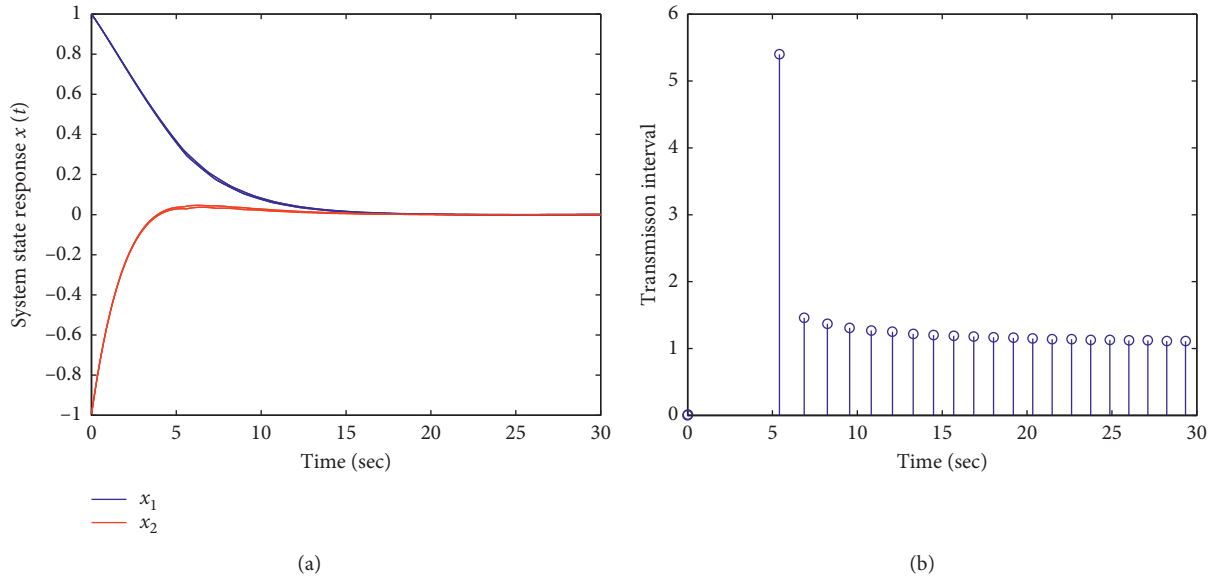


FIGURE 1: System state responses diagram and event-driven update picture. (a) Parameters' change of  $x(t)$ . (b) Event-driven updates.

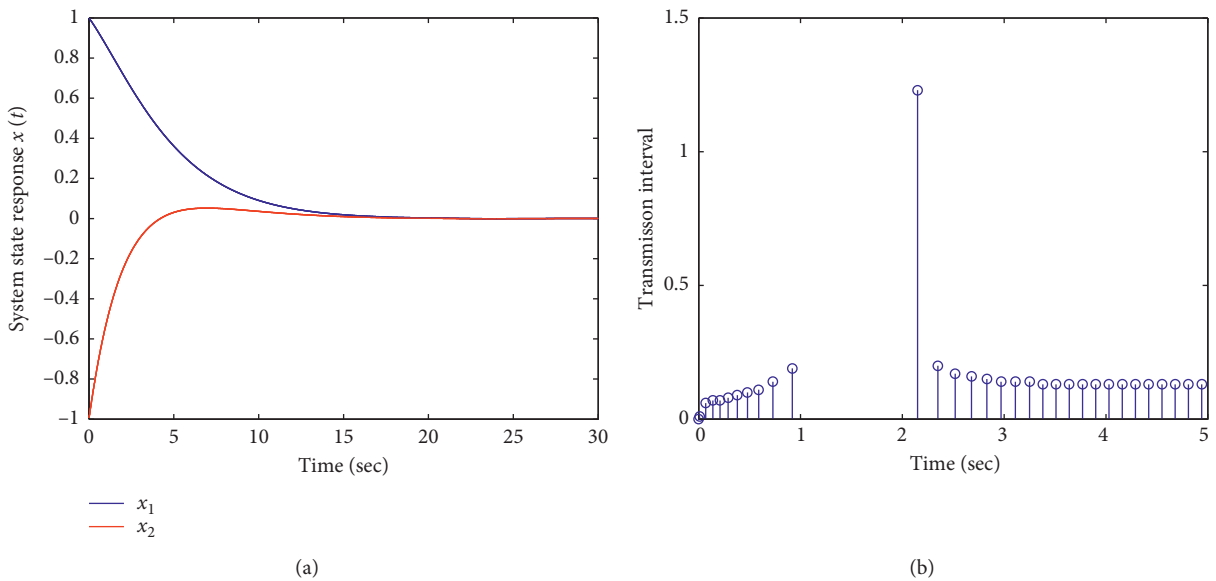


FIGURE 2: System state response diagram and event-driven update picture. (a) Parameters' change of  $x(t)$ . (b) Event-driven updates.

threshold is related not only to the system state but also to the initially set  $\beta$  value. We can see that the number of system updates is significantly reduced and the update interval is longer.

Through the above simulation, it can be found that different trigger mechanisms can stabilize the system, but the

update time of the system state is obviously different. Among them, the hybrid trigger mechanism proposed in this paper has more effective results, which can greatly reduce the network burden and save network bandwidth compared with the other two trigger methods.



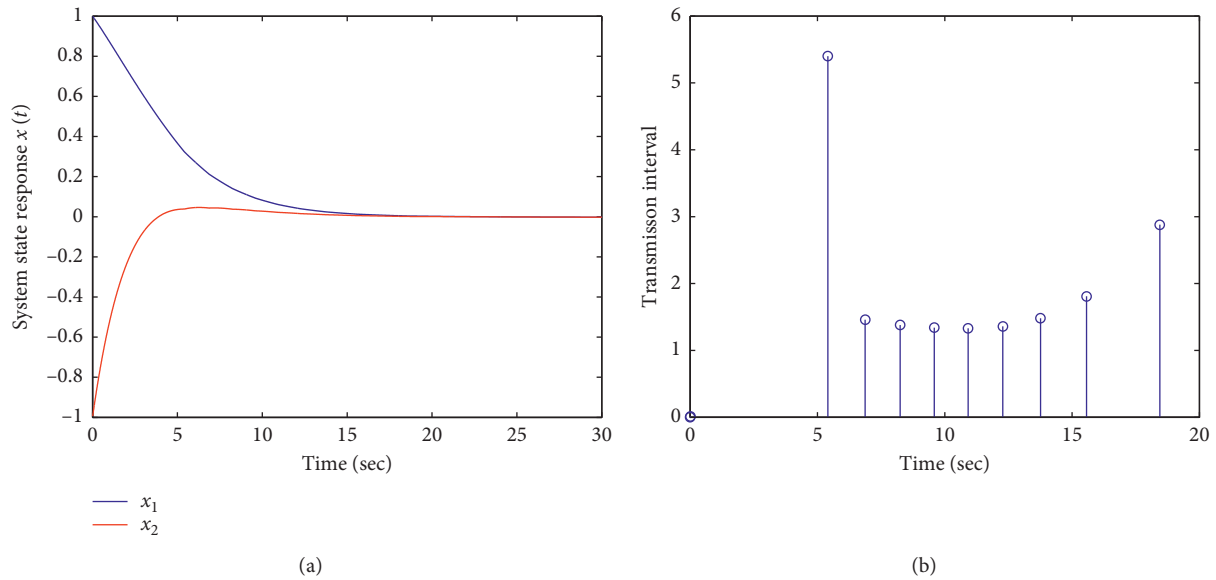


FIGURE 3: System state response diagram and event-driven update picture. (a) Parameters' change of  $x(t)$ . (b) Event-driven updates.

## 5. Conclusion

This paper has investigated the event-driven problem about NCSs. A mixed event trigger mechanism is introduced, which contains absolute trigger mechanism and relative trigger. The event triggering mechanism can be expressed by a time-delay model. The coupling of the system is reduced by introducing additional parameters and matrices. The sufficient condition can be obtained by LMI. By using the Wirtinger inequality method, relatively event-driven controller can be obtained, which meets an  $H_\infty$  performance index level of NCSs. Finally, two numerical simulation examples illustrate the effectiveness of the proposed method. In networked control systems, besides time delay, packet loss and quantization are also important factors that affect system performance. How to comprehensively consider the above two factors combined with trigger mechanism will be the focus of future work.

## Data Availability

The data used to support the findings of this study are included within the article. Because it is a numerical simulation example, readers can get the same results as this article by using the LMI toolbox of Matlab and the theorem given in this article.

## Conflicts of Interest

The authors declare that they have no conflicts of interest.

## Acknowledgments

This work was supported by National Natural Science Foundation of China (Grant nos. 61403278 and 61503280).

## References

- [1] X. M. Zhang, Q. L. Han, and X. H. Ge, "Networked control systems: a survey of trends and techniques," *IEEE-CAA Journal of Automatica Sinica*, vol. 7, no. 1, pp. 1–17, 2020.
- [2] H. Yan, C. Hu, H. Zhang, H. R. Karimi, X. Jiang, and M. Liu, " $H_\infty$  output tracking control for networked systems with adaptively adjusted event-triggered scheme," *IEEE Transactions on Systems, Man, and Cybernetics: Systems*, vol. 49, no. 10, pp. 2050–2058, 2019.
- [3] N. Xu and L. Sun, "An improved delay-dependent stability analysis for markovian jump systems with interval time-varying-delays," *IEEE Access*, vol. 6, pp. 33055–33061, 2018.
- [4] N. Xu and L. Sun, "Synchronization control of markov jump neural networks with mixed time-varying delay and parameter uncertain based on sample point controller," *Nonlinear Dynamics*, vol. 98, no. 3, pp. 1877–1890, 2019.
- [5] Z. Li, H. Yan, H. Zhang, X. Zhan, and C. Huang, "Stability analysis for delayed neural networks via improved auxiliary polynomial-based functions," *IEEE Transactions on Neural Networks and Learning Systems*, vol. 30, no. 8, pp. 2562–2568, 2019.
- [6] X. Li, B. Zhang, P. Li et al., "Finite-horizon  $H_\infty$  state estimation for periodic neural networks over fading channels," *IEEE Transactions on Neural Networks and Learning Systems*, vol. 31, no. 5, pp. 1450–1460, 2020.
- [7] G. Nagamani, Y. H. Joo, and T. Radhika, "Delay-dependent dissipativity criteria for markovian jump neural networks with random delays and incomplete transition probabilities," *Nonlinear Dynamics*, vol. 91, no. 56, pp. 2503–2522, 2018.
- [8] X.-M. Li, Q. Zhou, P. Li, H. Li, and R. Lu, "Event-triggered consensus control for multi-agent systems against false data-injection attacks," *IEEE Transactions on Cybernetics*, vol. 50, no. 5, pp. 1856–1866, 2020.
- [9] M. S. Ali and R. Saravanakumar, "Robust  $h_\infty$  control of uncertain systems with two additive time-varying delays," *Chinese Physics B*, vol. 24, no. 9, pp. 90202–90211, 2015.
- [10] R. Saravanakumar, M. S. Ali, and H. R. Karimi, "Robust  $h_\infty$  control of uncertain stochastic markovian jump systems with

- mixed time-varying delays,” *International Journal of Systems Science*, vol. 48, no. 4, pp. 862–872, 2017.
- [11] M. Shen, J. H. Park, and D. Ye, “A separated approach to control of markov jump nonlinear systems with general transition probabilities,” *IEEE Transactions on Cybernetics*, vol. 46, no. 9, pp. 2010–2018, 2016.
- [12] M. Shen, S. Yan, and G. M. Zhang, “A new approach to event-triggered static output feedback control of networked control systems,” *ISA Transactions*, vol. 65, pp. 468–474, 2016.
- [13] C. Peng and Q.-L. Han, “On designing a novel self-triggered sampling scheme for networked control systems with data losses and communication delays,” *IEEE Transactions on Industrial Electronics*, vol. 63, no. 2, pp. 1239–1248, 2016.
- [14] Y. Shen and M. Q. Shen, “Guangming zhanga: “extended event-driven observer-based output control of networked control systems,” *Nonlinear Dynamics*, vol. 86, no. 17, pp. 1639–1648, 2016.
- [15] H. Zhang, Z. Wang, H. Yan, F. Yang, and X. Zhou, “Adaptive event-triggered transmission scheme and  $\mathcal{H}_\infty$  filtering co-design over a filtering network with switching topology,” *IEEE Transactions on Cybernetics*, vol. 49, no. 12, pp. 4296–4307, 2019.
- [16] Z. Gu, P. Shi, and D. Yue, “An adaptive event-triggering scheme for networked interconnected control system with stochastic uncertainty,” *International Journal of Robust and Nonlinear Control*, vol. 27, no. 12, pp. 236–251, 2017.
- [17] Z. Gu, E. Tian, and J. Liu, “Adaptive event-triggered control of a class of nonlinear networked systems,” *Journal of the Franklin Institute*, vol. 354, no. 9, pp. 3854–3871, 2017.
- [18] Q. Zhou, W. Wang, H. Ma et al., “Event-triggered fuzzy adaptive containment control for nonlinear multi-agent systems with unknown bouc-wen hysteresis input,” *IEEE Transactions on Fuzzy Systems*, 2019.
- [19] Q. Zhou, W. Wang, H. Liang et al., “Observer-based event-triggered fuzzy adaptive bipartite containment control of multi-agent systems with input quantization,” *IEEE Transactions on Fuzzy Systems*, 2019.
- [20] H. Yan, H. Zhang, X. Zhan, Z. Li, and C. Yang, “Event-based  $\mathcal{H}_\infty$  fault detection for buck converter with multiplicative noises over network,” *IEEE Transactions on Circuits and Systems I: Regular Papers*, vol. 66, no. 6, pp. 2361–2370, 2019.
- [21] H. Shen, F. Li, H. Yan, H. R. Karimi, and H.-K. Lam, “Finite-time event-triggered  $\mathcal{H}_\infty$  control for t-s fuzzy markov jump systems,” *IEEE Transactions on Fuzzy Systems*, vol. 26, no. 5, pp. 3122–3135, 2018.
- [22] A. Rahnama, M. Xia, and P. J. Antsaklis, “Passivity-based design for event-triggered networked control systems,” *IEEE Transactions on Automatic Control*, vol. 63, no. 9, pp. 2755–2770, 2018.
- [23] Z. Gu, P. Shi, D. Yue, and Z. Ding, “Decentralized adaptive event-triggered  $\mathcal{H}_\infty$  filtering for a class of networked nonlinear interconnected systems,” *IEEE Transactions on Cybernetics*, vol. 49, no. 5, pp. 1570–1579, 2019.
- [24] J. Qiu, K. Sun, T. Wang, and H. Gao, “Observer-based fuzzy adaptive event-triggered control for pure-feedback nonlinear systems with prescribed performance,” *IEEE Transactions on Fuzzy Systems*, vol. 27, no. 11, pp. 2152–2162, 2019.
- [25] K. Zhang, T. Zhao, and S. Dian, “Dynamic output feedback control for nonlinear networked control systems with a two-terminal event-triggered mechanism,” *Nonlinear Dynamics*, vol. 100, no. 3, pp. 2537–2555, 2020.
- [26] K. Gu, J. Chen, and V. Kharitonov, “Stability of time-delay systems,” *Birkhauser Boston*, vol. 5, no. 4, pp. 213–217, 2003.
- [27] H.-B. Zeng, Y. He, M. Wu, and S.-P. Xiao, “Less conservative results on stability for linear systems with a time-varying delay,” *Optimal Control Applications and Methods*, vol. 34, no. 6, pp. 670–679, 2013.
- [28] H. B. Zeng, Y. He, and M. Wu, “Free-matrix-based integral inequality for stability analysis of systems with time-varying delay,” *IEEE Transactions on Automatic Control*, vol. 60, no. 10, pp. 2768–2772, 2017.
- [29] G. Chen, J. Xia, G. Zhuang, and J. Zhao, “Improved delay-dependent stabilization for a class of networked control systems with nonlinear perturbations and two delay components,” *Applied Mathematics and Computation*, vol. 316, pp. 1–17, 2018.
- [30] N. Xu and L. Sun, “Parallel distributed compensation controller design for markovian jump system with time-varying delays using bessel-legendre inequality method and improved positive definite rule,” *Transactions of the Institute of Measurement and Control*, vol. 42, no. 7, pp. 1313–1322, 2019.
- [31] P. Chen and J. Zhang, “Event-triggered output-feedback h $\infty$  control for networked control systems with time-varying sampling,” *Control Theory and Applications*, vol. 9, no. 9, pp. 1384–1391, 2015.
- [32] A. Seuret and F. Gouaisbaut, “Wirtinger-based integral inequality: application to time-delay systems,” *Automatica*, vol. 49, no. 9, pp. 2860–2866, 2013.
- [33] F. Li, J. Fu, and D. Du, “An improved event-triggered communication mechanism and L $\infty$  control co-design for network control systems,” *Information Sciences*, vol. 370, pp. 743–762, 2016.
- [34] H. K. Khalil, *Nonlinear Systems*, Prentice-Hall, Upper Saddle River, NJ, USA, 3rd edition, 2002.

## Research Article

# Decentralized Suboptimal State Feedback Integral Tracking Control Design for Coupled Linear Time-Varying Systems

Mohamed Sadok Attia, Mohamed Karim Bouafoura , and Naceur Benhadj Braiek

*Ecole Polytechnique de Tunisie, BP. 743, La Marsa 2078, Tunisia*

Correspondence should be addressed to Mohamed Karim Bouafoura; mohamed.bouafoura@ept.rnu.tn

Received 3 February 2020; Revised 30 April 2020; Accepted 3 June 2020; Published 26 July 2020

Guest Editor: Xiao Ling Wang

Copyright © 2020 Mohamed Sadok Attia et al. This is an open access article distributed under the Creative Commons Attribution License, which permits unrestricted use, distribution, and reproduction in any medium, provided the original work is properly cited.

In this paper, a suboptimal state feedback integral decentralized tracking control synthesis for interconnected linear time-variant systems is proposed by using orthogonal polynomials. Particularly, the use of operational matrices allows, by expanding the subsystem input states and outputs over a shifted Legendre polynomial basis, the conversion of time-varying parameter differential state equations to a set of time-independent algebraic ones. Hence, optimal open-loop state and control input coefficients are forwardly determined. These data are used to formulate a least-square problem, allowing the synthesis of decentralized state feedback integral control gains. Closed-loop asymptotic stability LMI conditions are given. The proposed approach effectiveness is proved by solving a nonconstant reference tracking problem for coupled inverted pendulums.

## 1. Introduction

The decentralized control has given rise to increasing attention in the automatic control community. Obviously, studies are mainly related to the so-called large-scale interconnected dynamic system class. The latter family of plants finds its application in several fields such as mechanical systems [1–3], power-generating plants [4, 5], aircraft dynamics [6], aerospace transportation [7], and economic models [8]. The decentralized control of an interconnected system essence aims at making each subsystem being controlled using only its own local state variables. However, ensuring the global stability of the whole system still remains a challenging concern [1, 9, 10].

Over the past years, many research results have been dedicated to the decentralized control approach for linear [11, 12] and nonlinear large-scale systems [1, 10, 13]. We recall here some works in the literature such as decentralized optimal control using the successive approximation approach [14], state-dependent Riccati equation (SDRE) optimal control [10], feedback decentralized polynomial control for the multimachine power system [9], robust  $H_{\infty}$  decentralized observation and control [15], and Chebyshev

wavelet-based collocation scheme [16]. In most cases, particular classes of interconnected systems are handled, and specific mathematical conditions should be met at first in order to achieve the problem resolution.

On the contrary, linear time-variant (LTV) systems are known to be an immediate generalization of time-invariant systems. In fact, this class of linear systems is the result of nonlinear systems linearizing along a trajectory. Hence, it permits to cover a wider operating conditions of the systems to be studied, and as a consequence, ensures the applicability of the resulting control approaches. It is worth noting that the decentralized tracking problem of time-varying systems has not been addressed excessively in the literature. Using time-varying parameters for interconnected system modeling has been considered recently in order to solve various control problems. Among the latest contributions, one may cite [17], where authors combine an operator form of discrete-time linear systems with the classical Youla parameterization to characterize the set of stably realizable decentralized controllers for LTI, LTV, or even linear switched systems. Mohamed et al. [18] addressed the problem of the adaptive sliding mode observer for nonlinear interconnected systems with time-varying parameters.

Besides, the time-variation concept has concerned the delay modeling [19] or the output constraint modeling [20] of large-scale systems. For the tracking problem, we particularly recall the method in [1], where authors developed a decentralized tracking control for a class of time-varying systems based on the backstepping technique. The time-variant parameters in the global systems are unknown, bounded (that bounds need to be estimated and not literally using the time-varying parameters), and should verify some analytical assumptions in order to prove the stability of the closed-loop system.

Moreover, approaches based on similar mathematical tools (orthogonal functions, wavelets, and polynomials) used in this work have considered only the optimal control problem of time-varying systems. To our best knowledge, the decentralized scheme for LTV interconnected systems has not been treated yet. One may refer to [12, 21] and references therein that exhibit a review on orthogonal function approaches to solve the optimal control problem for time-varying systems. It is clear that most techniques are based on product operational matrices, and two formulations could be distinguished:

- (i) The Lagrange approach: Lagrange multipliers are introduced, and then a parameter optimization problem is formulated by giving the necessary conditions for optimization. Resolution could be done via a nonlinear optimization tool.
- (ii) The Riccati approach: here, the state transition matrix of the two-point boundary value problem (TPBVP) should be identified by the mean of an orthogonal basis that leads to multiple least-square problems.

However, in most works in the literature, as it is the case for the above described techniques, only open-loop optimal solutions are given, which is an important limitation since such control could not be efficiently implemented in practice.

On the other side, several orthogonal function-based contributions have been extensively proposed during the last three decades for the analysis, identification, optimal control, and model reduction of linear [22, 23] and some classes of nonlinear systems [24–27]. In the literature, there are several orthogonal function bases dedicated to solve the above cited problems arising in control theory. One may refer to research activities based on Legendre polynomials [22, 28], Chebyshev [12], Hermite polynomials [29], block pulse [25], Walsh functions [30], or even hybrid of piecewise and polynomials [31]. In our work, shifted Legendre polynomials are chosen to develop time-variant systems and manipulate related operational matrices, more specifically the Kronecker product operational matrix, to solve the posed optimal tracking problem.

In this paper, we aim to design a suboptimal decentralized state feedback integral tracking control technique applied for interconnected linear time-variant systems. This approach consists in expanding all variables involved in the considered dynamic subsystems over shifted Legendre basis.

It will be then possible to reduce the corresponding interconnected time-variant parameter differential equations into some coupled time-independent algebraic equations. Thus, computations become clearly more easier to be undertaken. More precisely, the proposed approach is achieved by following the below 2 steps :

- (1) Consider the global time-varying system and solve the related optimal control problem with a direct approach based on shifted Legendre polynomials. This permits to avoid the resolution of a high-order TPBVP with time-varying parameters and allows to obtain global state and control coefficients on the basis by just finding a direct relation between the coefficients and deducing the control from the approached expression of the criterion.
- (2) Once open-loop global state and control coefficients are obtained, we inject each subsystem state and control coefficients in the proposed decentralized state feedback with an integral action equation. That leads, by the mean of the integration operational matrix of the basis, to an algebraic equation where unknowns are only control gains. A formulated least-square problem is then solved.

Finally, we will be interested to study the stability of the overall system controlled with the proposed feedback action. As a consequence, an augmented system is constructed and LMI conditions are given, guaranteeing asymptotic stability of the closed loop.

This article is organized as follows: shifted Legendre polynomial properties and problem formulation are presented in Section 2. Open-loop optimal control synthesis and suboptimal state feedback integral control determination are given Section 3. Section 4 is reserved to the stability analysis. A numerical simulated example based on coupled inverted pendulums is provided in the Section 5, and it highlights the achieved developments.

## 2. Preliminaries and Problem Statement

**2.1. Legendre Polynomials.** The Legendre polynomials are orthogonal on the interval  $[-1, 1]$ , with a weight function  $w(\tau) = 1$ . The set of Legendre polynomials is obtained from the formula of Olinde Rodrigues [23]:

$$\ell_n(\tau) = \frac{1}{2^n n!} \frac{d^n (\tau^2 - 1)^n}{d\tau^n}. \quad (1)$$

This gives

$$\begin{aligned} \ell_0(\tau) &= 1, \\ \ell_1(\tau) &= \tau, \\ \ell_2(\tau) &= \frac{3\tau^2 - 1}{2}. \end{aligned} \quad (2)$$

These polynomials can also be obtained from the recursive relationship [23]:

$$(n+1)\ell_{n+1}(\tau) = (2n+1)\tau\ell_n(\tau) - n\ell_{n-1}(\tau), \quad (3)$$

with  $\ell_0(\tau) = 1$  and  $\ell_1(\tau) = \tau$ .

**2.2. Shifted Legendre Polynomials.** In order to obtain orthogonal Legendre polynomials over the time interval  $[0, t_f]$ , which is more useful in control synthesis, we perform the following change of variable:

$$\tau = \frac{2t}{t_f} - 1 \text{ with } 0 \leq t \leq t_f. \quad (4)$$

The recursive relationship (3) becomes [32]

$$(n+1)s_{n+1}(t) = (2n+1)\left(\frac{2t}{t_f} - 1\right)s_n(t) - ns_{n-1}(t), \quad (5)$$

where  $s_n(t)$  denotes an elementary shifted Legendre polynomial defined over  $0 \leq t \leq t_f$ , in which  $s_0(t) = 1$  and  $s_1(t) = (2t/t_f) - 1$ .

The principle of orthogonality of the shifted Legendre polynomials (SLPs) is expressed by the following equation [33]:

$$\int_0^{t_f} s_i(t)s_j(t)dt = \frac{t_f}{2i+1}\delta_{ij}, \quad (6)$$

where  $\delta_{ij}$  is the Kronecker symbol.

**2.3. The Operational Matrix of Integration of Shifted Legendre Polynomials.** In the case of shifted Legendre polynomials, the operational matrix of integration  $P_N$  is defined as follows [28]:

$$\int_0^t \mathcal{S}_N(\tau)d\tau \cong P_N \mathcal{S}_N(t), \quad (7)$$

where

$$P_N = \frac{t_f}{2} \begin{pmatrix} 1 & 1 & 0 & 0 & \cdots & 0 & 0 & 0 \\ -\frac{1}{3} & 0 & \frac{1}{3} & 0 & \cdots & 0 & 0 & 0 \\ 0 & -\frac{1}{5} & 0 & \frac{1}{5} & \cdots & 0 & 0 & 0 \\ \vdots & \vdots & \vdots & \vdots & \cdots & \vdots & \vdots & \vdots \\ 0 & 0 & 0 & 0 & \cdots & \frac{1}{2N-3} & 0 & \frac{1}{2N-3} \\ 0 & 0 & 0 & 0 & \cdots & 0 & -\frac{1}{2N-1} & 0 \end{pmatrix}, \quad (8)$$

is an  $(N \times N)$  constant matrix and  $\mathcal{S}_N(t) = [s_0(t), s_1(t), \dots, s_{N-1}(t)]^T$  denotes a shifted Legendre basis of dimension  $N$ .

**2.4. The Integration of the Cross Product.** The integration of the cross product of two shifted Legendre polynomial vectors can be obtained as [31]

$$C_p = \int_0^{t_f} \mathcal{S}_N(t)\mathcal{S}_N^T(t)dt = t_f \begin{bmatrix} 1 & 0 & \cdots & 0 \\ 0 & \frac{1}{3} & \cdots & 0 \\ \vdots & \vdots & \ddots & \vdots \\ 0 & 0 & \cdots & \frac{1}{2M-1} \end{bmatrix}, \quad (9)$$

where  $C_p$  is an  $(N \times N)$  constant matrix.

**2.5. Operational Matrix of the Kronecker Product.** The product of two shifted Legendre polynomials  $s_i(t)$  and  $s_j(t)$  can be expressed by [32]

$$s_i(t)s_j(t) \cong \sum_{k=0}^{M-1} \psi_{ijk}L_k(t), \quad (10)$$

with

$$\psi_{ijk} = \frac{2k+1}{t_f} \int_0^{t_f} s_i(t)s_j(t)s_k(t)dt. \quad (11)$$

Then, we may write

$$s_j(t)\mathcal{S}_N(t) = \begin{bmatrix} \psi_{i00} \\ \psi_{i11} \\ \vdots \\ \psi_{i(N-1)(N-1)} \end{bmatrix} = K_s^i \mathcal{S}_N(t), \quad (12)$$

where  $K_s^i$  is an  $N \times N$  constant matrix, and then it becomes

$$\mathcal{S}_N(t) \otimes \mathcal{S}_N(t) = \begin{bmatrix} K_s^0 \\ K_s^1 \\ \vdots \\ K_s^{N-1} \end{bmatrix} = K_{\mathcal{S}} \mathcal{S}_N(t), \quad (13)$$

where  $K_{\mathcal{S}} \in \mathbb{R}^{N^2 \times N}$  is the Kronecker product operational matrix of shifted Legendre polynomials.

**2.6. Problem Statement.** Consider the following optimal control problem: find the optimal control  $u_i^*(t)$ , which minimizes the following quadratic performance index:

$$J = \frac{1}{2} \sum_i^M \int_{t_0}^{t_f} [e_i^T(t)Q_i e_i(t) + u_i^T(t)R_i u_i(t)]dt, \quad (14)$$

where  $M$  is the number of interconnected subsystems and  $e_i(t)$  is the tracking error defined by

$$e_i(t) = y_i(t) - y_{ri}(t), \quad (15)$$

with  $y_i(t) \in \mathbb{R}^{P_i}$  being the output of the  $i$ -th subsystem and  $y_{ri}(t)$  being the reference submodel output.

Particularly, in this framework, we consider a global LTV system (S) consisting of  $M$  interconnected subsystems ( $S_i$ ) described by the following state equation:

$$(S_i) \begin{cases} \dot{x}_i(t) = A_i(t)x_i(t) + B_i(t)u_i(t) + \sum_{\substack{j=1 \\ j \neq i}}^M H_{ij}(t)x_j(t), \\ y_i(t) = C_i x_i(t), \end{cases} \quad (16)$$

where  $x_i(t) \in \mathbb{R}^{n_i}$ ,  $u_i(t) \in \mathbb{R}^{m_i}$ , and  $y_i(t) \in \mathbb{R}^{p_i}$  are, respectively, the state vector, the control vector, and the output vector of the subsystem ( $S_i$ ) and  $A_i(t) = [a_{ij}(t)]$ ,  $B_i(t) = [b_{ij}(t)]$ , and  $C_i$  and  $H_{ij}(t) = [h_{ij}(t)]$  are some time-dependent matrices characterising the subsystem ( $S_i$ ) with respective dimensions  $(n_i \times n_i)$ ,  $(n_i \times m_i)$ ,  $(p_i \times n_i)$ , and  $(n_i \times n_j)$ .

We assume that each subsystem is assumed to be fully measurable and controllable, and its matrices have the following bounds:

$$\begin{aligned} \underline{A} &\leq a_{ij}(t) \leq \bar{A}, \\ \underline{B} &\leq b_{ij}(t) \leq \bar{B}, \\ \underline{H} &\leq h_{ij}(t) \leq \bar{H}, \end{aligned} \quad (17)$$

where notations  $\underline{A}$  and  $\bar{A}$  correspond, respectively, to the minimum and maximum of a time-dependent variable  $\lambda_{ij}(t)$ .

The linear time-invariant reference models to be used in this study are obviously stable and encompass all desired performances to be conferred to the controlled subsystems. These LTI models are described by the following state equations:

$$\begin{cases} \dot{x}_{ri}(t) = E_i x_{ri}(t) + F_i r_i(t), \\ y_{ri}(t) = G_i x_{ri}(t), \end{cases} \quad (18)$$

where  $x_{ri}(t) \in \mathbb{R}^{\tilde{n}_{ri}}$  is the state vector of the  $i$ -th reference submodel,  $r_i(t) \in \mathbb{R}^{m_{ri}}$  is a nonconstant input, and  $y_{ri}(t) \in \mathbb{R}^{p_{ri}}$  its output vector generating, hence, a path to be tracked and  $E_i$ ,  $F_i$ , and  $G_i$  are the chosen matrices characterising the reference model with respective dimensions  $(\tilde{n}_{ri} \times \tilde{n}_{ri})$ ,  $(\tilde{n}_{ri} \times m_{ri})$ , and  $(p_{ri} \times \tilde{n}_{ri})$ .

In the sequel, we will be concerned with the synthesis of state feedback integral suboptimal controllers of the following form:

$$u_i(t) = \bar{N}_i r_i(t) + K_i x_i(t) + L_i \int_0^t (y_i(\tau) - r_i(\tau)) d\tau, \quad (19)$$

which are aimed to make each subsystem outputs track nonconstant inputs with respect to the corresponding reference submodel dynamics.

### 3. Optimal Tracking Control Synthesis

**3.1. Criterion Approximation.** A global criterion to be minimised could be defined as follows:

$$J = \frac{1}{2} \int_0^{t_f} (e^T(t) Q e(t) + u^T(t) R u(t)) dt, \quad (20)$$

where  $e(t) \in \mathbb{R}^p$  and  $u(t) \in \mathbb{R}^m$  denote the global system tracking error and the control input, respectively. Notice that this criterion is associated to the global system (S):

$$\begin{cases} \dot{x}(t) = A_g(t)x(t) + B_g(t)u(t), \\ y(t) = C_g x(t), \end{cases} \quad (21)$$

where global system matrices  $A_g(t) \in \mathbb{R}^{n \times n}$ ,  $B_g(t) \in \mathbb{R}^{m \times m}$ , and  $C_g \in \mathbb{R}^{p \times p}$  are given by

$$\begin{aligned} A_g(t) &= \text{diag}(A_i(t)) + H, \text{ with } H = [H_{ij}], H_{ii} = 0, \\ &\quad \forall i, j = 1, \dots, M, \\ B_g(t) &= \text{diag}(B_i(t)), \\ C_g &= \text{diag}(C_i). \end{aligned} \quad (22)$$

Applying the vec operator and related Kronecker product property [34] yields

$$\begin{aligned} \text{vec}(e(t)) &\approx (\mathcal{S}_N(t)^T(t) \otimes I_p) \text{vec}(e_N^T), \\ \text{vec}(u(t)) &\approx (\mathcal{S}_N(t)^T(t) \otimes I_m) \text{vec}(u_N^T), \end{aligned} \quad (23)$$

where  $I_p$  and  $I_m$  are, respectively, the  $(p \times p)$  and  $(m \times m)$  identity matrices and  $e_N^T$  and  $u_N^T$  are the coefficients obtained by developing, respectively, the error and the control input over the shifted Legendre basis.

With this approximation, the globalization of equation (2) gives

$$\text{vec}(e_N^T) \approx (I_N \otimes C_g) \text{vec}(x_N^T) - \text{vec}(y_{rN}^T), \quad (24)$$

where  $x_N^T$  and  $y_{rN}^T$  are the coefficients obtained by developing, respectively, the global system state and the global reference model output over the shifted Legendre basis.

Let us denote

$$\begin{aligned} z_x &= \text{vec}(x_N^T), \\ z_u &= \text{vec}(u_N^T), \\ Y_N &= \text{vec}(y_{rN}^T), \\ \Gamma_N &= \text{vec}(r_N^T). \end{aligned} \quad (25)$$

Exploiting the vec property (see Appendix), the global criterion to be minimised is expressed as follows:

$$J \approx [z_x^T (I_N \otimes C_g^T) - Y_N^T] \tilde{Q} [(I_N \otimes C_g) z_x - Y_N] + z_u^T \tilde{R} z_u, \quad (26)$$

where  $\tilde{Q} = (C_p \otimes Q)$  and  $\tilde{R} = (C_p \otimes R)$  with  $C_p$  the cross product matrix presented in the previous section.

The expression of  $Y_N$  in (26) depends on  $\Gamma_N$  and will be replaced by the following relation:

$$Y_N = (I_N \otimes G) (I_{nN} - P_N^T \otimes E) (P_N^T \otimes F) \Gamma_N, \quad (27)$$

where matrices  $E = \text{diag}(E_i)$ ,  $F = \text{diag}(F_i)$ , and  $G = \text{diag}(G_i)$  define the global reference model.

**3.2. Dynamic Constraint Expansion over the Orthogonal Basis.** The development of time-dependent matrices in (21), over shifted Legendre basis, yields

$$A_g(t) \approx \sum_{k=0}^{N-1} A_{gk} s_k(t) = \underbrace{\begin{bmatrix} s_0(t) \cdot I_n & & & 0 \\ & s_1(t) \cdot I_n & & \\ & & \ddots & \\ 0 & & & s_{N-1}(t) \cdot I_n \end{bmatrix}}_{\mathcal{S}_N^T(t) \otimes I_n} \cdot \begin{bmatrix} A_{g0} \\ \dots \\ A_{g1} \\ \dots \\ \vdots \\ \dots \\ A_{gN-1} \end{bmatrix} = (\mathcal{S}_N^T(t) \otimes I_n) \cdot \tilde{A}_g, \quad (28)$$

where  $A_{gk} \in^{n \times n}$  and  $\tilde{A}_g \in^{nN \times n}$ .

Similarly, one may state

$$B_g(t) \approx (\mathcal{S}_N^T(t) \otimes I_n) \tilde{B}_g. \quad (29)$$

Now, the system expansion over the SLP base is given by

$$\begin{aligned} x_N^T \mathcal{S}_N(t) - x_{N0}^T \mathcal{S}_N(t) &= (\mathcal{S}_N^T(t) \otimes I_n) \tilde{A}_g x_N^T P_N \mathcal{S}_N(t) \\ &+ (\mathcal{S}_N^T(t) \otimes I_n) \tilde{B}_g u_N^T P_N \mathcal{S}_N(t), \end{aligned} \quad (30)$$

with  $x_{N0}^T$  being the initial state projection over the considered basis.

Applying the vec operator to (30) gives

$$\begin{aligned} &(\mathcal{S}_N^T(t) \otimes I_n) z_x - (\mathcal{S}_N^T(t) \otimes I_n) z_{x0} \\ &= [(\mathcal{S}_N^T(t) P_N) \otimes (\mathcal{S}_N^T(t) \otimes I_n) \tilde{A}_g] z_x \\ &+ [(\mathcal{S}_N^T(t) P_N) \otimes (\mathcal{S}_N^T(t) \otimes I_n) \tilde{B}_g] z_u. \end{aligned} \quad (31)$$

Notice that

$$\begin{aligned} &(\mathcal{S}_N^T(t) P_N) \otimes (\mathcal{S}_N^T(t) \otimes I_n) \tilde{A}_g \\ &= (\mathcal{S}_N(t) \otimes \mathcal{S}_N(t) \otimes I_n) (P_N^T \otimes \tilde{A}_g) \\ &= (\mathcal{S}_N(t) \otimes I_n) (K_S^T \otimes I_n) (P_N^T \otimes \tilde{A}_g). \end{aligned} \quad (32)$$

Hence, (31) becomes

$$z_x = Vz_u + Wz_{x0}, \quad (33)$$

where

$$\begin{aligned} W &= (I_n - (K_S^T \otimes I_n) (P_N^T \otimes \tilde{A}_g))^{-1}, \\ V &= W \cdot (K_S^T \otimes I_n) (P_N^T \otimes \tilde{B}_g). \end{aligned} \quad (34)$$

**3.3. Optimal Open-Loop Control.** Substituting (33) in (26) and setting the optimization condition  $\partial J/z_u = 0$  yield the following optimal control:

$$z_u^* = -(\hat{Q}V + \tilde{R})^{-1} (z_{x0}^T W^T \hat{Q}V + Y_N^T \tilde{Q}C_g V), \quad (35)$$

where  $\hat{Q} = C_g^T \tilde{Q} C_g$ .

Finally, the optimal state coefficient  $z_x^*$  could be also recovered by injecting (35) in (33).

**3.4. Suboptimal State Feedback Integral Synthesis.** We are interested now, based on open-loop optimal results ( $z_u^*, z_x^*$ ), to synthesize a suboptimal control of type (19).

It is possible now to capture, for each subsystem, optimal state  $x_{iN}^{*T}$  and input  $u_{iN}^{*T}$  coefficients from the optimal global system ones.

On the other hand, expansion of the decentralized state feedback integral control over SLP basis yields

$$\begin{aligned} u_{iN}^T \mathcal{S}_N(t) &= \bar{N}_i r_{iN}^T \mathcal{S}_N(t) + K_i x_{iN}^T \\ &+ L_i (y_{iN}^T - y_{riN}^T) P_N \mathcal{S}_N(t). \end{aligned} \quad (36)$$

Simplifying the basis and applying the vec operator with optimal coefficients, the synthesis of control parameters could be done by solving the following least-square problem:

$$\mathcal{A} \cdot \Delta = \mathcal{B}, \quad (37)$$

with

$$\mathcal{A} = \text{diag} \left( \left[ r_{iN}^T \otimes I_{m_i} : x_{iN}^{*T} \otimes I_{m_i} : (C_i x_{iN}^{*T} P_N - r_{iN}^T P_N)^T \otimes I_{m_i} \right] \right),$$

$$\mathcal{B} = \begin{bmatrix} z_{u1}^* \\ z_{u2}^* \\ \vdots \\ z_{uM}^* \end{bmatrix},$$

(38)

where  $z_{ui}^* = \text{vec}(u_{iN}^{*T})$  and

$$\Delta = \begin{bmatrix} \text{vec}(\bar{N}_1) \\ \text{vec}(K_1) \\ \text{vec}(L_1) \\ \dots \\ \text{vec}(\bar{N}_2) \\ \text{vec}(K_2) \\ \text{vec}(L_2) \\ \dots \\ \vdots \\ \dots \\ \text{vec}(\bar{N}_M) \\ \text{vec}(K_M) \\ \text{vec}(L_M) \end{bmatrix}. \quad (39)$$

#### 4. Closed-Loop Stability Analysis

Consider the following augmented state space submodel:

$$\begin{bmatrix} \dot{x}_i(t) \\ \dot{x}_{ai}(t) \end{bmatrix} = \begin{bmatrix} A_i(t) & 0 \\ C_i & 0 \end{bmatrix} \begin{bmatrix} x_i(t) \\ x_{ai}(t) \end{bmatrix} + \begin{bmatrix} B_i(t) \\ 0 \end{bmatrix} u_i(t) + \begin{bmatrix} 0 \\ -1 \end{bmatrix} r_i(t), \quad (40)$$

where  $x_{ai} = \int_0^t (y_i(\tau) - r_i(\tau)) d\tau$ . Hence, each controlled subsystems with input (19) may be written as

$$\dot{X}_i(t) = \bar{A}_i(t)X_i(t) + \bar{B}_i(t)r_i(t), \quad (41)$$

where  $X_i(t) = \begin{bmatrix} x_i(t) \\ x_{ai}(t) \end{bmatrix}$  is the augmented state for each subsystem and

$$\begin{aligned} \bar{A}_i(t) &= \begin{bmatrix} A_i(t) + B_i(t)K_i & B_i(t)L_i \\ C_i & 0 \end{bmatrix}, \\ \bar{B}_i(t) &= \begin{bmatrix} B_i(t)\bar{N}_i \\ -1 \end{bmatrix}. \end{aligned} \quad (42)$$

The closed-loop global system may be constructed as follows:

$$\dot{X}_g(t) = \bar{A}_{cl}(t)X_g(t) + \bar{B}_{cl}(t)r(t), \quad (43)$$

where  $\bar{A}_{cl} = \text{diag}(\bar{A}_i(t))$  and  $\bar{B}_{cl} = \text{diag}(\bar{B}_i(t))$ , for  $i = 1, \dots, M$ .

As a consequence, the linear time-varying model defined by equation (43) can be expressed in the following polytopic form such as  $\mathbb{M} = [A_{cl} | \bar{B}_{cl}]$  belongs to a polytope of matrices  $\mathcal{M}$  defined by [35]

$$\begin{aligned} \mathcal{M} &= \left\{ \mathbb{M} = M(\theta) = [\bar{A}_{cl}(\theta) | \bar{B}_{cl}(\theta)] / M(\theta) \right. \\ &= \left. \sum_{i=1}^q (\theta_i [\bar{A}_{cli} | \bar{B}_{cli}]) \right\}, \end{aligned} \quad (44)$$

where  $\theta \in \Theta$ , the set of all barycentric coordinates:

$$\Theta = \left\{ \theta = \begin{bmatrix} \theta_1 \\ \theta_2 \\ \vdots \\ \theta_q \end{bmatrix} / \sum_{i=1}^q \theta_i = 1 \right\}. \quad (45)$$

The closed-loop system (43) is a mean square asymptotically stable with an  $H_\infty$  disturbance attenuation  $\gamma$  if and only if there exists a positive definite matrix  $P \in \mathbb{R}^{(n+M) \times (n+M)}$  such that [36]

$$\begin{bmatrix} \bar{A}_{cli}^T P + P \bar{A}_{cli} & P \bar{B}_{cli} & C_g^T \\ \bar{B}_{cli} P & -\gamma I_m & 0 \\ C_g & 0 & -I_p \end{bmatrix} < 0, \quad \forall i = 1, \dots, M. \quad (46)$$

#### 5. Application to Coupled Inverted Pendulums

The considered benchmark [1, 37] consists of two identical pendulums which are coupled through a moving spring and move in a plane (Figure 1). We assume that the pivot position of the moving spring is a function of time  $a(t)$  which can change along the full length  $l$  of the pendulums.

The objective of the decentralized controller is to control each pendulum with mass  $m$  independently, such that each pendulum will follow its own desired (reference) trajectory, while the connected spring is moving. The linearized dynamic equations of the two pendulum systems (for small displacements about the equilibrium) are

$$\begin{aligned} \dot{x}_1 &= \begin{bmatrix} 0 & 1 \\ \frac{g}{l} - \frac{ka(t)^2}{ml^2} & 0 \end{bmatrix} x_1 + \begin{bmatrix} 0 \\ \frac{1}{ml^2} \end{bmatrix} u_1 + \begin{bmatrix} 0 & 0 \\ \frac{ka(t)^2}{ml^2} & 0 \end{bmatrix} x_2, \\ \dot{x}_2 &= \begin{bmatrix} 0 & 1 \\ \frac{g}{l} - \frac{ka(t)^2}{ml^2} & 0 \end{bmatrix} x_2 + \begin{bmatrix} 0 \\ \frac{1}{ml^2} \end{bmatrix} u_1 + \begin{bmatrix} 0 & 0 \\ \frac{ka(t)^2}{ml^2} & 0 \end{bmatrix} x_1, \end{aligned} \quad (47)$$

where  $x_1 = [\theta_1, \dot{\theta}_1]^T$  and  $x_2 = [\theta_2, \dot{\theta}_2]^T$ ,  $k$  and  $g$  are the spring and gravity constants, and  $u_1$  and  $u_2$  are the torque inputs applied at the pivot points.

It is clear that  $a(t) \in [0, l]$ , then we know that the displacement of the pendulums and the connected spring is bounded, so the constant bounds of matrices characterising the two subsystems can be obtained.



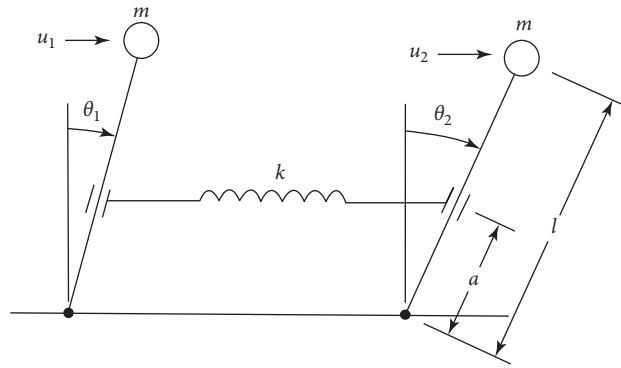


FIGURE 1: Two interconnected inverted pendulums.

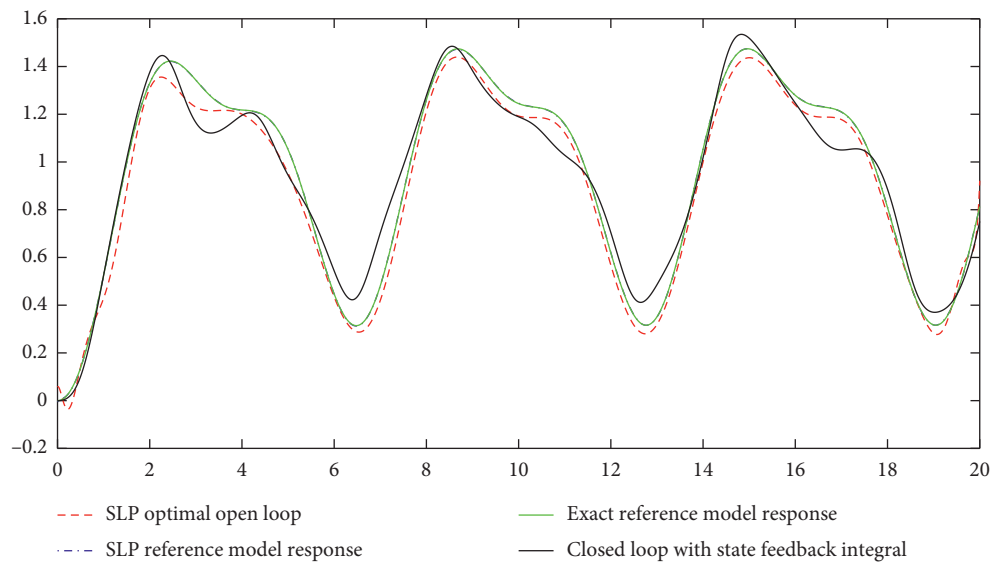


FIGURE 2: Optimal and suboptimal state trajectories of subsystem 1.

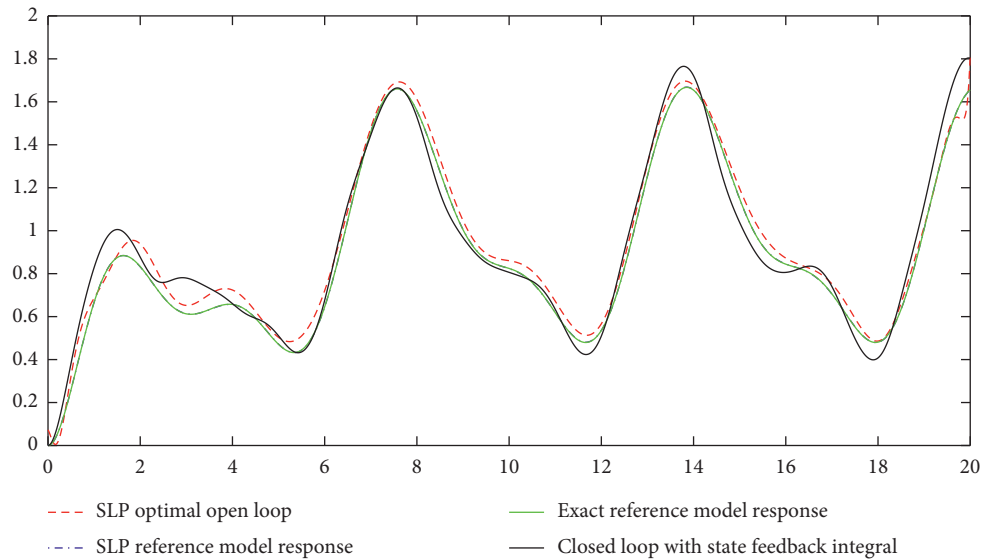


FIGURE 3: Optimal and suboptimal state trajectories of subsystem 2.

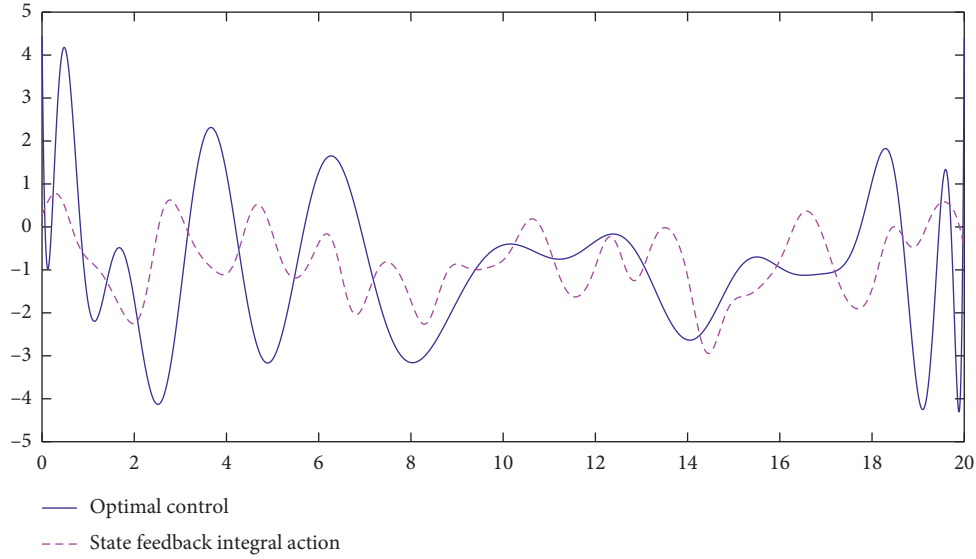


FIGURE 4: Optimal and suboptimal control signals of subsystem 1.

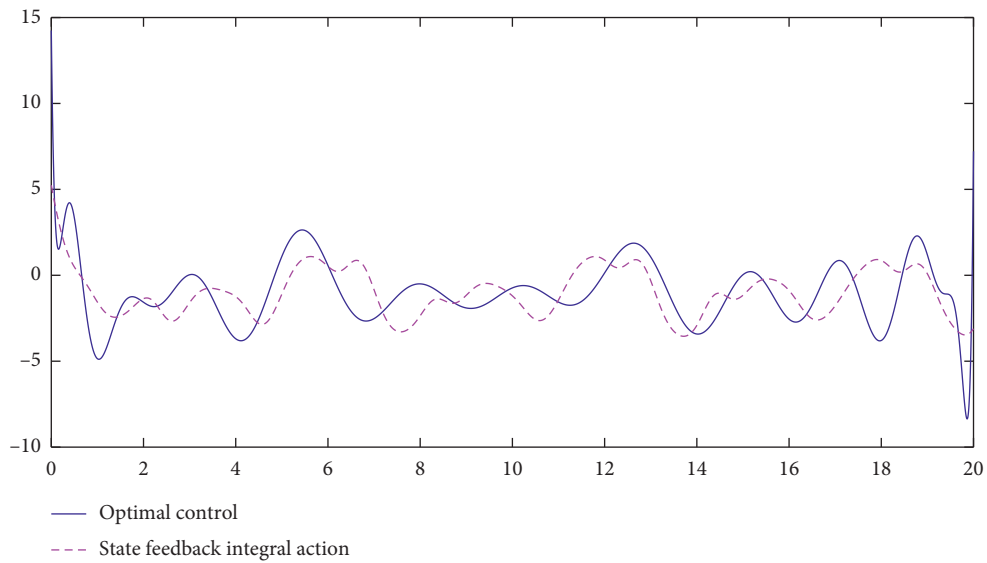


FIGURE 5: Optimal and suboptimal control signals of subsystem 2.

For simulations, we set the time-varying function  $a(t) = (l/2)(1 + \sin(\omega t))$  and choose  $g/l = 1$ ,  $1/ml^2 = 1$ , and let  $kl^2/4 = 25$  and  $\omega = \pi$ .

The reference model (18) for each pendulum is chosen as

$$\begin{aligned} E_{1,2} &= \begin{bmatrix} 0 & 1 \\ -1 & -2 \end{bmatrix}, \\ F_{1,2} &= \begin{bmatrix} 0 \\ 1 \end{bmatrix}, \\ G_{1,2} &= [1 \ 0]. \end{aligned} \quad (48)$$

The reference trajectories used in simulation were chosen as

$$\begin{aligned} r_1(t) &= 1 + \sin(t) + \sin(2t), \\ r_2(t) &= 1 + \cos(t) + \cos(2t). \end{aligned} \quad (49)$$

Optimal open-loop trajectories for both subsystems 1 and 2 are depicted, respectively, in Figures 2 and 3. Optimal tracking results are obtained for the horizon time  $t_f = 20$  and  $N = 26$  which is the shifted Legendre basis dimension. The tracking is ensured by minimising the quadratic criterion with  $Q_{1,2} = \text{diag}(10^3)$  and  $R_{1,2} = 1$ .

The feedback approach applied to the interconnected pendulums leads to the following decentralized state feedback integral actions:

$$\begin{aligned}
\bar{N}_1 &= 0.274, \\
K_1 &= [-7.2635 - 3.6248], \\
L_1 &= -2.9728, \\
\bar{N}_2 &= 1.7476, \\
K_2 &= [-8.3477 - 4.8091], \\
L_2 &= -3.4561.
\end{aligned} \tag{50}$$

Closed loop for both subsystems is also given in Figures 2 and 3. It is then clear that controlled states reproduce the shape of the optimal ones.

State feedback integral actions compared to optimal open-loop inputs are drawn in Figures 4 and 5. It appears that both optimal and suboptimal signals are in the same variation range.

The asymptotic stability with an  $H_\infty$  disturbance attenuation of the closed-loop system is verified by the feasible solution of the formulated LMI. The obtained LMI variables are

$$P = \begin{bmatrix} 2.9401 & 0.4237 & 0.7387 & -0.9920 & -0.1118 & -0.2182 \\ 0.4237 & 0.3752 & 0.2994 & 0.1285 & -0.0110 & -0.0081 \\ 0.7387 & 0.2994 & 2.6532 & -0.4524 & -0.0103 & -0.7878 \\ -0.9920 & 0.1285 & -0.4524 & 3.8961 & 0.6411 & 0.9556 \\ -0.1118 & -0.0110 & -0.0103 & 0.6411 & 0.4731 & 0.3503 \\ -0.2182 & -0.0081 & -0.7878 & 0.9556 & 0.3503 & 3.1039 \end{bmatrix},$$

$$\gamma = 0.3058. \tag{51}$$

## 6. Conclusion

In this paper, a new suboptimal decentralized control technique is designed by using orthogonal functions as an interesting tool of dynamical system approximation, more specifically shifted Legendre polynomials with operational matrices of integration and Kronecker product are exploited.

The main advantage of the proposed technique is its applicability to the class of time-varying interconnected systems. Hence, the suboptimal decentralized state feedback integral controller parameters are adjusted such that each subsystem has a specific desired performance of a chosen reference model by solving a time-independent least-square problem.

In the future work, we intend to extend the actual study to the synthesis of the optimal tracking control for interconnected nonlinear time-varying systems.

## Appendix

### Kronecker Product and $\text{vec}(\cdot)$ Function Property

For any matrices  $X$ ,  $Y$ , and  $Z$  having appropriate dimensions, the following property of the Kronecker product is given [34]:

$$\text{vec}(XYZ) = (Z^T \otimes X)\text{vec}(Y), \tag{A.1}$$

where  $\text{vec}$  denotes the vectorization operator of a matrix [34] and  $\otimes$  stands for the Kronecker product.

Let  $A$ ,  $B$ ,  $C$ , and  $D$  be matrices with appropriate dimensions, and we recall the following property [34]:

$$(A \otimes B)(C \otimes D) = AC \otimes BD. \tag{A.2}$$

## Data Availability

System parameters used for simulation in the paper are given in the manuscript.

## Conflicts of Interest

The authors declare that there are no conflicts of interest regarding the publication of this paper.

## References

- [1] C. Wang and Y. Lin, "Decentralized adaptive tracking control for a class of interconnected nonlinear time-varying systems," *Automatica*, vol. 54, pp. 16–24, 2015.
- [2] C.-H. Xie and G.-H. Yang, "Decentralized adaptive fault-tolerant control for large-scale systems with external disturbances and actuator faults," *Automatica*, vol. 85, pp. 83–90, 2017.
- [3] D. Belogalov, V. Finaev, I. Shapovalov, V. Soloviev, and M. Medvedev, "Decentralized control of a group of robots using fuzzy logic," *Journal of Engineering and Applied Sciences*, vol. 12, no. 9, pp. 2492–2498, 2017.
- [4] A. S. Tlili, "Proportional integral observer-based decentralized stabilization design scheme for nonlinear complex interconnected systems," *Transactions of the Institute of Measurement and Control*, vol. 41, no. 7, pp. 1811–1823, 2018.
- [5] T. N. Pham, S. Nahavandi, H. Trinh, and L. V. Hien, "Decentralized bounded input bounded output stabilization of perturbed interconnected time-delay power systems with energy storages," *International Journal of Electrical Power & Energy Systems*, vol. 93, pp. 51–64, 2017.
- [6] D. Xu, B. Jiang, H. Liu, and P. Shi, "Decentralized asymptotic fault tolerant control of near space vehicle with high order actuator dynamics," *Journal of the Franklin Institute*, vol. 350, no. 9, pp. 2519–2534, 2013.
- [7] H. Hou, X. Nian, S. Xu, M. Sun, and H. Xiong, "Robust decentralized control for large-scale web-winding systems: a linear matrix inequality approach," *Transactions of the Institute of Measurement and Control*, vol. 39, no. 7, pp. 953–964, 2017.
- [8] M. Miranbeigi, B. Moshiri, and A. Rahimi-Kian, "Decentralized manufacturing management by a multi-agent optimal control method," *Transactions of the Institute of Measurement and Control*, vol. 36, no. 8, pp. 935–945, 2014.
- [9] H. Rtibi, S. Elloumi, and N. Benhadj Braiek, "Development of a decentralized nonlinear controller for a class of uncertain polynomial interconnected systems: application for a large scale power system," *Transactions of the Institute of Measurement and Control*, vol. 41, no. 8, pp. 2236–2249, 2019.
- [10] A. Feydi, S. Elloumi, C. Jammazi, and N. Benhadj Braiek, "Decentralized finite-horizon suboptimal control for nonlinear interconnected dynamic systems using SDRE

- approach," *Transactions of the Institute of Measurement and Control*, vol. 41, no. 11, pp. 3264–3275, 2019.
- [11] M. S. Mahmoud, M. F. Hassan, and M. G. Darwish, *Large Scale Control Systems, Theories and Techniques*, Marcel Dekker, New York, NY, USA, 1985.
  - [12] S. Radhoush, M. Samavat, and M. A. Vali, "Optimal control of linear time-varying systems using the Chebyshev wavelets (a comparative approach)," *Systems Science & Control Engineering*, vol. 2, no. 1, pp. 691–698, 2014.
  - [13] S. Stankovic and D. Siljak, "Robust stabilization of nonlinear interconnected systems by decentralized dynamic output feedback," *System and Control Letters*, vol. 58, pp. 271–275, 2009.
  - [14] S. Elloumi, B. Abidi, and N. Benhadj Braiek, "Decentralized optimal controller design for multimachine power systems using successive approximation approach," *Journal of the Franklin Institute*, vol. 350, no. 10, pp. 2994–3010, 2013.
  - [15] S. Dhbaibi, A. S. Tlili, S. Elloumi, and N. Benhadj Braiek, " $H_\infty$  decentralized observation and control of nonlinear interconnected systems," *ISA Transactions*, vol. 48, no. 4, pp. 458–467, 2009.
  - [16] M. Mortezaee and A. Nazemi, "Solving infinite horizon optimal control problems of nonlinear interconnected large-scale dynamic systems via a Haar wavelet collocation scheme," *Iranian Journal of Operations Research*, vol. 6, no. 2, pp. 19–35, 2015.
  - [17] M. Naghnaeian, P. G. Voulgaris, and N. Elia, "A unified framework for decentralized control synthesis," in *Proceedings of the 2018 European Control Conference (ECC)*, Limassol, Cyprus, 2018.
  - [18] M. Mohamed, X.-G. Yan, Z. Mao, and B. Jiang, "Adaptive sliding mode observer for nonlinear interconnected systems with time varying parameters," *Asian Journal of Control*, vol. 21, no. 1, pp. 1–10, 2019.
  - [19] W. Qian, W. Qiangde, Z. W. Zhengqiang, and Z. Zhang, "Decentralized adaptive tracking control for high-order interconnected stochastic nonlinear time-varying delay systems with stochastic input-to-state stable inverse dynamics by neural networks," *Transactions of the Institute of Measurement and Control*, vol. 41, no. 13, pp. 3612–3625, 2019.
  - [20] M. Wan and Y. Yin, "Adaptive decentralized output feedback tracking control for large-scale interconnected systems with time-varying output constraints," *Mathematical Problems in Engineering*, vol. 2020, Article ID 6760521, 14 pages, 2020.
  - [21] I. Malmir, "Optimal control of linear time-varying systems with state and input delays by Chebyshev wavelets," *Statistics, Optimization & Information Computing*, vol. 5, no. 4, pp. 302–324, 2017.
  - [22] C. Hwang and T.-Y. Guo, "Transfer-function matrix identification in MIMO systems via shifted Legendre polynomials," *International Journal of Control*, vol. 39, no. 4, pp. 807–814, 1984.
  - [23] K. B. Datta and B. M. Mohan, *Orthogonal Functions in Systems and Control*, World Scientific Publishing, Singapore, 1995.
  - [24] M. Dadkhah, M. H. Farahi, and A. Heydari, "Optimal control of a class of non-linear time-delay systems via hybrid functions," *IMA Journal of Mathematical Control and Information*, vol. 34, no. 1, pp. 255–270, 2017.
  - [25] B. Iben Warrad, M. K. Bouafoura, and N. Benhadj Braiek, "Static output tracking control for non-linear polynomial time-delay systems via block-pulse functions," *Journal of the Chinese Institute of Engineers*, vol. 41, no. 3, pp. 194–205, 2018.
  - [26] M. K. Bouafoura and N. Benhadj Braiek, "Hybrid functions direct approach and state feedback optimal solutions for a class of nonlinear polynomial time delay systems," *Complexity*, vol. 2019, Article ID 9596253, 14 pages, 2019.
  - [27] S. Bichiou, M. K. Bouafoura, and N. Benhadj Braiek, "Time optimal control laws for bilinear systems," *Mathematical Problems in Engineering*, vol. 2018, Article ID 5217427, 10 pages, 2018.
  - [28] P. Paraskevopoulos and S. G. Mouroutsos, "Legendre series approach to identification and analysis of linear systems," *IEEE Transactions on Automatic Control*, vol. 30, no. 6, pp. 585–589, 1985.
  - [29] G. T. Kekkeris and P. N. Paraskevopoulos, "Hermite series approach to optimal control," *International Journal of Control*, vol. 47, no. 2, pp. 557–567, 1988.
  - [30] C. F. Chen and C. H. Hsiao, "Time-domain synthesis via walsh functions," *Proceedings of the Institution of Electrical Engineers*, vol. 122, no. 5, pp. 565–570, 1975.
  - [31] H. R. Marzban and M. Razzaghi, "Optimal control of linear delay systems via hybrid of block-pulse and Legendre polynomials," *Journal of the Franklin Institute*, vol. 341, no. 3, pp. 279–293, 2004.
  - [32] C. Hwang and M.-Y. Chen, "Analysis and parameter identification of time-delay systems via shifted legendre polynomials," *International Journal of Control*, vol. 41, no. 2, pp. 403–415, 1985.
  - [33] I. S. Gradshteyn and I. M. Ryzhik, *Tables of Integrals*, Academic Press, Cambridge, MA, USA, 1979.
  - [34] J. Brewer, "Kronecker products and matrix calculus in system theory," *IEEE Transactions on Circuits and Systems*, vol. 25, no. 9, pp. 772–781, 1978.
  - [35] J. Bosche and A. El Hajjaji, *An Output Feedback Controller Design for Lateral Vehicle Dynamic*, The International Federation of Automatic Control, Seoul, Korea, 2008.
  - [36] D. Boyd, L. El Ghaoui, E. Peron, and V. Bala-krishnan, *Linear Matrix Inequalities in System and Control Theory*, SIAM Society for Industrial and Applied Mathematics, Philadelphia, PA, USA, 1994.
  - [37] S. K. Singh and L. Shi, "Robust adaptive controllers for interconnected mechanical systems: influence of types of interconnections on time-invariant and time-varying systems," *Journal of Dynamic Systems, Measurement, and Control*, vol. 116, no. 3, pp. 456–473, 1994.

## Research Article

# A Model-Based Decoupling Method for Surge Speed and Heading Control in Vessel Path Following

Xudong Wang,<sup>1</sup> Jin Zhao ,<sup>1</sup> and Tao Geng<sup>2</sup>

<sup>1</sup>Guangdong HUST Industrial Technology Research Institute, Guangdong Province Key Laboratory of Digital Manufacturing Equipment, Key Laboratory of Image Processing and Intelligent Control of the Ministry of Education of China, School of Artificial Intelligence and Automation, Huazhong University of Science and Technology, Wuhan 430074, China  
<sup>2</sup>Guangdong HUST Industrial Technology Research Institute, Dongguan 523000, Guangdong, China

Correspondence should be addressed to Jin Zhao; jinzhao617@163.com

Received 16 March 2020; Accepted 27 June 2020; Published 22 July 2020

Guest Editor: Xiao Ling Wang

Copyright © 2020 Xudong Wang et al. This is an open access article distributed under the Creative Commons Attribution License, which permits unrestricted use, distribution, and reproduction in any medium, provided the original work is properly cited.

In this paper, to solve the surge speed loss problem generated by sway-yaw motion in the path-following control, a model-based decoupling (MBD) method for surge speed and heading control in vessel path following is proposed. The guidance law is designed independently in the kinematic level. In the kinetic level, the surge model and sway-yaw model can be decoupled by assuming that the surge speed varies slowly, and the heading controller and surge speed controller are designed under the framework of the MBD method. Commonly, the surge speed controller is ignored in the path following or designed separately. In the MBD method, the heading controller is designed first through the MPC method, and the coupling terms between the surge model and sway-yaw model are treated as time-varying disturbances, which can be predicted through the outcomes of the heading controller. Then, the time-varying disturbances are compensating in the surge speed controller so that the surge speed can be feedforward compensated to achieve better performance. The simulation results compared the surge speed performance in path following of the MBD method and usual approaches to illustrate the effectiveness of the MBD method.

## 1. Introduction

Unmanned Aerial Vehicle (UAV), Unmanned Ground Vehicle (UGV), and Unmanned surface vessel (USV) have attracted more and more attention in recent years. The unmanned agents have great potentials in applications such as patrol, hydrologic exploration, and transportation when they are cooperative as multiagent systems. The coordinated control for multiagent systems has received increasing attention recently [1–6], also the control of single agent is essential to the whole multiagent system. Path following is a very crucial technology for Unmanned surface vessels (USVs) sailing in the ocean; many applications require that the USVs have the capability to drive to the task area along a predefined path. The purpose of the path following controller is to minimize the error between the real position of USVs and the predefined path in vessel sailing. The path

guidance laws designed at the kinematic level can be used for way-point path following [7–9] and curve path following [10–14]. For example, autopilot is a kind of path-following controller at the kinematic level which has been widely used in ocean transportation.

Many other methods which combine the kinematic model and kinetics model are also proposed to achieve the goal of path following. Some robust nonlinear methods are used to force the vessel to follow the predefined path. In [15], Lyapunov's direct approach and backstepping method are used to design the controller. In [16], several coordinate transformations and the backstepping technique are used to design a global controller for vessel path following. In [17], the backstepping nonlinear controller design is based on feedback dominance, and the experiment results demonstrate the effectiveness of the proposed method. In [18], the path following controller design is divided into two parts via

backstepping technique. In [19], a backstepping-based path-following control algorithm is presented to ensure that the tracking errors of the surface vessel remain within the required performance constraints. In [20], a neural sliding mode controller is designed for vessel path following in the external disturbance and parameter perturbation. In [21, 22], the stability of integral line-of-sight (ILOS) guidance method for a path-following system of underactuated marine vehicles is analyzed. In order to reduce the large cross-track error in turning by adjusting vessel speed, an inverse optimal control method is proposed in [23]. In [24], a reference governor is used for generating the optimal reference signals within the state and input constraints, and the optimization problem is solved by a projection neural network.

It is a challenge to address the actuator saturation and state constraints in controller design for robust nonlinear methods. In [25], the error constraint of the vessel position is handled by integrating a novel tan-type barrier Lyapunov function. However, how to handle lots of different actuators and state constraints is still difficult in the robust method. Due to the advantage of dealing with constraints, many methods under the framework of MPC are proposed to solve path-following problems. In [17], the path-following problem is solved by using a linear MPC controller with rudder and roll constraints. In [26], an LOS decision variable can be incorporated into the MPC design. The lookahead distance is optimized in solving the MPC problem so that the path following has a better performance than the constant lookahead distance LOS method. In [27], a nonlinear state-space model consists of a path following error model and a kinetic model as the tracking model is established; then, a nonlinear MPC controller is designed. In [28], a robust MPC method is proposed for vessel path following control under the constraints of the rudder angle and roll angle. In [29], a nonlinear MPC controller is designed to solve the combined path planning and tracking control problem for an AUV.

In the application of the way-point path following, surge speed control is essential since time constraint is a condition that cannot be ignored. In [7], the speed is controlled through the state feedback linearization method. In [30], different approaches such as proportional-integral and feedback linearization are tested in vessel speed control experiments. Except for designing a speed controller independently, the speed and yaw subsystem can be designed together. In [31], a dynamic window-based controller is used to control the surge speed under the actuator constraints. In [32], the speed and yaw subsystem are controlled through the backstepping and Lyapunov method.

In this paper, to improve the speed and heading controller performance in path following, a model-based decoupling (MBD) method is proposed. The heading controller is designed first under the framework of MPC; then, the coupling terms between the surge model and yaw subsystem are predicted through the output of heading controller. In the speed MPC controller, the coupling terms are compensated as a time-varying disturbance. The speed and heading control of the vessel using a kinetic model is a nonlinear control problem under the framework

of MPC. By using the MBD method, the original nonlinear MPC control problem breaks down into two low-dimensional nonlinear MPC problem or two linear MPC problem.

The organization of this paper is as follows. Section 2 states the problem formulation. Section 3 presents the design of the path following guidance laws and MBD method. Section 4 illustrates and analyzes the simulation results. Section 5 summarizes conclusions.

## 2. Problem Formulation

*2.1. Mathematical Model for Vessel Path Following.* In this section, the kinematic and kinetic model of USVs is introduced first. The vessel model normally is a six degree-of-freedom (DOF) nonlinear model, including surge, lateral, vertical velocity, and pitch, roll, and yaw angle. The states in 6-DOF model such as pitch angle and roll angle can be neglected in path-following control, so, the kinematic model in north-east coordinate such as equation (1a) and the 3-DOF kinetic model proposed in [33] such as equation (1b), are used here to describe path following:

$$\dot{\eta} = R(\eta)v, \quad (1a)$$

$$M\dot{v} + C(v)v + D(v)v = B\tau + \tau_{\text{wind}} + \tau_{\text{wave}}, \quad (1b)$$

where the vector  $\eta = [x \ y \ \psi]^T$  denotes the position and yaw angle in the north-east coordinate and  $R(\eta)$  is the rotation matrix. The detail form of equation (1a) is

$$\dot{x} = u \cos(\psi) - v \sin(\psi), \quad (2a)$$

$$\dot{y} = u \sin(\psi) + v \cos(\psi), \quad (2b)$$

$$\dot{\psi} = r, \quad (2c)$$

where  $v = [u \ v \ r]^T$  denotes the surge velocity, lateral velocity, and yaw angle velocity in the body-fixed coordinate. Vector  $\tau = [\tau_x \ 0 \ \tau_z]^T$  denotes actuator force and torques,  $\tau_{\text{wind}}$  denotes force and torques caused by wind,  $\tau_{\text{wave}}$  denotes force and torques caused by the wave,  $M$  accounts for inertial effects, matrix  $C(v)$  accounts for centrifugal and Coriolis effects, and matrix  $D(v)$  accounts for viscous and dissipative effects. The exact expression of the matrix is

$$M = \begin{bmatrix} m - Xu & 0 & 0 \\ 0 & m - Y_v & mX_g - Y_f \\ 0 & mX_g - N_v & I_z - N_r \end{bmatrix},$$

$$C(v) = \begin{bmatrix} 0 & 0 & c13 \\ 0 & 0 & c23 \\ -c13 & -c23 & 0 \end{bmatrix}, \quad (3)$$

$$D(v) = \begin{bmatrix} d11 & 0 & 0 \\ 0 & d22 & d23 \\ 0 & d32 & d33 \end{bmatrix},$$

where

$$\begin{aligned}
c13 &= -m(X_g r + v) + Y_{\dot{v}} v + \frac{1}{2}(Y_r + N_v)r, \\
c23 &= mu - X_{\dot{u}} u, \\
d11 &= -X_u - X_{|u|u}|u| - X_{uu}u^2, \\
d22 &= -Y_v - Y_{|v|v}|v| - Y_{|r|v}|r|, \\
d23 &= -Y_r - Y_{|v|r}|v| - Y_{|r|r}|r|, \\
d32 &= -N_v - N_{|v|v}|v| - N_{|r|r}|r|, \\
d33 &= -N_r - N_{|v|r}|v| - N_{|r|r}|r|.
\end{aligned} \tag{4}$$

The vessel named CyberShip II in [33] has two main propellers, two rudders aft, and one bow thruster fore. For simple but without loss of generality, the vessel model of CyberShip II used in this paper has no bow thruster, but one propeller and one rudder. The surging force generated by one propeller is equal to two propellers of CyberShip II, and so is the steering moment. The exact expression of actuator configuration matrix  $B$  is

$$B = \begin{bmatrix} 2 & 0 \\ 0 & 2 \\ 0 & -|l_x R_1| - |l_x R_2| \end{bmatrix}. \tag{5}$$

The kinetic model can be rewritten as  $\dot{v} = -M^{-1}C(v)v + M^{-1}D(v)v + M^{-1}B\tau$ . The detail form of the kinetic model is

$$\dot{u} = a_1 u + a_2 u^2 + a_3 u^3 + a_4 vr + a_5 r^2 + a_6 u^2 \delta^2 + a_7 \tau_x, \tag{6a}$$

$$\dot{v} = b_1 uv + b_2 ur + b_3 v|v| + b_4 v|r| + b_5 r|v| + b_6 r|r| + b_7 \tau_z, \tag{6b}$$

$$\dot{r} = c_1 uv + c_2 ur + c_3 v|v| + c_4 v|r| + c_5 r|v| + c_6 r|r| + c_7 \tau_z. \tag{6c}$$

**2.2. Path-following Formulation.** The guidance law used in this paper is designed at the kinematic level. Usually, the  $C^1$  parametrized path  $(x_p(\theta), y_p(\theta))$  with  $\theta \geq 0$  are used to denote path including curve path or way-point path. In this paper, the cross-error of the path following is our concern, and the expected surge speed is given by manual. Since many path-following guidance laws are valid in both curve path following and way-point path following, the situation of the way-point path following is only considered in this paper for simplicity. For a vessel located at  $(x, y)$ , the orthogonal distance  $y_e$  to the path can be calculated by equation (7) proposed in [10]:

$$y_e = -(x - x_p)\sin(\theta) + (y - y_p)\cos(\theta), \tag{7}$$

where  $\theta$  is the slop of straight line between two way-point  $(x_i, y_i)$  and  $(x_{i+1}, y_{i+1})$ , for  $i = 1, 2, \dots, N$ , and  $\theta$  can be

calculated by  $\theta = \tan^{-1}(y_{i+1} - y_i / x_{i+1} - x_i)$ . The cross point  $(x_p, y_p)$  can be calculated by the following equation.

$$\begin{cases} y_{i+1} - y_p = \tan(\theta)(x_{i+1} - x_p), \\ y - y_p = -\frac{1}{\tan(\theta)}(x - x_p), \quad \theta \neq 0 \text{ and } \theta \neq \frac{\pi}{2}, \end{cases} \tag{8}$$

when  $\theta = 0$ , cross point  $(x_p, y_p) = (x, y_{i+1})$ , and when  $\theta = \pi/2$ , cross point  $(x_p, y_p) = (x_{i+1}, y)$ .

Equation (7) is differentiable, and the differential form is

$$\frac{\partial y_e}{\partial \psi} = -(u \cos(\psi) - v \sin(\psi))\sin(\theta) + (u \sin(\psi) \tag{9}$$

$$+ v \cos(\psi)\cos(\theta).$$

Equation (9) can be written in a more compact form as

$$\dot{y}_e = U \sin(\psi - \theta + \beta), \tag{10}$$

where  $U = \sqrt{u^2 + v^2}$  and  $\beta = \tan^{-1}(v/u)$  is the speed sideslip angle. In this paper, all the states including sideslip assumption can be measured directly. Assuming that sideslip angle  $\beta$  is small and constant implies  $\cos(\beta) \approx 1$  and  $\sin(\beta) \approx \beta$ . Equation (10) can be simplified as

$$\dot{y}_e = U \sin(\psi - \theta) + U \cos(\psi - \theta)\beta. \tag{11}$$

### 3. MBD Method for Surge Speed and Heading Control

In this section, the path-following guidance law is introduced first, since the focus of this paper is the MBD method, and the path-following guidance law equation (12) proposed in [10] is used in this paper to generated reference heading  $\psi_d$ ; the stability of the guidance laws can be referred to [10]

$$\psi_d = y_p + \tan^{-1}\left(\frac{1}{\Delta} y_e + \beta\right). \tag{12}$$

Robust nonlinear methods such as the backstepping method and direct Lyapunov method can be used to design surge speed and heading controller based on the nonlinear 3-DOF maneuvering model. However, these methods cannot handle the constraints of state and actuator. Also, it is a challenge to design such a controller when the maneuvering model is complex.

The nonlinear MPC method based on the 3-DOF maneuvering model can be used to control heading and surge speed together under the constraints [34]; the solution of the nonlinear MPC problem can only be solved through numerical iteration methods such as Gauss-Newton method. All solutions based on gradient iteration method can only guarantee the local minimum, also it is a huge computation burden for on-board computer in real-time control.

To reduce the complexity of designing controller, usually, the surge speed controller and heading controller are designed independently due to which the 3-DOF maneuvering model can be decoupled in a forward speed (surge) model and a sway-yaw subsystem for maneuvering [35]. The

independent surge speed and heading controller both have good performance when the reference heading and reference speed are steady. However, there is an inevitable speed loss when there is sway-yaw motion.

The MBD method for surge speed and heading control are designed under the framework of MPC. Figure 1 shows the guidance and control architecture for vessel path following. The MPC heading controller is designed independently based on the sway-yaw model linearized at a given work point. The MPC surge speed controller is also based on the linearized surge model. The time-varying added resistance generated by sway-yaw motion is only considered in the process of solving the optimal sequence, which does not add much computation burden. The nonlinear MPC problem breaks down into two low-dimensional linear MPC problem through the MBD method. Since the heading controller and the surge speed controller are designed independently, it is much more convenient for parameters turning in the controller design process.

During every MBD method control interval, the MPC heading controller is solved first. Then, the coupling terms of the surge model are calculated through the outcome sequence of the MPC heading controller, and these coupling terms are treated as time-varying added resistance. Next, the MPC surge model is solved considering the time-varying added resistance. Finally, the first element of the heading controller outcome sequence and the speed controller outcome sequence are used as controller output.

The rest of this section now focuses on the derivation of the MBD method.

**3.1. Heading Controller.** In this section, the MPC heading controller with actuator constraints is first designed. The purpose of the heading controller is to steer the vessel heading to the expected heading  $\psi_d$ .

During the path-following task, the surge speed is controlled by a speed controller, so we assume that the surge speed is constant during every control interval, and the sway-yaw subsystem equations (6b) and (6c) can be decoupled from an original nonlinear system. The linear state-space model is derived by linearizing the sway-yaw subsystem at a given work point to reduce the complexity of designing the controller. Assuming surge speed  $u = u_o$ , lateral velocity  $v \approx 0$ , yaw angular velocity  $r \approx 0$ , and the right hand of equations (6b) and (6c) can express in a Taylor series by taking the partial derivative. By retaining the first-order terms of Taylor series and incorporating equation with  $\dot{\psi} = r$ , the linearized sway-yaw subsystem can be written as

$$\dot{x} = A_c x + B_c \tau z, \quad (13)$$

$$\text{where } \dot{x} = \begin{bmatrix} \dot{v} \\ \dot{r} \\ \dot{\psi} \end{bmatrix}, A_c = \begin{bmatrix} b_1 u & b_2 u & 0 \\ c_1 u & c_2 u & 0 \\ 0 & 1 & 0 \end{bmatrix}, \text{ and } B_c = \begin{bmatrix} b_7 \\ c_7 \\ 0 \end{bmatrix}.$$

The controllers are designed in a discrete form; the heading model can be simplified to a first-order transfer

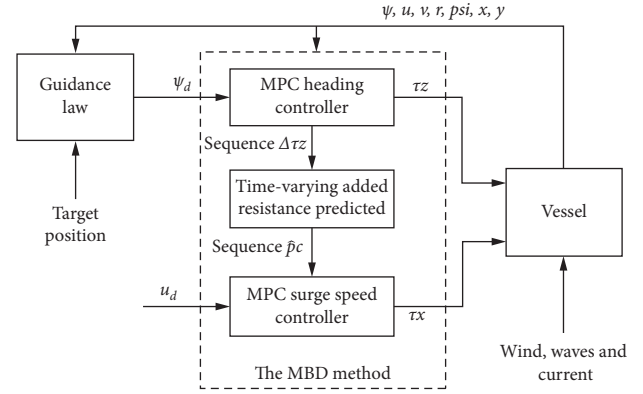


FIGURE 1: Architecture of the MBD method.

function model. Normally, the sampling interval  $T_s$  is chosen as one-tenth of the time constant in the simplified first-order function model. When the sampling interval  $T_s$  is given, the discrete form of equation (13) can be easily calculated by the following transform:

$$x_{k+1} = A_d x_k + B_d \tau z_k, \quad (14)$$

where  $x_{k+1} = [v_{k+1} \ r_{k+1} \ \psi_{k+1}]^T$ ,  $A_d = e^{A_c T_s}$ , and  $B_d = \int_0^{T_s} e^{A_c T} dt B_c$ . Due to the effect of wind, current, wave, and unknown disturbance, the predicted progress incorporating the external disturbance  $d$  is used to correct the prediction results at every control interval. For the simplicity of solving online optimization, equation (14) is written in the augmented form as

$$z_{k+1} = A z_k + B \Delta \tau z_k + d_k, \quad (15a)$$

$$\psi_{k+1} = C z_{k+1}, \quad (15b)$$

where  $z_{k+1} = \begin{bmatrix} v_{k+1} \\ r_{k+1} \\ \psi_{k+1} \\ \tau z_{k+1} \end{bmatrix}$ ,  $A = \begin{bmatrix} A_d & B_d \\ 0 & I \end{bmatrix}$ ,  $B = \begin{bmatrix} B_d \\ I \end{bmatrix}$ ,  $C = [0 \ 0 \ 1 \ 0]$ , and  $I$  is the identity matrix.

As we all know, the energy output by the physical system is not infinite, and the torque force generated by vessel actuators such as a rudder or water-jet system has the torque rate constraints and bounded value constraints. So, the constraints of the actuator are considered in the heading control online optimal progress,  $\Delta \underline{\tau z}$  and  $\Delta \overline{\tau z}$  are the lower and upper bounds of the  $\tau z$  varying rate, respectively, and  $\underline{\tau z}$  and  $\overline{\tau z}$  are the lower and upper bounds of the  $\tau z$  value, respectively.

The cost function consists of two quadratic terms, the heading error quadratic term guarantee that the real heading convergence to the reference heading and the rudder varying rate quadratic term can reduce the rudder movement. Then, the heading control problem is transformed into a constrained online optimization problem as equation (16),  $N_p$  is the prediction horizon, and  $N_u$  is the control horizon:



$$\begin{aligned} \min J(z_k, \Delta\tau z) &= \sum_{j=1}^{N_p} (Cz_{k+j} - \psi_d)^T Q (Cz_{k+j} - \psi_d) \\ &+ \sum_{j=1}^{N_u} \Delta\tau z_{k+j}^T R \Delta\tau z_{k+j}, \end{aligned} \quad (16)$$

which subjects to

$$\underline{\Delta\tau z} \leq \Delta\tau z_{k+j-1} \leq \overline{\Delta\tau z}, \quad j = 1, 2, \dots, N_u, \quad (17a)$$

$$\underline{\tau z} \leq \tau z_{k+j} \leq \overline{\tau z}, \quad j = 1, 2, \dots, N_u. \quad (17b)$$

The online optimization problem equation (16) can be transformed into a quadratic problem to solve the optimal solution sequence  $\Delta\tau z^* = \{\Delta\tau z_k^*, \Delta\tau z_{k+2}^*, \dots, \Delta\tau z_{k+N_u-1}^*\}$  at each time  $k$ . According to equations (15a) and (15b), the state prediction with prediction horizon  $N_p$  and control horizon  $N_u$  can be written as

$$\psi_{\text{pre}} = Pz_k + H\Delta\tau z + Ed_k, \quad (18)$$

where  $\psi_{\text{pre}} = \begin{bmatrix} \psi_{k+1} \\ \psi_{k+2} \\ \vdots \\ \psi_{k+N_p} \end{bmatrix}$ ,  $P = \begin{bmatrix} CA \\ CA^2 \\ \vdots \\ CA^{N_p} \end{bmatrix}$ ,  $H = \begin{bmatrix} CB & 0 & \dots & 0 \\ \vdots & \vdots & \vdots & \vdots \\ CA^{N_u-1}B & CA^{N_u-2}B & \dots & B \\ \vdots & \vdots & \vdots & \vdots \\ CA^{N_u-1}B & CA^{N_u-2}B & \dots & B \end{bmatrix}$ , and  $E = \begin{bmatrix} C \\ CA + I \\ \vdots \\ \sum_{j=0}^{N_p-1} CA^j \end{bmatrix}$ . The

disturbance at time  $k$  is updated by the error of real state and predicted state as

$$d_k = z_k - (Az_{k-1} + B\Delta\tau z_{k-1}). \quad (19)$$

Substituting equation (18) into equation (16) and ignoring the constant value terms which do not affect the solution of solving the optimization problem, the cost function can be written as a quadratic form:

$$\min J(z_k, \Delta\tau z) = \frac{1}{2} \Delta\tau z^T S \Delta\tau z + f^T \Delta\tau z. \quad (20)$$

Matrix  $S = H^T Q H + R$  is the quadratic objective term, and matrix  $f = H^T Q (Pz_k + Ed_k - \psi_d)$  is the linear term. The constrained quadratic programming can be solved by the numerical method. The controller output  $\tau z_k = \tau z_{k-1} + \Delta\tau z_k$ , and  $\Delta\tau z_k$  is the first element of  $\Delta\tau z^*$ . The stability of the MPC controller without terminal constraints can be guaranteed by choosing a large prediction horizon [36].

**3.2. Surge Speed Controller.** In this section, the MPC surge speed controller with surge force constraints is designed. Under the framework of MPC, the constraints of the state and actuator can be handled easily. The standard MPC (SMPC) method is first introduced to the design surge speed controller; then, the surge speed controller based on the MBD method is introduced. The discretized linear surge

model equation (21) can be derived by linearizing the nonlinear surge model equation (6a) at a given work point:

$$u_{k+1} = A_1 u_k + B_1 \tau x, \quad (21)$$

where  $A_1 = e^{a_1 T_s}$  and  $B_1 = \int_0^{T_s} e^{a_1 T_s} dt a_7$ .

When a vessel is in the surge motion, yawing motion due to steering can result in added resistance in calm water as well as yawing due to wave motion [37], and the added resistance can significantly reduce surge speed. Usually, the surge speed controller is designed independently based on the linear surge model equation (21) through the standard MPC method and all the disturbance, including the added resistance and the effect of the wave, wind, and current are treated as an unknown disturbance.

The derivation of the SMPC method is introduced as follows. Considering the unknown disturbance  $\omega$  and re-writing the surge model equation (21) as augmented for simplicity, the modified surge model is

$$y_{k+1} = A_u y_k + B_u \tau x_k + du_k, \quad (22a)$$

$$u_{k+1} = C_u y_{k+1}, \quad (22b)$$

where  $y_{k+1} = \begin{bmatrix} u_{k+1} \\ \tau x_{k+1} \end{bmatrix}$ ,  $A_u = \begin{bmatrix} A_1 & B_1 \\ 0 & 1 \end{bmatrix}$ ,  $B_u = \begin{bmatrix} B_1 \\ 1 \end{bmatrix}$ ,

$du_k = \begin{bmatrix} \omega_k \\ 0 \end{bmatrix}$ , and  $C_u = [1 \ 0]$ . The disturbance  $\omega_k$  at time  $k$  is updated by the error of real surge speed and predicted surge speed as

$$\omega_k = u_k - (A_1 u_{k-1} + B_1 \Delta\tau x_{k-1}). \quad (23)$$

Then, the augmented surge model is used to construct a MPC controller.

Based on the modified surge model, the surge speed control problem with excepted surge speed  $u_d$  now is an online optimization problem as cost function equation (24). The speed error quadratic term in equation (24) grantee that the real speed convergence to the reference speed and the force varying rate quadratic term in equation (24) can reduce the force varying. The first element of optimal solution sequence  $\Delta\tau x^* = \{\Delta\tau x_k^*, \Delta\tau x_{k+2}^*, \dots, \Delta\tau x_{k+N_u-1}^*\}$  is the surge force increment at each time  $k$ . The prediction horizon is  $N_{pu}$ , and control horizon is  $N_{uu}$ :

$$\begin{aligned} \min J(y_k, \Delta\tau x) &= \sum_{j=1}^{N_{pu}} (C_u y_{k+j} - u_d)^T Q (C_u y_{k+j} - u_d) \\ &+ \sum_{j=1}^{N_{uu}} \Delta\tau x_{k+j}^T R \Delta\tau x_{k+j}, \end{aligned} \quad (24)$$

which subjects to

$$\underline{\Delta\tau x} \leq \Delta\tau x_{k+j-1} \leq \overline{\Delta\tau x}, \quad j = 1, 2, \dots, N_{uu}, \quad (25a)$$

$$\underline{\tau x} \leq \tau x_{k+j} \leq \overline{\tau x}, \quad j = 1, 2, \dots, N_{uu}. \quad (25b)$$

The drawback of the SMPC is that there will be no compensating force of disturbance until there is an offset in

surge speed since the process of updating disturbance  $\omega$  at time  $k$  always occurs at the next control interval. The MBD method is proposed in this paper to overcome the delay in updating disturbance. In the MBD method, the sway-yaw motion due to the steering is predicted by the actuator sequence  $\Delta\tau\mathbf{z}^*$  and compensated as a time-varying disturbance  $\widehat{\mathbf{p}}\mathbf{c} = \{\widehat{p}c_k, \widehat{p}c_{k+1}, \dots, \widehat{p}c_{k+N_{pd}-1}\}$  in forward speed control. The calculation of  $\widehat{\mathbf{p}}\mathbf{c}$  involves several steps, as described in the sequel:

- (1) At time  $k$ , calculate the predicted sequence of  $\widehat{\mathbf{v}}, \widehat{\mathbf{r}}$  through equations (15a) and (15b) by using  $\Delta\tau\mathbf{z}^*$ .
- (2) Calculate the time-varying disturbance  $\widehat{p}c_k$  by using part terms of equation (6a),  $\widehat{p}c_k = a_4 v_k r_k + a_5 r_k^2$ . The states  $v_k$  and  $r_k$  are measured directly at present time  $k$ .
- (3) Calculate the rest of time-varying disturbance sequence by using part terms of equation (6a),  $\widehat{p}c_{k+1} = a_4 \widehat{v}_{k+1} \widehat{r}_{k+1} + a_5 \widehat{r}_{k+1}^2$ . The predicted state  $\widehat{v}_{k+j}$  and  $\widehat{r}_{k+j}$ ,  $j = 1, \dots, N_{pd} - 1$ , are calculated at step 1.

Substituting  $\widehat{\mathbf{p}}\mathbf{c}$  into equations (22a) and (22b), the surge model is modified as follows:

$$y_{k+1} = A_u y_k + B_u \tau x_k + d u_k, \quad (26a)$$

$$u_{k+1} = C_u y_{k+1} + \widehat{p}c_k, \quad (26b)$$

and the equation of updating  $\omega_k$  is modified as

$$\omega_k = u_k - (A_1 u_{k-1} + B_1 \Delta\tau x_{k-1} + \widehat{p}c_{k-1}). \quad (27)$$

The cost function based on equations (26a) and (26b) and equation (27) can be written as

$$\min J(y_k, \Delta\tau x) = \sum_{j=1}^{N_{pu}} (C_u y_{k+j} + \widehat{p}c_{k+j-1} - u_d)^T Q (C_u y_{k+j} + \widehat{p}c_{k+j-1} - u_d) + \sum_{j=1}^{N_u} \Delta\tau x_{k+j}^T R \Delta\tau x_{k+j}^T, \quad (28)$$

which subjects to

$$\Delta \underline{\tau x} \leq \Delta\tau x_{k+j-1} \leq \Delta \overline{\tau x}, \quad j = 1, 2, \dots, N_{uu}, \quad (29a)$$

$$\underline{\tau x} \leq \tau x_{k+j} \leq \overline{\tau x}, \quad j = 1, 2, \dots, N_{uu}. \quad (29b)$$

Also, the online optimization problem equations (25a), (25b), and (28) can be transformed into constrained quadratic programming, the controller output  $\tau x_k = \tau x_{k-1} + \Delta\tau x_k$ , and  $\Delta\tau x_k$  is the first element of  $\Delta\tau\mathbf{x}^*$ . The stability of the MPC controller can be guaranteed by choosing a large prediction horizon  $N_{pu}$ . Since the focus of this paper is the performance of the MBD method, the detailed proof of MPC stability can be referred to [36].

## 4. Simulation Results

In this section, the results of the way-point path following are presented. The simulation results of the MBD method and the standard MPC (SMPC) method are compared to illustrate the

TABLE 1: The parameters of the vessel.

$m$	23.8
$I_z$	17.6
$x_g$	0.046
$X_{udot}$	-2.0
$X_u$	-0.72253
$X_{absuu}$	-1.32742
$X_{uuu}$	-5.86643;
$Y_{vdot}$	-10.0
$Y_{rdot}$	-0.0
$Y_v$	-0.88965
$Y_{absvv}$	-36.47287
$Y_{absrv}$	-0.805
$Y_r$	-7.250
$Y_{absvr}$	-0.845
$Y_{absrr}$	-3.450
$N_{vdot}$	0
$N_{rdot}$	-1.0
$N_v$	0.03130
$N_{absvv}$	3.95645
$N_{absrv}$	0.130
$N_r$	-1.900
$N_{absvr}$	0.080
$N_{absrr}$	-0.750
$I_{xR1}$	-0.549
$I_{xR2}$	-0.549

superiority of the MBD method. Then, a time-varying disturbance incorporating white noise and constant offset force is added in path-following simulations to demonstrate the effectiveness and robustness of the MBD method. The parameters of the vessel are given in [33] and listed in Table 1.

In the simulation, the parameter  $\Delta$  in guidance law is chosen as  $\Delta = 8$  m. In the heading MPC Controller, the prediction horizon  $N_p$  and control horizon  $N_u$  are chosen as 70 and 30, respectively. The matrix  $Q_h$  is an identity matrix with dimension  $N_p \times N_p$ , the matrix  $R_h$  is also an identity matrix with dimension  $N_u \times N_u$ . In the surge speed controller, the prediction horizon  $N_{pu}$  and control horizon  $N_{uu}$  are chosen as 30 and 5, respectively. The matrix  $Q_u$  is an identity matrix with dimension  $N_{pu} \times N_{pu}$ ; the matrix  $R_u$  is also an identity matrix with dimension  $N_{uu} \times N_{uu}$ . In the surge speed controller, the vessel initial forward speed of the vessel is set at 0.5 m/s and the other state of vessel are all set to zero. The constraints of surge force are  $|\tau x| \leq 5$ . The constraints of steering moment are  $|\tau z| \leq 1$ , and the steering moment increment is  $|\Delta\tau z| \leq 0.5$ .

The path-following results of different methods with no external disturbance are shown in Figure 2, and the corresponding surge speed and surge force  $\tau x$  are shown in Figure 3. From the results shown in Figure 2, we can see that the path following results of different methods are very close and the actual path of the vessel converges to the reference path eventually.

In the surge speed control, as shown in Figure 3, the commanded speed is 0.8 m/s at the first 200 s then changed to 0.6 m/s. All the surge control method can guarantee the surge speed converge to the command speed. Due to the way-point changed, the sway and yawing motion result in added resistance. There is some speed loss in path following

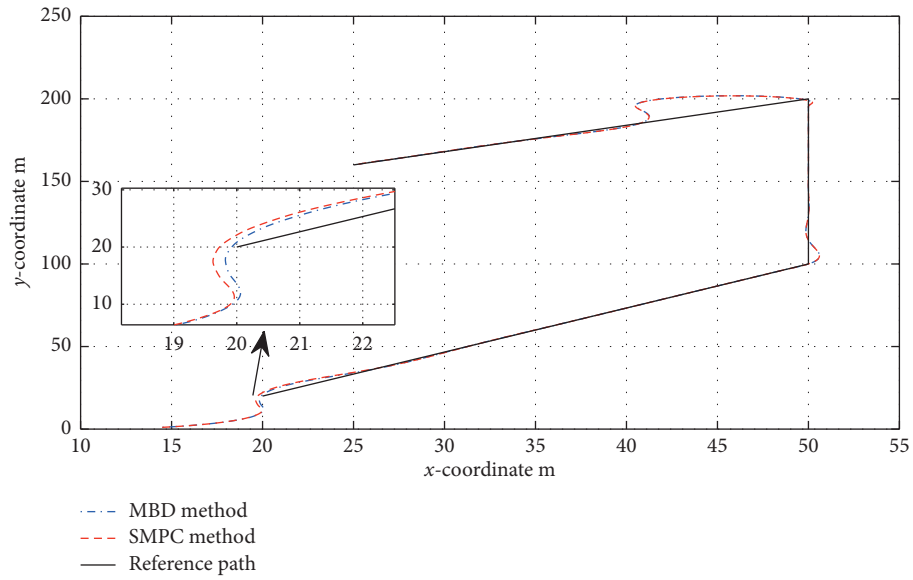
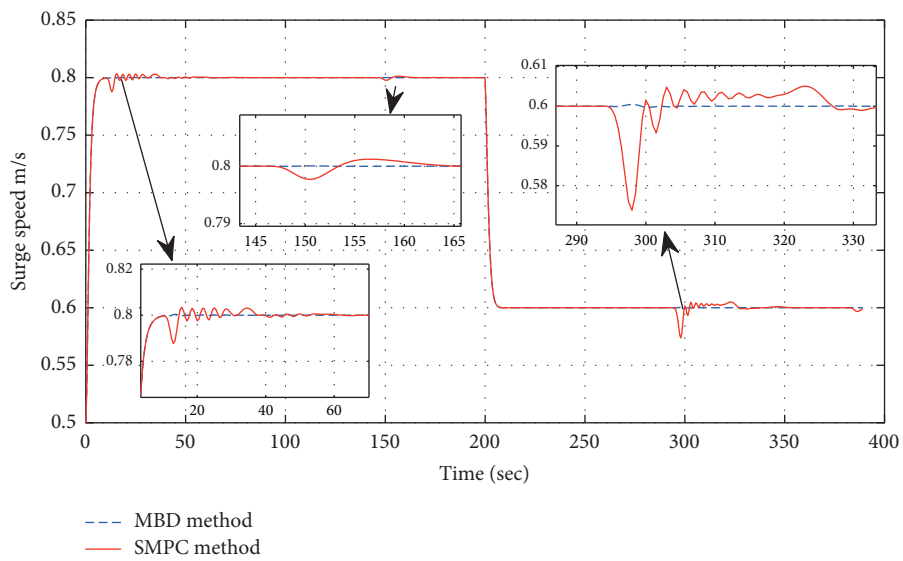
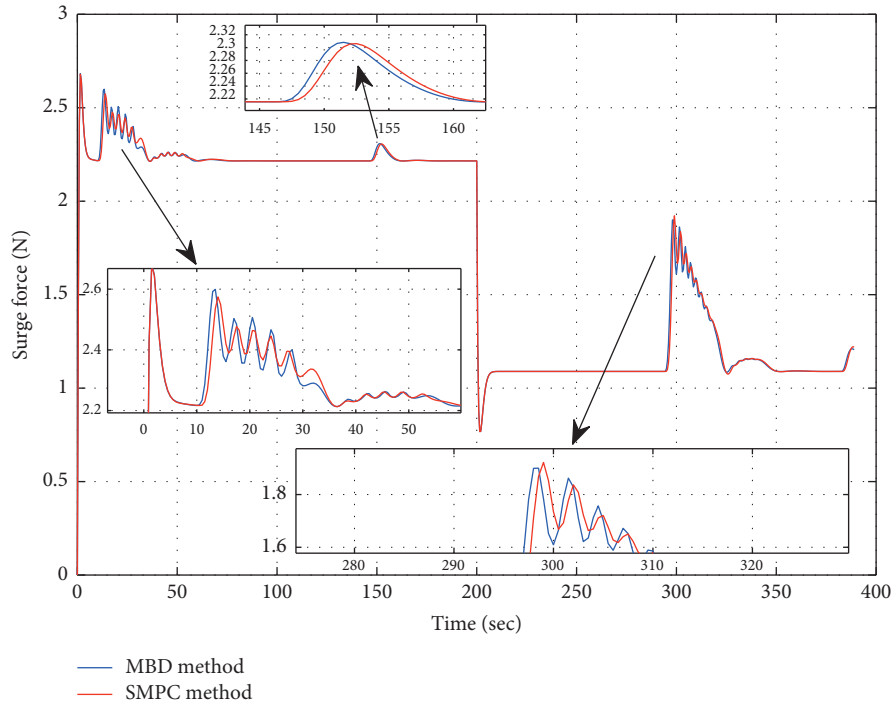


FIGURE 2: Path following results of different methods.



(a)

FIGURE 3: Continued.



(b)

FIGURE 3: Surge speed control performance of different methods. (a) Surge speed in path following of different methods. (b) Surge force in path following of different methods.

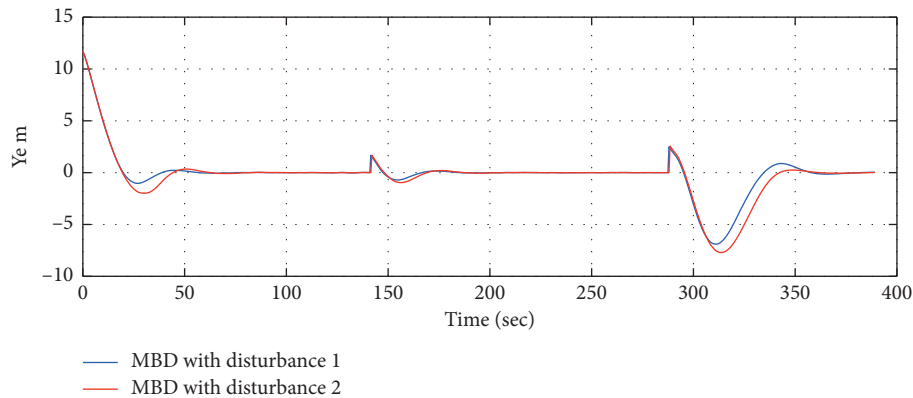


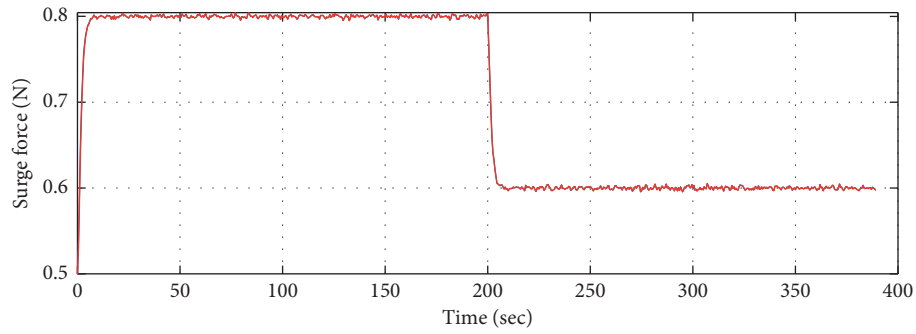
FIGURE 4: Cross-error in path following under different disturbances.

under the SMPC control method, but there are no significant fluctuations in surge speed under the control of the MBD method, see Figure 3(a) at about 20 s, 150 s, and 300 s. From the surge force output by different methods shown in Figure 3(b), we can see, comparing the surge force output by the MBD method and the SMPC method, that the surge force output by SMPC controller has a time delay when there is an add resistance. Moreover, the time delay of surge force is the reason why there is a significant surge speed loss in speed control.

In the MBD method, the sway and yawing motion generated by the steering moment is predicted as a time-

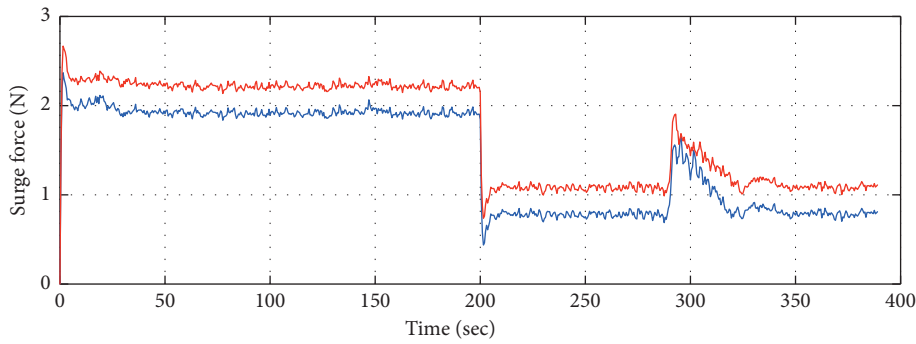
varying disturbance, which is compensated at the speed control. Nevertheless, in SMPC control, there will be no external force to compensate disturbance until there is an offset in surge speed. So, the MBD method has a better performance than the SMPC method in heading and speed control of the vessel in path following.

To further demonstrate the effectiveness of the MBD method in the real sea environment, the path following results with time-varying disturbance is shown in Figures 4–6. The disturbance one shown in Figures 5 and 6 consists of white noise with noise power of 0.0025, and a constant force of 0.3N; the disturbance two shown in



— MBD with disturbance 1  
— MBD with disturbance 2

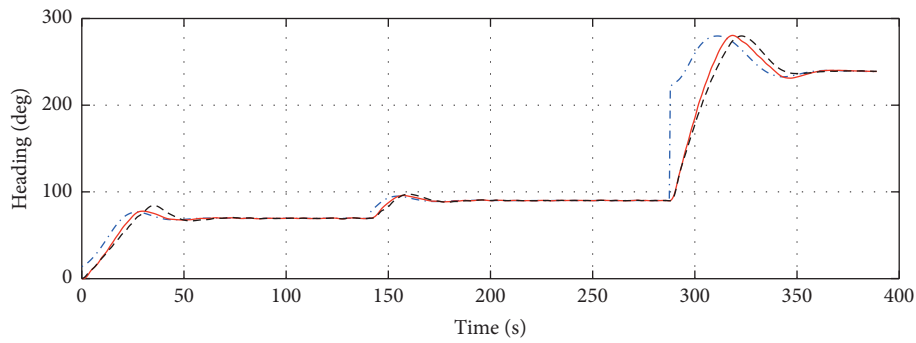
(a)



— MBD with disturbance 1  
— MBD with disturbance 2

(b)

FIGURE 5: Surge speed in path following under different disturbances. (a) Surge speed control results under different disturbances. (b) Surge force results under different disturbances.



- - -  $\psi_d$   
—  $\psi$  with disturbance 1  
- - -  $\psi$  with disturbance 2

(a)

FIGURE 6: Continued.

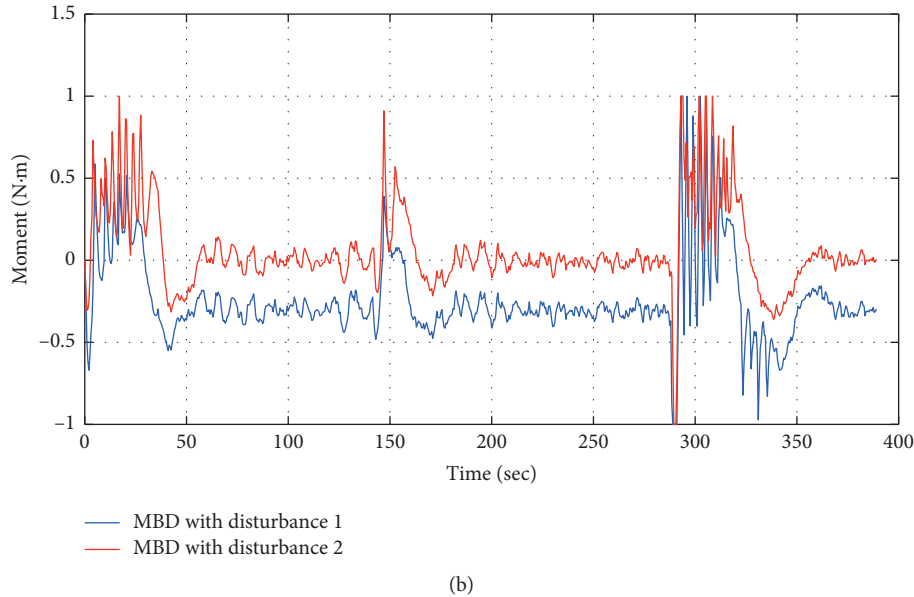


FIGURE 6: Heading control results in path following under different disturbances. (a) Heading control results under different disturbances. (b) Steering moment under different disturbances.

Figures 5 and 6 is a white noise with noise power of 0.0025.

From Figure 4, we can see that the cross error  $Y_e$  in path following converges to zero; the addition unknown time-varying disturbance has no influence in the overall performance. The heading and speed control results shown in Figures 5 and 6 demonstrate the effectiveness of the MBD method under unknown time-varying disturbance. Also, the steering moment  $\tau z$ , the increment of steering moment  $\Delta\tau z$ , and the surge force  $\tau x$  are all restricted to the constraints.

## 5. Conclusions

In this paper, to solve the surge speed loss in path following due to the added resistance generated by sway-yaw motion, the MBD method for surge speed and heading control in vessel path following is presented. In the MBD method, the heading controller and the surge speed controller can be designed under the framework of MPC, independently. The nonlinear control problem of control vessel heading and controller together can be decoupled into two MPC control problems based on the linear heading model and linear surge model, which makes the progress of designing the controller easier. The output of the heading controller is used to predict the time-varying add resistance, which is treated as time-varying disturbance and compensated in surge speed control.

Compared to the control results of the SMPC method, the surge speed has no significant fluctuations in path following under the control of the MBD method, which demonstrates the superiority of the MBD method. The path-following results under the unknown time-varying disturbance demonstrate the effectiveness and robustness of the MBD method.

## Data Availability

The data used to support the findings of this study are included within the article.

## Conflicts of Interest

The authors of this paper declare that there are no conflicts of interest regarding the publication of this article.

## Acknowledgments

This work was supported in part by the Guangdong Innovative and Entrepreneurial Research Team Program under Grant 2014ZT05G304 and National Natural Science Foundation of China under Grants 61573159 and 61273174.

## References

- [1] X. Wang, H. Su, X. Wang, and G. Chen, "Fully distributed event-triggered semiglobal consensus of multi-agent systems with input saturation," *IEEE Transactions on Industrial Electronics*, vol. 64, no. 6, pp. 5055–5064, 2016.
- [2] X. L. Wang, H. Su, M. Z. Chen, X. F. Wang, and G. Chen, "Reaching non-negative edge consensus of networked dynamical systems," *IEEE Transactions on Cybernetics*, vol. 48, no. 9, pp. 2712–2722, 2018.
- [3] X. Wang, H. Su, M. Z. Chen, and X. Wang, "Observer-based robust coordinated control of multiagent systems with input saturation," *IEEE Transactions on Neural Networks and Learning Systems*, vol. 29, no. 5, pp. 1933–1946, 2017.
- [4] Y. Liu and H. Su, "Containment control of second-order multi-agent systems via intermittent sampled position data communication," *Applied Mathematics and Computation*, vol. 362, Article ID 124522, 2019.

- [5] X. Wang and H. Su, "Self-triggered leader-following consensus of multi-agent systems with input time delay," *Neurocomputing*, vol. 330, pp. 70–77, 2019.
- [6] Y. Liu and H. Su, "Some necessary and sufficient conditions for containment of second-order multi-agent systems with sampled position data," *Neurocomputing*, vol. 378, pp. 228–237, 2020.
- [7] L. Moreira, T. I. Fossen, and C. G. Soares, "Path following control system for a tanker ship model," *Ocean Engineering*, vol. 34, no. 14–15, pp. 2074–2085, 2007.
- [8] A. M. Lekkas and T. I. Fossen, "A time-varying lookahead distance guidance law for path following," *IFAC Proceedings Volumes*, vol. 45, no. 27, pp. 398–403, 2012.
- [9] A. M. Lekkas and T. I. Fossen, "Integral los path following for curved paths based on a monotone cubic hermite spline parametrization," *IEEE Transactions on Control Systems Technology*, vol. 22, no. 6, pp. 2287–2301, 2014.
- [10] T. I. Fossen, K. Y. Pettersen, and R. Galeazzi, "Line-of-sight path following for dubins paths with adaptive sideslip compensation of drift forces," *IEEE Transactions on Control Systems Technology*, vol. 23, no. 2, pp. 820–827, 2015.
- [11] L. Liu, D. Wang, and Z. Peng, "ESO-based line-of-sight guidance law for straight line path following with exact sideslip compensation," in *Proceedings of the 12th World Congress on Intelligent Control and Automation (WCICA)*, pp. 677–681, IEEE, Guilin, China, June 2016.
- [12] L. Liu, D. Wang, Z. Peng, and H. Wang, "Predictor-based los guidance law for path following of underactuated marine surface vehicles with sideslip compensation," *Ocean Engineering*, vol. 124, pp. 340–348, 2016.
- [13] Z. Zheng and L. Sun, "Path following control for marine surface vessel with uncertainties and input saturation," *Neurocomputing*, vol. 177, pp. 158–167, 2016.
- [14] Y. Qu, L. Cai, and H. Xu, "Curved path following for unmanned surface vehicles with heading amendment," *IEEE Transactions on Systems, Man, and Cybernetics: Systems*, 2019.
- [15] K. D. Do, J. Pan, and Z.-P. Jiang, "Robust and adaptive path following for underactuated autonomous underwater vehicles," *Ocean Engineering*, vol. 31, no. 16, pp. 1967–1997, 2004.
- [16] K. D. Do and J. Pan, "Robust path-following of underactuated ships: theory and experiments on a model ship," *Ocean Engineering*, vol. 33, no. 10, pp. 1354–1372, 2006.
- [17] Z. Li, J. Sun, and S. Oh, "Design, analysis and experimental validation of a robust nonlinear path following controller for marine surface vessels," *Automatica*, vol. 45, no. 7, pp. 1649–1658, 2009.
- [18] Z. Hui and S. Jihong, "Path following control of underactuated ship based on nonlinear backstepping," in *Proceedings of the IEEE International Conference on Information and Automation (ICIA)*, pp. 1–6, IEEE, Yinchuan, China, August 2013.
- [19] Z. Zheng and M. Feroskhan, "Path following of a surface vessel with prescribed performance in the presence of input saturation and external disturbances," *IEEE/ASME Transactions on Mechatronics*, vol. 22, no. 6, pp. 2564–2575, 2017.
- [20] L. Yang and J. Zhang, "Path following of underactuated surface vessels based on neural sliding mode," in *Proceedings of the IEEE International Conference on Mechatronics and Automation (ICMA)*, pp. 2261–2266, IEEE, Beijing, China, August 2015.
- [21] W. Caharija, K. Y. Pettersen, M. Bibuli et al., "Integral line-of-sight guidance and control of underactuated marine vehicles: theory, simulations, and experiments," *IEEE Transactions on Control Systems Technology*, vol. 24, no. 5, pp. 1623–1642, 2016.
- [22] M. S. Wiig, K. Y. Pettersen, and T. R. Krogstad, "Uniform semiglobal exponential stability of integral line-of-sight guidance laws," *IFAC-PapersOnLine*, vol. 48, no. 16, pp. 61–68, 2015.
- [23] Y. Qu, H. Xu, W. Yu, H. Feng, and X. Han, "Inverse optimal control for speed-varying path following of marine vessels with actuator dynamics," *Journal of Marine Science and Application*, vol. 16, no. 2, pp. 225–236, 2017.
- [24] Z. Peng, J. Wang, and Q.-L. Han, "Path-following control of autonomous underwater vehicles subject to velocity and input constraints via neurodynamic optimization," *IEEE Transactions on Industrial Electronics*, vol. 66, no. 11, pp. 8724–8732, 2018.
- [25] Z. Zheng, L. Sun, and L. Xie, "Error-constrained LOS path following of a surface vessel with actuator saturation and faults," *IEEE Transactions on Systems, Man, and Cybernetics: Systems*, vol. 48, no. 10, pp. 1794–1805, 2017.
- [26] S.-R. Oh and J. Sun, "Path following of underactuated marine surface vessels using line-of-sight based model predictive control," *Ocean Engineering*, vol. 37, no. 2–3, pp. 289–295, 2010.
- [27] H. Zheng, R. R. Negenborn, and G. Lodewijks, "Trajectory tracking of autonomous vessels using model predictive control," *IFAC Proceedings Volumes*, vol. 47, no. 3, pp. 8812–8818, 2014.
- [28] J. Zhang, T. Sun, and Z. Liu, "Robust model predictive control for path-following of underactuated surface vessels with roll constraints," *Ocean Engineering*, vol. 143, pp. 125–132, 2017.
- [29] C. Shen, Y. Shi, and B. Buckham, "Integrated path planning and tracking control of an AUV: a unified receding horizon optimization approach," *IEEE/ASME Transactions on Mechatronics*, vol. 22, no. 3, pp. 1163–1173, 2016.
- [30] B.-O. H. Eriksen and M. Breivik, "Modeling, identification and control of high-speed avsvs: theory and experiments," in *Sensing and Control for Autonomous Vehicles*, pp. 407–431, Springer, Berlin, Germany, 2017.
- [31] M. E. N. Sorensen, M. Breivik, and B.-O. H. Eriksen, "A ship heading and speed control concept inherently satisfying actuator constraints," in *Proceedings of the IEEE Conference on Control Technology and Applications (CCTA)*, pp. 323–330, IEEE, Mauna Lani, HI, USA, August 2017.
- [32] Y. Liao, Y. Pang, and L. Wan, "Combined speed and yaw control of underactuated unmanned surface vehicles," in *Proceedings of the 2nd International Asia Conference on Informatics in Control, Automation and Robotics (CAR 2010)*, vol. 1, pp. 157–161, IEEE, Wuhan, China, March 2010.
- [33] R. Skjetne, *The maneuvering problem*, vol. 1, NTNU, Trondheim, Norway, 2005, Ph.D.-Thesis.
- [34] M. Abdelaal, M. Franzle, and A. Hahn, "Nonlinear model predictive control for tracking of underactuated vessels under input constraints," in *Proceedings of the IEEE European Modelling Symposium (EMS)*, pp. 313–318, IEEE, Madrid, Spain, October 2015.
- [35] T. I. Fossen, *Handbook of Marine Craft Hydrodynamics and Motion Control*, John Wiley & Sons, Hoboken, NY, USA, 2011.
- [36] D. Limon, T. Alamo, and E. Camacho, "Stable constrained mpc without terminal constraint," in *Proceedings of the 2003 American Control Conference*, vol. 6, pp. 4893–4898, IEEE, Denver, CO, USA, June 2003.
- [37] Z. Liu, H. Jin, M. J. Grimble, and R. Katebi, "Ship forward speed loss minimization using nonlinear course keeping and roll motion controllers," *Ocean Engineering*, vol. 113, pp. 201–207, 2016.

## Research Article

# A New Method for Feature Extraction and Classification of Single-Stranded DNA Based on Collaborative Filter

Bingyong Yan <sup>1</sup>, Haixu Cui <sup>1</sup>, Haitao Fu,<sup>2</sup> Jiale Zhou,<sup>1,3</sup> and Huifeng Wang <sup>1</sup>

<sup>1</sup>Key Laboratory of Advanced Control & Optimization for Chemical Process of Ministry of Education, East China University of Science and Technology, Shanghai 200237, China

<sup>2</sup>School of Electronic Information Engineering, Beijing Institute of Technology, Beijing 100081, China

<sup>3</sup>Key Laboratory for Advanced Materials & Department of Chemistry, East China University of Science and Technology, Shanghai 200237, China

Correspondence should be addressed to Bingyong Yan; byyan@ecust.edu.cn and Huifeng Wang; whuifeng@ecust.edu.cn

Received 20 March 2020; Accepted 11 May 2020; Published 21 July 2020

Guest Editor: Hou-Sheng Su

Copyright © 2020 Bingyong Yan et al. This is an open access article distributed under the Creative Commons Attribution License, which permits unrestricted use, distribution, and reproduction in any medium, provided the original work is properly cited.

The traditional support vector machine algorithm is not enough to classify single-stranded DNA molecules, so this paper proposes an improved threshold extraction algorithm based on collaborative filter for the classification of single-stranded DNA. Firstly, according to the different characteristic curves of the blocking current signals formed by the four bases (A, T, C, and G) that make up DNA molecules crossing the nanopore, the collaborative filter feature extraction algorithm with improved threshold is proposed. Then, the feature information is reconstructed and sent to the SVM classifier for training. Finally, the unfiltered, collaborative filter, improved threshold collaborative filter, and Bessel filter data are, respectively, extracted and sent to the SVM classifier for classification and comparison research. The experimental results show that the improved collaborative filter algorithm has higher accuracy in single-stranded DNA molecular classification.

## 1. Introduction

In recent years, nanochannel technology has developed into an indispensable tool for single molecule experiments, which provides a new way for high sensitive detection of single molecules and the study of weak interaction between single molecules. This technology is widely used in DNA single molecule sequencing, protein structure analysis, and early diagnosis of major diseases. Nanochannel technology is mainly used to analyze the weak blocking current signal generated by the unknown molecule that passes through the nanopore and to study the information of biogenetics and life science. Compared with the traditional detection technology, it has the characteristics of simple operation, clear structure, and fast detection speed, so it is called the most promising third generation DNA sequencing technology [1–4].

Due to the huge amount of data of blocking current generated by the molecules to be measured crossing the

nanopore, the traditional data analysis and processing methods are far from meeting the requirements of DNA sequencing. Therefore, support vector machine and other auxiliary research tools have undoubtedly become one of the powerful tools for analyzing single-stranded DNA data [5].

At present, many researchers have applied SVM in bioinformatics recognition [6, 7]. For example, Balachandran et al. [8] used the SVM model to predict in vitro phage virus proteins. Zhao et al. [9] used the SVM model to recognize amino acids. Zhong et al. [10] used SVM as a base classifier to recognize miRNA precursors. Zhou et al. [11] used the SVM model to recognize the DNA sequences of analytes such as *Bacillus subtilis*. Kumar et al. [12] used SVM to classify RNA-binding and nonbinding proteins. Dai [13] used SVM to classify imbalanced protein data. Through the above research and analysis, we can see that the classification rate using traditional SVM for classification is difficult to improve. In order to further improve the recognition rate, Tabard-Cossa et al. [14] and Kowalczyk et al.



[15], respectively, studied the synthesis of enhanced nanopores, the mechanism of noise generation, and the noise model of nanopores. Dekker [16] and Goto et al. [17] designed low-noise I-V conversion sensor methods to denoise nanopores. These methods can improve the signal-to-noise ratio of the blocking current, and the accuracy of the recognition is improved to a certain extent. However, because the collected blocking current signal is a very weak picoampere signal, most of the research on denoising of blocking current signal is only based on the analysis of external physical conditions, while there is little research on the specific blocking current signal itself.

Considering the existing research problems, this paper proposes a new collaborative filter classification method based on improved threshold. The basic idea is to use a fixed force between a single base and a nanopore [9], while the force between adjacent bases is uncertain, so the fluctuation of blocking current signal value is in a small range, but the block current signal generated by the same base through the nanopore shows a certain similarity in the whole signal [18, 19]. Therefore, based on the self-similar structure of the nanopore blocking current signal in the entire time domain, the collaborative filter algorithm was first used to analyze the grouped signals. By introducing the compensation factor, an improved threshold selection algorithm was proposed to extract the characteristics of the signal. Then, the processed data are reconstructed and sent to the SVM for training. Finally, the above algorithm was used to analyze the blocking current signals generated by  $A_{14}$  and  $CA_3$  single-stranded DNA molecules through the nanopore.

## 2. Introduction to Improved Collaborative Filter Algorithm

Considering the similarity of blocking current signals with the same base in the entire blocking current signal, the new feature extraction and classification method proposed in this paper are shown in Figure 1.

The first step is to use the blocking current signal generated from the DNA molecule through the nanopore channel as raw data.

The second step is to find out the similar blocks of the raw data and divide the most similar  $n$  blocks into a group with a certain threshold.

The third step is to coprocess the  $n$  groups. At this time, each group is a matrix. First, the  $n$  group matrix is subjected to two-dimensional discrete transformation, respectively, and then processed by introducing improved thresholds to filter out noise. Finally, two-dimensional discrete inverse transformation is used to reconstruct the raw signal. The reconstructed signal is the filtered signal with obvious characteristics.

In the fourth step, the current blocking curves after reconstruction of the characteristics of the two DNA single-stranded molecules  $A_{14}$  and  $CA_3$  processed in the first three steps are labeled and mixed and then sent to the SVM for training, and the classification results are analyzed.

The details of each functional module are described below.

**2.1. Grouping of Signals.** Figure 2 is a schematic diagram of grouping similar blocks. Each grouping block with similar characteristics is grouped for collaborative processing to reveal the characteristics of noise coverage and provides guarantee for SVM classification.

The selected blocking current signal is marked as  $R$ , a reference segment is first selected from  $R$  as  $D$ , and the comparative segment  $L$  from  $R$  is then selected without repeating. And Euclidean distance is used to judge the similarity between  $D$  and  $L$  [20]:

$$d_{(D,L)} = \sqrt{\sum_{i=1}^n (D_i - L_i)^2}, \quad i = 1, 2, 3, \dots, n, \quad (1)$$

where  $i$  is the selected  $i$ -th segment.

Then, it is normalized [21]:

$$\bar{d}_{(D,L)} = \frac{\sqrt{\sum_{i=1}^n (D_i - L_i)^2}}{w}, \quad i = 1, 2, 3, \dots, n, \quad (2)$$

where  $w$  is the width of the selected reference segment.  $\bar{d}_{(D,L)}$  is smaller, with higher similarity between  $D$  and  $L$ .

Then, the fixed reference segment  $D$  is selected and searched in the entire area of the blocking current signal length  $l$  ( $l \gg w$ ). At the same time,  $L$  moves across the entire segment  $R$  in steps of  $k$  and obtains  $m$  segments with the smallest distance from the reference segment to form group ( $D$ ). And it is saved to a two-dimensional array of  $m$  rows and  $w$  columns, group ( $D$ ) $_{m \times w}$ .

Finally, the reference segment  $D$  traverses the entire blocking current signal in steps of  $k$  and records groups formed by different reference segments.

**2.2. Collaborative Processing.** For the  $n$  groups generated in Section 3.1, this section uses collaborative filter to perform filter processing on each group of signals in order to be able to extract the characteristic information of the grouped signals.

Collaboration: each segment in each group is traversed through the entire blocking current signal, and each group contains the information of other groups, so this process can be regarded as a ‘‘collaborative’’ process.

Collaborative filter consists of three steps:

The first step is the two-dimensional discrete transformation of groups, and each group forms a matrix.

The second step performs threshold processing on each group matrix to filter the noise information in the raw data.

The third step is to transform the two-dimensional discrete inverse transformation on the matrix after the threshold processing in the second step and reconstruct signal with obvious characteristic information.

Each step is explained in detail as follows:

(1) Two-dimensional discrete transformation of the group:

$$G(D) = \text{dct2}(\text{group}(D)), \quad (3)$$

where  $\text{dct2}(\cdot)$  is the two-dimensional discrete cosine transform.

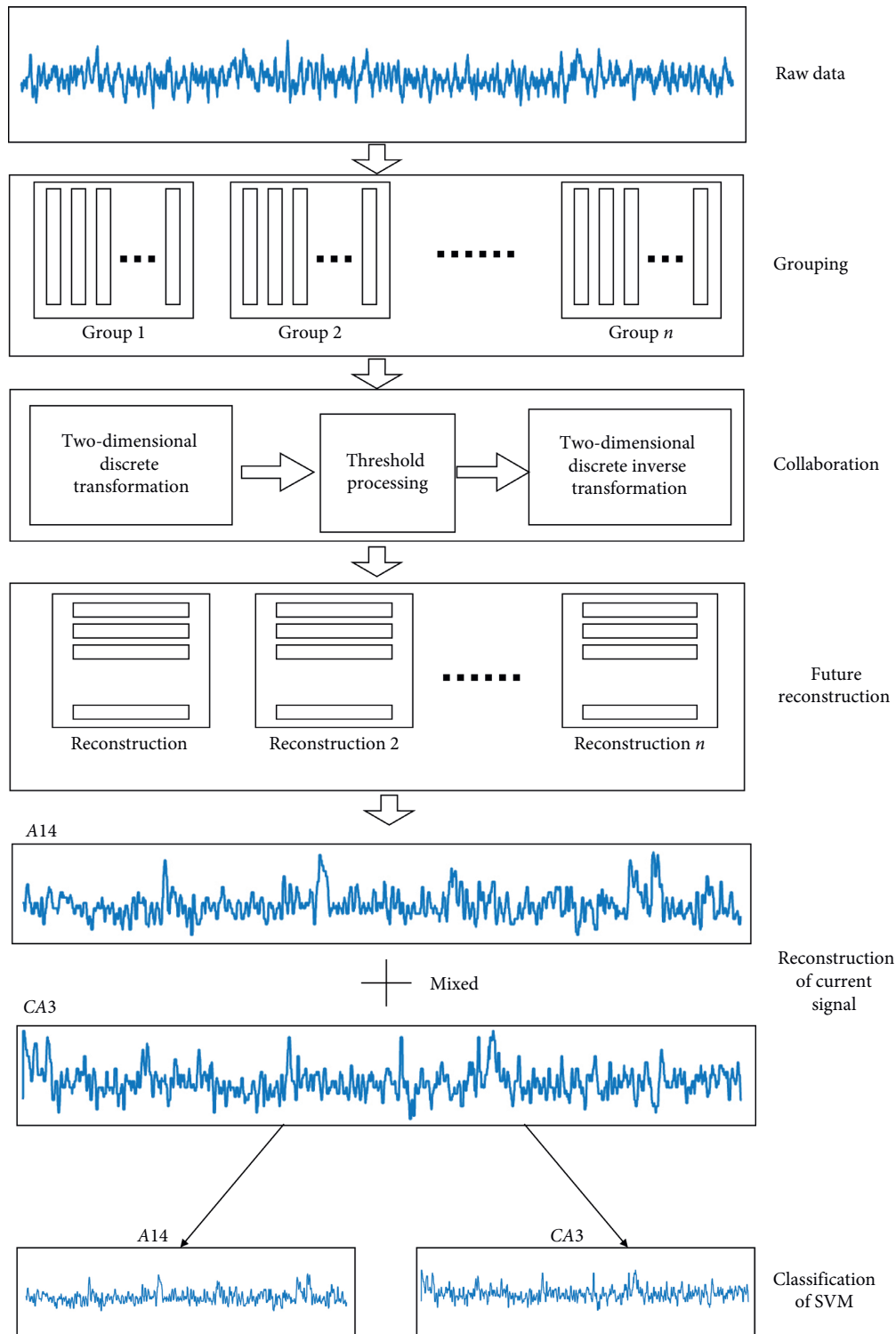


FIGURE 1: Flowchart of collaborative filter algorithm.

(2) A threshold value is selected for each group as  $\lambda$  and threshold noise reduction is performed in the transform domain. Coefficients smaller than the threshold

value are set to zero to attenuate noise, and coefficients larger than the threshold value are retained. This paper uses the hard threshold method, which is defined as

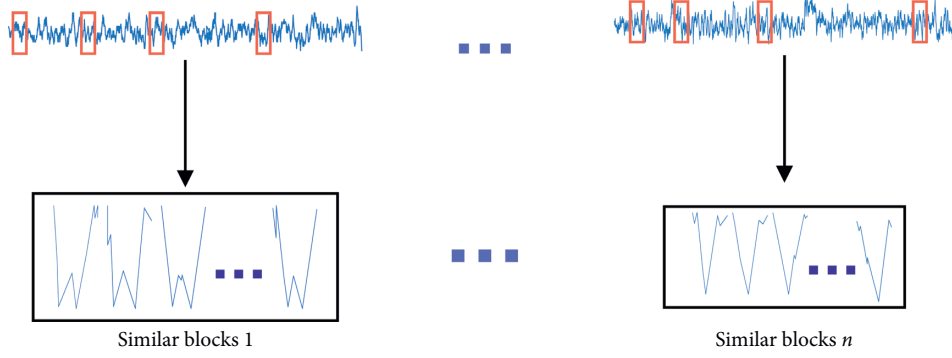


FIGURE 2: Similar block grouping.

$$T_H(g) = \begin{cases} g, & |g| < \lambda, \\ 0, & |g| \leq \lambda, \end{cases} \quad (4)$$

where  $\lambda$  is based on the threshold denoising method of Donoho, which is approximately optimal in the sense of mean square error, and at the same time can ensure that the reconstructed signal has the smoothness of the raw signal. The definition of threshold by VisuShrink proposed by Donoho and Johnstone is [22] as follows:

$$\lambda = \delta^* \sqrt{2 \log^*(m^*w)}, \quad (5)$$

where  $\delta$  is the noise standard deviation of the raw signal.

Since the noise of the blocking current signal of DNA passing through the nanopore is unknown, this paper uses the absolute deviation of the median of the coefficient matrix  $G(D)$  to estimate [18]:

$$\text{MAD} = \text{median}(|D_i - \text{median}(D_i)|), \quad i = 1, 2, 3, \dots, n, \quad (6)$$

where MAD is median absolute deviation,  $\text{median}(\cdot)$ .  $D_i$  is the element in the coefficient matrix  $G(D)$ . The estimated noise standard is defined as

$$\hat{\delta} = \frac{\text{MAD}}{k}, \quad (7)$$

where  $k$  is the scale factor constant, which is generally selected as 0.6745 [23].

- (3) After thresholding the transform coefficient matrix, the grouped filter results are obtained by two-dimensional discrete inverse cosine transform, as follows:

$$\text{group}(D) = \text{idct2}\{T_H(g)\}, \quad (8)$$

where  $\text{idct2}(\cdot)$  is the two-dimensional discrete cosine transform.

Through three steps, the  $n$  groups in 2.1 can be processed collaboratively, and finally,  $n$  group signals with noise removed can be obtained.

**2.3. Improved Threshold.** In the case of actual measurement, the additional noise changes caused by slight environmental differences and the small changes in hardware circuit components and reference ground can cause signal drift.

Although the data can be filtered using a collaborative filter to reduce noise interference, if the input signal has drift and contains nonzero mean noise interference, it will lead to the deviation of the final results of data processing. Therefore, it is necessary to compensate the drift of system.

This section improves the threshold value in the second step of collaborative filter data processing in Section 2.2 and introduces threshold compensation factor  $\lambda_c$  to compensate the drift of system.

The improved threshold is defined as

$$\lambda = \delta^* \sqrt{2 \log^*(m^*w) + \lambda_c}, \quad (9)$$

where when the circuit is at zero input signal, the output value of the acquisition circuit at this time is  $R_0$ . The data processing methods in Sections 2.1 and 2.2 are used to obtain the threshold  $\lambda_i$ ,  $i = 1, 2, \dots, n$  without input.

Compensation factor is defined as

$$\lambda_c = \frac{1}{n} \sum_{j=1}^n \lambda_j^i. \quad (10)$$

**2.4. Feature Extraction of Signals.** Because the traditional SVM-based method is used for classification, feature information of the raw data is drowned in noise, resulting in the unsatisfactory classification effect of SVM. In this paper, the raw signal is processed by the collaborative filter method and then reconstructing data with obvious characteristics.

The features of each group are displayed from the submerged noise, and the reconstructed obvious feature structure provides guarantee for the accuracy of the SVM classification.

Each group is composed of the  $m$  most similar to the original reference segment, so there is overlap between these  $m$  contrast segments. That is to say, a single point exists in multiple segments at the same time, so the reconstruction of the signal is to arithmetically average these  $m$  similar segments [24] to obtain the final output:

$$\text{Result}(i) = \frac{\sum_{i=1}^m \text{group}(D)_{i^*w}}{m}, \quad (11)$$

where  $\text{group}(D)_{i^*w}$  is the row vector in the group.

The characteristic reconstructed blocking current signal is

$$\text{signal} = \text{result}\{\text{result}(1), \text{result}(2), \dots, \text{result}(n)\}. \quad (12)$$

### 3. SVM Classification and Recognition Based on Improved Feature Extraction

**3.1. Experimental Data.** The block current signals generated by the two single-stranded DNA molecules  $A_{14}$  and  $CA_3$  to be recognized as they pass through the nanopore are shown in Figures 3 and 4, respectively.

The baseline current is 70.00 pA (both 800,000 sampling points).

**3.2. Parameter Selection.** This paper mainly uses signal-noise ratio and root mean squared error [25] as the evaluation criteria to determine the data based on cooperative filter and feature reconstruction and passes these two standards to determine the parameters that the collaborative filter algorithm needs to determine, that is, compare the moving step size  $k$  of the segmented segments with the number of sampling points included in each segment.

The definition of SNR used in this paper is

$$\text{SNR} = 10 \log\left(\frac{S}{N}\right) = 10 \log\left(\frac{\sum_{i=1}^N S^2(i)}{\sum_{i=1}^N (S_f(i) - S(i))^2}\right). \quad (13)$$

The definition of RMSE is

$$\text{RMSE} = \frac{\sum_{i=1}^N (S_f(i) - S(i))^2}{N}, \quad (14)$$

where  $S(i)$  is the value of the initial input signal,  $S_f(i)$  is the value of the output signal after collaborative filter, and  $N$  is the total length of the input signal. The larger the signal-to-noise ratio, the smaller the root mean square error, and the stronger the desiccation ability.

#### (a) Moving step of grouped fragments

It can be seen from the curve trend in Figure 5 that when the width of the segment is 50, the SNR is the largest, the RMSE is the smallest, and the denoising

effect is the best, so the moving step of the segment is 30.

#### (b) The width of the fragment

It can be seen from the curve trend in Figure 6 that when the moving step size of the fixed segment is 50, the SNR is the largest, the RMSE is the smallest, and the denoising effect is the best, so the width of the segment is 10.

Through the analysis of the above experimental data, it can be concluded that the collaborative filter algorithm has the best data processing effect when the moving step length of the segment is 30 and the width of the segment is 10. At this time, the SNR is 49.77 and the RMSE is 0.16.

**3.3. Comparison of Filter Results.** The parameters determined in Section 3.2 are segment moving step 30 and segment width 10. In order to highlight the performance of the algorithm, this section will compare it with the Bessel filter algorithm [26].

Figures 7 and 8 compare the data processing effect without and with improved threshold collaborative filter algorithm. Figure 7 shows the entire DNA molecule fragment, and Figure 8 shows a portion of the DNA molecule fragment. From Figures 7 and 8, it can be seen from the overall and partial filter results that the improved threshold collaborative filter algorithm (SNR = 49.77 and RMSE = 0.16) has a significantly better effect on data processing than the without improved threshold collaborative filter algorithm (SNR = 38.62 and RMSE = 0.89).

Figures 9 and 10 compare the data processing effect without improved threshold collaborative filter algorithm and Bessel algorithm. Figure 9 shows the entire DNA molecule fragment, and Figure 10 shows a portion of the DNA molecule fragment. From Figures 6 and 10, it can be seen from the overall and partial filter that the effect of the collaborative filter algorithm (SNR = 38.62 and RMSE = 0.89) on data processing is similar to that of Bessel filter (SNR = 38.62 and RMSE = 0.89).

Figures 11 and 12 compare the data processing effect of improved threshold collaborative filter algorithm and Bessel algorithm. Figure 11 shows the entire DNA molecule fragment, and Figure 12 shows a portion of the DNA molecule fragment. From Figures 11 and 12, it can be seen from the overall and partial filter that the effect of the improved threshold collaborative filter algorithm (SNR = 49.77 and RMSE = 0.16) on data processing is significantly better than that of Bessel filter on data processing (SNR = 39.71 and RMSE = 0.82).

From the above comparison results, it can be concluded that the denoising effect of the improved threshold collaborative filter algorithm is significantly better than without the improved threshold collaborative filter algorithm and Bessel Filter algorithm. Therefore, after the improved threshold collaborative filter algorithm is used to process the raw data, the characteristic information of the data is more obvious.

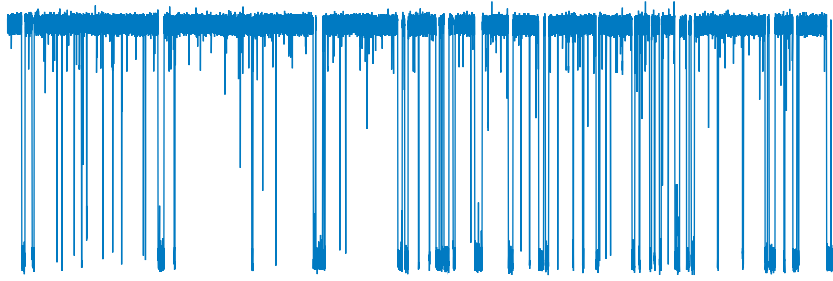
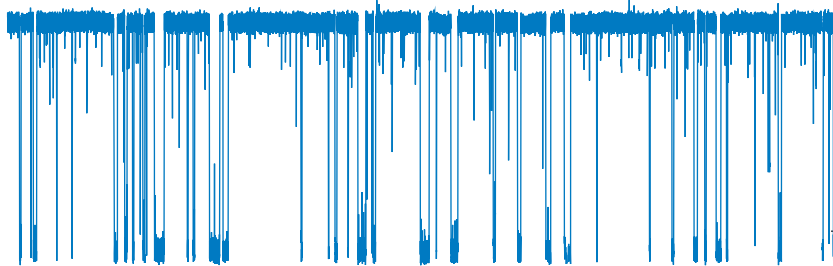
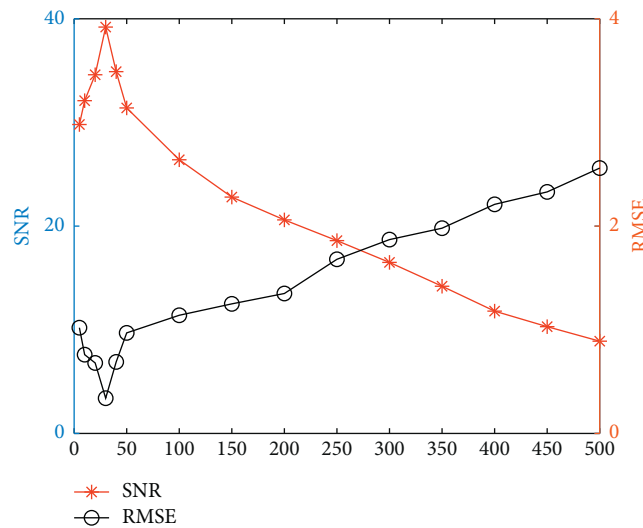
FIGURE 3:  $A_{14}$  raw data signal.FIGURE 4:  $CA_3$  raw data signal.

FIGURE 5: Change chart of step size.

**3.4. Comparison of Classification Results.** In order to verify the effectiveness of the algorithm proposed in this paper, SVM classification algorithm [27] is used to classify and study the collaborative filter, Bessel Filter, and improved threshold collaborative filter.

The blocking current sampling points of  $CA_3$  and  $A_{14}$  molecules are 15822 and 16628, respectively. 70% of the reconstructed datasets are used for training models and 30% for testing the effect of model recognition and classification.

Table 1 shows the classification accuracy of raw data, Bessel Filter data, collaborative filter data, and collaborative filter data with improved threshold using SVM. According to the classification accuracy in the table, it can be seen that the classification effect of collaborative filter without improved thresholds is similar to that of the Bessel filter by about 77%, while the classification effect of collaborative filter algorithm with improved thresholds is up to 95.88% better than the other two algorithms.

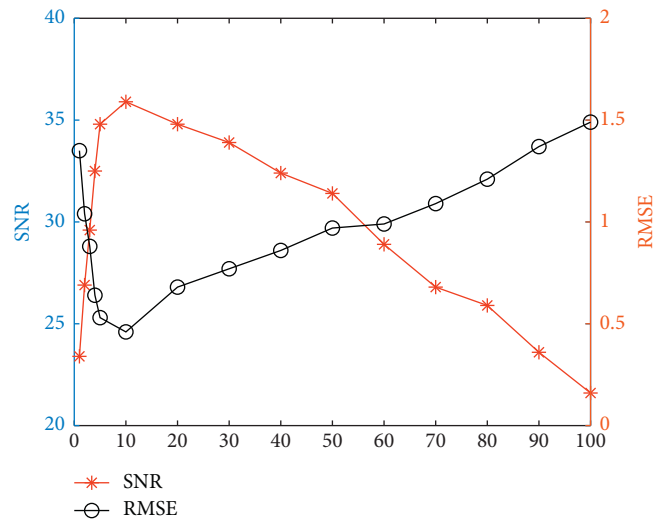


FIGURE 6: Change chart of width.

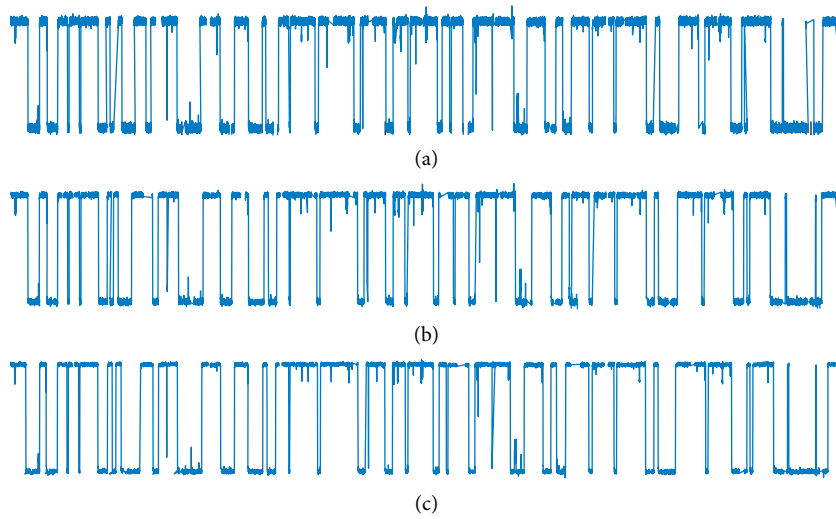


FIGURE 7: Comparison diagram with and without improved threshold collaborative filter: (a)  $A_{14}$  raw data; (b) collaborative filter; (c) improved threshold collaborative filter.

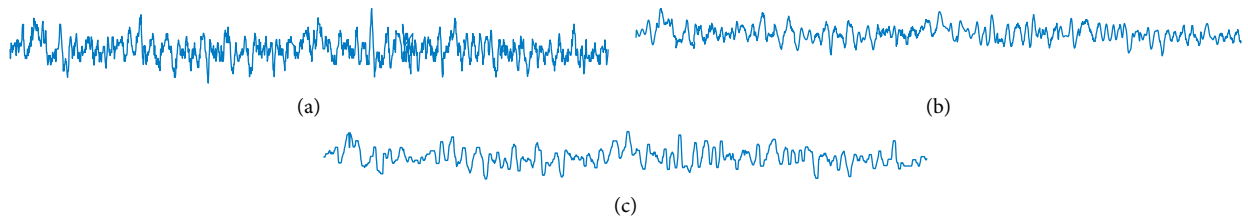


FIGURE 8: Partial diagram of collaborative filter with and without improved threshold collaborative filter: (a)  $A_{14}$  raw data; (b) collaborative filter; (c) improved threshold collaborative filter.

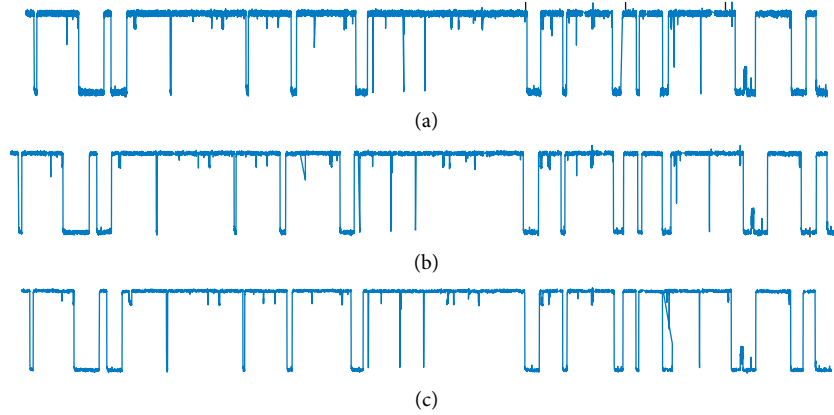


FIGURE 9: Comparison of Bessel and collaborative filters ( $A_{14}$  overall): (a)  $A_{14}$  raw data; (b) Bessel filter; (c) collaborative filter.

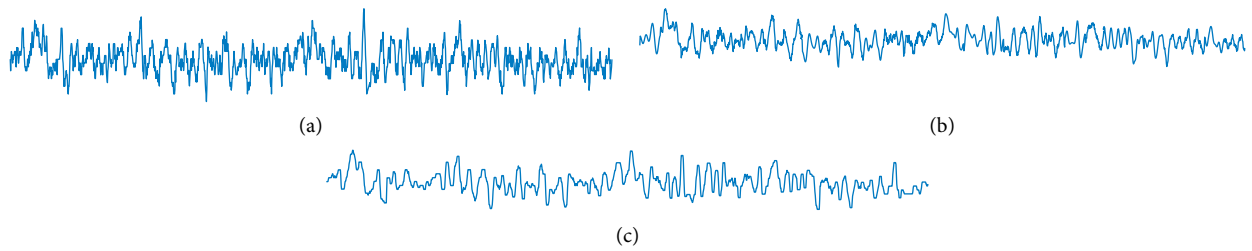


FIGURE 10: Comparison of Bessel and collaborative filters ( $A_{14}$  part): (a)  $A_{14}$  raw data; (b) Bessel filter; (c) collaborative filter.

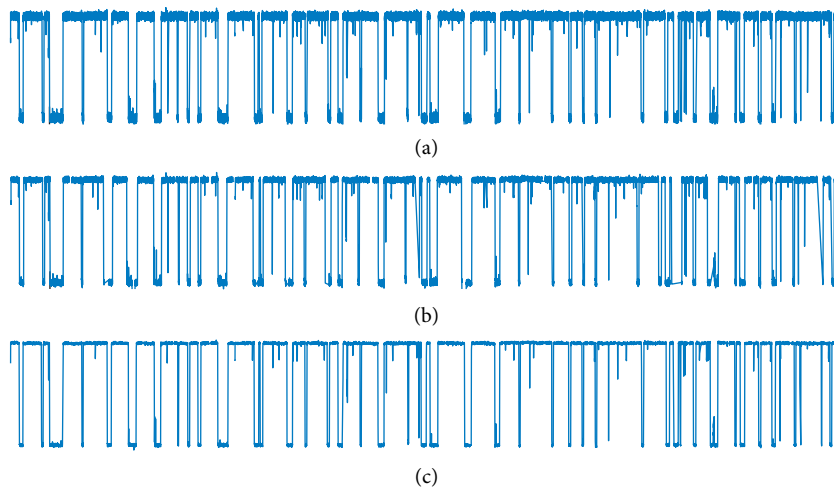


FIGURE 11: Comparison of Bessel and improved threshold collaborative filters ( $A_{14}$  overall): (a)  $A_{14}$  raw data; (b) Bessel filter; (c) improved threshold collaborative filter.

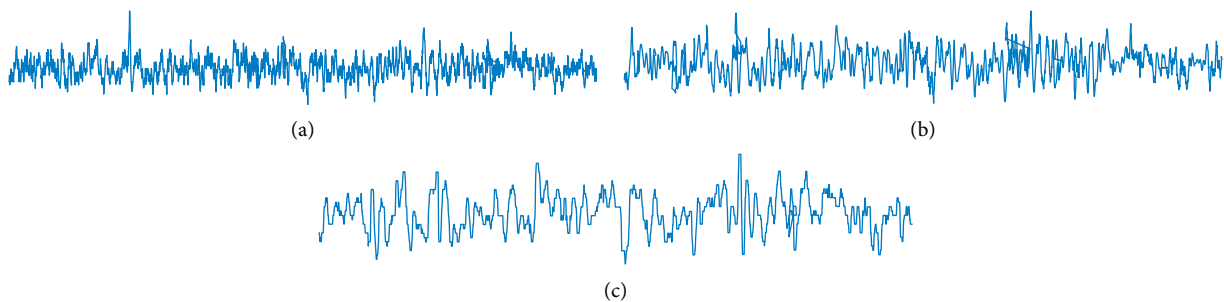


FIGURE 12: Comparison of Bessel and improved threshold collaborative filters ( $A_{14}$  part): (a)  $A_{14}$  raw data; (b) Bessel filter; (c) improved threshold collaborative filter.

TABLE 1: SVM classification results.

Filter algorithm	Classification accuracy (%)
Raw data	53.53
Bessel filter	77.05
Collaborative filter	76.38
Collaborative filter with improved threshold	95.88

#### 4. Conclusion

Due to the large amount of environmental noise and the instrument's own noise mixed in the raw sampling data, it is difficult to obtain the feature information of the raw data only by SVM for classification, resulting in low classification accuracy. Therefore, in consideration of signal drift caused by various noises, based on the premise of grouping, thresholding, and reconstruction of the raw data based on the collaborative filter algorithm, this paper improves the threshold value selected during the thresholding process in the collaborative algorithm and introduces the threshold drift compensation factor to compensate for signal drift to compensate for the effects of noise.

Then, the raw data are processed using a collaborative filter algorithm with improved thresholds to obtain data groups with obvious feature information, and data groups with obvious feature information are used for data reconstruction. Then, the data processing effect of improved threshold collaborative filter is compared with the data processing effect of the unimproved collaborative filter and Bessel filter. The data processing effect of improved threshold collaborative filter is significantly better than the other two data processing methods.

Finally, the data processed by the three data processing methods are sent to SVM for training, and the classification accuracy of the data processed by the improved threshold collaborative filter algorithm is obviously better than the other two data processing methods.

#### Data Availability

The nanopore current data belong to the School of Chemical Engineering and Molecular Engineering of East China University of Science and Technology, which belongs to the school cooperative relationship. Since the School of Chemical Engineering and Molecular Engineering still needs to apply this dataset to other biological research, the experimental dataset of this paper is not public.

#### Conflicts of Interest

The authors declare that they have no conflicts of interest.

#### Acknowledgments

This work was supported by the National Major Scientific Research Instrument Development Project (no. 21327807), National Natural Science Youth Fund (no. 51407078), and National Natural Science Foundation of China (no. 61773165).

#### References


- [1] H. Su, M. Long, and Z. Zeng, "Controllability of two-time-scale discrete-time multiagent systems," *IEEE Transactions on Cybernetics*, vol. 50, no. 4, pp. 1440–1449, 2020.
- [2] H. Su, J. Zhang, and X. Chen, "A stochastic sampling mechanism for time-varying formation of multiagent systems with multiple leaders and communication delays," *IEEE Transactions on Neural Networks and Learning Systems*, vol. 30, no. 12, pp. 3699–3707, 2019.
- [3] C. Cao, "Application of third generation sequencing technology to microbial research," *Microbiology*, vol. 43, no. 10, pp. 2269–2276, 2016.
- [4] S. Ambardar and M. Gowda, "High-resolution full-length HLA typing method using third generation (Pac-Bio SMRT) sequencing technology," *Methods in Molecular Biology*, vol. 1802, pp. 135–153, 2018.
- [5] M. Jain and M. Akeson, *High-Coverage Long Read DNA Sequencing with the Oxford Nanopore MinION*, UC Santa Cruz Electronic Theses and Dissertations, 2017.
- [6] X. Wang and H. Su, "Self-triggered leader-following consensus of multi-agent systems with input time delay," *Neurocomputing*, vol. 330, pp. 70–77, 2019.
- [7] P. Dixit and G. I. Prajapati, "Machine learning in bioinformatics: a novel approach for DNA sequencing," in *Proceedings of the 2015 Fifth International Conference on Advanced Computing & Communication Technologies (ACCT)*, pp. 41–47, Haryana, India, February 2015.
- [8] M. Balachandran, T. H. Shin, and L. Gwang, "PVP-SVM: sequence-based prediction of phage virion proteins using a support vector machine," *Frontiers in Microbiology*, vol. 9, p. 476, 2018.
- [9] Y. Zhao, B. Ashcroft, P. Zhang et al., "Single molecule spectroscopy of amino acids and peptides by recognition tunneling," *Nature Nanotechnology*, vol. 9, no. 6, pp. 466–473, 2014.
- [10] L. Zhong, J. T. L. Wang, D. Wen, and B. A. Shapiro, "Pre-miRNA classification via combinatorial feature mining and boosting," in *Proceedings of the 2012 IEEE International Conference on Bioinformatics and Biomedicine*, Philadelphia, PA, USA, October 2012.
- [11] Q. Zhou, Q. Jiang, and W. Dan, "A new method for classification in DNA sequence," in *Proceedings of the 2011 6th International Conference on Computer Science & Education (ICCSE)*, Singapore, August 2011.
- [12] M. Kumar, G. P. S. Gromiha, and G. P. S. Raghava, "SVM based prediction of RNA-binding proteins using binding residues and evolutionary information," *Journal of Molecular Recognition*, vol. 24, no. 2, pp. 303–313, 2011.
- [13] H.-L. Dai, "Imbalanced protein data classification using ensemble FTM-SVM," *IEEE Transactions on NanoBioscience*, vol. 14, no. 4, pp. 350–359, 2015.
- [14] V. Tabard-Cossa, M. D. Trivedi, and A. N. N. MarzaliJetha, "Noise analysis and reduction in solid-state nanopores," *Nanotechnology*, vol. 18, no. 30, Article ID 305505, 2007.
- [15] S. W. Kowalczyk, A. Y. Grosberg, and Y. C. Rabin, "Modeling the conductance and DNA blockade of solid-state nanopores," *Nanotechnology*, vol. 22, no. 31, Article ID 315101, 2011.
- [16] J. Dekker, W. B. K. Pedrotti, and W. B. Dunbar, "An area-efficient low-noise CMOS DNA detection sensor for multi-channel nanopore applications," *Sensors and Actuators B: Chemical*, vol. 176, pp. 1051–1055, 2013.
- [17] Y. Goto, I. Yanagi, and K. Matsui, "Integrated solid-state nanopore platform for nanopore fabrication via dielectric



- breakdown, DNA-speed deceleration and noise reduction,” *Scientific Reports*, vol. 6, no. 1, Article ID 31324, 2016.
- [18] Y. Liu and H. Su, “Containment control of second-order multi-agent systems via intermittent sampled position data communication,” *Applied Mathematics and Computation*, vol. 362, Article ID 124522, 2019.
- [19] Y. Liu and H. Su, “Some necessary and sufficient conditions for containment of second-order multi-agent systems with sampled position data,” *Neurocomputing*, vol. 378, pp. 228–237, 2020.
- [20] J. M. Smith, D. T. Lee, and J. S. Liebman, “An  $O(n \log n)$  heuristic for steiner minimal tree problems on the euclidean metric,” *Networks*, vol. 11, no. 1, pp. 23–39, 2010.
- [21] K. Dabov, V. A. Foi, and K. Egiazarian, “Image denoising by sparse 3-D transform-domain collaborative filtering,” *IEEE Transactions on Image Processing*, vol. 16, no. 8, pp. 2080–2095, 2007.
- [22] D. L. Donoho and I. M. Johnstone, “Ideal spatial adaptation by wavelet shrinkage,” *Biometrika*, vol. 81, no. 3, pp. 425–455, 1994.
- [23] Howell D. C, Median Absolute Deviation, 2008.
- [24] Zhaoyi, “Digital filtering arithmetic average method and weighted average method,” *Instrumentation Technology*, no. 4, p. 41, 2001.
- [25] T. Chai and R. R. Draxler, “Root mean square error (RMSE) or mean absolute error (MAE)?—arguments against avoiding RMSE in the literature,” *Geoscientific Model Development*, vol. 7, no. 3, pp. 1247–1250, 2014.
- [26] P. T. Trinh, R. Brossier, L. Métivier, J. Virieux, and P. Wellington, “Bessel smoothing filter for spectral-element mesh,” *Geophysical Journal International*, vol. 209, no. 3, pp. 1489–1512, 2017.
- [27] G. M. Foody and A. Mathur, “Toward intelligent training of supervised image classifications: directing training data acquisition for SVM classification,” *Remote Sensing of Environment*, vol. 93, no. 1-2, pp. 107–117, 2004.

## Research Article

# A Time-Delay-Bounded Data Scheduling Algorithm for Delay Reduction in Distributed Networked Control Systems

Zeming Fan,<sup>1</sup> Xiaojun Yu ,<sup>1</sup> Hao Wan,<sup>1</sup> Meilin Kang,<sup>1</sup> Yuan Liu,<sup>1</sup> Yuye He,<sup>1</sup> and Gaoxi Xiao<sup>2</sup>

<sup>1</sup>School of Automation, Northwestern Polytechnical University, Xi'an, Shaanxi 710129, China

<sup>2</sup>School of Electrical and Electronic Engineering, Nanyang Technological University, Singapore 639798

Correspondence should be addressed to Xiaojun Yu; e070035@e.ntu.edu.sg

Received 5 February 2020; Revised 19 May 2020; Accepted 9 June 2020; Published 21 July 2020

Guest Editor: Sahar Yazdani

Copyright © 2020 Zeming Fan et al. This is an open access article distributed under the Creative Commons Attribution License, which permits unrestricted use, distribution, and reproduction in any medium, provided the original work is properly cited.

As a key feature of networked control systems (NCSs), the time delays induced by communication medium sharing and data exchange over the system components could largely degrade the NCS performances or may even cause system instability, and thus, it is of critical importance to reduce time delays within NCSs. This paper studies the time-delay reduction problem in distributed NCSs and presents a dual-way data scheduling mechanism for time-delay reductions in delay-bounded NCSs with time-varying delays. We assess the time delays and their influences on the NCSs first with various delay factors being considered and then describe a one-way scheduling mechanism for network-delay reductions in NCSs. Based upon such a method, a dual-way scheduling algorithm is finally proposed for distributed NCSs with different types of transmitted data packets. Experiments are conducted on a remote teaching platform to verify the effectiveness of the proposed dual-way scheduling mechanism. Results demonstrate that, with the stability time-delay bound considered within the scheduling process, the proposed mechanism is effective for NCS time-delay reductions while addressing the stability, control accuracy, and settling time issues efficiently. Such a proposed mechanism could also be implemented together with some other existing control algorithms for time-delay reductions in NCSs. Our work could provide both useful theoretical guidance and application references for stable tracking control of delay-bounded NCSs.

## 1. Introduction

With the rapid advancements of networking technologies over the past decades, there is a growing trend in both industrial and commercial communities to integrate computing, communication, and control systems together to formulate a unified platform via network remote control. In such integrated platforms, the control commands from different information sources are transmitted and exchanged over networks, while their feedback control systems, whose control loops are formed via real-time communication channels, are called networked control systems (NCSs) [1]. Owing to its advantageous properties, e.g., low cost, high reliability, easy reconfiguration, satisfactory flexibility, robustness, and adaptation capabilities, NCS has attracted extensive research interest in recent years and been utilized in various fields, such as the power grids,

transportation networks, water distribution networks, telephone networks, global financial networks, and genetic expression networks [2].

In practical NCSs, there exist numerous information sources and nodes exchanging data over the networks simultaneously, and thus, the time delays induced by network resource sharing would generate inevitably [3–5]. Such time delays could largely degrade the system performances or sometimes may even cause the system to be instable. Furthermore, as the time delays within NCSs could either be constant, or bounded, or random, they also make the NCS system design and analysis complicated. Therefore, it is of critical importance to reduce the NCS time delays in engineering practice [5, 6].

Various mechanisms have been proposed for NCS time-delay reductions in the literature [7, 8]. Based on the

different time-delay models being adopted, such mechanisms could be divided into two main categories, namely, the NCS network control-based ones and the NCS system data scheduling-based ones [7]. Specifically, the NCS network control-based mechanisms treat the whole NCS system as a controlled network, and the main focus is on control of the networks, i.e., the main object is to propose efficient methods to address the raised networking issues, such as routing, congestion control, networking protocol, and data communications [6–8]. The NCS network control-based mechanisms have attracted extensive research interest over the past years, and readers could refer to [6–8] for comprehensive details.

The data scheduling-based mechanisms consider NCSs to be control systems and try to optimize performances of the overall NCSs [9, 10]. Initially, the data scheduling-based mechanisms assume that the NCSs have fixed data sampling period and propose methods to optimize resource allocations for competing demands [10]. Scheduling algorithms such as rate monotony (RM) scheduling, earliest deadline first (EDF) dynamic scheduling, and dead-bands scheduling, are of this category. Although such methods help reduce time delays, the practical system variables, such as varying transmission delays, transmission variables, packet loss, and communication constraints, have been ignored, and thus, these methods may not be adaptive to real-time network changes during the system operation process [11]. To further overcome these problems, scheduling mechanisms with variable sampling periods, such as dynamic feedback scheduling, fuzzy logic control or neural network-based scheduling, active sampling period scheduling, and delay compensation-based scheduling, have also been proposed [11–14]. Those methods are flexible in handling the time-varying traffic, yet some other constraints, such as the unknown network loads prior to scheduling, the lacks of upper and lower bounds for sampling period, and the difficulties in determining the key control parameters, have been largely ignored [14, 15].

Event-triggering feedback control mechanism is another kind of scheduling scheme being proposed to address the above network constraints and has attracted extensive research interest in recent years [16–18]. Specifically, by adopting a subsystem to broadcast the local state information to its neighbors, the distributed event-triggering feedback schemes were proposed for linear and nonlinear systems first [16, 17], and later, such algorithms were extended with various practical constraints, e.g., the data drops, transmission delays, probabilistic nonlinearities, sensor/actuator faults, and external attacks/disturbances, being taken into account, and have also achieved satisfactory results [18–21]. Currently, some other algorithms with more practical constraints taken into account are attracting increasing research interest. For more details of recent advances on event-triggering NCS control and the trends and techniques for NCS delay reductions, readers could refer to [6, 22]. It is worth mentioning that most of those existing mechanisms have ignored the influences of the upper and lower time-delay bounds on the performances of the system stability and the data scheduling schemes.

In practice, however, the permissible system time-delay bounds play a critical role in determining the system stability performances for NCSs. This is because, on the one hand, there usually exists a huge amount of information being exchanged over the networks, and such information would inevitably induce time delays, while on the other hand, such information is typically of different types, and each type of information may have its own transmitting priorities within the NCS. For such information being transmitted, once the transmission time exceeds the system permissible time-delay bounds, the system may become unstable or even divergent [23]. The case is especially true for distributed NCSs, since in decentralized systems, some of the plants are first-ordered, while the others may be higher-ordered with much stricter time-delay bound limitations. Therefore, to avoid causing system instability, scheduling in NCSs should be performed within the system time-delay bounds.

It is also worth noting that most of the existing scheduling mechanisms are one-way designed, making the scheduling operations inefficient for NCS delay reductions. For instance, for distributed NCSs as shown in Figure 1, those existing scheduling mechanisms typically operate either on the field sensor scheduler or on the network remote controller scheduler only. In practice, however, if the scheduling operations are conducted on the sensor scheduler and controller schedulers simultaneously, i.e., dual-way scheduling schemes are devised and adopted, the NCS time-delay reductions could be much more efficient. This is because, in such a case, both sensor terminals and remote controller could transmit their control demands simultaneously within the NCS for processing, and meanwhile, the sensor terminals and remote controllers could work cooperatively and more efficiently with the control variables being transmitted within the NCS control loops.

This paper studies the time-delay reduction problem within distributed NCSs and proposes a delay-bounded data scheduling mechanism for time-delay reductions in NCSs. Specifically, with the various delay factors being considered, the time delays and their influences on the NCSs are evaluated first, and then, a one-way scheduling algorithm is presented for data scheduling within NCSs. Based on such a one-way scheduling scheme, a novel dual-way dynamic scheduling algorithm, which is performed on controller and sensor schedulers simultaneously, is finally described. Both simulations and experiments are conducted to verify the effectiveness of the proposed data scheduling mechanism. Results obtained from experiments carried out on a practical remote teaching platform show that, with the scheduling operations conducted within the lower and upper NCS delay bounds, the proposed algorithm could help significantly improve the performances of the distributed NCSs while the system stability could also be guaranteed in different cases.

## 2. Time Delays and Their Impacts on Distributed NCSs

*2.1. Time Delays within NCSs.* A typical NCS comprised several control plants, sensors, controllers, and actuators shown in Figure 2. In such an NCS, there are numerous

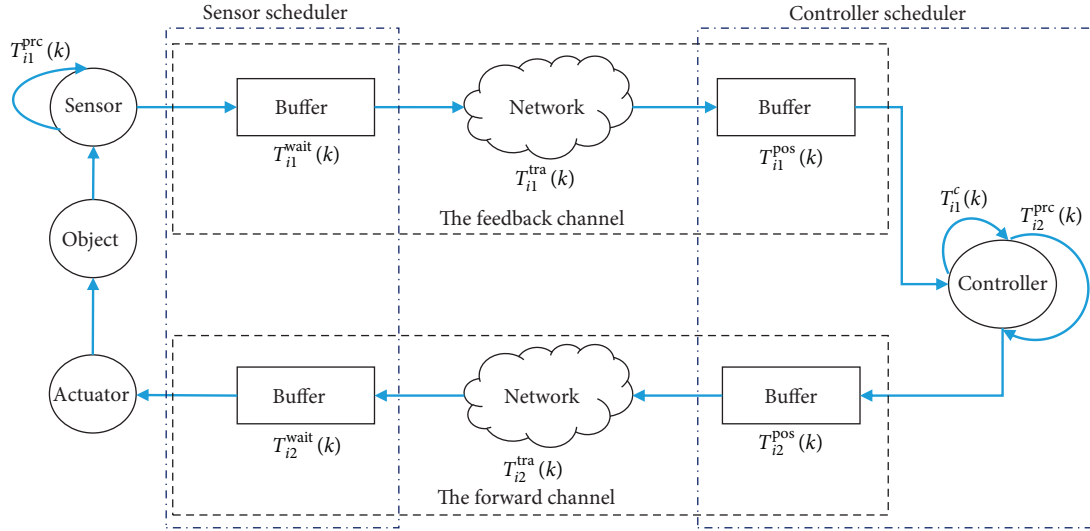


FIGURE 1: Structure of a typical NCS with time delays.

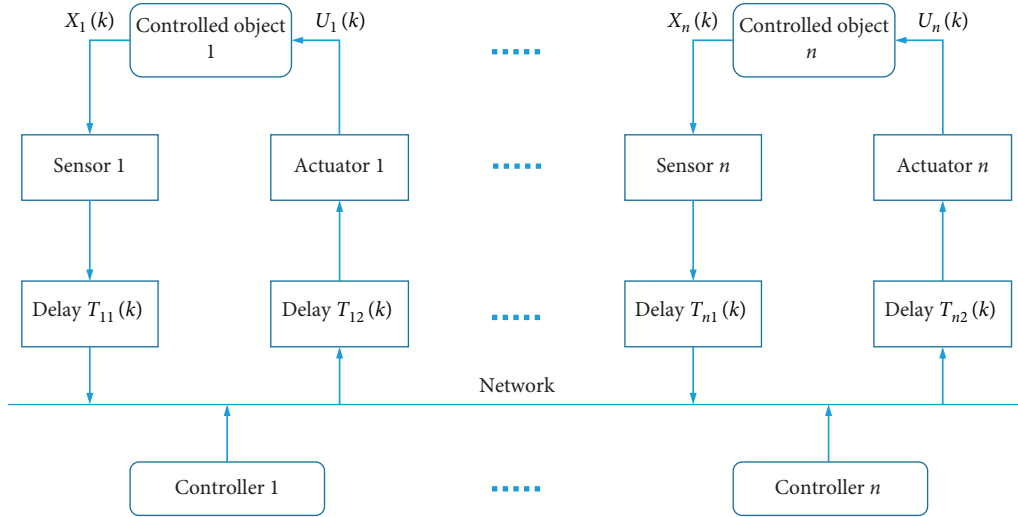


FIGURE 2: Topological structure of network with  $n$  controllers.

information sources sharing the network resources and transmitting data onto the network via communication channels. Once too much information are transmitted simultaneously via the same channel, the common network transmission issues, e.g., congestions, packet collisions, multipath transmissions, and link interruptions, may arise and thus would cause time delays inevitably [3, 4].

The time delays within NCSs could be categorized into control-induced delays and network-induced delays. While the former is the time consumed by the sensors, plants, and actuators to complete their respective noncommunication functions, the latter is induced by data transmissions within the NCS. For NCSs with feedback and forward channels as shown in Figure 1, we further divide the time delays in the system  $k$ th control cycle into five parts as follows:

- (1) Data preprocessing delay, i.e., the time required by sensors to pack data for transmission, and it is

denoted by  $T_{i1}^{prc}(K)$  and  $T_{i2}^{prc}(k)$  for the feedback and forward channels, respectively.

- (2) Data packet queuing delay, i.e., the time taken by a data packet to wait for its transmission, and it is denoted by  $T_{i1}^{wait}(k)$  and  $T_{i2}^{wait}(k)$  for the feedback and forward channels, respectively.
- (3) Data transmission delay, i.e., the time taken by a data packet to be transmitted within the system, which is determined by the packet length, network bandwidth, and transmission distance. Such a delay is denoted by  $T_{i1}^{tra}(k)$  and  $T_{i2}^{tra}(k)$  for the feedback and forward channels, respectively.
- (4) Data postprocessing delay, i.e., the time required for a controller to receive and store a data packet, and it is denoted by  $T_{i1}^{pos}(k)$  and  $T_{i2}^{pos}(k)$  for the feedback and forward channels, respectively.
- (5) Controller calculation delay is denoted by  $T_i^c(k)$ .

Denote the overall time delay for the feedback and forward channels to be  $T_{i1}(k)$  and  $T_{i2}(k)$ ; then, we can have

$$T_{i1}(k) = T_{i1}^{\text{prc}}(k) + T_{i1}^{\text{wait}}(k) + T_{i1}^{\text{tra}} + T_{i1}^{\text{pos}}(k), \quad (1)$$

$$T_{i2}(k) = T_{i2}^{\text{prc}}(k) + T_{i2}^{\text{wait}}(k) + T_{i2}^{\text{tra}} + T_{i2}^{\text{pos}}(k), \quad (2)$$

while the total time delay within the NCS is

$$T_i(k) = T_{i1}(k) + T_{i2}(k) + T_i^c(k), \quad (3)$$

which is also the control system round trip time (RTT), i.e., the interval between the time a plant receives its  $k$ th control command to the time when it receives its  $(k+1)$ th command.

In practice,  $T_i^c(k)$  is determined by computer performances. Specifically, since such a delay is much smaller as compared with the others and could be compensated by algorithms [24], the influences of  $T_i^c(k)$  are neglected and only those of  $T_{i1}(k)$  and  $T_{i2}(k)$  are evaluated in this paper.

**2.2. Influences of Time Delays on NCS Stability.** Assume that controllers in the NCS as shown in Figure 2 are event-driven, while those sensors and actuators are time-driven, then the theoretical discrete state equations for the  $i$ th plant are

$$x_i(k+1) = \mathbf{A}_i x_i(k) + \mathbf{B}_i u_i(k), \quad (4)$$

$$u_i(k) = K_i x_i(k), \quad (5)$$

where  $x_i(k) \in R^n$  is the state variable of the  $i$ th plant in its  $k$ th control cycle;  $\mathbf{A}_i$  and  $\mathbf{B}_i$  are constant matrices, while  $u_i(k)$  and  $K_i$  are control input and feedback gain of the  $i$ th control plant, respectively.

Further assume that the network-induced delays are time-varying and bounded, satisfying [25, 26]

$$0 < \leq T_i(k) \leq T_{iM}, \quad (6)$$

where  $T_{iM}$  is a constant, denoting the upper bound of the time-varying delay  $T_i(k)$ , and it could be characterized by the summation inequality presented in Theorem 5 in [27].

With the network-induced delays being taken into account, we have  $u_i(k) = K_i x_i(k - T_i(k))$  from (5), while the closed-loop NCS by (4) and (5) could be described as follows:

$$\begin{aligned} x_i(k+1) &= \mathbf{A}_i x_i(k) + \mathbf{B}_i K_i x_i(k - T_i(k)) \\ &= \mathbf{A}_i x_i(k) + \mathbf{A}_{id} x_i(k - T_i(k)), \quad (7) \\ y_i(k) &= c_i x_i(k), \end{aligned}$$

where  $\mathbf{A}_{id} = \mathbf{B}_i K_i$  is a loose variable introduced by Lyapunov's function to characterize the NCS. The schematic diagram of such a control system could be illustrated by Figure 3, wherein the two networks could either be the same or different depending on the practical implementation of the NCSs.

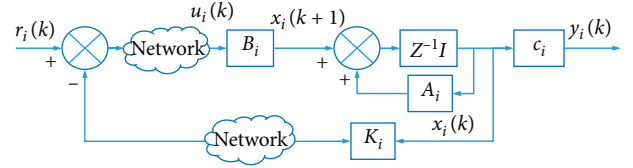


FIGURE 3: Schematic diagram of the control system evaluated.

### 3. Strategies for Network-Delay Reductions

As shown in (1), the time delay  $T_{i1}(k)$  in NCS is caused mainly by the data processing delay  $T_{i1}^{\text{prc}}(k)$ , queuing delay  $T_{i1}^{\text{wait}}(k)$ , transmission delay  $T_{i1}^{\text{tra}}(k)$ , and the postprocessing delay  $T_{i1}^{\text{pos}}(k)$ . Among all those factors, since  $T_{i1}^{\text{tra}}(k)$  is determined by the network conditions, while  $T_{i1}^{\text{prc}}(k)$  and  $T_{i1}^{\text{pos}}(k)$  are so short that could be negligible [28],  $T_{i1}^{\text{wait}}(k)$  is regarded to be the main delay factor. This is similar for  $T_{i2}(k)$  in the forward channels. However, since the data transmitted in NCS system include video/audio information, control commands, sensing data, and control data of all NCS components, which are either periodic or nonperiodic and to be transmitted either in real time or non-real time over the channels, the NCS time delays could be very large. In such a case, the transmission of all control data or system outputs within a single data packet is impractical. Moreover, since the queuing delays of both forward and backward channels could be manipulated by scheduling of the sensors and controllers, it is expected that appropriate scheduling algorithms could be devised to minimize the system time delays.

In this paper, we propose a two-way scheduling mechanism for an NCS, wherein scheduling operations are performed on both sensor and controller schedulers. Specifically, once there exist any data collisions, the scheduling mechanism is adopted to assign the data packets to each node different priorities, such that they could be transmitted with the shortest average delay.

**3.1. Scheduling Preprocessing.** To describe the scheduling operations for a plant within a control loop more clearly, we categorize the scheduling operations into data preprocessing on sensor schedulers, data postprocessing on controller schedulers, data queuing on controller schedulers, and data queuing on sensor schedulers. Hence, the time delays for each plant are mainly introduced by these four tasks and could be managed by a scheduling operation. Specifically, for any plant  $i$ , a transmission description function  $\tau_{in}$  could be established as shown in (8), which could be utilized to calculate the desired scheduling time slot for each data packet.

$$\tau_{in} = f(\tau_{imm}, \tau_{ina}, \tau_{inr}, \tau_{inf}, \tau_{ine}, \tau_{inb}), \quad (8)$$

where  $n = 1, 2, 3, 4$  denoting the four data packet scheduling operations. Hence, the time delays as shown in Figure 1 could also be denoted as  $T_{i1}^{\text{wait}} = \tau_{i1}$ ,  $T_{i1}^{\text{pos}} = \tau_{i2}$ ,  $T_{i2}^{\text{pos}} = \tau_{i3}$ , and  $T_{i2}^{\text{wait}} = \tau_{i4}$ .  $\tau_{imm}$  describes the significance level of each data packet and is defined to be the reciprocal of the packet

time-delay upper bound.  $\tau_{ina}$  is the actual packet transmission starting time, which is also utilized to order the scheduling operations for packets with the same significance level.  $\tau_{inr}$  is the longest execution time among all data packets, which is determined by the data packet length, network bandwidth, and transmission distances.  $\tau_{inf}$  and  $\tau_{ine}$  are the earliest and latest transmission starting time of a data packet, respectively.  $\tau_{inb}$  is the control cycle of the NCS.

Once the system delay bounds  $T_{i1M}$ ,  $T_{i2M}$  and the packet transmission description function  $\tau_{in}$  are determined, the scheduling operations then could be decided for each packet in the NCS. Specifically, for a packet to be transmitted, its scheduling operation includes two main steps, i.e., packet significance level determination and scheduling operation determination for all packets with the same significance level. In this study, we call the former as scheduling pre-processing and the latter as packet scheduling operation. The determinations of packet transmission property variables are discussed in the following sections.

### 3.2. Scheduling Mechanism for Sensor Scheduler

**3.2.1. Scheduling of Coupled Information.** In NCSs with coupled information, data packets are transmitted in pre-defined order, i.e., for a plant within a control loop, its control information should be sent to the actuator before it collects data from a sensor, while for a controller, it has to receive sensor data first, and then sends the control information to the local controller via network after executing the control mechanism. In this way, the real-time data transmission within NCSs could be guaranteed. To perform scheduling for packets with the same significance level, a data transmission set  $\tau_s$  has to be established as below according to the packet transmission time, while each packet should be assigned a time slot, within which the sensor scheduler or controller scheduler is fully occupied by the scheduling task specified:

$$\tau_s = \left\{ \left[ \tau_{in} \longrightarrow \tau_{jn} \right] \mid \tau_{in}, \tau_{jn} \in \tau \right\}, \quad (9)$$

where  $\tau$  represents all data packets to be transmitted, and  $[\tau_{in} \longrightarrow \tau_{jn}]$  defines the relative priority of two data packets within  $\tau$ , indicating that  $\tau_{jn}$  can be transmitted only when the transmission of  $\tau_{in}$  is completed.

However, since the processing of a packet may last for a period of time, the variables  $\tau_{inr}$ ,  $\tau_{inf}$ ,  $\tau_{ine}$  have to be calculated. For an existing data transmission set with  $u$  packets  $[\tau_{in}^k \longrightarrow \tau_{jn}^k] (k = 1, \dots, u)$  to be transmitted, the earliest transmission starting time  $\tau_{inf}^k$  among those packets can be calculated as follows:

$$\tau_{inf}^k = \tau_{ina}^k + \tau_{inr}, \quad (10)$$

where  $\tau_{inr} = T_{i1}^{tra}$ . The earliest transmission starting time  $\tau_{inf}$  among all packets within the set could be calculated:

$$\tau_{inf} = \max\left(\tau_{inf}^1, \dots, \tau_{inf}^u\right). \quad (11)$$

Similarly, if there exists a transmission set with  $v$  packets following  $[\tau_{in} \longrightarrow \tau_{in}^k] (k = 1, \dots, v)$ , then the latest transmission starting time  $\tau_{ine}^k$  for those data packets can be calculated as follows:

$$\tau_{ine}^k = \min\left(\tau_{ine}^k - \tau_{inr}, T_{i1M} - \tau_{inr}\right), \quad (12)$$

and the latest transmission starting time  $\tau_{ine}$  for packets within the transmission set could be determined by

$$\tau_{ine} = \min\left(\tau_{ine}^k, \tau_{inf}^k\right). \quad (13)$$

**3.2.2. Scheduling of Noncoupled Information.** In NCSs, there also exists noncoupled information with the packets being transmitted in an arbitrary order. To determine the scheduling operations for such packets, the packet transmission starting time  $\tau_{ina}$  has to be calculated. In practice, however, since the NCS time delay typically consists of the forward channel delay, feedback channel delay, and controller processing delay, while the forward and feedback channels are symmetric, it is reasonable to assume that half of the overall delay comes from the forward channel while the other half is from the feedback channel. Hence, in the scheduling process, half of the delay  $T_{iM}$  is assigned to the forward channel scheduler, and the other half is assigned to the feedback channel scheduler. In such a way, it is expected that the time slots reserved for the controller scheduler are enough for its scheduling operations. Hence, the longest allowable queuing delay  $T_{ilm}$  for those data packets could be determined as follows:

$$T_{ilm} = \frac{1}{2} \left[ T_{iM} - T_{i1}^{tra} (k-1) - T_{i1}^{prc} (k-1) - T_{i1}^{pos} (k-1) \right], \quad (14)$$

and the latest starting time would be

$$\tau_{ine} = T_{ilm}. \quad (15)$$

Moreover, since the noncoupled packets could be transmitted in an arbitrary order, the earliest transmission starting time of a packet could be set as  $\tau_{inf} = 0$ , while its execution time could be  $\tau_{inr} = T_{i1}^{tra}$ .

**3.2.3. Scheduling for Hybrid Coupled and Noncoupled Information.** In NCSs with both coupled and noncoupled information, assume that there are information coupled packets with  $u$  following  $[\tau_{in}^k \longrightarrow \tau_{in}^k] (k = 1, \dots, u)$  and  $v$  following  $[\tau_{in} \longrightarrow \tau_{in}^h] (h = 1, \dots, v)$ , which are determined by (11) and (13), respectively, as well as  $w$  information noncoupled packets. If there exists a parameter  $j (j \in (u - 2, u + w + 2))$  for the scheduled packets  $\tau_{in}^j$  satisfying

$$\begin{cases} \tau_{inf} \geq \tau_{ina}^j + \tau_{inr}^j, \\ \tau_{ina}^{j+1} \geq \tau_{inf} + \tau_{inr}, \end{cases} \quad (16)$$

or

$$\begin{cases} \tau_{inf} \leq \tau_{ina}^j + \tau_{inr}^j \leq \tau_{ine}, \\ \tau_{ina}^{j+1} \geq \tau_{ina}^j + \tau_{inr}^j + \tau_{inr}, \end{cases} \quad (17)$$

then we have the actual execution time for  $n$ th task of the  $i$ th plant as follows:

$$\tau_{ina} = \max(\tau_{inf}, \tau_{ina}^j + \tau_{inr}^j). \quad (18)$$

Hence, the time slot utilized for processing the packet within the control loop could be calculated as follows:

$$\tau_{ina} + \tau_{inr}. \quad (19)$$

The scheduling for any data packet to be transmitted within NCS could be conducted as shown in Algorithm 1.

**3.3. Scheduling Mechanism for Controller Scheduler.** To determine the scheduling operations for each packet, the execution time slot should be calculated for each data packet, and thus, the transmission time  $\tau_{if}$ ,  $\tau_{ie}$ , and  $\tau_{ia}$  should be calculated using (11) and (13) and (16)–(18), respectively. Finally, the transmission set  $\tau_s$  could be determined. The same scheduling operations shown in Algorithm 1 are executed within the controller scheduler for each packet of the plant.

While for any plant adopting an NCS structure as shown in Figure 1, the scheduling and transmission time slot distribution for each of its data packets could be illustrated in Figure 4.

## 4. Experimental Verification

To verify the effectiveness of the proposed time-delay bounded scheduling algorithm, experiments are conducted on a lab-customized teaching system. Figure 5 depicts the schematic of the system. As seen, it consists of four layers, with the first layer being the motion platforms connected to the local sensors and actuators and the second layer being the training platform server group connected with the campus network. The third layer is the school information center and the fourth layer is student clients, and they are connected to the public and the campus networks, respectively. Specifically, in our experiments, those motion platforms are located in the new campus acting as NCS control plants, and they are controlled by a local controller, while those student clients are located within the old campus acting as the remote controllers. As those two campuses are 34 kilometers away from each other, the teaching system within the two campuses is interconnected by public transmission networks. In the experiments, scheduling operations are conducted on the local controller and school information center server, respectively, to facilitate the packet transmissions.

The motion platform as shown in Figure 6 is a typical teaching instrument that has been commonly utilized in the laboratory for both load simulation and the position and attitude control of aircrafts. It has four degrees of freedom (4-DOFs), consisting of a linear motional freedom and three rotational freedoms that are orthogonal to each other.

Specifically, those 4-DOFs are along four separate axes, which are for inner ring motion, central ring motion, outer ring motion, and the line move motion, respectively, and each axis is equipped with two independent motors, with one for motion control and the other for force control. The force control system could be utilized to simulate the motion control loads or motion control interferences, while the motion control system could be used for force control interferences.

In our experiments, the 4-DOFs together with their respective two control systems are utilized to simulate eight independent control plants. Specifically, the system local controllers act as sensor schedulers of the feedback channels, while those student client controllers act as schedulers for the forward channels to control all experimental components, and the main purpose of our experiment is to realize simultaneous closed-loop control of the 8 objects. To realize stable control of the control plants, we measured their dead zones and then set the measured values to be their respective lower and upper thresholds of the adopted relay-based dead-time compensators [29, 30] in the motion platform. In such a way, influences of the frictions within those objects could be eliminated. Each of those objects could be described with the mathematical model presented by (7), wherein discrete-time model matrices  $\mathbf{A}_i$  and  $\mathbf{A}_{id}$  denote the system state matrix and input matrix, respectively. Both  $\mathbf{A}_i$  and  $\mathbf{A}_{id}$  are shown in (20), and the system stability time-delay bound limits could be determined with the stability criterion presented in [27]. The model parameters, together with the loads of the four motion and the other four torque motors, i.e., inner ring, central ring, outer ring, and line move, are shown in Tables 1 and 2, respectively.

$$\begin{aligned} \mathbf{A} &= \begin{bmatrix} A_{11} & A_{12} \\ A_{21} & A_{22} \end{bmatrix}, \\ \mathbf{A}_d &= \begin{bmatrix} A_{d11} & A_{d12} \\ A_{d21} & A_{d22} \end{bmatrix}. \end{aligned} \quad (20)$$

To evaluate the effectiveness of the proposed time-delay bounded scheduling mechanism, we compare the time-delay performances of the tested motion platform with and without adopting the proposed scheduling mechanisms. Specifically, for an  $i$ th system, we define the control time of a control loop to be  $T_i(k)$ , which starts from the  $k$ th control cycle to the time when the local controller sends its control signals. Table 3 presents the measured  $T_i(k)$  for the platform system without the proposed scheduling mechanism, while Table 4 shows the measured  $T_i(k)$  when the proposed scheduling mechanism is adopted. Results in Table 3 show that without the proposed scheduling mechanisms, there exist a number of measured delays, denoted with red color texts with  $T_i(k) > T_{iM}$ , i.e., such delays are larger than the time-delay bound shown in Tables 1 and 2. Such large time delays could largely degrade the system performances or may even cause system instability. However, once the proposed data scheduling mechanisms are adopted, the measured time delays for all 8 channels are significantly reduced with  $T_i(k) < T_{iM}$ . Such results indicate that with the

**Input:** an existing transmission set  $[\tau_{in}^k \rightarrow \tau_{jn}] (k = 1, \dots, u)$ ; a new data packet with  $\tau_{in}$ .  
**Output:** a new transmission set  $[\tau_{in}^k \rightarrow \tau_{jn}] (k = 1, \dots, u + 1)$ .

- (1) Calculate the time-delay upper bound  $T_{iM}$  with Theorem ?? for the data packet;
- (2) Calculate transmission priority  $\tau_{imm}$  with  $T_{iM}$ , i.e.,  $\tau_{imm} \propto (1/T_{iM})$ ;
- (3) Compare calculated  $\tau_{imm}$  to  $\tau_{imm}^k$  of  $\tau_{in}^k (k = 1, \dots, u)$  in the set;
- (4) **if** calculated  $\tau_{imm} = \tau_{imm}^k$  for  $1 \leq k \leq u$  **then**
- (5) Insert  $\tau_{in}$  into the end of set  $[\tau_{in}^k \rightarrow \tau_{jn}] (k = 1, \dots, u)$ , go to step 10;
- (6) **else**
- (7) Calculate information execution time  $\tau_{ia}$  using equations (10)–(18);
- (8) Insert  $\tau_{in}$  into set  $[\tau_{in}^k \rightarrow \tau_{jn}] (k = 1, \dots, u)$  according to  $\tau_{ina}$  in an increasing order;
- (9) **end if**
- (10) Calculate the actual packet execution time  $\tau_{ina}$  using equation (18);
- (11) Scheduling operation according to the order of transmission set  $[\tau_{in}^k \rightarrow \tau_{jn}] (k = 1, \dots, u + 1)$ ;

ALGORITHM 1: Scheduling mechanism in feedback channel for distributed NCSs.

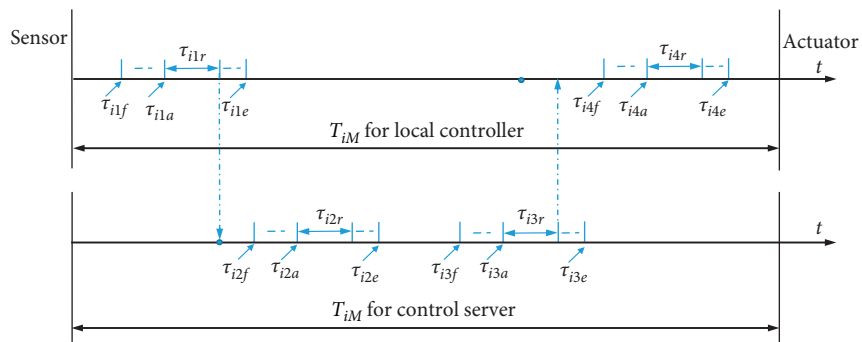


FIGURE 4: The scheduling and execution time distribution for each packet of the plant adopting an NCS structure as shown in Figure 1.

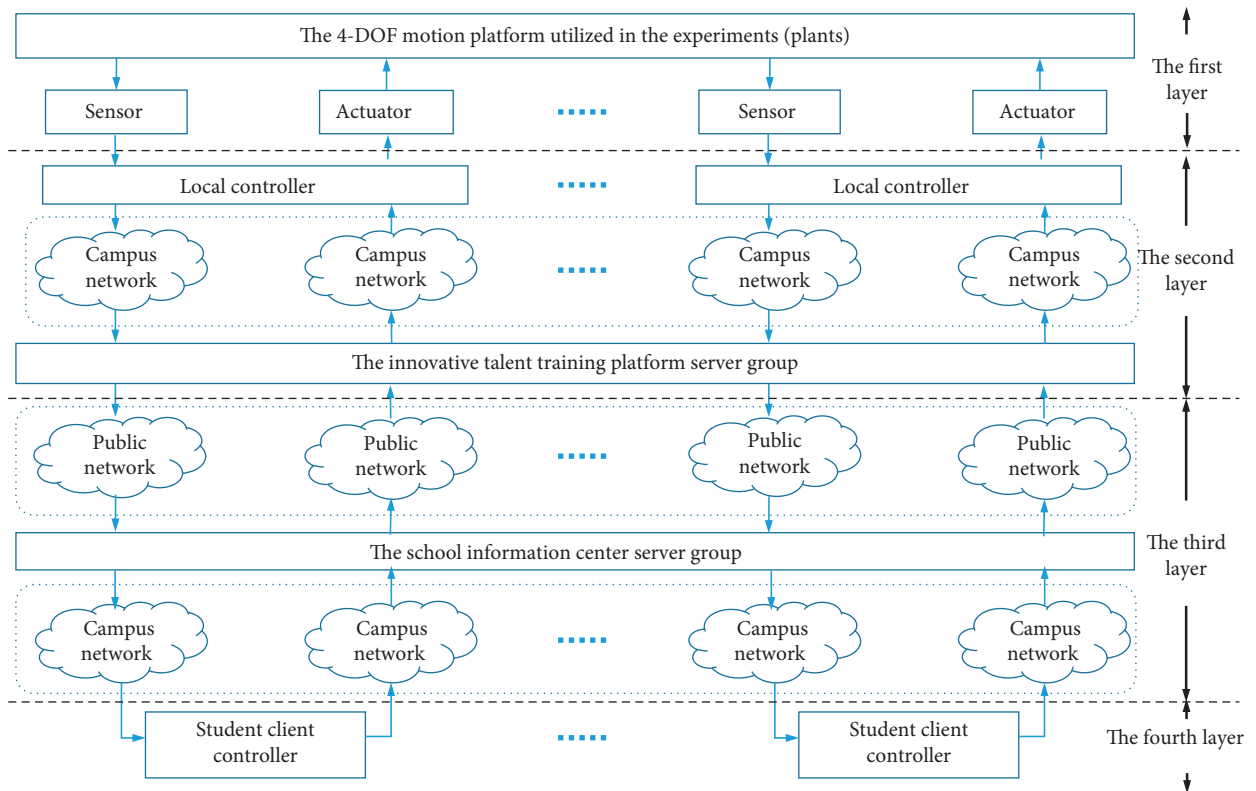


FIGURE 5: Experimental setup of the NCS being utilized in our experiments.



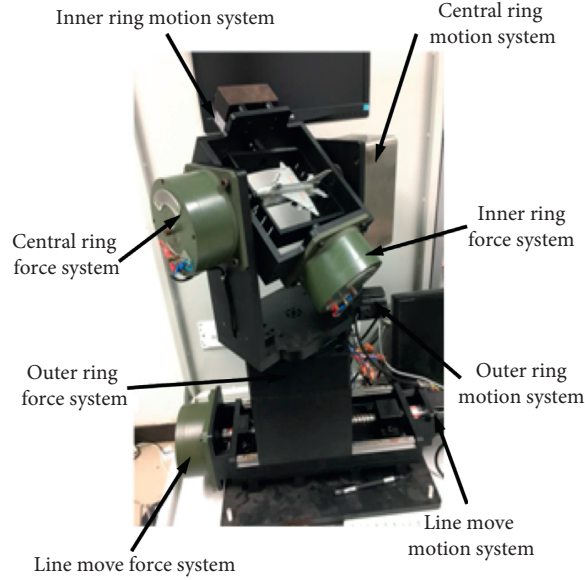


FIGURE 6: The experimental motion platform with four degrees of freedom.

TABLE 1: Model parameters of the four motion systems simulated in Figure 6 and the calculated upper limit of system time delay.

Motion system	$A_{11}$	$A_{12}$	$A_{21}$	$A_{22}$	$A_{d11}$	$A_{d12}$	$A_{d21}$	$A_{d22}$	$T_M$ (ms)
Inner ring motion	0.80	0	0.05	0.90	-0.10	0	-0.20	-0.10	38
Central ring motion	0.82	0	0.06	0.91	-0.11	0	-0.20	-0.09	37
Outer ring motion	0.79	0	0.05	0.93	-0.12	0	-0.21	-0.08	38
Line move motion	0.78	0	0.06	0.92	-0.13	0	-0.19	-0.12	38

TABLE 2: Model parameters of the four force systems simulated in Figure 6 and the upper limit of system delay calculated using (7) with the same controller.

Force system	$A_{11}$	$A_{12}$	$A_{21}$	$A_{22}$	$A_{d11}$	$A_{d12}$	$A_{d21}$	$A_{d22}$	$T_M$ (ms)
Inner ring force	1.01	0.11	0.11	0.83	0.21	0	0.11	-0.10	20
Central ring force	0.98	0.12	0.09	0.79	0.23	0	0.09	-0.11	21
Outer ring force	1.03	0.09	0.12	0.82	0.19	0	0.12	-0.13	21
Line move force	1.05	0.1	0.08	0.81	0.22	0	0.13	-0.14	19

TABLE 3: Measured NCS time delay for NCS without scheduling mechanism adopted.

System		$T_i$ (K)															
$i$ th control cycle		1	2	3	4	5	6	7	8	9	10	11	12	13	14	15	16
Inner ring	Motion	12	15	16	21	19	23	18	13	24	18	13	38	42	43	56	23
	Force	21	24	35	36	32	12	14	13	15	9	12	16	24	30	32	12
Central ring	Motion	15	16	21	19	23	32	37	23	48	65	89	47	45	32	23	24
	Force	12	15	26	43	25	36	42	12	14	15	9	14	16	16	13	10
Outer ring	Motion	27	32	45	87	67	45	57	36	56	23	34	38	18	19	32	19
	Force	9	13	14	15	8	16	13	15	14	34	23	25	34	14	13	16
Line move	Motion	64	54	34	54	39	45	21	23	25	34	23	18	24	23	29	24
	Force	10	13	8	15	15	34	23	21	32	43	12	16	17	12	18	19

time-delay bounds taken into account, the proposed scheduling mechanisms could help facilitate the data transmission for the plants, which, thus, helps realize stable system control.

The proposed scheduling mechanism together with different control schemes is also applied onto the teaching system to control the 4-DOFs motion platform online. Specifically, the control schemes are implemented to drive

TABLE 4: Measured NCS time delay for NCS with the proposed scheduling mechanism adopted.

System		$T_i(K)$															
<i>i</i> th control cycle		1	2	3	4	5	6	7	8	9	10	11	12	13	14	15	16
Inner ring	Motion	11	12	15	34	38	21	22	28	21	18	13	38	25	16	32	23
	Force	12	9	14	13	16	9	12	14	9	14	13	16	10	14	13	16
Central ring	Motion	15	16	21	19	23	32	37	23	21	19	26	27	31	32	23	24
	Force	9	12	14	9	14	13	16	10	14	13	16	12	9	14	13	16
Outer ring	Motion	27	32	23	34	21	31	32	12	32	23	21	12	18	19	32	19
	Force	11	15	13	12	10	9	12	14	9	14	13	10	13	14	16	13
Line move	Motion	32	34	21	28	32	18	21	23	25	21	23	18	24	23	24	24
	Force	13	16	10	14	13	16	10	13	14	16	12	9	14	13	16	13

TABLE 5: The detailed control parameters for the PID controller being utilized in the experiments.

Controller		Parameter being utilized		
Parameters		$K_p$	$K_i$	$K_d$
Inner ring	Motion	3.0	0.1	0
	Force	0.15	1.5	0
Central ring	Motion	3.5	0.15	0
	Force	0.16	1.6	0
Outer ring	Motion	10.5	0.5	0
	Force	0.1	1.75	0.01
Line move	Motion	25	0.5	0
	Force	0.05	1.5	0.01

the motion platform, and the proposed scheduling mechanism is utilized to facilitate the data transmission over the campus and the public communication networks. The dynamic performances of the teaching system with and without the scheduling mechanisms are evaluated in different cases.

- (1) Scheduling effect verification with the classical PID control strategy: we compare the performances of the outer ring force system before and after the schedule method being adopted. In the experiments, the influences of three main NCS delay factors, i.e., time delays, packet drops, and packet disordering, have been considered, wherein the influences of both packet drops and packet misordering were equivalently converted to be time delays. A simple PID controller was adopted for outer ring force system control, and the controller parameters were obtained with simple yet sophisticated modeling approach in the experiments [31], and they are also listed in Table 5. Figure 7 presents a state space description of such an adopted PID controller. Once the controller parameters are obtained, they would remain fixed for the whole experiments. The step signals starting from  $t = 0.1$  s are utilized as the system inputs; the theoretical and practical system responses are obtained. Figures 8 and 9 depict the theoretical and practical system responses with and without scheduling mechanisms being adopted, respectively. As seen in Figure 8, without adopting the scheduling mechanisms, the system response becomes divergent, i.e.,

the amplitude of the dashed curve increases with time and is away from the expected system response. In such a case, the system may finally become unstable. While once the scheduling mechanism is adopted, the system response converges, i.e., as shown in Figure 9, the practical system response converges to its expected state, and the system finally becomes stable. Such results demonstrate that the proposed scheduling algorithm could help facilitate the data transmission within NCS, which thus helps stabilize the system, even though the system dynamic performances are still not satisfactory as the system overshoot is large and the stability time is long as indicated in Figure 9.

- (2) Scheduling verification with an NCS control mechanism proposed in [32]: we implemented the NCS process control mechanism presented in [32] and applied it to remote control the motion platform in our teaching system. Specifically, the proposed scheduling algorithm was utilized to facilitate data transmission within the NCS.

Figures 10 and 11 present the step responses of the outer ring force system without and with the proposed scheduling algorithm being adopted, respectively. Results demonstrate that, owing to its predictive ability, the implemented control mechanism helps achieve satisfactory control effects even without adopting the scheduling algorithm. However, once the proposed scheduling algorithm is further adopted, the system control effects could be largely improved. As can be seen in Figure 11, the overshoot amplitude, overshoot time,

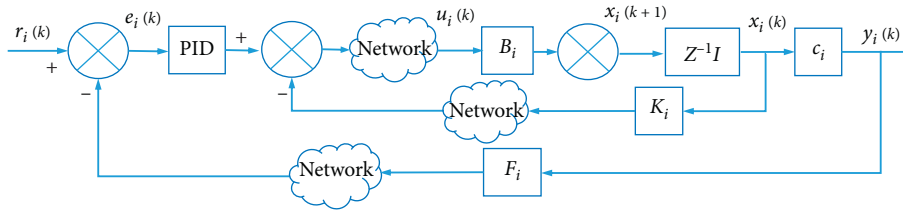


FIGURE 7: A state space description of the simple PID controller being the simplified PID control model adopted for the outer ring force system of the motion platform.

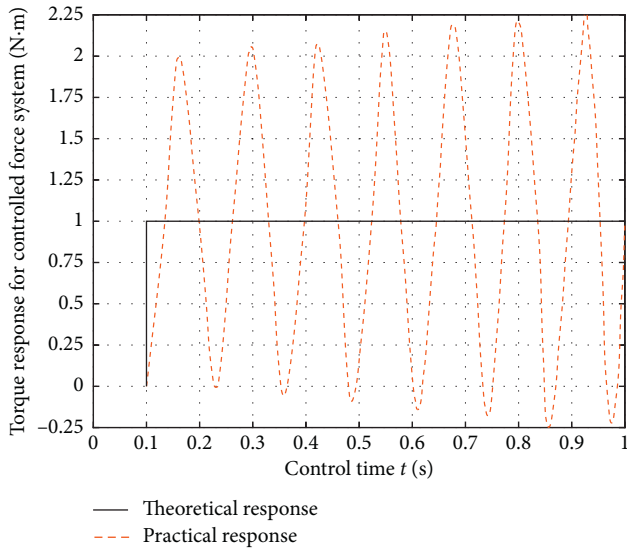


FIGURE 8: System step response before scheduling with PID controller.

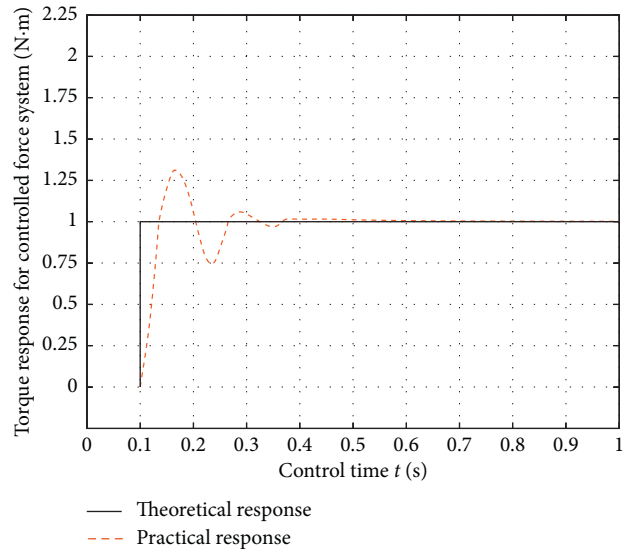


FIGURE 10: System step response for the control algorithm in [32] without scheduling mechanism.

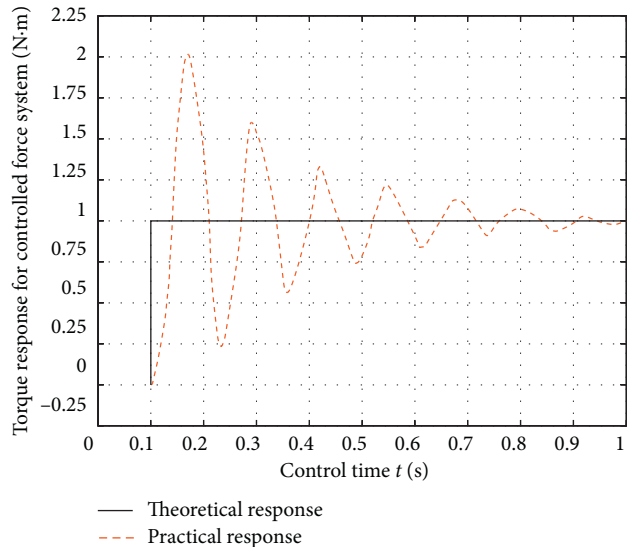


FIGURE 9: System step response after scheduling with PID controller.

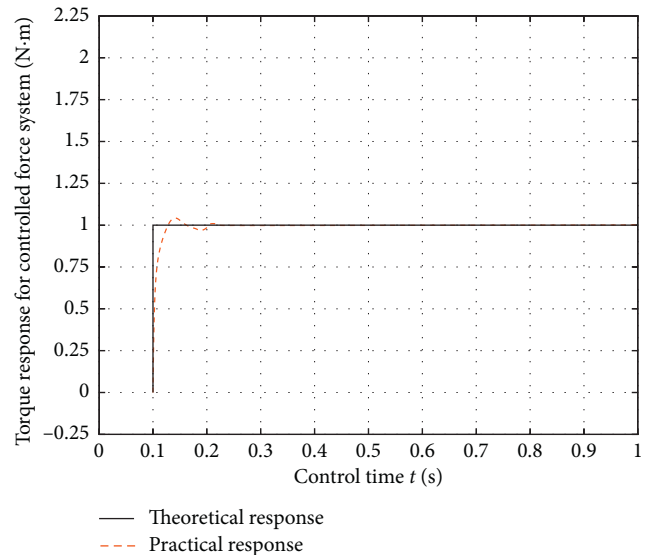


FIGURE 11: System step response for the control algorithm in [32] with scheduling mechanism adopted.

and the stabilization time are significantly reduced as compared with those in Figure 10. Such performance comparison further verifies the effectiveness of the proposed scheduling algorithm.

As discussed, for an NCS system, the main factors affecting the system stability are the time delays, packet drops, and packet misorders of the transmitted data within the system; the main objective of NCS control system design is

to achieve stable system control while minimizing the time delays. To address such an issue, the main idea of this study is to present a scheduling algorithm to reduce the time delays caused by data transmissions and postprocessing within NCS, i.e.,  $T_{i1}^{\text{wait}}(k)$ ,  $T_{i2}^{\text{wait}}(k)$ ,  $T_{i1}^{\text{pos}}(k)$ , and  $T_{i2}^{\text{pos}}(k)$ . Meanwhile, with the system time-delay bounds of the closed-loop NCSs being taken into account, the data within the NCS could be transmitted more efficiently within the system stability delay bound. In such a way, the system stability could be guaranteed while the time delays could be largely reduced. The above experimental results convincingly demonstrated the effectiveness of the proposed time-delay-bounded scheduling algorithm for NCS. Due to the large amount of data to be scheduled in real-time data transmission process, however, the proposed scheduling algorithm still suffers from the heavy data processing load, especially when the real-time audio/video data is huge. Specifically, once the time delay exceeds the time-delay bound characterized by an existing system stability criterion, the system would still be instable.

## 5. Conclusion

This paper investigates the time-delay reduction issue in distributed NCSs with time-varying delays and presents a dual-way data scheduling algorithm with the system stability time-delay bounds taken into account. Specifically, the paper analyzes the influences of various time-delay variables on the system stability first and then presents a one-way scheduling mechanism for data transmission within NCS, followed by an extended dual-way scheduling algorithm for time-delay reductions in NCSs. To verify the effectiveness of the proposed scheduling algorithm, both simulations and experiments are finally conducted on a teaching system to remote control a motion platform in different cases. Results show that the proposed scheduling algorithm could largely facilitate data transmission over the networks, which thus helps improve the NCS stability and control accuracy in different cases. It is believed that with the system time-delay bounds being considered, such a proposed scheduling algorithm could not only help reduce time-delays in NCSs, but also achieve stable system control for NCSs.

## Data Availability

All data, models, or code generated or used during the study are available from the corresponding author upon request.

## Conflicts of Interest

The authors declare that they have no conflicts of interest regarding the publication of this paper.

## Acknowledgments

The authors would like to acknowledge the financial support provided by the Fundamental Research Funds for the Central Universities (Grant no. G2018KY0308), China Postdoctoral Science Foundation (Grant no. 2018M641013), Postdoctoral Science Foundation of Shaanxi Province

(Grant no. 2018BSHYDZZ05), and the Seed Foundation of Innovation and Creation for Graduate students in Northwestern Polytechnical University (Grant nos. ZZ2019028 and ZZ2019191).

## References

- [1] T. C. Yang, "Networked control system: a brief survey," *IEE Proceedings—Control Theory and Applications*, vol. 153, no. 4, pp. 403–412, 2006.
- [2] K.-Y. You and L.-H. Xie, "Survey of recent progress in networked control systems," *Acta Automatica Sinica*, vol. 39, no. 2, pp. 101–117, 2013.
- [3] W.-A. Zhang and L. Yu, "Modelling and control of networked control systems with both network-induced delay and packet-dropout," *Automatica*, vol. 44, no. 12, pp. 3206–3210, 2008.
- [4] R. A. Gupta and M.-Y. Chow, "Networked control system: overview and research trends," *IEEE Transactions on Industrial Electronics*, vol. 57, no. 7, pp. 2527–2535, 2010.
- [5] M. S. Mahmoud and M. M. Hamdan, "Fundamental issues in networked control systems," *IEEE/CAA Journal of Automatica Sinica*, vol. 5, no. 5, pp. 902–922, 2018.
- [6] X.-M. Zhang, Q.-L. Han, X. Ge et al., "Networked control systems: a survey of trends and techniques," *IEEE/CAA Journal of Automatica Sinica*, vol. 7, no. 1, pp. 1–17, 2019.
- [7] Y. Tupsuwan and M.-Y. Chow, "Control methodologies in networked control systems," *Control Engineering Practice*, vol. 11, no. 10, pp. 1099–1111, 2003.
- [8] E. Joeliyanto, "Networked control systems: time delays and robust control design issues," in *Proceedings of the 2011 2nd International Conference on Instrumentation Control and Automation*, pp. 16–25, IEEE, Bandung, Indonesia, November 2011.
- [9] X. Ge, F. Yang, and Q.-L. Han, "Distributed networked control systems: a brief overview," *Information Sciences*, vol. 380, pp. 117–131, 2017.
- [10] H. Benítez-Pérez, J. L. Ortega-Arjona, P. E. Méndez-Monroy, E. Rubio-Acosta, and O. A. Esquivel-Flores, "Modelling of networked control systems," in *Control Strategies and Co-Design of Networked Control Systems*, pp. 25–40, Springer, Berlin, Germany, 2019.
- [11] W. P. M. H. Heemels, A. R. Teel, N. Van de Wouw, and D. Nešić, "Networked control systems with communication constraints: tradeoffs between transmission intervals, delays and performance," *IEEE Transactions on Automatic Control*, vol. 55, no. 8, pp. 1781–1796, 2010.
- [12] D. Simon, Y.-Q. Song, and C. Aubrun, *Co-design Approaches to Dependable Networked Control Systems*, John Wiley & Sons, Hoboken, NJ, USA, 2013.
- [13] D. Freirich and E. Fridman, "Decentralized networked control of systems with local networks: a time-delay approach," *Automatica*, vol. 69, pp. 201–209, 2016.
- [14] K. Liu, A. Selivanov, and E. Fridman, "Survey on time-delay approach to networked control," *Annual Reviews in Control*, vol. 48, pp. 57–79, 2019.
- [15] Y.-B. Zhao, G.-P. Liu, Y. Kang, and L. Yu, "Stability of networked control systems: a new time delay systems approach," in *Packet-Based Control for Networked Control Systems*, pp. 87–97, Springer, Berlin, Germany, 2018.
- [16] X. Wang and M. D. Lemmon, "Event-triggered broadcasting across distributed networked control systems," in *Proceedings of the 2008 American Control Conference*, pp. 3139–3144, IEEE, Seattle, WA, USA, June 2008.

- [17] X. Wang and M. D. Lemmon, "Decentralized event-triggered broadcasts over networked control systems," in *Hybrid Systems: Computation and Control*, pp. 674–677, Springer, Berlin, Germany, 2008.
- [18] X. Wang and M. D. Lemmon, "Event-triggering in distributed networked systems with data dropouts and delays," in *Hybrid Systems: Computation and Control*, pp. 366–380, Springer, Berlin, Germany, 2009.
- [19] Z. Gu, Z. Huan, D. Yue, and F. Yang, "Event-triggered dynamic output feedback control for networked control systems with probabilistic nonlinearities," *Information Sciences*, vol. 457–458, pp. 99–112, 2018.
- [20] Y.-L. Wang, C.-C. Lim, and P. Shi, "Adaptively adjusted event-triggering mechanism on fault detection for networked control systems," *IEEE Transactions on Cybernetics*, vol. 47, no. 8, pp. 2299–2311, 2017.
- [21] H. Sun, C. Peng, Y. Wang, and Y.-C. Tian, "Output-based resilient event-triggered control for networked control systems under denial of service attacks," *IET Control Theory & Applications*, vol. 13, no. 16, pp. 2521–2528, 2019.
- [22] C. Peng and F. Li, "A survey on recent advances in event-triggered communication and control," *Information Sciences*, vol. 457–458, pp. 113–125, 2018.
- [23] C. Ma, S. Chen, and W. Liu, "Maximum allowable delay bound of networked control systems with multi-step delay," *Simulation Modelling Practice and Theory*, vol. 15, no. 5, pp. 513–520, 2007.
- [24] R. Luck and A. Ray, "An observer-based compensator for distributed delays," *Automatica*, vol. 26, no. 5, pp. 903–908, 1990.
- [25] C.-H. Chen, C.-L. Lin, and T.-S. Hwang, "Stability of networked control systems with time-varying delays," *IEEE Communications Letters*, vol. 11, no. 3, pp. 270–272, 2007.
- [26] L. Zhang, Y. Shi, T. Chen, and B. Huang, "A new method for stabilization of networked control systems with random delays," *IEEE Transactions on Automatic Control*, vol. 50, no. 8, pp. 1177–1181, 2005.
- [27] A. Seuret, F. Gouaisbaut, and E. Fridman, "Stability of discrete-time systems with time-varying delays via a novel summation inequality," *IEEE Transactions on Automatic Control*, vol. 60, no. 10, pp. 2740–2745, 2015.
- [28] L. Zhang, H. Gao, and O. Kaynak, "Network-induced constraints in networked control systems—a survey," *IEEE Transactions on Industrial Informatics*, vol. 9, no. 1, pp. 403–416, 2012.
- [29] J. E. Normey-Rico and E. F. Camacho, "Dead-time compensators: a survey," *Control Engineering Practice*, vol. 16, no. 4, pp. 407–428, 2008.
- [30] K. K. Tan, T. H. Lee, and R. Ferdous, "Online relay automatic tuning of multi-loop pi controllers," *Intelligent Automation & Soft Computing*, vol. 9, no. 3, pp. 155–167, 2003.
- [31] J. B. Rawlings and D. Q. Mayne, *Model Predictive Control: Theory and Design*, Nob Hill Publishing, Madison, WI, USA, 2009.
- [32] T. Wang, H. Gao, and J. Qiu, "A combined adaptive neural network and nonlinear model predictive control for multirate networked industrial process control," *IEEE Transactions on Neural Networks and Learning Systems*, vol. 27, no. 2, pp. 416–425, 2016.

## Research Article

# Control of Multiple Viruses Interacting and Propagating in Multilayer Networks

Xiao Tu <sup>1</sup>, Guo-Ping Jiang <sup>2</sup>, Yurong Song <sup>2</sup> and Xiaoling Wang<sup>2</sup>

<sup>1</sup>School of Computer Science, Nanjing University of Posts and Telecommunications, Nanjing 210003, China

<sup>2</sup>College of Automation, Nanjing University of Posts and Telecommunications, Nanjing 210003, China

Correspondence should be addressed to Guo-Ping Jiang; [jianggp@njupt.edu.cn](mailto:jianggp@njupt.edu.cn)

Received 26 March 2020; Accepted 9 June 2020; Published 10 July 2020

Academic Editor: Bo Shen

Copyright © 2020 Xiao Tu et al. This is an open access article distributed under the Creative Commons Attribution License, which permits unrestricted use, distribution, and reproduction in any medium, provided the original work is properly cited.

Experimental studies involving control against virus propagation have attracted the interest of scientists. However, most accomplishments have been constrained by the simple assumption of a single virus in various networks, but this assumption apparently conflicts with recent developments in complex network theory, which details that each node might play multiple roles in different topological connections. Multiple viruses propagate through individuals via different routes, and thus, each individual component could be located in various positions of differing importance in each virus propagation process in each network. Therefore, we propose several control strategies for establishing a multiple-virus interaction and propagation model involving multiplex networks, including a novel Multiplex PageRank target control model and a multiplex random control model. Using computer experiments and simulations derived from actual examples, we exploit several actual cases to determine the relationship of the relative infection probability with the immunization probability. The results demonstrate the differences between our multiple-virus interaction and propagation model and the single-virus propagation model and verify the effectiveness of our novel Multiplex PageRank target control strategy. Moreover, we use parallel computing for simulating and identifying the relationships of the immunization thresholds with both interaction coefficients, which is beneficial for further practical applications because it can reduce the multiple interactions between viruses and allows achieving a greater effect through the immunization of fewer nodes in the multilayer networks.

## 1. Introduction

The structure and dynamics of multilayer networks have attracted much attention from scientific communities [1–24]. Comprised of a set of networks combined with interacting layers, these multilayer networks properly describe a variety of realistic complex systems, such as financial networks [18], ecological networks [19], information networks [20], and transportation networks [21].

Recently, many studies have attempted to discover the dynamics of viral propagation in multiplex networks. Along this line, various methods aiming at studying the virus propagation process in multilayer networks have been proposed and explored, and some examples include competing epidemics [25], the effect of the interconnected network structure [17], and the interaction of viruses and

information [26]. More explicitly, several virus spreading models in partially overlapped networks have been proposed, and these networks are described as distinct networks that contain partially identical individuals [27–29]. By considering one virus spreading via multiple routes [6] or one virus spreading in multiple species [30], corresponding virus spreading models in multilayer networks have been proposed. Interestingly, these measures are not considerably affected by multiple viral interactions.

As mentioned above, although some accomplishments have been achieved by focusing on the effect of multilayer topology on virus dynamics and the resulting threshold, the influence of such improved complexity on control strategies remains unexplored [31–36]. In conventional research on virus control, the vaccinated candidate nodes are commonly chosen randomly or spontaneously according to their

topological properties, such as degree, betweenness,  $k$ -shell, and PageRank [37–42]. Therefore, an interesting problem presents itself, which we aim to address in this work. If we consider the basic control cases in multilayer networks, how do they affect virus propagation?

Here, using the multiple-virus spreading model in multilayer networks, we study the performance of some novel control strategies, including novel Multiplex PageRank targeted control and multiplex random control strategies, in multilayer networks. Based on the generating function theory, extensive computational simulations are performed to assess our measure in various cases, and we find that the effectiveness of the proposed control strategies relies on the interaction relationship between multiple viruses in multilayer networks.

## 2. Multiple-Virus Interaction and Propagation

Unlike the existing research on single-virus propagation in overlapping networks and double virus propagation in conventional networks, we focus on multiple viruses propagating through individuals, who are integrated into all layers of a multilayer network formed by different propagation routes. In our model, we briefly exploit a double-layer network containing network  $A$  and network  $B$  of the same size  $N$  in which the nodes in both layers adopt one-to-one links. A schematic of the multilayer network is shown in Figure 1. The dashed lines represent the inner links of integrated individuals and their correspondence in the other layer. For the simulation, we construct each layer using a BA scale-free network model consisting of  $N$  nodes; this network was primarily constructed based on a random network of  $m_0$  nodes, and a new node with  $m$  links to the existing nodes was then introduced until the network contained a total of  $N$  nodes. In our model, we assume that the two viruses propagate according to their respective transmissibility in each layer, and the simulation is initiated by infecting several randomly chosen individuals in the multilayer network.

The propagation process follows a multiple-virus propagation model ( $S_A I_A S_A - S_B I_B S_B$ ) in a multilayer network, where each node can be divided into four compartments relevant to the two viruses: the individuals who are susceptible to both the virus in network  $A$  and the virus in network  $B$  ( $S_A S_B$ ), the individuals who are susceptible to the virus propagated in  $A$  while infected with the virus propagated in  $B$  ( $S_A I_B$ ), the individuals who are infected with the virus propagated in  $A$  while susceptible to the virus propagated in  $B$  ( $I_A S_B$ ), and the individuals who are infected with both the virus propagated in  $A$  and the virus propagated in  $B$  ( $I_A I_B$ ). An individual at state  $S_A$  in  $A$  can be converted to state  $I_A$  if it comes in contact with any neighbor at state  $I_A$ , which occurs with the probability  $\alpha_A^{S_B}$  if the individual is at state  $S_B$  in  $B$ . An individual at state  $S_A$  in  $A$

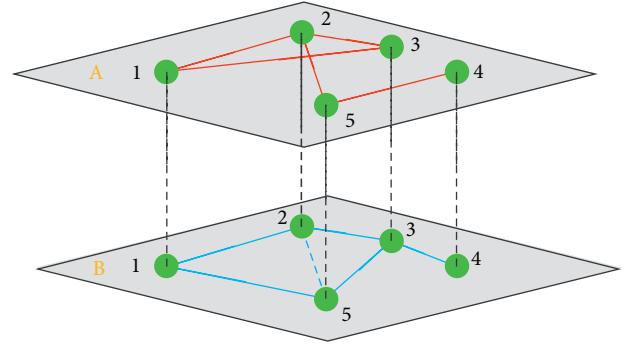


FIGURE 1: Multilayer network; the dashed lines show the inner links of the integrated nodes. Prior to the initiation of propagation, all individuals are in the susceptible state, which is represented by a green circle.

can be converted to state  $I_A$  with the probability  $\alpha_A^{I_B}$  if the individual is at state  $I_B$  in  $B$ . Similar to  $A$ , an individual at state  $S_B$  in  $B$  can be converted to state  $I_B$  with the probability  $\alpha_B^{S_A}$  if the individual is at state  $S_A$  in  $A$ . An individual at state  $S_B$  in  $B$  can be converted to  $I_B$  state with the probability  $\alpha_B^{I_A}$  if the individual is at state  $I_A$  in  $A$ . An individual at state  $I_A$  might be cured and returned to state  $S_A$  with the probability  $\mu_A$ , whereas an individual at state  $I_B$  might be cured and return to state  $S_B$  with the probability  $\mu_B$ .

Moreover,  $\alpha_A^{S_B}$  and  $\alpha_A^{I_B}$  are related by the interaction coefficient  $c_A^{I_B}$  such that  $\alpha_A^{I_B} = c_A^{I_B} \alpha_A^{S_B}$ , where  $c_A^{I_B}$  indicates the influence of the virus in  $B$  on the spreading probability of the virus in  $A$ , whereas  $\alpha_B^{S_A}$  and  $\alpha_B^{I_A}$  are related by the interaction coefficient  $c_B^{I_A}$  such that  $\alpha_B^{I_A} = c_B^{I_A} \alpha_B^{S_A}$ , where  $c_B^{I_A}$  refers to the influence of the virus in  $A$  on the propagation probability of the virus in  $B$ . Notably,  $c_A^{I_B} \geq 0$ ,  $\alpha_A^{S_B} \in [0, 1]$ , and  $\alpha_A^{I_B} \in [0, 1]$ . In particular,  $c_A^{I_B} = 0$  indicates that the virus in  $B$  is immune to the virus in  $A$ ;  $0 < c_A^{I_B} < 1$  indicates that the virus in  $B$  inhibits the virus in  $A$ ;  $c_A^{I_B} = 1$  indicates that the virus in  $B$  has no effect on the virus in  $A$ ; and  $c_A^{I_B} > 1$  indicates that the virus in  $B$  enhances the virus in  $A$ . In addition, the spreading probability  $\alpha_A^{I_B}$  must satisfy  $\alpha_A^{I_B} \leq 1$ ; therefore, if  $c_A^{I_B} \alpha_A^{S_B} > 1$ , then  $\alpha_A^{I_B} = 1$ . The conditions in  $B$  are similar to those in  $A$ .

Because we use  $A$  and  $B$  to denote the two virus propagation routes,  $A_{ji}$  and  $B_{ji}$  are denoted as the edges from individual  $j$  to individual  $i$  by the routes of each propagated virus, which are equal to 1 if edges exist and 0 otherwise. We adopt the process of a continuous time Markov chain to describe the interaction of multiple propagating viruses by defining  $X_i^t$  and  $Y_i^t$  as measures of the random variables  $X$  and  $Y$  of node  $i$  at time  $t$ , respectively. For each  $i \in \{1, 2, \dots, N\}$ , the random variables  $X_i$  and  $Y_i$  satisfy  $X_i: \{S_A, I_A\} \rightarrow \{0, 1\}$  and  $Y_i: \{S_B, I_B\} \rightarrow \{0, 1\}$ . Therefore, the continuous time Markov chain equation of the node state evolution over time is represented as follows:

$$\begin{aligned}
\Pr[X_i^{t+1} = 1, Y_i^{t+1} = 0 | X_i^t = 0, Y_i^t = 0] &= \alpha_A^{S_B} \Delta t \sum_{j \in N_i} 1_{\{X_j^t=1\}} + o(\Delta t), \\
\Pr[X_i^{t+1} = 1, Y_i^{t+1} = 1 | X_i^t = 0, Y_i^t = 1] &= \alpha_A^{I_B} \Delta t \sum_{j \in N_i} 1_{\{X_j^t=1\}} + o(\Delta t), \\
\Pr[X_i^{t+1} = 0, Y_i^{t+1} = 0 | X_i^t = 1, Y_i^t = 0] &= \mu_A \Delta t + o(\Delta t), \\
\Pr[X_i^{t+1} = 0, Y_i^{t+1} = 1 | X_i^t = 0, Y_i^t = 0] &= \alpha_B^{S_A} \Delta t \sum_{j \in N_i} 1_{\{Y_j^t=0\}} + o(\Delta t), \\
\Pr[X_i^{t+1} = 1, Y_i^{t+1} = 1 | X_i^t = 1, Y_i^t = 0] &= \alpha_B^{I_A} \Delta t \sum_{j \in N_i} 1_{\{Y_j^t=1\}} + o(\Delta t), \\
\Pr[X_i^{t+1} = 0, Y_i^{t+1} = 0 | X_i^t = 0, Y_i^t = 1] &= \mu_B \Delta t + o(\Delta t).
\end{aligned} \tag{1}$$

where  $\Pr$  is the probability and  $\Delta t > 0$  is a time step,  $1_{\{\chi\}}$ , which is equal to 1 if  $\chi$  is true or 0 otherwise. If  $\lim_{\Delta t \rightarrow 0} (f(\Delta t)/\Delta t) = 0$ ,  $f(\Delta t)$  can be written as  $o(\Delta t)$ . In particular,  $1_{\{X_j^t=1\}}$  can be represented by  $\Pr[X_j = 1]$ . Thus,

the continuous Markov chain equation (1) can be transformed to a new random stochastic equation:

$$\begin{aligned}
\Pr[X_i^{t+1} = 1, Y_i^{t+1} = 0 | X_i^t = 0, Y_i^t = 0] &= \alpha_A^{S_B} \Delta t \sum_{j \in N_i} \Pr[X_j^t = 1] + o(\Delta t), \\
\Pr[X_i^{t+1} = 1, Y_i^{t+1} = 1 | X_i^t = 0, Y_i^t = 1] &= \alpha_A^{I_B} \Delta t \sum_{j \in N_i} \Pr[X_j^t = 1] + o(\Delta t), \\
\Pr[X_i^{t+1} = 0, Y_i^{t+1} = 0 | X_i^t = 1, Y_i^t = 0] &= \mu_A \Delta t + o(\Delta t), \\
\Pr[X_i^{t+1} = 0, Y_i^{t+1} = 1 | X_i^t = 0, Y_i^t = 0] &= \alpha_B^{S_A} \Delta t \sum_{j \in N_i} \Pr[Y_j^t = 1] + o(\Delta t), \\
\Pr[X_i^{t+1} = 1, Y_i^{t+1} = 1 | X_i^t = 1, Y_i^t = 0] &= \alpha_B^{I_A} \Delta t \sum_{j \in N_i} \Pr[Y_j^t = 1] + o(\Delta t), \\
\Pr[X_i^{t+1} = 0, Y_i^{t+1} = 0 | X_i^t = 0, Y_i^t = 1] &= \mu_B \Delta t + o(\Delta t).
\end{aligned} \tag{2}$$

The value of the nodes reflects the average probability of the four states at time  $t$ , which are, respectively, denoted by  $p_i^{S_A S_B}(t)$ ,  $p_i^{S_A I_B}(t)$ ,  $p_i^{I_A S_B}(t)$ , and  $p_i^{I_A I_B}(t)$  and satisfy

$$p_i^{S_A S_B}(t) + p_i^{S_A I_B}(t) + p_i^{I_A S_B}(t) + p_i^{I_A I_B}(t) = 1. \tag{3}$$

Thus, the average probability of the virus in  $A$  at time  $t$  is represented as  $p_i^{I_A}(t) = p_i^{I_A S_B}(t) + p_i^{I_A I_B}(t)$  and that of the

virus in  $B$  at time  $t$  is represented as  $p_i^{I_B}(t) = p_i^{S_A I_B}(t) + p_i^{I_A I_B}(t)$ . We defined the new state as  $Z_i (\in [p_i^{S_A S_B}, p_i^{S_A I_B}, p_i^{I_A S_B}, p_i^{I_A I_B}])$ . According to the correlation theorem and the properties of the continuous time Markov chain, the transfer matrix  $Q$  of the stochastic process can be obtained as follows:

$$Q = \begin{bmatrix} -\alpha_A^{S_B} \sum_j A_{ji} p_j^{I_A} - \alpha_B^{S_A} \sum_j B_{ji} p_j^{I_B} & -\alpha_A^{I_B} \sum_j A_{ji} p_j^{I_A} + \mu_B & \mu_A - \alpha_B^{S_A} \sum_j B_{ji} p_j^{I_B} & \mu_A + \mu_B \\ -\alpha_A^{S_B} \sum_j A_{ji} p_j^{I_A} + \alpha_B^{S_A} \sum_j B_{ji} p_j^{I_B} & -\alpha_A^{I_B} \sum_j A_{ji} p_j^{I_A} - \mu_B & \mu_A + \alpha_B^{S_A} \sum_j B_{ji} p_j^{I_B} & \mu_A - \mu_B \\ \alpha_A^{S_B} \sum_j A_{ji} p_j^{I_A} - \alpha_B^{S_A} \sum_j B_{ji} p_j^{I_B} & \alpha_A^{I_B} \sum_j A_{ji} p_j^{I_A} + \mu_B & -\mu_A - \alpha_B^{S_A} \sum_j B_{ji} p_j^{I_B} & -\mu_A + \mu_B \\ \alpha_A^{S_B} \sum_j A_{ji} p_j^{I_A} + \alpha_B^{S_A} \sum_j B_{ji} p_j^{I_B} & \alpha_A^{I_B} \sum_j A_{ji} p_j^{I_A} - \mu_B & -\mu_A + \alpha_B^{S_A} \sum_j B_{ji} p_j^{I_B} & -\mu_A - \mu_B \end{bmatrix}^T. \tag{4}$$

Therefore, the Kolmogorov forward differential equations of the stochastic process (2) can be represented as follows:

$$\dot{Z}_i = Z_i Q, \quad i \in \{1, 2, \dots, N\}. \tag{5}$$

We can expand the differential equations of node  $i$  to obtain



$$\begin{aligned}
\dot{p}_i^{S_A S_B} &= \left( -\alpha_A^{S_B} \sum_j A_{ji} p_j^{I_A} - \alpha_B^{S_A} \sum_j B_{ji} p_j^{I_B} \right) p_i^{S_A S_B} + \left( -\alpha_A^{I_B} \sum_j A_{ji} p_j^{I_A} + \mu_B \right) p_i^{S_A I_B} \\
&\quad + \left( \mu_A - \alpha_B^{S_A} \sum_j B_{ji} p_j^{I_B} \right) p_i^{I_A S_B} + (\mu_A + \mu_B) p_i^{I_A I_B}, \\
\dot{p}_i^{S_A I_B} &= \left( -\alpha_A^{S_B} \sum_j A_{ji} p_j^{I_A} + \alpha_B^{S_A} \sum_j B_{ji} p_j^{I_B} \right) p_i^{S_A S_B} + \left( -\alpha_A^{I_B} \sum_j A_{ji} p_j^{I_A} - \mu_B \right) p_i^{S_A I_B} \\
&\quad + \left( \mu_A + \alpha_B^{S_A} \sum_j B_{ji} p_j^{I_B} \right) p_i^{I_A S_B} + (\mu_A - \mu_B) p_i^{I_A I_B}, \\
\dot{p}_i^{I_A S_B} &= \left( \alpha_A^{S_B} \sum_j A_{ji} p_j^{I_A} - \alpha_B^{S_A} \sum_j B_{ji} p_j^{I_B} \right) p_i^{S_A S_B} + \left( \alpha_A^{I_B} \sum_j A_{ji} p_j^{I_A} + \mu_B \right) p_i^{S_A I_B} \\
&\quad + \left( -\mu_A - \alpha_B^{S_A} \sum_j B_{ji} p_j^{I_B} \right) p_i^{I_A S_B} + (-\mu_A + \mu_B) p_i^{I_A I_B}, \\
\dot{p}_i^{I_A I_B} &= \left( \alpha_A^{S_B} \sum_j A_{ji} p_j^{I_A} + \alpha_B^{S_A} \sum_j B_{ji} p_j^{I_B} \right) p_i^{S_A S_B} + \left( \alpha_A^{I_B} \sum_j A_{ji} p_j^{I_A} - \mu_B \right) p_i^{S_A I_B} \\
&\quad + \left( -\mu_A + \alpha_B^{S_A} \sum_j B_{ji} p_j^{I_B} \right) p_i^{I_A S_B} + (-\mu_A - \mu_B) p_i^{I_A I_B}.
\end{aligned} \tag{6}$$

### 3. Multiplex Control Strategy

In contrast to the control of each noninteracted virus in each conventional network individually, the multiplex control strategy aims to immunize fewer nodes but achieve a greater effect on both of the interacting viruses in the multilayer network simultaneously. Thus, we compare our novel Multiplex PageRank target control with multiplex random control in a multilayer network.

Recently, researchers have focused on measuring the centrality of multiplex networks. The eigenvector multiplex centrality hypothesizes that the centrality of a node in one layer is impacted by its centrality in other layers by an overlapped influence matrix [43]. The versatility of nodes highlights the relevance of related nodes in different layers and applies to multilayer networks in which the corresponding nodes in different layers are connected by interlinks [44]. The Multiplex PageRank centrality utilizes the correlations among the degrees of nodes in different layers by means of a random walk subject to teleportation [45–49].

Among these centrality measures, the versatility of nodes is the only measure that considers the interlinks, whereas both the Multiplex PageRank centrality and the eigenvector multiplex centrality stipulate one-to-one links among the nodes in different layers, which are denoted inner links throughout the rest of the manuscript paper. An inner link induces a coupling relationship that will impact the distribution of centrality inside the same node. The major challenge when identifying the centrality of a node in a multiplex network with inner links is that the centrality depends on the relationship among the distinct types of links, which are also known as traditional links, between

different nodes in the same layer. This study attempts to address the issue of the centrality distribution through a generalization of PageRank by considering the coupling relationship.

Our novel Multiplex PageRank measure is derived from a random population migration in an urban multilayer transport network, including a flight network  $A$  and a railway network  $B$ , to obtain the rankings of the hub cities in terms of transportation. Because we aim to obtain the rankings of the hub cities in terms of transportation, two or more train stations or airports in a same city are considered single stations or airports. The connections between train stations or airports in different cities are identified by the existence of railways or airlines. The population is migrating according to the distribution coefficients  $\beta_A$  and  $\beta_B$ , which satisfy  $0 \leq \beta_A + \beta_B \leq 1$ . This relationship indicates that some of the population ( $\beta_A$ ) prefer travelling by aircraft, some of the population ( $\beta_B$ ) prefer travelling by train, and some of the population ( $1 - \beta_A - \beta_B$ ) refuse to travel because they are choosing to remain in cities due to personal interests. The total population of city  $i$  at time  $t$  is defined as  $S_i(t)$ . Therefore, we can obtain  $S_i(t+1)$  as

$$S_i(t+1) = \sum_j A_{ji} \frac{\beta_A S_j(t)}{H_j^{(A)}} + \sum_j B_{ji} \frac{\beta_B S_j(t)}{H_j^{(B)}} + (1 - \beta_A - \beta_B) v_i, \tag{7}$$

where  $H_j^{(A)} = \sum_r A_{jr} + \delta(0, \sum_r A_{jr})$ ,  $H_j^{(B)} = \sum_r B_{jr} + \delta(0, \sum_r B_{jr})$ , and  $\delta(x, y)$  is the Kronecker delta, which equals one if  $x = y$  and zero if  $x \neq y$  and can be exploited to control city  $j$  without any transportation to other cities to keep the population of  $j$  in itself, and  $v_i$  is the personalized interests of

the population staying in city  $i$ . By initializing each  $S_i(0)$  by the value  $N^{-1}$ , as determined by the number of cities and repeating the migration process, we can obtain the rankings of the hub cities in terms of transportation and derive the rankings in terms of node importance in a multilayer network.

Based on our urban multiplex transport network, which has two layers, the generated Multiplex PageRank centrality

measure is applied to a multiplex network of  $M$  layers with  $N$  nodes in each layer as follows:

$$S_i(t+1) = \sum_L \sum_j g_{ji}^{(L)} \frac{\alpha_L S_i(t)}{H_j^{(L)}} + \left(1 - \sum_L \alpha_L\right) v_i, \quad (8)$$

where  $H_j^{(L)} = \sum_r g_{jr}^{(L)} + \delta(0, \sum_r g_{jr}^{(L)})$ ,

$$\begin{aligned} \dot{p}_i^{S_A S_B} &= \left( -\alpha_A^{S_B} \sum_j A_{ji} p_j^{I_A} - \alpha_B^{S_A} \sum_j B_{ji} p_j^{I_B} \right) p_i^{S_A S_B} (1 - w_i) + \left( -\alpha_A^{I_B} \sum_j A_{ji} p_j^{I_A} + \mu_B \right) p_i^{S_A I_B} (1 - w_i) \\ &\quad + \left( \mu_A - \alpha_B^{S_A} \sum_j B_{ji} p_j^{I_B} \right) p_i^{I_A S_B} (1 - w_i) + (\mu_A + \mu_B) p_i^{I_A I_B} (1 - w_i), \\ \dot{p}_i^{S_A I_B} &= \left( -\alpha_A^{S_B} \sum_j A_{ji} p_j^{I_A} + \alpha_B^{S_A} \sum_j B_{ji} p_j^{I_B} \right) p_i^{S_A S_B} (1 - w_i) + \left( -\alpha_A^{I_B} \sum_j A_{ji} p_j^{I_A} - \mu_B \right) p_i^{S_A I_B} (1 - w_i) \\ &\quad + \left( \mu_A + \alpha_B^{S_A} \sum_j B_{ji} p_j^{I_B} \right) p_i^{I_A S_B} (1 - w_i) + (\mu_A - \mu_B) p_i^{I_A I_B} (1 - w_i), \\ \dot{p}_i^{I_A S_B} &= \left( \alpha_A^{S_B} \sum_j A_{ji} p_j^{I_A} - \alpha_B^{S_A} \sum_j B_{ji} p_j^{I_B} \right) p_i^{S_A S_B} (1 - w_i) + \left( \alpha_A^{I_B} \sum_j A_{ji} p_j^{I_A} + \mu_B \right) p_i^{S_A I_B} (1 - w_i) \\ &\quad + \left( -\mu_A - \alpha_B^{S_A} \sum_j B_{ji} p_j^{I_B} \right) p_i^{I_A S_B} (1 - w_i) + (-\mu_A + \mu_B) p_i^{I_A I_B} (1 - w_i), \\ \dot{p}_i^{I_A I_B} &= \left( \alpha_A^{S_B} \sum_j A_{ji} p_j^{I_A} + \alpha_B^{S_A} \sum_j B_{ji} p_j^{I_B} \right) p_i^{S_A S_B} (1 - w_i) + \left( \alpha_A^{I_B} \sum_j A_{ji} p_j^{I_A} - \mu_B \right) p_i^{S_A I_B} (1 - w_i) \\ &\quad + \left( -\mu_A + \alpha_B^{S_A} \sum_j B_{ji} p_j^{I_B} \right) p_i^{I_A S_B} (1 - w_i) + (-\mu_A - \mu_B) p_i^{I_A I_B} (1 - w_i). \end{aligned} \quad (9)$$

We start the multiplex target control strategy by immunizing the top  $\phi \in [0, 1]$  ranked individuals in the multilayer network or the multiplex random control strategy by immunizing an arbitrary number of  $\phi$  individuals in the multilayer network before virus propagation begins. An immunized individual is aware of, takes preventive action against, and is immunized to both viruses in both layers and thus cannot be infected or is infectious throughout the propagation process. We define the immunization state of an individual  $i$  as  $w_i$ , which is equal to 1 if  $i$  is immunized and to 0 otherwise.

After immunization, we propagate both viruses in the multilayer network, and this process is initiated by infecting several random susceptible nonimmunized individuals in each layer. We then obtain expansion of the Kolmogorov forward differential equations of the stochastic process of the continuous time Markov Chains for the multiple-virus propagation model, which is constrained by the multiplex control strategy for each node  $i$  as represented in (9).

#### 4. Simulation

Considering the interaction relationships between the two viruses, several actual cases are investigated through computer experiments and simulations. By adopting  $\rho_\phi$  as the infection probability at an immunization probability  $\phi$  at the steady state and  $\rho_0$  as the infection probability without control at the steady state, we can obtain the immunized probability versus the steady infection probability for the following. The common parameters are set to  $N = 10000$ ,  $\alpha_A^{S_B} = 0.2$ ,  $\alpha_B^{S_A} = 0.2$ ,  $\mu_A = 0.8$ , and  $\mu_B = 0.8$ , and  $\phi$  ranges from 0 to 1 at 1% intervals. Moreover, we adopt  $m_0 = 20$  and  $m = 8$  to construct network  $A$ , and  $m_0 = 30$  and  $m = 12$  are used to construct network  $B$ . Moreover,  $I_A$  means the nodes infected with the virus in network  $A$ ,  $I_B$  means the nodes infected with the virus in network  $B$ , and  $I_A \cup I_B$  means the union of  $I_A$  and  $I_B$ , i.e., all infected nodes without considering the types of viruses. The control results are averaged by simulating 100 time steps 1000 times in 50 multilayer networks.

Because an individual who is affected with whooping cough or measles will infect another individual [50], we adopt  $c_A^{I_B} = 0$  for whooping cough or  $c_B^{I_A} = 0$  for measles. Because there are more propagation routes for measles than whooping cough, we adopt  $A$  to denote the propagation routes of whooping cough and  $B$  to denote the propagation routes of measles. By deciding to mainly immunize against measles and to immunize against whooping cough indirectly, we adopt the distribution coefficients  $\beta_A = 0.35$  and  $\beta_B = 0.5$  because measles is more dangerous than whooping cough. The simulation results are shown in Figure 2. As shown in Figure 2(a), the immunization threshold of the multiplex random control of whooping cough is in a high value about 0.8, and the decreasing rate of the curve is smaller and smaller, whereas the immunization threshold of the multiplex target control of whooping cough is constrained to a very low value, which is affected by the control of measles with our novel Multiplex PageRank method and the limitations caused by the existence of fewer propagation routes for whooping cough compared with those of multiplex random control. In addition, as shown in Figure 2(b), the immunization threshold of the multiplex random control of whooping cough is about equal to that of measles, but the decreasing rate of the curve is constant, whereas a turning point can be found in the curve of the multiplex target control of measles before the immunization threshold is reached. This finding indicates that measles benefits from a greater number of propagation routes, and thus, the infection probability of our Multiplex PageRank target control decreases at a lower rate compared with that observed with multiplex random control. The turning point occurs at the value of approximately 0.12 when the population has been completely immunized against whooping cough, and thus, the control of the population to whooping cough results in a decrease in the immunization rate of measles. Figure 2(c) presents the union of infections of whooping cough and measles in the multilayer network. The decreasing infection probability rate remains at a steady rate. As shown by the results, the Multiplex PageRank target control strategy immunizes fewer nodes and has a greater effect on both viruses simultaneously in the multilayer network.

A computer that is affected by countermeasures, which are also classified as infectious malware in China, can avoid infection by some computer viruses [51]. In addition, a computer affected by these computer viruses is not affected by the propagation of countermeasures; thus, we adopt  $c_A^{I_B} = 1$  for countermeasures and  $c_B^{I_A} = 0$  for computer viruses. Because the propagation routes of computer viruses are increased compared with those of countermeasures, we adopt  $A$  to denote the propagation routes of countermeasures and  $B$  to denote the propagation routes of computer viruses. By deciding to mainly immunize against computer viruses and to immunize against countermeasures indirectly, we adopt the distribution coefficients  $\beta_A = 0.35$  and  $\beta_B = 0.5$  because computer viruses are more dangerous than countermeasures. The simulation results are shown in Figure 3. The results shown in Figure 3(a) demonstrate that the immunization threshold of the multiplex target control of the countermeasures is constrained to a lower value than

that of multiplex random control. Even if we mainly concentrate on immunizing against computer viruses, the propagation of countermeasures is constrained by the decreased propagation routes. However, the immunization threshold of the multiplex random control of the countermeasures is at a high value about 0.8, and the decreasing rate of the curve is constant. In addition, Figure 3(b) shows the existence of several turning points in the curve of multiplex target control against computer viruses prior to attaining the immunization threshold. However, the immunization threshold of the multiplex random control of computer viruses is in a high value about 0.8, and the decreasing rate of the curve is constant. This finding indicates that the computer viruses are first immunized by the countermeasures. The first turning point is found at a value of approximately 0.2 when the countermeasures propagate within the top-ranked nodes are mostly immunized, which results in an increase in the probability of infection with computer viruses. However, the infection probability soon begins to decrease at a value of approximately 0.27 after the population is fully immunized against countermeasures, which also immunizes against computer viruses. Figure 3(c) presents the union of the infections by countermeasures and computer viruses in the multilayer network. The decreasing rate of the infection probability remains unchanged, and the results show that our Multiplex PageRank target control strategy involves the control of fewer nodes to achieve greater effects on both viruses simultaneously in the multilayer network.

Assuming that an individual who is affected with hepatitis C or B virus will show inhibition against the other virus and that the inhibition of hepatitis B virus by hepatitis C virus is stronger than that of hepatitis C virus by hepatitis B virus [52], we adopt  $c_A^{I_B} = 0.5$  for hepatitis C virus and  $c_B^{I_A} = 0.3$  for hepatitis B virus. Because there are more propagation routes for hepatitis B virus than for hepatitis C virus, we adopt  $A$  to denote the propagation routes of hepatitis C virus and  $B$  to denote the propagation routes of hepatitis B virus. Based on the decision to mainly immunize against hepatitis B virus and sometimes immunize against hepatitis C virus, we adopt the distribution coefficients  $\beta_A = 0.35$  and  $\beta_B = 0.5$  because hepatitis B virus is more dangerous than hepatitis C virus. The simulation results are shown in Figure 4. As shown in Figure 4(a), the immunization threshold of the multiplex random control of hepatitis C virus is at a high value about 0.8, and the decreasing rate of the curve is constant, whereas the immunization threshold of the multiplex target control of the hepatitis C virus is constrained to a lower value based on control with our novel Multiplex PageRank, the suppression of hepatitis B virus, and the limitation of the propagation routes of hepatitis C virus compared with multiplex random control. Moreover, the results in Figure 4(b) demonstrate a change in the decreasing rate of the infection probability obtained with multiplex target control of hepatitis B virus before attaining the immunization threshold. However, the immunization threshold of the multiplex random control of hepatitis B virus is in a high value about 0.8, and the decreasing rate of the curve is constant. These results indicate that hepatitis B

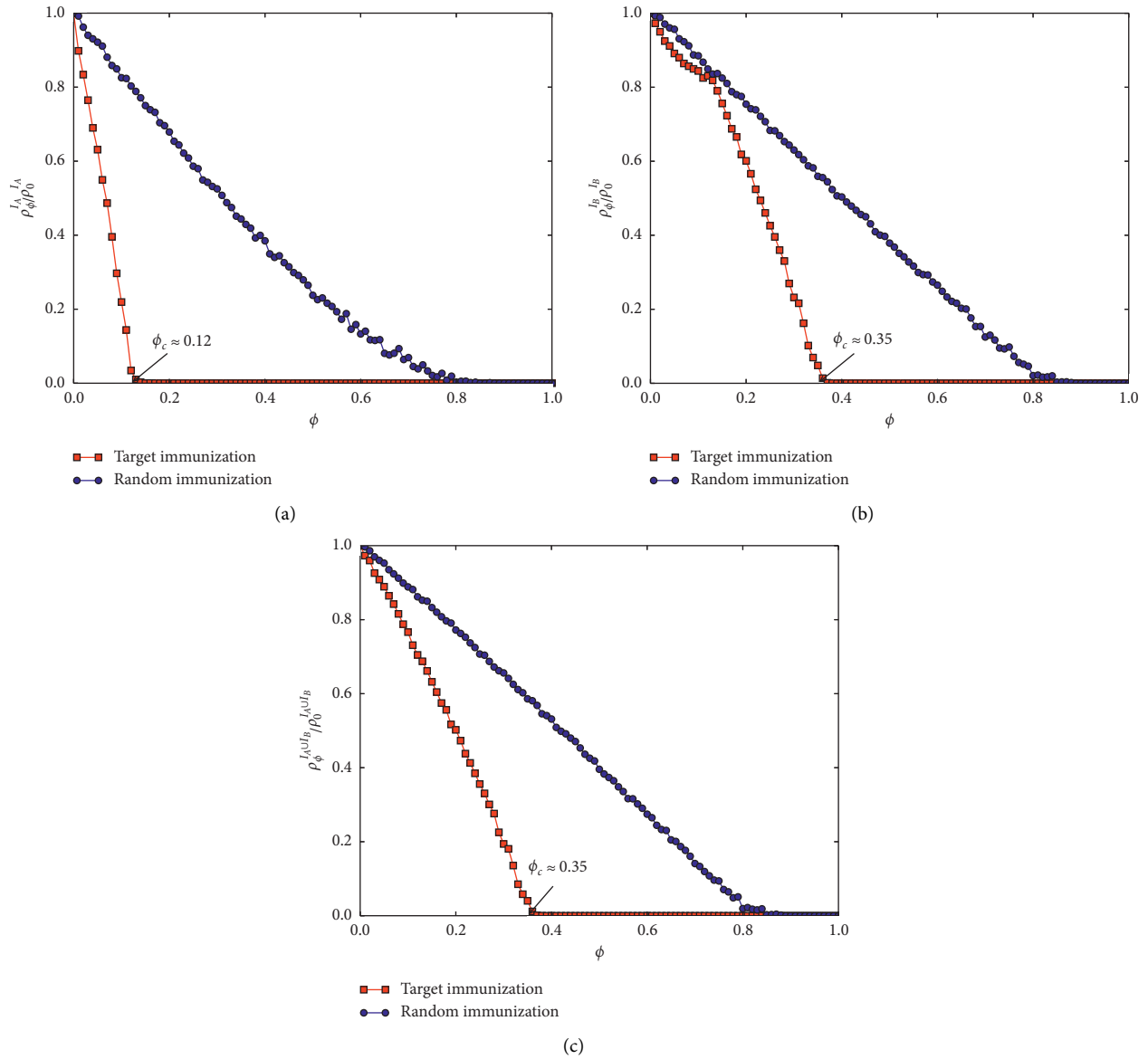


FIGURE 2: Relative size ( $\rho_\phi/\rho_0$ ) of infected clusters versus the immunization probability  $\phi$  for multiple targets or random control in a double layer network that involves whooping cough and measles: (a) whooping cough-infected clusters, (b) measles-infected clusters, and (c) clusters infected with both whooping cough and measles. The arrow denotes the immunization threshold  $\phi_c$  of our novel Multiplex PageRank target control.

virus is first suppressed by hepatitis C virus. The change in the decreasing rate of the infection is probability at a value of approximately 0.24 occurred when the population is completely immunized against hepatitis C virus, which occasioning results in a decline in the decreasing rate of the infection probability of hepatitis B virus. However, the decreasing rate of the infection probability soon increases with an increase in the immunization probability. Figure 4(c) presents the union of infection with hepatitis C and B viruses in the multilayer network. The decreasing rate of the infection probability is maintained at a constant rate. Our Multiplex PageRank target control strategy indicates that the control of fewer nodes can achieve a greater effect on both viruses simultaneously in the multilayer network.

Because tuberculosis does not affect HIV but an individual who is infected with HIV will be more susceptible to infection by tuberculosis [53], we adopt  $c_A^{I_B} = 1.5$  for tuberculosis and  $c_B^{I_A} = 1$  for HIV. Due to the higher number of propagation routes for HIV compared with tuberculosis, we adopt  $A$  to denote the propagation routes of tuberculosis and  $B$  to denote the propagation routes of HIV. By deciding to mainly immunize against HIV and only slightly immunize against tuberculosis, we adopt the distribution coefficients  $\beta_A = 0.35$  and  $\beta_B = 0.5$  because HIV is more dangerous than tuberculosis. The simulation results are shown in Figure 5. The results in Figure 5(a) reveal a small change in the decreasing rate of the infection probability with multiplex target control of tuberculosis before attaining the

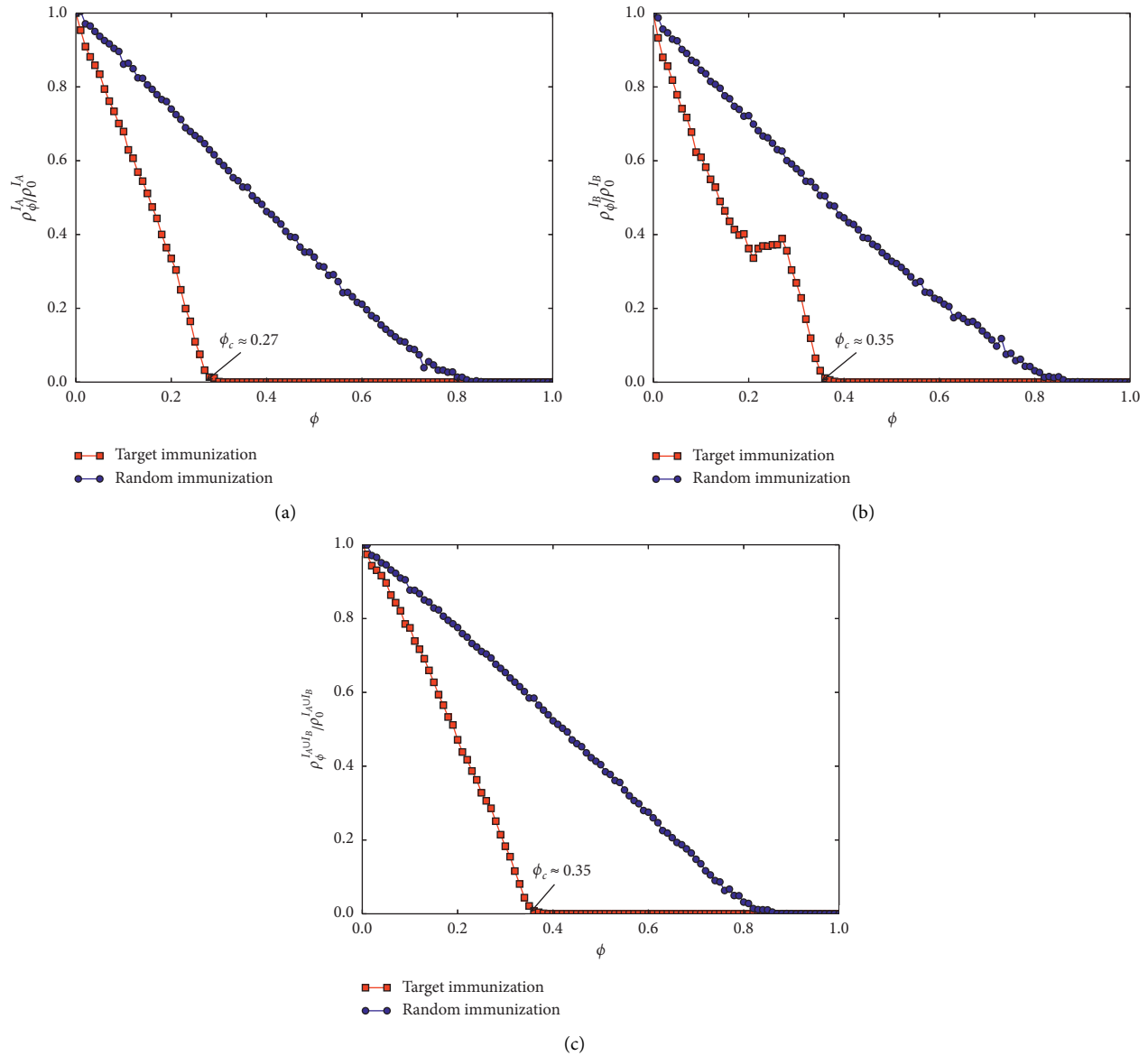


FIGURE 3: Relative size ( $\rho_\phi/\rho_0$ ) of infected clusters versus the immunization probability  $\phi$  for multiplex target or random control in a double-layer network that includes countermeasures and computer viruses: (a) countermeasures-infected clusters, (b) computer virus-infected clusters, and (c) clusters infected with both countermeasures and computer viruses. The arrow denotes the immunization threshold  $\phi_c$  of our novel Multiplex PageRank target control.

immunization threshold. However, the immunization threshold of the multiplex random control of tuberculosis is at a high value about 0.8, and the decreasing rate of the curve is constant. This finding indicates that tuberculosis is first enhanced by HIV. The change in the decreasing rate of the infection probability occurs at the value of approximately 0.22 when HIV is propagated in the top ranking nodes, which are mostly immunized, and this finding results in a small increase in the decreasing rate of the infection probability of tuberculosis. However, even if tuberculosis infection has been enhanced, it is constrained by its fewer propagation routes; thus, the population is completely immunized against tuberculosis before it is immunized against HIV. Moreover, as shown in Figure 5(b), the immunization

threshold of the multiplex random control of HIV is at a high value about 0.8, and the decreasing rate of the curve is constant. We also find a small change in the rate of the infection probability obtained through multiplex target control for HIV before the immunization threshold is attained. The change in the decreasing rate of the infection is probability obtained at a value of approximately 0.29 when the population is completely immunized against tuberculosis, which results in a greater decreasing rate for control against HIV. Figure 5(c) shows the union of the infection probability of tuberculosis and HIV in the multilayer network. A decreasing rate of the infection probability increases at a value of approximately 0.22 due to the increase in the decreasing rate of tuberculosis and decreases at a value of

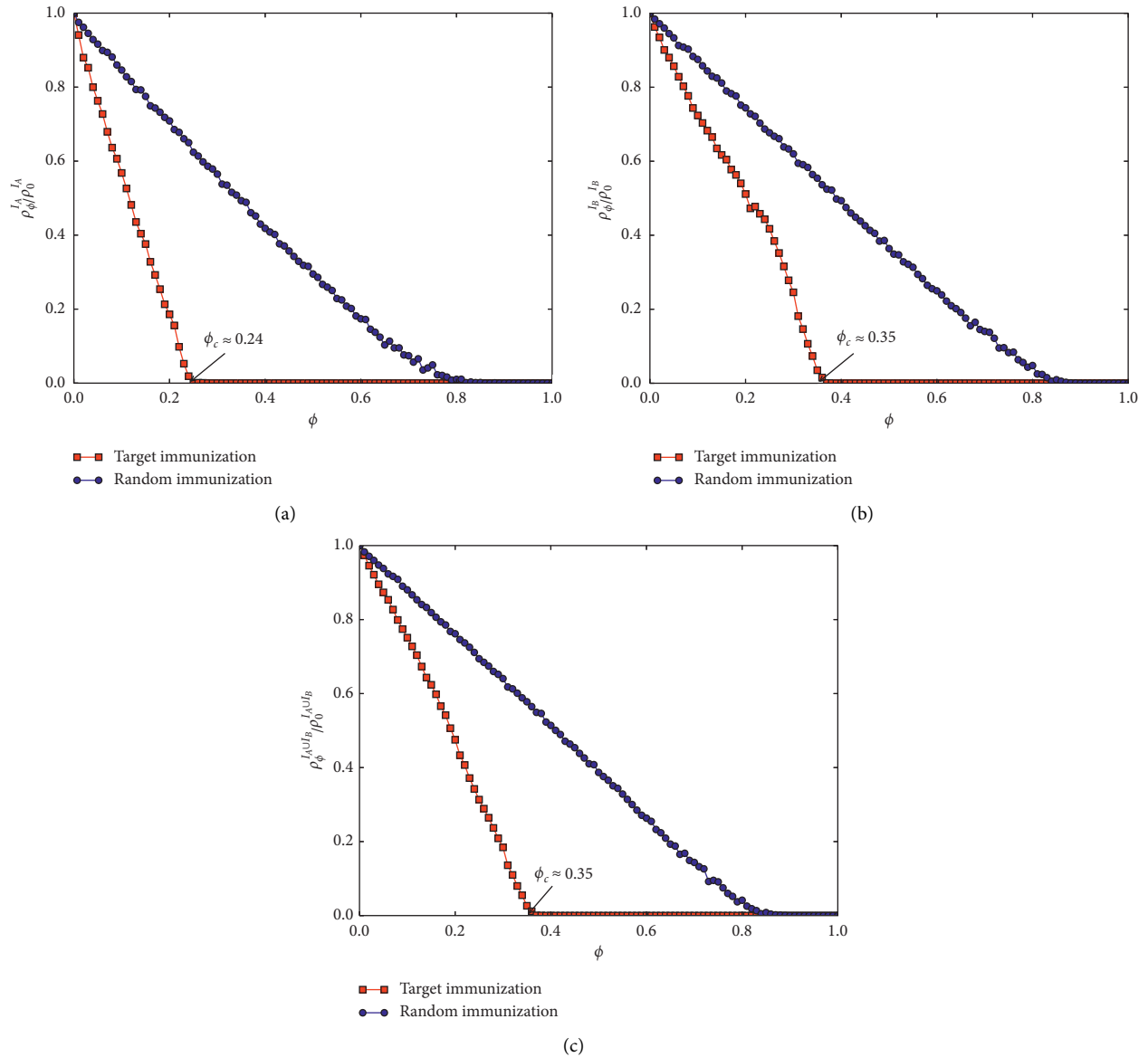


FIGURE 4: Relative size ( $\rho_\phi/\rho_0$ ) of infected clusters versus the immunization probability  $\phi$  for multiplex target or random control in a double-layer network that includes hepatitis B virus and hepatitis C virus: (a) hepatitis C virus-infected clusters, (b) hepatitis B virus-infected clusters, and (c) clusters infected with both hepatitis C and B viruses. The arrow denotes the immunization threshold  $\phi_c$  of our novel Multiplex PageRank target control.

approximately 0.29 because only the HIV rate decreases. We find that our Multiplex PageRank target control strategy is capable of immunizing fewer nodes to achieve a greater effect on both viruses simultaneously in the multilayer network.

Because an individual who is infected with malaria or HIV will be more susceptible to the other virus and the degree of enhancement of HIV obtained with malaria infection is stronger than that of malaria with HIV [54], we adopt  $c_A^{I_B} = 1.8$  for malaria and  $c_B^{I_A} = 1.5$  for HIV. As there are more propagation routes for HIV than malaria, we adopt  $A$  to denote the propagation routes of malaria and  $B$  to denote the propagation routes of HIV. Based on the decision to mainly immunize against HIV and only sometimes

immunize against malaria, we adopt the distribution coefficients  $\beta_A = 0.35$  and  $\beta_B = 0.5$  because HIV is more dangerous than malaria. The simulation results are shown in Figure 6. As shown in Figure 6(a), the immunization threshold of the multiplex random control of malaria is at a high value about 0.8, and the decreasing rate of the curve is constant. We also find a change in the decreasing rate of the infection probability before the immunization threshold is reached, which indicates that malaria is first enhanced by HIV. The change in the decreasing rate of the infection probability occurs at a value of approximately 0.25 when HIV has propagated to the top-ranked nodes, which are immunized, and this propagation results in an increase in the decreasing rate of the

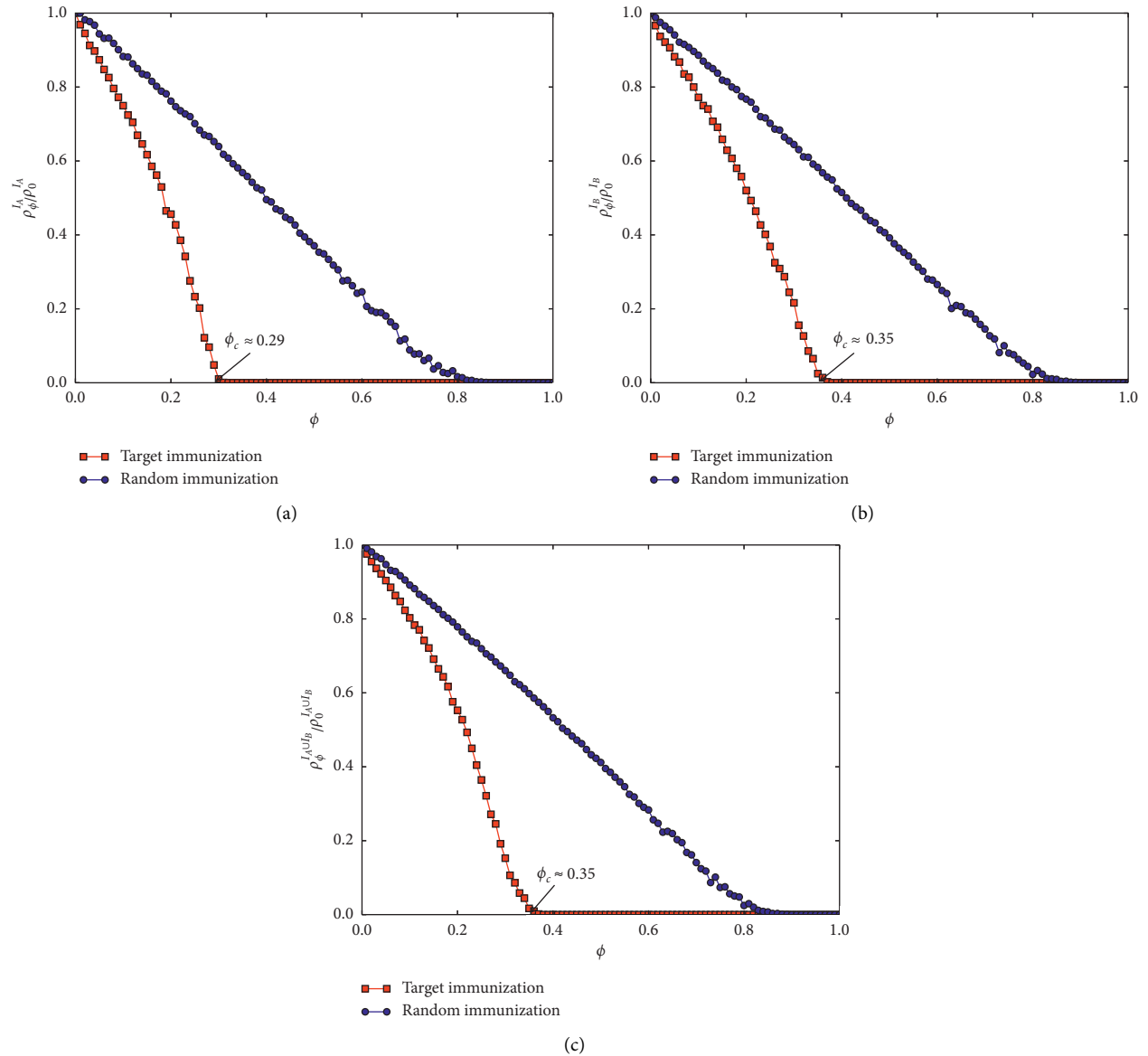


FIGURE 5: Relative size ( $\rho_\phi/\rho_0$ ) of infected clusters versus the immunization probability  $\phi$  for multiplex target or random control in a double-layer network that includes tuberculosis and HIV: (a) clusters infected with tuberculosis, (b) clusters infected with HIV, and (c) clusters infected with both tuberculosis  $\phi_c$  of our novel Multiplex PageRank target control.

infection probability of malaria. However, even though the enhancement of HIV obtained with malaria is stronger than that of malaria achieved with HIV, malaria is constrained by its fewer propagation routes, and thus, the population is completely immunized against malaria before it is immunized against HIV. Moreover, as shown in Figure 6(b), the immunization threshold of the multiplex random control of HIV is at a high value about 0.8, and the decreasing rate of the curve is constant. We also find some changes in the decreasing rate of the infection probability of multiplex target control of HIV before the immunization threshold is achieved, which indicates that malaria is first enhanced by HIV. The first change in the decreasing rate of the infection probability occurs at a value of approximately 0.25 when malaria has propagated to the top-ranked nodes, which are mostly immunized, and this results in an increase in the

decreasing rate of the HIV infection probability. The second change observed at a value of approximately 0.30 refers to an increase in the decreasing rate due to complete control against malaria, which leads HIV without any enhancement. Figure 6(c) presents the union of the infection probabilities of malaria and HIV in the multilayer network. The decreasing rate of the infection probability increases at a value of approximately 0.25 due to increases in both malaria and HIV and declines at a value of approximately 0.30 because only HIV infection remained. The results show that our Multiplex PageRank target control strategy immunizes fewer nodes to achieve a greater effect on both viruses simultaneously in the multilayer network.

Figures 2–6 show the relative sizes of the infected clusters versus the immunization probability in several actual cases. It is noted that the multiplex random control strategy in

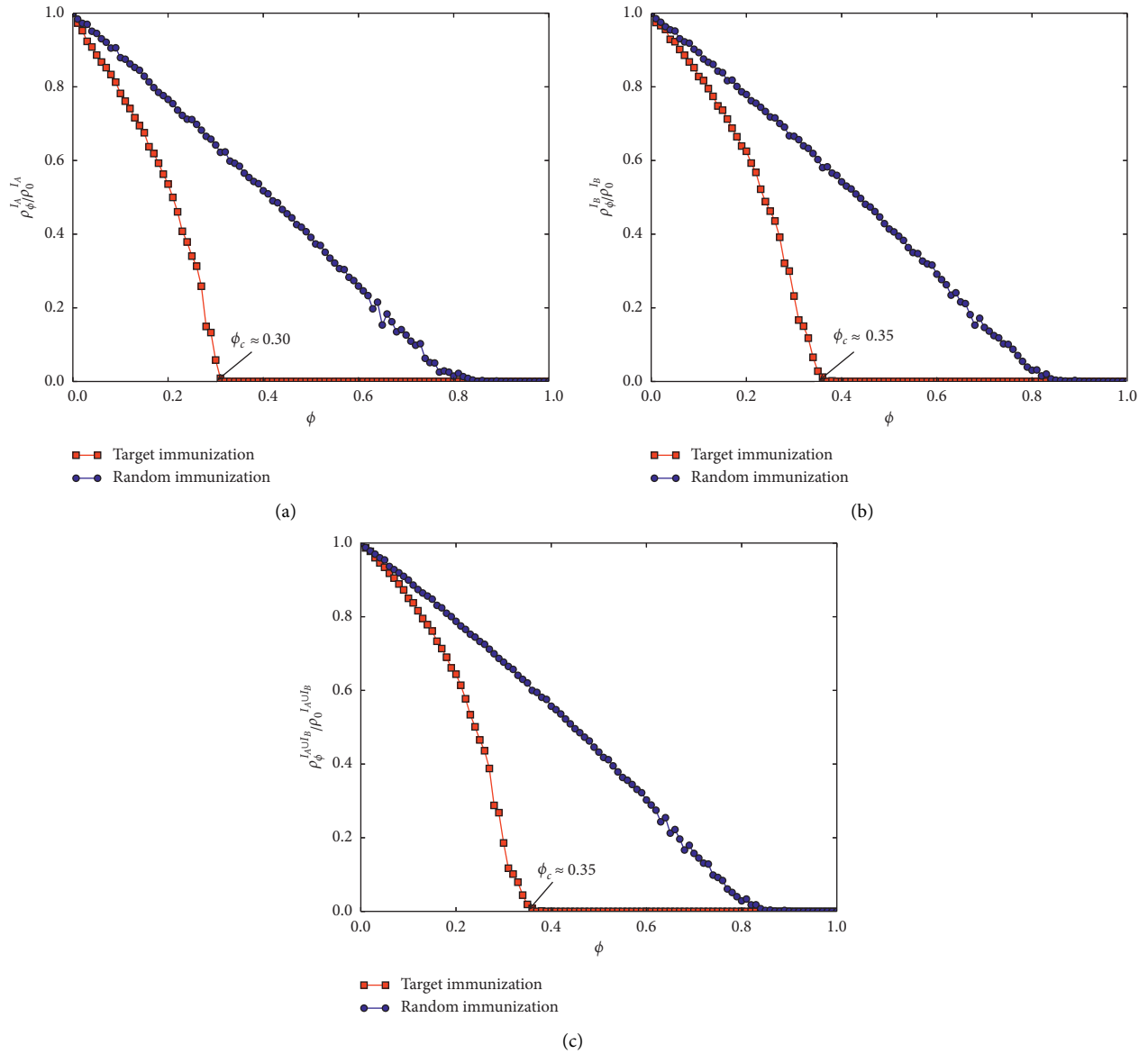


FIGURE 6: Relative size ( $\rho_\phi/\rho_0$ ) of infected clusters versus the immunization probability  $\phi$  for multiplex target or random control in a double-layer network including malaria and HIV: (a) malaria-infected clusters, (b) HIV-infected clusters, and (c) clusters infected with both malaria and HIV. The arrow denotes the immunization threshold  $\phi_c$  of our novel Multiplex PageRank target control.

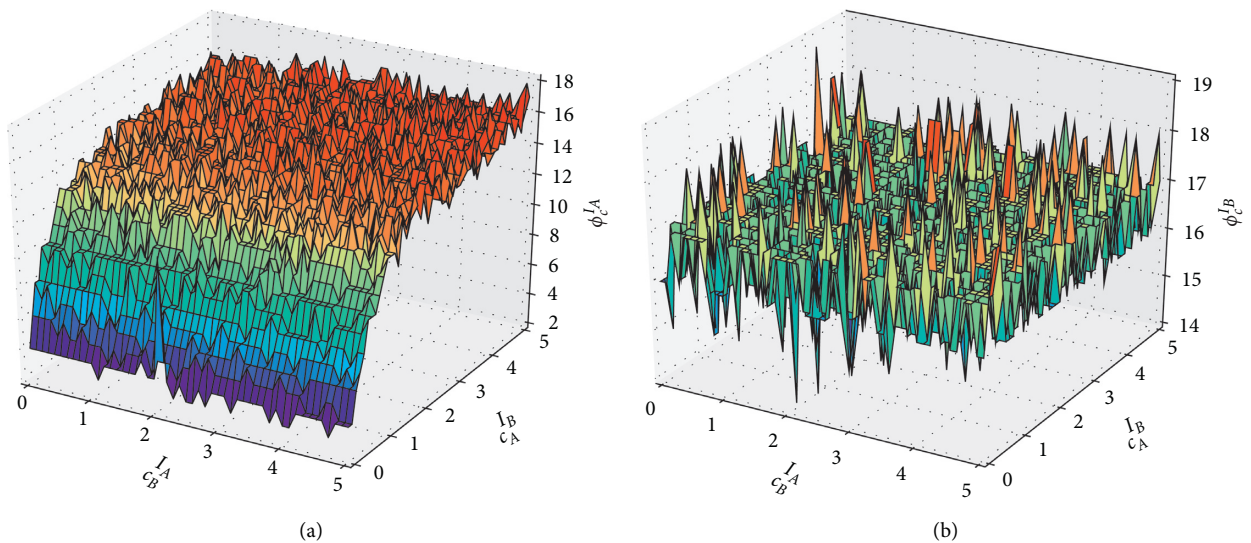


FIGURE 7: Continued.



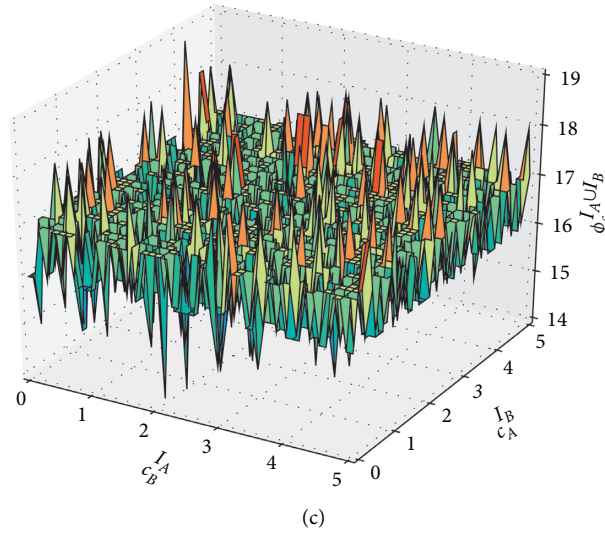


FIGURE 7: Novel Multiplex PageRank target immunization thresholds  $\phi_c$  versus interaction coefficients of multiple-virus propagation. (a) Target immunization threshold of  $I_A$ . (b) Target immunization threshold of  $I_B$ . (c) Target immunization threshold of  $I_A \cup I_B$ .

these double-layer networks with different interaction coefficients has little difference. The results demonstrate the effectiveness of our multiplex target control strategy in multilayer networks. Furthermore, the figures present the immunization threshold  $\phi_c$  of our novel Multiplex PageRank target control versus the interaction coefficients  $c_A^{I_B}$  and  $c_B^{I_A}$ . By setting  $\alpha_A^{S_B} = 0.2$  and  $\alpha_B^{S_A} = 0.2$ , both the interaction coefficients are limited from 0 to 5 because  $\alpha_A^{I_B} \leq 1$  and  $\alpha_B^{I_A} \leq 1$ . Using 0.1 intervals for the interaction coefficients, we divide both of them into 51 partitions. The immunization probability  $\phi$  ranges from 0 to 1 at a 0.01 interval, which results in the division of the probability into 101 compartments. Adopting 100 time steps 1000 times for 50 networks with a size of 10,000, the computer simulations take a long time. We exploit parallel computing, including multiple CPUs and multiple GPUs, to solve this problem, and the results are shown in Figure 7. As shown in Figure 7(a), the immunization threshold of the virus in A is majorly impacted by the interaction coefficient  $c_A^{I_B}$ . The results shown in Figure 7(b) demonstrate that the immunization threshold of the virus in B is impacted by the ratio of  $c_B^{I_A}$  to  $c_A^{I_B}$ . Figure 7(c) reveals that the immunization threshold of the total infectious is decided by the virus in B because it has more propagation routes.

## 5. Conclusion

This paper has presented a novel Multiplex PageRank target control strategy on multiple-virus interaction and propagation in multilayer networks compared with the multiplex random control. Using the proposed strategy, we have simulated several computer experiments that allow us to obtain the relative size of the steady probability versus the immunization probability and the critical immunization threshold for several actual cases. Furthermore, we have shown the critical immunization threshold of our novel Multiplex PageRank target control versus different

interaction coefficients of our multiple-virus propagation, which is useful for further practical applications.

## Data Availability

All the network data used in the paper are artificial network data, and the constructing measures are included with the supplementary information file.

## Conflicts of Interest

The authors declare that they have no conflicts of interest.

## References

- [1] Z. Wang, L. Wang, and M. Perc, "Degree mixing in multilayer networks impedes the evolution of cooperation," *Physical Review E*, vol. 89, no. 5, Article ID 052813, 2014.
- [2] Q. Jin, L. Wang, C.-Y. Xia, and Z. Wang, "Spontaneous symmetry breaking in interdependent networked game," *Scientific Reports*, vol. 4, no. 1, p. 4095, 2014.
- [3] L. Wang, Y. Zhang, Z. Wang, and X. Li, "The impact of human location-specific contact pattern on the SIR epidemic transmission between populations," *International Journal of Bifurcation and Chaos*, vol. 23, no. 05, Article ID 1350095, 2013.
- [4] L. Wang, Z. Wang, Y. Zhang, and X. Li, "How human location-specific contact patterns impact spatial transmission between populations?" *Scientific Reports*, vol. 3, no. 1, p. 1468, 2013.
- [5] L. Wang, X. Li, Y.-Q. Zhang, Y. Zhang, and K. Zhang, "Evolution of scaling emergence in large-scale spatial epidemic spreading," *PLoS ONE*, vol. 6, no. 7, Article ID e21197, 2011.
- [6] D. Zhao, L. Li, H. Peng, Q. Luo, and Y. Yang, "Multiple routes transmitted epidemics on multiplex networks," *Physics Letters A*, vol. 378, no. 10, pp. 770–776, 2014.
- [7] B. Min, S. Do Yi, K.-M. Lee, and K.-I. Goh, "Network robustness of multiplex networks with interlayer degree correlations," *Physical Review E*, vol. 89, no. 4, Article ID 042811, 2014.

- [8] C. Buono, L. G. Alvarez-Zuzek, P. A. Macri, and L. A. Braunstein, "Epidemics in partially overlapped multiplex networks," *PLoS ONE*, vol. 9, no. 3, Article ID e92200, 2014.
- [9] O. Yagan, D. Qian, J. Zhang, and D. Cochran, "Conjoining speeds up information diffusion in overlaying social-physical networks," *IEEE Journal on Selected Areas in Communications*, vol. 31, no. 6, pp. 1038–1048, 2013.
- [10] J. Gómez-Gardenes, I. Reinares, A. Arenas, and L. M. Floría, "Evolution of cooperation in multiplex networks," *Scientific Reports*, vol. 2, no. 1, p. 620, 2012.
- [11] J. Y. Kim and K.-I. Goh, "Coevolution and correlated multiplexity in multiplex networks," *Physical Review Letters*, vol. 111, no. 5, Article ID 058702, 2013.
- [12] F. Battiston, V. Nicosia, and V. Latora, "Structural measures for multiplex networks," *Physical Review E*, vol. 89, no. 3, Article ID 032804, 2014.
- [13] C. Granell, S. Gómez, and A. Arenas, "Dynamical interplay between awareness and epidemic spreading in multiplex networks," *Physical Review Letters*, vol. 111, no. 12, Article ID 128701, 2013.
- [14] V. Nicosia, G. Bianconi, V. Latora, and M. Barthelemy, "Growing multiplex networks," *Physical Review Letters*, vol. 111, no. 5, Article ID 058701, 2013.
- [15] S. Gomez, A. Diaz-Guilera, J. Gomez-Gardenes, C. J. Perez-Vicente, Y. Moreno, and A. Arenas, "Diffusion dynamics on multiplex networks," *Physical Review Letters*, vol. 110, no. 2, Article ID 028701, 2013.
- [16] M. Salehi, R. Sharma, M. Marzolla, M. Magnani, P. Siyari, and D. Montesi, "Spreading processes in multilayer networks," *IEEE Transactions on Network Science and Engineering*, vol. 2, no. 2, pp. 65–83, 2015.
- [17] S. Boccaletti, G. Bianconi, R. Criado et al., "The structure and dynamics of multilayer networks," *Physics Reports*, vol. 544, no. 1, pp. 1–122, 2014.
- [18] F. Caccioli, M. Shrestha, C. Moore, and J. D. Farmer, "Stability analysis of financial contagion due to overlapping portfolios," *Journal of Banking & Finance*, vol. 46, pp. 233–245, 2014.
- [19] M. J. O. Pocock, D. M. Evans, and J. Memmott, "The robustness and restoration of a network of ecological networks," *Science*, vol. 335, no. 6071, pp. 973–977, 2012.
- [20] J. Iacovacci and G. Bianconi, "Extracting information from multiplex networks," *Chaos: An Interdisciplinary Journal of Nonlinear Science*, vol. 26, no. 6, Article ID 065306, 2016.
- [21] R. Gallotti and M. Barthelemy, "Anatomy and efficiency of urban multimodal mobility," *Scientific Reports*, vol. 4, no. 1, p. 6911, 2014.
- [22] X. Wang and H. Su, "Completely model-free RL-based consensus of continuous-time multi-agent systems," *Applied Mathematics and Computation*, vol. 382, Article ID 125312, 2020.
- [23] Y. Zhang, G. Wen, G. Chen et al., "Gaming temporal networks," *IEEE Transactions on Circuits and Systems II: Express Briefs*, vol. 66, no. 4, pp. 672–676, 2018.
- [24] X. Wang, X. Wang, H. Su, and J. Lam, "Coordination control for uncertain networked systems using interval observers," *IEEE Transactions on Cybernetics*, 2019.
- [25] B. Karrer and M. E. Newman, "Competing epidemics on complex networks," *Physical Review E*, vol. 84, no. 3, Article ID 036106, 2011.
- [26] B. Min and K. Goh, "Layer-crossing overhead and information spreading in multiplex social networks," *Seed*, vol. 21, no. T22, p. T12, 2013.
- [27] V. Marceau, P.-A. Noël, L. Hébert-Dufresne, A. Allard, and L. J. Dubé, "Modeling the dynamical interaction between epidemics on overlay networks," *Physical Review E*, vol. 84, no. 2, Article ID 026105, 2011.
- [28] S. Funk and V. A. Jansen, "Interacting epidemics on overlay networks," *Physical Review E*, vol. 81, no. 3, Article ID 036118, 2010.
- [29] M. E. Newman and C. R. Ferrario, "Interacting epidemics and coinfection on contact networks," *PLoS ONE*, vol. 8, no. 8, Article ID e71321, 2013.
- [30] Y.-Y. Ahn, H. Jeong, N. Masuda, and J. D. Noh, "Epidemic dynamics of two species of interacting particles on scale-free networks," *Physical Review E*, vol. 74, no. 6, Article ID 066113, 2006.
- [31] C. Gao and J. Liu, "Modeling and restraining mobile virus propagation," *IEEE Transactions on Mobile Computing*, vol. 12, no. 3, pp. 529–541, 2013.
- [32] D. Zhao, H. Peng, L. Li, Y. Yang, and S. Li, "An efficient patch dissemination strategy for mobile networks," *Mathematical Problems in Engineering*, vol. 2013, pp. 1–13, 2013.
- [33] D. Zhao, L. Li, S. Li, Y. Huo, and Y. Yang, "Identifying influential spreaders in interconnected networks," *Physica Scripta*, vol. 89, no. 1, Article ID 015203, 2013.
- [34] C. Gao, J. Liu, and N. Zhong, "Network immunization with distributed autonomy-oriented entities," *IEEE Transactions on Parallel and Distributed Systems*, vol. 22, no. 7, pp. 1222–1229, 2011.
- [35] B. Gao, Z. Deng, and D. Zhao, "Competing spreading processes and immunization in multiplex networks," *Chaos, Solitons & Fractals*, vol. 93, pp. 175–181, 2016.
- [36] L. G. A. Zuzek, C. Buono, and L. A. Braunstein, "Epidemic spreading and immunization strategy in multiplex networks," *Journal of Physics: Conference Series*, vol. 640, no. 1, Article ID 012007, 2015.
- [37] R. Cohen, S. Havlin, and D. Ben-Avraham, "Efficient immunization strategies for computer networks and populations," *Physical Review Letters*, vol. 91, no. 24, Article ID 247901, 2003.
- [38] L. K. Gallos, F. Liljeros, P. Argyrakis, A. Bunde, and S. Havlin, "Improving immunization strategies," *Physical Review E*, vol. 75, no. 4, Article ID 045104, 2007.
- [39] Y. Chen, G. Paul, S. Havlin, F. Liljeros, and H. E. Stanley, "Finding a better immunization strategy," *Physical Review Letters*, vol. 101, no. 5, Article ID 058701, 2008.
- [40] L. Wang, Y. Zhang, T. Huang, and X. Li, "Estimating the value of containment strategies in delaying the arrival time of an influenza pandemic: a case study of travel restriction and patient isolation," *Physical Review E*, vol. 86, no. 3, Article ID 032901, 2012.
- [41] L. Wang and X. Li, "Spatial epidemiology of networked metapopulation: an overview," *Chinese Science Bulletin*, vol. 59, no. 28, pp. 3511–3522, 2014.
- [42] H. Ishii, R. Tempo, and E.-W. Bai, "A web aggregation approach for distributed randomized PageRank algorithms," *IEEE Transactions on Automatic Control*, vol. 57, no. 11, pp. 2703–2717, 2012.
- [43] L. Solá, M. Romance, R. Criado, J. Flores, A. García del Amo, and S. Boccaletti, "Eigenvector centrality of nodes in multiplex networks," *Chaos: An Interdisciplinary Journal of Nonlinear Science*, vol. 23, no. 3, Article ID 033131, 2013.
- [44] M. D. Domenico, A. Solé-Ribalta, E. Omodei, S. Gómez, and A. Arenas, "Ranking in interconnected multilayer networks reveals versatile nodes," *Nature Communications*, vol. 6, no. 1, 2015.
- [45] A. Solé-Ribalta, M. Domenico, S. Gómez, and A. Arenas, "Centrality rankings in multiplex networks," in *Proceedings of*

- the 2014 ACM conference on Web science*, vol. 9, Bloomington, Indiana, June 2014.
- [46] F. Pedroche, M. Romance, and R. Criado, "A biplex approach to PageRank centrality: from classic to multiplex networks," *Chaos*, vol. 26, no. 6, 2016.
  - [47] B. Jiang, K. Kloster, D. F. Gleich, and M. Gribskov, "AptRank: an adaptive PageRank model for protein function prediction on Bi-relational graphs," *Bioinformatics*, vol. 33, no. 12, 2016.
  - [48] J. Iacovacci, C. Rahmede, A. Arenas, and G. Bianconi, "Functional multiplex PageRank," *Europhysics Letters*, vol. 116, no. 2, 2016.
  - [49] A. Halu, R. J. Mondragón, P. Panzarasa, and G. Bianconi, "Multiplex pagerank," *PLoS ONE*, vol. 8, no. 10, Article ID e78293, 2013.
  - [50] H. Emerson, "Measles and whooping cough," *American Journal of Public Health and the Nations Health*, vol. 27, no. 6\_Suppl, pp. 1–58, 1937.
  - [51] L.-C. Chen and K. M. Carley, "The impact of countermeasure propagation on the prevalence of computer viruses," *IEEE Transactions on Systems, Man and Cybernetics, Part B (Cybernetics)*, vol. 34, no. 2, pp. 823–833, 2004.
  - [52] A. Alberti et al., "The interaction between hepatitis B virus and hepatitis C virus in acute and chronic liver disease," *Journal of Hepatology*, vol. 22, no. 1 Suppl, pp. 38–41, 1995.
  - [53] E. L. Corbett, C. J. Watt, N. Walker et al., "The growing burden of tuberculosis," *Archives of Internal Medicine*, vol. 163, no. 9, pp. 1009–1021, 2003.
  - [54] A. Alemu, Y. Shiferaw, Z. Addis, B. Mathewos, and W. Birhan, "Effect of malaria on HIV/AIDS transmission and progression," *Parasites & Vectors*, vol. 6, no. 1, p. 18, 2013.

## Research Article

# Sampled-Data-Based Adaptive Group Synchronization of Second-Order Nonlinear Complex Dynamical Networks with Time-Varying Delays

Bo Liu <sup>1</sup>, Jiahui Bai,<sup>2</sup> Yue Zhao,<sup>1</sup> Chao Liu <sup>3</sup>, Xuemin Yan,<sup>4</sup> and Hongtao Zhou <sup>5</sup>

<sup>1</sup>School of Information Engineering, Minzu University of China, Beijing 100081, China

<sup>2</sup>College of Science, North China University of Technology, Beijing 100144, China

<sup>3</sup>School of Mathematics, Shanghai University of Finance and Economics, Shanghai 200433, China

<sup>4</sup>National Institute of Education Sciences, Beijing 100088, China

<sup>5</sup>Key Laboratory of Imaging Processing and Intelligence Control, School of Artificial Intelligence and Automation, Huazhong University of Science and Technology, Wuhan 430074, China

Correspondence should be addressed to Bo Liu; [boliu@ncut.edu.cn](mailto:boliu@ncut.edu.cn)

Received 23 April 2020; Accepted 5 June 2020; Published 27 June 2020

Academic Editor: Zhiwei Gao

Copyright © 2020 Bo Liu et al. This is an open access article distributed under the Creative Commons Attribution License, which permits unrestricted use, distribution, and reproduction in any medium, provided the original work is properly cited.

This paper studies the adaptive group synchronization of second-order nonlinear complex dynamical networks with sampled-data and time-varying delays by designing a new adaptive strategy to feedback gains and coupling strengths. According to Lyapunov stability properties, it is shown that the agents of subgroups can converge the given synchronous states, respectively, under some conditions on the sampled period. Moreover, some simulation results are given.

## 1. Introduction

Complex dynamical networks are used to describe the large size and complexity of the research object to solve the practical application problem by constructing the mathematical models in essence. In nature, synchronization is a ubiquitous phenomenon, such as the synchronization of beating rhythm of cardiac myocytes and consistency of fireflies twinkling. Recently, the synchronization problem of complex systems with nonlinear dynamical has attracted increasing attention and wide application including physics, mathematics, chemistry, biology, information science, electronics, and medicine [1–16]. Because of the extensive application value of synchronization in engineering technology, complex network synchronization has become a hot issue in the field of nonlinearity science, for example, the evolutionary origin of asymptotically stable consensus in [7] and the application of synchronization in engineering was introduced in [8].

In order to achieve network synchronization, some advisable methods are introduced in outstanding works

(e.g., [17–28]), such as pinning control [17–19] and adaptive strategies [20–28]. In [25], the authors introduced the adaptive coupling strengths and studied the adaptive synchronization of two heterogeneous second-order nonlinear coupled dynamical systems. The synchronization of fractional-order complex networks were well considered in [26–28] and applying decentralized adaptive strategies, pinning control and adaptive control strategy, respectively. The authors [29–31] investigated the synchronization of complex dynamical systems with time-varying delays. Works [32, 33] discussed adaptive consensus of networks with single-integrator nonlinear dynamics and adaptive synchronization of networks with double-integrator nonlinear dynamics, respectively. In [34], the author investigated the adaptive synchronization for first-order complex systems with local Lipschitz nonlinearity. Su et al. [35] also researched the adaptive flocking of multiagent networks with local Lipschitz nonlinearity. In engineering practice, the whole network (group) can be partitioned into several subnetworks (subgroups) to study the synchronization

problems, called as group synchronization. Li et al. [36] investigated the group synchronization for complex systems with nonlinear dynamics. Some conditions were established in [37] for solving consensus problem of multiagent complex systems with double-integrator and sampled control. The consensus of complex networks with sampled data and time-delay topology was studied in [38].

Inspired by these works, the adaptive group synchronization of second-order nonlinear complex dynamical undirected networks with sampled-data and time-varying delays will be discussed in this paper. And its main contributions are threefold: (1) the new second-order model with sampled-data and time-varying delays is established; (2) the communication delays of all the neighboring agents'

positions and velocities are time varying; (3) adaptive laws for solving the group synchronization of second-order nonlinear complex dynamical systems are introduced.

The rest of this paper is arranged as follows. The mathematical model with time delays and sampled data and some necessary preliminaries are given in Section 2. Section 3 presents the main results. Some numerical simulations are given in Section 4. Finally, Section 5 shows the conclusion.

## 2. Problem Formulation and Preliminaries

A second-order complex network with nonlinear dynamics consists of  $N$  nodes and each node obeys

$$\left\{ \begin{array}{l} \dot{x}_i(t) = v_i(t), \\ \dot{v}_i(t) = \begin{cases} f(v_i(t_s), v_i(T_s)) + \sum_{j \in \mathcal{M}_{1i}} c_{ij}(t_s) a_{ij} (x_j(T_s) - x_i(T_s)) + \sum_{j \in \mathcal{M}_{2i}} d_{ij}(t_s) b_{ij} x_j(T_s) + \sum_{j \in \mathcal{M}_{1i}} \alpha_{ij}(t_s) p_{ij} (v_j(T_s) - v_i(T_s)) \\ + \sum_{j \in \mathcal{M}_{2i}} \beta_{ij}(t_s) q_{ij} v_j(T_s) + u_i, \quad \forall i \in \ell_1, \forall t \in [t_s, t_{s+1}] \\ f(v_i(t_s), v_i(T_s)) + \sum_{j \in \mathcal{M}_{2i}} c_{ij}(t_s) a_{ij} (x_j(T_s) - x_i(T_s)) + \sum_{j \in \mathcal{M}_{1i}} d_{ij}(t_s) b_{ij} x_j(T_s) + \sum_{j \in \mathcal{M}_{2i}} \alpha_{ij}(t_s) p_{ij} (v_j(T_s) - v_i(T_s)) \\ + \sum_{j \in \mathcal{M}_{1i}} \beta_{ij}(t_s) q_{ij} v_j(T_s) + u_i, \quad \forall i \in \ell_2, \forall t \in [t_s, t_{s+1}], \end{cases} \end{array} \right. \quad (1)$$

where  $x_i(t) \in R^n$  is the position vector of agent  $i$ ;  $v_i(t) \in R^n$  is its velocity vector, for  $i = 1, \dots, N$  as  $t \in [0, +\infty)$ ;  $f: R^n \rightarrow R^n$  is a continuous differentiable function;  $T_s = t_s - \tau(t_s)$  and  $\tau > 0$ ;  $\mathcal{M}_i$  is the neighbor set of node  $i$ ,  $\mathcal{M}_i \in \mathcal{M}_{1i} \cup \mathcal{M}_{2i}$  with  $\mathcal{M}_{1i} = \{x_j \in \mathcal{X}_1: a_{ij} \geq 0, i, j \in \ell_1\}$  and  $\mathcal{M}_{2i} = \{x_j \in \mathcal{X}_2: a_{ij} \geq 0, i, j \in \ell_2\}$ , where  $\mathcal{X} = \mathcal{X}_1 \cup \mathcal{X}_2$ ,  $\ell = \ell_1 \cup \ell_2$  with  $\mathcal{X}_1 = \{x_1, \dots, x_L\}$ ,  $\mathcal{X}_2 = \{x_{L+1}, \dots, x_N\}$ ,  $\ell_1 =$

$1, \dots, L$ ,  $\ell_2 = L + 1, \dots, N$ , and  $L < N$ ;  $c_{ij}(t_s)$ ,  $d_{ij}(t_s)$ ,  $\alpha_{ij}(t_s)$ , and  $\beta_{ij}(t_s)$  are the position's and velocity's coupling strengths between agent  $i$  and agent  $j$ ; and nonnegative numbers  $a_{ij}$ ,  $b_{ij}$ ,  $p_{ij}$ , and  $q_{ij}$  are the edge-weights connecting agent  $i$  and agent  $j$ .

Design the control input as

$$u_i = \begin{cases} -c_i(t_s) h_i (x_i(T_s) - \bar{x}_1(T_s)) - d_i(t_s) l_i (v_i(T_s) - \bar{v}_1(T_s)), & i \in \ell_1, \\ -c_i(t_s) h_i (x_i(T_s) - \bar{x}_2(T_s)) - d_i(t_s) l_i (v_i(T_s) - \bar{v}_2(T_s)), & i \in \ell_2, \end{cases} \quad (2)$$

where  $h_i$  and  $l_i$  are on-off controls, if node  $i$  is steered, then  $h_i = 1$  and  $l_i = 1$ , otherwise  $h_i = 0$  and  $l_i = 0$ ,  $c_i(t_s)$  and  $d_i(t_s)$  represent the position's and velocity's feedback gains,

respectively,  $\bar{x}_1(t) \in R^n$  and  $\bar{x}_2(t) \in R^n$  are the given synchronous positions, and  $\bar{v}_1(t) \in R^n$  and  $\bar{v}_2(t) \in R^n$  are their velocities, respectively.

According to (1) and (2), we design the adaptive laws for coupling strengths respectively as

$$\begin{aligned} \dot{c}_{ij}(t_s) &= \begin{cases} a_{ij}k_{ij} \left[ (x_i(T_s) - x_j(T_s))^T (x_i(T_s) - x_j(T_s)) + (\dot{x}_i(t) - \dot{x}_j(t))^T (\dot{x}_i(t) - \dot{x}_j(t)) \right], & i, j \in \ell_1, \\ a_{ij}k_{ij} \left[ (x_i(T_s) - x_j(T_s))^T (x_i(T_s) - x_j(T_s)) + (\dot{x}_i(t) - \dot{x}_j(t))^T (\dot{x}_i(t) - \dot{x}_j(t)) \right], & i, j \in \ell_2, \end{cases} \\ \dot{\alpha}_{ij}(t_s) &= \begin{cases} p_{ij}\varepsilon_{ij} \left[ (v_i(T_s) - v_j(T_s))^T (v_i(T_s) - v_j(T_s)) + (\dot{v}_i(t) - \dot{v}_j(t))^T (\dot{v}_i(t) - \dot{v}_j(t)) \right], & i, j \in \ell_1, \\ p_{ij}\varepsilon_{ij} \left[ (v_i(T_s) - v_j(T_s))^T (v_i(T_s) - v_j(T_s)) + (\dot{v}_i(t) - \dot{v}_j(t))^T (\dot{v}_i(t) - \dot{v}_j(t)) \right], & i, j \in \ell_2, \end{cases} \end{aligned} \quad (3)$$

$$\begin{aligned} \dot{d}_{ij}(t_s) &= \begin{cases} b_{ij}k_{ij} (x_j(T_s) - \bar{x}_2(T_s))^T (x_j(T_s) - \bar{x}_2(T_s)), & i \in \ell_1, j \in \ell_2, \\ b_{ij}k_{ij} (x_j(T_s) - \bar{x}_1(T_s))^T (x_j(T_s) - \bar{x}_1(T_s)), & i \in \ell_2, j \in \ell_1, \end{cases} \\ \dot{\beta}_{ij}(t_s) &= \begin{cases} q_{ij}\varepsilon_{ij} (v_j(T_s) - \bar{v}_2(T_s))^T (v_j(T_s) - \bar{v}_2(T_s)), & i \in \ell_1, j \in \ell_2, \\ q_{ij}\varepsilon_{ij} (v_j(T_s) - \bar{v}_1(T_s))^T (v_j(T_s) - \bar{v}_1(T_s)), & i \in \ell_2, j \in \ell_1. \end{cases} \end{aligned} \quad (4)$$

where  $k_{ij} > 0$  and  $\varepsilon_{ij} > 0$  are the weights of  $c_{ij}(t_s)$  and  $\alpha_{ij}(t_s)$ , respectively.

Similarly, we design the adaptive laws for the feedback gains, respectively, as

$$\begin{aligned} \dot{c}_i(t_s) &= \begin{cases} h_i k_i \left[ (x_i(T_s) - \bar{x}_1(T_s))^T (x_i(T_s) - \bar{x}_1(T_s)) + (\dot{x}_i(t) - \dot{\bar{x}}_1(t))^T (\dot{x}_i(t) - \dot{\bar{x}}_1(t)) \right], & i \in \ell_1, \\ h_i k_i \left[ (x_i(T_s) - \bar{x}_2(T_s))^T (x_i(T_s) - \bar{x}_2(T_s)) + (\dot{x}_i(t) - \dot{\bar{x}}_2(t))^T (\dot{x}_i(t) - \dot{\bar{x}}_2(t)) \right], & i \in \ell_2, \end{cases} \\ \dot{d}_i(t_s) &= \begin{cases} l_i \varepsilon_i \left[ (v_i(T_s) - \bar{v}_1(T_s))^T (v_i(T_s) - \bar{v}_1(T_s)) + (\dot{v}_i(t) - \dot{\bar{v}}_1(t))^T (\dot{v}_i(t) - \dot{\bar{v}}_1(t)) \right], & i \in \ell_1, \\ l_i \varepsilon_i \left[ (v_i(T_s) - \bar{v}_2(T_s))^T (v_i(T_s) - \bar{v}_2(T_s)) + (\dot{v}_i(t) - \dot{\bar{v}}_2(t))^T (\dot{v}_i(t) - \dot{\bar{v}}_2(t)) \right], & i \in \ell_2, \end{cases} \end{aligned} \quad (5)$$

in which  $k_i > 0$  and  $\varepsilon_i > 0$  are the weights of  $c_i(t_s)$  and  $d_i(t_s)$ , respectively.

The position's and velocity's weighted coupling configuration matrices of system (1) can be represented as

$$\begin{aligned} A &= \begin{bmatrix} A_{11}^{L \times L} & B_{12}^{L \times (N-L)} \\ B_{21}^{(N-L) \times L} & A_{22}^{(N-L) \times (N-L)} \end{bmatrix}, \\ P &= \begin{bmatrix} P_{11}^{L \times L} & Q_{12}^{L \times (N-L)} \\ Q_{21}^{(N-L) \times L} & P_{22}^{(N-L) \times (N-L)} \end{bmatrix}, \end{aligned} \quad (6)$$

where

$$\begin{aligned} A_{11} &= \begin{bmatrix} a_{11} - \sum_{j=1}^L a_{1j} & \cdots & a_{1L} \\ \vdots & \ddots & \vdots \\ a_{L1} & \cdots & a_{LL} - \sum_{j=1}^L a_{Lj} \end{bmatrix}, & A_{22} &= \begin{bmatrix} a_{(L+1)(L+1)} - \sum_{j=L+1}^N a_{(L+1)j} & \cdots & a_{(L+1)N} \\ \vdots & \ddots & \vdots \\ a_{N(L+1)} & \cdots & a_{NN} - \sum_{j=L+1}^N a_{Nj} \end{bmatrix}, \\ P_{11} &= \begin{bmatrix} p_{11} - \sum_{j=1}^L p_{1j} & \cdots & p_{1L} \\ \vdots & \ddots & \vdots \\ p_{L1} & \cdots & p_{LL} - \sum_{j=1}^L p_{Lj} \end{bmatrix}, & P_{22} &= \begin{bmatrix} p_{(L+1)(L+1)} - \sum_{j=L+1}^N p_{(L+1)j} & \cdots & p_{(L+1)N} \\ \vdots & \ddots & \vdots \\ p_{N(L+1)} & \cdots & p_{NN} - \sum_{j=L+1}^N p_{Nj} \end{bmatrix}. \end{aligned} \quad (7)$$

In order to solve the synchronization problem, we briefly give some assumptions, lemmas, and definitions used in this paper.

*Assumption 1* (see [39]). The coupling strengths and feedback gains are all bounded, that is,

$$\begin{aligned} \|c_{ij}(t_s)\| &\leq c_{ij}, \|d_{ij}(t_s)\| \leq d_{ij}, \|c_i(t_s)\| \leq c_i, \|\alpha_{ij}(t_s)\| \\ &\leq \alpha_{ij}, \|\beta_{ij}(t_s)\| \leq \beta_{ij}, \|d_i(t_s)\| \leq d_i, \end{aligned} \quad (8)$$

where  $\|\cdot\|$  is the Euclidean norm and  $c_{ij}, d_{ij}, c_i, \alpha_{ij}, \beta_{ij}$ , and  $d_i$  are positive constants. In fact, the coupling strengths and feedback gains are usually bounded.

*Assumption 2* (see [39]).  $0 \leq \tau(t) \leq \tau$ , when  $t \geq 0$  and  $\tau > 0$  are constants.

Unlike some existing works, such as [40],  $0 \leq \dot{\tau}(t) \leq 1$  is required; however, this paper does not need to know any information about the derivative of  $\tau(t)$ .

*Assumption 3*  $\exists \rho_1 > 0, \rho_2 > 0$  such that

$$\|f(\alpha, \beta) - f(\gamma, \delta)\| \leq \rho_1 \|\alpha - \gamma\| + \rho_2 \|\beta - \delta\|, \quad \forall \alpha, \beta, \gamma, \delta \in R^n, \quad (9)$$

which can guarantee the boundedness of the nonlinear term for system (1).

**Lemma 1** (see [39]). *Suppose that  $x, y \in R^N$  are arbitrary vectors and matrix  $Q \in R^{N \times N}$  is positive definite; then, the inequality satisfies*

$$2x^T y \leq x^T Q x + y^T Q^{-1} y. \quad (10)$$

**Lemma 2** (see [39]). *If  $A = (a_{ij}) \in R^{N \times N}$  is symmetric irreducible, each eigenvalue of  $A - B$  is negative, where  $a_{ii} = -\sum_{j=1, j \neq i}^N a_{ij}$  and  $B = \text{diag}(b, 0, \dots, 0)$  with  $b > 0$ .*

**Lemma 3** (see [39]). *For an undirected graph  $G$ , its corresponding coupling matrix  $A$  is irreducible iff  $G$  is connected.*

**Lemma 4** (see [39]). *If  $\forall x(t) \in R^n$  is real differentiable and  $W = W^T > 0$  is a constant matrix, we can have*

$$\begin{aligned} &\left[ \int_{t-\tau(t)}^t x(k) dk \right]^T W \left[ \int_{t-\tau(t)}^t x(k) dk \right] \\ &\leq \tau \int_{t-\tau(t)}^t x^T(k) W x(k) dk, \quad t \geq 0, \end{aligned} \quad (11)$$

where  $0 \leq \tau(t) \leq \tau$ .

### 3. Main Results

For  $\alpha > 0$  and the sample periodic  $\mathbf{T}$ , we assume that

$$t_{i+1} - t_i = \alpha \mathbf{T}_i, \quad \forall i = 0, 1, 2, \dots, \quad (12)$$

where  $t_0 < t_1 < \dots$  are the discrete time periods and integer  $\mathbf{T}_i > 0$  is a sampled time with  $\mathbf{T}_i \leq \mathbf{T}$ . Inspired by [36], we design a linear synchronization protocol under the sampling period as

$$\begin{cases} \dot{v}_i(t_s + \alpha) = \dot{v}_i(t_s) - \frac{1}{\mathbf{T}} \dot{v}_i(t_s) = \left(1 - \frac{1}{\mathbf{T}}\right) \dot{v}_i(t_s), \\ \dot{v}_i(t_s + 2\alpha) = \dot{v}_i(t_s + \alpha) + (\dot{v}_i(t_s + \alpha) - \dot{v}_i(t_s)) = \left(1 - \frac{2}{\mathbf{T}}\right) \dot{v}_i(t_s), \\ \vdots \\ \dot{v}_i(t_{s+1} - \alpha) = \dot{v}_i(t_s + \mathbf{T}_s \alpha - \alpha) = \left(1 - \frac{\mathbf{T}_s - 1}{\mathbf{T}}\right) \dot{v}_i(t_s). \end{cases} \quad (13)$$

Let  $h = 0, 1, \dots, \mathbf{T}_s - 1$ ; thus, we have

$$\dot{v}_i(t) = \begin{cases} \left(1 - \frac{h}{\mathbf{T}}\right) \times \left[ f(v_i(t_s), v_i(\mathbf{T}_s)) + \sum_{j \in \mathcal{M}_{1i}} c_{ij}(t_s) a_{ij} (x_j(\mathbf{T}_s) - x_i(\mathbf{T}_s)) + \sum_{j \in \mathcal{M}_{2i}} d_{ij}(t_s) b_{ij} x_j(\mathbf{T}_s) + \sum_{j \in \mathcal{M}_{1i}} \alpha_{ij}(t_s) p_{ij} (v_j(\mathbf{T}_s) - v_i(\mathbf{T}_s)) \right. \\ \left. + \sum_{j \in \mathcal{M}_{2i}} \beta_{ij}(t_s) q_{ij} v_j(\mathbf{T}_s) + u_i \right], \quad \forall i \in \ell_1, \forall t \in [t_s, t_{s+1}], \\ \left(1 - \frac{h}{\mathbf{T}}\right) \times \left[ f(v_i(t_s), v_i(\mathbf{T}_s)) + \sum_{j \in \mathcal{M}_{2i}} c_{ij}(t_s) a_{ij} (x_j(\mathbf{T}_s) - x_i(\mathbf{T}_s)) + \sum_{j \in \mathcal{M}_{1i}} d_{ij}(t_s) b_{ij} x_j(\mathbf{T}_s) + \sum_{j \in \mathcal{M}_{2i}} \alpha_{ij}(t_s) p_{ij} (v_j(\mathbf{T}_s) - v_i(\mathbf{T}_s)) \right. \\ \left. + \sum_{j \in \mathcal{M}_{1i}} \beta_{ij}(t_s) q_{ij} v_j(\mathbf{T}_s) + u_i \right], \quad \forall i \in \ell_2, \forall t \in [t_s, t_{s+1}]. \end{cases} \quad (14)$$

**Theorem 1.** Consider connected network (1) with control input (2) steered by (3)–(5) under Assumptions 1–3 and Lemmas 1–4; then, each node's position and velocity can asymptotically synchronize.

*Proof.* Let

$$\begin{aligned}\tilde{x}_i(t_s) &\triangleq x_i(t_s) - \bar{x}_1(t_s), \\ \tilde{v}_i(t_s) &\triangleq v_i(t_s) - \bar{v}_1(t_s),\end{aligned}\quad (15)$$

for  $i \in \ell_1$ , and

$$\begin{aligned}\tilde{x}_i(t_s) &\triangleq x_i(t_s) - \bar{x}_2(t_s), \\ \tilde{v}_i(t_s) &\triangleq v_i(t_s) - \bar{v}_2(t_s),\end{aligned}\quad (16)$$

for  $i \in \ell_2$ ; then, we obtain

$$\dot{\tilde{v}}_i(t) = \begin{cases} \left(1 - \frac{h}{T}\right) \times \left[ f(v_i(t_s), v_i(T_s)) - f(\bar{v}_1(t_s), \bar{v}_1(T_s)) + \sum_{j \in \mathcal{M}_{1i}} c_{ij}(t_s) a_{ij} (\tilde{x}_j(T_s) - \tilde{x}_i(T_s)) + \sum_{j \in \mathcal{M}_{2i}} d_{ij}(t_s) b_{ij} \tilde{x}_j(T_s) \right. \\ \left. + \sum_{j \in \mathcal{M}_{1i}} \alpha_{ij}(t_s) p_{ij} (\tilde{v}_j(T_s) - \tilde{v}_i(T_s)) + \sum_{j \in \mathcal{M}_{2i}} \beta_{ij}(t_s) q_{ij} \tilde{v}_j(T_s) + u_i \right], & \forall i \in \ell_1, \forall t \in [t_s, t_{s+1}], \\ \left(1 - \frac{h}{T}\right) \times \left[ f(v_i(t_s), v_i(T_s)) - f(\bar{v}_2(t_s), \bar{v}_2(T_s)) + \sum_{j \in \mathcal{M}_{2i}} c_{ij}(t_s) a_{ij} (\tilde{x}_j(T_s) - \tilde{x}_i(T_s)) + \sum_{j \in \mathcal{M}_{1i}} d_{ij}(t_s) b_{ij} \tilde{x}_j(T_s) \right. \\ \left. + \sum_{j \in \mathcal{M}_{2i}} \alpha_{ij}(t_s) p_{ij} (\tilde{v}_j(T_s) - \tilde{v}_i(T_s)) + \sum_{j \in \mathcal{M}_{1i}} \beta_{ij}(t_s) q_{ij} \tilde{v}_j(T_s) + u_i \right], & \forall i \in \ell_2, \forall t \in [t_s, t_{s+1}]. \end{cases}\quad (17)$$

Construct a Lyapunov function as

$$V(t_s) = V_1(t_s) + V_2(t_s) + V_3(t_s), \quad (18)$$

where

$$\begin{aligned}V_1(t_s) &= \frac{1}{2} \sum_{i \in \mathcal{M}_{1i}} \tilde{x}_i^T(t_s) \tilde{x}_i(t_s) + \sum_{i \in \mathcal{M}_{1i}} \sum_{j \in \mathcal{M}_{1i}} \frac{(c_{ij}(t_s) - 2c_{ij} - p)^2}{4k_{ij}} + \sum_{i \in \mathcal{M}_{1i}} \sum_{j \in \mathcal{M}_{2i}} \frac{(d_{ij}(t_s) - 2d_{ij} - 1)^2}{4k_{ij}} + \sum_{i \in \mathcal{M}_{1i}} \frac{(c_i(t_s) - (3/2)c_i - p)^2}{2k_i} \\ &+ \frac{1}{2} \sum_{i \in \mathcal{M}_{1i}} \tilde{v}_i^T(t_s) \tilde{v}_i(t_s) + \sum_{i \in \mathcal{M}_{1i}} \sum_{j \in \mathcal{M}_{1i}} \frac{(p_{ij}(t_s) - 2p_{ij} - p)^2}{4\epsilon_{ij}} + \sum_{i \in \mathcal{M}_{1i}} \sum_{j \in \mathcal{M}_{2i}} \frac{(q_{ij}(t_s) - 2q_{ij} - 1)^2}{4\epsilon_{ij}} + \sum_{i \in \mathcal{M}_{1i}} \frac{(d_i(t_s) - (3/2)d_i - p)^2}{2\epsilon_i}, \\ V_2(t_s) &= \frac{1}{2} \sum_{i \in \mathcal{M}_{2i}} \tilde{x}_i^T(t_s) \tilde{x}_i(t_s) + \sum_{i \in \mathcal{M}_{2i}} \sum_{j \in \mathcal{M}_{2i}} \frac{(c_{ij}(t_s) - 2c_{ij} - p)^2}{4k_{ij}} + \sum_{i \in \mathcal{M}_{2i}} \sum_{j \in \mathcal{M}_{1i}} \frac{(d_{ij}(t_s) - 2d_{ij} - 1)^2}{4k_{ij}} + \sum_{i \in \mathcal{M}_{2i}} \frac{(c_i(t_s) - (3/2)c_i - p)^2}{2k_i} \\ &+ \frac{1}{2} \sum_{i \in \mathcal{M}_{2i}} \tilde{v}_i^T(t_s) \tilde{v}_i(t_s) + \sum_{i \in \mathcal{M}_{2i}} \sum_{j \in \mathcal{M}_{2i}} \frac{(\alpha_{ij}(t_s) - 2\alpha_{ij} - p)^2}{4\epsilon_{ij}} + \sum_{i \in \mathcal{M}_{2i}} \sum_{j \in \mathcal{M}_{1i}} \frac{(\beta_{ij}(t_s) - 2\beta_{ij} - 1)^2}{4\epsilon_{ij}} + \sum_{i \in \mathcal{M}_{2i}} \frac{(d_i(t_s) - (3/2)d_i - p)^2}{2\epsilon_i}, \\ V_3(t_s) &= \tau \sum_{i \in \mathcal{M}_{1i}} \left[ 2\rho_1 + \rho_2 + 1 + \left( \sum_{i \in \mathcal{M}_{1i}} c_{ij}(t_s) a_{ij} \right) + \left( \sum_{i \in \mathcal{M}_{1i}} \alpha_{ij}(t_s) p_{ij} \right) + \left( \sum_{i \in \mathcal{M}_{2i}} d_{ij}(t_s) b_{ij} \right) + \left( \sum_{i \in \mathcal{M}_{2i}} \beta_{ij}(t_s) q_{ij} \right) \right. \\ &+ (c_i(t_s) h_i) + (d_i(t_s) l_i) \left. \right] \int_{T_s}^{t_s} (k - t_s + \tau) \tilde{x}_i^T(k) \dot{\tilde{x}}_i(k) dk + \tau \sum_{i \in \mathcal{M}_{1i}} \int_{T_s}^{t_s} (k - t_s + \tau) \tilde{x}_i^T(k) \dot{\tilde{x}}_i(k) dk \\ &+ \tau \sum_{i \in \mathcal{M}_{2i}} \left[ 2\rho_3 + \rho_4 + 1 + \left( \sum_{i \in \mathcal{M}_{2i}} c_{ij}(t_s) a_{ij} \right) + \left( \sum_{i \in \mathcal{M}_{2i}} \alpha_{ij}(t_s) p_{ij} \right) + \left( \sum_{i \in \mathcal{M}_{1i}} d_{ij}(t_s) b_{ij} \right) + \left( \sum_{i \in \mathcal{M}_{1i}} \beta_{ij}(t_s) q_{ij} \right) \right. \\ &+ (c_i(t_s) h_i) + (d_i(t_s) l_i) \left. \right] \int_{T_s}^{t_s} (k - t_s + \tau) \tilde{x}_i^T(k) \dot{\tilde{x}}_i(k) dk + \tau \sum_{i \in \mathcal{M}_{2i}} \int_{T_s}^{t_s} (k - t_s + \tau) \tilde{x}_i^T(k) \dot{\tilde{x}}_i(k) dk,\end{aligned}\quad (19)$$



and  $p > 0$  is sufficiently large. Next, there are two cases to discuss.  $\square$

Differentiating  $V_1(t_s)$ , under Assumptions 1–3 and Lemmas 1–4, we can have

Case 1.  $A_{11}, A_{22}, P_{11}$ , and  $P_{22}$  are symmetric.

$$\begin{aligned}
\dot{V}_1(t_s) \leq & \frac{1}{2} \sum_{i \in \mathcal{M}_{1i}} \tilde{x}_i^T(t) \tilde{x}_i(t) + \frac{1}{2} \rho_2 \sum_{i \in \mathcal{M}_{1i}} \tilde{v}_i^T(T_s) \tilde{v}_i(T_s) + \frac{1}{2} \sum_{i \in \mathcal{M}_{1i}} \xi_{1i} \tilde{v}_i^T(t) \tilde{v}_i(t) \\
& - \frac{p}{2} \sum_{i \in \mathcal{M}_{1i}} \sum_{j \in \mathcal{M}_{1i}} a_{ij} \left[ (\tilde{x}_i(T_s) - \tilde{x}_j(T_s))^T (\tilde{x}_i(T_s) - \tilde{x}_j(T_s)) + (\dot{\tilde{x}}_i(t) - \dot{\tilde{x}}_j(t))^T (\dot{\tilde{x}}_i(t) - \dot{\tilde{x}}_j(t)) \right] \\
& - \frac{p}{2} \sum_{i \in \mathcal{M}_{1i}} \sum_{j \in \mathcal{M}_{1i}} p_{ij} \left[ (\tilde{v}_i(T_s) - \tilde{v}_j(T_s))^T (\tilde{v}_i(T_s) - \tilde{v}_j(T_s)) + (\dot{\tilde{v}}_i(t) - \dot{\tilde{v}}_j(t))^T (\dot{\tilde{v}}_i(t) - \dot{\tilde{v}}_j(t)) \right] \quad (20) \\
& - \frac{1}{2} \sum_{i \in \mathcal{M}_{1i}} \sum_{j \in \mathcal{M}_{2i}} b_{ij} \tilde{x}_j^T(T_s) \tilde{x}_j(T_s) - \frac{1}{2} \sum_{i \in \mathcal{M}_{1i}} \sum_{j \in \mathcal{M}_{2i}} q_{ij} \tilde{v}_j^T(T_s) \tilde{v}_j(T_s) \\
& - \frac{p}{2} \sum_{i \in \mathcal{M}_{1i}} h_i \left[ \tilde{x}_i^T(T_s) \tilde{x}_i(T_s) + \dot{\tilde{x}}_i^T(t) \dot{\tilde{x}}_i(t) \right] - \frac{p}{2} \sum_{i \in \mathcal{M}_{1i}} l_i \left[ \tilde{v}_i^T(T_s) \tilde{v}_i(T_s) + \dot{\tilde{v}}_i^T(t) \dot{\tilde{v}}_i(t) \right],
\end{aligned}$$

where  $\xi_{1i} = 1 + 2\rho_1 + \rho_2 + \sum_{j \in \mathcal{M}_{1i}} c_{ij}(t_s) a_{ij} + \sum_{j \in \mathcal{M}_{1i}} \alpha_{ij}(t_s) p_{ij} + \sum_{j \in \mathcal{M}_{2i}} d_{ij}(t_s) b_{ij} + \sum_{j \in \mathcal{M}_{2i}} \beta_{ij}(t_s) q_{ij} + c_i(t_s) h_i + d_i(t_s) l_i$ .

Using Leibniz–Newton formula,

$$x(t_s) - x(T_s) = \int_{T_s}^{t_s} \dot{x}(k) dk, \quad (21)$$

then

$$(x(t_s))^T = (x(T_s))^T + \left( \int_{T_s}^{t_s} \dot{x}(k) dk \right)^T, \quad (22)$$

and then

$$\begin{aligned}
(\tilde{x}(t_s))^T (\tilde{x}(t_s)) &= \left[ (\tilde{x}(T_s))^T + \left( \int_{T_s}^{t_s} \dot{\tilde{x}}(k) dk \right)^T \right] \left[ (\tilde{x}(T_s)) + \left( \int_{T_s}^{t_s} \dot{\tilde{x}}(k) dk \right) \right] \\
&\leq 2(\tilde{x}(T_s))^T (\tilde{x}(T_s)) + 2 \left( \int_{T_s}^{t_s} \dot{\tilde{x}}(k) dk \right)^T \left( \int_{T_s}^{t_s} \dot{\tilde{x}}(k) dk \right) \quad (23) \\
&\leq 2(\tilde{x}(T_s))^T (\tilde{x}(T_s)) + 2\tau \int_{V_s}^{t_s} \dot{\tilde{x}}_i^T(k) \dot{\tilde{x}}_i(k) dk.
\end{aligned}$$

Similarly,

$$(\tilde{v}(t_s))^T (\tilde{v}(t_s)) \leq 2(\tilde{v}(T_s))^T (\tilde{v}(T_s)) + 2\tau \int_{T_s}^{t_s} \dot{\tilde{v}}_i^T(k) \dot{\tilde{v}}_i(k) dk. \quad (24)$$

Substituting (23) and (24) into (20), we obtain

$$\begin{aligned}
\dot{V}_1(t_s) \leq & \sum_{i \in \mathcal{M}_{1i}} \tilde{x}_i^T(T_s) \tilde{x}_i(T_s) + \tau \sum_{i \in \mathcal{M}_{1i}} \int_{T_s}^{t_s} \dot{\tilde{x}}_i^T(k) \dot{\tilde{x}}_i(k) dk - \frac{1}{2} \sum_{i \in \mathcal{M}_{1i}} \sum_{j \in \mathcal{M}_{2i}} b_{ij} \tilde{x}_j^T(T_s) \tilde{x}_j^T(T_s) \\
& + \sum_{i \in \mathcal{M}_{1i}} \left( \xi_{1i} + \frac{1}{2} \rho_2 \right) \tilde{v}_i^T(T_s) \tilde{v}_i(T_s) + \tau \sum_{i \in \mathcal{M}_{1i}} \xi_{1i} \int_{T_s}^{t_s} \dot{\tilde{v}}_i^T(k) \dot{\tilde{v}}_i(k) dk - \frac{1}{2} \sum_{i \in \mathcal{M}_{1i}} \sum_{j \in \mathcal{M}_{2i}} q_{ij} \tilde{v}_j^T(T_s) \tilde{v}_j(T_s) \\
& + \sum_{i \in \mathcal{M}_{1i}} p \lambda_1 \|\tilde{x}_i(T_s)\|^2 + \sum_{i \in \mathcal{M}_{1i}} p \lambda_1 \|\dot{\tilde{x}}_i(t_s)\|^2 + \sum_{i \in \mathcal{M}_{1i}} p \lambda_3 \|\tilde{v}_i(T_s)\|^2 + \sum_{i \in \mathcal{M}_{1i}} p \lambda_3 \|\dot{\tilde{v}}_i(t_s)\|^2,
\end{aligned} \tag{25}$$

where  $\xi_{1i} = 1 + 2\rho_1 + \rho_2 + \sum_{j \in \mathcal{M}_{1i}} c_{ij}(t_s) a_{ij} + \sum_{j \in \mathcal{M}_{1i}} \alpha_{ij}(t_s) p_{ij} + \sum_{j \in \mathcal{M}_{2i}} d_{ij}(t_s) b_{ij} + \sum_{j \in \mathcal{M}_{2i}} \beta_{ij}(t_s) q_{ij} + c_i(t_s) h_i + d_i(t_s) l_i$  and  $\lambda_1$  and  $\lambda_3$  are the minimum eigenvalues of  $A_{11} - H_1$  and  $P_{11} - L_1$ , respectively.

Similarly, differentiating  $V_2(t_s)$  and  $V_3(t_s)$ , we can obtain

$$\begin{aligned}
\dot{V}_2(t_s) \leq & \sum_{i \in \mathcal{M}_{2i}} \tilde{x}_i^T(T_s) \tilde{x}_i(T_s) + \tau \sum_{i \in \mathcal{M}_{2i}} \int_{T_s}^{t_s} \dot{\tilde{x}}_i^T(k) \dot{\tilde{x}}_i(k) dk - \frac{1}{2} \sum_{i \in \mathcal{M}_{2i}} \sum_{j \in \mathcal{M}_{1i}} b_{ij} \tilde{x}_j^T(T_s) \tilde{x}_j(T_s) \\
& + \sum_{i \in \mathcal{M}_{2i}} \left( \xi_{2i} + \frac{1}{2} \rho_4 \right) \tilde{v}_i^T(T_s) \tilde{v}_i(T_s) + \tau \sum_{i \in \mathcal{M}_{2i}} \xi_{2i} \int_{T_s}^{t_s} \dot{\tilde{v}}_i^T(k) \dot{\tilde{v}}_i(k) dk - \frac{1}{2} \sum_{i \in \mathcal{M}_{2i}} \sum_{j \in \mathcal{M}_{1i}} q_{ij} \tilde{v}_j^T(T_s) \tilde{v}_j(T_s) \\
& + \sum_{i \in \mathcal{M}_{2i}} p \lambda_2 \|\tilde{x}_i(T_s)\|^2 + \sum_{i \in \mathcal{M}_{2i}} p \lambda_2 \|\dot{\tilde{x}}_i(t_s)\|^2 + \sum_{i \in \mathcal{M}_{2i}} p \lambda_4 \|\tilde{v}_i(T_s)\|^2 + \sum_{i \in \mathcal{M}_{2i}} p \lambda_4 \|\dot{\tilde{v}}_i(t_s)\|^2,
\end{aligned} \tag{26}$$

where  $\xi_{2i} = 1 + 2\rho_3 + \rho_4 + \sum_{j \in \mathcal{M}_{2i}} c_{ij}(t_s) a_{ij} + \sum_{j \in \mathcal{M}_{2i}} \alpha_{ij}(t_s) p_{ij} + \sum_{j \in \mathcal{M}_{1i}} d_{ij}(t_s) b_{ij} + \sum_{j \in \mathcal{M}_{1i}} \beta_{ij}(t_s) q_{ij} + c_i(t_s) h_i + d_i(t_s) l_i$

and  $\lambda_2$  and  $\lambda_4$  are the minimum eigenvalues of  $A_{22} - H_2$  and  $P_{22} - L_2$ , respectively:

$$\begin{aligned}
\dot{V}_3(t_s) = & \tau^2 \sum_{i \in \mathcal{M}_{1i}} \dot{\tilde{x}}_i^T(t_s) \dot{\tilde{x}}_i(t_s) - \tau \sum_{i \in \mathcal{M}_{1i}} \int_{T_s}^{t_s} \dot{\tilde{x}}_i^T(k) \dot{\tilde{x}}_i(k) dk + \tau^2 \sum_{i \in \mathcal{M}_{1i}} \xi_{1i} \dot{\tilde{v}}_i^T(t_s) \dot{\tilde{v}}_i(t_s) - \tau \sum_{i \in \mathcal{M}_{1i}} \xi_{1i} \int_{T_s}^{t_s} \dot{\tilde{v}}_i^T(k) \dot{\tilde{v}}_i(k) dk \\
& + \tau^2 \sum_{i \in \mathcal{M}_{2i}} \dot{\tilde{x}}_i^T(t_s) \dot{\tilde{x}}_i(t_s) - \tau \sum_{i \in \mathcal{M}_{2i}} \int_{T_s}^{t_s} \dot{\tilde{x}}_i^T(k) \dot{\tilde{x}}_i(k) dk + \tau^2 \sum_{i \in \mathcal{M}_{2i}} \xi_{2i} \dot{\tilde{v}}_i^T(t_s) \dot{\tilde{v}}_i(t_s) - \tau \sum_{i \in \mathcal{M}_{2i}} \xi_{2i} \int_{T_s}^{t_s} \dot{\tilde{v}}_i^T(k) \dot{\tilde{v}}_i(k) dk.
\end{aligned} \tag{27}$$

Combining  $\dot{V}_1(t_s)$ ,  $\dot{V}_2(t_s)$ , and  $\dot{V}_3(t_s)$ , we obtain

$$\begin{aligned}
\dot{V}(t_s) \leq & \sum_{i \in \mathcal{M}_{1i}} (1 + p \lambda_1) \|\tilde{x}_i(T_s)\|^2 + \sum_{i \in \mathcal{M}_{1i}} (\tau^2 + p \lambda_1) \|\dot{\tilde{x}}_i(t_s)\|^2 + \sum_{i \in \mathcal{M}_{2i}} (1 + p \lambda_2) \|\tilde{x}_i(T_s)\|^2 + \sum_{i \in \mathcal{M}_{2i}} (\tau^2 + p \lambda_2) \|\dot{\tilde{x}}_i(t_s)\|^2 \\
& + \sum_{i \in \mathcal{M}_{1i}} \left( \xi_{1i} + \frac{1}{2} \rho_2 - \frac{1}{2} \sum_{j \in \mathcal{M}_{2i}} b_{ji} - \frac{1}{2} \sum_{j \in \mathcal{M}_{2i}} q_{ji} + p \lambda_3 \right) \|\tilde{v}_i(T_s)\|^2 + \sum_{i \in \mathcal{M}_{1i}} (\tau^2 \xi_{1i} + p \lambda_3) \|\dot{\tilde{v}}_i(t_s)\|^2 \\
& + \sum_{i \in \mathcal{M}_{2i}} \left( \xi_{2i} + \frac{1}{2} \rho_4 - \frac{1}{2} \sum_{j \in \mathcal{M}_{1i}} b_{ji} - \frac{1}{2} \sum_{j \in \mathcal{M}_{1i}} q_{ji} + p \lambda_4 \right) \|\tilde{v}_i(T_s)\|^2 + \sum_{i \in \mathcal{M}_{2i}} (\tau^2 \xi_{2i} + p \lambda_4) \|\dot{\tilde{v}}_i(t_s)\|^2,
\end{aligned} \tag{28}$$

where  $\lambda_1, \lambda_2, \lambda_3$ , and  $\lambda_4$  are the minimum eigenvalues of  $A_{11} - H_1, A_{22} - H_2, P_{11} - L_1$ , and  $P_{22} - L_2$ , respectively; with  $H_1 = \text{diag}\{h_i\}$  and  $L_1 = \text{diag}\{l_i\}$  for  $\forall i \in \ell_1$ , and  $H_2 = \text{diag}\{h_i\}$  and  $L_2 = \text{diag}\{l_i\}$  for  $\forall i \in \ell_2$ . Furthermore, since  $A_{11}, A_{22}, P_{11}$ , and  $P_{22}$  are both symmetric and diagonal matrices  $H_1, H_2, L_1$ , and  $L_2$  have at least one element being 1,  $\lambda_i < 0, i = 1, 2, 3, 4$  based on Lemma 2. Therefore,  $\dot{V}(t_s) < 0$ , if  $p > 0$  is sufficiently large.

Case 2.  $A_{11}, A_{22}, P_{11}$ , and  $P_{22}$  are asymmetric.

It is known that  $(A_{11} + A_{11}^T)/2, (A_{22} + A_{22}^T)/2, (P_{11} + P_{11}^T)/2$ , and  $(P_{22} + P_{22}^T)/2$  are symmetric, even if  $A_{11}, A_{22}, P_{11}$ , and  $P_{22}$  are asymmetric. Therefore, all eigenvalues of  $(A_{11} + A_{11}^T)/2 - H_1, (A_{22} + A_{22}^T)/2 - H_2, (P_{11} + P_{11}^T)/2 - L_1$ , and  $(P_{22} + P_{22}^T)/2 - L_2$  are negative from Lemma 2. Similarly, we can have

$$\begin{aligned} \dot{V}_1(t_s) \leq & \sum_{i \in \mathcal{M}_{1i}} \tilde{x}_i^T(T_s) \tilde{x}_i(T_s) + \tau \sum_{i \in \mathcal{M}_{1i}} \int_{T_s}^{t_s} \dot{\tilde{x}}_i^T(k) \dot{\tilde{x}}_i(k) dk - \frac{1}{2} \sum_{i \in \mathcal{M}_{1i}} \sum_{j \in \mathcal{M}_{2i}} b_{ij} \tilde{x}_j^T(T_s) \tilde{x}_j(T_s) \\ & + \sum_{i \in \mathcal{M}_{1i}} \left( \xi_{1i} + \frac{1}{2} \rho_2 \right) \tilde{v}_i^T(T_s) \tilde{v}_i(T_s) + \tau \sum_{i \in \mathcal{M}_{1i}} \xi_{1i} \int_{T_s}^{t_s} \dot{\tilde{v}}_i^T(k) \dot{\tilde{v}}_i(k) dk - \frac{1}{2} \sum_{i \in \mathcal{M}_{1i}} \sum_{j \in \mathcal{M}_{2i}} q_{ij} \tilde{v}_j^T(T_s) \tilde{v}_j(T_s) \\ & + \sum_{i \in \mathcal{M}_{1i}} p \lambda_1 \|\tilde{x}_i(T_s)\|^2 + \sum_{i \in \mathcal{M}_{1i}} p \lambda_1 \|\dot{\tilde{x}}_i(t_s)\|^2 + \sum_{i \in \mathcal{M}_{1i}} p \lambda_3 \|\tilde{v}_i(T_s)\|^2 + \sum_{i \in \mathcal{M}_{1i}} p \lambda_3 \|\dot{\tilde{v}}_i(t_s)\|^2, \end{aligned} \quad (29)$$

where  $\xi_{2i} = 1 + 2\rho_3 + \rho_4 + \sum_{j \in \mathcal{M}_{2i}} c_{ij}(t_s) a_{ij} + \sum_{j \in \mathcal{M}_{2i}} \alpha_{ij}(t_s) p_{ij} + \sum_{j \in \mathcal{M}_{1i}} d_{ij}(t_s) b_{ij} + \sum_{j \in \mathcal{M}_{1i}} \beta_{ij}(t_s) q_{ij} + c_i(t_s) h_i + d_i(t_s) l_i$ ,

and  $\lambda_2$  and  $\lambda_4$  are the minimum eigenvalue of  $(A_{22} + A_{22}^T)/2 - H_2$  and  $(P_{22} + P_{22}^T)/2 - L_2$ , respectively.

$$\begin{aligned} \dot{V}_2(t_s) \leq & \sum_{i \in \mathcal{M}_{2i}} \tilde{x}_i^T(T_s) \tilde{x}_i(T_s) + \tau \sum_{i \in \mathcal{M}_{2i}} \int_{T_s}^{t_s} \dot{\tilde{x}}_i^T(k) \dot{\tilde{x}}_i(k) dk - \frac{1}{2} \sum_{i \in \mathcal{M}_{2i}} \sum_{j \in \mathcal{M}_{1i}} b_{ij} \tilde{x}_j^T(T_s) \tilde{x}_j(T_s) \\ & + \sum_{i \in \mathcal{M}_{2i}} \left( \xi_{2i} + \frac{1}{2} \rho_4 \right) \tilde{v}_i^T(T_s) \tilde{v}_i(T_s) + \tau \sum_{i \in \mathcal{M}_{2i}} \xi_{2i} \int_{T_s}^{t_s} \dot{\tilde{v}}_i^T(k) \dot{\tilde{v}}_i(k) dk - \frac{1}{2} \sum_{i \in \mathcal{M}_{2i}} \sum_{j \in \mathcal{M}_{1i}} q_{ij} \tilde{v}_j^T(T_s) \tilde{v}_j(T_s) \\ & + \sum_{i \in \mathcal{M}_{2i}} p \lambda_2 \|\tilde{x}_i(T_s)\|^2 + \sum_{i \in \mathcal{M}_{2i}} p \lambda_2 \|\dot{\tilde{x}}_i(t_s)\|^2 + \sum_{i \in \mathcal{M}_{2i}} p \lambda_4 \|\tilde{v}_i(T_s)\|^2 + \sum_{i \in \mathcal{M}_{2i}} p \lambda_4 \|\dot{\tilde{v}}_i(t_s)\|^2, \end{aligned} \quad (30)$$

where  $\xi_{1i} = 1 + 2\rho_1 + \rho_2 + \sum_{j \in \mathcal{M}_{1i}} c_{ij}(t_s) a_{ij} + \sum_{j \in \mathcal{M}_{1i}} \alpha_{ij}(t_s) p_{ij} + \sum_{j \in \mathcal{M}_{2i}} d_{ij}(t_s) b_{ij} + \sum_{j \in \mathcal{M}_{2i}} \beta_{ij}(t_s) q_{ij} + c_i(t_s) h_i + d_i(t_s) l_i$ .

and  $\lambda_1$  and  $\lambda_3$  are the minimum eigenvalue of  $(A_{11} + A_{11}^T)/2 - H_1, (P_{11} + P_{11}^T)/2 - L_1$ , respectively:

Combining  $\dot{V}_1(t_s), \dot{V}_2(t_s)$ , and  $\dot{V}_3(t_s)$ , we obtain

$$\begin{aligned} \dot{V}(t_s) \leq & \sum_{i \in \mathcal{M}_{1i}} (1 + p \lambda_1) \|\tilde{x}_i(T_s)\|^2 + \sum_{i \in \mathcal{M}_{1i}} (\tau^2 + p \lambda_1) \|\dot{\tilde{x}}_i(t_s)\|^2 + \sum_{i \in \mathcal{M}_{2i}} (1 + p \lambda_2) \|\tilde{x}_i(T_s)\|^2 + \sum_{i \in \mathcal{M}_{2i}} (\tau^2 + p \lambda_2) \|\dot{\tilde{x}}_i(t_s)\|^2 \\ & + \sum_{i \in \mathcal{M}_{1i}} \left( \xi_{1i} + \frac{1}{2} \rho_2 - \frac{1}{2} \sum_{j \in \mathcal{M}_{2i}} b_{ji} - \frac{1}{2} \sum_{j \in \mathcal{M}_{2i}} q_{ji} + p \lambda_3 \right) \|\tilde{v}_i(T_s)\|^2 + \sum_{i \in \mathcal{M}_{1i}} (\tau^2 \xi_{1i} + p \lambda_3) \|\dot{\tilde{v}}_i(t_s)\|^2 \\ & + \sum_{i \in \mathcal{M}_{2i}} \left( \xi_{2i} + \frac{1}{2} \rho_4 - \frac{1}{2} \sum_{j \in \mathcal{M}_{1i}} b_{ji} - \frac{1}{2} \sum_{j \in \mathcal{M}_{1i}} q_{ji} + p \lambda_4 \right) \|\tilde{v}_i(T_s)\|^2 + \sum_{i \in \mathcal{M}_{2i}} (\tau^2 \xi_{2i} + p \lambda_4) \|\dot{\tilde{v}}_i(t_s)\|^2, \end{aligned} \quad (31)$$

where  $\lambda_1, \lambda_2, \lambda_3$ , and  $\lambda_4$  are the minimum eigenvalue of  $(A_{11} + A_{11}^T/2) - H_1$ ,  $(A_{22} + A_{22}^T/2) - H_2$ ,  $(P_{11} + P_{11}^T/2) - L_1$ , and  $(P_{22} + P_{22}^T/2) - L_2$ , respectively. Even though matrix  $A_{11}, A_{22}, P_{11}$ , and  $P_{22}$  are asymmetric, matrix  $(A_{11} + A_{11}^T)/2$ ,  $(A_{22} + A_{22}^T)/2$ ,  $(P_{11} + P_{11}^T)/2$ , and  $(P_{22} + P_{22}^T)/2$  are symmetric; thus, from Lemma 2, we can obtain all eigenvalues of  $(A_{11} + A_{11}^T/2) - H_1$ ,  $(A_{22} + A_{22}^T/2) - H_2$ ,  $(P_{11} + P_{11}^T/2) - L_1$ , and  $(P_{22} + P_{22}^T/2) - L_2$  are negative. So,  $\lambda_i < 0, \forall i \in 1, 2, 3, 4$  and  $\dot{V}(t_s) < 0$ , if  $p > 0$  is sufficiently large.

Therefore, all the agents of sampled-data based network (1) with time-varying delays can achieve the given synchronous states asymptotically.

*Remark 1.* When the topology structure is connected regardless of the coupled weighted matrices, the sampled-data-based network (1) with time-varying delays can be asymptotically group synchronized by controller (2).

#### 4. Simulations

A complex dynamical system with  $N = 6$  and  $L = 3$ . Let the initial values be  $X(0) = [29 \ 12 \ 20 \ 17 \ 25 \ -7 \ 22 \ 9]$  and  $c_{ij}(0) = d_{ij}(0) = \alpha_{ij}(0) = \beta_{ij}(0) = c_i(0) = d_i(0) = 0.01$ .

Let  $A_{11}, A_{22}, P_{11}$ , and  $P_{22}$  be symmetric as

$$\begin{aligned} A_{11} &= \begin{bmatrix} -2 & 1 & 0 \\ 1 & -3 & 1 \\ 0 & 1 & -1 \end{bmatrix} * 0.1, \\ A_{22} &= \begin{bmatrix} -3 & 2 & 1 \\ 2 & -4 & 1 \\ 1 & 1 & -3 \end{bmatrix} * 0.05, \\ P_{11} &= \begin{bmatrix} 0 & 2 & 0 \\ 2 & 0 & 1 \\ 0 & 1 & 0 \end{bmatrix} * 0.01, \\ P_{22} &= \begin{bmatrix} 0 & 2 & 1 \\ 2 & 0 & 2 \\ 1 & 2 & 0 \end{bmatrix} * 0.005, \end{aligned} \tag{32}$$

and  $A_{11}, A_{22}, P_{11}$ , and  $P_{22}$  be asymmetric as

$$\begin{aligned} A_{11} &= \begin{bmatrix} -3 & 0 & 3 \\ 2 & -3 & 1 \\ 0 & 1 & -1 \end{bmatrix} * 0.1, \\ A_{22} &= \begin{bmatrix} -2 & 2 & 0 \\ 3 & -6 & 3 \\ 1 & 2 & -3 \end{bmatrix} * 0.05, \\ P_{11} &= \begin{bmatrix} 0 & 3 & 0 \\ 2 & 0 & 1 \\ 0 & 1 & 0 \end{bmatrix} * 0.01, \\ P_{22} &= \begin{bmatrix} 0 & 2 & 0 \\ 3 & 0 & 3 \\ 0 & 2 & 0 \end{bmatrix} * 0.005, \end{aligned} \tag{33}$$

respectively.

Take

$$\begin{aligned} B_{12} &= \begin{bmatrix} 0 & 1 & 0 \\ 2 & 0 & 0 \\ 0 & 0 & 0.5 \end{bmatrix} * 0.1, \\ B_{21} &= \begin{bmatrix} 1 & 2 & 0 \\ 0 & 0 & 0 \\ 0 & 0 & 0 \end{bmatrix} * 0.1, \\ H_1 &= \text{diag}\{0.1 \ 0 \ 0\}, \\ H_2 &= \text{diag}\{0 \ 0.1 \ 0\}. \end{aligned} \tag{34}$$

Figure 1 presents that the effects of adaptive strategies for the synchronization of complex networks with non-linear dynamical. Figure 1(a) shows the position and velocity of all nodes without adaptive strategies, and Figure 1(b) shows the position and velocity of all nodes with adaptive laws, respectively, in which the subgroups' coupling matrices are symmetric. It is obvious to see the fact that all the nodes with adaptive laws can achieve their given synchronous states asymptotically, while all the nodes without adaptive laws cannot converge. Figures 2 and 3 show the simulations of network (1) with  $\tau = 0.1$ , in which the subnetworks' coupling matrices are symmetric or asymmetric described as Figures 2 and 3, respectively. Figures 2(a) and 2(b) present that the position and velocity of all nodes of network (1) with  $\tau = 0.1$ , where subgroups' coupling matrices are symmetric, and the coupling strengths  $c_{ij}, d_{ij}, \alpha_{ij}$ , and  $\beta_{ij}$  and the feedback gains  $c_i$  and  $d_i$  are presented in Figures 2(c)–2(h), respectively. Similarly, Figures 3(a) and 3(b) present that the position and velocity of all nodes of network (1) with  $\tau = 0.1$ , where the subgroups' coupling matrices are asymmetric, the coupling strengths  $c_{ij}, d_{ij}, \alpha_{ij}$ , and  $\beta_{ij}$  and the feedback gains  $c_i$  and  $d_i$  presented as Figures 3(c)–3(h), respectively. From Figures 2 and 3, we can find that all nodes of network (1) can achieve synchronization and the coupling strengths and the feedback gains also converge to be consistent. However, compared with Figure 3, the system in Figure 2 can achieve synchronization faster than that in Figure 3. Figure 4 is the simulation of network (1) with adaptive laws, in which the subgroups' coupling matrices are symmetric, where Figures 4(a) and 4(b) are the positions and velocities of all nodes of network (1) with  $\tau = 0.1$  and  $\tau = 1$ , respectively. We can know that, with the time delay  $\tau$  increasing, the system cannot achieve synchronization.

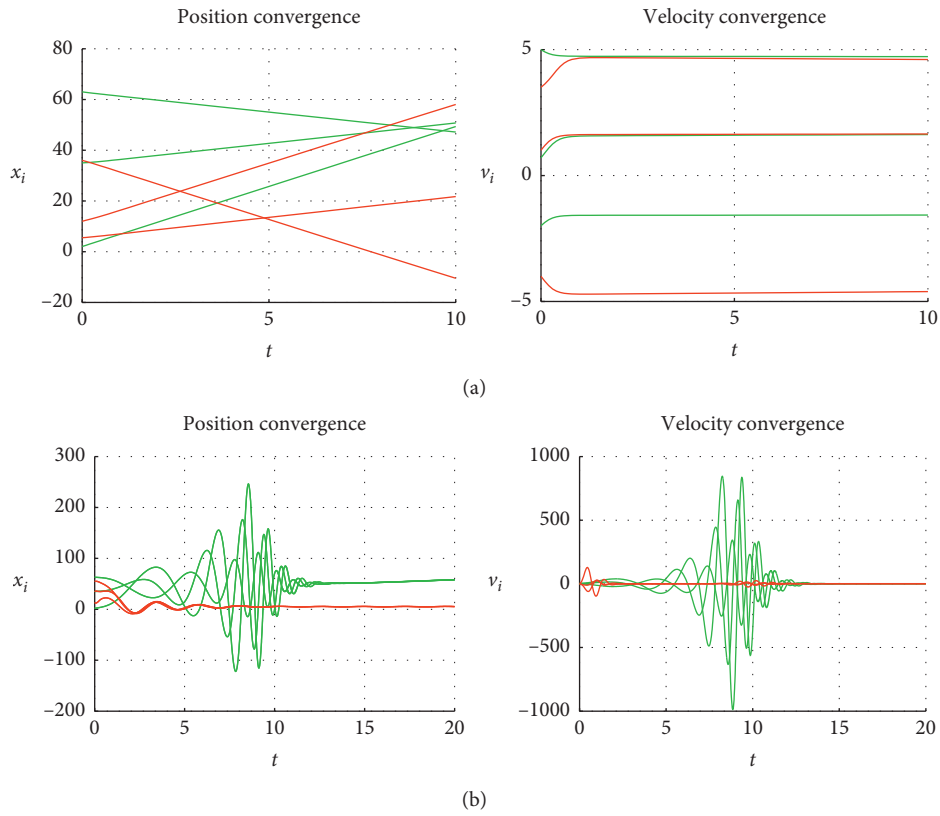


FIGURE 1: (a) Without adaptive strategies. (b) With adaptive strategies.

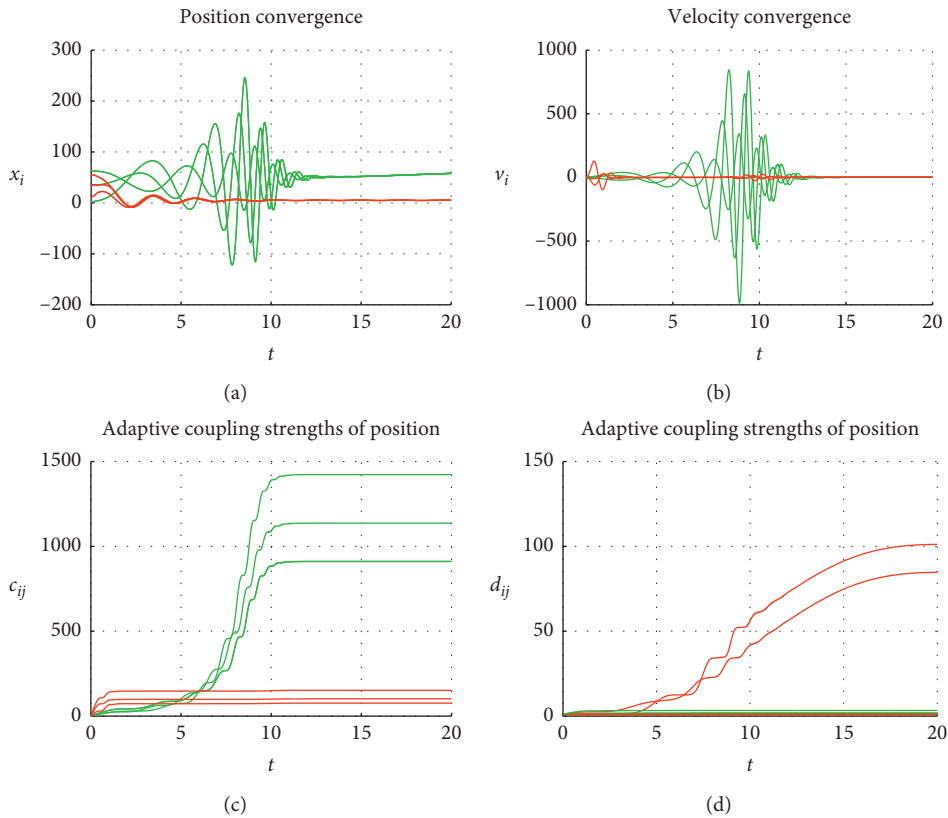


FIGURE 2: Continued.

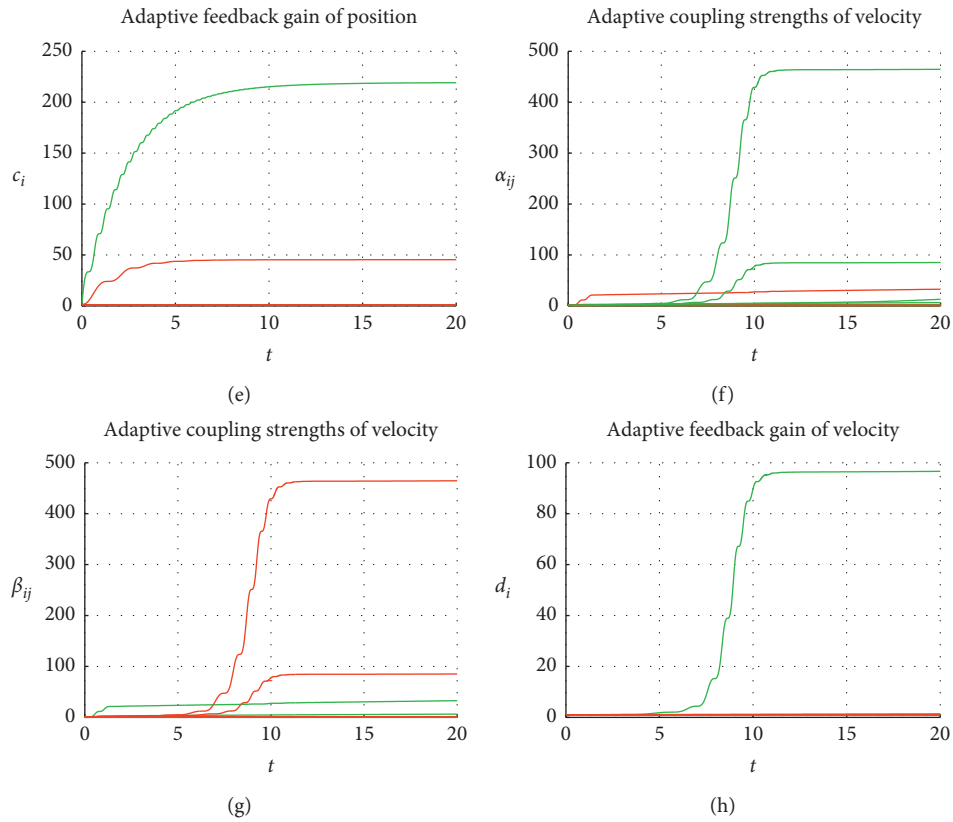


FIGURE 2: Intragroup coupling matrix is symmetric and time delay  $\tau = 0.1$ . (a) Positions. (b) Velocities. (c)  $c_{ij}$ . (d)  $d_{ij}$ . (e)  $c_i$ . (f)  $\alpha_{ij}$ . (g)  $\beta_{ij}$ . (h)  $d_i$ .

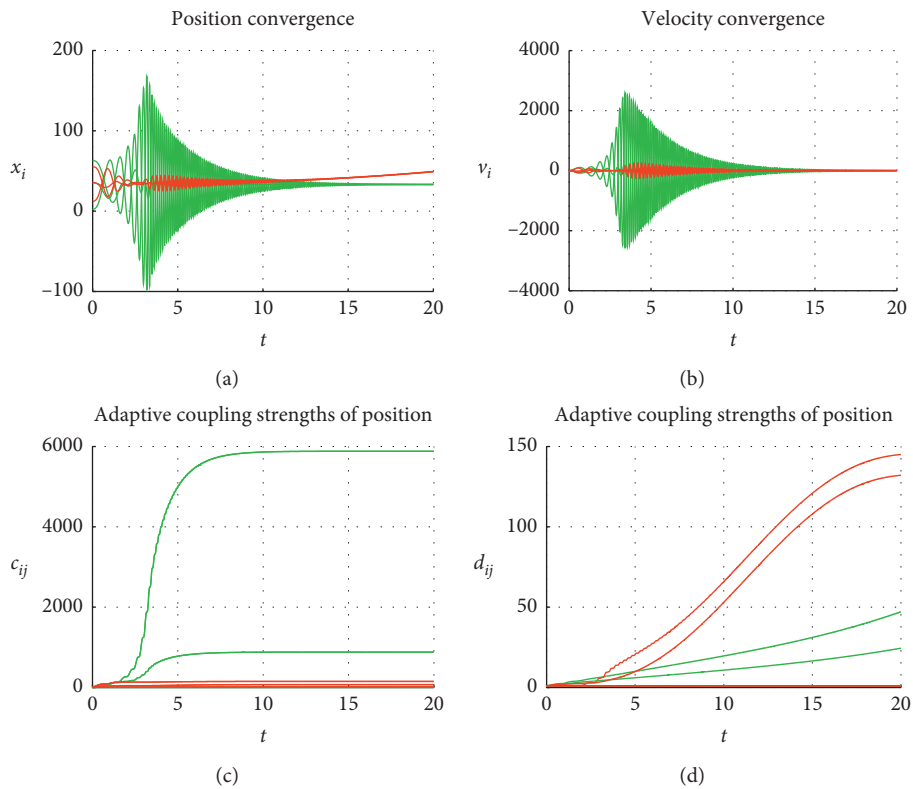


FIGURE 3: Continued.

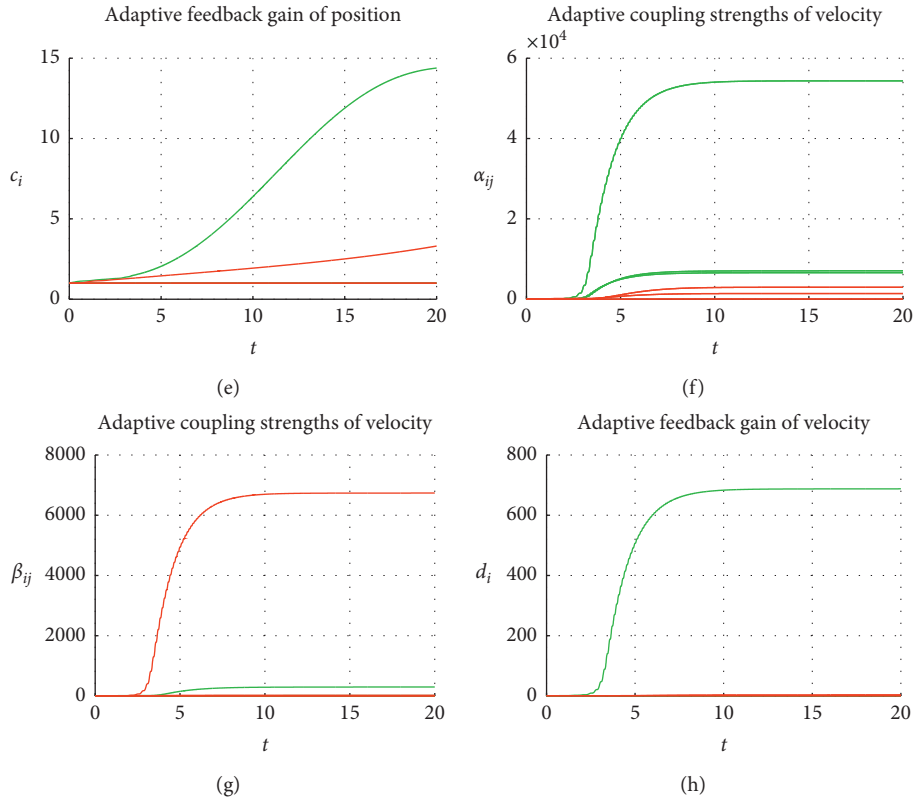


FIGURE 3: Intragroup coupling matrix is asymmetric and time delay  $\tau = 0.1$ . (a) Positions. (b) Velocities. (c)  $c_{ij}$ . (d)  $d_{ij}$ . (e)  $c_i$ . (f)  $\alpha_{ij}$ . (g)  $\beta_{ij}$ . (h)  $d_i$ .

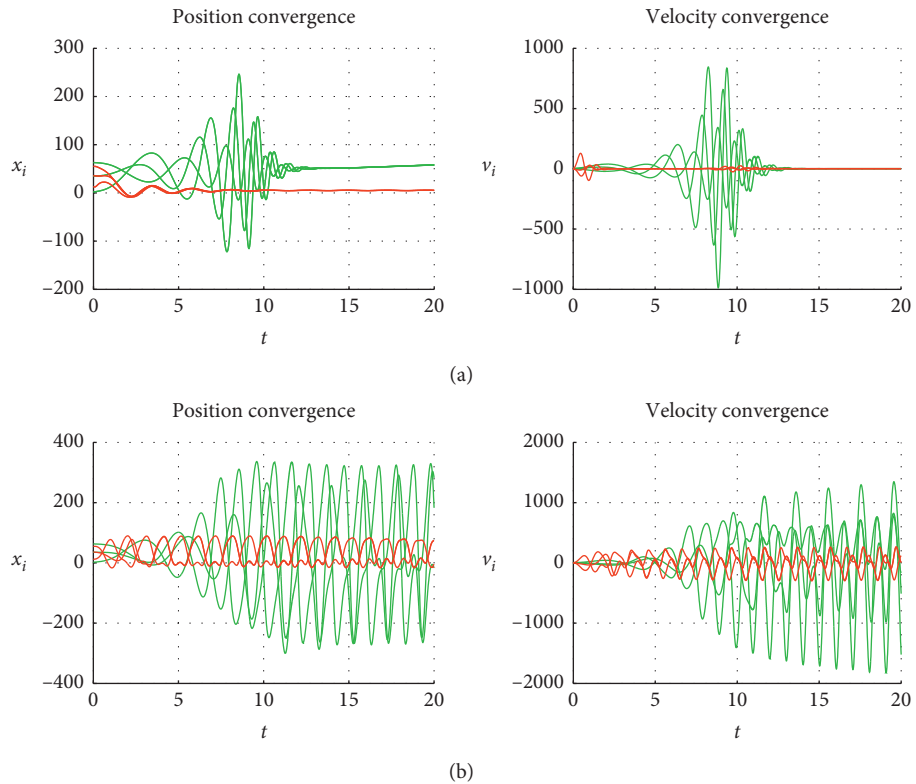


FIGURE 4: Intragroup coupling matrix is symmetric and with adaptive strategies. (a) Time delay  $\tau = 0.1$ . (b) Time delay  $\tau = 1$ .

## 5. Conclusion

The adaptive group synchronization of second-order nonlinear complex dynamical networks with time-varying delays and sampled data has been researched in this paper. A new adaptive law has been designed, and we have proved that the second-order system with sampled data can achieve group synchronization no matter whether the coupling matrix is symmetric or not. Moreover, we have discussed the influences of time-varying delays and adaptive laws for group synchronization of complex networks with nonlinear dynamics in the different simulations. Finally, some simulations have been represented.

## Data Availability

No data were used in this study.

## Conflicts of Interest

The authors declare that there are no conflicts of interest regarding the publication of this paper.

## Acknowledgments

This work was supported by the achievements of the important project “Class Teaching Experiment Research in Basic Education School” of Beijing Education Science “12th Five Year Plan” in 2015 (no. ABA15009) and National Natural Science Foundation of China (Grant no. 61773023).

## References

- [1] G. Chen and Z. Duan, “Network synchronizability analysis: a graph theoretic approach,” *Chaos: An Interdisciplinary Journal of Nonlinear Science*, vol. 18, no. 3, Article ID 37102, 2008.
- [2] C. Wu and L. Chua, “Application of graph theory to the synchronization in an array of coupled nonlinear oscillators,” *IEEE Transactions on Circuits and Systems I: Fundamental Theory and Applications*, vol. 42, no. 8, pp. 494–497, 1995.
- [3] A. Papachristodoulou, A. Jadbabaie, and U. Münz, “Effects of delay in multi-agent consensus and oscillator synchronization,” *IEEE Transactions on Automatic Control*, vol. 55, no. 6, pp. 1471–1477, 2010.
- [4] X. L. Wang, H. Su, M. Z. Q. Chen, X. F. Wang, and G. Chen, “Reaching non-negative edge consensus of networked dynamical systems,” *IEEE Transactions on Cybernetics*, vol. 48, no. 9, pp. 2712–2722, 2018.
- [5] X. Liu, H. Su, and M. Z. Q. Chen, “A switching approach to designing finite-time synchronization controllers of coupled neural networks,” *IEEE Transactions on Neural Networks and Learning Systems*, vol. 27, no. 2, pp. 471–482, 2016.
- [6] B. Liu, N. Xu, H. Su, L. Wu, and J. Bai, “On the observability of leader-based multiagent systems with fixed topology,” *Complexity*, vol. 2019, Article ID 9487574, 10 pages, 2019.
- [7] C. Tang, B. Wu, J. Wang, and L. Xiang, “Evolutionary origin of asymptotically stable consensus,” *Scientific Reports*, vol. 4, p. 4590, 2014.
- [8] I. Z. Kiss, “Synchronization engineering,” *Current Opinion in Chemical Engineering*, vol. 21, pp. 1–9, 2018.
- [9] H. Su, Y. Sun, and Z. Zeng, “Semiglobal observer-based non-negative edge consensus of networked systems with actuator saturation,” *IEEE Transactions on Cybernetics*, vol. 50, no. 6, pp. 2827–2836, 2020.
- [10] H. Su, Y. Liu, and Z. Zeng, “Second-order consensus for multiagent systems via intermittent sampled position data control,” *IEEE Transactions on Cybernetics*, vol. 50, no. 5, pp. 2063–2072, 2020.
- [11] H. Su, M. Long, and Z. Zeng, “Controllability of two-time-scale discrete-time multiagent systems,” *IEEE Transactions on Cybernetics*, vol. 50, no. 4, pp. 1440–1449, 2020.
- [12] H. Su, J. Zhang, and X. Chen, “A stochastic sampling mechanism for time-varying formation of multiagent systems with multiple leaders and communication delays,” *IEEE Transactions on Neural Networks and Learning Systems*, vol. 30, no. 12, pp. 3699–3707, 2019.
- [13] S. Liu, Z. Ji, H. Ma, and S. He, “A new perspective to algebraic characterization on controllability of multiagent systems,” *Complexity*, vol. 2020, Article ID 9703972, 12 pages, 2020.
- [14] B. Liu, H. Su, L. Wu, X. Li, and X. Lu, “Fractional-order controllability of multi-agent systems with time-delay,” *Neurocomputing*, 2020.
- [15] X. Wang, H. Su, X. Wang, and G. Chen, “Fully distributed event-triggered semiglobal consensus of multi-agent systems with input saturation,” *IEEE Transactions on Industrial Electronics*, vol. 64, no. 6, pp. 5055–5064, 2017.
- [16] W. Yu, L. Zhou, X. Yu, J. Lu, and R. Lu, “Consensus in multi-agent systems with second-order dynamics and sampled data,” *IEEE Transactions on Industrial Informatics*, vol. 9, no. 4, pp. 2137–2146, 2013.
- [17] B. Liu, P. Wei, and X. Wang, “Group synchronization of complex network with nonlinear dynamics via pinning control,” in *Proceeding of the 32nd Chinese Control Conference*, IEEE, Xi’an, China, pp. 235–240, July 2013.
- [18] W. Yu, G. Chen, and J. Lu, “On pinning synchronization of complex dynamical networks,” *Automatica*, vol. 45, no. 2, pp. 429–435, 2009.
- [19] Y. Lü, J. Lu, J. Liang, and J. Cao, “Pinning synchronization of nonlinear coupled Lure networks under hybrid impulses,” *IEEE Transactions on Circuits and Systems II-Express Briefs*, vol. 66, no. 3, pp. 432–436, 2018.
- [20] H. Su, Z. Rong, M. Chen, X. Wang, G. Chen, and H. Wang, “Decentralized adaptive pinning control for cluster synchronization of complex dynamical networks,” *IEEE Transactions on Systems, Man and Cybernetics, Cybernetics*, vol. 43, no. 1, pp. 394–399, 2013.
- [21] P. Delellis, M. Bemnardo, and F. Garofalo, “Synchronization of complex networks through local adaptive coupling,” *Chaos*, vol. 18, no. 3, p. 175, 2008.
- [22] J. Hu and W. X. Zheng, “Adaptive tracking control of leader-follower systems with unknown dynamics and partial measurements,” *Automatica*, vol. 50, no. 5, pp. 1416–1423, 2014.
- [23] B. Liu, S. Li, and L. Wang, “Adaptive synchronization of two time-varying delay nonlinear coupled networks,” in *Proceedings of the 33rd Chinese Control Conference*, pp. 3800–3804, IEEE, Nanjing, China, July 2014.
- [24] Y. Zhao, G. Wen, Z. Duan, and G. Chen, “Adaptive consensus for multiple nonidentical matching nonlinear systems: an edge-based framework,” *IEEE Transactions on Circuits and Systems II: Express Briefs*, vol. 62, no. 1, pp. 85–89, 2015.
- [25] B. Liu, S. Li, and X. Tang, “Adaptive second-order synchronization of two heterogeneous nonlinear coupled networks,” *Mathematical Problems in Engineering*, vol. 2015, Article ID 578539, 7 pages, 2015.



- [26] Q. Xu, S. Zhuang, Y. Zeng, and J. Xiao, "Decentralized adaptive strategies for synchronization of fractional-order complex networks," *IEEE/CAA Journal of Automatica Sinica*, vol. 4, no. 3, pp. 543–550, 2017.
- [27] D. Ding, J. Yan, N. Wang, and D. Liang, "Adaptive synchronization of fractional order complex-variable dynamical networks via pinning control," *Communications in Theoretical Physics*, vol. 68, no. 9, pp. 366–374, 2017.
- [28] L. Du, Y. Yang, and Y. Lei, "Synchronization in a fractional-order dynamic network with uncertain parameters using an adaptive control strategy," *Applied Mathematics and Mechanics*, vol. 39, no. 3, pp. 353–364, 2018.
- [29] S. Wang, H. Yao, S. Zheng, and Y. Xie, "A novel criterion for cluster synchronization of complex dynamical networks with coupling time-varying delays," *Communications in Nonlinear Science and Numerical Simulation*, vol. 17, no. 7, pp. 2997–3004, 2012.
- [30] Z.-J. Tang, T.-Z. Huang, J.-L. Shao, and J.-P. Hu, "Consensus of second-order multi-agent systems with nonuniform time-varying delays," *Neurocomputing*, vol. 97, no. 1, pp. 410–414, 2012.
- [31] B. Liu, X. Wang, H. Su, H. Zhou, Y. Shi, and R. Li, "Adaptive synchronization of complex dynamical networks with time-varying delays," *Circuits, Systems, and Signal Processing*, vol. 33, no. 4, pp. 1173–1188, 2014.
- [32] Y. Liang and X. Wang, "Adaptive synchronization in complex networks through nonlinearly coupling," *Computer Engineering and Applications*, vol. 48, no. 10, pp. 25–28, 2012.
- [33] H. Su, G. Chen, X. Wang, and Z. Lin, "Adaptive second-order consensus of networked mobile agents with nonlinear dynamics," *Automatica*, vol. 47, no. 2, pp. 368–375, 2011.
- [34] B. Liu, X. Wang, Y. Gao, G. Xie, and H. Su, "Adaptive synchronization of complex dynamical networks governed by local lipschitz nonlinearity on switching topology," *Journal of Applied Mathematics*, vol. 2013, Article ID 818242, 7 pages, 2013.
- [35] H. Su, N. Zhang, M. Z. Chen, H. Wang, and X. Wang, "Adaptive flocking with a virtual leader of multiple agents governed by locally Lipschitz nonlinearity," *Nonlinear Analysis: Real World Applications*, vol. 23, no. 9, pp. 978–990, 2013.
- [36] M. Li, B. Liu, Y. Zhu, L. Wang, and M. Zhou, "Group synchronization of nonlinear complex dynamics networks with sampled data," *Mathematical Problems in Engineering*, vol. 2014, Article ID 142061, 8 pages, 2014.
- [37] H. Liu, G. Xie, and L. Wang, "Necessary and sufficient conditions for solving consensus problems of double-integrator dynamics via sampled control," *International Journal of Robust and Nonlinear Control*, vol. 20, no. 15, pp. 1706–1722, 2010.
- [38] Y. Gao and L. Wang, "Sampled-data based consensus of continuous-time multi-agent systems with time-varying topology," *IEEE Transactions on Automatic Control*, vol. 56, no. 5, pp. 1226–1231, 2011.
- [39] B. Liu, X. Wang, H. Su, Y. Gao, and L. Wang, "Adaptive second-order consensus of multi-agent systems with heterogeneous nonlinear dynamics and time-varying delays," *Neurocomputing*, vol. 118, pp. 289–300, 2013.
- [40] J. Zhang, M. Li, and B. Liu, "Synchronization of a complex network for neighboring agents with time-varying delays," *Communications in Computer and Information Science*, vol. 225, pp. 73–81, 2011.

## Research Article

# Consensus Control of Nonlinear Multiagent Systems with Incremental Quadratic Constraints and Time Delays

Dachao Wang , Fang Song , Wei Zhang , and Zhi Hu 

Laboratory of Intelligent Control and Robotics, Shanghai University of Engineering Science, Shanghai 201620, China

Correspondence should be addressed to Fang Song; [songfang2005@163.com](mailto:songfang2005@163.com)

Received 26 March 2020; Accepted 28 May 2020; Published 24 June 2020

Guest Editor: Xiao Ling Wang

Copyright © 2020 Dachao Wang et al. This is an open access article distributed under the Creative Commons Attribution License, which permits unrestricted use, distribution, and reproduction in any medium, provided the original work is properly cited.

This paper considers the problem of consensus control for a class of nonlinear multiagent systems with incremental quadratic constraints and time delays. Each agent exchanges state information through a strongly connected communication topology. Based on the information obtained from neighboring agents, a distributed consensus protocol is designed. A delay-independent consensus condition is formed for the protocol to solve the consensus problem by employing Lyapunov–Krasovskii functional method. In order to deal with the nonlinear terms in matrix inequalities, an iterative algorithm is proposed by using the Schur complement lemma and the cone complementary linearization method. The nonlinearities under consideration are more general than many other nonlinearities considered in related literature studies since the incremental quadratic constraints include many other known nonlinearities as some special cases. Finally, we give a numerical example to illustrate the effectiveness of the proposed consensus control protocol.

## 1. Introduction

The consensus control problem of multiagent systems (MAS) has drawn lots of attention from researchers of systems and control community over the past few decades [1]. This is partly because the consensus problem has wide applications in different areas such as optimization, formation control, sensor network, dynamic agents of network, and cooperative surveillance.

In the past few years, researchers have made considerable progresses in the consensus control area and many aspects of consensus control are fully investigated. Many important results have been analyzed and published about the consensus control for linear, second-order, and high-order MAS, as seen in [2–7]. Finite-time consensus problem also attracts much attention from researchers [8, 9], and they mainly investigated how MAS can reach consensus within a certain time. In [10], the authors worked on the consensus problem for linear MAS under a time-invariant communication topology. In order to save energy in real-world mechanical systems, many different methods, such as event-trigger-based control [11, 12], intermittent control [13], and

sampled-data-based control [14], are invented to help solving consensus problem [15]. Instead of focusing on node consensus, authors in [16] studied nonnegative edge consensus due to physical considerations. As an important topic, group consensus also received much attention and many important works are published [17, 18].

It is worth mentioning that most of the existing papers are focusing on linear MAS, but physical systems always contain complicated nonlinearities. Therefore, consensus problem for nonlinear MAS deserves more attention. However, there exists no universal approach to solve the consensus problem for nonlinear MAS, and researchers are mostly concentrating on some types of systems with special nonlinearities (see, e.g., [19–21]). Researchers in [19] provided a linear matrix inequality-based method to design adaptive consensus control protocols for nonlinear MAS with Lipschitz nonlinearities by introducing adaptive coupling weights. Further, this method was extended to solve the consensus problem for nonlinear MAS whose nonlinearities satisfy one-side Lipschitz constraints in [20].

Time delays often appear in systems control and may bring instability to systems. Therefore, it is essential to

consider time delays in system control. Liu et al. [22] studied the consensus problem for nonlinear Lipschitz time-delay systems with input saturation. In [23], by applying a reduction method, the authors investigated the consensus problem for Lipschitz nonlinear MAS with input delays. Time delays also appear in communication between agents and pose a grave threat on consensus control, so many authors considered the consensus problem with communication delay (see, e.g., [24, 25]).

On the other hand, the incremental quadratic constraints ( $\delta$ QC) were first proposed in [26]. As stated in [27],  $\delta$ QC can be described by a set of multiplier matrices which we call incremental multiplier matrices ( $\delta$  MMs) in a particular form, and many other types of nonlinearities, such as Lipschitz, one-side Lipschitz, and incremental sector bound nonlinearities, can be rewritten in a unified form of  $\delta$ QC. Many references consider the control and observation problem for systems with nonlinearities satisfying  $\delta$ QC [26–32]. In [28], the authors proposed a secure chaotic communication scheme of chaotic systems which satisfy  $\delta$ QC. In [31], full-order and reduced-order observers for discrete-time systems whose nonlinearities satisfy  $\delta$ QC are designed. Adaptive state observers are designed for incremental quadratically nonlinear systems in [32]. However, to the best of our knowledge, we can hardly find any papers that investigate the consensus control for nonlinear MAS whose nonlinearities satisfy  $\delta$ QC.

In this paper, we aim to focus on investigating the consensus problem for nonlinear MAS whose nonlinearities satisfy  $\delta$ QC with time delays. Compared with the current literature, there are about two main contributions in this work. Firstly, we design a distributed consensus protocol for incremental quadratically nonlinear MAS, and the considered nonlinearities include many common nonlinearities as some special cases. In other words, our results generalize and unify quite a few consensus protocol-design problems for many nonlinear systems. Secondly, this paper considers the sabotage of time delays, and a delay-independent consensus condition is established for the proposed consensus protocol by employing Lyapunov–Krasovskii functional method. Moreover, an iterative algorithm was proposed to handle nonlinear terms in matrix inequalities by applying cone complement linearization (CCL) method. We transform the non-convex feasibility problem to some sequential optimization problem. Consequently, it can solve the proposed sufficient conditions via the linear matrix inequalities (LMI) method. Furthermore, the gain matrix and coupling weight can be computed through the proposed iterative algorithm.

The rest of this paper is organized as follows. Preliminaries are given in Section 2. The consensus problem for incremental quadratically nonlinear systems with time delays is investigated in Section 3. In Section 4, we provide a numerical example to illustrate the effectiveness of the developed results. Finally, Section 5 draws the conclusions.

In this paper, we use  $x \in \mathbb{R}^n$  representing a vector of  $n$  real elements.  $\mathbb{R}^{m \times n}$  denotes the set of all  $m$  by  $n$  real matrices.  $\langle \cdot, \cdot \rangle$  is the inner product in  $\mathbb{R}$ , i.e., given  $x, y \in \mathbb{R}^n$ ,

then  $\langle \cdot, \cdot \rangle = x^T y$ .  $\| \cdot \|$  denotes the Euclidean norm.  $E > 0$  means  $E$  is a symmetric positive definite matrix and  $E \geq 0$  denotes symmetric positive semidefinite matrix.  $E - F \geq 0$  represents that the matrix  $E - F$  is symmetric semipositive definite.  $I_n$  represents an identity matrix of dimension  $n$ .  $I$  is an identity matrix of any appropriate dimension.  $E \otimes F$  denotes the Kronecker product of matrices  $E$  and  $F$ . Minimize  $\text{Tr}(\sum_{i=1}^N A_i)$  represents the minimum trace for a set of matrices  $A_i$ . The notation  $*$  is used to denote the blocks induced by symmetry.

## 2. Preliminaries

In this paper, we consider an incremental quadratically nonlinear MAS with  $N$  agents represented as follows:

$$\begin{aligned} \dot{x}_i(t) &= Ax_i(t) + A_h x_i(t-h) + B\varphi(t, z_i(t)) + Fu_i(t), \\ z_i(t) &= Cx_i(t) + C_h x_i(t-h), \end{aligned} \quad (1)$$

with

$$x_i(t) = \eta_i(t), \quad \forall t \in [-h, 0], i = 1, 2, \dots, N, \quad (2)$$

where  $A \in \mathbb{R}^{n \times n}$ ,  $A_h \in \mathbb{R}^{n \times n}$ ,  $B \in \mathbb{R}^{n \times m}$ ,  $F \in \mathbb{R}^{n \times r}$  and  $C, C_h \in \mathbb{R}^{q \times n}$  are constant matrices.  $x_i(t) \in \mathbb{R}^n$  is the state vector and  $x_i(t-h) \in \mathbb{R}^n$  is the time-delay state.  $u_i \in \mathbb{R}^r$  is the control input or protocol. The scalar  $h > 0$  is the constant delay.  $\eta_i$  is the continuous initial condition. We put all the nonlinear time-varying terms into a vector-valued nonlinear function  $\varphi(t, z) \in \mathbb{R}^m$ .

Those agents exchange information via a network modeled by a communication graph  $\mathcal{G}$  with  $\mathcal{G} = (\mathcal{V}, \mathcal{E})$ .  $\mathcal{V} = \{1, \dots, N\}$  means the set of nodes, and  $\mathcal{E} \subset \mathcal{V} \times \mathcal{V}$  represents the set of edges. In this paper, nodes denote agents while edges represent communication links. The adjacency matrix of a graph  $\mathcal{G}$  is denoted by  $A = [a_{ij}]_{N \times N}$ , where  $N$  means the number of agents in this network and

$$a_{ij} = \begin{cases} 0, & \text{if } (v_i, v_j) \notin \mathcal{E}, \\ 0, & \forall i = j, \\ 1, & \text{if } (v_i, v_j) \in \mathcal{E}, \end{cases} \quad (3)$$

where  $a_{ij}$  denotes the connection between agents  $i$ th and  $j$ th of the network of all agents.  $a_{ij} = 0$  means there is no connection between agents  $i$ th and  $j$ th.  $a_{ij} = 1$  means connection between agents  $i$ th and  $j$ th exists. Given an undirected communication graph, we have  $a_{ij} = a_{ji}$ . The Laplacian matrix  $\mathcal{L}$  for MAS is defined as follows:

$$\mathcal{L} = [\mathcal{L}_{ij}]_{N \times N}, \quad (4)$$

where

$$\mathcal{L}_{ij} = \begin{cases} \sum_{j=1, i \neq j}^N a_{ij}, & \forall i = j, \\ -a_{ij}, & \forall i \neq j. \end{cases} \quad (5)$$

In this paper, we consider a distributed consensus protocol based on the states feedback of neighboring agents (see [19]):

$$u_i(t) = cK \sum_{j=1}^N a_{ij} (x_i(t) - x_j(t)), \quad (6)$$

where  $c > 0$  is the coupling weight between neighboring agents,  $K \in \mathbb{R}^{p \times n}$  is the feedback gain matrix and that will be computed later.

**Lemma 1** (see [33]). *The network  $\mathcal{G}$  has a spanning tree that connects any two agents in the MAS if and only if Laplacian matrix  $\mathcal{L}$  of  $\mathcal{G}$  has a simple zero eigenvalue and all the other eigenvalues have positive real parts.*

**Lemma 2** (see [34]). *For any given symmetric matrix  $R \in \mathbb{R}^{n \times n}$  with the form  $R = \begin{bmatrix} R_{11} & R_{12} \\ R_{12}^T & R_{22} \end{bmatrix}$  where  $R_{11} \in \mathbb{R}^{r \times r}$ ,  $R_{12} \in \mathbb{R}^{r \times (n-r)}$ , and  $R_{22} \in \mathbb{R}^{(n-r) \times (n-r)}$ , then the following three conditions are equal:*

$$\begin{aligned} 1: & R < 0, \\ 2: & R_{11} < 0, R_{22} - R_{12}^T R_{11}^{-1} R_{12} < 0, \\ 3: & R_{22} < 0, R_{11} - R_{12} R_{22}^{-1} R_{12}^T < 0. \end{aligned} \quad (7)$$

**Definition 1** (see [30]). A symmetric matrix  $M \in \mathbb{R}^{(q+m) \times (q+m)}$  is an incremental multiplier matrix ( $\delta$ MM) for vector-valued function  $\varphi(t, z(t))$  if it satisfies the following incremental quadratic constraints ( $\delta$ QC):

$$\begin{bmatrix} \delta z \\ \delta \varphi \end{bmatrix}^T M \begin{bmatrix} \delta z \\ \delta \varphi \end{bmatrix} \geq 0, \quad (8)$$

for all  $z_1(t), z_2(t) \in \mathbb{R}^q$  and all  $\varphi(t, z_1(t)), \varphi(t, z_2(t)) \in \mathbb{R}^m$ , where  $M = \begin{bmatrix} M_{11} & M_{12} \\ M_{12}^T & M_{22} \end{bmatrix}$ , in which  $M_{11} = M_{11}^T \in \mathbb{R}^{q \times q}$  and  $M_{22} = M_{22}^T \in \mathbb{R}^{m \times m}$ , and  $\delta z = z_1(t) - z_2(t)$  and  $\delta \varphi = \varphi(t, z_1(t)) - \varphi(t, z_2(t))$ .

In this paper, we consider a vector-valued nonlinear function  $\varphi$ , which can be described in the form of  $\delta$ QC characterized by a set of symmetric matrices. Actually,  $\delta$ QC include many common nonlinearities as some special cases, such as the sector constraint, slope-restricted, Lipschitz, and one-side Lipschitz nonlinearities. We refer the interested readers to [26–32] for more details. Some nonlinearities satisfying  $\delta$ QC will be listed.

**Remark 1.** If  $\varphi$  is globally Lipschitz nonlinearity for  $z$  (see, e.g., [31]), there is a positive constant  $L_g > 0$  for any  $z_1, z_2 \in \mathbb{R}^q$  such that

$$\|\delta \varphi\| \leq L_g \|\delta z\|, \quad (9)$$

which is equivalent to (where  $q = m$ )

$$L_g^2 \delta z^T \delta z - \delta \varphi^T \delta \varphi \geq 0. \quad (10)$$

Therefore, inequality (8) is satisfied by choosing

$$M = \nu \begin{bmatrix} L_g^2 I_q & 0 \\ 0 & -I_m \end{bmatrix}, \quad (11)$$

with  $\nu > 0$ .

**Remark 2.** If  $\varphi$  satisfies quadratically inner bounded constraints with respect to  $z$  (see, e.g., [31]), there exist some scalars  $\alpha_2, \alpha_3 \in \mathbb{R}$  such that (where  $q = m$ )

$$\|\delta \varphi\|^2 \leq \alpha_2 \|z\|^2 + \alpha_3 \langle \delta \varphi, \delta z \rangle. \quad (12)$$

The incremental multiplier matrix can be chosen as follows:

$$M = \nu \begin{bmatrix} \alpha_2 I_q & \frac{\alpha_3}{2} I_q \\ \frac{\alpha_3}{2} I_q & -I_q \end{bmatrix}, \quad (13)$$

with  $\nu > 0$ .

It is worth mentioning that as shown in [26, 27], by properly selecting the incremental multiplier matrix, most of the nonlinearities can be rewritten in the form of (8). So the nonlinearities considered in this paper are more common than other nonlinearities considered in recent literature studies.

**Assumption 1.** All the nonlinear agents as described by (1) communicate with each other through a strongly connected graph  $\mathcal{G}$ .

**Assumption 2.** The nonlinear vector-valued functions  $\varphi$  in (1) satisfies  $\delta$ QC as defined in Definition 1 with a known incremental multiplier matrix  $M \in \mathbb{M}$ .

**Remark 3.** For MAS described by (1), we can have the following condition from Assumption 2:

$$\begin{bmatrix} \bar{z}(t) \\ \bar{\varphi}(t, z(t)) \end{bmatrix}^T \bar{M} \begin{bmatrix} \bar{z}(t) \\ \bar{\varphi}(t, z(t)) \end{bmatrix} \geq 0, \quad (14)$$

where

$$\begin{aligned} \bar{z}^T(t) &= [(z_1(t) - z^*)^T, (z_2(t) - z^*)^T, \dots, (z_3(t) - z^*)^T], \\ \bar{\varphi}(t, z(t)) &= [(\varphi(t, z_1(t)) - \varphi(t, z^*))^T, \dots, \\ & \quad (\varphi(t, z_N(t)) - \varphi(t, z^*))^T]^T, \\ M &= \begin{bmatrix} M_{11} & M_{12} \\ M_{12}^T & M_{22} \end{bmatrix}, \\ \bar{M} &= \begin{bmatrix} I_N \otimes M_{11} & I_N \otimes M_{12} \\ I_N \otimes M_{12}^T & I_N \otimes M_{22} \end{bmatrix}. \end{aligned} \quad (15)$$

### 3. Main Results

The consensus problem under Assumptions 1 and 2 for the nonlinear MAS (1) with a constant time delay is investigated in the following section.

**Theorem 1.** Consider the MAS described in (1) satisfying Assumptions 1 and 2 with a given incremental multiplier matrix  $M$ . Suppose that there exist matrices  $P > 0, Q > 0$  and scalars  $\alpha > 0, \tau > 0$  such that the following matrix inequality is satisfied:

$$\begin{bmatrix} \bar{\Phi}_{11} & A_h & B \\ * & -Q & 0 \\ * & * & 0 \end{bmatrix} + \alpha \Psi \Psi^T M \Psi < 0, \quad (16)$$

where

$$\begin{aligned} \bar{\Phi}_{11} &= AP + PA^T + PQP - \tau FF^T, \\ \Psi &= \begin{bmatrix} C & C_h & 0 \\ 0 & 0 & I \end{bmatrix}, \\ \psi &= \text{diag}(P, I_N, I_N). \end{aligned} \quad (17)$$

Then, the consensus control protocol given by (6) can asymptotically solve the consensus problem for MAS (1) with the feedback control gain  $K = -F^T P^{-1}$  and the coupling weight  $c \geq \tau/2 \partial(L)$ , where  $\partial(L)$  represents the minimum nonzero eigenvalue of the graph  $\mathcal{G}$ .

*Proof.* Letting  $e_i(t) = x_i(t) - (1/N) \sum_{j=1}^N x_j(t)$ , it follows that  $e_i(t)$  and  $z_i(t)$  satisfy the following dynamics:

$$\begin{aligned} \dot{e}_i(t) &= Ae_i(t) + A_h e_i(t-h) + B\varphi(t, z_i(t)) \\ &\quad - \frac{1}{N} \sum_{j=1}^N B\varphi(t, z_j(t)) \\ &\quad + \sum_{j=1}^N ca_{ij} FK(e_i(t) - e_j(t)), \end{aligned}$$

$$z_i(t) - \frac{1}{N} \sum_{j=1}^N z_j(t) = Ce_i(t) + C_h e_i(t-h),$$

$$i = 1, 2, \dots, N.$$

(18)

Firstly, we consider the following Lyapunov function candidate:

$$\begin{aligned} V(t) &= \sum_{i=1}^N e_i^T(t) P^{-1} e_i(t) \\ &\quad + \sum_{i=1}^N \int_{t-h}^t e_i(\alpha)^T Q e_i(\alpha) d\alpha, \end{aligned} \quad (19)$$

where  $P > 0, Q > 0$  and  $P, Q \in \mathbb{R}^{n \times n}$ .

The time derivative of  $V(t)$  along the trajectory of the consensus error dynamic system in (18) is given by

$$\begin{aligned} \dot{V}(t) &= 2 \sum_{i=1}^N e_i(t)^T P^{-1} (Ae_i(t) + A_h e_i(t-h)) \\ &\quad + 2 \sum_{i=1}^N e_i(t)^T P^{-1} B \left( \varphi(t, z_i(t)) - \frac{1}{N} \sum_{j=1}^N \varphi(t, z_j(t)) \right) \\ &\quad + 2 \sum_{i=1}^N e_i(t)^T P^{-1} FK \sum_{j=1}^N ca_{ij} (e_i(t) - e_j(t)) \\ &\quad + \sum_{i=1}^N (e_i(t)^T Q e_i(t) - e_i(t-h)^T Q e_i(t-h)). \end{aligned} \quad (20)$$

Noticing that  $\sum_{i=1}^N e_i^T(t) = 0$ , so one can have

$$\sum_{i=1}^N e_i(t)^T P^{-1} B \left( \varphi(t, z^*) - \frac{1}{N} \sum_{j=1}^N \varphi(t, z_j(t)) \right) = 0. \quad (21)$$

Then, relative terms in (20) satisfy

$$\begin{aligned} &2 \sum_{i=1}^N e_i(t)^T P^{-1} B \left( \varphi(t, z_i(t)) - \frac{1}{N} \sum_{j=1}^N \varphi(t, z_j(t)) \right) \\ &= 2 \sum_{i=1}^N e(t)^T P^{-1} B (\varphi(t, z_i(t)) - \varphi(t, z^*)). \end{aligned} \quad (22)$$

Let  $e(t) = [e_1^T(t), e_2^T(t), \dots, e_N^T(t)]^T$  and  $e(t-h) = [e_1^T(t-h), e_2^T(t-h), \dots, e_N^T(t-h)]^T$ .

Then, the following inequality is derived by (20) with  $K = -F^T P^{-1}$ :

$$\begin{aligned} \dot{V}(t) &= e^T(t) (I_N \otimes (P^{-1}A + A^T P^{-1})) e(t) \\ &\quad + e^T(t) (I_N \otimes 2P^{-1}A_h) e(t-h) \\ &\quad - e^T(t) (2c\mathcal{L} \otimes P^{-1}FF^T P^{-1}) e(t) \\ &\quad + e^T(t) (I_N \otimes 2P^{-1}B) \bar{\varphi}(t, z(t)) \\ &\quad + e^T(t) (I_N \otimes Q) e(t) - e^T(t-h) (I_N \otimes Q) e(t-h), \end{aligned} \quad (23)$$

where  $\bar{\varphi}(t, z(t)) = [(\varphi(t, z_1(t)) - \varphi(t, z^*))^T, \dots, (\varphi(t, z_N(t)) - \varphi(t, z^*))^T]^T$ .

Let  $\Omega^T \mathcal{L} \Omega = \Lambda$  and  $\Lambda = \text{diag}(0, \lambda_2, \dots, \lambda_i, \dots, \lambda_N)$ , where  $\Omega$  is an unitary matrix satisfying  $\Omega^{-1} = \Omega^T$  and  $\lambda_i$  denotes the positive eigenvalues of the Laplacian matrix  $\mathcal{L}$ . By substituting  $\mathcal{L} = \Omega \Lambda \Omega^T$ ,  $\tilde{\xi} = I \otimes (\Omega^T \otimes I_n) \xi$ , and  $\xi = [ce^T(t) \ e^T(t-h) \ (\bar{\varphi}(t, z(t)))^T]^T$ , one can have

$$\begin{aligned} &- e^T(t) (2c\mathcal{L} \otimes P^{-1}FF^T P^{-1}) e(t) \\ &= - \sum_{i=1}^N \tilde{e}_i^T(t) 2c\lambda_i P^{-1} FF^T P^{-1} \tilde{e}_i(t). \end{aligned} \quad (24)$$

Notice that

$$\begin{aligned}
& - \sum_{i=1}^N \tilde{e}_i^T(t) 2c\lambda_i P^{-1} F F^T P^{-1} \tilde{e}_i(t) \\
& \leq -\tilde{e}^T(t) (I_N \otimes 2\partial(L)cP^{-1} F F^T P^{-1}) \tilde{e}(t).
\end{aligned} \tag{25}$$

Then, we choose the coupling weight  $c$  such that  $2\partial(L)c \geq \tau$ , which implicates

$$\begin{aligned}
& -\tilde{e}^T(t) (I_N \otimes 2\partial(L)cP^{-1} F F^T P^{-1}) \tilde{e}(t) \\
& \leq -\tilde{e}^T(t) (I_N \otimes \tau P^{-1} F F^T P^{-1}) \tilde{e}(t).
\end{aligned} \tag{26}$$

So (23) can be written into a compact form as follows:

$$\dot{V}(t) = \tilde{\xi}^T \Phi \tilde{\xi}, \tag{27}$$

where

$$\Phi = \begin{bmatrix} \Phi_{11} & I_N \otimes P^{-1} A_h & I_N \otimes P^{-1} B \\ * & I_N \otimes -Q & 0 \\ * & * & 0 \end{bmatrix}, \tag{28}$$

$$\Phi_{11} = I_N \otimes (P^{-1} A + A P^{-1} + Q - \tau P^{-1} F F^T P^{-1}).$$

Secondly, we have the following equality from (1):

$$\begin{bmatrix} \bar{z}(t) \\ \bar{\varphi}(t, z(t)) \end{bmatrix} = \bar{\Psi} \xi, \tag{29}$$

where

$$\bar{\Psi} = \begin{bmatrix} I_N \otimes C & I_N \otimes C_h & 0 \\ 0 & 0 & I \end{bmatrix}. \tag{30}$$

Substituting (29) into (14) yields

$$\xi^T \bar{\Psi}^T \bar{M} \bar{\Psi} \xi \geq 0. \tag{31}$$

The nonlinear  $\varphi(t, z_i(t))$  satisfies Definition 1 with a symmetric matrix  $M$ , so we can define a set of incremental multiplier matrices by  $\bar{M}_\Omega = \{\alpha \bar{M}; \alpha > 0\}$ , where  $\bar{M}_\Omega \in M$ . Now by substituting  $\bar{M}$  with  $\alpha \bar{M}$  in (31) and applying  $\tilde{\xi} = I \otimes (\Omega^T \otimes I_n) \xi$ , (31) can be further expressed as follows:

$$\tilde{\xi}^T \bar{\Psi}^T \alpha \bar{M} \bar{\Psi} \tilde{\xi} \geq 0. \tag{32}$$

Adding the terms on the left side of (31) to the right side of (27) yields

$$\dot{V}(t) \leq \tilde{\xi}^T \left( \Phi + \bar{\Psi}^T \alpha \bar{M} \bar{\Psi} \right) \tilde{\xi}. \tag{33}$$

If  $\dot{V}(t) < 0$ , the synchronization error  $e$  will converge to the origin according to the Lyapunov stability theory. Therefore, we need to verify that

$$\Phi + \bar{\Psi}^T \alpha \bar{M} \bar{\Psi} < 0. \tag{34}$$

By utilizing the Kronecker product, it can be validated that the inequality (34) is equivalent to

$$I_N \otimes \left( \begin{bmatrix} \Phi_{11} & P^{-1} A_h & P^{-1} B \\ * & -Q & 0 \\ * & * & 0 \end{bmatrix} + \Psi^T \alpha M \Psi \right) < 0, \tag{35}$$

where  $\Psi$  is defined in Theorem 1.

Since  $I_N > 0$ , the condition (35) holds if and only if

$$\begin{bmatrix} \tilde{\Phi}_{11} & P^{-1} A_h & P^{-1} B \\ * & -Q & 0 \\ * & * & 0 \end{bmatrix} + \Psi^T \alpha M \Psi < 0, \tag{36}$$

where

$$\tilde{\Phi}_{11} = P^{-1} A + A P^{-1} + Q - \tau P^{-1} F F^T P^{-1}. \tag{37}$$

Then multiply both the left and right sides of the matrix in (36) by a reversible matrix  $\psi = \text{diag}(P, I_N, I_N)$  for a similar transformation, and we have condition (16). If condition (16) holds, then  $\dot{V}(t) < 0$ . Hence, the consensus error dynamic system (18) is asymptotically stable, and the consensus error  $e \rightarrow 0$  as  $t \rightarrow \infty$ . Therefore, the considered MAS can reach consensus. This completes the proof of Theorem 1.  $\square$

*Remark 4.* Theorem 1 offers a sufficient condition that the nonlinear time-delay MAS can reach consensus. Then, we need to find a solution to the constraint in Theorem 1 to retrieve the consensus control gain matrix  $K$  and the coupling weight  $c$ .

After partitioning  $M$  in the form of (8) and applying the Schur complement lemma to (16), the inequality (16) is equivalent to

$$\begin{bmatrix} AP + PA^T - \tau FF^T + \alpha PC^T M_{11} CP & A_h + \alpha PC^T M_{11} C_h & B + \alpha PC^T M_{12} & P \\ * & -Q + \alpha C_h^T M_{11} C_h & \alpha C_h^T M_{12} & 0 \\ * & * & \alpha M_{22} & 0 \\ * & * & * & -Q^{-1} \end{bmatrix} < 0. \tag{38}$$

It should be noted that inequality (38) is not linear with the variables  $P$  and  $Q$  so we cannot directly utilize a convex optimization algorithm to find a solution. Therefore, in order to complete the design of the consensus control law in this paper, we can transform the nonlinear constraints into

corresponding convex optimization problems subject to LMI constraints. A general treatment to (38) is to employ the cone complementary linearization [20, 35–37]. On the other hand, a necessary condition for the feasibility of (38) is  $M_{22} < 0$  obviously. Further, when  $M_{11} > 0$ ,  $M_{11} = 0$  or

$C^T M_{11} C < 0$ , the matrix inequality (38) can be transformed to different sequential corresponding convex optimization problems subject to LMI constraints, respectively, which deserve further concrete discussions.

Based on the above discussions, we have the following corollaries to Theorem 1.

**Corollary 1.** Consider the MAS described in (1) satisfying Assumptions 1 and 2 and the given incremental multiplier  $M$  satisfying  $M_{22} < 0$  and  $M_{11} = 0$ . Suppose that there exist matrices  $P > 0, W > 0, \tilde{W} > 0, Q > 0, \tilde{Q} > 0$  and scalars  $\alpha > 0, \tau > 0$  such that the following matrix inequalities are satisfied:

$$\begin{bmatrix} AP + PA^T - \tau FF^T & A_h & (B + \alpha PC^T M_{12}) & P \\ * & -Q & \alpha C_h^T M_{12} & 0 \\ * & * & \alpha M_{22} & 0 \\ * & * & * & -W \end{bmatrix} < 0, \quad (39)$$

$$\begin{bmatrix} \tilde{W} & I \\ * & \tilde{Q} \end{bmatrix} \geq 0, \quad (40)$$

$$\begin{aligned} \tilde{W}W &= I, \\ \tilde{Q}Q &= I. \end{aligned} \quad (41)$$

Then, the consensus control protocol given by (6) can asymptotically solve the consensus problem for MAS given by (1) with the feedback control gain  $K = -F^T P^{-1}$  and the coupling weight  $c \geq \tau/2 \partial(L)$ , where  $\partial(L)$  represents the minimum nonzero eigenvalue of the graph  $\mathcal{G}$ .

*Proof.* Firstly, (38) turns into the following with  $M_{11} = 0$ :

$$\begin{bmatrix} AP + PA^T - \tau FF^T & A_h & (B + \alpha PC^T M_{12}) & P \\ * & -Q & \alpha C_h^T M_{12} & 0 \\ * & * & \alpha M_{22} & 0 \\ * & * & * & -Q^{-1} \end{bmatrix} < 0. \quad (42)$$

Secondly, we here introduce a new matrix variable  $W > 0$  and make sure that

$$Q^{-1} \geq W. \quad (43)$$

Note that (43) is equivalent to

$$\begin{bmatrix} \tilde{W} & I \\ * & \tilde{Q} \end{bmatrix} \geq 0, \quad (44)$$

where  $\tilde{W} = W, \tilde{Q} = Q^{-1}$ . Then, we replace  $Q^{-1}$  with  $W$  in (42) and have (39). If (39)–(41) hold, (42) is satisfied. This completes the proof of Corollary 1.  $\square$

Similarly, we have the following two corollaries when  $M_{11} > 0$  and  $C^T M_{11} C < 0$ , respectively. We omit proofs here.

**Corollary 2.** Consider the MAS described in (1) satisfying Assumptions 1 and 2 and the given incremental multiplier  $M$  satisfying  $M_{22} < 0$  and  $M_{11} > 0$ . Suppose that there exist matrices  $P > 0, Q > 0, \tilde{Q} > 0, W > 0, \tilde{W} > 0$ , and scalars  $\alpha > 0, \tau > 0$ , such that the following inequalities are satisfied:

$$\begin{bmatrix} AP + PA^T - \tau FF^T & (A_h + \alpha PC^T M_{11} C)_h & (B + \alpha PC^T M_{12}) & P & \sqrt{\alpha} PC^T M_{11} \\ * & (-Q + \alpha C_h^T M_{11} C)_h & \alpha C_h^T M_{12} & 0 & 0 \\ * & * & \alpha M_{22} & 0 & 0 \\ * & * & * & -W & 0 \\ * & * & * & * & -M_{11} \end{bmatrix} < 0. \quad (45)$$

$$\begin{bmatrix} \tilde{W} & I \\ * & \tilde{Q} \end{bmatrix} \geq 0,$$

$$\begin{aligned} \tilde{W}W &= I, \\ \tilde{Q}Q &= I. \end{aligned} \quad (46)$$

Then, the consensus control protocol given by (6) can asymptotically solve the consensus problem for MAS given by (1) with the feedback control gain  $K = -F^T P^{-1}$  and the coupling weight  $c \geq \tau/2 \partial(L)$ , where  $\partial(L)$  represents the minimum nonzero eigenvalue of the graph  $\mathcal{G}$ .

**Corollary 3.** Consider the MAS described in (1) satisfying Assumptions 1 and 2 and the given incremental multiplier  $M$  satisfying  $M_{22} < 0$  and  $C^T M_{11} C < 0$ . Suppose that there exist matrices  $P > 0, Q > 0, W_1 > 0, W_2 > 0, \tilde{P} > 0, \tilde{Q} > 0, \tilde{W}_1 > 0$ ,

$\tilde{W}_2 > 0$ , and scalars  $\alpha > 0, \tau > 0$ , such that the following inequalities are satisfied:

$$\begin{aligned} & \begin{bmatrix} AP + PA^T - \tau FF^T - \alpha W_2 & (A_h + \alpha PC^T M_{11} C_h) & (B + \alpha PC^T M_{12}) & P \\ * & (-Q + \alpha C_h^T M_{11} C_h) & \alpha C_h^T M_{12} & 0 \\ * & * & \alpha M_{22} & 0 \\ * & * & * & -W_1 \end{bmatrix} < 0, \\ & \begin{bmatrix} \tilde{W}_1 & I \\ * & \tilde{Q} \end{bmatrix} \geq 0, \\ & \begin{bmatrix} -C^T M_{11} C & \tilde{P} \\ * & \tilde{W}_2 \end{bmatrix} \geq 0, \\ & \tilde{W}_1 W_1 = I, \\ & \tilde{W}_2 W_2 = I, \\ & \tilde{Q} Q = I, \\ & \tilde{P} P = I. \end{aligned} \quad (47)$$

Then, the consensus control protocol given by (6) can asymptotically solve the consensus problem for MAS given by (1) with the feedback control gain  $K = -F^T P^{-1}$  and the coupling weight  $c \geq \tau/2 \partial(L)$ , where  $\partial(L)$  represents the minimum nonzero eigenvalue of the graph  $\mathcal{G}$ .

As mentioned in [20, 35, 36], we can deal with the original feasibility problem in Corollary 1 by solving the following optimization with variables  $\tilde{W}, W, P, Q$ , and  $\tilde{Q}$ :

$$\begin{cases} \min \text{Trace} & (\tilde{W}W + \tilde{Q}Q) \\ \text{subject to} & \begin{bmatrix} \tilde{W} & I \\ * & W \end{bmatrix} \geq 0, \begin{bmatrix} \tilde{Q} & I \\ * & Q \end{bmatrix} \geq 0 \\ & \text{and inequalities (39), (40).} \end{cases} \quad (48)$$

In (48), equalities (46) are transformed into inequalities  $\begin{bmatrix} \tilde{W} & I \\ * & W \end{bmatrix} \geq 0, \begin{bmatrix} \tilde{Q} & I \\ * & Q \end{bmatrix} \geq 0$ . It ensures that we can attain  $\tilde{W} = W^{-1}$  and  $\tilde{Q} = Q^{-1}$  with the required accuracy. The specific algorithm is given in Algorithm 1.

The original feasibility problem in Corollary 2 can be tackled by solving the following optimization subject to LMI constraints with variables  $\tilde{W}, W, P, Q$ , and  $\tilde{Q}$ :

$$\begin{cases} \min \text{Trace} & (\tilde{W}W + \tilde{Q}Q) \\ \text{subject to} & \begin{bmatrix} \tilde{W} & I \\ * & W \end{bmatrix} \geq 0, \begin{bmatrix} \tilde{Q} & I \\ * & Q \end{bmatrix} \geq 0 \\ & \text{and inequalities (45).} \end{cases} \quad (49)$$

The original feasibility problem in Corollary 3 can be tackled by solving the following optimization subject to

LMI constraints with variables  $\tilde{W}_1, W_1, \tilde{W}_2, W_2, \tilde{P}, P, Q$ , and  $\tilde{Q}$ :

$$\begin{cases} \min \text{Trace} & (\tilde{W}_1 W_1 + \tilde{W}_2 W_2 + \tilde{P} P + \tilde{Q} Q) \\ \text{subject to} & \begin{bmatrix} \tilde{W}_1 & I \\ * & W_1 \end{bmatrix} \geq 0, \begin{bmatrix} \tilde{W}_2 & I \\ * & W_2 \end{bmatrix} \geq 0 \\ & \begin{bmatrix} \tilde{Q} & I \\ * & Q \end{bmatrix} \geq 0, \begin{bmatrix} \tilde{P} & I \\ * & P \end{bmatrix} \geq 0 \\ & \text{and inequalities (47).} \end{cases} \quad (50)$$

*Remark 5.* It is worth mentioning that during the derivation process in the proof of Theorem 1, we introduced a positive scalar  $\tau$  that  $2\partial(\mathcal{L})c \geq \tau$ , where  $\partial(\mathcal{L})$  represents the minimum nonzero eigenvalue of the graph  $G$ . Hence, we need to find a positive  $\tau$  to choose  $c$ . In our results,  $\tau > 0$  needs to be chosen such that the inequality in Theorem 1 is satisfied. In fact,  $\tau$  needs to be adjusted few times to find a feasible solution in Algorithm 1. Once the inequality in Theorem 1 is satisfied with a positive  $\tau$ , then we can select the coupling weight  $c$  as long as it satisfies  $2\partial(\mathcal{L})c \geq \tau$ , which will be exemplified in the simulation part.

*Remark 6.* The inequalities in corollaries can be solved by applying CCL algorithm and LMI-tools. After using LMI-tools of MATLAB, we can find a feasible solution to the constraints in (48) with respect to variables  $\tilde{W}, W, P, Q$ , and  $\tilde{Q}$ . Those constraints ensure  $\tilde{Q}$  and  $\tilde{W}$  are the inverses of  $Q$  and  $W$ , respectively. We can attain the variables with the required accuracy from a freedom in



- (1) Choose proper scalars  $\tau > 0$  and  $\alpha > 0$  to guarantee a feasible solution to the inequalities in (48).
- (2) Find a feasible set  $\bar{W}_0, W_0, \bar{Q}_0, Q_0, P_0$  so that inequalities in (48) can be satisfied. Adjust scalars  $\tau$  and  $\alpha$  and try again when feasible solutions cannot be found. Then, set  $k = 0$ .
- (3) Solve the following minimization optimization problem with respect to variables  $\bar{W}, W, P, Q$ , and  $\bar{Q}$ .  $\min \text{Trace}(W_k \bar{W} + W \bar{W}_k + \bar{Q}_k Q + \bar{Q} Q_k)$ , subject to inequalities in (48). Find the new optimization solution  $\bar{W}, W, P, Q, \bar{Q}$ , then set  $\bar{W}_{k+1} = \bar{W}, W_{k+1} = W, \bar{Q}_{k+1} = \bar{Q}, Q_{k+1} = Q, P_{k+1} = P$ .
- (4) If the inequality (42) is satisfied with the matrices  $Q, P$  obtained in Step 3, then we can choose coupling weight  $c$  according to  $2 \partial(\mathcal{L})c \geq \tau$  and obtain the control gain matrix  $K$  by  $K = -F^T P^{-1}$ . Stop when inequality (42) is still not feasible after a certain number of iterations. Then, set  $k = k + 1$  and go to Step 3.

ALGORITHM 1: The constraints in Corollary 1 can be tackled by solving (48) through the following iterative algorithm.

minimization. After verifying conditions in Corollary 1 are satisfied, we can design the gain matrix via  $K = -F^T P^{-1}$  and the coupling weight  $c$  to complete the consensus control law design. The interested readers refer to [35–37] for more details about CCL algorithm. By making appropriate modifications to Algorithm 1, we can easily derive algorithms for Corollary 2 and Corollary 3.

*Remark 7.*  $\delta$ QC include many common nonlinearities as some special cases. In the sense,  $\delta$ QC can be employed for more general scenarios. Therefore, the results in this paper have wider application scenarios compared with the existing references ([20, 21], etc.).

#### 4. Simulation Example

In this section, we provide a numerical simulation to illustrate the effectiveness of the proposed consensus control protocol. For simplicity, we only simulate Corollary 1. Consider a network of mobile agents. Each agent with nonlinear dynamics remains the same as in (1) with the following parameters (from [38]):

$$\begin{aligned}
 A &= \begin{bmatrix} -2 & 0 \\ 0 & -0.9 \end{bmatrix}, \\
 A_h &= \begin{bmatrix} -1 & 0 \\ -1 & -1 \end{bmatrix}, \\
 B &= \begin{bmatrix} 0.2 & 0.7 \\ 0.3 & 0.4 \end{bmatrix}, \\
 F &= [1 \ 1]^T, \\
 C &= [0.6 \ 0.8], \\
 C_h &= [0.5 \ 0.9],
 \end{aligned} \tag{51}$$

$$\varphi(t, z) = 0.5[0.5(1 + \sin t)0.5(1 - \sin t)]^T * z,$$

where  $\varphi$  is a nonlinear function since  $t$  is changeable.  $z$  contains the time-delay term  $C_h x(t - h)$ , and  $h = 4$  in this simulation.  $\varphi(t, z)$  and  $z$  satisfy  $\delta$ QC with an incremental multiplier matrix [38]:

$$M = \begin{bmatrix} 0 & 0.5 & 0.5 \\ 0.5 & -1 & 0 \\ 0.5 & 0 & -1 \end{bmatrix}. \tag{52}$$

Those agents exchange information under a connection graph as shown in Figure 1. Thus, we can obtain the following Laplacian matrix, the communication matrix between agents:

$$\mathcal{L} = \begin{bmatrix} 2 & -1 & 0 & 0 & 0 & -1 & 0 & 0 \\ -1 & 3 & -1 & -1 & 0 & 0 & 0 & 0 \\ 0 & -1 & 3 & -1 & 0 & -1 & 0 & 0 \\ 0 & -1 & -1 & 4 & -1 & 0 & 0 & -1 \\ 0 & 0 & 0 & -1 & 2 & 0 & -1 & 0 \\ -1 & 0 & -1 & 0 & 0 & 2 & 0 & 0 \\ 0 & 0 & 0 & 0 & -1 & 0 & 2 & -1 \\ 0 & 0 & 0 & -1 & 0 & 0 & -1 & 2 \end{bmatrix}. \tag{53}$$

The minimum nonzero eigenvalue of the graph  $G\partial(\mathcal{L}) = 0.29$ . Let  $\tau = 2.3$  and  $\alpha = 0.2$ . By applying Algorithm 1 with the LMI toolbox of MATLAB, we can find a feasible solution to (42) with

$$\begin{aligned}
 P &= \begin{bmatrix} 2.9926 & -0.6004 \\ -0.6004 & 5.2398 \end{bmatrix}, \\
 Q &= \begin{bmatrix} 13.2397 & 0.0000 \\ 0.0000 & 13.2397 \end{bmatrix}.
 \end{aligned} \tag{54}$$

We choose  $c = 4$  here for  $2 \partial(\mathcal{L})c \geq \tau$ . The feedback control gain matrix  $K = -F^T P^{-1} = [-0.3812 \ -0.2345]$ . Now we have completed the consensus control protocol design.

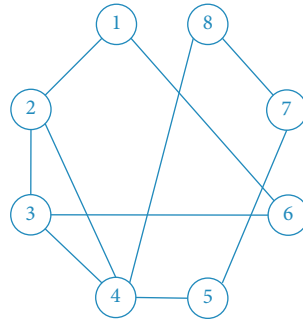


FIGURE 1: Communication topology of MAS in (1).

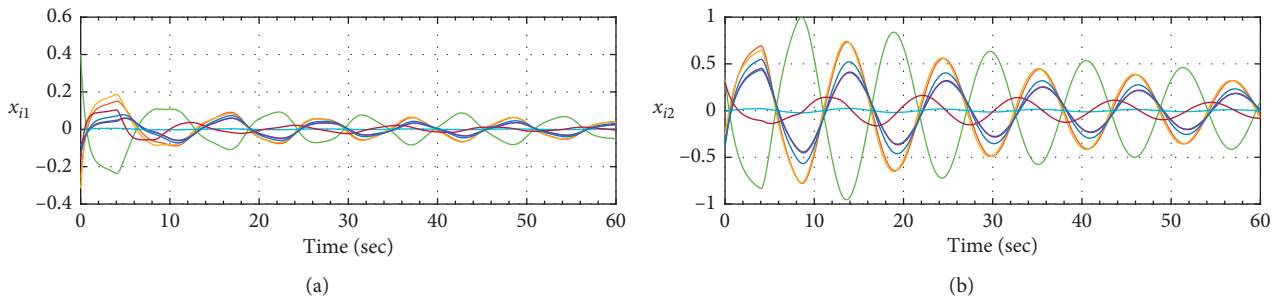


FIGURE 2: The state for agents 1, 2, ..., 8 without consensus control.

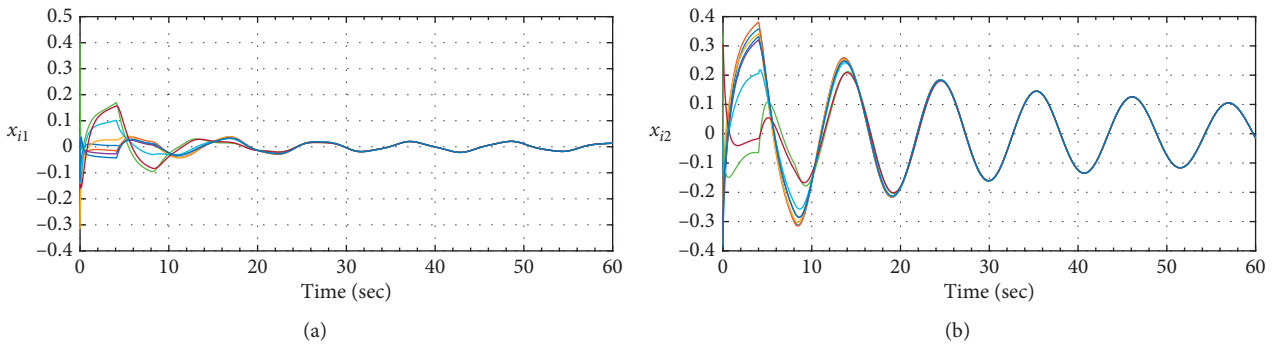


FIGURE 3: The state for agents 1, 2, ..., 8 under consensus control.

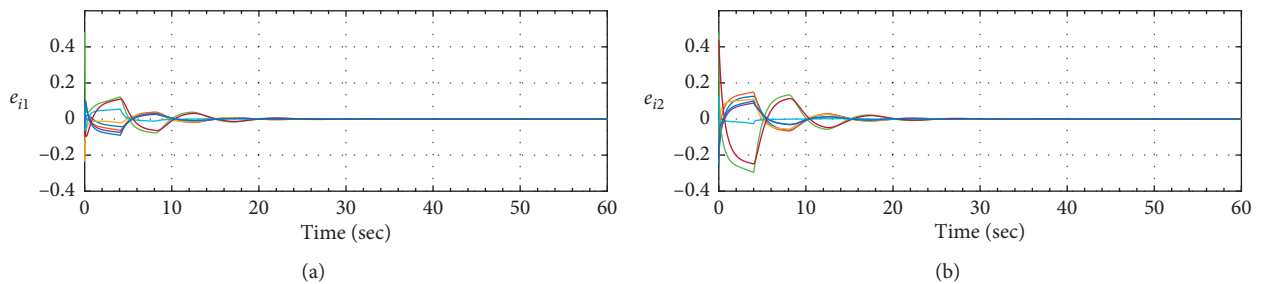


FIGURE 4: The consensus error for agents 1, 2, ..., 8 under consensus control.

As we can see in Figure 2, the nonlinear time-delay MAS did not reach consensus without the consensus control law. The state trajectories are shown in Figure 3. We can see that all agents reach consensus after applying

the designed consensus law. All the corresponding states of each agent change synchronously over time. In Figure 4, the state errors of each agent converged to the origin for about 20 seconds. This demonstrated the effectiveness

of the proposed consensus control law design method in this paper.

## 5. Conclusion

The consensus control problem has been investigated for the nonlinear time-delay MAS whose nonlinearities satisfy  $\delta$ QC under an undirected communication graph. A distributed consensus control protocol-design criterion was proposed for nonlinear MAS. We have considered a more general class of nonlinearities which satisfy  $\delta$ QC. By utilizing graph theory and Lyapunov theory, we analyzed the consensus error dynamic stability of the proposed control law. Then, sufficient conditions have been deduced as the form of matrix inequalities to solve the consensus problem for the considered MAS. In order to cope with the nonlinear terms, we transformed the nonlinear constraints into some optimization problems subject to LMI constraints and proposed iterative algorithms by resorting to the Schur complement lemma and the CCL method. Then, the gain matrix and the coupling weight in the protocol can be easily computed to complete our consensus control law design. A numerical example is provided to illustrate the effectiveness of the developed results.

## Data Availability

The data used to support the findings of this study are available from the corresponding author upon request.

## Conflicts of Interest

The authors declare that they have no conflicts of interest.

## Acknowledgments

This work was supported by the National Natural Science Foundation (NNSF) of China under Grant 51505273.

## References

- [1] J. Zhou, C. Sang, X. Li, M. Fang, and Z. Wang, "Consensus for nonlinear stochastic multi-agent systems with time delay," *Applied Mathematics and Computation*, vol. 325, pp. 41–58, 2018.
- [2] X. L. Wang and H. Su, "Completely model-free RL-based consensus of continuous-time multi-agent systems," *Applied Mathematics and Computation*, vol. 382, Article ID 125312, 2020.
- [3] X. Wang, H. Su, M. Z. Q. Chen, and X. Wang, "Observer-based robust coordinated control of multiagent systems with input saturation," *IEEE Transactions on Neural Networks and Learning Systems*, vol. 29, no. 5, pp. 1933–1946, 2018.
- [4] Y. Qian, W. Zhang, M. Ji, and C. Yan, "Observer-based positive edge consensus for directed nodal networks," *IET Control Theory & Applications*, vol. 14, no. 2, pp. 352–357, 2020.
- [5] N. Mu, X. Liao, and T. Huang, "Event-based consensus control for a linear directed multiagent system with time delay," *IEEE Transactions on Circuits and Systems II: Express Briefs*, vol. 62, no. 3, pp. 281–285, 2015.
- [6] H. Yan, Y. Shen, H. Zhang, and H. Shi, "Decentralized event-triggered consensus control for second-order multi-agent systems," *Neurocomputing*, vol. 133, pp. 18–24, 2014.
- [7] B. Zhou and Z. Lin, "Consensus of high-order multi-agent systems with large input and communication delays," *Automatica*, vol. 50, no. 2, pp. 452–464, 2014.
- [8] L. Wang and F. Xiao, "Finite-time consensus problems for networks of dynamic agents," *IEEE Transactions on Automatic Control*, vol. 55, no. 4, pp. 950–955, 2010.
- [9] D. Meng and Y. Jia, "Iterative learning approaches to design finite-time consensus protocols for multi-agent systems," *Systems & Control Letters*, vol. 61, no. 1, pp. 187–194, 2012.
- [10] Z. Li, Z. Duan, G. Chen, and L. Huang, "Consensus of multiagent systems and synchronization of complex networks: a unified viewpoint," *IEEE Transactions on Circuits and Systems I: Regular Papers*, vol. 57, no. 1, pp. 213–224, 2010.
- [11] D. V. Dimarogonas, E. Frazzoli, and K. H. Johansson, "Distributed event-triggered control for multi-agent systems," *IEEE Transactions on Automatic Control*, vol. 57, no. 5, pp. 1291–1297, 2012.
- [12] X. Wang, H. Su, X. Wang, and G. Chen, "Fully distributed event-triggered semiglobal consensus of multi-agent systems with input saturation," *IEEE Transactions on Industrial Electronics*, vol. 64, no. 6, pp. 5055–5064, 2017.
- [13] A. Hu, J. Cao, and M. Hu, "Consensus of leader-following multi-agent systems in time-varying networks via intermittent control," *International Journal of Control, Automation and Systems*, vol. 12, no. 5, pp. 969–976, 2014.
- [14] Y. Cao and W. Ren, "Sampled-data discrete-time coordination algorithms for double-integrator dynamics under dynamic directed interaction," *International Journal of Control*, vol. 83, no. 3, pp. 506–515, 2010.
- [15] Z. Ma, Z. Liu, and Z. Chen, "Modified leader-following consensus of time-delay multi-agent systems via sampled control and smart leader," *International Journal of Control, Automation and Systems*, vol. 15, no. 6, pp. 2526–2537, 2017.
- [16] X. L. Wang, H. Su, M. Z. Q. Chen, X. F. Wang, and G. Chen, "Reaching non-negative edge consensus of networked dynamical systems," *IEEE Transactions on Cybernetics*, vol. 48, no. 9, pp. 2712–2722, 2018.
- [17] H.-X. Hu, G. Wen, W. Yu, Q. Xuan, and G. Chen, "Swarming behavior of multiple Euler-Lagrange systems with cooperation-competition interactions: an auxiliary system approach," *IEEE Transactions on Neural Networks and Learning Systems*, vol. 29, no. 11, pp. 5726–5737, 2018.
- [18] H.-x. Hu, W. Yu, G. Wen, Q. Xuan, and J. Cao, "Reverse group consensus of multi-agent systems in the cooperation-competition network," *IEEE Transactions on Circuits and Systems I: Regular Papers*, vol. 63, no. 11, pp. 2036–2047, 2016.
- [19] Z. Li, W. Ren, X. Liu, and M. Fu, "Consensus of multi-agent systems with general linear and Lipschitz nonlinear dynamics using distributed adaptive protocols," *IEEE Transactions on Automatic Control*, vol. 58, no. 7, pp. 1786–1791, 2013.
- [20] R. Agha, M. Rehan, C. K. Ahn, G. Mustafa, and S. Ahmad, "Adaptive distributed consensus control of one-sided Lipschitz nonlinear multiagents," *IEEE Transactions on Systems, Man, and Cybernetics: Systems*, vol. 49, no. 3, pp. 568–578, 2019.
- [21] W. Song, X. Cheng, C. Cattani, and E. Zio, "Multi-fractional Brownian motion and quantum-behaved partial swarm optimization for bearing degradation forecasting," *Complexity*, Article ID 8543131, 9 pages, 2000, In press.
- [22] X. Liu, J.-W. Xiao, D. Chen, and Y.-W. Wang, "Dynamic consensus of nonlinear time-delay multi-agent systems with

- input saturation: an impulsive control algorithm,” *Nonlinear Dynamics*, vol. 97, no. 2, pp. 1699–1710, 2019.
- [23] C. Wang, Z. Zuo, Z. Lin, and Z. Ding, “A truncated prediction approach to consensus control of Lipschitz nonlinear multi-agent systems with input delay,” *IEEE Transactions on Control of Network Systems*, vol. 4, no. 4, pp. 716–724, 2017.
- [24] Y. Pei and J. Sun, “Consensus of discrete-time linear multi-agent systems with Markov switching topologies and time-delay,” *Neurocomputing*, vol. 151, pp. 776–781, 2015.
- [25] X. Liu, K. Zhang, and W.-C. Xie, “Consensus of multi-agent systems via hybrid impulsive protocols with time-delay,” *Nonlinear Analysis: Hybrid Systems*, vol. 30, pp. 134–146, 2018.
- [26] B. Açıkmeşe and M. Corless, “Observers for systems with nonlinearities satisfying incremental quadratic constraints,” *Automatica*, vol. 47, no. 7, pp. 1339–1348, 2011.
- [27] W. Zhang, H. Su, F. Zhu, and G. M. Azar, “Unknown input observer design for one-sided Lipschitz nonlinear systems,” *Nonlinear Dynamics*, vol. 79, no. 2, pp. 1469–1479, 2015.
- [28] Y. Zhao, W. Zhang, H. Su, and J. Yang, “Observer-based synchronization of chaotic systems satisfying incremental quadratic constraints and its application in secure communication,” *IEEE Transactions on Systems, Man, and Cybernetics: Systems*, pp. 1–12. In press, 2019.
- [29] W. Zhang, H. Su, F. Zhu, and S. P. Bhattacharyya, “Improved exponential observer design for one-sided Lipschitz nonlinear systems,” *International Journal of Robust and Nonlinear Control*, vol. 26, no. 18, pp. 3958–3973, 2016.
- [30] Y. Zhao, W. Zhang, W. Zhang, and F. Song, “Exponential reduced-order observers for nonlinear systems satisfying incremental quadratic constraints,” *Circuits, Systems, and Signal Processing*, vol. 37, no. 9, pp. 3725–3738, 2018.
- [31] W. Zhang, Y. Zhao, and M. Abbaszadeh, “Full-order and reduced-order exponential observers for discrete-time nonlinear systems with incremental quadratic constraints,” *Journal of Dynamic Systems, Measurement, and Control*, vol. 141, Article ID 041005, 9 pages, 2019.
- [32] H. Zhang, W. Zhang, Y. Zhao, M. Ji, and L. Huang, “Adaptive state observers for incrementally quadratic nonlinear systems with application to chaos synchronization,” *Circuits, Systems, and Signal Processing*, vol. 39, no. 3, pp. 1290–1306, 2020.
- [33] L. Peng, Y. Jia, and L. Li, “Distributed robust  $H_\infty$  consensus control in directed networks of agents with time-delay,” *Systems & Control Letters*, vol. 57, no. 8, pp. 643–653, 2008.
- [34] S. Boyd, L. Ghaoui, E. Feron, and V. Balakrishnan, *Linear Matrix Inequalities in System and Control Theory*, Society for Industrial and Applied Mathematics, Philadelphia, PA, USA, 1994.
- [35] L. E. Ghaoui, F. Oustry, and M. A. Rami, “A cone complementary linearization algorithm for static output feedback and related problems,” *IEEE Transactions on Automatic Control*, vol. 42, no. 8, pp. 1171–1176, 1997.
- [36] F. Song, S. Yu, T. Chen, and L.-N. Sun, “Research on CNC simulation system with instruction interpretations possessed of wireless communication,” *The Journal of Supercomputing*, vol. 72, no. 7, pp. 2703–2719, 2016.
- [37] K. Hu and J. Yuan, “Finite sum equality approach to  $H_\infty$  output-feedback control for switched linear discrete-time systems with time-varying delay,” *IET Control Theory & Applications*, vol. 3, no. 8, pp. 1006–1016, 2009.
- [38] M. Ekrastian, M. Ataei, and S. Talebi, “Stability of nonlinear time-delay systems satisfying a quadratic constraint,” *Transactions of the Institute of Measurement and Control*, vol. 40, no. 3, pp. 712–718, 2016.

## Research Article

# Epidemic Spreading Combined with Age and Region in Complex Networks

Xu Zhang,<sup>1</sup> Yurong Song ,<sup>2</sup> Haiyan Wang ,<sup>3</sup> and Guo-Ping Jiang <sup>2</sup>

<sup>1</sup>School of Computer Science, Nanjing University of Posts and Telecommunications, Nanjing 210023, China

<sup>2</sup>College of Automation & College of Artificial Intelligence, Nanjing University of Posts and Telecommunications, Nanjing 210023, China

<sup>3</sup>School of Mathematical and Natural Sciences, Arizona State University, Phoenix, AZ 85069, USA

Correspondence should be addressed to Yurong Song; songyr@njupt.edu.cn

Received 6 April 2020; Accepted 16 May 2020; Published 22 June 2020

Guest Editor: Michael Z. Q. Chen

Copyright © 2020 Xu Zhang et al. This is an open access article distributed under the Creative Commons Attribution License, which permits unrestricted use, distribution, and reproduction in any medium, provided the original work is properly cited.

In social networks, the age and the region of individuals are the two most important factors in modeling infectious diseases. In this paper, a spatial susceptible-infected-susceptible (SIS) model is proposed to describe epidemic spreading over a network with region and age by establishing several partial differential equations. Numerical simulations are performed, and the simulation of the proposed model agrees well with real influenza-like illness (ILI) in the USA reported by the Centers for Disease Control (CDC). Moreover, the proposed model can be used to predict the infected density of individuals. The results show that our model can be used as a tool to analyze influenza cases in the real world.

## 1. Introduction

Epidemic spreading [1], which was dramatic historical events, continues to pose health threats to humans today. Recently, epidemic outbreaks have caused the death of many people, such as during the spread of SARS [2] and H1N1 [3, 4] influenza. Thus, to reduce the danger of epidemic spreading, the study of the dynamics of epidemics is an important issue and has raised a great deal of concern. The spread of epidemics in complex networks [5] has been extensively studied by many researchers from different disciplines, including computer science, mathematics, biology, and physics.

Mathematical modeling is a useful tool that has been used to reveal many phenomena of disease propagation in complex networks. One of the most widely used models for the spread of an infectious disease is the susceptible-infected-susceptible (SIS) model [6–8], where the disease is transmitted from infected individuals to their susceptible neighbors with an infection rate, and the infected individuals can recover to become susceptible again with a recovery rate.

In the real world, many studies on real diseases, such as cholera [9, 10], have revealed that diseases might have

different infection rates and mortality rates for different age groups [11]. Individuals of different ages might also have different behaviors, and behavioral changes are crucial in the control and prevention of many infectious diseases. Young individuals tend to be more active in interactions with or between populations and in disease transmissions [12]. Thus, many investigators have developed the age-structured models, composed of partial differential equations [13], for the spread of the epidemics. The age-structured models [14, 15], where the density of the infected individuals was expressed as a function of multiple independent variables, and the epidemic process were modeled as partial differential equations. Kuniya [16] studied the global asymptotic stability by discretizing the age-structured multigroup model. Inaba et al. [17] established an age-structured model of epidemic spreading for the demographic transition and obtained the stability condition using reproduction numbers. So et al. [18] derived the equation of a reaction-diffusion model for a single species population with the age structure.

Meanwhile, the other significant factor is spatial location [19]. Individuals in different regions may have different reproductive and survival capacities. Especially, disease or

information spreading has different behaviors in different spatial locations. Therefore, several researchers have proposed epidemic models based on partial differential equations on a network whose underlying edge represents the physical distance between nodes. Bustamante-Castaneda et al. [20] extended a Kermack–McKendrick model to a geographical network, and different parameters influenced this model and obtained a simple criterion for the onset of the epidemic. The characteristics of influenza are more diverse in subtropical and tropical regions [21]. Wang et al. [22] established a number of partial differential equations of the second order over networks to characterize information spreading in temporal and spatial dimensions.

From the above, studies usually focus on the epidemic models with either the region or age factor based on partial differential equations separately. The main contribution of this study is to combine age and region together based on partial differential equations. Thus, in this paper, we will establish several partial differential equations to describe the epidemic spreading in combination with age and region.

This paper has the following structure: the classification of individuals in complex networks is introduced in Section 2, and the mathematical model is constructed in Section 3. The numerical simulations are given in Section 4. In Section 5, we provide concluding remarks.

## 2. Embedding of a Network with Age and Region to the X-Axis

In social networks, individuals are likely to come into contact with individuals of the same age, especially during the teenage years and in old age. Students of the same age are always in the same grade, and apart from their parents and teachers, they are most exposed to their peers. Additionally, individuals of different ages have different behaviors in epidemic spreading. Therefore, the individuals in complex networks are divided into different communities based on an age structure. Meanwhile, individuals are always divided into different communities by distance. For example, a person is always in contact with his neighbors, friends, colleagues, or others who are in the same place or same region, and together, they form a community in a contact network. Thus, from the beginning, individuals in complex networks can be divided into different communities based on their spatial location.

First, in a social network or complex network, we consider the cluster of individuals of different classifications: age and region. We group individuals of the same age and region together in the complex network.

Suppose that  $P(t)$  denotes the total population in the networks at time  $t$ . Individuals in networks have their age factors and spatial locations or regions. We combine region and age as group  $\{r_n, a_m\}$ , where the region  $r$  is divided into several groups  $r = \{r_1, r_2, \dots, r_N\}$  and the age  $a = \{a_1, a_2, \dots, a_M\}$ . Here,  $r_N$  is the maximum region group, and  $a_M$  is the maximum age group. Based on this group, one could divide the total population into a set of groups, i.e.,  $P(t) = \{P_{r_n, a_m}(t)\}$ . Individuals in group  $P_{r_n, a_m}(t)$  share the same age  $a_m$  in the same region  $r_n$ , where we denote group  $\{r_n, a_m\}$  as the combination of region and age. Then, we use the  $x$ -axis as the

group and embed the density  $P_x(t)$  at the location  $x$ , where  $x$  denotes the combination of region and age, satisfying

$$x = m + (n - 1) \times M. \quad (1)$$

Let  $\rho(x, t)$  represent the density  $P_x(t)$  at the location  $x$ , where  $x \in (0, X]$ , and  $X \in (0, +\infty)$  is the upper bound of  $x$ . By setting  $m = M$  and  $n = N$  into equation (1), we obtain

$$X = MN. \quad (2)$$

Then, we have

$$\int_0^X \rho(x, t) dx = P(t). \quad (3)$$

## 3. Partial Differential Equation Model

This section describes the system of differential equations that describes the multifactor epidemic model. We aim to establish a realistic model that can provide a broad perspective for the prediction and control of disease propagation in real-world networks.

Individuals are classified into different groups. Based on this classification, we establish several equations that describe the evolution of the individuals in the classification system. Then, we establish a new SIS model to analyze the spread of the epidemic.

Generally, we consider a given human population that is divided into two classes: susceptible and infected. At each time step, each individual adopts one of these two states. During one time step, a susceptible individual will be infected when he comes into contact with an infected individual. Meanwhile, the infected individual will become susceptible when he has recovered.

For each classification, we consider both the density of the combination of region and age and the population changes over time. Thus, we describe the density of humans in each class as  $s = s(x, t)$  and  $i = i(x, t)$ , which are susceptible density and infected density of the combination of region and age  $x$  and time  $t$ , respectively.

$$\rho(x, t) = s(x, t) + i(x, t). \quad (4)$$

The dynamic equation can be written as

$$\left\{ \begin{array}{l} \left( \frac{\partial}{\partial t} + \frac{\partial}{\partial x} \right) s(x, t) = \gamma(x) i(x, t) - \lambda(x) s(x, t) i(x, t) \\ \quad - \mu(x) s(x, t), \\ \left( \frac{\partial}{\partial t} + \frac{\partial}{\partial x} \right) i(x, t) = -\gamma(x) i(x, t) + \lambda(x) s(x, t) i(x, t) \\ \quad - \mu(x) i(x, t), \\ s(x, 0) = \phi(x), i(x, 0) = \varphi(x), \quad x > 0, \\ s(0, t) = \xi(t), i(0, t) = \zeta(t), \quad t > 0, \end{array} \right. \quad (5)$$

where  $\mu(x)$  is the age-region-specific mortality rate,  $\gamma(x)$  is the recovery rate which is a function of  $x$ , and  $\lambda(x)$  is the infection rate as a function of  $t$ .  $\phi$  and  $\varphi$  and  $\xi$  and  $\zeta$  are the initial distributions of the susceptible and infected individuals, respectively. Additionally, there is the birth condition, which is assumed that all newborns are susceptible:

$$s(0, t) = \int_0^{\infty} \beta(x)\rho(x, t)dx, \quad (6)$$

where  $\beta(x)$  is the birth rate.

In the real world, the number of deaths due to the spreading of disease is far less than the number of infected individuals. Therefore, we can ignore the death rates and assume that there is no migration.

For simplicity, we assume that  $\rho(x, t) =: \rho^*(x)$  is independent of time, and the population is  $\int_0^X \rho(t, x)dx = \int_0^X \rho^*(x)dx$ , which is in a stationary state.

$$\frac{\partial i(x, t)}{\partial t} + \frac{\partial i(x, t)}{\partial x} = -\gamma(x)i(x, t) + \lambda(x)[\rho(x) - i(x, t)]i(x, t), \quad (7)$$

where the boundary conditions are  $i(x, 0) = \varphi(x)$ ,  $x > 0$ , and  $i(0, t) = \zeta(t)$ ,  $t > 0$ . The first term in equation (7) considers the infected individuals whose location is  $x$ . The second term considers the probability that an individual with  $x$  is healthy  $s(x, t)$  and will become infected via a connection with an infected individual. The transmission dynamics of the disease are governed by equation (7), where a susceptible individual with location  $x$  becomes infected with the probability  $\lambda(x)$  when the individual connects to an infected one, while an infected individual becomes susceptible with the recovery rate  $\gamma(x)$  spontaneously. It is worth mentioning that the conclusion in this paper can be extended to other epidemic models, such as the SIR model.

#### 4. Simulation

To support our model, we verify it with real weekly data on influenza-like illness (ILI) in the community from the 42<sup>nd</sup> week of 2017 to the 4<sup>th</sup> week of 2018, as reported by the CDC. This paper uses fifteen classifications and fifty classifications to conduct the simulations. To simplify the simulation, the unit of time is one week.

**4.1. Simulation Results of Fifteen Classifications.** The regions of the USA [19] defined by the CDC are shown in Figure 1. In our model simulation, we rezone the entire area into three new regions. Here, we set  $M = 5$  and  $N = 3$ . The 1<sup>st</sup>, 2<sup>nd</sup>, 3<sup>rd</sup>, and 4<sup>th</sup> regions are rezoned into Region 1; the 5<sup>th</sup>, 6<sup>th</sup>, and 7<sup>th</sup> regions are rezoned into Region 2; and the 8<sup>th</sup>, 9<sup>th</sup>, and 10<sup>th</sup> regions are rezoned into Region 3. Meanwhile, the ages are divided into five intervals, namely,  $[0, 4]$ ,  $[5, 24]$ ,  $[25, 49]$ ,  $[50, 64]$ , and  $[65, A]$ , where  $A$  is the upper bound of individuals. Here, setting  $M = 5$  and  $N = 3$  into equation (1), we obtain  $x = 1, 2, \dots, 15$ , and the details are shown in Table 1. By combining the age and region, fifteen classifications are derived.

The initial guess parameter values are

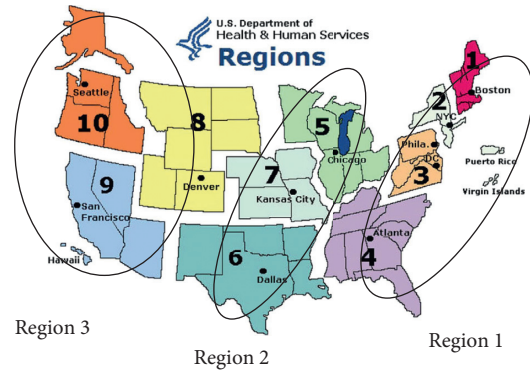


FIGURE 1: The region map defined by this paper.

$$\lambda(x) = 0.01 + \exp[-5.20 \times (x - 2.70)], \quad (8)$$

$$\gamma(x) = 0.30 + \exp[-0.60 \times (x - 3.00)], \quad (9)$$

where the exponent form is chosen based on the distribution of displacement lengths of individuals [23].

The final parameter values are

$$\lambda(x) = 0.01 + \exp[-5.23 \times (x - 2.72)], \quad (10)$$

$$\gamma(x) = 0.30 + \exp[-0.60 \times (x - 3.02)].$$

The information in Table 1 and Figure 2 shows how a change in the value of  $x$ , the combined region and age, changes the density of the infected individuals, which means that all of the data have been divided into fifteen classifications. Based on the initial guess parameter values, we simulate the equation by adjusting the parameter values. Figure 2 gives the simulation results, where the red-dotted line is the data for the 19<sup>th</sup> week of ILI cases reported by the CDC. The blue solid line is the simulated result using our model in the 19<sup>th</sup> week. As shown in Figure 2, these two lines match well, especially for integer values of  $x$ .

**4.2. Simulation Results of Fifty Classifications.** Here, we further set  $M = 5$  and  $N = 10$ . The ages are divided as described in Section 4, and the regions are shown in Figure 1 according to the 10 regions of the USA. Setting  $M = 5$  and  $N = 10$  into equation (1), we obtain  $x = 1, 2, \dots, 50$ , and the details are shown in Table 2. By combining the age and region, fifty classifications are obtained.

The initial guess parameter values satisfy equations (8) and (9). The information in Table 2 and Figure 3 shows that all the data have been divided into fifty classifications. Figure 3 gives the simulation results, where the red-dotted line is the data from the 18<sup>th</sup> week of ILI cases reported by the CDC. The blue solid line is the simulated result using our model in the 18<sup>th</sup> week. As shown in Figure 3, these two lines match well, especially at integer values of  $x$ . The simulation of the model agrees well with the real cases provided by the CDC. Our model can very accurately simulate real conditions.

TABLE 1: Fifteen classifications for the combined ages and regions,  $x$ .

$x$ (combination of region and age)	$m$ (age groups)	$n$ (region groups)
1	From 0 to 4	Region 1
2	From 5 to 24	Region 1
3	From 25 to 49	Region 1
4	From 50 to 64	Region 1
5	From 65 to upper bound	Region 1
6	From 0 to 4	Region 2
7	From 5 to 24	Region 2
8	From 25 to 49	Region 2
9	From 50 to 64	Region 2
10	From 65 to upper bound	Region 2
11	From 0 to 4	Region 3
12	From 5 to 24	Region 3
13	From 25 to 49	Region 3
14	From 50 to 64	Region 3
15	From 65 to upper bound	Region 3

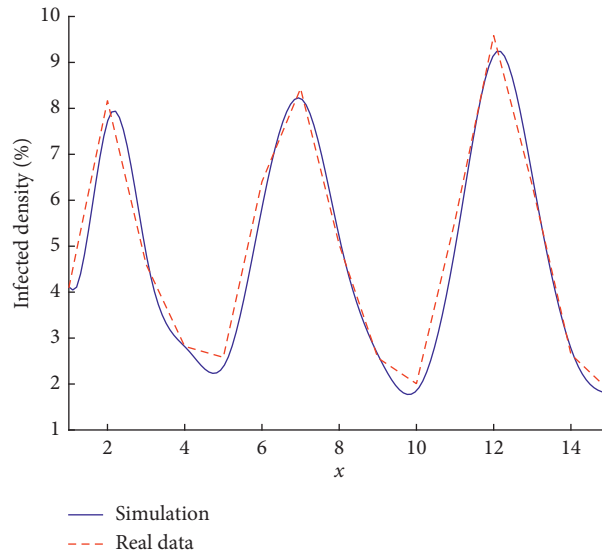


FIGURE 2: The density of infected individuals as a function of time for the SIS model with fifteen classifications.

4.3. *Prediction Accuracy.* From the above, we can see that our model agrees well with the reported ILI cases provided by the CDC. Here, we use our model to predict the infected density of individuals in the next three weeks, and the prediction accuracy is calculated by using fifteen classifications mentioned in Section 4. The prediction accuracy of the model against the actual value is defined as

$$\text{accuracy} = 1 - \frac{|\text{predv} - \text{actv}|}{\text{actv}}, \quad (11)$$

where  $\text{predv}$  is the prediction value of our model and  $\text{actv}$  is the actual value of the real data reported by the CDC.

We use data from the 1<sup>st</sup> week to the 4<sup>th</sup> week for training, find the suitable parameters where simulation of our model agrees well with the data from the CDC, and predict the data of ILI cases reported by the CDC for the next three weeks.

Following the same procedure, we train the data from the 1<sup>st</sup> week to the 7<sup>th</sup> week and predict the data from the 8<sup>th</sup> week to the 10<sup>th</sup> week; train the data from the 1<sup>st</sup> week to the 10<sup>th</sup> week and predict the data from the 11<sup>th</sup> week to the 13<sup>th</sup> week; and train the data from the 1<sup>st</sup> week to the 13<sup>th</sup> week and predict the data from the 14<sup>th</sup> week to the 16<sup>th</sup> week. Figure 4 shows the average prediction accuracy for fifteen classifications. And the results demonstrate that our model can predict the data of ILI cases reported by the CDC for fifteen classifications with similar accuracy.

Figure 4 shows that a prediction accuracy of 85.01% is obtained if the data of the first 4 weeks are used for training. Similarly, a prediction accuracy of 76.95%, 83.20%, and 87.31% is obtained if the data of the first 7 weeks, first 10 weeks, and first 13 weeks are used for training, respectively. It can be seen that our model can obtain high prediction accuracy for fifteen classifications.



TABLE 2: Fifty classifications of combined ages and regions,  $x$ .

$x$ (combination of age and region)	$m$ (age groups)	$n$ (region groups)
1	From 0 to 4	Region 1
2	From 5 to 24	Region 1
3	From 25 to 49	Region 1
4	From 50 to 64	Region 1
5	From 65 to upper bound	Region 1
6	From 0 to 4	Region 2
7	From 5 to 24	Region 2
8	From 25 to 49	Region 2
9	From 50 to 64	Region 2
10	From 65 to upper bound	Region 2
11	From 0 to 4	Region 3
12	From 5 to 24	Region 3
13	From 25 to 49	Region 3
14	From 50 to 64	Region 3
15	From 65 to upper bound	Region 3
16	From 0 to 4	Region 4
17	From 5 to 24	Region 4
18	From 25 to 49	Region 4
19	From 50 to 64	Region 4
20	From 65 to upper bound	Region 4
21	From 0 to 4	Region 5
22	From 5 to 24	Region 5
23	From 25 to 49	Region 5
24	From 50 to 64	Region 5
25	From 65 to upper bound	Region 5
26	From 0 to 4	Region 6
27	From 5 to 24	Region 6
28	From 25 to 49	Region 6
29	From 50 to 64	Region 6
30	From 65 to upper bound	Region 6
31	From 0 to 4	Region 7
32	From 5 to 24	Region 7
33	From 25 to 49	Region 7
34	From 50 to 64	Region 7
35	From 65 to upper bound	Region 7
36	From 0 to 4	Region 8
37	From 5 to 24	Region 8
38	From 25 to 49	Region 8
39	From 50 to 64	Region 8
40	From 65 to upper bound	Region 8
41	From 0 to 4	Region 9
42	From 5 to 24	Region 9
43	From 25 to 49	Region 9
44	From 50 to 64	Region 9
45	From 65 to upper bound	Region 9
46	From 0 to 4	Region 10
47	From 5 to 24	Region 10
48	From 25 to 49	Region 10
49	From 50 to 64	Region 10
50	From 65 to upper bound	Region 10

4.4. Comparison and Summary. As shown in Figures 2 and 3, the curve simulated by our model has better performance with fifty classifications than with fifteen classifications. This is because in numerical simulations of differential equations, the denser the points, the more accurate the results. In summary, the empirical results agree well with the real data of weekly reported cases provided by the CDC. From

Figure 4, a high accuracy is achieved to predict the reported ILI cases provided by the CDC. This indicates that our model can be used as a tool to analyze flu cases in terms of the regions or ages. Since the simulation of the model agrees well with the reported ILI cases provided by the CDC in terms of the regions or ages, we argue that our model can be used to analyze flu cases in real-world networks.

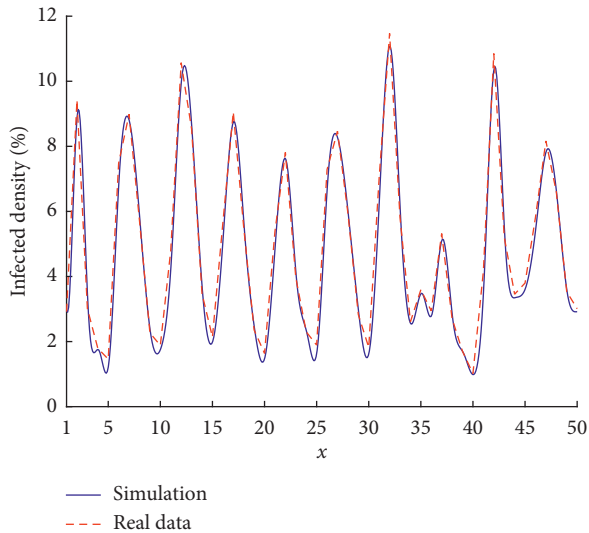


FIGURE 3: The density of infected individuals as a function of time for the SIS model with fifty classifications.

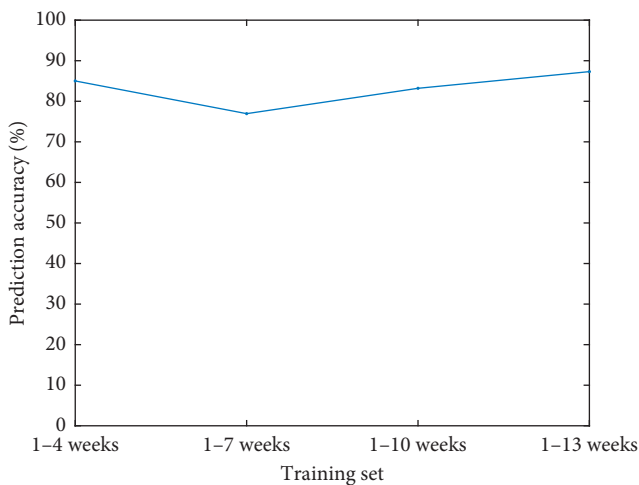


FIGURE 4: Three-week prediction accuracy for fifteen classifications.

## 5. Conclusion

In real networks, age and region are two of the most important characteristics of epidemic processes. Individuals of different ages may engage in different behaviors in disease spreading. Individuals in different regions may also have different reproductive and survival capacities. Based on the SIS model, a new propagation model has been proposed to describe epidemic spreading combined with age and region as a system of partial differential equations. Then, numerical simulations have been performed to show that the simulation of this model agrees well with real influenza-like illness in the USA as reported by the CDC. This implies that our model can be a tool to analyze and predict flu cases with granularity at the regional or age level. However, some other factors, such as migration and time delay, are also important that impact the spreading of disease, which will be our near future work.

## Data Availability

The data used to support the findings of this study may be released upon application to the Centers for Disease Control (CDC).

## Conflicts of Interest

The authors declare that they have no conflicts of interest.

## Acknowledgments

Xu Zhang, Yurong Song, and Guo-Ping Jiang were supported by the National Natural Science Foundation of China (Grant nos. 61672298, 61873326, 61802155, and 61802201) and the Philosophy Social Science Research Key Project Fund of Jiangsu University (Grant no. 2018SJZD1142).

## References

- [1] D. J. Daley, J. Gani, and J. M. Gani, *Epidemic Modelling: An Introduction*, Cambridge University Press, Cambridge, UK, 2001.
- [2] C. Dye and N. Gay, "Modeling the SARS epidemic," *Science*, vol. 300, no. 5627, pp. 1884-1885, 2003.
- [3] J. Zarocostas, "World health organization declares A (H1N1) influenza pandemic," *BMJ*, vol. 338, p. 2425, 2009.
- [4] V. P. Maru, C. Nagarathna, B. S. Shakuntala, and H. K. Navin, "Mongrelised genetics of H1N1 virus: a bird's eyeview," *Indian Journal of Dental Research*, vol. 21, no. 4, pp. 586-590, 2010.
- [5] R. Pastor-Satorras, C. Castellano, P. V. Mieghem, and A. Vespignani, "Epidemic processes in complex networks," *Review of Modern Physics*, vol. 87, no. 3, pp. 120-131, 2014.
- [6] P. V. Mieghem, "The  $N$ -intertwined SIS epidemic network model," *Computing*, vol. 93, no. 2-4, pp. 147-169, 2011.
- [7] E. Cator and P. V. Mieghem, "Susceptible-infected-susceptible epidemics on the complete graph and the star graph: exact analysis," *Physical Review E*, vol. 87, no. 1, Article ID 012811, 2013.
- [8] C. Li, R. V. D. Bovenkamp, and P. V. Mieghem, "Susceptible-infected-susceptible model: a comparison of  $N$ -intertwined and heterogeneous mean-field approximations," *Physical Review E*, vol. 86, no. 2, Article ID 026116, 2012.
- [9] A. Alexanderian, M. K. Gobbert, K. R. Fister, H. Gaff, S. Lenhart, and E. Schaefer, "An age-structured model for the spread of epidemic cholera: analysis and simulation," *Nonlinear Analysis: Real World Applications*, vol. 12, no. 6, pp. 3483-3498, 2011.
- [10] A. Agheksanterian and M. K. Gobbert, "Modeling the spread of epidemic cholera: an age-structured model," 2007.
- [11] R. M. Anderson and R. M. May, *Infectious Diseases of Humans, Dynamics and Control*, Oxford University Press, Oxford, UK, 1991.
- [12] H. W. Hethcote, "The mathematics of infectious disease," *SIAM Review*, vol. 42, no. 4, pp. 599-653, 2000.
- [13] H. Wang and X.-S. Wang, "Traveling wave phenomena in a Kermack-McKendrick SIR model," *Journal of Dynamics and Differential Equations*, vol. 28, no. 1, pp. 143-166, 2016.
- [14] J. Wang, J. Lang, and X. Zou, "Analysis of an age structured HIV infection model with virus-to-cell infection and cell-to-cell transmission," *Nonlinear Analysis: Real World Applications*, vol. 34, pp. 75-96, 2017.

- [15] M. Cecchini, S. Cividino, R. Turco, and L. Salvati, "Population age structure, complex socio-demographic systems and resilience potential: a spatio-temporal, evenness-based approach," *Sustainability*, vol. 11, no. 7, p. 2050, 2019.
- [16] T. Kuniya, "Global stability analysis with a discretization approach for an age-structured multigroup SIR epidemic model," *Nonlinear Analysis: Real World Applications*, vol. 12, no. 5, pp. 2640–2655, 2011.
- [17] H. Inaba, R. Saito, and N. Bacaër, "An age-structured epidemic model for the demographic transition," *Journal of Mathematical Biology*, vol. 77, no. 5, pp. 1299–1339, 2018.
- [18] J. W.-H. So, J. Wu, and X. Zou, "A reaction-diffusion model for a single species with age structure. I travelling wavefronts on unbounded domains," *Proceedings of the Royal Society A*, vol. 457, no. 2012, pp. 1841–1853, 2001.
- [19] F. Wang, H. Wang, K. Xu et al., "Regional level influenza study with geo-tagged twitter data," *Journal of Medical Systems*, vol. 40, no. 8, p. 189, 2016.
- [20] F. Bustamante-Castaneda, J.-G. Caputo, G. Cruz-Pacheco, A. Knippel, and F. Mouatamide, "Analysis of an epidemic model on a network," 2019, <http://arxiv.org/abs/1906.07449>.
- [21] W. Yang, B. J. Cowling, E. H. Y. Lau, and J. Shaman, "Forecasting influenza epidemics in Hong Kong," *PLoS Computational Biology*, vol. 11, no. 7, Article ID e1004383, 2015.
- [22] H. Wang, F. Wang, and K. Xu, "Modeling information diffusion in online social networks with partial differential equations," in *Surveys and Tutorials in the Applied Mathematical Sciences*, Springer, Berlin, Germany, 2020.
- [23] D. H. Barmak, C. O. Dorso, and M. Otero, "Modelling dengue epidemic spreading with human mobility," *Physica A: Statistical Mechanics & its Applications*, vol. 447, pp. 129–140, 2015.

## Research Article

# Trajectory Planning and Tracking for Carrier Aircraft-Tractor System Based on Autonomous and Cooperative Movement

Minghui Yu,<sup>1</sup> Xue Gong ,<sup>1</sup> Guowei Fan,<sup>2</sup> and Yu Zhang <sup>2</sup>

<sup>1</sup>School of Artificial Intelligence and Automation, Huazhong University of Science and Technology, Wuhan 430074, China

<sup>2</sup>China Ship Development and Design Center, Wuhan 430064, China

Correspondence should be addressed to Xue Gong; [gongxue@hust.edu.cn](mailto:gongxue@hust.edu.cn)

Received 5 March 2020; Accepted 29 April 2020; Published 13 June 2020

Guest Editor: Xiao Ling Wang

Copyright © 2020 Minghui Yu et al. This is an open access article distributed under the Creative Commons Attribution License, which permits unrestricted use, distribution, and reproduction in any medium, provided the original work is properly cited.

The solution of how to plan out the cooperative moving trajectory autonomously and control the motion of carrier-based aircraft timely and accurately is the key to helping improve the overall deck operation efficiency. The main problem discussed in this article is coordinated trajectory planning strategy for multicarrier aircraft and cooperative control between tractor and carrier aircraft. First, the kinematic model and three-degree-of-freedom dynamics model of the towbarless traction system are established. Then, a coevolution mechanism for aircraft systems is proposed to ensure coordinated trajectory planning among multiple aircraft and a trajectory adapted to the tractor-aircraft system is generated based on the hybrid RRT\* algorithm. Next, a double-layer closed-loop controller is designed for the trajectory tracking of the tractor-aircraft system on the deck under the constraints of incomplete constraints and various physical conditions. It includes an outer model predictive controller which effectively controls the cooperative motion between the carrier aircraft and tractor and an inner torque control strategy based on adaptive fuzzy PID control which strictly ensures the stability of the system. Simulation results demonstrate that the controller is more rapid, more accurate, and more robust in tracking line trajectory with initial deviation, sine curve with large curvature, and complex trajectories on decks compared with backstepping control and LQR algorithm.

## 1. Introduction

Aircraft carrier is one of the extra-large maritime combat platforms. The number and the launch-recovery efficiency of carrier-based aircraft is quite important for the platform's combat effectiveness. The efficiency and safety of transfer operations in hangar and flight deck directly affect the launching efficiency of carrier-based aircraft. At present, the dispatching operation mainly adopts the coordinated control method of the tractor and guide. However, with the rapid development of the intelligent industry, automatic tractors will become the trend of ground movement of carrier-based aircraft, which will place further demands on the speed and safety of carrier-based aircraft's movement. Path planning is one of the most important links in transportation operations and many scholars have done research [1, 2]. To the best of our knowledge, there is little research to deal with the problem of cooperative trajectory

generation of multiple aircraft traction systems. At the same time, there are numerous shortages and restrictions in practice [3–8]. Due to the complicated movement process of the tractor-aircraft system, the planned trajectory is generally under ideal conditions, which means it is difficult to consider the error factors such as the initial deviation [9–11]. Therefore, the quality of trajectory tracking is a key factor in judging the overall control system.

The trajectory tracking problem of carrier-based aircraft traction system is defined as follows: the system starts from an initial position on the hangar or flight deck, moves along a desired time-related trajectory under the controller, and finally reaches the specified position steadily. Moreover, the core of the research is to design the controller to make the tracking accuracy higher. Trajectory tracking problem of tractor-aircraft system on deck has not been explored to a large extent. If the factors such as the mass of the aircraft and the constraints of trajectory planning are ignored, it can be

regarded as a drag-pull system to a certain degree. According to the structural characteristics of the traction system, the aircraft can be regarded as a trailer. The main goal is to track the trajectory of the aircraft, so that the aircraft can reach the predetermined position according to the ideal trajectory as much as possible. Many studies about the trajectory tracking of the tractor system have been carried out and many representative methods have been proposed during the past decades.

For the preliminary research of trajectory tracking problems, traditional control methods are mainly used, such as PID control or sliding mode control (SMC) [12]. Due to the complex kinematics and dynamics of the tractor system, the performance of the trajectory tracking system designed by the classic control method is quite limited, which makes the controller must be adjusted in an adaptive manner [13]. It is convenient to use the PID controller for Simple Input Simple Output (SISO) systems, while tractor-trailer systems have multiple inputs and outputs. Traditionally, decentralized control is performed by designing a controller for each SISO subsystem, but it is difficult to consider the interaction between each system [14]. Therefore, control method of dynamic state feedback has been proposed. For the towed wheeled mobile robot (TTWR), Khalaji and Moosavian proposed a robust adaptive feedback linearized dynamic controller (RAFLDC) and verified the stability of the control algorithm using the Lyapunov method [15]. Huofeng et al. designed a linear dynamic feedback controller based on the internal model principle, which can ensure the boundedness of the tracking error [16]. A controller that combines kinematics and dynamics has been created by Lashkari [17]. The speed input of the system is determined by the kinematic controller, and then the required torque of the trailer is calculated to achieve the given speed input. This method guarantees the stability of the controller and can adjust the parameters according to the number of trailers. In addition, linear quadratic regulator- (LQR-) based controllers are widely applied in the field of trajectory tracking. A linear secondary regulator was proposed in [18] to control the position of the trailer. However, it has been pointed out that feedforward control is needed to compensate for the curve with large curvature.

Model predictive control (MPC) has developed rapidly in recent decades, but too little work has been devoted to the trajectory tracking of carrier-based aircraft. In the trajectory tracking of mobile robots, the nonlinear model is usually linearized first and then transformed into a linear time-invariant system for control. Bin et al. developed a control framework based on the MPC method and used hybrid logic dynamics (MLD) to model the axleless tractor-trailer system. Then, a hybrid integer quadratic programming method is used to design an optimal reversing controller [19]. Yue et al. designed a dynamic controller based on MPC and SMC. The latter drives the vehicle's speed to track the expected speed generated by the former, which guarantees the progressive convergence of the inner loop from the perspective of stability [20]. Kayacan et al. created a control method based on linear model predictive controller and combined it with

feedforward control and robust control [21]. At the same time, some scholars have applied nonlinear model predictive control to the trajectory tracking of tractor-trailer systems. In [22], Backman et al. studied the NMPC implementation of the tractor-trailer system, which can control them to track straight lines and curves. Reference [23] mentioned a nonlinear rolling time-domain estimator and a nonlinear model predictive controller based on an adaptive model and gave relatively successful experimental results. Unfortunately, NMPC requires a very large amount of calculations [24]. Although its tracking accuracy is good, it is still difficult to achieve online real-time controlling.

There are three main ways of carrier-based aircraft movement on aircraft carriers: aircraft taxi motion, towbarless tractor traction motion, and towbar tractor traction motion. Shipboard aircraft do not have the conditions for taxiing on aircraft carrier decks with relatively narrow spaces, compact deployments, and inaccessibility. The towbarless tractor uses its own clamping and lifting device to directly act on the aircraft's front landing gear. This method does not require a towbar to connect to the aircraft, which is more flexible than a towbar tractor [25]. In view of the above problems, this paper focuses on the trajectory tracking model of the towbarless traction system.

This article is highly motivated by the strong demand in the military and other related fields. We expect to employ advanced control technology to help the aircraft reach the designated position quickly and accurately, so as to increase the flight sorties rate. The summary of our contributions is listed as follows.

- (1) We describe a novel application scenario (i.e., towbarless tractor-aircraft trajectory tracking) for model predictive control (MPC). A full-state controller is designed through MPC to drive all state variables to converge to the desired trajectory.
- (2) We generate trajectories suitable for the carrier aircraft on the deck using the hybrid RRT\* algorithm based on the collaborative strategy and convex the obstacles on deck and define a distance function that is particularly suitable for carrier aircraft. Taking into account the driving characteristics of carrier-based aircraft, the RRT node is expanded using the Reeds-Shepp route, which is different from other path planning algorithms.
- (3) In order to improve the dynamic stability of the system, we propose a self-adaptive fuzzy PID controller to control the system's centroid yaw and yaw rate by adding yaw moment.
- (4) We conduct many sets of simulation experiments to verify the effectiveness and advantages of the method for this scenario.

In the remainder of this paper, the description of the towbarless tractor-aircraft system is introduced in Section 2, the trajectory generation and trajectory tracking controller are proposed in Section 3 and Section 4, respectively. Section 5 shows experimental results of different trajectory. The conclusion of this paper is presented in Section 6.

## 2. Towbarless Tractor-Aircraft System

Consider a towbarless traction system with carrier aircraft, as sketched in Figure 1. In the inertial coordinate system  $OXY$ ,  $P_1(x_1, y_1)$  and  $P_2(x_2, y_2)$  are the position coordinates of the tractor and the aircraft;  $\theta_1$  and  $\theta_2$  are the direction angles of the tractor and the carrier.  $\delta$  is the steering angle of the front wheels and  $v$  is the axial speed of the rear axle of the tractor.  $v_i$  and  $\omega_i$  are the lateral speed and yaw rate of the tractor and the aircraft, respectively.  $m_i$  and  $I_i$  are the mass and moment of inertia of the tractor and the aircraft, respectively.  $F_{x_i}$  and  $F_{y_i}$  are the longitudinal and lateral forces on the tires of the tractor and the aircraft, and  $T$  is the steering torque, where  $i = 1, 2$ .

For its motion on the deck, the following assumptions are made:

- Assuming a pure rolling motion, both the tractor and the aircraft are rigid bodies
- Both the tractor and the carrier aircraft are symmetrical along the longitudinal axis
- The aircraft's front landing gear is directly articulated at the midpoint of the two rear wheels of the tractor
- Regardless of the effects of air resistance and friction, only the lateral movement of the tractor along the  $y$ -axis and the yaw movement around the center of mass are considered

**2.1. Kinematic Model.** When the speed of the traction system is small, the kinematics model can better describe the motion of the system [26]. According to the incomplete constraints of the towbarless tractor system, the kinematic relationship of the system can be simplified. The kinematic equation of the carrier-based traction system is described as follows:

$$\begin{cases} \dot{x}_1 = v \cos \theta_1, \\ \dot{y}_1 = v \sin \theta_1, \\ \dot{\theta}_1 = \frac{v \tan \delta}{L_1}, \\ \dot{x}_2 = v [\cos(\theta_1 - \theta_2) \cos \theta_2], \\ \dot{y}_2 = v [\cos(\theta_1 - \theta_2) \sin \theta_2], \\ \dot{\theta}_2 = \frac{v \sin(\theta_1 - \theta_2)}{L_2}. \end{cases} \quad (1)$$

According to the geometric relationship between the two adjacent car bodies in the trailer system, the complete system constraints are obtained:

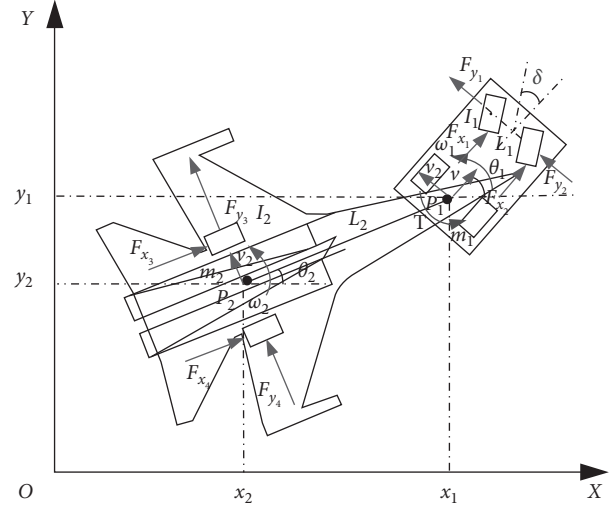


FIGURE 1: Towbarless traction system with carrier aircraft.

$$\begin{bmatrix} x_1 \\ y_1 \end{bmatrix} = \begin{bmatrix} x_2 \\ y_2 \end{bmatrix} + L_2 \begin{bmatrix} \cos \theta_2 \\ \sin \theta_2 \end{bmatrix}. \quad (2)$$

The main task of trajectory tracking is to track the movement trajectory of the carrier-based aircraft, so that the carrier-based aircraft can reach the target position quickly and accurately. Therefore, the configuration of the whole system is completely given by  $(\theta_1, x_2, y_2, \theta_2)$ . The state variable is  $\xi = [\theta_1, x_2, y_2, \theta_2]^T \in \Omega$ , the output variable is  $Y = [\theta_1, x_2, y_2, \theta_2]^T$ , and the control variable is  $U = [v, \delta]^T \in \psi$ . The system can be expressed as the following state space expression:

$$\dot{\xi}_0 = f(\xi_0, u_0). \quad (3)$$

Since the linearized system is simple to control and easy to solve, we linearize the above model.

$$\dot{\xi} = f(\xi_0, u_0) + A(t)(\xi - \xi_0) + B(t)(u - u_0). \quad (4)$$

Subtracting (3) and (4), we get

$$\dot{\tilde{\xi}} = A(t)\tilde{\xi} + B(t)\tilde{u}, \quad (5)$$

where  $\tilde{\xi} = \xi - \xi_0$ ,  $\tilde{u} = u - u_0$ ,  $A(t) = (\partial f / \partial \xi)|_{\xi_0, u_0}$ , and  $B(t) = (\partial f / \partial u)|_{\xi_0, u_0}$ .

This state space expression is continuous. The linear parameter-varying (LVP) model after discretization is described as

$$\begin{cases} \tilde{\xi}(k+1) = A_{k,t}\tilde{\xi}(k) + B_{k,t}\tilde{u}(k), \\ \eta(k) = C_{k,t}\tilde{\xi}(k), \end{cases} \quad (6)$$

where

$$A_{k,t} = \begin{bmatrix} 0 & 0 & 0 & 0 \\ -\sin(\theta_1 - \theta_2)\cos\theta_2 vt & 0 & 0 & [-\sin(\theta_1 - \theta_2)\cos\theta_2 - \cos(\theta_1 - \theta_2)\sin\theta_2]vt \\ -\sin(\theta_1 - \theta_2)\sin\theta_2 vt & 0 & 0 & [-\sin(\theta_1 - \theta_2)\sin\theta_2 - \cos(\theta_1 - \theta_2)\cos\theta_2]vt \\ \frac{vt \cos(\theta_1 - \theta_2)}{L_2} & 0 & 0 & \frac{\cos(\theta_1 - \theta_2)vt}{L_2} \end{bmatrix}, \quad (7)$$

$$B_{k,t} = \begin{bmatrix} \frac{t \tan \delta}{L_1} & \frac{vt}{L_1 \cos^2 \delta} \\ \cos(\theta_1 - \theta_2)\cos\theta_2 t & 0 \\ \cos(\theta_1 - \theta_2)\sin\theta_2 t & 0 \\ \frac{t}{L_2} \sin(\theta_1 - \theta_2) & 0 \end{bmatrix}.$$

Let  $\widehat{\xi}(k|t) = \begin{bmatrix} \xi(k|t) \\ u(k-1|t) \end{bmatrix}$ ; then get the new state equation as

$$\begin{cases} \widehat{\xi}(k+1) = A_t \widehat{\xi}(k|t) + B_t \Delta u(k), \\ \eta(k) = C_t \widehat{\xi}(k|t), \end{cases} \quad (8)$$

where  $A_t = \begin{bmatrix} A_{k,t} & B_{k,t} \\ 0_{2 \times 4} & I \end{bmatrix}$ ,  $B_t = \begin{bmatrix} B_{k,t} \\ I \end{bmatrix}$ , and  $C_t = [C_{k,t} \ 0_{4 \times 2}]$ .

**2.2. Dynamics Model.** When the traction system's speed is large, the dynamic stability of the system needs to be considered. The three-degree-of-freedom dynamics equation of tractor-aircraft system is established based on Newtonian mechanics [27]:

$$\begin{cases} m_1 a_{y_1} + m_2 a_{y_2} - (F_{y_1} + F_{y_2}) - (F_{y_3} + F_{y_4}) = 0, \\ (I_1 + m_1 L_1^2) \dot{\omega}_1 - (F_{y_1} + F_{y_2}) L_1 - F_{x_1} b + F_{x_2} b - T = 0, \\ (I_2 + m_2 L_2^2) \dot{\omega}_2 + (F_{y_3} + F_{y_4}) L_2 - F_{x_3} c + F_{x_4} c + T = 0. \end{cases} \quad (9)$$

Among them,  $b$  and  $c$  are one-half of the wheel gap between the tractor and the aircraft, respectively,  $a_{y_1}$ ,  $a_{y_2}$  are the centroid accelerations of the tractor and the aircraft, and

$$\begin{cases} a_{y_1} = \dot{v}_1 + v\omega_1, \\ a_{y_2} = \dot{v}_1 - L_2 \dot{\omega}_1 + L_2 \ddot{\psi} + v\omega_1, \psi = \theta_1 - \theta_2, \dot{\theta}_1 = \omega_1, \dot{\theta}_2 = \omega_2. \end{cases} \quad (10)$$

When the system travels along a curve with a large curvature, the steering system is equivalent to a torsion spring acting on the hinge point, and the spring stiffness is represented by  $K_\psi$ . Then, the steering torque  $T$ , the tire yaw angle  $\beta_i$  ( $i = 1, 2, 3, 4$ ), the tractor yaw angle  $\beta_{\text{tractor}}$ , and the lateral force  $F_{y_i}$  ( $i = 1, 2, 3, 4$ ) are as follows:

$$T = -K_\psi \psi, \quad (11)$$

$$\beta_1 = \beta_2 = \frac{v_1 + L_1 \omega_1}{v}, \quad (12)$$

$$\beta_3 = \beta_4 = \frac{v_1 - L_2 \omega_1 + L_2 \dot{\psi}}{v}, \quad (13)$$

$$\beta_{\text{tractor}} = \frac{v_1}{v}, \quad (14)$$

$$F_{y_1} = F_{y_2} = k_1 \beta_1, \quad (15)$$

$$F_{y_3} = F_{y_4} = k_2 \beta_3, \quad (16)$$

where  $k_1$  and  $k_2$  are the tire cornering stiffness. According to equations (9)~(16), the state equations in matrix form can be obtained:

$$M \dot{X} + JX = H, \quad (17)$$

where  $M$  is the system inertia matrix,  $J$  is the Jacobian state matrix, and the state variable  $X = [v_1 \ \omega_1 \ \omega_2 \ \psi]^T$ .

In order to study the stability of the system, this paper uses an additional torque to drive the tractor-aircraft system to run stably. Applying torque  $\pm F_x$  to the left and right front wheels of the tractor is equivalent to applying yaw moment  $M'$  to the entire body. By integrating equations (14) and (17), the dynamics model of the entire system is obtained as follows:

$$\dot{X}' = AX' + B\dot{\psi} + C\psi + LM'. \quad (18)$$

Among them,

$$\begin{aligned}
A &= \begin{bmatrix} a_{11} & a_{12} \\ a_{21} & a_{22} \end{bmatrix}, \\
B &= \begin{bmatrix} b_1 \\ 0 \end{bmatrix}, \\
C &= \begin{bmatrix} c_1 \\ c_2 \end{bmatrix}, \\
L &= \begin{bmatrix} 0 \\ h_2 \end{bmatrix}, \\
X' &= \begin{bmatrix} \beta_{\text{tractor}} \\ \omega_1 \end{bmatrix}, \\
h_2 &= \frac{1}{I_1}, \\
a_{11} &= \frac{2(k_1 + k_2)}{(m_1 + m_2)v} - \frac{2m_2k_2L_2^2}{(I_2 + m_2L_2^2)(m_1 + m_2)v}, \\
a_{12} &= \frac{2k_2m_2L_2^3}{(I_2 + m_2L_2^2)(m_1 + m_2)v^2} + \frac{2k_1L_1 - 2k_2L_2}{(m_1 + m_2)v^2} - 1, \\
a_{21} &= \frac{2k_1L_1}{I_1}, \\
a_{22} &= \frac{2k_1L_1^2}{I_1v}, \\
c_2 &= \frac{K_\psi}{I_1}, \\
b_1 &= \frac{2k_2L_2}{(m_1 + m_2)v^2} - \frac{2k_2m_2L_2^2}{(I_2 + m_2L_2^2)(m_1 + m_2)v^2}, \\
c_1 &= \frac{m_2K_\psi I_2 - 2m_2k_2L_2^2}{(I_2 + m_2L_2^2)(m_1 + m_2)v} + \frac{2k_2}{(m_1 + m_2)v}.
\end{aligned} \tag{19}$$

This dynamics model considers the differential term of the articulation angle and controls the system's centroid yaw and yaw rate through additional torque.

### 3. Path Planning and Trajectory Generation

**3.1. Collaborative Strategy for Tractor-Aircraft System.** When a carrier-based aircraft moves on the deck, the state of other carrier-based aircraft and environmental information will affect its movement trajectory, and the information collected from only one aircraft is quite limited. Therefore, the current operation trend is that the "Captain" in the system manages the transfer of all carrier aircraft and organizes the basic communication between the aircraft.

Through the communication between different carrier aircrafts, the coordinated trajectory planning can be carried out for a dispatching task, so as to avoid all obstacles and seek the overall optimal route. In this mode, coordinate position, speed, steering angle, attitude, and other information of each other can be communicated. Each carrier aircraft has its own local trajectory planner and trajectory tracking controller. Figure 2 shows the coordination mechanism in the process of carrier aircraft dispatching. This mechanism not only considers the behavior of a single carrier aircraft but also considers the state of other carrier aircraft moving on the deck [28].

Through the above cooperation mechanism, we can complete trajectory generation and obstacle avoidance, and the overall controller design of a single aircraft is as follows.

According to the kinematics and dynamics model established in Section 2, we establish the control structure shown in Figure 3. First, the feasible path is generated by RRT\*. Second, in order to meet the various constraints of the system, a model predictive controller is designed to track the trajectory, and GA is used to iteratively optimize the parameters of MPC. Next, considering the disturbance factors when the system turns, it may have different degrees of influence on the dynamic performance of the vehicle, so an adaptive fuzzy PID controller is designed to observe and improve the stability of the system. The meaning of the variables in the figure will be defined in the following paragraphs.

**3.2. RRT\* Algorithm Based on Reeds-Shepp.** When the carrier-based aircraft is towed from the initial position to the target position on the deck, it is essential to achieve the optimal path while avoiding all obstacles. In order to track the mission route on the deck, this paper first uses RRT\* algorithm to search the optimal path.

The RRT algorithm is a random algorithm that covers the search space by constructing tree nodes. This method can easily add obstacle constraints when expanding nodes. Using feature graphics to describe the obstacles on the deck, the folded and spread wings of the carrier-based aircraft can be simplified into two different shapes of convex edges, as shown in the Figure 4. When the carrier-based aircraft is regarded as an obstacle, the length of the vertical line between the center point of the traction system and the convex contour of the obstacle must exceed the safety distance between the two carrier-based aircraft.

Different from the ordinary RRT algorithm, the Reeds-Shepp path is used when expanding nodes. Reeds-Shepp path is a kind of shortest path composed of straightforward, backward, turn left, turn right, and other basic curves [29]. By limiting the curvature of the curve, it is ensured that the traction system has a sufficient turning radius and is more in line with the actual movement of the carrier-based aircraft.

The hybrid RRT\* algorithm flow is shown in Figure 5. First, the starting node  $q_{\text{start}}$  is used as the root node to build the search tree *Tree*. The node  $q_{\text{rand}}$  is obtained by random sampling. After traversing the *Tree* to find the node  $q_{\text{nearest}}$  closest to  $q_{\text{rand}}$ , the Reeds-Shepp path between



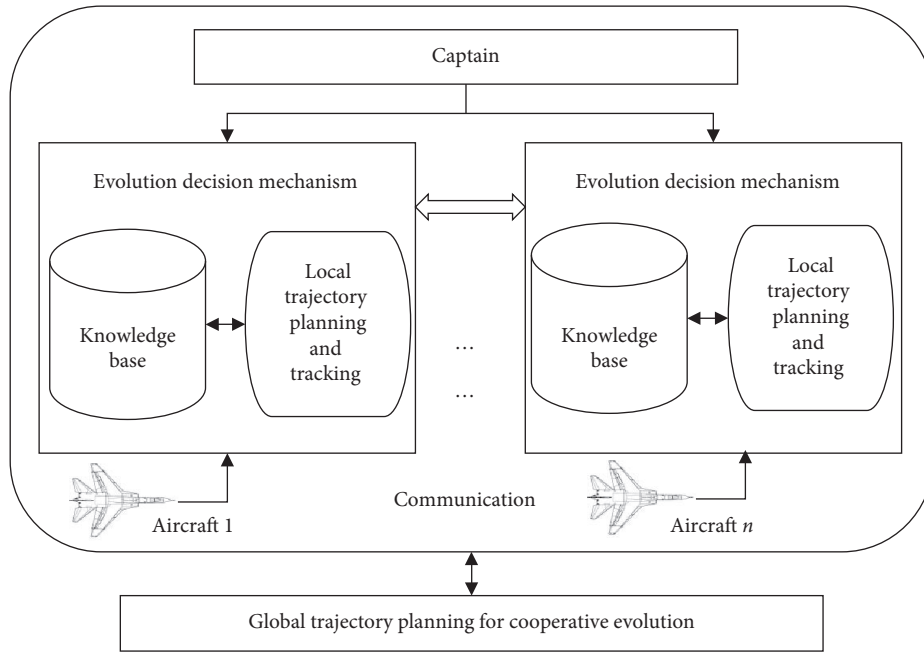


FIGURE 2: Mechanism of coevolution for aircraft systems.

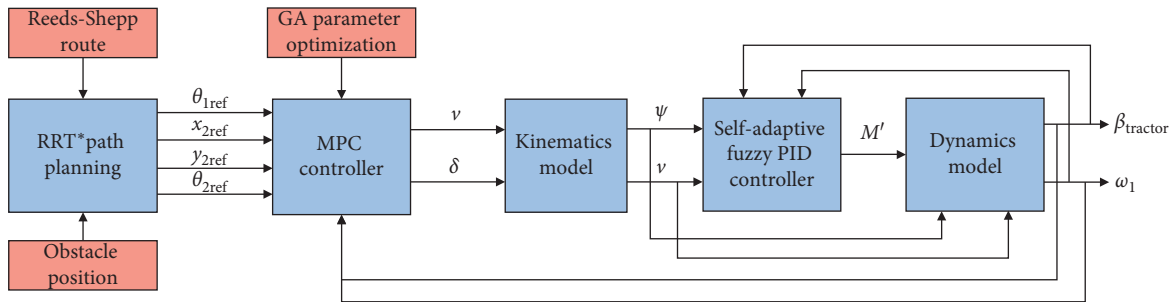


FIGURE 3: Block diagram of control structure.

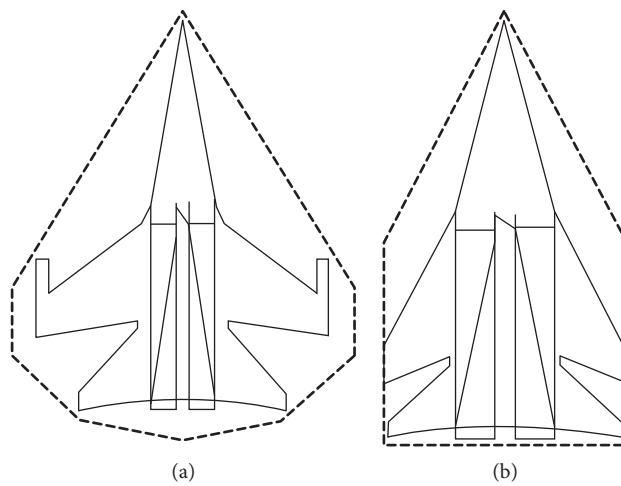


FIGURE 4: Convex outline of (a) spread and (b) folded wings.

```

Generate_Path( $q\_start, q\_goal, max\_iter, obstacle$ )
1   $Tree \leftarrow q\_start$ 
2  for  $i=1$  to  $max\_iter$  do
3     $q\_rand \leftarrow Random\_Node()$ 
4     $q\_nearest \leftarrow Nearest\_Node(Tree, q\_rand)$ 
5     $q\_new \leftarrow New\_Node\_ByRS(q\_rand, q\_nearest)$ 
6    if no_collision( $q\_new, obstacle$ )
7       $near\_nodes \leftarrow Near\_Nodes(q\_new)$ 
8       $q\_new \leftarrow Select\_Parent(near\_nodes)$ 
9      if  $q\_new$ 
10      $Tree.add\_node(q\_new)$ 
11   $q\_last \leftarrow Best\_Goal\_Node(Tree, q\_goal)$ 
12  if  $q\_last$  return  $q\_last$ 
13  else return None

```

FIGURE 5: Hybrid RRT\* algorithm pseudocode.

the two is generated and stored in the new node  $q\_new$ . Collision detection is performed on the generated path. If it is within a safe distance, the parent node of  $q\_new$  is searched again in the  $Tree$ . It is required that the path cost between this parent node and  $q\_new$  be minimal and there is no collision. If  $q\_new$  exists, it is added to the random expansion tree as a new leaf node. The above process is continuously iterated until the maximum number of generations is exceeded, and the search is ended. The target node  $q\_goal$  is traced back to the starting node  $q\_start$ , and the planned path is obtained.

In the above algorithm, to calculate the distance between two nodes, Euclidean distance can usually be used in systems with complete constraints. But, for the traction system in this article, more consideration should be given to its own motion characteristics. The direction angle is an important factor in determining whether the system needs to make a large turn. In order to obtain a more accurate distance measurement and reduce the amount of calculation, the approximate distance is employed in (20) [30]. Among them,  $R$  is the minimum turning radius, and  $O_1$  and  $O_2$  are the centers of the circles on both sides with  $Q_0$  as the center, as shown in Figure 6.

$$D(Q_0, Q_1) = \begin{cases} 2\pi R, & \text{if } \|O_1 - Q_1\| < R \text{ or } \|O_2 - Q_1\| < R, \\ \|Q_1 - Q_0\|, & \text{otherwise.} \end{cases} \quad (20)$$

The final distance can be expressed as

$$M(Q_0, Q_1) = \sqrt{D^2(Q_0, Q_1) + \alpha(\varphi_0 - \varphi_1)}, \quad (21)$$

where  $\varphi$  is the direction angle of the point and  $\alpha$  is the weight of  $\varphi$ .

Premeditating the adverse effect of the turn on the movement, the weighted sum of the path length and the number of turns is applied as the calculation standard of the path cost. The weight of the number of turns can be expressed by  $\beta$ .

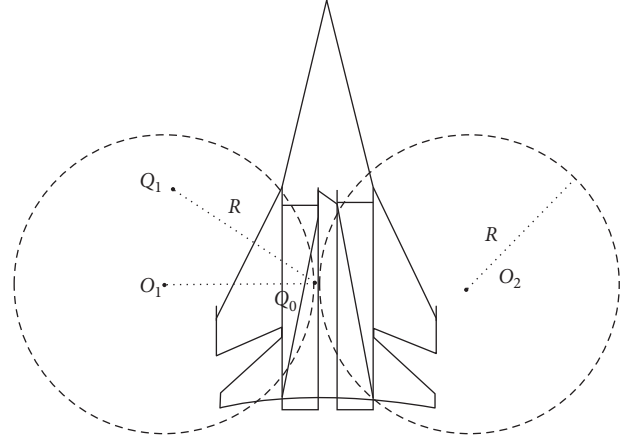


FIGURE 6: Circle with the minimum turning radius.

$$\text{cost} = \sum l + \beta \sum \text{turns}. \quad (22)$$

**3.3. Reference Trajectory Generation.** In the tracking problem, the generated path will be transformed into an allowable trajectory, that is, the solution of the differential equation of the traction system motion model [31]. The reference trajectory can be indicated as

$$\begin{aligned} x_{2r} &= x(t), \\ y_{2r} &= y(t). \end{aligned} \quad (23)$$

From the kinematics model of equation (1), we can get

$$v_r = \pm \sqrt{\left(\frac{dx_{1r}}{dt}\right)^2 + \left(\frac{dy_{1r}}{dt}\right)^2}, \quad (24)$$

where  $x_{1r} = x_{2r} + l_2 \cos \theta_{2r}$ ,  $y_{1r} = y_{2r} + l_2 \sin \theta_{2r}$ .

Simultaneously,  $\theta_{2r} = \arctan(y'_{2r}/x'_{2r}) = (y''_{2r}x'_{2r} - y'_{2r}x''_{2r})/(x'^2_{2r} + y'^2_{2r})$  and  $\theta_{1r} = \theta_{2r} + \arctan(l_2\theta'_{2r}/v_r)$ . So far, the system's reference trajectory input  $[\theta_{1\text{ref}} \ x_{2\text{ref}} \ y_{2\text{ref}} \ \theta_{2\text{ref}}]^T$  is obtained, and the reference trajectory and its derivatives are continuous and uniformly bounded [4].

## 4. Trajectory Tracking

Aiming at the various state constraints of the system, we use a model predictive controller to track any reference trajectory and then achieve control of the driving torque through adaptive control in dynamics.

### 4.1. Model Predictive Controller

**4.1.1. Controller Design.** According to the discrete linearized state equation in Section 2.1, the trajectory tracking control is performed using the model predictive control method. The design structure of the controller is shown in Figure 7.

Let  $N_p$  be the predicted time domain and  $N_c$  be the control time domain; the system output in the predicted time domain can be presented by the following formula:

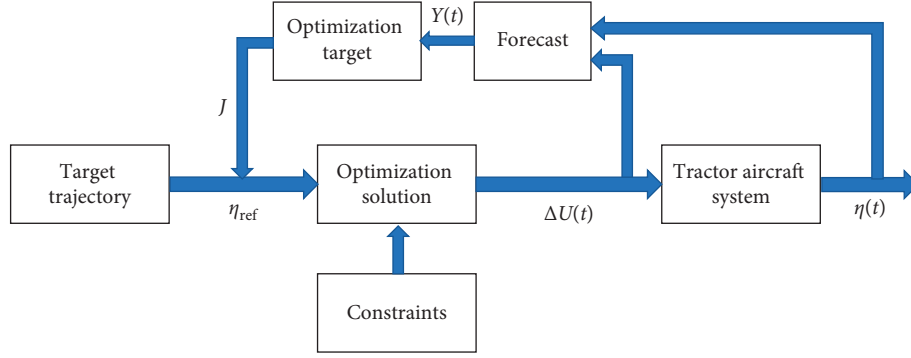


FIGURE 7: Structure of MPC controller.

$$Y(t) = \begin{bmatrix} \eta(t+1|t) \\ \eta(t+2|t) \\ \vdots \\ \eta(t+N_p|t) \end{bmatrix}. \quad (25)$$

The system input is defined as the amount of change in the input variable at each moment in the control time domain:

$$\Delta U(t) = \begin{bmatrix} \Delta u(t|t) \\ \Delta u(t+1|t) \\ \vdots \\ \Delta u(t+N_c|t) \end{bmatrix}. \quad (26)$$

Then, the prediction output in the system prediction time domain can be formulated by

$$Y(t) = \psi_t \xi(t|t) + \Lambda_t \Delta U(t), \quad (27)$$

where

$$\psi_t = \begin{bmatrix} C_t A_t \\ C_t A_t^2 \\ \vdots \\ C_t A_t^{N_p-1} \end{bmatrix}, \quad (28)$$

$$\Lambda_t = \begin{bmatrix} C_t B_t & 0 & 0_{4 \times 2} & 0_{4 \times 2} \\ C_t A_t B_t & C_t B_t & 0_{4 \times 2} & 0_{4 \times 2} \\ \vdots & \vdots & \ddots & \vdots \\ C_t A_t^{N_c-1} B_t & C_t A_t^{N_c-2} B_t & \cdots & C_t B_t \\ C_t A_t^{N_c} B_t & C_t A_t^{N_c-1} B_t & \cdots & C_t A_t B_t \\ \vdots & \vdots & \ddots & \vdots \\ C_t A_t^{N_p-1} B & C_t A_t^{N_p-2} B & \cdots & C_t A_t^{N_p-N_c-1} B \end{bmatrix}.$$

The purpose of designing the controller is to enable the carrier-based aircraft to track the target trajectory quickly and with as little error as possible and make it possible for the change of the control amount to be smoother. The objective function  $J$  mainly considers the tracking performance of the controller.

$$J_1 = \sum_{i=1}^{N_p} \|\eta(t+i|t) - \eta_{ref}(t+i|t)\|_Q^2, \quad (29)$$

where  $Q$  is the output weighting matrix and  $\eta_{ref} = [\theta_{1ref} \ x_{2ref} \ y_{2ref} \ \theta_{2ref}]^T$  is the reference trajectory. At the same time, the control variable is considered to make the control variable change to the minimum in the control time domain:

$$J_2 = \sum_{i=1}^{N_c-1} \|\Delta u(t+i|t)\|_R^2, \quad (30)$$

where  $R$  is the control weighting matrix. At the same time, a relaxation factor  $\varepsilon$  is added to ensure that the system that changes in real time has a feasible solution at every moment. The final objective function is:

$$\min J = J_1 + J_2 + \sigma \varepsilon^2. \quad (31)$$

In the actual control system, constraints such as control variable constraints, control increment constraints, and output constraints must be met:

$$\text{s.t.} \begin{cases} u_{\min}(t+k|t) \leq u(t+k|t) \leq u_{\max}(t+k|t), \\ \Delta u_{\min}(t+k|t) \leq \Delta u(t+k|t) \leq \Delta u_{\max}(t+k|t), \\ k = 0, 1, \dots, N_c - 1, \\ \eta_{\min}(t+k|t) - \varepsilon \leq \eta(t+k|t) \leq \eta_{\max}(t+k|t) + \varepsilon. \end{cases} \quad (32)$$

Solving the above optimization problem will get the input increment in the control time domain:  $\Delta U_t^* = [\Delta u_t^*, \Delta u_{t+1}^*, \dots, \Delta u_{t+N_c-1}^*]^T$ . In each step, the first element in the control increment is taken as the input of the system, and the control system executes this input until the next step. Through continuous feedback optimization, a new control increment sequence is obtained for each cycle, and the cycle ends until the system completes the optimization of the entire control process.

**4.1.2. Parameter Optimization.** Controller parameters are usually adjusted by engineering experience, which takes a long time. Genetic algorithm is a heuristic swarm intelligence optimization algorithm, which has fast convergence speed and is not easy to fall into a local optimum. This article

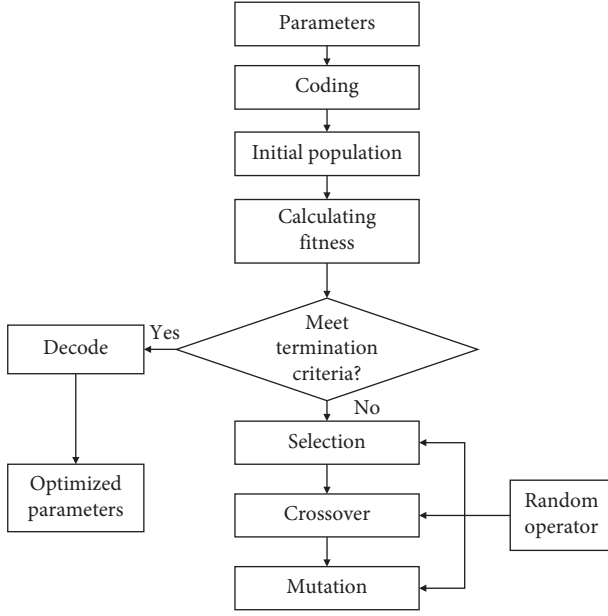


FIGURE 8: Flowchart of the genetic algorithm.

uses genetic algorithms to optimize the parameters in the MPC controller. The algorithm flow diagram is shown in Figure 8.

The parameters are first encoded and the initial population is generated. The parameters to be optimized include the prediction time domain, the control time domain, and the weighting matrix. Randomly generate  $P_N$  initial string structure data in the parameter solution space (i.e., one chromosome), set the maximum number of iterations  $k$ , and randomly generate  $P_M$  chromosomes as the initial population  $P(0)$ . The fitness function maps the quality of the solution. Considering the stability, accuracy, and speed of the system, the following fitness function is used:

$$J_{\text{opt}} = \frac{\sum_{i=0}^N (w_1 |E_i| + w_2 u_i^2 + w_3 |EY_i|)}{N}. \quad (33)$$

Among them,  $w_1, w_2, w_3$  is the weight coefficient;  $E_i = \sqrt{(\sum_{j=1}^{N_p} (Y(i+j) - Y_{\text{ref}}(i+j))^2 / N_p)}$  represents the tracking error at each step;  $u_i$  is the control input, that is, the MPC controller output; each step of the system overshoots  $EY_i = Y(i) - Y(i-1)$ , and when the overshoot exceeds a certain threshold, this index is used as an index in the fitness function; when it is not exceeded,  $w_3 = 0$ . The smaller the fitness value is, the better the solution is.

The genetic algorithm calls the controller model a subfunction. The parameters of the genetic algorithm are set as follows: population size  $P_M = 20$ , number of iterations  $k = 50$ , and weight  $w_1 = 0.9, w_2 = 0.1, w_3 = \begin{cases} 0, & EY_i < EY_{\text{threshold}} \\ 10, & EY_i \geq EY_{\text{threshold}} \end{cases}$ .

**4.2. Self-Adaptive Fuzzy PID Dynamics Controller.** The tractor-aircraft system has a complicated working environment on the deck and is prone to unstable driving under external interference. Therefore, it is necessary to regulate the stability of the system. The yaw rate and the centroid yaw

angle can reflect the yaw stability of the tractor, so they are selected as the control variables. In this process, by adding a yaw moment to the tractor, the actual state and ideal state deviation of the centroid yaw angle and yaw rate during the tractor's driving process are controlled as targets, so that the system is stable within a reasonable range.

Design a fuzzy PID controller with the control variable error and error change rate as input signals. The PID parameters are adjusted online by the fuzzy controller, so that the center of mass sideslip angle and yaw rate tend to ideal values. The control structure diagram of the control system is shown in Figure 9, where  $\omega_{r-1}$  is yaw rate of ideal model and  $\beta_{r-tractor}$  is the centroid yaw angle of ideal model.

The ideal transfer function and ideal state space equation of the system are

$$X_r(s) = \begin{bmatrix} \beta_{r-tractor}(s) \\ \omega_{r-1}(s) \end{bmatrix} = \begin{bmatrix} \frac{k_\beta}{1 + t_\omega s} \\ \frac{k_\omega}{1 + t_\omega s} \end{bmatrix} \psi(s), \quad (34)$$

$$\dot{X}_r = A_r X_r + C_r \psi, \quad (35)$$

where

$$A_r = \begin{pmatrix} -\frac{1}{t_\beta} & 0 \\ 0 & -\frac{1}{t_\omega} \end{pmatrix},$$

$$C_r = \begin{bmatrix} b_r + \frac{k_\beta}{t_\beta} \\ \frac{k_\omega}{t_\omega} \end{bmatrix}, \quad (36)$$

$$k_\beta = \frac{c_1 a_{22} - a_{12} c_2 + a_{12} h_2 z_1}{a_{11} a_{22} - a_{12} a_{21}},$$

$$z_1 = \frac{a_{22} c_1 + a_{12} c_2}{a_{12} h_2},$$

$$t_\beta = \frac{1}{(zh_1 - c)} k_\beta,$$

$$k_\omega = \frac{(a_{21} h_1 - a_{11} h_2) z - a_{21} c_1 - a_{12} c_2}{a_{11} a_{22} - a_{12} a_{21}},$$

$$t_\omega = \frac{1}{(c_2 + zh_2)} k_\omega.$$

Because the differential term  $\dot{\psi}$  is added to the dynamics model (18), there is a constant in  $C_r$  of the state equation, which is the structural parameter  $b_r$  of the tractor system.

According to the ideal state space equation, the ideal sideslip angle and ideal yaw rate  $X_r$  can be estimated. The

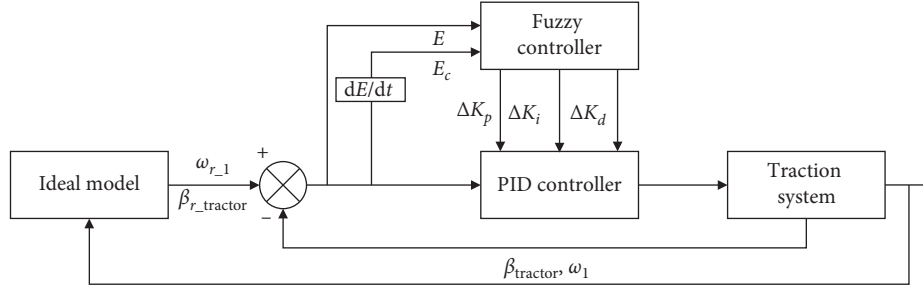


FIGURE 9: Adaptive fuzzy PID controller structure.

deviation of the actual control variable from the ideal control variable is

$$e(k) = X'(k) - X_r(k). \quad (37)$$

The function of deviation evaluation index is

$$E(k) = e(k)^T Q e(k). \quad (38)$$

Let  $Q = [1 \ 0; 0 \ 1]$ . The additional yaw moment is

$$M_f(k) = (K_p + \Delta K_p) \cdot E(k) + (K_i + \Delta K_i) \cdot \sum_{i=0}^k E(k) + (K_d + \Delta K_d) \cdot [E(k) - E(k-1)], \quad (39)$$

where  $K_p, K_i$ , and  $K_d$  are PID control parameters and  $\Delta K_p, \Delta K_i$ , and  $\Delta K_d$  are fuzzy controller output parameters.

The error  $E$  and the error variety rate  $E_c$  are defined as the discourse domain on the fuzzy set  $U_1$ , both of which are  $\{-1, -0.8, \dots, 0.8, 1\}$ , and the output variable domain  $U_2$  is  $\{-3, -2, -1, 0, 1, 2, 3\}$ . The membership function is shown in Figures 10 and 11. The input and output fuzzy subsets are defined as  $\{NB, NM, NS, ZE, PS, PM, PB\}$ . The membership functions are all triangles. This sharper membership function has higher resolution and sensitivity.

To ensure the real-time control, the fuzzy control rule table is obtained by offline calculation. With reference to the general experience of fuzzy adaptive control strategies, the fuzzy control rules are given in Table 1.

## 5. Simulation and Analysis

In order to verify the accuracy and stability of the controller, the classic trajectory and deck travel task trajectory in the tracking problem were simulated respectively, and their tracking effects were compared.

### 5.1. Classical Trajectories

**5.1.1. Line Trajectory with Initial Deviation.** According to the movement of the carrier-based aircraft on the deck, set the connection parameters  $L_1 = 1, L_2 = 0.2$ , traction speed constraints  $|v| \leq 2\text{m/s}$ , acceleration constraints  $|a| \leq 2\text{m/s}^2$ , and front wheel steering angle incremental constraints  $|\Delta\delta| \leq 1$ . Assuming the initial states  $[\theta_1, x_2, y_2, \theta_2]^T = [0, 0, 0, 0]^T$ , the above controller is employed to control the

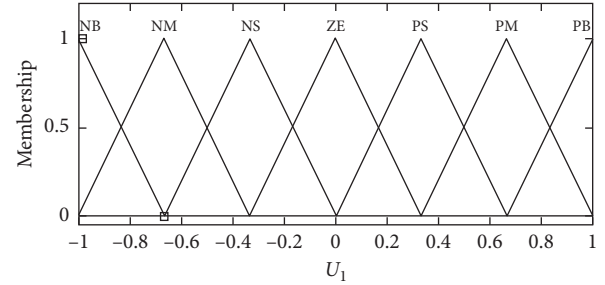


FIGURE 10: Membership function of input universe.

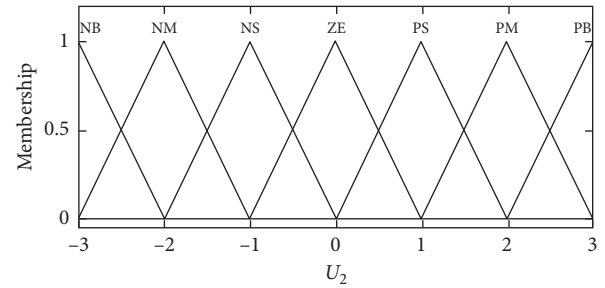


FIGURE 11: Membership function of output universe.

TABLE 1: Fuzzy control rules.

$E_c$	$E$						
	NB	NM	NS	ZE	PS	PM	PB
NB	PB	PB	PM	PM	PS	PS	ZE
NM	PB	PB	PM	PS	PS	ZE	ZE
NS	PB	PM	PM	PS	ZE	NS	NS
ZE	PM	PM	PA	ZE	NS	NS	NM
PS	PM	PS	ZE	NS	NS	NM	NM
PM	PS	ZE	NS	NS	NM	NM	NB
PB	ZE	NS	NS	NM	NM	NB	NB

traction system to track the expected straight line. The simulation results are as shown in Figure 12.

It can be seen that the system is adjusted by the controller in about 2 s, which completely suppresses the initial error and achieves accurate tracking of the linear trajectory.

In order to display the effect of different initial deviations on the system, different initial deviation combinations shown in Table 2 were used for simulation. The results obtained are as follows.

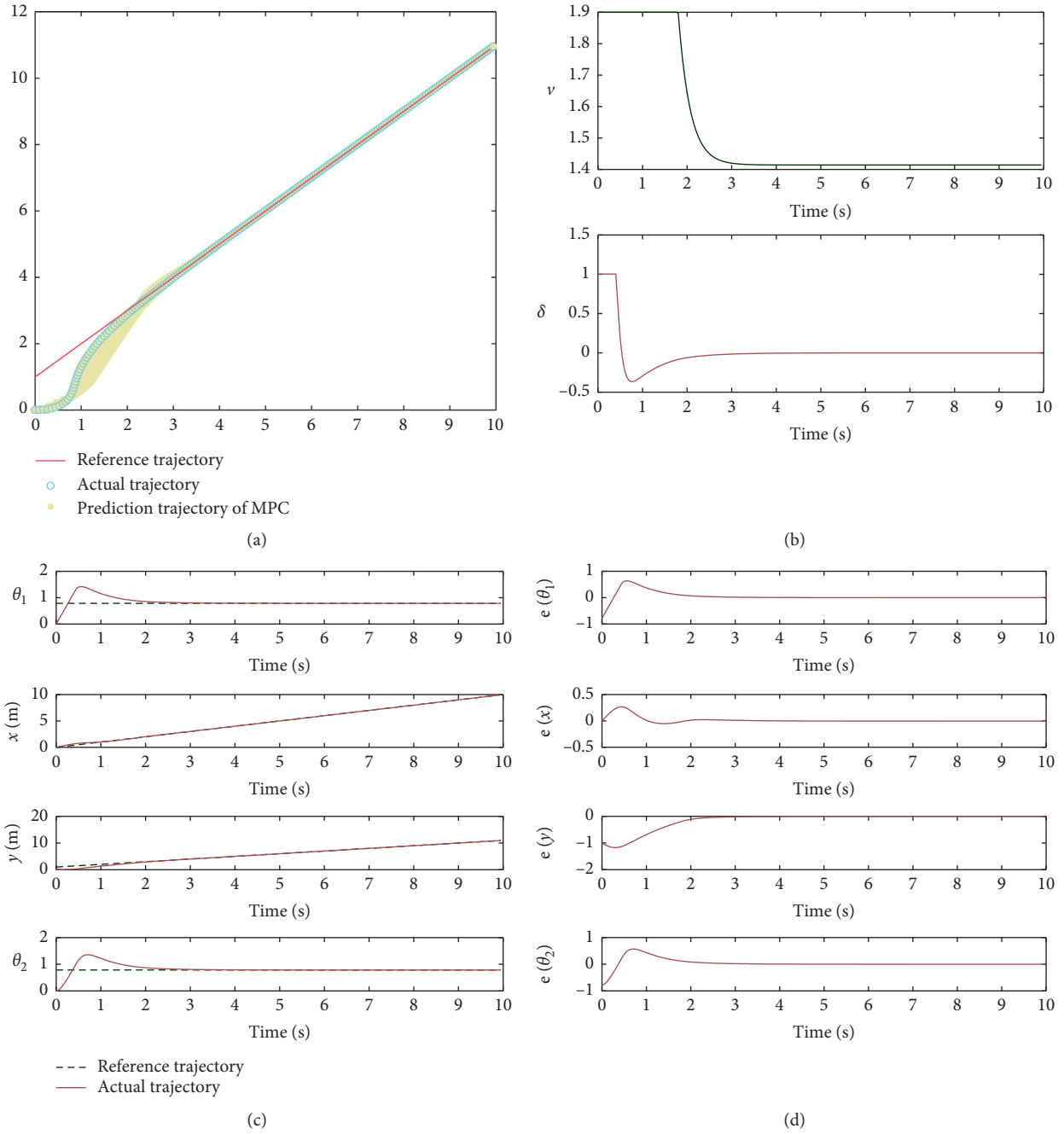


FIGURE 12: Simulation results of line trajectory with initial deviation. (a) Linear trajectory tracking result. (b) Changes of control variables. (c) Changes of state variables. (d) Tracking errors of state variables.

TABLE 2: The parameters of initial deviation.

	$\Delta\theta_1$	$\Delta x$	$\Delta y$	$\Delta\theta_2$
1	0.1	0.5	-2.0	0.1
2	0.1	-0.5	3.0	0.1
3	0.1	-0.5	-4.0	0.1
4	1	0	-1.0	1

Figures 13(a)–13(d) show the errors of the tractor’s orientation angle, aircraft’s abscissa, aircraft’s ordinate, and aircraft’s yaw angle under different initial errors,

respectively. Although the system has some overshoot when the initial error is too large, the suppression of the initial error is basically completed within 5 s in all four cases. In

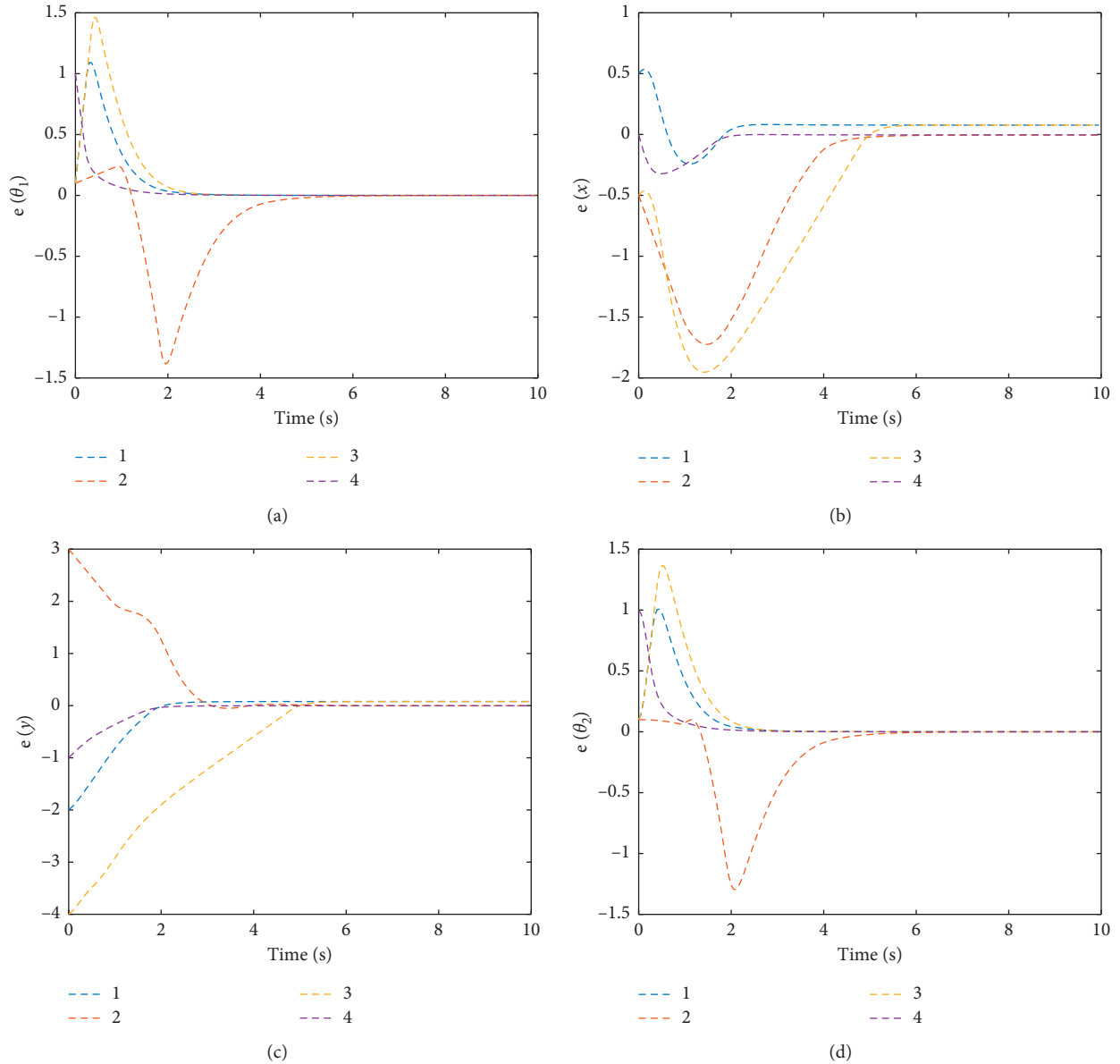


FIGURE 13:  $e(\theta_1), e(x), e(y), e(\theta_2)$  for different initial deviation.

addition, the control input changes smoothly and is constantly adjusted within the bounds to achieve the optimum. The simulation shows that the control algorithm in this paper can quickly suppress the initial error of the linear trajectory without the steady-state error.

### 5.1.2. Sine Curve with Large Curvature

(1) *MPC Results.* Assume that the connection parameters  $L_1 = 1, L_2 = 0.2$ , traction speed constraint  $|v| \leq 5\text{m/s}$ , acceleration constraint  $|a| \leq 2\text{m/s}^2$ , and front wheel steering angle incremental constraint  $|\Delta\delta| \leq 1$ . Assuming the initial error is 0, the above controller is used to control the traction system to track a sine curve with a large curvature.

As can be seen from Figures 14(a)–14(d), the designed controller can always move forward and the tracking error in the horizontal and vertical directions does not exceed 1. The input variable is continuously adjusted within the constraint range. Due to the large curvature of the curve, the steering angle of the front wheel needs to be continuously adjusted. Overshoot occurs only when the steering angle needs to be adjusted significantly, and good performance of the system is shown in other times.

(2) *Track Tracking with Initial Deviation.* Similarly, in order to show the influence of the initial deviation on the sine curve's tracking, four different initial deviation parameters shown in Table 3 are mainly selected for simulation. The simulation result is shown in Figure 15.

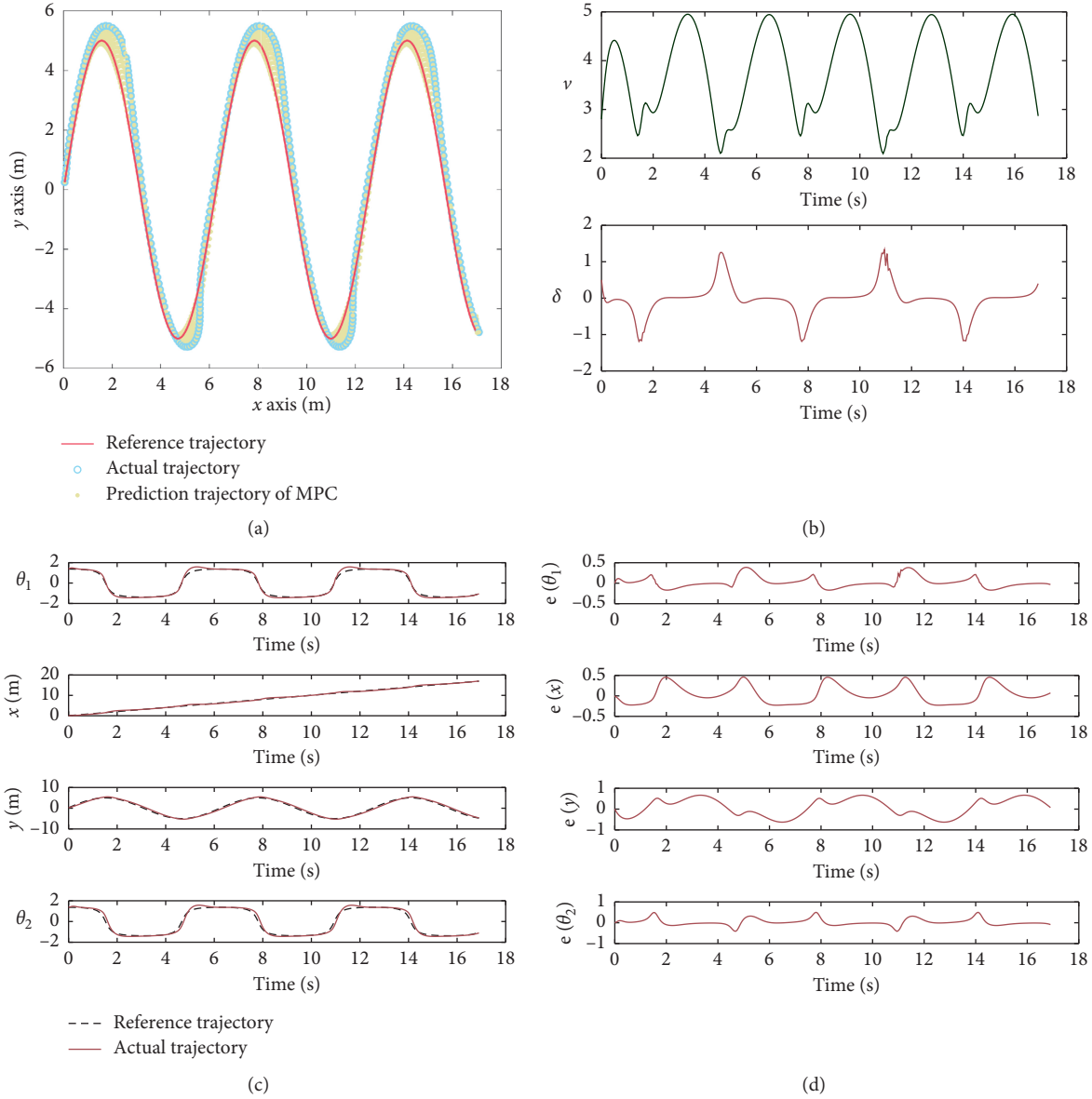


FIGURE 14: Simulation result of sine curve with large curvature. (a) Sine curve tracking result. (b) Changes of control variables. (c) Changes of state variables. (d) Tracking errors of state variables.

TABLE 3: The parameters of initial deviation.

	$\Delta\theta_1$	$\Delta x$	$\Delta y$	$\Delta\theta_2$
1	0.1	0.5	0.5	0.1
2	0.1	1.0	1.0	0.1
3	0.6	0.5	0.5	0.6
4	1	0.5	0.5	1

From Figures 15(a)–15(d), it can be seen that when the initial horizontal and vertical coordinate errors are large, the system will have some overshoot, while other cases can gradually converge to the desired trajectory within the allowable error range. In case 4, when the initial angle deviation reaches 1, it can also quickly converge to the target trajectory.

## 5.2. Deck Trajectories

### 5.2.1. Transfer Route between Flight Deck Stations

(1) *Route via RRT\* Algorithm.* The task of carrier-based aircraft transfer on the flight deck requires it to move from the initial station to the target station and avoid collision



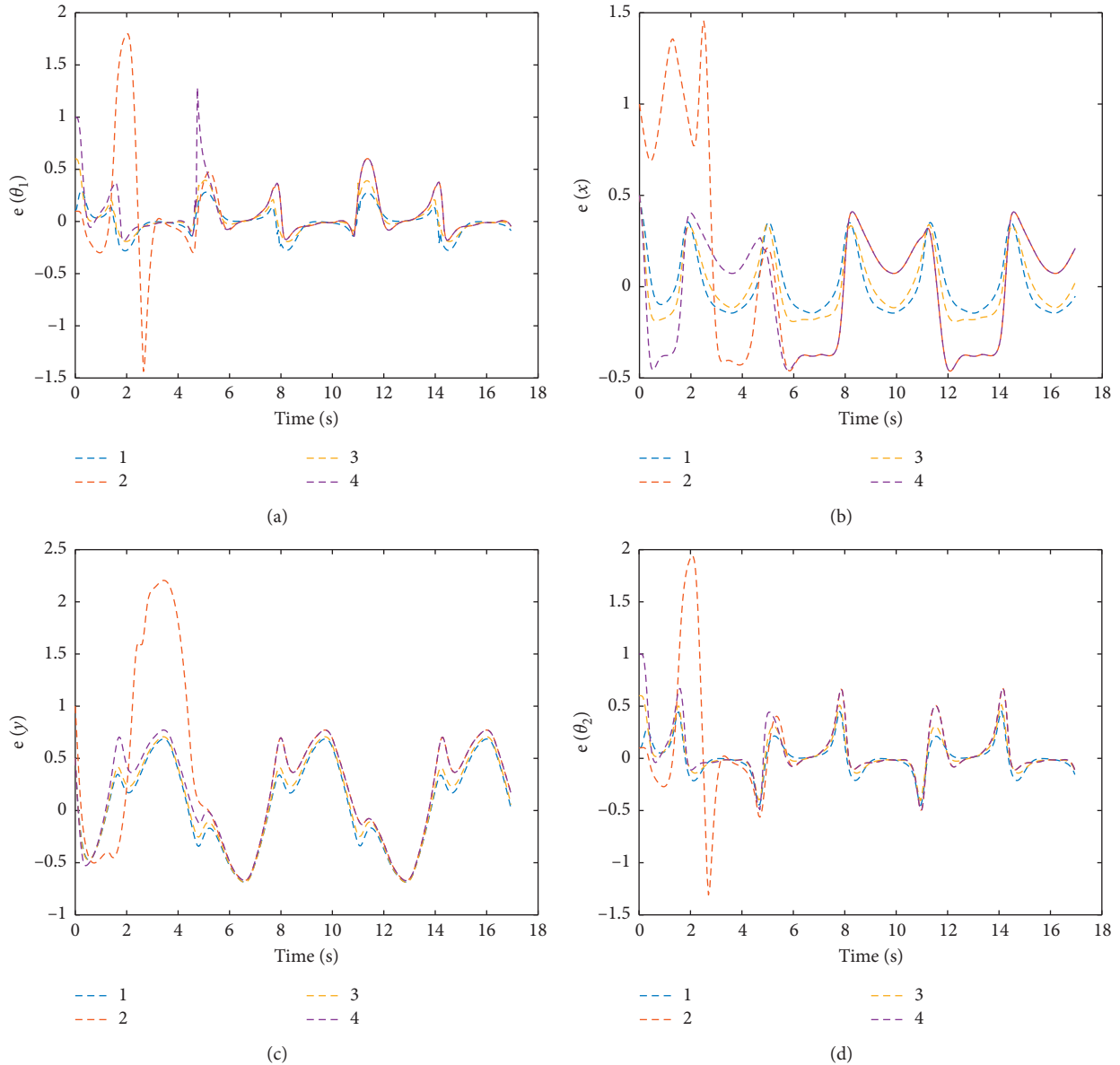
FIGURE 15:  $e(\theta_1), e(x), e(y), e(\theta_2)$  for different initial deviation.

TABLE 4: Parameters for ship obstacle.

Station name	$x$ (m)	$y$ (m)	Direction angle ( $^\circ$ )	Wing condition
A2	-5.500	-14.500	90	Folded wings
A3	-23.502	-13.031	90	Spread wings
A11	-76.526	32.360	342	Folded wings
Z5	-44.001	-14.500	90	Spread wings
H4	-30.328	22.999	0	Folded wings
A12	-97.526	29.861	340	Folded wings

with all carrier-based aircraft parked on the deck, and a certain safety distance is required. The following figure shows an example where six carrier-based aircraft are parked on the surface of the ship. The specific parameters are shown in the Table 4 and the parameters of traction system are shown in Table 5.

TABLE 5: Parameters of traction system.

Parameter	Value
$l_1$ (m)	5
$l_2$ (m)	10
Turning radius of aircraft (m)	10
Weight of aircraft (t)	20
Wight of tractor (t)	5
Safe distance (m)	3
Initial position (m)	(12.5, -30.5)
Target position (m)	(-129.828, 7.0)

The optimal Reed-Shepp path between two stations on the deck is calculated by the algorithm in Section 3.2, which meets the end position and direction requirements and can effectively avoid all obstacles. The aircraft first makes a left turn motion, and the direction angle gradually becomes larger. After the left turn is completed, it enters a linear motion. After

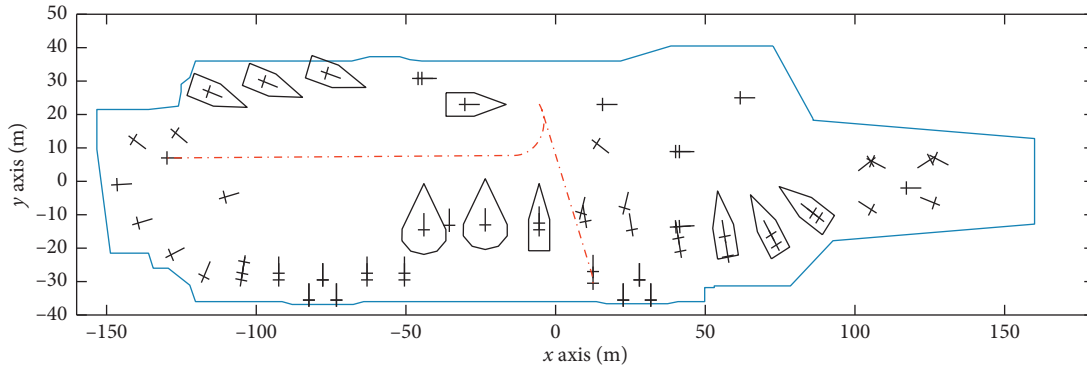


FIGURE 16: Path generation between stations with collision avoidance on deck.

the linear motion ends, it needs to return to the target station by reversing. The path is shown in Figure 16.

(2) *Experimental Results.* In order to verify the tracking effect of the controller on the deck, the above-mentioned trajectory was simulated without initial errors and the parameter optimization algorithm. Simultaneously, stability controller proposed in Chapter 3 was applied to the system.

The genetic algorithm's parameters are set as follows: population size  $n=20$ , maximum iteration number  $max\_gen=50$ , cross probability  $p_{cross}=0.7$ , and mutation probability  $p_{mutation}=0.01$ ; the fitness curve and trajectory tracking results are shown in Figures 17 and 18, and the optimized parameters of the controller are shown in Table 6.

As can be seen from the above Figure 19, the algorithm can better track the expected trajectory when the system is backing up. At the beginning, due to the large change in direction angle, the steering angle of the front wheel changes rapidly, and it can be quickly stabilized in the straight phase. When entering the back-up phase, the control input can be adjusted quickly. The carrier-based aircraft keeps up with the reference trajectory and immediately stabilizes. The error converges to zero. It shows that the control algorithm in this paper can track the motion trajectory of the carrier-based aircraft on the deck well. At the same time, due to the chattering phenomenon of turning vehicles, the stability of the tractor after control is better than the data before dynamics control. This stability is mainly reflected in the fact that the yaw angular velocity and centroid skew angle after the yaw moment control can meet the requirements of vehicle handling stability better than before.

For the purpose of studying whether the controller can achieve good robustness in the presence of errors, different initial deviation combinations are used for the above simulation experiments. The main initial deviations are as follows.

The error change curves in the four cases are shown in Figure 20. It can be seen that, in the four cases, the final system can gradually converge to a stable state. The direction angle deviation and the system overshoot of case 4 are large, but it can accurately track to the predetermined position after about 10s. For cases 1–3, the corresponding error changes are relatively gentle, indicating that, for this complex trajectory, the algorithm proposed in this paper can effectively suppress the initial error.

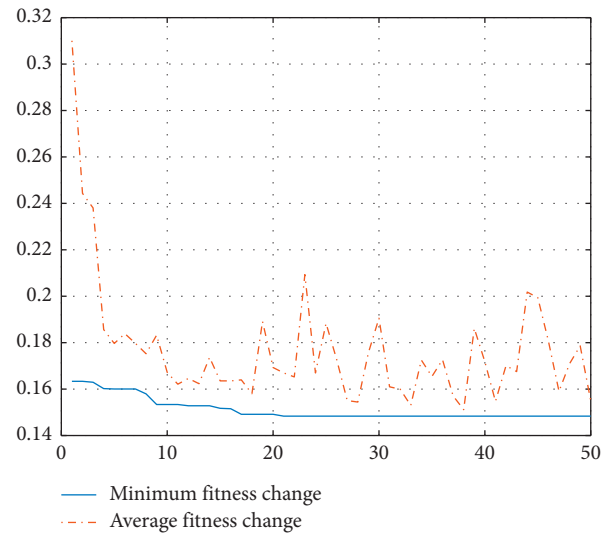


FIGURE 17: Fitness curve of GA.

### 5.2.2. Route between Recycling Station and Waiting Station

(1) *Route via RRT\* Algorithm.* After landing on the flight deck, the carrier-based aircraft will dock at the recycling station. If the carrier-based aircraft is to prepare for the next wave of take-off, it needs to be towed to a waiting position for subsequent support operations. Assume the following situation of obstacles; the RRT\* algorithm is applied to generate the traction route from the recycling station to the waiting station as shown in Figure 21.

(2) *Experimental Results.* Without the initial error, the control algorithm proposed in Section 3 is used to track the above trajectory, and the tracking results are shown in Figures 22 and 23.

It can be seen from the tracking error graph that the algorithm can perform stable tracking in the straight phase, but for the instantaneous reversing path or the path with a rapidly changing direction angle, the algorithm needs an adjustment time. During 138~148 s, the tractor drags the carrier-based aircraft to make a turning movement. Since the steering angle of the tractor needs to be continuously changed during this process, the system control is more

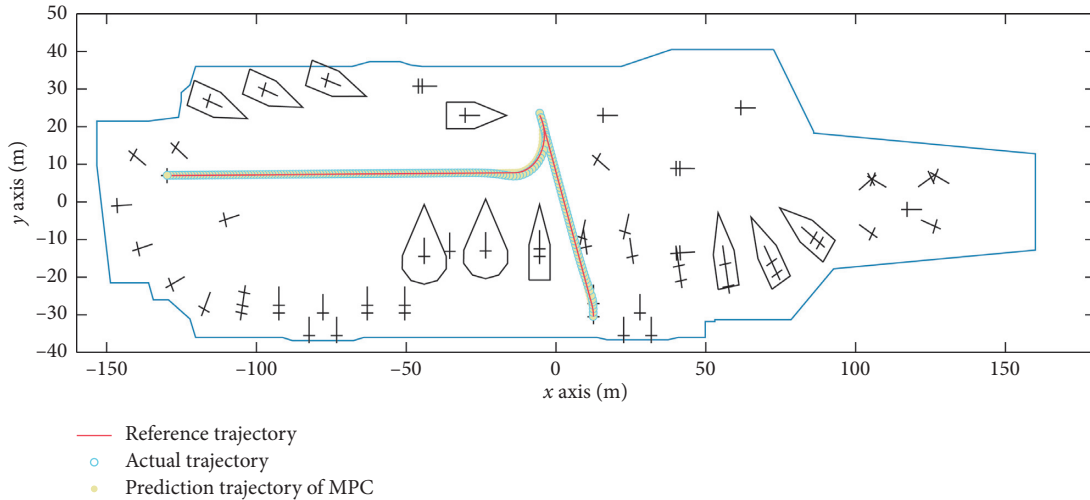


FIGURE 18: Trajectory tracking results between deck stations.

unstable and more sensitive to errors. The overall overshoot is within the range of  $[-1, 1]$ , which is an acceptable error range for carrier-based aircraft movement. In Figures 23(d) and 23(e), after adjusting the additional torque, the overshoot of the yaw angular velocity and the center of mass side deviation angle are smaller, the adjustment time is shorter, and the system has better stability.

Similarly, simulation experiments with different initial deviation were performed on the recycling station route, and the initial deviation parameters in Table 7 were used. Figures 24(a)–24(d) are the error change curves in the four cases, and it can be seen that the four cases are all effective in suppressing the initial error. Among them, case 4 caused greater fluctuations due to the change in direction angle, but all achieved good suppression in about 20 s. This shows that the algorithm used in this paper can effectively track the complex path between the recycling station and the waiting station and meets various constraints of the system.

**5.3. Controller Comparison.** In order to prove the superiority of the algorithm in this paper, especially for the tracking of complex trajectories, we performed comparative simulations on the straight lines with initial deviations, the sine curves, and the trajectories between deck stations. The classical backstepping control [17] and LQR algorithm [32] are compared with the algorithm in this paper.

Figures 25–27 show the tracking trajectory and the relationship between the abscissa, ordinate, and angle error of the aircraft-tractor system over time under three algorithms. It can be analyzed from three different trajectories:

- (1) For tracking of linear trajectory, both backstepping control and LQR algorithm can finally reach steady state, but the adjustment time is too long. Throughout the tracking process, the algorithm in

TABLE 6: Controller parameters after optimization.

Parameter	Value
Sampling time: $T$	1
$N_p$	50
$N_c$	6
$Q$	$[0.01 \ 0 \ 0 \ 0; 0 \ 1 \ 0 \ 0; 0 \ 0 \ 1 \ 0; 0 \ 0 \ 0 \ 1]$
$v_r$	1.0032
$\delta_r$	0.0032

this paper shows strong superiority, and the effect on suppressing the initial error is obviously greater than the other two algorithms.

- (2) For tracking of sine curve, the errors of three algorithms have amplifying tendency at sharp turns, and they gradually stabilize on gentle road sections. Backstepping control regulates the direction angle in real time through the feedback of steering angle to minimize the error. However, it can be seen that the speed control is unsatisfactory, which results in a large lateral tracking error compared with MPC algorithm. From the graph, we can see that the LQR algorithm has obvious fluctuation, and the maximum error is more than twice that of the algorithm in this paper. The algorithm in this paper also has an advantage in tracking the sine curve.
- (3) For the traction path of the towbarless tractor system on deck, LQR algorithm does not track well. The reason is that when the system changes from forward driving to reverse parking, the speed direction changes. The algorithm cannot converge to a stable state finally due to the changes during reversing, and the tracking error is larger than the algorithm proposed in this paper. As for backstepping control, the controller is not sensitive and stable to the speed's adjustment, which results in a very large overshoot.

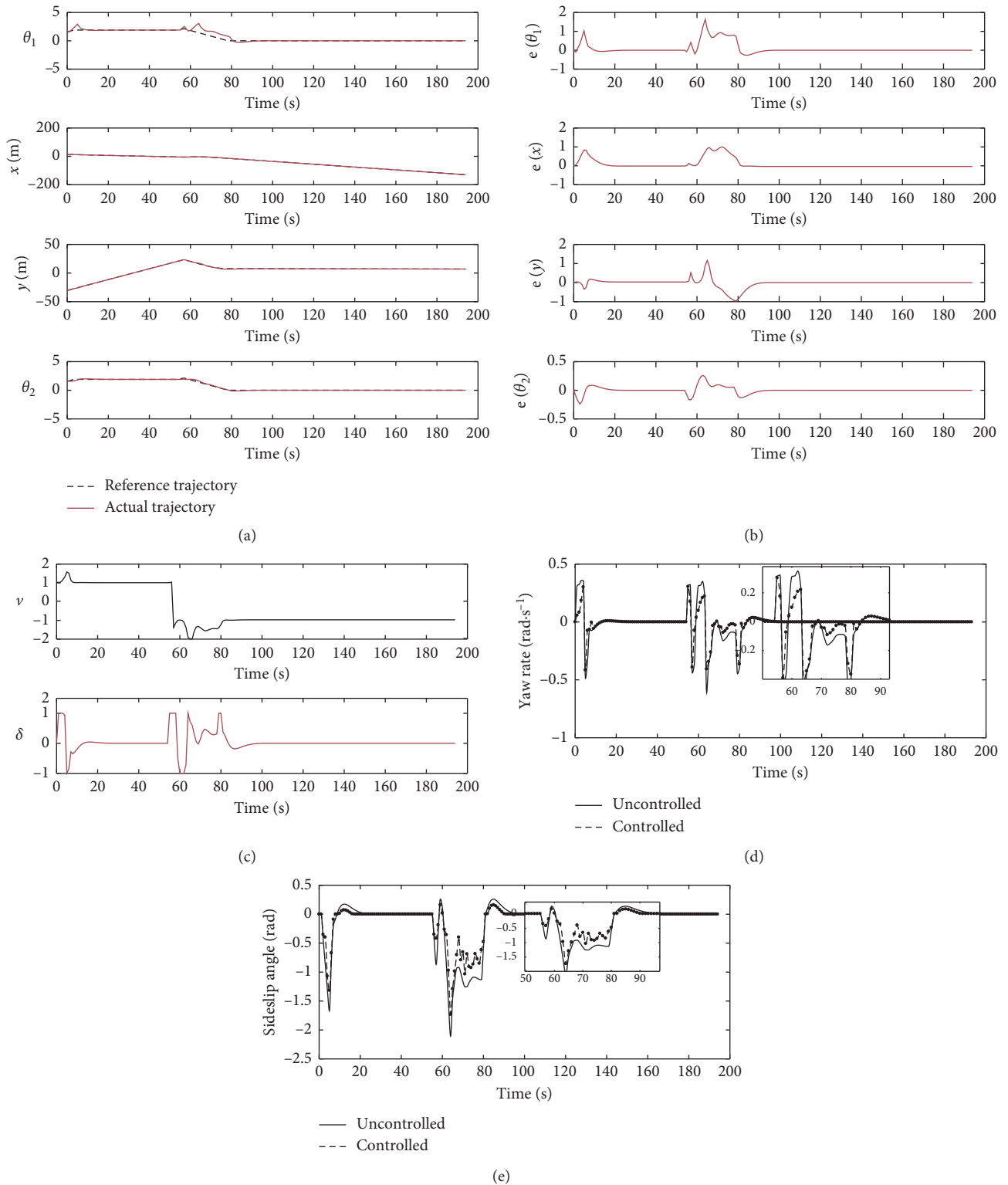


FIGURE 19: Tracking simulation results of transfer paths between deck stations. (a) Changes of state variables. (b) Tracking errors of state variables. (c) Changes of control variables. (d) Changes of yaw angular velocity. (e) Changes of centroid skew angle.

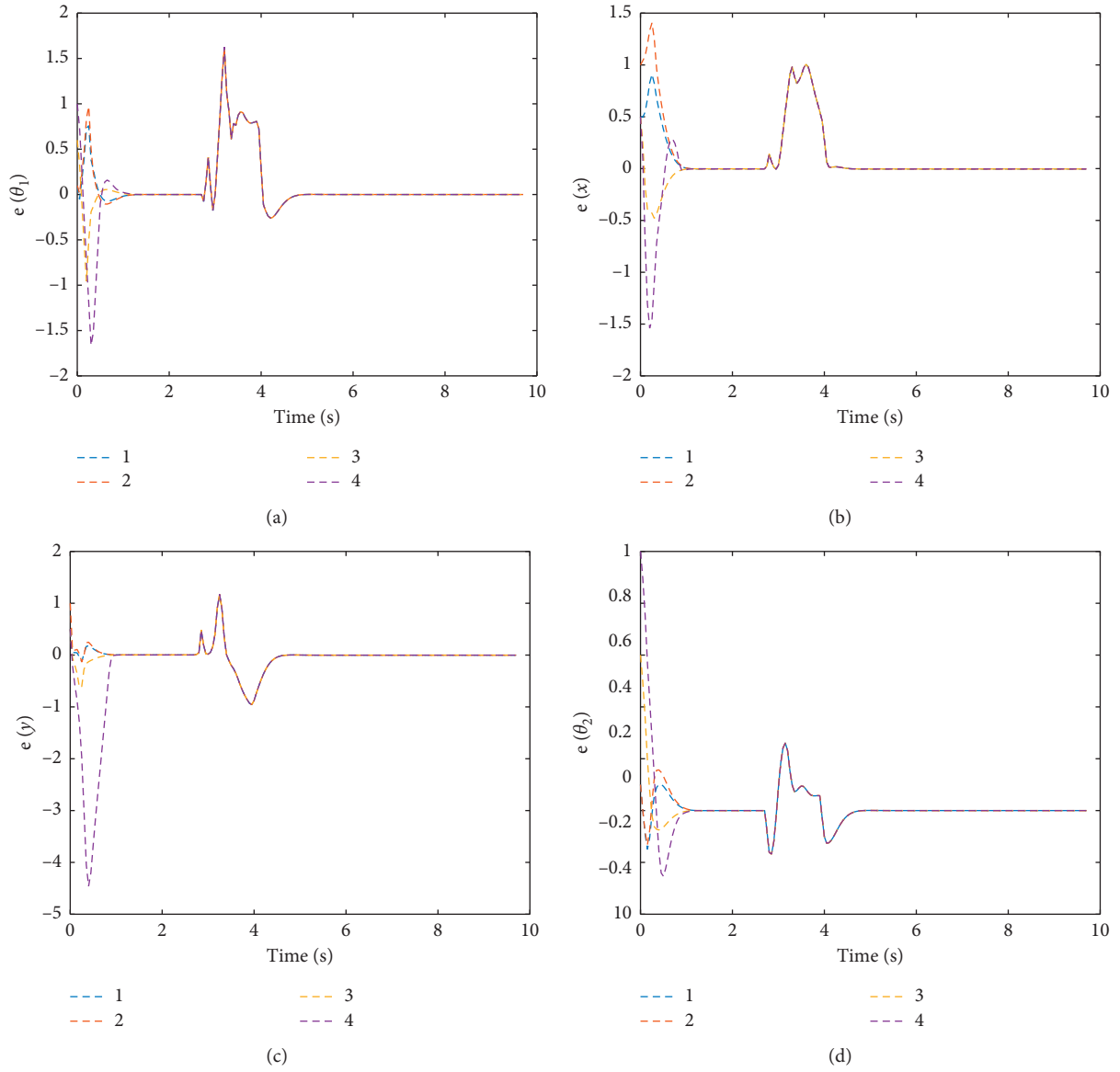


FIGURE 20:  $e(\theta_1), e(x), e(y), e(\theta_2)$  for different initial deviation.

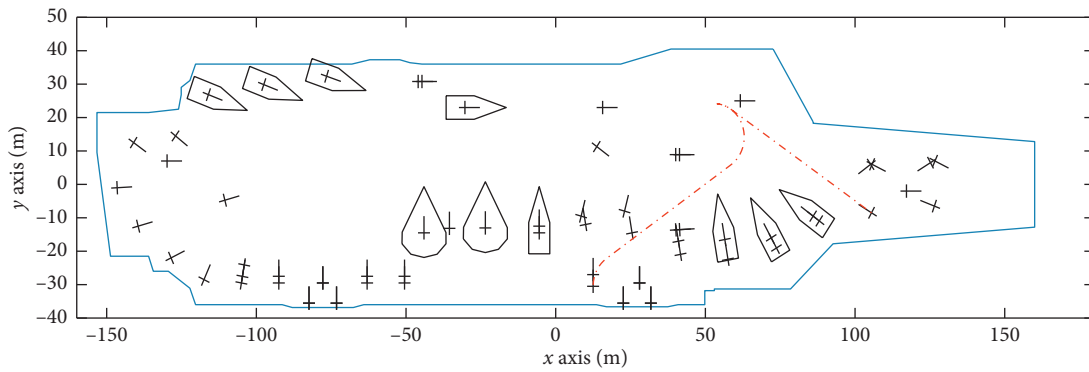


FIGURE 21: Path generation between recycling station and deck station.

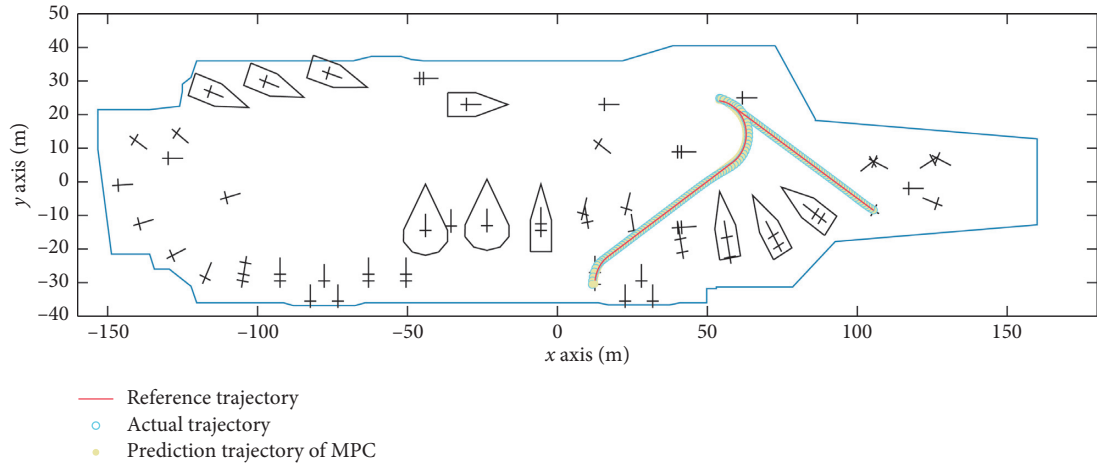
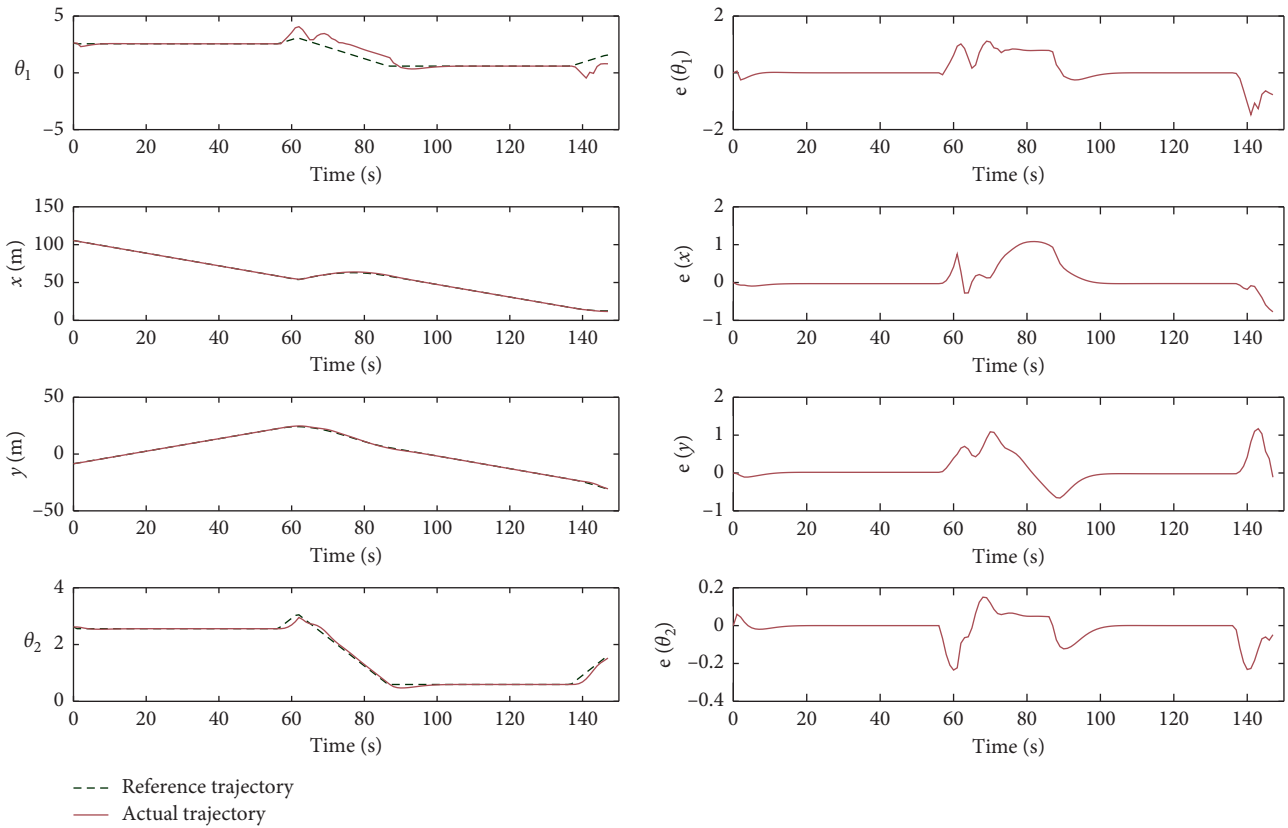


FIGURE 22: Trajectory tracking results between recycling station and waiting station.



(a)

(b)

FIGURE 23: Continued.

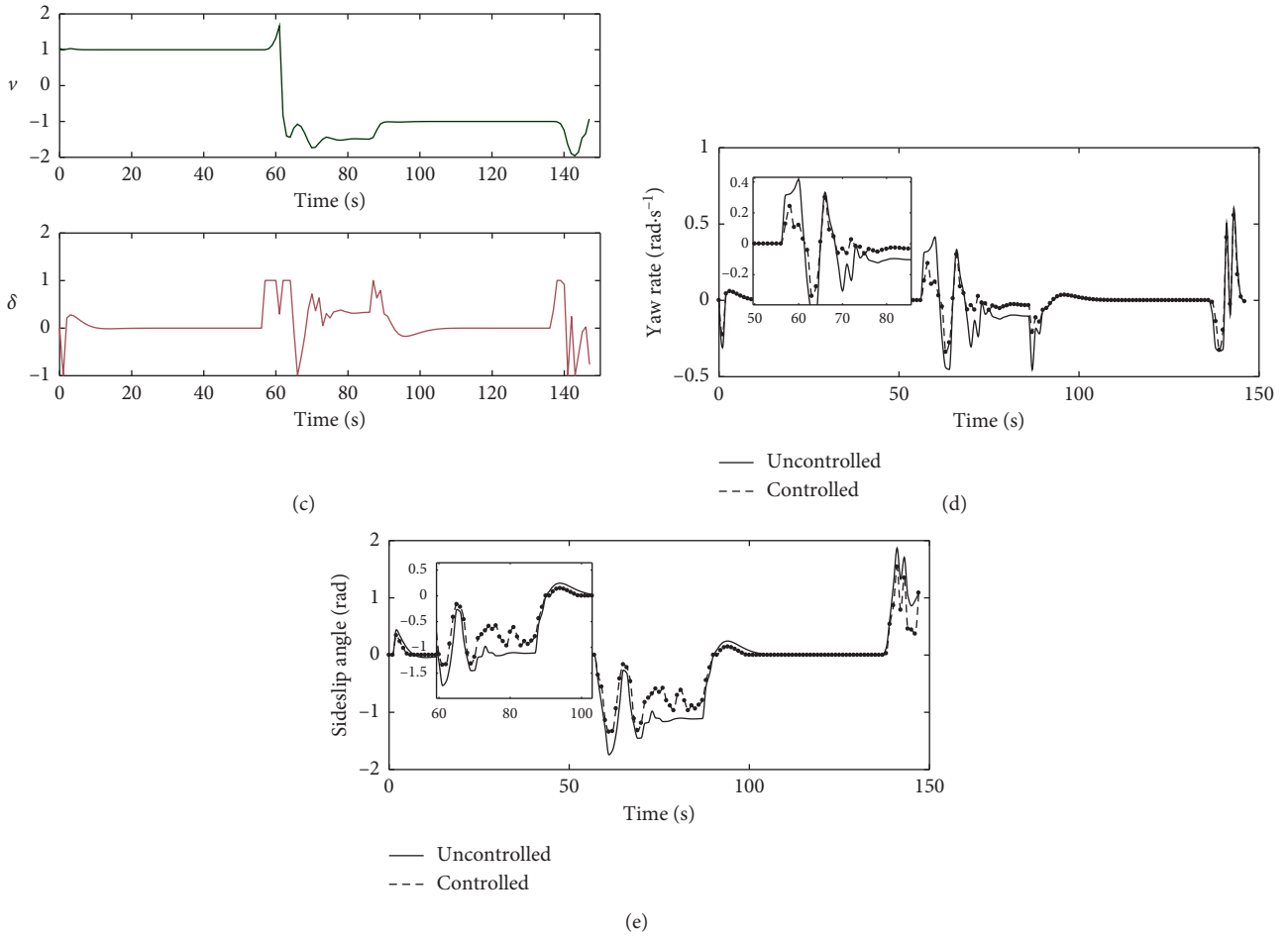


FIGURE 23: Tracking simulation results of transfer paths between recycling station and waiting station. (a) Changes of state variables. (b) Tracking errors of state variables. (c) Changes of control variables. (d) Changes of yaw angular velocity. (e) Changes of centroid skew angle.

TABLE 7: The parameters of initial deviation.

	$\Delta\theta_1$	$\Delta x$	$\Delta y$	$\Delta\theta_2$
1	0.1	0.5	0.5	0.1
2	0.1	1.0	1.0	0.1
3	0.6	0.5	0.5	0.6
4	1	0.5	0.5	1

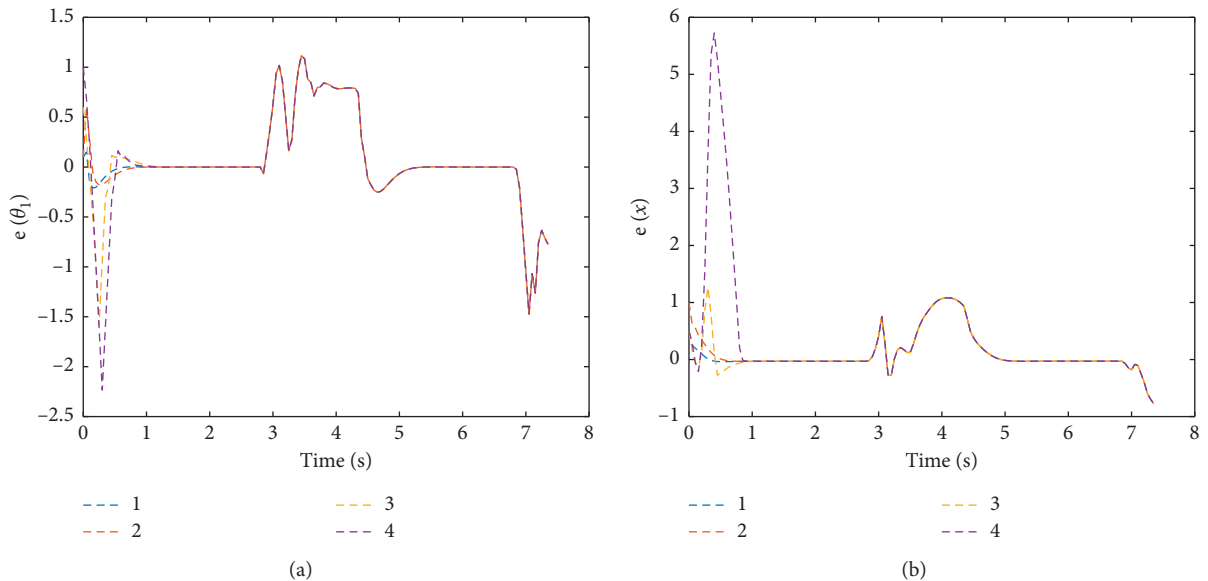


FIGURE 24: Continued.

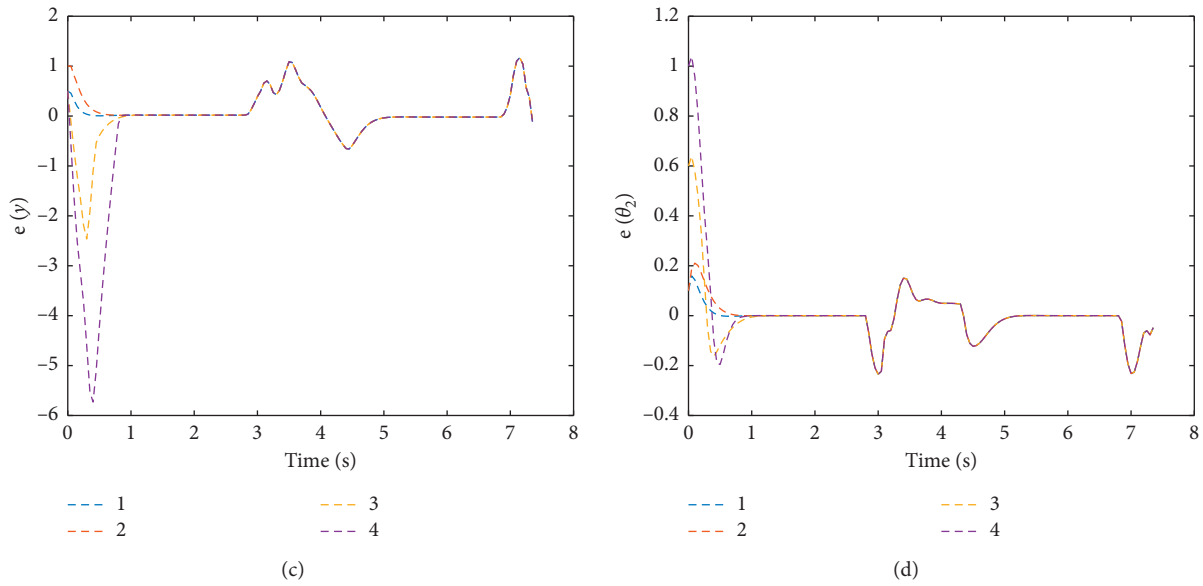


FIGURE 24:  $e(\theta_1), e(x), e(y), e(\theta_2)$  for different initial deviation.

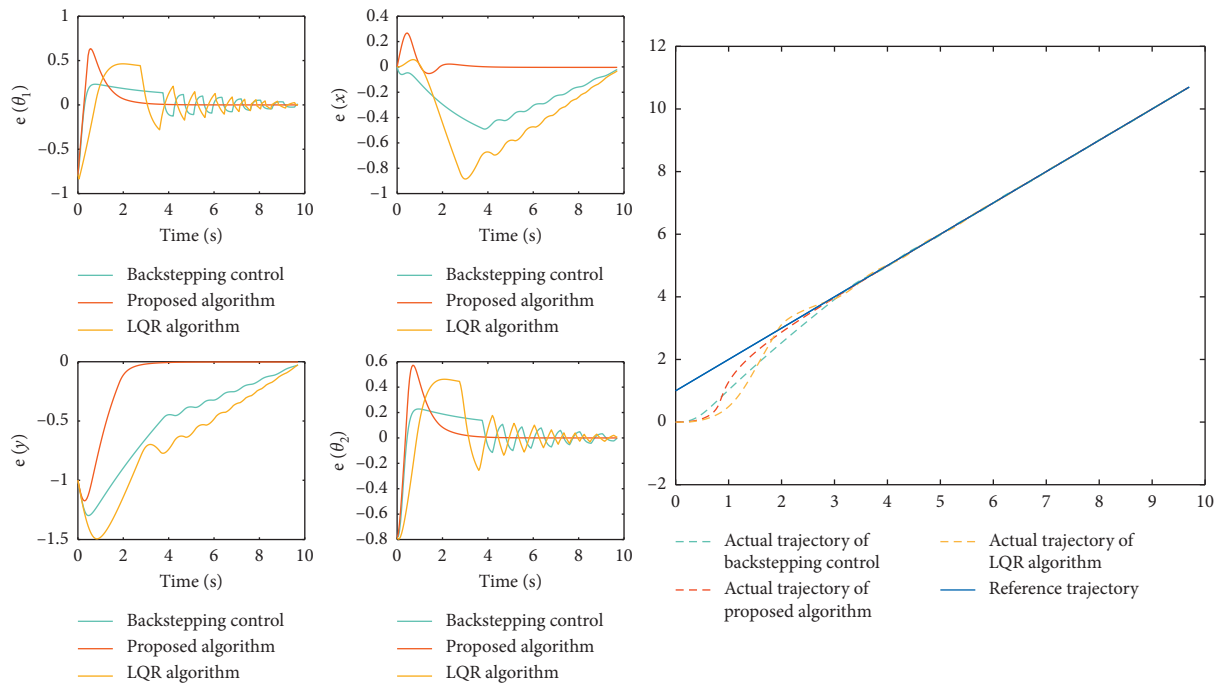


FIGURE 25: Line trajectories with initial deviation.

There is a certain degree of fluctuation in the second half. In contrast, the algorithm in this paper has small overshoot and fast response, which is more suitable for tracking complex trajectories on deck.

In summary, the trajectory tracking algorithm based on MPC proposed in this paper can be effectively applied to the trajectory tracking problem of towbarless traction systems.



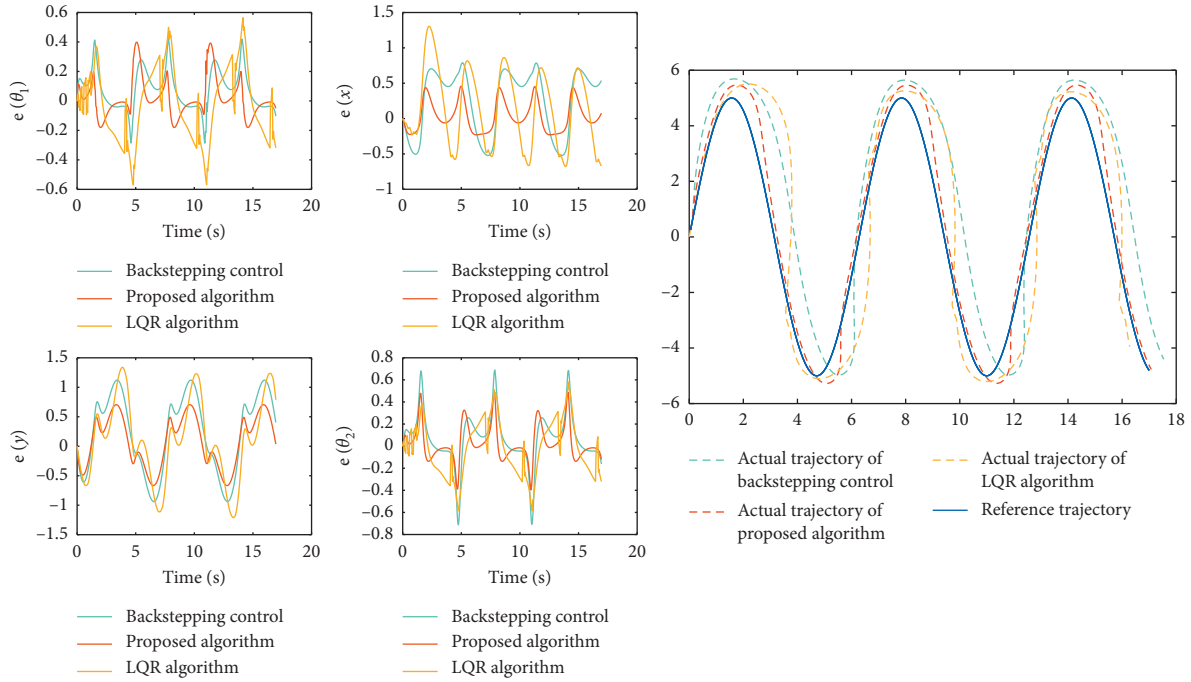


FIGURE 26: Sine curve with large curvature.

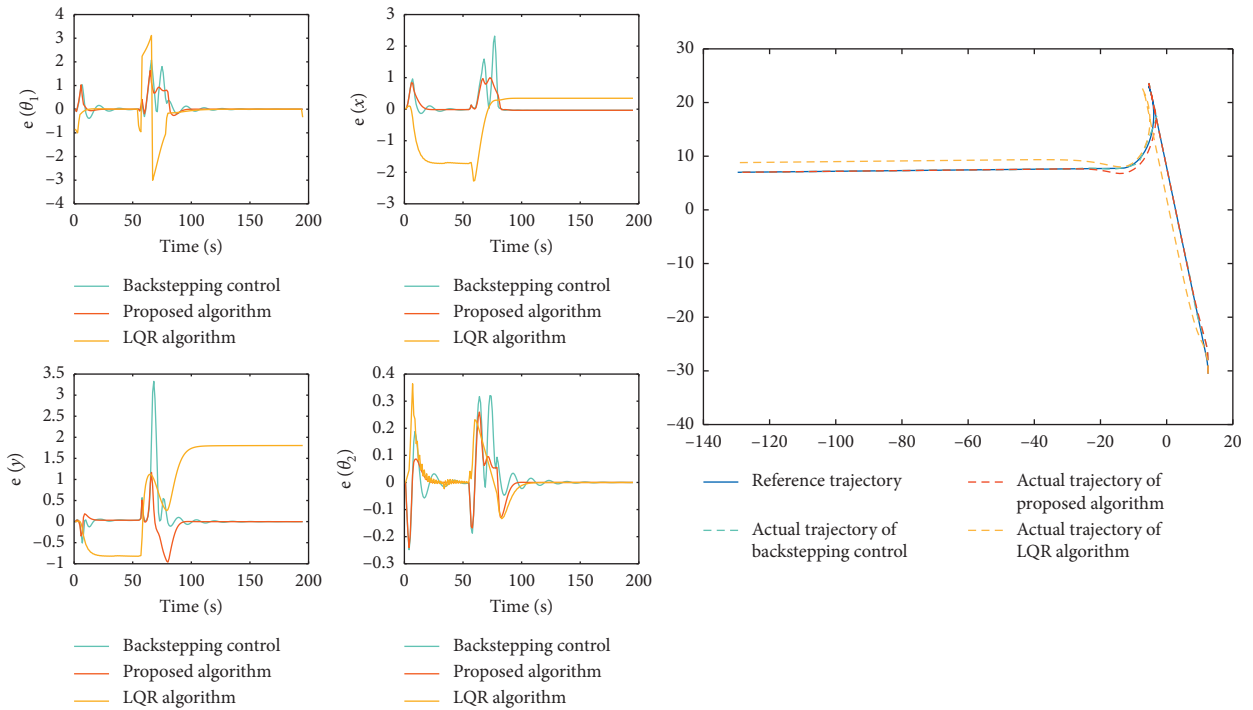


FIGURE 27: Deck trajectory.

### 6. Conclusion

In this paper, considering the noncontact constraints and various conditions, we propose a solution to the problem of tracking complex trajectories on the deck of a towbarless tractor-aircraft system. First, the strategy is proposed to

control multiple aircrafts to plan trajectory cooperatively and the method based on RRT\* is used to generate optimal path with obstacle. Then we construct model predictive controller (MPC) to track the reference trajectory and fully consider the dynamic performance of the system. Moreover, self-adaptive fuzzy PID controller is applied to control the

dynamics parameter to ensure the stable operation of the plane and greatly improve the anti-interference ability of the system. By tracking straight lines, sine curves with large curvature, and two complex trajectories on the deck, the controller can make the system quickly converge to the desired trajectory, which proves the robustness and accuracy of the system. At the same time, compared with feedback control and LQR control, the tracking accuracy and speed of the algorithm in this paper are far superior to the other two control methods. It shows that the traditional method finds difficulty in solving the complex state constraints and the strict control constraints at the same time. In other words, the proposed method can achieve the promising accuracy and stability and has practical application potential. In the near future, we plan to apply the algorithm in an aircraft carrier simulation system to evaluate our method in a real environment, which will be more challenging.

### Data Availability

The data used to support the findings of this study are included within the article. Because of ethical concerns, the original data cannot be made openly available.

### Conflicts of Interest

The authors declare that they have no conflicts of interest.

### Acknowledgments

This work was supported by the National Natural Science Foundation of China under Grant no. 61403255 and the National Defense Science Foundation Project of China under Grant no. JCKY 2017207B005.

### References

- [1] B. Michini and J. How, "A human-interactive course of action planner for aircraft carrier deck operations," in *Proceedings of the AIAA Information Technology*, March 2011.
- [2] B. Li, T. Acarman, Y. Zhang, L. Zhang, C. Yaman, and Q. Kong, "Tractor-trailer vehicle trajectory planning in narrow environments with a progressively constrained optimal control approach," *IEEE Transactions on Intelligent Vehicles*, p. 1, 2020.
- [3] X. Wang, H. Su, X. Wang, and G. Chen, "Fully distributed event-triggered semiglobal consensus of multi-agent systems with input saturation," *IEEE Transactions on Industrial Electronics*, vol. 64, no. 6, pp. 5055–5064, 2017.
- [4] X. L. Wang, H. Su, M. Z. Q. Chen, X. F. Wang, and G. Chen, "Reaching non-negative edge consensus of networked dynamical systems," *IEEE Transactions on Cybernetics*, vol. 48, no. 9, pp. 2712–2722, 2018.
- [5] X. L. Wang, H. Su, M. Z. Q. Chen, and X. Wang, "Observer-based robust coordinated control of multi-agent systems with input saturation," *IEEE Transactions on Neural Networks and Learning Systems*, vol. 529, no. 5, pp. 1933–1946, 2018.
- [6] Y. Liu and H. Su, "Containment control of second-order multi-agent systems via intermittent sampled position data communication," *Applied Mathematics and Computation*, vol. 362, no. 362, p. 124522, 2019.
- [7] X. Wang and H. Su, "Self-triggered leader-following consensus of multi-agent systems with input time delay," *Neurocomputing*, vol. 330, pp. 70–77, 2019.
- [8] Y. Liu and H. Su, "Some necessary and sufficient conditions for containment of second-order multi-agent systems with sampled position data," *Neurocomputing*, vol. 378, no. 378, pp. 228–237, 2020.
- [9] R. Kong, "Accurate parking planning of tractor-trailer-trailer mobile robot," in *Proceedings of the 2012 IEEE International Conference on Mechatronics and Automation*, pp. 1220–1226, IEEE, Chengdu, China, August 2012.
- [10] N. T. Binh, N. A. Tung, D. P. Nam, and N. H. Quang, "An adaptive backstepping trajectory tracking control of a tractor trailer wheeled mobile robot," *International Journal of Control Automation and Systems*, vol. 17, no. 2, pp. 465–473, 2019.
- [11] J. Cai, H. Jiang, L. Chen, J. Liu, Y. Cai, and J. Wang, "Implementation and development of a trajectory tracking control system for intelligent vehicle," *Journal of Intelligent & Robotic Systems*, vol. 94, no. 1, pp. 251–264, 2019.
- [12] Y. Wu, L. Sun, and X. Qu, "A sequencing model for a team of aircraft landing on the carrier," *Aerospace Science and Technology*, vol. 54, pp. 72–87, 2016.
- [13] D. Wu, Q. Zhang, and J. F. Reid, "Adaptive steering controller using a Kalman estimator for wheel-type agricultural tractors," *Robotica*, vol. 19, no. 5, pp. 527–533, 2001.
- [14] E. Kayacan, E. Kayacan, H. Ramon, O. Kaynak, and W. Saeys, "Towards agrobots: trajectory control of an autonomous tractor using type-2 fuzzy logic controllers," *IEEE/ASME Transactions on Mechatronics*, vol. 20, no. 1, pp. 287–298, 2015.
- [15] A. K. Khalaji and S. A. A. Moosavian, "Robust adaptive controller for a tractor-trailer mobile robot," *IEEE/ASME Transactions on Mechatronics*, vol. 19, no. 3, pp. 943–953, 2014.
- [16] Z. Huofeng, M. Baoli, S. Lihui, and F. F. Zhang, "Path following control of tractor-trailers with off-axle hitching," *Acta Automatica Sinica*, vol. 36, no. 9, pp. 1272–1278, 2010.
- [17] N. Lashkari, M. Biglarbegian, and S. X. Yang, "Backstepping tracking control design for a tractor robot pulling multiple trailers," in *Proceedings of the 2018 Annual American Control Conference (ACC)*, pp. 2715–2720, IEEE, Milwaukee, WI, USA, June 2018.
- [18] R. Werner, G. Kormann, and S. Mueller, "Systematic model based path tracking control of actively steered implements in simulation and experiment," *IFAC Proceedings Volumes*, vol. 46, no. 18, pp. 85–90, 2013.
- [19] Y. Bin, T. Shim, F. Nenglian, and D. Zhou, "Path tracking control for backing-up tractor-trailer system via model predictive control," in *Proceedings of the 24th Chinese Control and Decision Conference (CCDC)*, pp. 198–203, IEEE, Taiyuan, China, 2012.
- [20] M. Yue, X. Hou, M. Fan, and R. Jia, "Coordinated trajectory tracking control for an underactuated tractor-trailer vehicle via MPC and SMC approaches," in *Proceedings of the 2nd International Conference on Advanced Robotics and Mechatronics (ICARM)*, pp. 82–87, IEEE, Hefei, China, August 2017.
- [21] E. Kayacan, H. Ramon, and W. Saeys, "Robust trajectory tracking error model-based predictive control for unmanned ground vehicles," *IEEE/ASME Transactions on Mechatronics*, vol. 21, no. 2, pp. 806–814, 2016.
- [22] J. Backman, T. Oksanen, and A. Visala, "Navigation system for agricultural machines: nonlinear model predictive path tracking," *Computers and Electronics in Agriculture*, vol. 82, no. 82, pp. 32–43, 2012.

- [23] E. Kayacan, E. Kayacan, H. Ramon, and W. Saeys, "Learning in centralized nonlinear model predictive control: application to an autonomous tractor-trailer system," *IEEE Transactions on Control Systems Technology*, vol. 23, no. 1, pp. 197–205, 2015.
- [24] H. Fan, S. Li, H. Ding, and J. Zhang, "Simulation analysis of vehicle trajectory tracking based on model predictive control," in *Proceedings of the 2009 IEEE 28th International Symposium on Industrial Electronics (ISIE)*, pp. 1892–1897, IEEE, Vancouver, BC, Canada, June 2019.
- [25] N. Wang, H. Liu, and W. Yang, "Simulation study of the backward-motion for a aircraft towbarless tractor," in *Proceedings of the IEEE Conference Anthology*, pp. 1–5, IEEE, China, January 2013.
- [26] M. Karkee and B. L. Steward, "Study of the open and closed loop characteristics of a tractor and a single axle towed implement system," *Journal of Terramechanics*, vol. 47, no. 6, pp. 379–393, 2010.
- [27] W. Jianchun and L. Wang, "Transient and steady responses of articulated vehicle to disturbance moment(I)," *Mining and Processing Equipment*, vol. 9, no. 36, pp. 26–29, 2008.
- [28] F. You, R. Zhang, G. Lie, H. Wang, H. Wen, and J. Xu, "Trajectory planning and tracking control for autonomous lane change maneuver based on the cooperative vehicle infrastructure system," *Expert Systems with Applications*, vol. 42, no. 14, pp. 5932–5946, 2015.
- [29] J. M. Kim, K. I. Lim, and J. H. Kim, "Auto parking path planning system using modified Reeds-Shepp curve algorithm," in *Proceedings of the 2014 11th International Conference on Ubiquitous Robots and Ambient Intelligence (URAI)*, pp. 311–315, IEEE, Kuala Lumpur, Malaysia, November 2014.
- [30] L. Han, Q. H. Do, and S. Mita, "Unified path planner for parking an autonomous vehicle based on RRT," in *Proceedings of the 2011 IEEE International Conference on Robotics and Automation*, pp. 5622–5627, IEEE, Shanghai, China, May 2011.
- [31] J. Yuan, F. Sun, and Y. Huang, "Trajectory generation and tracking control for double-steering tractor-trailer mobile robots with on-axle hitching," *IEEE Transactions on Industrial Electronics*, vol. 62, no. 12, pp. 7665–7677, 2015.
- [32] B. Paden, M. Cap, S. Z. Yong, D. Yershov, and E. Frazzoli, "A survey of motion planning and control techniques for self-driving urban vehicles," *IEEE Transactions on Intelligent Vehicles*, vol. 1, no. 1, pp. 33–55, 2016.

## Research Article

# Distributed Optimal Control of Transient Stability for a Power Information Physical System

Shiming Chen and Kaiqiang Li 

East China Jiaotong University, Nanchang 330013, China

Correspondence should be addressed to Kaiqiang Li; 601613012@qq.com

Received 26 March 2020; Accepted 9 May 2020; Published 26 May 2020

Guest Editor: Michael Z. Q. Chen

Copyright © 2020 Shiming Chen and Kaiqiang Li. This is an open access article distributed under the Creative Commons Attribution License, which permits unrestricted use, distribution, and reproduction in any medium, provided the original work is properly cited.

The development of power energy structures and information communication technology has promoted the renewal of smart grid information-physical structures. At the same time, the changes in the smart grid energy structure and the vulnerability of the information network threaten the stability of the power system and uses multiagent control theory to improve the transient stability of the power grid which has strong practicability. In this paper, an optimized distributed control scheme is proposed for application to the smart grid model so that the grid system can flexibly adapt to the external operating conditions and recover to stable operating conditions after being disturbed. In this paper, an intelligent power grid information-physical network simulation system is established. According to the information exchange within the multiagent system, groups of coherent generators in the disturbed power grid in different regions are identified and controlled. Distributed control is applied to maintain the exponential frequency synchronization and phase angle aggregation of the synchronous generators to achieve transient stability. Finally, the effectiveness and rapidity of the proposed distributed optimal control scheme are verified by simulation analysis of the IEEE 39 node model.

## 1. Introduction

With the reorganization and renewal of the energy structure in recent years, the standards of smart grid systems in terms of their transient stability have been raised. A smart grid itself is based on the ultra-high-voltage UHV backbone transmission network and deeply integrates more stable information network technology to establish a strong power system network, realizing close connection and integration of the power system and information system [1]. The development of CPSs promotes the deep integration of physical power systems and power information systems. It provides a new way to realize the goal of power grid intelligence [2]. In the smart grid model, the information network dispatching centre node collects and processes the information of each physical power station and sends corresponding control instructions. Each physical power station supplies power to the information node to ensure its normal operation. Through this connection, the mutual

dependent relationship between the physical network and the information network is formed (Figure 1) [3]. With the intelligent development of smart grids, there is a dynamic interaction among the five “generation, transmission, supply, distribution, and use” terminals of smart grids with the two-way flow of energy and information [4], new energy, and other distributed energy grid connections and huge data processing between the information network and the physical network. Additionally, the basic characteristics of smart grid informatization, automation, and interaction are the operational belt of the great smart grid challenge [5, 6].

Information systems and information networks play an important role in enhancing the safe operation of smart grids. In actual operation, the dependence of the physical system on the information system will significantly affect the stable operation of the physical system in the case of information system failure. In actual operation, the cost of communication and information processing should also be considered. The use of redundant information and weakly

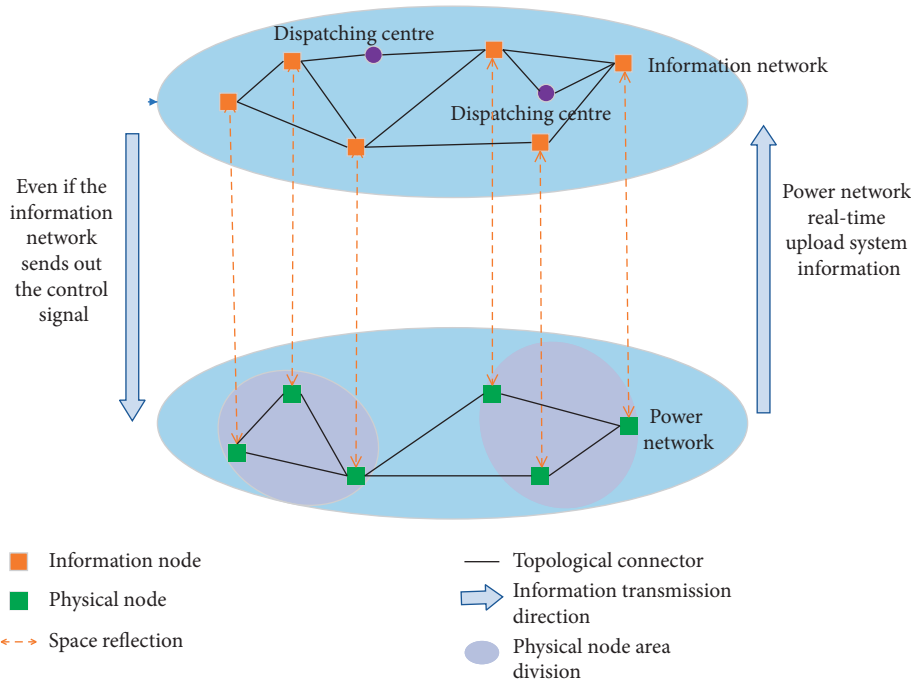


FIGURE 1: Model of a cyber-physical smart grid.

correlated information in computing will cause a too high computational burden, resulting in poor performance of the system state. The stability and flexibility of smart grids can be effectively improved by determining an appropriate dependency on the information network and information flow. For phasor measurement units (PMUs), which are synchronous phasor measurement devices, a reasonable number of them at suitable locations can synchronously collect the corresponding parameters of the power system at the installation site and achieve the overall observability, economic and reliability goals of the system online state calculation, and system state prediction [7–9]. In this paper, PMUs are introduced into the optimal configuration of the power system network structure to measure the voltage vectors of some nodes, which can improve the dependence on information, providing strong initial conditions and a discrimination basis for system stability analysis, protection, and reconstruction. This is of great significance for system online state calculation and system state prediction.

The traditional power grid control strategy mostly adopts a centralized scheduling method, and the dispatching centre needs to communicate with all generators and load nodes through the information network, with a high degree of communication dependence [10]. The “plug and play” technology required by the grid connection and independent operation of new energy and power components make the topological structure of the information network and physical network of the smart grid changeable [11]. The centralized control strategy has difficulty avoiding the high cost of communication facility construction. Distributed control technology can meet the flexibility requirements and provide high-efficiency control constraints [12]. In [13], a smart grid scheduling strategy considering flexible load is

designed, which have better convergence and application prospect compared with the centralized scheduling strategy.

In [14, 15], distributed control is used to reduce the cost of the communication network, and power distribution and frequency stability are achieved. Energy storage technology provides a new technology choice for the safe and economic operation of power grids, stabilization of power fluctuations, and distributed control [16–19]. In [16–18], the influence of flywheel energy storage on the power balance and stability of the power grid is studied. In [19], a fast control method for a battery energy storage system is adopted to improve the transient stability of the power grid. In [20], a distributed control method of energy storage system based on real-time wind power output regulation of energy sharing is proposed. In [21], a distributed intelligent power grid controller based on the Robust Consistency Algorithm of the second-order multiagent system is proposed. The controller is composed of a physical topology model of the network. The delay characteristics and anti-interference ability of the controller are verified by the IEEE39 node system.

In [22], the problem of cluster behavior and target consistent tracking of heterogeneous multi-inertial bodies with limited communication distance is studied. A distributed control protocol is designed to enable agents to achieve stable group behavior. In [23], a distributed observer is designed to estimate the relatively complete state of a general linear multiagent system that does not directly enter the real-time state, and it is used to track the consistency protocol, so as to achieve the overall consistency. In [24], a distributed multiclustor method based on partial information exchange is designed by studying the multiobjective consistency pursuit of the multiagent system, and sufficient conditions are given to realize the dynamic goal consistency

pursuit, so that the agent can adaptively select the target for tracking. In [25], we study the problem of consistency tracking of heterogeneous interdependent group systems with fixed communication topology and propose a distributed consistency tracking control protocol, which uses local information to achieve the consistency tracking of heterogeneous interdependent group systems. In [26], a new scale consistency protocol is proposed to solve the problem of time-varying delay in nonlinear dynamics and communication networks. In this paper, based on the rules of speed consistency and group concentration of a multiagent system, the phase angle (rotor angle) aggregation and frequency consistency of power grid generators are realized by using the local and associated node information to inject power into or absorb power from generator nodes through an external energy storage device (such as a flywheel) to ensure synchronous operation of the generators and realize transient stability of the power system.

In the context of transient stability, this paper integrates information and physical nodes into an agent, adopts the distributed control strategy of a “leading assisting” agent, and utilizes the information of local and other regional physical nodes and the coupling relationship of the physical network. It also realizes global information flow and stable operation of the system through the interaction of the information and physical networks and external energy storage. In this paper, the IEEE 39 node grid model is used as an example to demonstrate the effectiveness of the application of optimized distributed control in the smart grid model to maintain the stability of the system [27].

## 2. Transient Stability Control of a Smart Grid

To ensure that the power grid can quickly respond after being disturbed by information and a physical disturbance

and reduce the implementation time of transient stability zone control, necessary information network reliability optimization measures are taken to reduce information redundancy and unnecessary calculation and achieve the purpose of real-time control.

*2.1. Reliability Optimization of a Smart Grid Information Network.* Considering the reliability of the data processing of the information network under the influence of a single line fault in the physical network, the goal of a fully observable power network can be achieved by ensuring the optimal configuration of PMUs (synchronous vector measurement devices) with different channel capacities in the information network. Based on the configuration rule [28] of the minimum number of PMUs in the information network, the PMU optimization method to avoid scheme repetition is adopted, and the model is defined as follows:

$$\begin{cases} \min \left( x = \sum_k^n y_i x_k \right), \\ s.t \ AX \geq 1, \\ \max \left( f = \sum_k^n f_k \right), \end{cases} \quad (1)$$

where  $x_k$  is 1 or 0, which indicates whether physical grid node  $k$  has a PMU installed;  $A = (a_{ij})$  is the node correlation matrix, where if the two nodes  $i, j$  are adjacent or the same, then  $a_{ij} = 1$  and otherwise,  $a_{ij} = 0$ ;  $\mathbf{1}$  is the column vector whose elements are all 1;  $f_k = x_k + \sum_{l \in G} a_{lk} x_l$ ; and  $G$  indicates the set of all nodes connected to node  $k$ . Considering the 39-node grid model, the node correlation matrix is as follows:

$$A = \begin{bmatrix} A_1 \\ A_2 \\ A_3 \\ \vdots \\ A_{38} \\ A_{39} \end{bmatrix} = \begin{bmatrix} a_{1,1} & a_{1,2} & a_{1,3} & \cdots & a_{1,38} & a_{1,39} \\ a_{2,1} & a_{2,2} & a_{2,3} & \cdots & a_{2,38} & a_{2,39} \\ a_{3,1} & a_{3,2} & a_{3,3} & \cdots & a_{3,38} & a_{3,39} \\ \vdots & \vdots & \vdots & \vdots & \vdots & \vdots \\ a_{38,1} & a_{38,2} & a_{38,3} & \cdots & a_{38,38} & a_{38,39} \\ a_{39,1} & a_{39,2} & a_{39,3} & \cdots & a_{39,38} & a_{39,39} \end{bmatrix} = \begin{bmatrix} 1 & 1 & 0 & \cdots & 0 & 1 \\ 1 & 1 & 1 & \cdots & 0 & 0 \\ 0 & 1 & 1 & \cdots & 0 & 0 \\ \vdots & \vdots & \vdots & \vdots & \vdots & \vdots \\ 0 & 0 & 0 & \cdots & 1 & 0 \\ 1 & 0 & 0 & \cdots & 0 & 1 \end{bmatrix}. \quad (2)$$

The cost of installing PMU equipment at node  $i$  is as follows:

$$y_i = 1 + 0.1n_{ch}. \quad (3)$$

The cost of equipment installation is the sum of a fixed cost and a variable cost,  $n_{ch}$  is the number of PMU channels,

indicating the number of observable adjacent lines, generally 1–5, and the variable cost is increased by 0.1 for each additional line.

According to the above constraint rules, the following formula can be obtained to realize the fully observable IEEE 39 node power network topology:

$$\begin{cases} f_1 = x_1 + x_2 + x_{39} \geq 1, \\ f_2 = x_1 + x_2 + x_3 + x_{25} + x_{30} \geq 1, \\ f_3 = x_2 + x_3 + x_4 + x_{18} \geq 1, \\ \vdots \\ f_{38} = x_{24} + x_{38} \geq 1, \\ f_{39} = x_1 + x_9 + x_{39} \geq 1. \end{cases} \quad (4)$$

To further explain the impact of the number of channels, the following variables are introduced:

$$w_{i,j} = \begin{cases} 1 & \text{PMU was installed on node } i \text{ and made node } j \text{ observable,} \\ 0 & \text{Other.} \end{cases} \quad (5)$$

Then, the above formula can be rewritten to obtain the following inequalities:

$$\begin{cases} g_1 = x_1 + w_{2,1} + w_{39,1} \geq 1, \\ g_2 = x_2 + w_{1,2} + w_{3,2} + w_{25,2} + w_{30,2} \geq 1, \\ g_3 = x_3 + w_{2,3} + w_{4,3} + w_{18,3} \geq 1, \\ \vdots \\ g_{38} = x_{38} + w_{24,38} \geq 1, \\ g_{39} = x_{39} + w_{1,39} + w_{9,39} \geq 1. \end{cases} \quad (6)$$

In the case of a single line fault in the physical network, the number of channels on the right side of the fault point at the end of the node line is accordingly changed (i.e., multiplied by 2 to ensure that each node is observed by at least two PMUs). The configuration with the lowest cost is 2, 6, 8, 15, 16, 17, 20, 23, 25, 26, 29, and 35. In the distributed control framework, the sensitivity of the information nodes is considered to select the dominant generator in the area.

**2.2. Smart Grid Distributed Framework.** According to the information network reliability optimization results and the multiagent system model, a distributed control framework is designed for cooperation between the generator and the external energy storage system in the smart grid. In this framework, the corresponding information and physical equipment at each generator node are combined to form an agent. Each agent represents its main properties by the physical quantities of the generator. The information equipment includes a measurement unit (PMU) and a controller, both of which perform calculations and applications related to information and data. The physical equipment also includes external energy storage equipment in addition to the generator. Only when external energy storage is needed to inject power or absorb a certain power,  $P_{L,i}$  will the corresponding controller of the generator agent be activated.

The agents that describe the information-physical network interaction and the system model (Figure 2). The generator participating in stability control of the physical power grid and frequency adjustment without difference is

the leading generator, which is realized by the information network through selective control; the power regulation of other generators in the same zone is controlled by the information network to proportionally change with the power of the leading generator to assist in frequency regulation of the leading generator.

The synchronous generators play a leading role in the physical power grid, and thus the stability of the power grid is largely a problem of keeping the interconnected generators synchronized [19]. A smart grid maintains synchronous generator frequency synchronization and phase-angle aggregation by using a distributed control framework based on the multiagent model. According to the requirements of frequency synchronization, the normalized speed corresponding to the grid frequency is selected and denoted by  $\omega$ , and the generator label in the physical grid is  $i \in V, V = \{1, 2, \dots, Z\}$ , with

$$\omega_i(t) \longrightarrow 1 (t \longrightarrow \infty). \quad (7)$$

To avoid the rapid drop of the node voltage caused by the phase angle difference of the generator terminal voltage exceeding a certain range, thus affecting the safe operation of the unit, the phase angle aggregation requires that generators  $i$  and  $j$  satisfy the following:

$$|\theta_i - \theta_j| \leq \gamma, \quad (8)$$

where  $\gamma$  is a predefined threshold, usually  $5\pi/9$ .

**2.3. Smart Grid Control Target Model.** The information network selection coefficient  $h_i$  is set as follows:

$$h_i = \begin{cases} 1, & \text{the } i\text{-th agent contains the leading generator,} \\ 0, & \text{others.} \end{cases} \quad (9)$$

This coefficient is used to determine the selective control behaviour of the information network with respect to the physical network and ensure timely control of the main generator agent contained in each partition.

If there is a controller that connects the physical power grid with the information network, then the oscillating equation between motors can be obtained under the constant voltage condition [29]:

$$\begin{aligned} M_i \dot{\omega}_i &= -D_i \omega_i + P_{m,i} - |E_i|^2 G_{ii} \\ &- \sum_{j=1, j \neq i}^Z P_{ij} \sin(\theta_i - \theta_j + \varphi_{ij}) + h_i u_i. \end{aligned} \quad (10)$$

The transient stability problem of a smart grid is described as the control task of multiagent swarm concentration with consistent speed, and then the second-order dynamics model of multiagents is used to describe each agent as follows [30]:

$$\begin{cases} \dot{\theta}_i = \omega_i, \\ D_i \dot{\omega}_i = -M_i \ddot{\omega}_i - l_{ij} \omega_i + h_i \dot{u}_i. \end{cases} \quad (11)$$

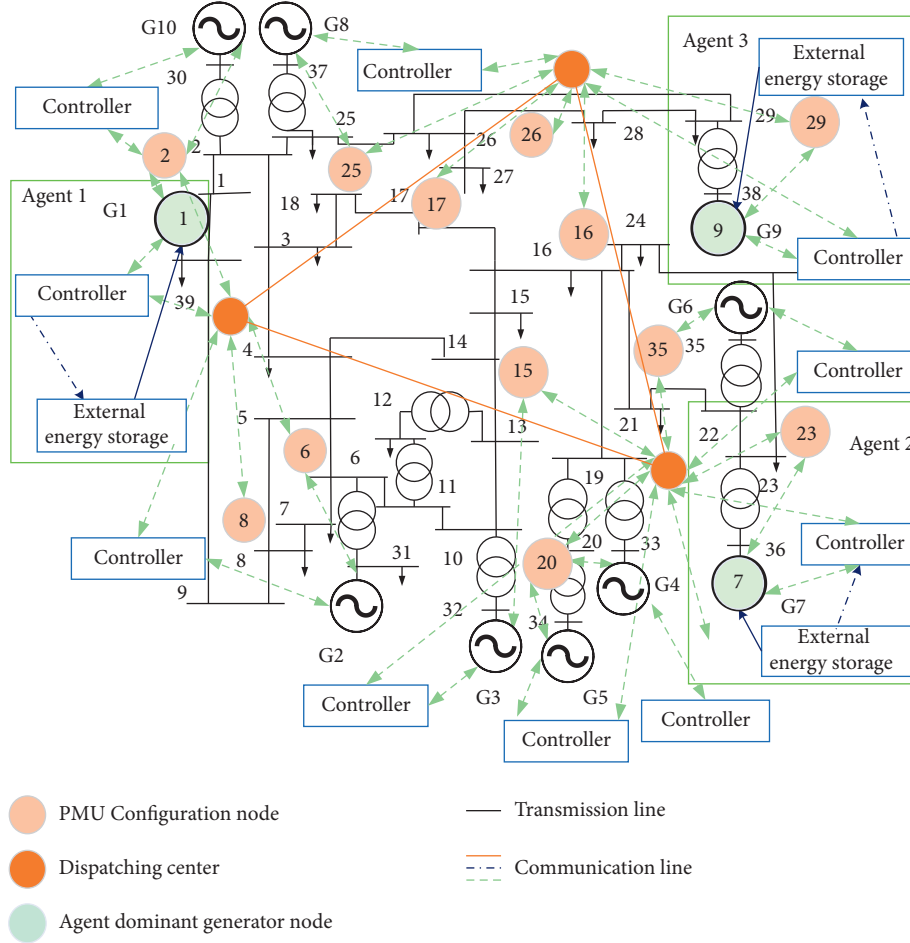


FIGURE 2: Model of the IEEE 39-bus cyber-physical smart grid with agents.

The controller signal is defined as  $u_i = P_{L,i}$  for agent  $i = 1, \dots, F$ , which corresponds to the agent containing the main generator. Since only one main generator is selected for each partition,  $F$  also represents the number of physical power grid zones.  $h = \text{diag}[h_1, \dots, h_i, h_{i+1}, \dots, h_Z]$ . Generally,  $h_i = 1$  is set for  $i \leq F$ ; otherwise,  $h_i = 1$  corresponds to other agents in the partition that assist in the adjustment,  $V_{mf} = \{F + i, \dots, Z\}$ . The auxiliary regulated power of the corresponding generator is  $P_{F+i} = a_{F+i} \cdot P_{L,i}$ , where  $a$  is a proportional coefficient that varies with the power of the leading generator and  $l_{ij}$  is an element of the physical relation matrix  $L$ , which is represented as

$$l_{ij} = \begin{cases} \sum_{j=1, j \neq i}^Z P_{ij} \cos(\theta_i - \theta_j + \varphi_{ij}), & i = j. \\ -P_{ij} \cos(\theta_i - \theta_j + \varphi_{ij}), & i \neq j. \end{cases} \quad (12)$$

In this case, a new control quantity  $\tilde{u}_i$  is introduced to define the controller signal  $u_i$  as

$$\dot{u}_i = \tilde{u}_i + l_{ij}\omega_i - B_i\dot{\omega}_i, \quad (13)$$

where  $B_i \geq (100 * D_i)$  is an element in information relation matrix  $B$ .

### 3. Distributed Area Optimal Control for the Transient Stability of a Smart Grid

**3.1. Smart Grid Area Division.** The main properties of each agent in the smart grid are described by the physical quantities of the generators in the physical grid. Let the state information carried by agent  $i$  at time  $t = k$  be

$$\begin{cases} x_i(k) = \theta(k), \\ v_i(k) = \omega_i(k). \end{cases} \quad (14)$$

When the time step is  $t = k$ ,  $\theta_i(k)$  and  $\omega_i(k)$  are the rotor angle and speed of the  $i$ -th generator, respectively, which are physical quantities directly obtained from the PMU.  $S_i(k) = [x_i(k), v(k)]^T$  describes the status information carried by individuals, where  $x_i(k)$  and  $v_i(k)$  correspond to the position and speed of the individual at time step  $t = k$ . If the distance between two individuals is less than the threshold  $r$ , then they are considered as being in each other's neighbourhood. The neighbourhood set for the  $i$ -th individual is defined as follows:



$$N_i(k) = \left\{ j \in V \mid \|x_i(k) - x_j(k)\| < r \right\}. \quad (15)$$

According to the similarity of the individual dynamic state quantities, the region is divided; for  $j \in N_i(k)$ , the relationship between individuals  $i$  and  $j$  in the same group meets the following requirement:

$$S_i(k) - S_j(k) < S_{th}(k), \quad (16)$$

where  $S_{th}(k)$  is the set threshold value.

The following dynamic model is used:

$$x_i(k+1) = x_i(k) + \Delta t v_i(k). \quad (17)$$

The physical dynamic quantity of the agent has been transformed into the individual state quantity in the information space, and multiple groups containing different individuals are simultaneously obtained, which are composed of agents with close physical coupling in the actual smart grid corresponding to the partition.

**3.2. Smart Grid Distributed Controller.** According to formula (13), letting  $\underline{M}_i = D_i + B_i$ , the second-order system of the set containing the leading generator agent is determined as

$$\begin{cases} \dot{\theta}_i = \omega_i, \\ \underline{M}_i \dot{\omega}_i = \tilde{u}_i. \end{cases} \quad (18)$$

To achieve transient stability of the smart grid, the distributed control signal applied to the agent (label  $i = 1, 2, \dots, F$ ) with the leading generator in each partition is as follows:

$$\tilde{u}_i = -\nabla V(\theta_{ij}) - \tilde{L}_{ij} \omega_i - c(\omega_i - \omega^*). \quad (19)$$

where  $c$  is a constant representing the coefficient of the feedback term;  $\omega$  is the expected normalized speed value.  $\tilde{L}_{ij}$  is an element in the velocity matching matrix  $\tilde{L}$ , and the first term is the  $V(\theta_{ij})$  gradient, where the potential function  $V(\theta_{ij})$  is defined as follows:

$$V(\theta_{ij}) = \frac{1}{2} \sum_{i=1}^F \sum_{j=1, j \neq i}^F \chi(\theta_i - \theta_j). \quad (20)$$

The above functions ensure that the rotor angle difference between agents is bounded.

### 3.3. Analysis of the Distributed Control Stability of a Smart Grid

**Theorem 1.** Consider a second-order system with expected values of the guidance feedback terms in kinetic equations (18) and (19). Suppose that the initial velocity does not match the expected value and that the initial energy  $H_0$  is finite; under the action of control protocol equation (19), all agents asymptotically and uniformly converge to the corresponding reference speed, corresponding to the expected speed of the generator of  $\omega^*$ , and the group behaviour is consistent with global stability.

*Proof.* Let  $\tilde{\theta}_i = \theta_i - \theta^*$  and  $\tilde{\omega}_i = \omega_i - \omega^*$  represent the differences between the physical quantities of the agent and the expected values, respectively, then:

$$\begin{cases} \dot{\tilde{\theta}}_i = \tilde{\omega}_i, \\ \underline{M}_i \dot{\tilde{\omega}}_i = \tilde{u}_i. \end{cases} \quad (21)$$

According to equations (18), (19), and (21), the control function can be obtained as follows:

$$\tilde{u}_i = -\nabla V(\tilde{\theta}_{ij}) - \tilde{L}_{ij} \tilde{\omega}_i - c \tilde{\omega}_i. \quad (22)$$

The *Lyapunov* function is defined as the total energy of the system, that is, the sum of the total potential energy between agents and the relative potential energy and kinetic energy between the physical quantities of the agents and the expected reference quantities:

$$H(\tilde{\theta}_i, \tilde{\omega}_i) = \frac{1}{2} \sum_{i=1}^F V(\tilde{\theta}_{ij}) + \frac{1}{2} \sum_{i=1}^F \tilde{\omega}_i^T \underline{M}_i \tilde{\omega}_i. \quad (23)$$

Since the potential function  $V(\theta_{ij})$  is symmetric with respect to  $\theta_{ij}$  ( $i, j = 1, \dots, F$ ),

$$\frac{\partial V(\tilde{\theta}_{ij})}{\partial \tilde{\theta}_{ij}} = \frac{\partial V(\tilde{\theta}_{ij})}{\partial \tilde{\theta}_i} = -\frac{\partial V(\tilde{\theta}_{ij})}{\partial \tilde{\theta}_j}. \quad (24)$$

The derivative of equation (23) can be obtained:

$$\dot{H} = \frac{1}{2} \sum_{i=1}^F \frac{\partial V(\tilde{\theta}_{ij})}{\partial \tilde{\theta}_i} + \sum_{i=1}^F \tilde{\omega}_i^T \underline{M}_i \dot{\tilde{\omega}}_i = \sum_{i=1}^F \tilde{\omega}_i^T \nabla V(\tilde{\theta}_{ij}) + \sum_{i=1}^F \tilde{\omega}_i^T \tilde{u}_i. \quad (25)$$

Equation (22) can be substituted into equation (25) to obtain

$$\begin{aligned} \dot{H} &= \sum_{i=1}^F \tilde{\omega}_i^T \nabla V(\tilde{\theta}_{ij}) - \sum_{i=1}^F \tilde{\omega}_i^T \nabla V(\tilde{\theta}_{ij}) - \sum_{i=1}^F \tilde{\omega}_i^T \tilde{L}_{ij} \tilde{\omega}_i - \sum_{i=1}^F \tilde{\omega}_i^T c \tilde{\omega}_i \\ &= -\sum_{i=1}^F \tilde{\omega}_i^T \tilde{L}_{ij} \tilde{\omega}_i - \sum_{i=1}^F \tilde{\omega}_i^T c \tilde{\omega}_i = -\sum_{i=1}^F \tilde{\omega}_i^T [(\tilde{L}_{ij} + c)] \tilde{\omega}_i \\ &= -\tilde{\omega}^T [(\tilde{L} + cI)] \tilde{\omega}. \end{aligned} \quad (26)$$

Since  $\tilde{L}$  is a semipositive definite Laplace matrix and  $c > 0$ ,  $\tilde{L} + cI$  is a positive definite matrix, and thus,  $\tilde{\omega}^T [(\tilde{L} + cI)] \tilde{\omega} > 0$  and  $\dot{H} < 0$ . Therefore, the agents asymptotically stably converge to their expected reference values under control input (19).  $\square$

## 4. Simulation Example

In this paper, the IEEE 39 node smart grid model is analysed as an example, which includes 19 loads and 46 lines, which are simulated by the MATLAB/Simulink platform. According to the classification of a short-circuit fault, centralized control after a fault and swarm control after a fault, the examples are divided into four scenarios.

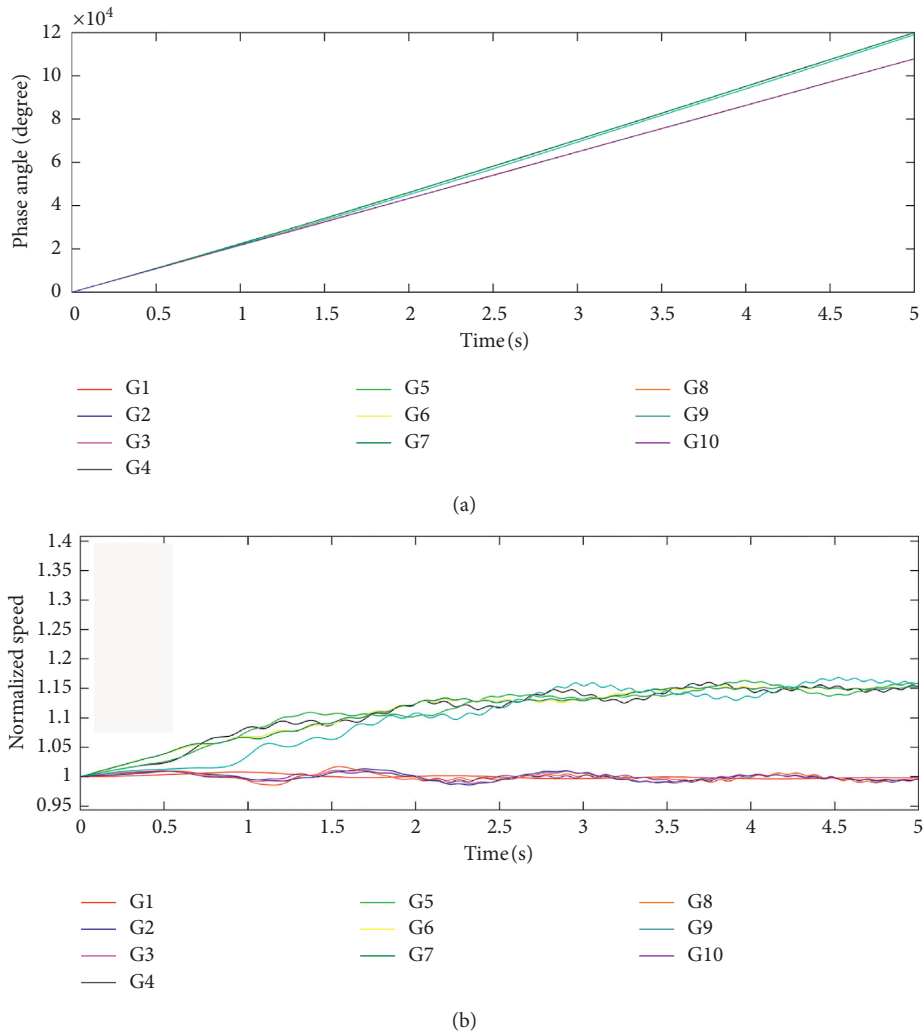


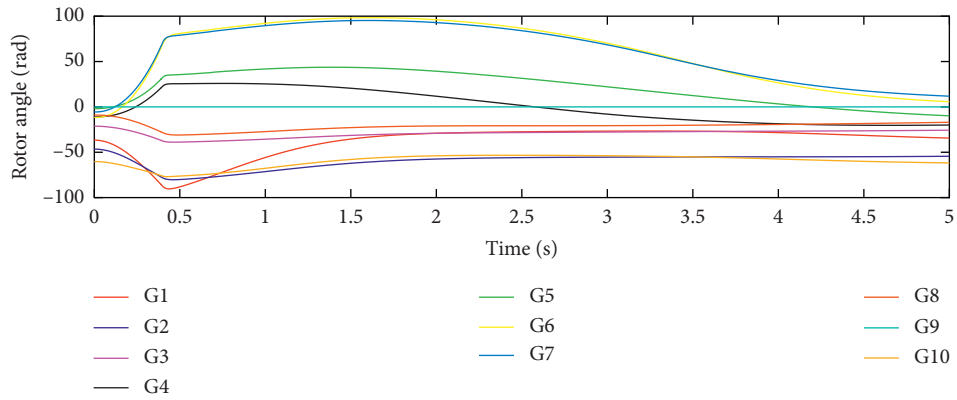
FIGURE 3: Relative rotor angles and rotor speeds of generators after the fault.

*Scenario 1.* Suppose at  $t = 0$  s, a three-phase short-circuit fault occurs on disturbed line 21–22 of the power grid. Disconnect the fault line and set  $h_i = 0$  for  $i \in V, V = \{1, 2, \dots, Z\}$ , that is, the controller connecting the information and physical networks is not activated and the information network traffic and calculation amount are minimal. The relationships between the speeds of each generator and the rotor angles are given in Figure 3. The system operation is obviously unstable, the rotor angle has an increasing difference trend, and the power network has a serious fault.

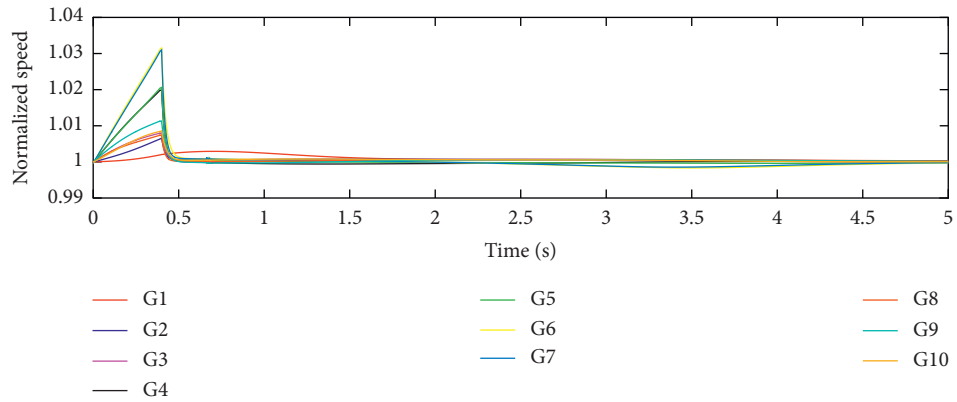
*Scenario 2.* Under centralized control, each node of the power grid needs to transmit information to the dispatching centre. After centralized processing, a large number of PMUs and communication lines are needed to ensure information collection and transmission. In the period before centralized control after fault removal, it is necessary to collect the state information of the whole power grid, assuming that the data can be collected and processed within the preset critical time after fault treatment under ideal conditions. When  $t = 0.15$  s, set  $h_i = 0$  for  $i \in V$ ,

$V = \{1, 2, \dots, Z\}$ , so that all generator nodes are controlled by no difference regulation. Under ideal conditions (Figure 4), the rotor angles and speeds of the generators change with time and the system achieves a stable state in a short time. However, the system is in the state of maximum information transmission and processing. The control equipment of each generator node frequently uses external energy devices to adjust the power of the corresponding nodes. The overall energy consumption of the whole regulation process is large, and the network topology and performance of the related equipment are not fully utilized.

*Scenario 3.* The flocking control method leads to a stable performance (Figure 5). Distributed flocking control can reduce the equipment cost and improve the centralized control of information processing, the energy consumption, and the critical stability range in the 5 s of the observation period, but the fluctuation range is larger. The smart grid after using each agent to facilitate control tends to be stable for a long time.

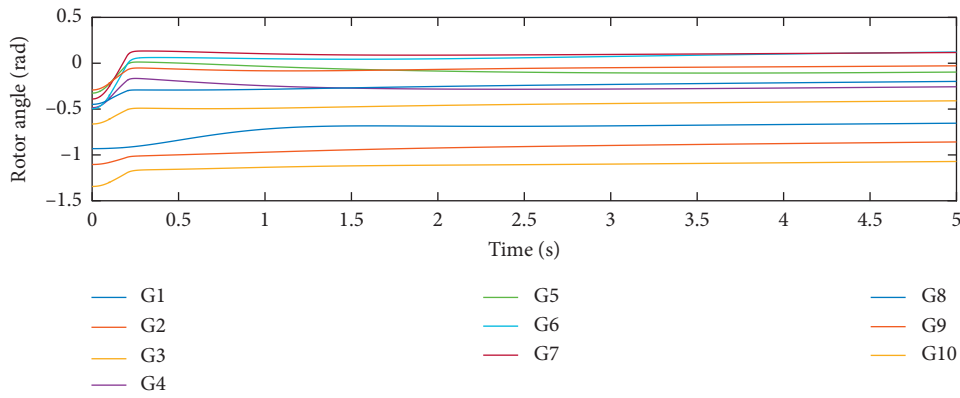


(a)



(b)

FIGURE 4: Relative rotor angles and rotor speeds of generators under centralized control after the fault.



(a)

FIGURE 5: Continued.

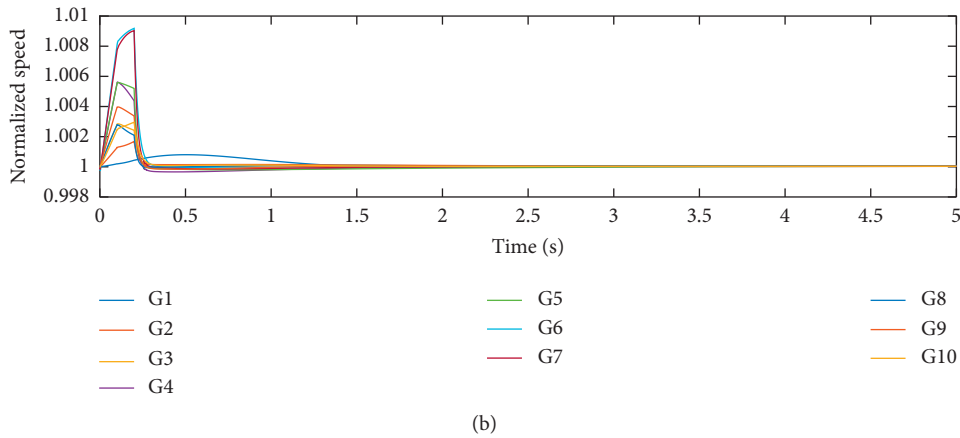


FIGURE 5: Relative rotor angles and rotor speeds of generators under flocking control after the fault.

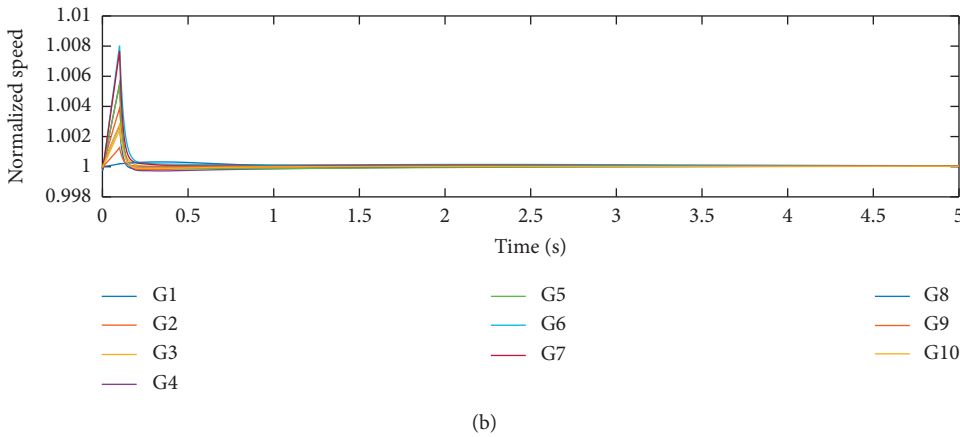
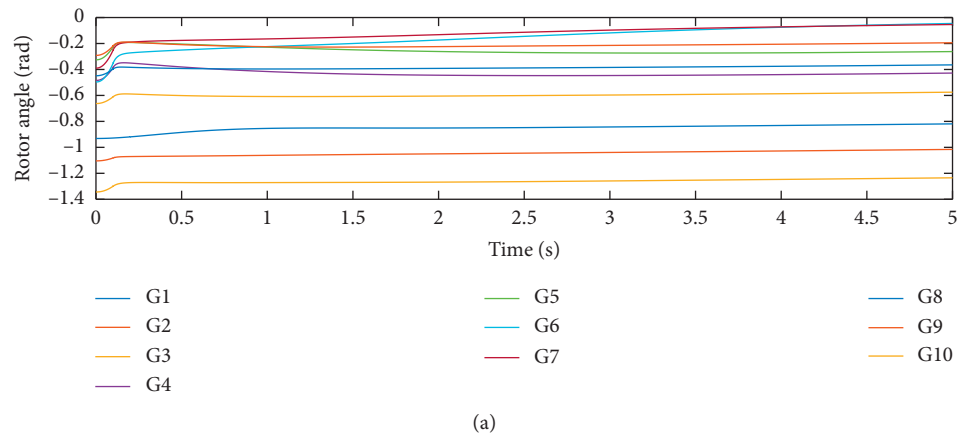


FIGURE 6: Relative rotor angles and rotor speeds of generators under distributed optimal control after the fault.

*Scenario 4.* The distributed optimal control method in this paper is used to control the performance (Figure 6). The smart grid partition identification scheme should be enabled within the preset critical time point after fault treatment to avoid more damage and improve the ability of the smart grid to restore transient stability. The distributed optimal control is applied to the agents containing the main generators, that is, setting  $h_i = 1$  for  $i = 1, \dots, F$ .

First, determine the smart grid partition based on the similarity of the intelligent agent dynamic characteristics; that is, the smart grid agent quantity changes corresponding to the movement trend of individuals in the information space. Next, obtain the state information of individual trajectories, described as individual motion curves in a two-dimensional space. From the trend of separation of individuals in the information space, that is, the change of the

physical quantities of each agent after the failure, it can be found which individuals are obviously far from other individuals and which movement trends are the closest. The following partitions can be obtained from the partitioning scheme of dynamic recognition of each agent:  $\{G1\}$ ,  $\{G2\ G3\ G8\ G9\ G10\}$ , and  $\{G4\ G5\ G6\ G7\}$ .

Second, on the basis of information network reliability optimization combined with the actual active power output for each agent and sensitivity weight arrangement of the node data, reasonable leading generators  $G1$ ,  $G7$ , and  $G9$  are selected for each partition, and distributed optimal control is applied to the intelligent agent with the leading generator to achieve the goal of system transient stability.

Within the critical time after the fault is cut off, partition identification and leading generator selection are completed. At  $t = 0.15$  s, the distributed control scheme combining the information and physical networks is applied to the smart grid. The state quantities of each agent change with time (Figure 6). The control objective is achieved for each agent in each partition, and the corresponding physical quantity converges to a certain value according to the partition. Since external energy injection could impact actual operation and lead to certain fluctuations, we quickly recover to the stable operation of the steady-state power system. The generator speeds are stable and gradually converge, and the rotor angles satisfy the requirements of the constraint and stable state. Under the conditions of information use and smaller external energy injection, the good effect of a shorter stable system recovery time, a smaller physical quantity fluctuation range, and an increased stability margin of the system are achieved.

Under the action of centralized control method, the system can resume stable operation in a short time, but the disadvantage is that the system is in the state of maximum information transmission and processing and the overall energy consumption is large. Compared with centralized control, distributed swarm control improves the disadvantages of large amount of information processing and energy consumption, but the time of system stability is prolonged. The distributed optimal control method proposed in this paper can quickly restore the stability of the system, reduce the energy consumption, and improve the stability margin of the smart grid.

## 5. Conclusions

In this paper on transient stability control of the smart grid model, the distributed multiagent control method adopted in the power grid model after reliability optimization of the information network is described. In the distributed control framework, the dynamic similarity of the physical parameters of the generators is used to form each zone, and external energy storage is used to adjust the agents in each zone. The leading generator realizes no difference adjustment, and other generators in the same zone adjust their power proportional to the adjusted power of the leading generator to achieve asymptotic stability of each zone. The simulation results in this paper verify the effectiveness of the proposed control scheme, which finally achieves transient stability and control of the smart grid model, and it has fast and stable performance compared with swarm control. The idea

presented in this paper has a certain reference value for improving the transient stability of smart grids in practical projects.

## Data Availability

The data used to support the findings of this study are included within the article.

## Conflicts of Interest

The authors declare that they have no conflicts of interest.

## Acknowledgments

This work was supported in part by the National Natural Science Foundation of China under Grant no. 11662002.

## References

- [1] S. Y. Chen, S. F. Song, and L. X. Li, "Survey on smart grid technology," *Power System Technology*, vol. 33, no. 8, pp. 1–7, 2009.
- [2] P. Kundur, N. J. Balu, and M. G. Lauby, *Power System Stability and Control*, McGraw-Hill, New York, NY, USA, 1994.
- [3] H. Li, Z. Han, A. D. Dimitrovski, and Z. Zhang, "Data traffic scheduling for cyber physical systems with application in voltage control of distributed generations: a hybrid system framework," *IEEE Systems Journal*, vol. 8, no. 2, pp. 542–552, 2014.
- [4] E. Mengelkamp, B. Notheisen, C. Beer et al., "A blockchain-based smart grid: towards sustainable local energy markets," vol. 33, no. 1–2, pp. 207–214, Computer Science Research & Development, 2018.
- [5] K. Muralitharan, R. Sakthivel, and R. Vishnuvarthan, "Neural network based optimization approach for energy demand prediction in smart grid," *Neurocomputing*, vol. 273, pp. 199–208, 2018.
- [6] Q. Y. Sun, F. Teng, H. G. Zhang et al., "Construction of dynamic coordinated optimization control system for energy internet," *Proceedings of the CSEE*, vol. 14, pp. 3667–3677, 2015.
- [7] D. Carrion and J. W. Gonzalez, "Optimal PMU location in electrical power systems under N-1 contingency," in *Proceedings of the International Conference on Information Systems and Computer Science*, (INCISCOS) IEEE Computer Society, Kuala Lumpur, Malaysia, March 2018.
- [8] E. Abiri, F. Rashidi, and T. Niknam, "An optimal PMU placement method for power system observability under various contingencies," *International Transactions on Electrical Energy Systems*, vol. 25, no. 4, pp. 589–606, 2015.
- [9] F. Rashidi, E. Abiri, T. Niknam, and M. R. Salehi, "Optimal placement of PMUs with limited number of channels for complete topological observability of power systems under various contingencies," *International Journal of Electrical Power & Energy Systems*, vol. 67, pp. 125–137, 2015.
- [10] Z. Wang and W. Jie, "A novel finite-time control scheme for enhancing smart grid frequency stability and resilience," *IEEE Transactions on Power Systems*, vol. 10, no. 6, pp. 6538–6551, 2019.
- [11] A. Q. Huang, M. L. Crow, G. T. Heydt, J. P. Zheng, and S. J. Dale, "The future renewable electric energy delivery and management (FREEDM) system: the energy internet : the

- energy internet,” *Proceedings of the IEEE*, vol. 99, no. 1, pp. 133–148, 2011.
- [12] Z. Li, W. Ren, X. Liu, and M. Fu, “Distributed containment control of multi-agent systems with general linear dynamics in the presence of multiple leaders,” *International Journal of Robust and Nonlinear Control*, vol. 23, no. 5, pp. 534–547, 2013.
- [13] D. U. Jia-Bing, C. Yan-Peng, L. Man-Fa et al., “Design and implementation of smart grid control system based on distributed real-time scheduling strategy,” *Electronic Design Engineering*, vol. 26, no. 7, pp. 119–127, 2018.
- [14] Y. Xu, W. Zhang, M.-Y. Chow, H. Sun, H. B. Gooi, and J. Peng, “A distributed model-free controller for enhancing power system transient frequency stability,” *IEEE Transactions on Industrial Informatics*, vol. 15, no. 3, pp. 1361–1371, 2019.
- [15] Y. Zhou, K. Wang, and G. Li, “Distributed hierarchical control for microgrid based on multi-agent consensus Algorithm,” *Automation of Electric Power Systems*, vol. 41, no. 11, pp. 142–149, 2017.
- [16] G. Dekker and J. Frunt, *Frequency Stability Contribution of Wartsila Combustion on Engines*, Wartsila Finland OY, Vaasa, Finland, 2012.
- [17] A. Farraj, E. Hammad, D. Kundur et al., “On the use of energy storage systems and linear feedback optimal control for transient stability,” *IEEE Transactions on Industrial Informatics*, vol. 13, no. 4, pp. 1575–1585, 2017.
- [18] H. Silva-Saravia, H. Pulgar-Painemal, and J. Mauricio, “Flywheel energy storage model, control and location for improving stability: the Chilean case,” *IEEE Transactions on Power Systems*, vol. 1, no. 1, p. 99, 2016.
- [19] K. Kawabe and A. Yokoyama, “Improvement of transient stability and short-term voltage stability by rapid control of batteries on EHV network in power systems,” *Electrical Engineering in Japan*, vol. 188, no. 3, pp. 1–10, 2014.
- [20] S. Baros and M. D. Ili, “A consensus approach to real-time distributed control of energy storage systems in wind farms,” *IEEE Transactions on Smart Grid*, vol. 10, no. 1, pp. 613–625, 2019.
- [21] W. Ziqiang and W. Jie, “A distributed control considering the cyber-physical characteristics of smart grid,” *Proceedings of the CSEE*, vol. 39, no. 23, pp. 6921–6933, 2019.
- [22] S. Chen, H. Pei, Q. Lai et al., “Multitarget tracking control for coupled heterogeneous inertial agents systems based on flocking behavior,” in *Proceedings of the IEEE Transactions on Systems Man & Cybernetics Systems*, pp. 1–7, January 2018.
- [23] C. Shiming, G. Junjie, G. Yanli et al., “Observer-based event-triggered tracking consensus of non-ideal general linear multi-agent systems,” *Journal of the Franklin Institute*, vol. 356, no. 17, 2019.
- [24] H. Pei, S. Chen, and Q. Lai, “Multi-target consensus circle pursuit for multi-agent systems via a distributed multi-flocking method,” *International Journal of Systems Science*, vol. 47, no. 16, 2016.
- [25] H. Pei, S. Chen, Q. Lai et al., “Consensus tracking for heterogeneous interdependent group systems,” *IEEE Transactions on Cybernetics*, vol. 50, no. 4, 2020.
- [26] Z. Zhang, S. Chen, and H. Su, “Scaled consensus of second-order nonlinear multiagent systems with time-varying delays via aperiodically intermittent control,” *IEEE Transactions on Cybernetics*, no. 99, pp. 1–14, 2019.
- [27] A. MOEINI, I. KAMWA, P. BRUNELLE et al., *Open Data IEEE Test Systems Implemented in SimPowerSystems for Education and Research in Power Grid Dynamics and Control*, in *Proceedings of the 2015 50th International Universities Power Engineering Conference*, pp. 1–6, Stoke-on-Trent, UK, September 2015.
- [28] Z. Zhuoli, Y. Ping, X. U. Zhirong et al., “Review on large-disturbance transient stability research of microgrid with multiple energy resources and multiple conversions,” *Power System Technology*, vol. 41, no. 7, pp. 2195–2204, 2017.
- [29] F. Dorfler, M. Chertkov, and F. Bullo, “Synchronization in complex oscillator networks and smart grids,” *Proceedings of the National Academy of Sciences*, vol. 110, no. 6, pp. 2005–2010, 2013.
- [30] R. Olfati-Saber, “Flocking for multi-agent dynamic systems: algorithms and theory,” *IEEE Transactions on Automatic Control*, vol. 51, no. 3, pp. 401–420, 2006.

## Research Article

# Multimotor Improved Relative Coupling Cooperative Control Based on Sliding-Mode Controller

Changfan Zhang , Mingjie Xiao , and Jing He 

*College of Electrical and Information Engineering, Hunan University of Technology, Zhuzhou 412007, China*

Correspondence should be addressed to Jing He; [hejing@263.net](mailto:hejing@263.net)

Received 23 March 2020; Accepted 2 May 2020; Published 20 May 2020

Guest Editor: Xiao Ling Wang

Copyright © 2020 Changfan Zhang et al. This is an open access article distributed under the Creative Commons Attribution License, which permits unrestricted use, distribution, and reproduction in any medium, provided the original work is properly cited.

To provide cooperative control under complex working conditions of a filling multimotor system, this paper proposes a relative coupling control strategy with a switching system structure. Firstly, a multistation transmission system composed of a filling motor and a transfer motor is designed according to different filling processes. Secondly, a stable sliding-mode surface common to the multimotor system is selected, and an equivalent sliding-mode controller corresponding to each motor is designed. Thirdly, public Lyapunov stability theory is used to prove that the switched system can move from any initial state to the common sliding surface of the system, thereby ensuring the asymptotic stability of the entire system. Simulation results show that this method has a more significant control effect on the system error of each motor in comparison with the traditional relative coupling control structure.

## 1. Introduction

As a major technical problem in filling production, multi-machine collaborative control is widely explored by researchers in the food packaging industry [1, 2]. Multimotor synchronous control is an important part of multimachine collaborative control technology for filling production. A long period of research produced numerous results [3, 4]. However, two main problems remain in the filling process of thick sauces and sticky foods. First, the system starts and stops frequently during the filling operation. Second, when the filling operation is completed, the filling motor exhibits an abrupt load torque. In view of the two problems, this study focuses on how to realize the multimotor synchronous control of the filling system under complex working conditions.

In terms of synchronous topology, parallel synchronous control and master-slave synchronous control are non-coupling structures [5]. The motors lack connection, and the synchronization performance is easily affected by external disturbances and load torque changes. Thence, Zhang et al. [6] proposed a virtual total axis control structure based on an

equivalent load observer, therefore addressing the difficult synchronization between the multi-axis system of the printing press when the load disturbance is large. However, they did not consider the coordination between multiple variables. For high-speed EMU, Yang et al. [7] established a multiadaptive neural fuzzy inference system (ANFIS) model and designed a predictive controller to achieve the EMU operational control. Zhao and Zhang [8] first proposed the relative coupling control structure, but adding a speed feedback module would complicate its structure as the number of motors increased. Thus, to solve these problems, Shi et al. [9] improved the relative coupling control strategy by introducing an additional speed controller and simplified the system structure. Sun et al. [10] adopted a fuzzy SMC based on ring-coupling synchronous control structure to enhance the reliability and control accuracy of the multimotor drive system. Zhang et al. [11] proposed a switching structure control method based on state switching and designed a nonlinear SMC to achieve synchronous control of the printing press multi-axis system in the case of time delay. Li et al. [12] proposed a second-order adaptive SMC method based on average relative coupling. The adaptive law

overcame the effects of bounded external disturbances and parameter perturbations on the system, thus improving robustness. Huang et al. [13] proposed an external coercion mechanism to analyze the problem of extensive cooperation. By modeling the agent on a simple conventional network, it proved that the mechanism has a significant promotion effect on cooperation.

In terms of synchronous control algorithms, researchers are prone to enhancing control accuracy by improving the algorithm [14]. Li et al. [15] introduced the adaptive sliding-mode algorithm to the ring-coupling control strategy and solved the poor synchronization performance of multiple motors in the case of uncertain perturbation of system parameters. Xia et al. [16] used a two-degree-of-freedom PI velocity controller and improved the effect of noise and time delay on synchronization performance by using Kalman filtering. He et al. [17] used a sliding-mode controller to achieve multi-axis servo cooperative control under variable proportional conditions. Yang et al. [18] studied the event-triggered consensus (ETC) problem based on multiagent systems with linear dynamics and implemented multiagent consistency control by using the ETC controller. Zhang et al. [19] solved the problem of distributed robust cooperative control of multimotor systems with unknown compound disturbances, and they further proposed a distributed robust cooperative control algorithm based on a disturbance observer. Xia et al. [20] combined a cross-coupling structure with a sliding-mode control algorithm and used an exponential approach law and a saturation function to propose a synchronous control strategy. Wang et al. [21] proposed an adaptive and robust  $H^\infty$  control strategy using the combination of a robust tracking controller and a distributed synchronous controller which implemented load tracking and synchronous control of a multiservo system. Liu et al. [22] added a mismatched relay node to the complex motor network to reduce the coupling threshold for synchronization of the entire complex motor network and thus improve the synchronization performance of the entire network. Acknowledging that the status information of adjacent objects cannot be obtained between agents, Wu et al. [23] solved the problem of positive edge consistency in undirected networks, proposed an iterative linear LMI algorithm, and obtained the feedback matrix and the observer matrix. Through the output feedback protocol, Su et al. [24] studied the positive edge consistency of undirected and directed networks. Wang et al. [25] considered the input saturation problem of multiagent systems and adopted low-parameter, high-gain feedback techniques and high-gain observer methods to achieve consistent and robust control of multiagents. Wu and Su [26] studied the edge consistency problem of undirected network systems with positive constraints and input saturation. In contrast to the general conclusion of input saturation, the author improved the system consistency to a global level.

To sum up, the scholars performed substantial research on multimotor synchronous control [27, 28]. However, the results in switching synchronous control are rare, especially for the study of motor load torque abrupt change which has always been the least of concern. Therefore, the current work

explored the complex working conditions of the filling motor appearing in the filling multiservo motor system during the stop-start time when the load torque changes abruptly. It appropriately improves the filling motor model in accordance with actual production and proposes a relative coupling control strategy of multimotor with switching system structure. It then designs an equivalent SMC which can solve the poor coordination performance of multi-machine in complex production conditions effectively during filling production and thus ensure the smooth operation of the system. The main research work of this paper can be summarized as following two points, consequently:

- (1) This work proposes a multimotor system with a switching system structure which mainly addresses the complex working conditions of the filling motor during the stop-start time and the sudden change of the motor load torque. The system is optimized to make the model consistent with the actual engineering background.
- (2) For the switching system structure of the filling motor, the common Lyapunov function is selected so that it could be switched at any initial state and reach the common sliding-mode surface, thereby ensuring the asymptotic stability of the multimotor system.

This paper is organized as follows: according to the structural advantages of the switching system, an improved relative coupling control strategy based on the filling multimotor system is designed in Section 2. The equivalent sliding-mode controller is designed to ensure single-axis error convergence and the multimotor system Lyapunov function is selected to ensure the progressive stability of the system in Section 3. Comparative simulations and analysis are illustrated in Section 4. Finally, this paper's conclusion is given in Section 5.

## 2. Multimotor Cooperative Control Structure Based on Improved Relative Coupling

In this section, a sliding-mode control method with a switching system structure for the filling multimotor system is designed. In the traditional control method generally, the processing of the sudden load of the motor is usually conservative. The control structure proposed in this section can improve the filling motor model to overcome the impact of the sudden change in load torque at the stop-start time, thereby tracking and controlling motor speed synchronously. The main advantage of designing the switching system is to solve a special working condition that occurs in the actual filling process; that is, the load torque of the filling motor jumped at the moment when the filling multimotor system is stopped-started, resulting in a large synchronization error in the system. When the switching system is designed, the filling motor can achieve smooth switching under complex working conditions when the load torque changes suddenly. At the same time, because the multimotor system selects the common Lyapunov function, it can ensure that the system reaches the common sliding-mode surface. It



is gradually stabilized, so as to effectively overcome the impact of sudden change of load torque on the synchronization performance. The designed relative coupling control diagram of the  $n$ -improved motors is shown in Figure 1:

Because of the different functions of each station in the filling operation, the multimotor system is composed of a filling motor and a conveying motor. In Figure 1, considering that the system contains  $n$  motors and motor 1 was the filling motor, other motors were taken as the transfer motors. The model of motor 1 is designed to switch the system structure. During the filling operation, the filling motor is stationary and stopped. Upon completion of the filling operation, the filling system needs to transport the filled finished product to the next station. Hence, the load torque of motor 1 is abruptly changed at the moment of stop-start, that is, changing from no-load to the increased load torque of the filling material which causes the filling motor to switch from subsystem 1 to subsystem 2. However, for the transmission motor system, the load torque does not change abruptly. Thus, a standard motor model can be used.

For the filling production transmission system, this study takes the permanent magnet synchronous motor as the research object. In the ideal permanent magnet synchronous model [29], the vector control strategy of  $i_d = 0$  is adopted to obtain the state equation of the  $j$  motor in the multimotor system [30]:

$$\begin{cases} \frac{d\theta_j}{dt} = \omega_j, \\ \frac{d\omega_j}{dt} = -\frac{R_{\Omega j}}{J_j}\omega_j + \frac{3}{2} \cdot \frac{n_{pj}^2 \psi_{fj}}{J_j} i_{qj} - \frac{T_{Lj} n_{pj}}{J_j}, \end{cases} \quad (1)$$

where  $\theta_j$  is the rotor position;  $\omega_j$  is the rotor electrical angular velocity;  $T_{Lj}$  is the load torque;  $R_{\Omega j}$  is the rotational resistance coefficient of motor;  $J_j$  is the moment of inertia;  $n_{pj}$  is the number of pole pairs of motor;  $\psi_{fj}$  is the rotor flux; and  $i_{dj}$  and  $i_{qj}$  are the  $d$ -axis and  $q$ -axis components of the stator current.

Let  $(R_{\Omega j}/J_j) = a_j$ ,  $(3/2) \cdot (n_{pj}^2 \psi_{fj}/J_j) = b_j$ ,  $(T_{Lj} n_{pj}/J_j) = p_j$ , and formula (1) can be expressed as follows:

$$\dot{\omega}_j = -a_j \omega_j + b_j u_j - p_j, \quad j = 1, k, k = 2, \dots, n, \quad (2)$$

where  $u_j = i_{qj}$  is the controller to be designed.

A filling motor model is established. Motor 1 is used as the filling motor. Because its load torque  $T_{L1}$  is abrupt, the state equation of motor 1 with switching system structure is designed, mainly including two subsystems under different states of stop and start. From formula (2), we can obtain the following:

$$\begin{cases} f_1(\omega_{11}, t) = \dot{\omega}_{11} = -a_1 \omega_{11} + b_1 u_1, \\ f_2(\omega_{12}, t) = \dot{\omega}_{12} = -a_1 \omega_{12} + b_1 u_1 - p_1, \end{cases} \quad (3)$$

where  $f_1(\omega_{11}, t)$  and  $\omega_{11}$  are the subsystems and speeds when motor 1 is stopped, and the filling motor is no-load at this time;  $f_2(\omega_{12}, t)$  and  $\omega_{12}$  are the subsystems and speeds when motor 1 is started. Define the state variables as

$x_{11} = \omega_{11}$ ,  $x_{12} = \omega_{12}$ , and rewrite formula (3) as matrix form as follows:

$$\begin{pmatrix} f_1(x_{11}, t) \\ f_2(x_{12}, t) \end{pmatrix} = \begin{pmatrix} \dot{x}_{11} \\ \dot{x}_{12} \end{pmatrix} = -a_1 \begin{pmatrix} x_{11} \\ x_{12} \end{pmatrix} + b_1 \begin{pmatrix} u_1 \\ u_1 \end{pmatrix} - p_1 \begin{pmatrix} 0 \\ 1 \end{pmatrix}. \quad (4)$$

A transfer motor model is built, and the motors in formula (2) excluding motor 1 are redefined as

$$\dot{\omega}_k = -a_k \omega_k + b_k u_k - p_k, \quad k = 2, \dots, n, \quad (5)$$

where  $\omega_k$  is the speed of the transfer motor in the multimotor system.

For a system consisting of a filling motor and a transfer motor, the tracking error of each motors is defined as follows:

$$e_j^* = \omega_j^* - \omega_j, \quad j = 1, k, k = 2, \dots, n, \quad (6)$$

where  $\omega_j^*$  and  $\omega_j$  are the given speed value and actual output speed of the  $j$ th motor of the system, respectively.

Define the synchronization error between the motors as follows:

$$\tau_{ji} = \omega_j - \omega_i, \quad j = 1, k, k = 2, \dots, n, i = 1, 2, \dots, n, i \neq j, \quad (7)$$

where  $\tau_{ji}$  indicates the synchronization error between the  $j$ th motor and the  $i$ th motor.

In the relative coupling control strategy, the speed compensator is often used for feedback adjustment for the synchronization error. To eliminate the influence of different motor rotational inertia on the synchronization performance, the speed compensator module used a fixed gain compensator. The synchronization error compensation signal is as follows [31]:

$$\Delta\omega_j = \sum_{i=1}^n \lambda_{ji} \tau_{ji}, \quad j = 1, k, k = 2, \dots, n, i = 1, 2, \dots, n, i \neq j, \quad (8)$$

where  $\lambda_{ji}$  is the ratio of the rotational inertia between adjacent motors. Its specific expression is

$$\lambda_{ji} = \frac{J_j}{J_i}. \quad (9)$$

### 3. Sliding-Mode Controller Design and Stability Analysis

**3.1. Sliding-Mode Controller Design.** This section designs a controller for a multimotor system to ensure that each axis has a better tracking and synchronization control effect. The equivalent sliding-mode controller is designed as follows [32]:

$$u_j = \frac{(1 + \sum_{i=1}^n \lambda_{ji}) a_j \omega_j + \dot{\omega}_j^* + \sum_{i=1}^n \lambda_{ji} \dot{\omega}_i}{(1 + \sum_{i=1}^n \lambda_{ji}) b_j} + \frac{K_j}{b_j} \text{sgn}(s_j), \quad j = 1, k, k = 2, \dots, n, i = 1, 2, \dots, n, i \neq j, \quad (10)$$

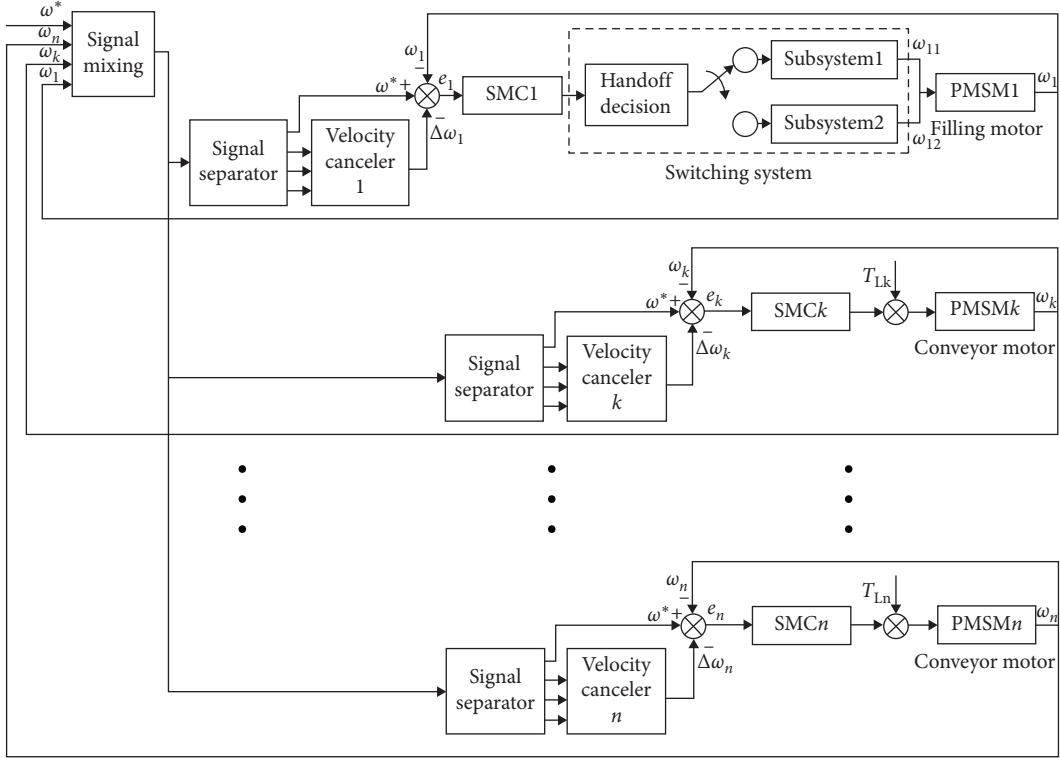


FIGURE 1: The designed relative coupling control diagram of the  $n$ -improved motors.

where  $K_j$  is the sliding-mode coefficient to be designed and  $s_j$  is the sliding surface to be designed.

Define the single-axis error of the multimotor synchronous system, and from formulas (6) and (8), we can obtain the following [17]:

$$e_j = e_j^* - \Delta\omega_j = \omega_j^* - \omega_j - \Delta\omega_j, \quad j = 1, k, k = 2, \dots, n. \quad (11)$$

After the derivation of formula (11), we get

$$\begin{aligned} \dot{e}_j &= \dot{\omega}_j^* - \dot{\omega}_j - \sum_{i=1}^n \lambda_{ji} (\dot{\omega}_j - \dot{\omega}_i) \\ &= - \left( 1 + \sum_{i=1}^n \lambda_{ji} \right) \dot{\omega}_j + \dot{\omega}_j^* + \sum_{i=1}^n \lambda_{ji} \dot{\omega}_i. \end{aligned} \quad (12)$$

Define the sliding surface as follows:

$$s_j = c_j e_j, \quad j = 1, k, k = 2, \dots, n. \quad (13)$$

Design the sliding-mode parameter  $c_j > 0$ , and calculate the derivation of formula (13) as follows:

$$\dot{s}_j = c_j \dot{e}_j = c_j \left[ - \left( 1 + \sum_{i=1}^n \lambda_{ji} \right) \dot{\omega}_j + \dot{\omega}_j^* + \sum_{i=1}^n \lambda_{ji} \dot{\omega}_i \right]. \quad (14)$$

Let  $\dot{s}_j = 0$ , and the equivalent control term  $u_{jeq}$  is as follows:

$$u_{jeq} = \frac{(1 + \sum_{i=1}^n \lambda_{ji}) a_j \omega_j + \dot{\omega}_j^* + \sum_{i=1}^n \lambda_{ji} \dot{\omega}_i}{(1 + \sum_{i=1}^n \lambda_{ji}) b_j}. \quad (15)$$

Define the switching control term as follows:

$$u_{jsw} = \frac{1}{b_j} K_j \text{sgn}(s_j). \quad (16)$$

Thus, the sliding-mode control law of formula (10) consists of equivalent and switching control terms as follows:

$$u_j = u_{jeq} + u_{jsw}. \quad (17)$$

**3.2. Stability Analysis.** The multimotor system Lyapunov function is selected, and this function can also be used as the public Lyapunov function of the switching system. Finally, results prove that the switching system can go from any initial state to the public sliding surface, thus ensuring the asymptotic stability of the entire system.

The stability of the transfer motor system is analyzed, and the Lyapunov function is selected:

$$V_k = \frac{1}{2} s_k^2, \quad k = 2, \dots, n. \quad (18)$$

After the derivation of formula (18), we get

$$\begin{aligned} \dot{V}_k = s_k \dot{s}_k = s_k \cdot c_k \left[ - \left( 1 + \sum_{i=1}^n \lambda_{ki} \right) (-a_k \omega_k + b_k u_k - p_k) \right. \\ \left. + \dot{\omega}_k^* + \sum_{i=1}^n \lambda_{ki} \dot{\omega}_i \right]. \end{aligned} \quad (19)$$

Substituting formula (10) into (19) and reducing it results in

$$\begin{aligned} \dot{V}_k &= -s_k L_k (K_k \operatorname{sgn}(s_k) - p_k) \\ &= -L_k K_k |s_k| + L_k p_k s_k \\ &\leq -L_k (K_k - p_k) |s_k|, \end{aligned} \quad (20)$$

where

$$L_k = c_k \left( 1 + \sum_{i=1}^n \lambda_{ki} \right) > 0. \quad (21)$$

Design a proper sliding-mode coefficient  $K_k > p_k + \eta_k$ .  $\eta_j$  is an arbitrarily small normal number which obtains

$$\dot{V}_k < -L_k \eta_k |s_k|. \quad (22)$$

The sliding-mode principle [33] shows that the occurrence of the sliding-mode motion will cause  $s_k \rightarrow 0$  in limited time. According to formula (13), the single-axis error of each transfer motor  $e_k \rightarrow 0$  can be acquired.

The stability of the filling motor system is analyzed to select the common sliding-mode surface  $s_1$  and the common Lyapunov function  $V_1$  of the switching system:

$$V_1 = \frac{1}{2} s_1^2. \quad (23)$$

For the switching subsystem  $f_1(x_{11}, t)$ , derive formula (23) which gives

$$\begin{aligned} \dot{V}_1 &= s_1 \dot{s}_1 \\ &= s_1 \cdot c_1 \left[ - \left( 1 + \sum_{i=2}^n \lambda_{1i} \right) (-a_1 \omega_{11} + b_1 u_1) + \dot{\omega}_1^* + \sum_{i=2}^n \lambda_{1i} \dot{\omega}_i \right]. \end{aligned} \quad (24)$$

Substituting formula (10) into (24) and reducing it results in

$$\dot{V}_1 = -s_1 L_1 K_1 \operatorname{sgn}(s_1) = -L_1 K_1 |s_1|, \quad (25)$$

where

$$L_1 = c_1 \left( 1 + \sum_{i=2}^n \lambda_{1i} \right) > 0. \quad (26)$$

Design a proper sliding-mode coefficient  $K_1 > \eta_1$ ;  $\eta_1$  is an arbitrarily small normal number which obtains the following:

$$\dot{V}_1 < -L_1 \eta_1 |s_1|. \quad (27)$$

That is, the uniaxial error  $e_1$  of the switching subsystem  $f_1(x_{11}, t)$  gradually converges to 0.

For the switching subsystem  $f_2(x_{12}, t)$ , just design the appropriate sliding-mode coefficient  $K_1 > p_1 + \eta_1$  that can obtain formula (27) in the same way; that is, the uniaxial error  $e_1$  of the switching subsystem  $f_2(x_{12}, t)$  gradually converges to 0. The common Lyapunov function shows that  $\dot{V}_1$  exists regardless of the subsystem activated. Thus, the sliding-mode function  $s_1 \neq 0$  is attenuated. To sum up, when  $t \rightarrow \infty, e_j \rightarrow 0, j = 1, k = 2, \dots, n$ .

The convergence of tracking error and synchronization error is to be proved as follows [34].

From simultaneous formulas (6), (8), and (11), the following can be obtained:

$$e_j = \left( 1 + \sum_{i=1}^n \lambda_{ji} \right) e_j^* - \sum_{i=1}^n \lambda_{ji} e_i^*. \quad (28)$$

Rewrite formula (28) as matrix form:

$$\begin{pmatrix} e_1 \\ \vdots \\ e_j \\ \vdots \\ e_n \end{pmatrix} = \begin{pmatrix} 1 + \sum_{i=1}^n \lambda_{1i} & \cdots & -\lambda_{1i} & \cdots & -\lambda_{1n} \\ \vdots & \ddots & \vdots & & \vdots \\ -\lambda_{j1} & & 1 + \sum_{i=1}^n \lambda_{ji} & & -\lambda_{jn} \\ \vdots & & \vdots & \ddots & \vdots \\ -\lambda_{n1} & \cdots & -\lambda_{ni} & \cdots & 1 + \sum_{i=1}^n \lambda_{ni} \end{pmatrix} \begin{pmatrix} e_1^* \\ \vdots \\ e_j^* \\ \vdots \\ e_n^* \end{pmatrix}. \quad (29)$$

Define the matrix of coefficient  $G_{n \times n}$  as

$$G_{n \times n} = \begin{pmatrix} 1 + \sum_{i=1}^n \lambda_{1i} & \cdots & -\lambda_{1i} & \cdots & -\lambda_{1n} \\ \vdots & \ddots & \vdots & & \vdots \\ -\lambda_{j1} & & 1 + \sum_{i=1}^n \lambda_{ji} & & -\lambda_{jn} \\ \vdots & & \vdots & \ddots & \vdots \\ -\lambda_{n1} & \cdots & -\lambda_{ni} & \cdots & 1 + \sum_{i=1}^n \lambda_{ni} \end{pmatrix}. \quad (30)$$

The coefficient matrix  $G_{n \times n}$  is a nonsingular matrix. Because  $e_j \rightarrow 0$  has been proven above,  $[e_1^* \cdots e_j^* \cdots e_n^*]^T$  can be obtained with only unique zero solution. Therefore, the tracking error of each axis can be converged to 0, and the synchronous compensation signal  $\Delta \omega_j$  also converges to 0.

The proof is completed.

#### 4. Simulation and Experimental Results Analysis

To verify the theoretical research and control method in this paper, this section uses Matlab/Simulink to perform a

TABLE 1: The physical parameter setting of each motor.

Parameter	Motor 1	Motor 2	Motor 3
$R_\Omega$ (N · m · s)	$4.831 \times 10^{-5}$	$4.846 \times 10^{-5}$	$4.827 \times 10^{-5}$
$\psi_f$ (Wb)	0.175	0.173	0.178
$n_p$	2	2	2
$J$ (kg · m <sup>2</sup> )	$8.5 \times 10^{-4}$	$8.47 \times 10^{-4}$	$8.51 \times 10^{-4}$

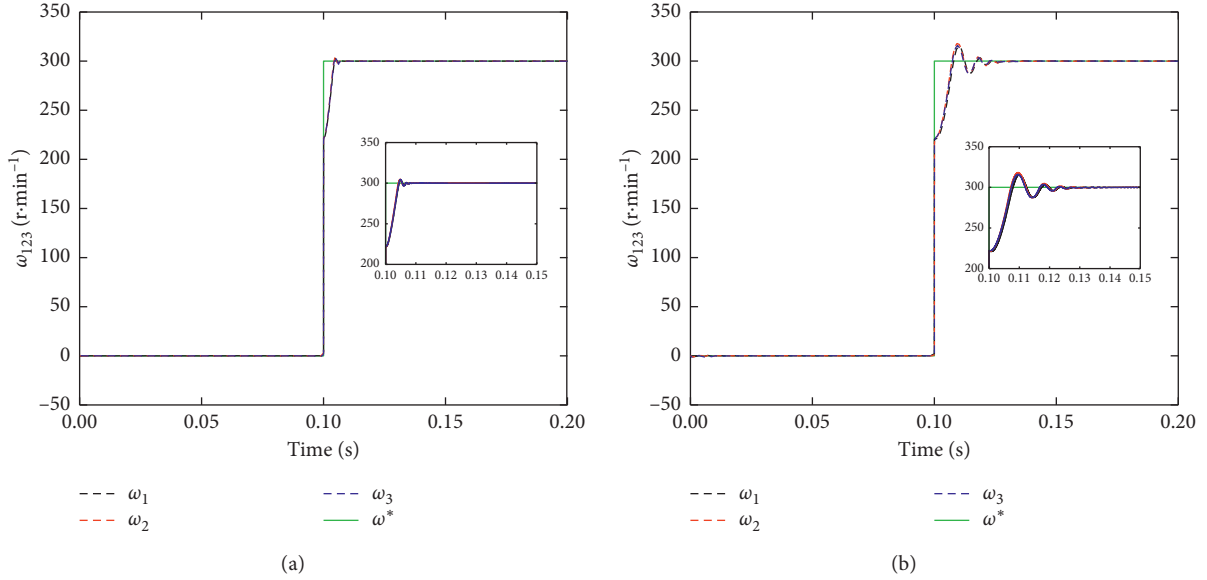


FIGURE 2: Comparative simulation results of the speed follow of each motor.

simulation analysis of the system and thus verify the research of multimotor cooperative control under complex working conditions of filling production. At the same time, to highlight the advantages of the improved control structure, this section also adds a comparative experiment simulation. Under the traditional control structure, the PI controller is used to adjust the system error, and the sudden load torque is also applied to the filling motor. For the stop-start process during the filling system operation, the speed given curve of the designed multimotor system is as follows:

$$\omega^* = \begin{cases} 0, & 0 \leq t \leq 0.1, \\ 300, & 0.1 < t \leq 0.2. \end{cases} \quad (31)$$

The physical parameter setting of each motor used in Matlab/Simulink is shown in Table 1:

The entire experimental simulation duration is set to 0.2 s. For the experimental simulation of the improved control structure, designed motor 1 is switched in 0.1 s, and the load torque of the given subsystem  $f_2(x_{12}, t)$  is 1 N · m. For the experimental simulation of the traditional control structure, a load torque 1 N · m is suddenly applied to motor 1 at 0.1 s. To simulate the process of conveying the empty bottle to the filling station by the transfer motor, the load torque of given motor 2 is 0.1 N · m. To simulate the process of conveying the finished product to the next station by transfer the motor, the load torque of the given motor 3 is

1 N · m. In the controller, the sliding-mode coefficient is  $K_1 = K_2 = K_3 = 10000$ , and the sliding surface parameter is  $c_1 = c_2 = c_3 = 1000$ . Figure 2 is the comparison simulation diagrams of the speed following curves of each motors.

Figure 2 is the speed following curve diagrams of each motor. Among them, (a) and (b) show the running trajectory of each motor speed under the improved and traditional relative coupling control strategy, respectively. The designed system speed-given curve simulates the stop-start process of filling production, and 0.1 s is the speed jump time. Analysis and simulation results show that, in comparison with the traditional control structure, the speed of motor 1 with the switching system structure runs more stably at the initial stage and the switching time. In addition, the rising curve is smoother, and the speeds of motors 2 and 3 can also be better tracked with the fixed value of the load torque, especially because the controller adjustment time only needs about 0.01 s at the time of switching, with no obvious overshoot of the speed.

(a), (b), and (c) in Figure 3 are the simulation comparison diagrams of the rotational speed-tracking errors of motors 1, 2, and 3, respectively. Among them, the red dashed line and the blue solid line, respectively, represent the tracking error under the traditional and the improved control strategy, and a supplementary explanation is made to Figure 2. Analysis and simulation results show that, Figure 3

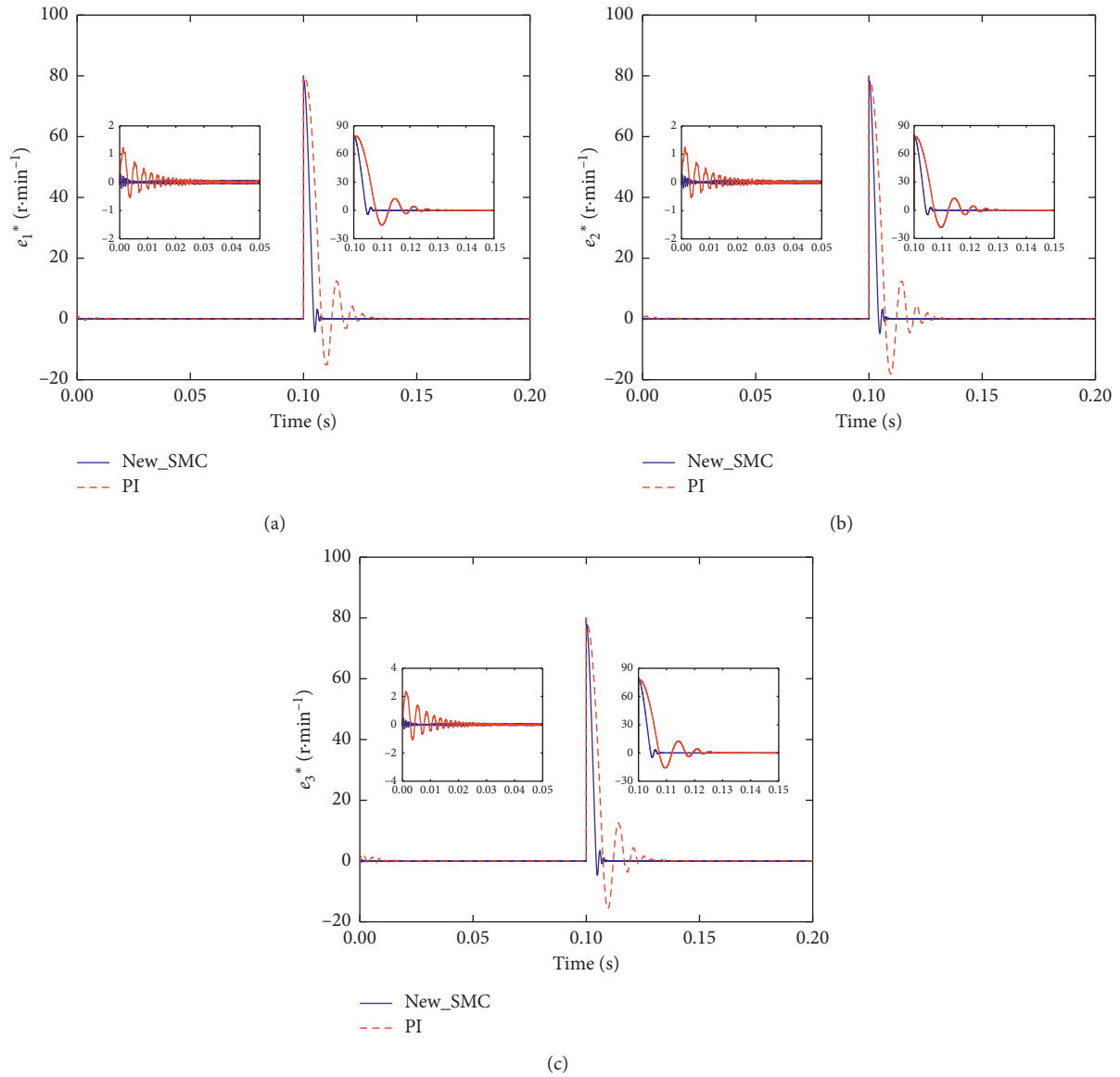


FIGURE 3: Comparative simulation results of tracking errors of each motor.

shows the situation of each motor tracking a given value more intuitively. At the same time, each motor in the improved control structure can achieve rapid convergence of the tracking error within 0.01 s, especially at the stop-start time of 0.1 s, when the impact of load torque mutation has good robustness. However, in the initial stage within 0 ~ 0.1 s, the tracking error jitter of motor 3 is larger than that of other motors, which is mainly caused by the larger load torque than that of other motors. At the moment of stop-start, the set value of the speed of each motor suddenly jumps from 0  $\text{rad} \cdot \text{min}^{-1}$  to 300  $\text{rad} \cdot \text{min}^{-1}$ , and the actual motor speed value cannot jump, so a large tracking error (about 80  $\text{rad} \cdot \text{min}^{-1}$ ) will occur in 0.1 s. On the other hand, it also confirmed the authenticity and rationality of the simulation.

(a), (b), and (c) in Figure 4 are the simulation comparison diagrams of the synchronous errors between motors

1 and 2, between motors 1 and 3 and between motors 2 and 3, respectively. Among them, the red dashed line and the blue solid line represent the synchronous error under the traditional and the improved control strategy, respectively. In terms of error suppression time, the synchronous error among the motors in the improved control structure can be quickly converged within 0.01 s. However, in the traditional control structure, the error will not converge until about 0.15 s. In terms of error suppression effect, the improved method proposed in this paper can make the error jitter suppression is more significant and change amplitude is smaller. Among them, motors 1 and 2 have a smaller initial synchronous error in 0 ~ 0.1 s, and it also includes the case where the error curve between the motors is significantly different at the switching time of 0.1 s. This result is mainly caused by the large difference in load torque of each motor, and it is real and reasonable.

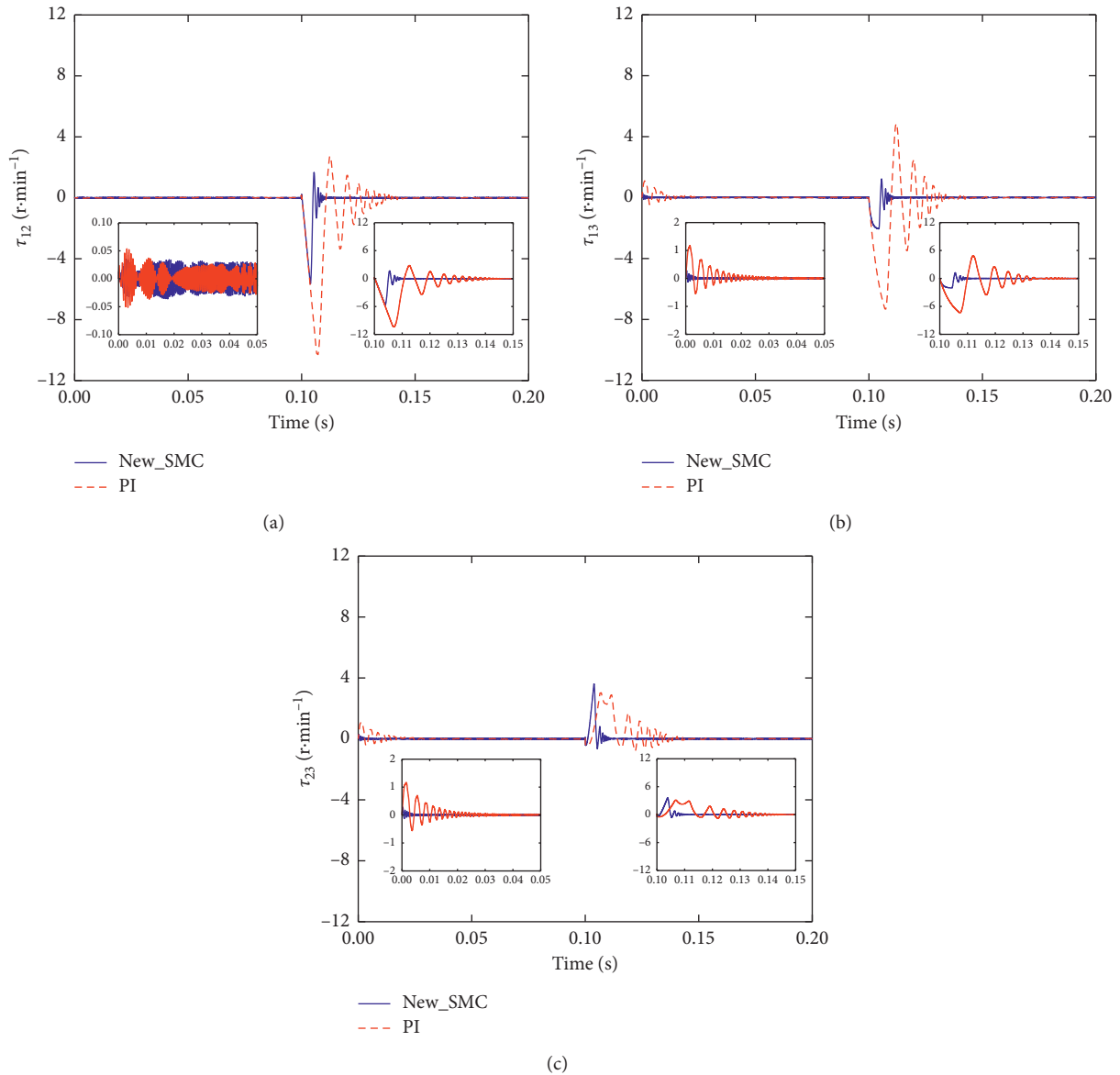


FIGURE 4: Comparative simulation results of synchronization errors of each motor.

## 5. Conclusions

To realize the follow-up control and synchronous control of the filling multimotor system under complex working conditions, the relative coupling control strategy including the switching system structure is firstly established. Secondly, the common sliding-mode surface is selected based on the filling motor, and the equivalent sliding-mode controller is designed. Thirdly, by selecting the common Lyapunov function, the switching system can reach the common sliding-mode surface in any initial state. Hence, the entire system reaches an asymptotic stable state. By adopting the proposed method, the adverse effects of sudden changes in load torque can be effectively weakened. As such, the system has better dynamic and static characteristics and is particularly robust to torque parameter jumps that occur during the switching process. Simulation results verify the

effectiveness of this method for multimotor collaborative control of filling.

## Data Availability

The model data used to support the findings of this study are available from the corresponding author upon request.

## Conflicts of Interest

The authors declare that there are no conflicts of interest regarding the publication of this paper.

## Acknowledgments

The study was supported by the National Key R&D Program of China (no. 2018YFD0400705).

## References

- [1] H. Yan, Y. Tian, H. Li, H. Zhang, and Z. Li, "Input-output finite-time mean square stabilisation of nonlinear semi-Markovian jump systems," *Automatica*, vol. 104, pp. 82–89, 2019.
- [2] H. Su, Y. Ye, Y. Qiu, Y. Cao, and M. Z. Q. Chen, "Semi-global output consensus for discrete-time switching networked systems subject to input saturation and external disturbances," *IEEE Transactions on Cybernetics*, vol. 49, no. 11, pp. 3934–3945, 2019.
- [3] H. Su, J. Zhang, and X. Chen, "A stochastic sampling mechanism for time-varying formation of multi-agent systems with multiple leaders and communication delays," *IEEE Transactions on Neural Networks and Learning Systems*, vol. 30, no. 12, pp. 3699–3707, 2019.
- [4] S. Mao, H. Wu, M. Lu, and C.-W. Cheng, "Multiple 3D marker localization and tracking system in image-guided radiotherapy," *International Journal of Robotics and Automation*, vol. 32, no. 5, pp. 517–523, 2017.
- [5] C. Xu, Y. Zhao, B. Qin, and H. Zhang, "Adaptive synchronization of coupled harmonic oscillators under switching topology," *Journal of the Franklin Institute*, vol. 356, no. 2, pp. 1067–1087, 2019.
- [6] C.-F. Zhang, Y.-Y. Xiao, J. He, and M. Yan, "Improvement of electronic line-shafting control in multi-axis systems," *International Journal of Automation and Computing*, vol. 15, no. 4, pp. 474–481, 2018.
- [7] H. Yang, Y. Fu, and D. Wang, "Multi-ANFIS model based synchronous tracking control of high-speed electric multiple unit," *IEEE Transactions on Fuzzy Systems*, vol. 26, no. 3, pp. 1472–1484, 2018.
- [8] W. Zhao and H. Zhang, "Coupling control strategy of force and displacement for electric differential power steering system of electric vehicle with motorized wheels," *IEEE Transactions on Vehicular Technology*, vol. 67, no. 9, pp. 8118–8128, 2018.
- [9] T. Shi, H. Liu, Q. Geng, and C. Xia, "An improved relative coupling control structure for multi-motor speed synchronous driving system," *IET Electric Power Applications*, vol. 10, no. 6, pp. 451–457, 2016.
- [10] C. Sun, G. Gong, H. Yang, and F. Wang, "Fuzzy sliding mode control for synchronization of multiple induction motors drive," *Transactions of the Institute of Measurement and Control*, vol. 41, no. 11, pp. 3223–3234, 2019.
- [11] C. Zhang, H. Wu, B. Liu, J. He, and B. Li, "Hybrid structure based tracking and consensus for multiple motors," *Mathematical Problems in Engineering*, vol. 2014, Article ID 967578, 9 pages, 2014.
- [12] L. Li, L. Sun, and S. Zhang, "Mean deviation coupling synchronous control for multiple motors via second-order adaptive sliding mode control," *ISA Transactions*, vol. 62, pp. 222–235, 2016.
- [13] K. Huang, Y. Zhang, Y. Li, C. Yang, and Z. Wang, "Effects of external forcing on evolutionary games in complex networks," *Chaos: An Interdisciplinary Journal of Nonlinear Science*, vol. 28, no. 9, Article ID 093108, 2018.
- [14] J. He, X. Chen, S. Mao, C. Zhang, and J. Liu, "Virtual line shafting-based total-amount coordinated control of multi-motor traction power," *Journal of Advanced Transportation*, vol. 2020, Article ID 4735397, 9 pages, 2020.
- [15] L.-B. Li, L.-L. Sun, S.-Z. Zhang, and Q.-Q. Yang, "Speed tracking and synchronization of multiple motors using ring coupling control and adaptive sliding mode control," *ISA Transactions*, vol. 58, pp. 635–649, 2015.
- [16] C. Xia, Y. Yan, B. Ji, and T. Shi, "Two-degree-of-freedom proportional integral speed control of electrical drives with Kalman-filter-based speed estimation," *IET Electric Power Applications*, vol. 10, no. 1, pp. 18–24, 2016.
- [17] J. He, X. Jiang, C. Zhang et al., "Multiaxis servo synergic control based on sliding mode controller," *Journal of Control Science and Engineering*, vol. 2019, Article ID 9249270, 16 pages, 2019.
- [18] D. Yang, W. Ren, X. Liu, and W. Chen, "Decentralized event-triggered consensus for linear multi-agent systems under general directed graphs," *Automatica*, vol. 69, pp. 242–249, 2016.
- [19] C. Zhang, H. Wu, J. He, and C. Xu, "Consensus tracking for multi-motor system via observer based variable structure approach," *Journal of the Franklin Institute*, vol. 352, no. 8, pp. 3366–3377, 2015.
- [20] C. Xia, L. Li, G. Xin, and T. Shi, "Speed synchronization control of dual-PMSM system," *Diangong Jishu Xuebao/Transactions of China Electrotechnical Society*, vol. 32, no. 23, pp. 1–8, 2017.
- [21] M. Wang, X. Ren, and Q. Chen, "Robust tracking and distributed synchronization control of a multi-motor servomechanism with H-infinity performance," *ISA Transactions*, vol. 72, pp. 147–160, 2018.
- [22] L. Liu, D. Wei, and B. Zhang, "Synchronization control of chaos in complex motor networks with small-world topology based on dynamic relaying," *Jisuan Wuli/Chinese Journal of Computational Physics*, vol. 35, no. 6, pp. 750–756, 2018.
- [23] H. Wu, J. Lam, and H. Su, "Global consensus of positive edge system with sector input nonlinearities," *IEEE Transactions on Systems, Man, and Cybernetics: Systems*, pp. 1–10, 2019.
- [24] H. Su, H. Wu, and J. Lam, "Positive edge-consensus for nodal networks via output feedback," *IEEE Transactions on Automatic Control*, vol. 64, no. 3, pp. 1244–1249, 2018.
- [25] X. Wang, H. Su, M. Z. Q. Chen, and X. Wang, "Observer-based robust coordinated control of multiagent systems with input saturation," *IEEE Transactions on Neural Networks and Learning Systems*, vol. 29, no. 5, pp. 1933–1946, 2018.
- [26] H. Wu and H. Su, "Positive edge consensus of networked systems with input saturation," *ISA Transactions*, vol. 96, pp. 210–217, 2020.
- [27] J. He, B. Yang, C. Zhang et al., "Robust consensus braking algorithm for distributed EMUs with uncertainties," *IET Control Theory & Applications*, vol. 13, no. 17, pp. 2766–2774, 2019.
- [28] C. Xu, H. Su, C. Liu, and G. Zhang, "Robust adaptive synchronization of complex network with bounded disturbances," *Advances in Difference Equations*, vol. 2019, no. 1, 2019.
- [29] P. Gao, G. Zhang, H. Ouyang, and L. Mei, "A sliding mode control with nonlinear fractional order PID sliding surface for the speed operation of surface-mounted PMSM drives based on an extended state observer," *Mathematical Problems in Engineering*, vol. 2019, Article ID 7130232, 13 pages, 2019.
- [30] J. He, J. Ding, C. Zhang et al., "Research on multi-axis servo synergic control system based on sliding mode variable structure," in *Proceedings of the IECON 2019-45th Annual Conference of the IEEE Industrial Electronics Society*, pp. 6908–6915, Lisbon, Portugal, October 2019.
- [31] Y. Xia, K. Xu, Y. Li, G. Xu, and X. Xiang, "Modeling and three-layer adaptive diving control of a cable-driven underwater parallel platform," *IEEE Access*, vol. 6, pp. 24016–24034, 2018.

- [32] Y. Pan, M. J. Er, T. Sun, B. Xu, and H. Yu, "Adaptive fuzzy PD control with stable  $H^\infty$  tracking guarantee," *Neurocomputing*, vol. 237, pp. 71–78, 2016.
- [33] V. I. Utkin, *Sliding Modes in Control and Optimization*, Springer-Verlag, Berlin, Germany, 1992.
- [34] J. He, L. Mi, J. Liu, X. Cheng, Z. Lin, and C. Zhang, "Ring coupling-based collaborative fault-tolerant control for multi-robot actuator fault," *International Journal of Robotics and Automation*, vol. 33, no. 6, pp. 672–680, 2018.



## Research Article

# An Improved Iterative Method for Solving the Discrete Algebraic Riccati Equation

Li Wang 

School of Mathematics and Computational Science, Hunan University of Science and Technology, Hunan 411201, China

Correspondence should be addressed to Li Wang; wanglileigh@163.com

Received 24 March 2020; Accepted 21 April 2020; Published 20 May 2020

Guest Editor: Hou-Sheng Su

Copyright © 2020 Li Wang. This is an open access article distributed under the Creative Commons Attribution License, which permits unrestricted use, distribution, and reproduction in any medium, provided the original work is properly cited.

The discrete algebraic Riccati equation has wide applications, especially in networked systems and optimal control systems. In this paper, according to the damped Newton method, two iterative algorithms with a stepsize parameter is proposed to solve the discrete algebraic Riccati equation, one of which is an extension of Algorithm (4.1) in Dai and Bai (2011). A numerical example demonstrates the convergence effect of the presented algorithm.

## 1. Introduction and Preliminaries

The discrete algebraic Riccati equation plays an important part in engineering, such as optimal control systems [1], modified filtering [2, 3], and networked systems [4–7]. Consider the following discrete-time linear system:

$$x(k+1) = Ax(k) + Bu(k), \quad (1)$$

where  $x(k) \in R^n$  is the state variable,  $u(k) \in R^r$  is the input variable,  $B \in R^{n \times r}$  is the input matrix, and  $A \in R^{n \times n}$  is the system matrix and is always invertible [8]. The optimal state feedback controller of (1) is

$$u^*(k) = -(G + B^T PB)^{-1} B^T PAx(k), \quad (2)$$

which minimizes the quadratic performance index of (1) and is closely related to the discrete algebraic Riccati equation (DARE):

$$P = A^T PA - A^T PB(G + B^T PB)^{-1} B^T PA + Q, \quad (3)$$

where  $Q \in R^{n \times n}$  is semipositive definite,  $G \in R^{r \times r}$  is positive definite, and  $P \in R^{n \times n}$  is the positive definite solution of the DARE (3). Let  $R = BG^{-1}B^T \geq 0$ . According to the matrix identity,

$$(X^{-1} + YZ)^{-1} = X - XY(I + ZXY)^{-1}ZX, \quad (4)$$

equation (3) can be transformed into

$$P = A^T(P^{-1} + R)^{-1}A + Q. \quad (5)$$

Due to the wide applications of the DARE, many works have been proposed to discuss the DARE. Various bounds and solutions about the DARE have been provided, such as upper and lower solution bounds [9–14], bounds about sum and product of eigenvalues [15, 16], determinant of the solution [17], and the existence of the solution [18–21]. However, in an optimal control system, we often need to compute the solution of the DARE to find the optimal state feedback controller which minimizes the quadratic performance index. It is very difficult to solve the DARE, especially when the dimensions of the coefficient matrices are high. So, many researchers provide a lot of iterative methods to solve this equation. Komaroff present a fixed-point iterative algorithm that needs to compute twice matrix inversion at each step [22]. By Newton's method, Guo derived the maximal symmetric solution of the DARE in [23]. The structure-preserving doubling algorithms are discussed in [24–27]. The Schur method is adopted to solve algebraic Riccati equations [28]. Recently, Dai and Bai propose an iterative algorithm that partially avoids computing the matrix inversions by making use of the Schulz iteration [29].

In Section 2, we propose two iterative algorithms with a stepsize parameter to solve the DARE by the damped Newton method. One of the iterative algorithms is an extension of Algorithm 4.1 in [29]. Numerical example is given in Section 3 to demonstrate the convergence effect of our algorithms.

We first introduce some symbol conventions.  $R$  denotes the real number field.  $R^{n \times m}$  denotes the set of  $n \times m$  real matrices. For  $X = (x_{ij}) \in R^{n \times n}$ , let  $X^T$ ,  $X^{-1}$ ,  $\|X\|$ , and  $\lambda_{\min}(X)$  denote the transpose, inverse, spectral norm, and the minimal eigenvalue of the matrix  $X$ , respectively. The inequality  $X > (\geq) 0$  means  $X$  is a symmetric positive (semi-) definite matrix; and the inequality  $X > (\geq) Y$  means  $X - Y$  is a symmetric positive (semi-) definite matrix. The identity matrix with appropriate dimensions is represented by  $I$ .

**Lemma 1** (see [30]). *If  $A, B \in R^{n \times n}$  are symmetric positive definite matrices, then*

$$A \geq B, \quad \text{if and only if} \quad B^{-1} \geq A^{-1}. \quad (6)$$

**Lemma 2** (see [31]). *Let  $C$  and  $P$  be Hermitian matrices of the same order and let  $P > 0$ . Then,*

$$CPC + P^{-1} \geq 2C. \quad (7)$$

**Lemma 3** (see [32]). *Let  $S$  and  $T$  be symmetric positive definite matrices. Then,*

$$\|S\| \geq \|T\|, \quad \text{if} \quad S \geq T \geq 0. \quad (8)$$

## 2. Improved Iterative Algorithms for Solving the DARE

To find the positive definite solution of the DARE (5), Dai and Bai, in [29], proposed an algorithm that partially avoids computing the matrix inversion as follows.

*Algorithm 1* (see [29]). Take  $Y_0 = (Q^{-1} + R)^{-1}$ . For  $k = 0, 1, 2, \dots$ , compute

$$\begin{cases} P_{k+1} = A^T Y_k A + Q, \\ Y_{k+1} = (1-t)Y_k + t[2Y_k - Y_k(P_k^{-1} + R)Y_k], \quad k = 0, 1, 2, \dots \end{cases} \quad (13)$$

About Algorithms 2 and 3, we have the following results.

**Theorem 1.** *Let  $P_-$  be the positive definite solution of the DARE (5) and  $Q > 0$ . The iterative sequences  $\{P_k\}$  and  $\{Y_k\}$  are generated by Algorithm 2 with  $t \in (0, 1]$ ; then,*

$$\begin{aligned} P_0 \leq P_1 \leq P_2 \leq \dots, \quad \lim_{k \rightarrow \infty} P_k &= P_-; \\ Y_0 \leq Y_1 \leq Y_2 \leq \dots, \quad \lim_{k \rightarrow \infty} Y_k &= (P_-^{-1} + R)^{-1}. \end{aligned} \quad (14)$$

$$\begin{cases} P_{k+1} = A^T Y_k A + Q, \\ Y_{k+1} = Y_k(2I - (P_{k+1}^{-1} + R)Y_k). \end{cases} \quad (9)$$

In this section, we propose two iterative algorithms to solve the DARE (5), which are motivated by the damped Newton method [33] and the methods in [34, 35]. Let us recall the damped Newton method to find the root of  $F(Z) = Z^{-1} - B$ :

$$Z_{k+1} = Z_k + tZ_k(I - BZ_k) = (1+t)Z_k - tZ_k BZ_k, \quad (10)$$

where  $t > 0$  is a stepsize parameter. If the initial matrix is near the solution of the problem, the unit stepsize  $t = 1$  can be accepted in the local Newton method. However, it is not suitable to choose  $t = 1$  if the initial matrix is far from the solution of the problem [33].

The DARE (5) can be translated into  $F(P) = 0$ , where

$$F(P) = [A^{-T}(P - Q)A^{-1}]^{-1} - (P^{-1} + R). \quad (11)$$

Let  $Z = A^{-T}(P - Q)A^{-1}$  and  $B = P^{-1} + R$ . Then, to find the root of  $F(P)$  is equivalent to find the root of  $F(Z)$ , we can solve the DARE (5) by constructing an iterative scheme. According to (10), we present the following iterative algorithms for the DARE (5).

*Algorithm 2*

Step 1: set  $P_0 = Q$ ,  $Y_0 = (Q^{-1} + R)^{-1}$  and  $t > 0$ .

Step 2: compute

$$\begin{cases} Y_{k+1} = (1-t)Y_k + t[2Y_k - Y_k(P_k^{-1} + R)Y_k], \\ P_{k+1} = A^T Y_{k+1} A + Q, \quad k = 0, 1, 2, \dots \end{cases} \quad (12)$$

*Algorithm 3*

Step 1: set  $Y_0 = (Q^{-1} + R)^{-1}$ ,  $P_0 = Q$  and  $t > 0$ .

Step 2: compute

*Proof.* We first prove  $P_k$  and  $Y_k$  are monotone increasing by induction. Since  $P_-$  is positive definite solution of DARE (5), then

$$P_- = A^T(P_-^{-1} + R)^{-1}A + Q. \quad (15)$$

Thus,  $P_- \geq Q$ .

(i) Since

$$\begin{aligned}
 Y_1 &= (1-t)Y_0 + t[2Y_0 - Y_0(P_0^{-1} + R)Y_0] \\
 &= (1-t)Y_0 + t[2Y_0 - Y_0(Q^{-1} + R)Y_0] \\
 &= (1-t)Y_0 + t[2Y_0 - Y_0] \\
 &= Y_0,
 \end{aligned} \tag{16}$$

then by Lemma 1, we obtain

$$\begin{aligned}
 P_1 &= A^T Y_1 A + Q = A^T Y_0 A + Q \\
 &= A^T (Q^{-1} + R)^{-1} A + Q,
 \end{aligned} \tag{17}$$

$$\begin{aligned}
 &\leq A^T (P_-^{-1} + R)^{-1} A + Q \\
 &= P_-.
 \end{aligned} \tag{18}$$

From (17), we also obtain  $P_1 \geq Q = P_0$ ; then,

$$P_- \geq P_1 \geq P_0, \tag{19}$$

$$Y_0 = Y_1 = (Q^{-1} + R)^{-1} \leq (P_1^{-1} + R)^{-1} \leq (P_-^{-1} + R)^{-1}. \tag{20}$$

By Lemma 2 and (20), we have

$$\begin{aligned}
 Y_2 &= (1-t)Y_1 + t[2Y_1 - Y_1(P_1^{-1} + R)Y_1] \\
 &\leq (1-t)Y_1 + t(P_1^{-1} + R)^{-1} \\
 &\leq (1-t)(P_1^{-1} + R)^{-1} + t(P_1^{-1} + R)^{-1} \\
 &= (P_1^{-1} + R)^{-1} \leq (P_-^{-1} + R)^{-1}.
 \end{aligned} \tag{21}$$

By (20) and Lemma 1, we obtain

$$\begin{aligned}
 Y_2 &= (1-t)Y_1 + t[2Y_1 - Y_1(P_1^{-1} + R)Y_1] \\
 &\geq (1-t)Y_1 + t[2Y_1 - Y_1(Q^{-1} + R)Y_1] \\
 &= (1-t)Y_1 + t[2Y_1 - Y_1] \\
 &= Y_1,
 \end{aligned} \tag{22}$$

thereby,

$$\begin{aligned}
 P_2 &= A^T Y_2 A + Q \\
 &\geq A^T Y_1 A + Q = P_1.
 \end{aligned} \tag{23}$$

By (21), we obtain

$$\begin{aligned}
 P_2 &= A^T Y_2 A + Q \\
 &\leq A^T (P_1^{-1} + R)^{-1} A + Q \\
 &\leq A^T (P_-^{-1} + R)^{-1} A + Q = P_-.
 \end{aligned} \tag{24}$$

Thus, from the above-mentioned proof, we have

$$\begin{aligned}
 P_0 \leq P_1 \leq P_2 \leq P_-, \quad Y_0 = Y_1 \\
 \leq Y_2 \leq (P_1^{-1} + R)^{-1} \leq (P_-^{-1} + R)^{-1}.
 \end{aligned} \tag{25}$$

(ii) Assume that

$$\begin{aligned}
 P_{i-1} \leq P_i \leq \dots \leq P_-, \quad Y_{i-1} \leq Y_i \leq (P_{i-1}^{-1} + R)^{-1} \\
 \leq (P_-^{-1} + R)^{-1}, \quad i = 1, 2, \dots, k.
 \end{aligned} \tag{26}$$

From (26), we get  $Y_k \leq (P_{k-1}^{-1} + R)^{-1} \leq (P_k^{-1} + R)^{-1}$ ; then,

$$Y_k^{-1} \geq P_k^{-1} + R. \tag{27}$$

Thus,

$$\begin{aligned}
 Y_{k+1} &= (1-t)Y_k + t[2Y_k - Y_k(P_k^{-1} + R)Y_k] \\
 &\geq (1-t)Y_k + t[2Y_k - Y_k Y_k^{-1} Y_k] \\
 &\geq (1-t)Y_k + tY_k = Y_k,
 \end{aligned} \tag{28}$$

$$\begin{aligned}
 Y_{k+1} &= (1-t)Y_k + t[2Y_k - Y_k(P_k^{-1} + R)Y_k] \\
 &\leq (1-t)Y_k + t(P_k^{-1} + R)^{-1} \\
 &\leq (1-t)(P_k^{-1} + R)^{-1} + t(P_k^{-1} + R)^{-1} \\
 &\leq (P_k^{-1} + R)^{-1} \leq (P_-^{-1} + R)^{-1}.
 \end{aligned} \tag{29}$$

By (28) and (29), we have

$$\begin{aligned}
 P_{k+1} &= A^T Y_{k+1} A + Q \\
 &\geq A^T Y_k A + Q = P_k,
 \end{aligned} \tag{30}$$

$$\begin{aligned}
 P_{k+1} &= A^T Y_{k+1} A + Q \\
 &\leq A^T (P_-^{-1} + R)^{-1} A + Q = P_-.
 \end{aligned} \tag{31}$$

So, we obtain

$$\begin{aligned}
 P_k \leq P_{k+1} \leq P_-, \quad Y_k \leq Y_{k+1} \leq (P_k^{-1} + R)^{-1} \\
 \leq (P_-^{-1} + R)^{-1}, \quad k = 0, 1, 2, \dots
 \end{aligned} \tag{32}$$

Thus, the proof of induction is completed. Moreover, as  $P_k$  and  $Y_k$  are monotone increasing and they are bounded, then  $\lim_{k \rightarrow \infty} P_k$  and  $\lim_{k \rightarrow \infty} Y_k$  exist. Taking limits in Algorithm  $\lim_{k \rightarrow \infty} Y_k = (P_-^{-1} + R)^{-1}$  and  $\lim_{k \rightarrow \infty} P_k = P_-$ .  $\square$

**Theorem 2.** Let  $P_-$  be the positive definite solution of the DARE (5). After  $k$  steps of iteration for Algorithm 2, we have  $\|I - Y_k(P_k^{-1} + R)\| < \varepsilon$ ; then,

$$\|A^T(P_k^{-1} + R)^{-1}A + Q - P_k\| \leq \varepsilon\|P_- - Q\|. \quad (33)$$

*Proof.* According to (15), we have

$$A^T(P_-^{-1} + R)^{-1}A = P_- - Q. \quad (34)$$

Then, by Algorithm 2, Lemma 3, and (34), we obtain

$$\begin{aligned} \|A^T(P_k^{-1} + R)^{-1}A + Q - P_k\| &= \|A^T(P_k^{-1} + R)^{-1}A - A^TY_kA\| \\ &= \|A^T[(P_k^{-1} + R)^{-1} - Y_k]A\| \\ &= \|A^T[I - Y_k(P_k^{-1} + R)](P_k^{-1} + R)^{-1}A\| \\ &\leq \|I - Y_k(P_k^{-1} + R)\| \cdot \|A^T(P_k^{-1} + R)^{-1}A\| \\ &\leq \|I - Y_k(P_k^{-1} + R)\| \cdot \|A^T(P_-^{-1} + R)^{-1}A\| \\ &= \|I - Y_k(P_k^{-1} + R)\| \cdot \|P_- - Q\| \\ &\leq \varepsilon\|P_- - Q\| \end{aligned} \quad (35)$$

because of  $P_k \leq P_-$ .

As the proof method is similar to Theorem 1, we list the monotonicity and convergence of Algorithm 3 without proof.  $\square$

**Theorem 3.** Let  $P_-$  be the positive definite solution of the DARE (5) and  $Q > 0$ . The iterative sequences  $\{P_k\}$  and  $\{Y_k\}$  are generated by Algorithm 3 with  $t \in (0, 1]$  and start from  $Y_0 = (Q^{-1} + R)^{-1}$  and  $P_0 = Q$ ; then,  $P_k$  is monotone increasing and converges to  $P_-$ , and  $Y_k$  is monotone increasing and converges to  $(P_-^{-1} + R)^{-1}$ .

*Remark 1.* For Algorithms 2 and 3, we find the steps of iteration for Algorithm 2 are less than Algorithm 3 and the convergence speed of the Algorithm 2 is faster than Algorithm 3 from the numerical examples. Therefore, in the following example, we only discuss the superiority and effectiveness of Algorithm 2.

### 3. Numerical Examples

In this section, we present the following numerical example to show the effectiveness of our results. We also discuss the performance of Algorithm 2 with different  $t$  values. The whole process is carried out on Matlab 7.1 and the precision is  $10^{-8}$ .

*Example 1.* Consider the discrete system (1) with

$$\begin{aligned} A &= \begin{pmatrix} 2.27 & 0.13 & 0.12 & 0.1 \\ -0.13 & 2.34 & 0.12 & 0.05 \\ 0.11 & -0.17 & 1.9 & 0.03 \\ 0.01 & 0.07 & 0.02 & 1.1 \end{pmatrix}, \\ B &= \begin{pmatrix} 1.15 & 0 & 0.01 & 0 \\ 0 & 0.8 & 0 & 0 \\ 0 & 0.04 & 0.9 & 0 \\ 0.02 & 0 & 0 & 1.8 \end{pmatrix}, \\ Q &= \begin{pmatrix} 0.12 & 0 & 0.1 & 0 \\ 0 & 2.2 & 0 & 0 \\ 0.1 & 0 & 1.4 & 0 \\ 0 & 0 & 0 & 0.7 \end{pmatrix}, \\ G &= I. \end{aligned} \quad (36)$$

In [29], Dai and Bai choose the starting matrix  $Y_0 = (Q^{-1} + R)^{-1}$ . After 17 steps of iteration, the required precision is derived, and the residual  $\|A^T(P^{-1} + R)^{-1}A + Q - P\|$  is  $2.0754e - 009$ .

For Algorithm 2, we choose  $P_0 = Q$ ,  $Y_0 = (Q^{-1} + R)^{-1}$  and give the steps of iteration and the residual as Table 1 with

TABLE 1: Numerical results.

$t$	Iterations	Residual	$t$	Iterations	Residual
0.6	35	$9.0186e-009$	1.2	10	$5.6438e-009$
0.8	24	$5.4562e-009$	1.3	12	$9.2094e-009$
0.9	20	$4.7874e-009$	1.5	18	$9.4721e-009$
1	17	$2.0754e-009$	1.8	40	$8.6619e-009$
1.1	14	$1.0160e-009$	2.0	104	$9.1141e-009$

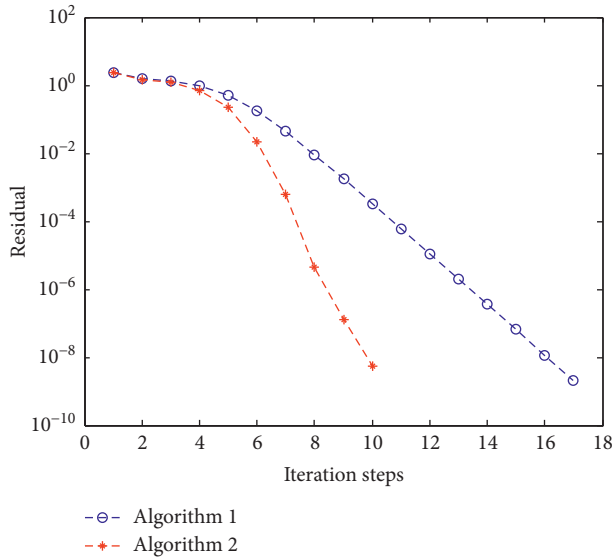


FIGURE 1: The relationship between iteration step and residual.

a different parameter  $t$  when the process is stopped under the required precision. When  $t$  is near 1, we find that the steps of iteration are less than [29]. Especially, when  $t = 1.2$ , it only needs 10 steps for Algorithm 2 to converge to the iterative solution:

$$P_{10} = \begin{pmatrix} 3.3299 & -0.3120 & 0.5202 & 0.1433 \\ -0.3120 & 9.6394 & -0.1292 & 0.1904 \\ 0.5202 & -0.1292 & 4.9731 & 0.0820 \\ 0.1433 & 0.1904 & 0.0820 & 0.9962 \end{pmatrix} \quad (37)$$

with the residual  $\|A^T(P^{-1} + R)^{-1}A + Q - P\| = 5.6438e-009$ , and Algorithm 2 has faster convergence speed than Algorithm 1 from Figure 1. Moreover, from Table 1, we see that Algorithm 2 is more efficient when  $t > 1$ . Although we only prove the convergence of Algorithm 2 when  $t \in (0, 1]$ , in this paper, Algorithm 2 works well in practical computation when  $t > 1$ .

### Data Availability

All data generated or analyzed during this study are included within this article.

### Conflicts of Interest

The authors declare that they have no conflicts of interest.

### Acknowledgments

The work was supported in part by the National Natural Science Foundation for Youths of China (11801164), National Natural Science Foundation of China (11971413), Key Project of National Natural Science Foundation of China (91430213), General Project of Hunan Provincial Natural Science Foundation of China (2015JJ2134), and the General Project of Hunan Provincial Education Department of China (15C1320).

### References

- [1] H. Kwakernaak and R. Sivan, *Linear Optimal Control Systems*, Wiley-Interscience, New York, NY, USA, 1972.
- [2] L. Wu and D. W. C. Ho, "Fuzzy filter design for Ito stochastic systems with application to sensor fault detection," *IEEE Transactions on Fuzzy Systems*, vol. 17, no. 1, pp. 233–242, 2009.
- [3] X. Su, P. Shi, L. Wu, and Y. D. Song, "A novel approach to filter design for TCS fuzzy discrete-time systems with time-varying delay," *IEEE Transactions on Fuzzy Systems*, vol. 20, no. 6, pp. 1114–1129, 2012.
- [4] W. N. Anderson, T. D. Morley, and G. E. Trapp, "Ladder networks, fixpoints, and the geometric mean," *Circuits, Systems and Signal Processing*, vol. 2, no. 3, pp. 259–268, 1983.
- [5] M. Z. Q. Chen, L. Zhang, H. Su, and G. Chen, "Stabilizing solution and parameter dependence of modified algebraic Riccati equation with application to discrete-time network synchronization," *IEEE Transactions on Automatic Control*, vol. 61, no. 1, pp. 228–233, 2016.
- [6] H. S. Su, H. Wu, and J. Lam, "Positive edge-consensus for nodal networks via output feedback," *IEEE Transactions on Automatic Control*, vol. 64, no. 3, pp. 1224–1249, 2019.
- [7] M. Lan and S. Chand, "Solving linear quadratic discrete-time optimal controls using neural networks," in *Proceedings of the IEEE Conference on Decision & Control*, IEEE, Honolulu, HI, USA, December 1990.
- [8] R. A. Kennedy, "Linear system theory," *Automatica*, vol. 30, no. 11, pp. 1811–1813, 1994.
- [9] C.-H. Lee, "Matrix bounds of the solutions of the continuous and discrete Riccati equations—a unified approach," *International Journal of Control*, vol. 76, no. 6, pp. 635–642, 2003.
- [10] H. H. Choi, "Upper matrix bounds for the discrete algebraic Riccati matrix equation," *IEEE Transactions on Automatic Control*, vol. 46, no. 3, pp. 504–508, 2001.
- [11] R. Davies, P. Shi, and R. Wiltshire, "New upper solution bounds of the discrete algebraic Riccati matrix equation," *Journal of Computational and Applied Mathematics*, vol. 213, no. 2, pp. 307–315, 2008.
- [12] J. Liu, L. Wang, and J. Zhang, "The solution bounds and fixed point iterative algorithm for the discrete coupled algebraic Riccati equation applied to automatic control," *IMA Journal of Mathematical Control and Information*, pp. 1–22, 2016.
- [13] J. Liu, L. Wang, and J. Zhang, "New matrix bounds and iterative algorithms for the discrete coupled algebraic Riccati equation," *International Journal of Control*, vol. 90, no. 11, pp. 2326–2337, 2017.
- [14] N. Komaroff, "Upper bounds for the solution of the discrete Riccati equation," *IEEE Transactions on Automatic Control*, vol. 37, no. 9, pp. 1370–1373, 1992.
- [15] J. Zhang, J. Liu, and Y. Zha, "The improved eigenvalue bounds for the solution of the discrete algebraic Riccati equation,"

- IMA Journal of Mathematical Control and Information*, pp. 1–20, 2016.
- [16] N. Komaroff and B. Shahian, “Lower summation bounds for the discrete Riccati and Lyapunov equations,” *IEEE Transactions on Automatic Control*, vol. 37, no. 7, pp. 1078–1080, 1992.
- [17] M. T. Tran and M. E. Sawan, “On the discrete Riccati matrix equation,” *SIAM Journal on Algebraic Discrete Methods*, vol. 6, no. 1, pp. 107–108, 1985.
- [18] J. Liu and J. Zhang, “The existence uniqueness and the fixed iterative algorithm of the solution for the discrete coupled algebraic Riccati equation,” *International Journal of Control*, vol. 84, no. 8, pp. 1430–1441, 2011.
- [19] R. Huang, J. Z. Liu, and L. Zhu, “Accurate solutions of diagonally dominant tridiagonal linear systems,” *BIT Numerical Mathematics*, vol. 54, no. 3, pp. 711–727, 2014.
- [20] Q. H. Liu, X. X. Li, and J. Yan, “On the large time behaviour of solutions for a class of time-dependent Hamilton-Jacobi equations,” *Science China Mathematics*, vol. 59, no. 5, pp. 875–8890, 2016.
- [21] Z.-H. He, “Some new results on a system of Sylvester-type quaternion matrix equations,” *Linear and Multilinear Algebra*, pp. 1–23, 2019.
- [22] N. Komaroff, “Iterative matrix bounds and computational solutions to the discrete algebraic Riccati equation,” *IEEE Transactions on Automatic Control*, vol. 39, no. 8, pp. 1676–1678, 1994.
- [23] C.-H. Guo, “Newton’s method for discrete algebraic Riccati equations when the closed-loop matrix has eigenvalues on the unit circle,” *SIAM Journal on Matrix Analysis and Applications*, vol. 20, no. 2, pp. 279–294, 1998.
- [24] W.-W. Lin and S.-F. Xu, “Convergence analysis of structure-preserving doubling algorithms for riccati-type matrix equations,” *SIAM Journal on Matrix Analysis and Applications*, vol. 28, no. 1, pp. 26–39, 2006.
- [25] E. K.-W. Chu, H.-Y. Fan, W.-W. Lin, and C.-S. Wang, “Structure-preserving algorithms for periodic discrete-time algebraic Riccati equations,” *International Journal of Control*, vol. 77, no. 8, pp. 767–788, 2004.
- [26] L.-Z. Lu, W.-W. Lin, and C. E. M. Pearce, “An efficient algorithm for the discrete-time algebraic Riccati equation,” *IEEE Transactions on Automatic Control*, vol. 44, no. 6, pp. 1216–1220, 1999.
- [27] T.-M. Hwang, E. K.-W. Chu, and W.-W. Lin, “A generalized structure-preserving doubling algorithm for generalized discrete-time algebraic Riccati equations,” *International Journal of Control*, vol. 78, no. 14, pp. 1063–1075, 2005.
- [28] A. Laub, “A Schur method for solving algebraic Riccati equations,” *IEEE Transactions on Automatic Control*, vol. 24, no. 6, pp. 913–921, 1979.
- [29] H. Dai and Z. Z. Bai, “On eigenvalue bounds and iteration methods for discrete algebraic Riccati equations,” *Journal of Computational Mathematics*, vol. 29, no. 3, pp. 341–366, 2011.
- [30] R. A. Horn and C. R. Johnson, *Matrix Analysis*, Cambridge University Press, Cambridge, UK, 2012.
- [31] X. Zhan, “Computing the extremal positive definite solutions of a matrix equation,” *SIAM Journal on Scientific Computing*, vol. 17, no. 5, pp. 1167–1174, 1996.
- [32] A. W. Marshall and I. Olkin, *Inequalities: Theory of Majorization and its Applications*, Academic Press, New York, NY, USA, 1979.
- [33] W. Sun and Y. Yuan, *Optimization Theory and Methods*, Springer Science and Business Media, LLC, New York, NY, USA, 2006.
- [34] M. Monsalve and M. Raydan, “A new inversion-free method for a rational matrix equation,” *Linear Algebra and Its Applications*, vol. 433, no. 1, pp. 64–71, 2010.
- [35] G. Schulz, “Iterative Berechnung der reziproken Matrix,” *ZAMM—Zeitschrift für Angewandte Mathematik und Mechanik*, vol. 13, no. 1, pp. 57–59, 1933.

## Research Article

# Robust Fault Detection for Permanent-Magnet Synchronous Motor via Adaptive Sliding-Mode Observer

Miaoying Zhang <sup>1</sup>, Fan Xiao <sup>2</sup>, Rui Shao <sup>1</sup> and Zhaojun Deng <sup>3</sup>

<sup>1</sup>College of Railway Transportation Locomotive and Vehicle College, Hunan Railway Professional Technology College, Zhuzhou, Hunan, China

<sup>2</sup>College of Electrical and Information Engineering, Hunan University of Technology, Zhuzhou, Hunan, China

<sup>3</sup>College of Railway Transportation Operation and Management, Hunan Railway Professional Technology College, Zhuzhou, Hunan, China

Correspondence should be addressed to Fan Xiao; 511191117@qq.com

Received 8 February 2020; Accepted 10 April 2020; Published 30 April 2020

Guest Editor: Hou-Sheng Su

Copyright © 2020 Miaoying Zhang et al. This is an open access article distributed under the Creative Commons Attribution License, which permits unrestricted use, distribution, and reproduction in any medium, provided the original work is properly cited.

In this paper, a robust fault detection problem is investigated for a permanent magnet synchronous motor (PMSM). By using the adaptive control and the sliding-mode control strategies, an observer is presented for estimating the amplitude demagnetization fault problem under inductance disturbance. The proposed method can effectively attenuate the inductance disturbance of the PMSM by the sliding-mode strategy. And the adaptive control estimation algorithm is adopted for guaranteeing that the real-time detection of demagnetization flux can be realized. The convergency is obtained by the Lyapunov stability theory. Finally, simulation is given for demonstrating the feasibility and effectiveness of the proposed method.

## 1. Introduction

With its high efficiency, low energy consumption, lightweight, low noise, maintainability, and many other advantages [1–3], the permanent-magnet synchronous motor (PMSM) has absorbed strong interest from many scholars. For the rapid development of rail transit, new energy vehicles, aviation, ships, and other fields, the application of the PMSM is becoming more and more widespread, and its research has become a hotspot of traction power.

In recent years, the study on stability of the PMSM has been highly concerned by researchers, and some achievements have been reported [4, 5]. In addition to the influence of various disturbance factors, the demagnetization of permanent magnet caused by disturbance is also a great threat to the stability of the PMSM. Due to the special permanent-magnet structure of the PMSM, the magnetization performance will decline or demagnetize under the disturbance. Once the permanent magnet demagnetizes, the PMSM fails to run stably and it will be even scrapped [6].

Therefore, the demagnetization detection of the PMSM is particularly important. The sliding-mode control is of great theoretical research significance on the stability of the PMSM because it is insensitive to model error and external disturbance of the research object [7–9]. The adaptive control can modify the control process according to the change of the dynamic characteristics of the controlled object and the disturbance. Its research object can contain the objective disturbance, and the adaptive control estimation algorithm can make a specified performance index reach and maintain the optimal state or approximately optimal state [10]. The sliding-mode control and the adaptive control with their unique advantages have made great improvement in recent years. Many scholars have conducted research studies on them and obtained a large number of excellent results [11–25].

At present, the sliding-mode control and the adaptive control in the PMSM are mainly used in speed control [11, 12], rotor position estimation [13], parameter identification [14], and other research fields. As for the sliding-mode

control, [15] introduces a hybrid controller (HC) for the speed control of the PMSM drive. Hosseyni et al. [16] present a speed control technique based on the sliding-mode observer (SMO) and the backstepping controller to estimate rotor speed and rotor position. The literature [14] implements parameter identification under parameter disturbance with the sliding-mode control. For the adaptive control, [17] proposes an adaptive PID controller for measurement and control of position or speed. Nguyen et al. [18] propose a simple adaptive control-based speed controller under parameter disturbance. Qutubuddin and Yadaiah [19] present an intelligent adaptive mechanism to estimate rotor speed, rotor position, and motor parameter identification.

In addition to separate the sliding-mode control and the adaptive control, there are also related studies that combine the two control strategies. Liu et al. [20] propose an adaptive sliding-mode control observer under the parameter disturbance. Xi et al. [12] propose a speed SMC with an adaptive law and an extended state observer (ESO).

In the above literature, the application of the sliding-mode control and the adaptive control in the PMSM has involved disturbance, but not including the flux demagnetization of the PMSM. In the actual operation process, disturbance will often cause demagnetization, and if demagnetization is not discovered and handled in time, the PMSM will be scrapped if demagnetization goes serious. Therefore, many scholars have studied the flux-linkage detection of the PMSM [21–24]. Zhang et al. [22] address permanent-magnet demagnetization fault in the PMSM, but no disturbance is involved. In [23], a stator flux-linkage observer based on the phase-locked loop is introduced which aims at the low-accuracy stator flux-linkage estimation in traditional direct control. In [24], a minimum-order extended flux-linkage sliding-mode observer is presented which can accurately observe torque and permanent-magnet flux.

These research studies on the permanent-magnet demagnetization fault detection of the PMSM do not consider the parameter change or only consider the resistance parameter change, so this paper selects a new field based on all above studies and proposes an observer which combines the sliding-mode control with the adaptive control aiming at the condition of the inductance disturbance. The characteristics of the sliding-mode control strategy are not sensitive to parameter and can overcome the inductance disturbance of the PMSM. The real-time adaptive control estimation algorithm is presented for realizing the real-time amplitude demagnetization fault detection of permanent-magnet flux linkage.

In this paper, the PMSM is taken as the main research object, and its stable control theory and real-time amplitude demagnetization fault detection of flux linkage are studied. Its successful development will not only enrich the research studies on the demagnetization fault detection theory of the PMSM but also be applied to further research studies about more disturbances for the PMSM on this basis.

## 2. Description of the Problem

In magnetic field-oriented coordinate  $d$ - $q$ , the mathematical model [25] of demagnetization current of the PMSM is

$$\begin{cases} \frac{di_d}{dt} = \frac{u_d}{L} - \frac{R}{L}i_d + \omega i_q + \omega \frac{\psi_{rq}}{L}, \\ \frac{di_q}{dt} = \frac{u_q}{L} - \frac{R}{L}i_q - \omega i_d - \omega \frac{\psi_{rd}}{L}, \end{cases} \quad (1)$$

where  $i_d$  and  $i_q$  are the current of the  $d$ - $q$  axis,  $u_d$  and  $u_q$  are the voltage of the  $d$ - $q$  axis,  $R$  is the resistance,  $\omega$  is the angular velocity,  $L$  is the inductance,  $\psi_{rd}$  is the flux linkage of the  $d$  axis, and  $\psi_{rq}$  is the flux linkage of  $q$  axis.

The permanent-magnet flux-linkage change of the PMSM is shown in Figure 1.  $ABC$  is the three-phase static coordinate, and axis  $A$  is coincidence with the axis of the actual stator  $A$  phase winding.  $d$ - $q$  is the magnetic field-oriented coordinate, and  $d$  axis points to the direction of rotor permanent-magnet flux-linkage and is coincidence with the magnetic pole axis of the rotor.  $\psi_f$  is flux-linkage under normal circumstances, and  $\theta$  is the intersection angle between  $\psi_f$  and the axis of  $A$  phase stator winding of motor.  $\psi_f$  rotates at angular velocity  $\omega$  in space along with the rotor, and  $q$  axis is  $90^\circ$  ahead of  $d$  axis counterclockwise. Deviation angle between direction of magnetic field orientation and direction of permanent-magnet flux-linkage direction is  $\gamma$ .

For amplitude demagnetization, demagnetization direction of the permanent-magnet flux linkage always occurs in the same direction of  $d$  axis, which has no effect on  $q$  axis. Formula (1) can be simplified as

$$\begin{cases} \frac{di_d}{dt} = \frac{u_d}{L} - \frac{R}{L}i_d + \omega i_q, \\ \frac{di_q}{dt} = \frac{u_q}{L} - \frac{R}{L}i_q - \omega i_d - \omega \frac{\psi_{rd}}{L}. \end{cases} \quad (2)$$

Under the inductance disturbance, the demagnetization mathematical model is given as follows:

$$\begin{cases} \frac{di_d}{dt} = \frac{u_d}{L + \Delta L} - \frac{R}{L + \Delta L}i_d + \omega i_q, \\ \frac{di_q}{dt} = \frac{u_q}{L + \Delta L} - \frac{R}{L + \Delta L}i_q - \omega i_d - \omega \frac{\psi_{rd}}{L + \Delta L}, \end{cases} \quad (3)$$

where  $\Delta L$  is the inductance disturbance.

We let  $1/(L + \Delta L) = (1/L) - (1/m)$ , where  $m = (L^2/\Delta L) + L$ , and equation (3) transfers into

$$\begin{cases} \frac{di_d}{dt} = \frac{u_d}{L} - \frac{R}{L}i_d + \omega i_q - \frac{u_d}{m} + \frac{R}{m}i_d, \\ \frac{di_q}{dt} = \frac{u_q}{L} - \frac{R}{L}i_q - \omega i_d - \omega \frac{\psi_{rd}}{L} - \frac{u_q}{m} + \frac{R}{m}i_q + \omega \frac{\psi_{rd}}{m}. \end{cases} \quad (4)$$

The state equation of the PMSM is obtained from equation (4):



$$\begin{cases} \dot{x} = Ax + Bu + Ef + d, \\ y = Cx, \end{cases} \quad (5)$$

where state variables are  $\begin{cases} x_1 = i_d, \\ x_2 = i_q, \end{cases} x = \begin{bmatrix} x_1 \\ x_2 \end{bmatrix}, u = \begin{bmatrix} u_d \\ u_q \end{bmatrix},$

$f = \begin{bmatrix} 0 \\ \psi_{rd} \end{bmatrix},$  and

$$d = \begin{bmatrix} -\frac{u_d}{m} + \frac{R}{m}i_d \\ -\frac{u_q}{m} + \frac{R}{m}i_q + \omega \frac{\psi_{rd}}{m} \end{bmatrix}, \quad (6)$$

and coefficient matrixes are

$$A = \begin{bmatrix} -\frac{R}{L} & \omega \\ -\omega & -\frac{R}{L} \end{bmatrix},$$

$$B = \begin{bmatrix} \frac{1}{L} & 0 \\ 0 & \frac{1}{L} \end{bmatrix}, \quad (7)$$

$$E = -\frac{\omega}{L},$$

$$C = \begin{bmatrix} 1 & 0 \\ 0 & 1 \end{bmatrix}.$$

### 3. Design of Adaptive Sliding-Mode Observer

For the PMSM system described in (5), an adaptive sliding-mode observer is constructed as follows:

$$\begin{cases} \dot{\hat{x}} = A\hat{x} + Bu + k \operatorname{sgn}(x - \hat{x}) + E\hat{f} + G(y - \hat{y}), \\ \hat{y} = C\hat{x}, \end{cases} \quad (8)$$

where  $\operatorname{sgn}(x - \hat{x})$  is the symbolic function,  $k$  is the to-be-designed constant,  $G$  is the to-be-designed matrix, superscript “ $\wedge$ ” is the observed value of relevant disturbances,  $k \operatorname{sgn}(x - \hat{x})$  is used to counteract influence of the parameter disturbance,  $\hat{f}$  is used to observe the demagnetization of the permanent-magnet flux linkage, and  $G(y - \hat{y})$  is used to control the convergence rate and optimize the stability of the system state.

Observer deviation is defined as  $e = x - \hat{x} =$

$$\begin{bmatrix} e_1 \\ e_2 \end{bmatrix} = \begin{bmatrix} x_1 - \hat{x}_1 \\ x_2 - \hat{x}_2 \end{bmatrix}.$$

Output deviation is defined as  $e_y = y - \hat{y}$ .

From formulas (5) and (8), we obtain

$$\begin{aligned} \dot{e} &= \dot{x} - \dot{\hat{x}} \\ &= (A - GC)e + Ee_f + d - k \operatorname{sgn}(x - \hat{x}), \end{aligned} \quad (9)$$

where fault estimation error  $e_f = f - \hat{f}$ .

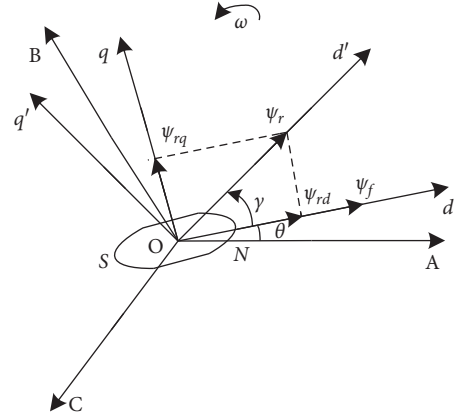


FIGURE 1: Permanent-magnet flux-linkage change of the PMSM.

The improved adaptive control estimation algorithm proposed in this paper is

$$\dot{\hat{f}} = -\Gamma F(e_y + e_y), \quad (10)$$

where  $\Gamma = \Gamma^T > 0$  is the adaptive learning rate and  $F$  is an optimal dimensional matrix which is the to-be-designed observer gain matrix.

*Remark 1.* Based on the improved adaptive control estimation algorithm (10), we can obtain the following real-time permanent-magnet flux-linkage estimation value:

$$\hat{f} = -\Gamma \int F(e_y + e_y). \quad (11)$$

**Lemma 1.** For any positive number  $\mu$  and symmetric positive definite matrix  $P$ , the following inequality holds:

$$2x^T P y \leq \frac{1}{\mu} x^T P x + \mu y^T P y. \quad (12)$$

**Theorem 1.** For formula (8), if  $k$  is large enough, a symmetric positive definite matrix  $F \in R^{r \times p}$  satisfies

$$\Theta = \begin{bmatrix} 2(A - GC) & FC(A - GC) + FC + E \\ * & 2FCE + H \end{bmatrix} < 0. \quad (13)$$

Improved adaptive control estimation algorithm such as formula (11) makes the state estimation error and the flux-linkage estimation error converge to zero.

### 4. Convergence Analysis

Choosing the following positive definite function as Lyapunov function, we can get

$$V = e^T e + e_f^T \Gamma^{-1} e_f. \quad (14)$$

The derivative of formula (14) is

$$\begin{aligned}
\dot{V} &= 2e^T \dot{e} + 2e_f^T \Gamma^{-1} \dot{e}_f \\
&= 2e^T (A - GC)e + 2e^T Ee_f + 2e^T (d - k \operatorname{sgn}(x - \hat{x})) \\
&\quad + 2e_f^T \Gamma^{-1} (\dot{f} - \hat{\dot{f}}) \\
&= 2e^T (A - GC)e + 2e^T Ee_f + 2e^T (d - k \operatorname{sgn}(x - \hat{x})) \\
&\quad + 2e_f^T \Gamma^{-1} \dot{f} \\
&\quad + 2e_f^T (FC(A - GC) + FC)e + 2e_f^T FCEe_f \\
&\quad + 2e_f^T FC(d - k \operatorname{sgn}(x - \hat{x})).
\end{aligned} \tag{15}$$

Let

$$\dot{V} = V_1 + V_2, \tag{16}$$

formula (16) can be divided into

$$\begin{aligned}
V_1 &= 2e^T (d - k \operatorname{sgn}(x - \hat{x})) + 2e_f^T FC(d - k \operatorname{sgn}(x - \hat{x})), \\
V_2 &= 2e^T (A - GC)e + 2e_f^T (FC(A - GC) + FC)e \\
&\quad + 2e_f^T FCEe_f + 2e^T Ee_f + 2e_f^T \Gamma^{-1} \dot{f}.
\end{aligned} \tag{17}$$

(a) For  $V_1$ ,

$$\begin{aligned}
V_1 &= 2e^T (d - k \operatorname{sgn}(x - \hat{x})) + 2e_f^T FC(d - k \operatorname{sgn}(x - \hat{x})) \\
&\leq 2\|e\|\|d\| - 2k\|e\| + 2\|e_f\|\|FC\|(\|d\| - k) \\
&= 2\|e\|(\|d\| - k) + 2\|e_f\|\|FC\|(\|d\| - k).
\end{aligned} \tag{18}$$

From the engineering point of view, both the stator resistance and the permanent-magnet flux-linkage are bounded. Thus, it can be assumed that  $d$  is bounded, that is, there is a positive constant  $\|d\| \leq \varepsilon$ , which makes  $\|d\| \leq \varepsilon$  bounded (the mathematical symbol represents the Euclidean norm of vector or spectral norm of matrix)

If  $k$  is large enough, it satisfies

$$\|d\| \leq \varepsilon < k. \tag{19}$$

From formula (18), the following formula is obtained:

$$2e^T (d - k \operatorname{sgn}(x - \hat{x})) + 2e^T Ee_f - 2e_f^T FCk \operatorname{sgn}(x - \hat{x}) < 0. \tag{20}$$

(b) For  $V_2$ ,

$$\begin{aligned}
V_2 &= 2e^T (A - GC)e + 2e_f^T (FC(A - GC) + FC)e \\
&\quad + 2e_f^T FCEe_f + 2e^T Ee_f + 2e_f^T \Gamma^{-1} \dot{f}.
\end{aligned} \tag{21}$$

TABLE 1: The setting value of motor parameters.

Motor parameters $\Omega$	The setting value
Resistance	2.875
Number of pole-pairs	4
Inductance (H)	0.0085
The rotor flux linkage (Wb)	0.175
The rotor inertia (Kgm)	0.008

According to Lemma 1, we obtain

$$\begin{aligned}
2e_f^T \Gamma^{-1} \dot{f} &\leq e_f^T H e_f + f^T \Gamma^{-1} H \Gamma^{-1} \dot{f} \\
&\leq e_f^T H e_f + f^2 \lambda_{\max}(\Gamma^{-1} H \Gamma^{-1}),
\end{aligned} \tag{22}$$

where  $H$  is a symmetric positive definite matrix.

We can obtain

$$\begin{aligned}
\dot{V}_2 &\leq 2e^T (A - GC)e + 2e_f^T (FC(A - GC) + FC)e \\
&\quad + 2e_f^T FCEe_f + 2e^T Ee_f \\
&\quad + e_f^T H e_f + f^2 \lambda_{\max}(\Gamma^{-1} H \Gamma^{-1}) \\
&= Z^T \Theta Z + \delta.
\end{aligned} \tag{23}$$

Here,  $Z = \begin{bmatrix} e \\ e_f \end{bmatrix}$ ,  $\Theta = \begin{bmatrix} 2(A-GC)FC(A-GC)+FC+E & \\ * & 2FCE+H \end{bmatrix}$ , and  $\delta = f^2 \lambda_{\max}(\Gamma^{-1} H \Gamma^{-1})$ .

If formula (13) holds, let  $\sigma = \lambda_{(\min)}(-\Theta)$ .

We obtain

$$\begin{aligned}
\dot{V} &\leq -\sigma \|Z\|^2 + \delta + 2e^T (d - k \operatorname{sgn}(x - \hat{x})) \\
&\quad + 2e_f^T FC(d - k \operatorname{sgn}(x - \hat{x})) \leq 0.
\end{aligned} \tag{24}$$

When  $\|Z\|^2 \geq (\delta/\sigma)$ ,  $k$  and  $F$  are large enough,  $\dot{V} \leq 0$ , that is,  $\langle Z \|Z\|^2 \geq (\delta/\sigma) \rangle$ , which makes the state estimation error  $e$  and the permanent-magnet flux-linkage estimation error  $e_f$  converge to zero.

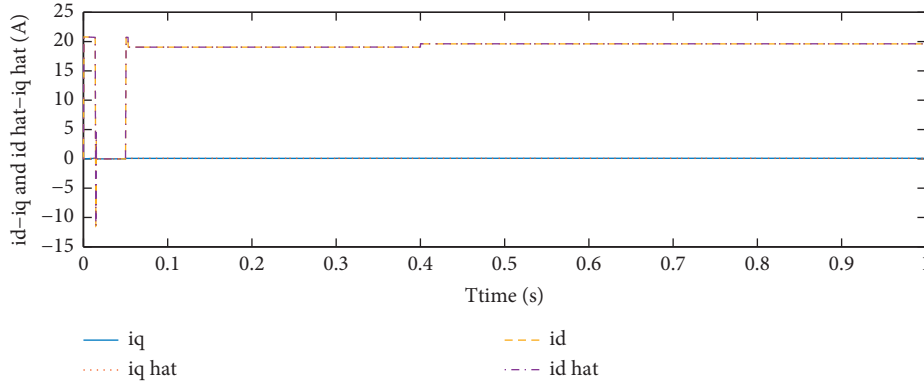
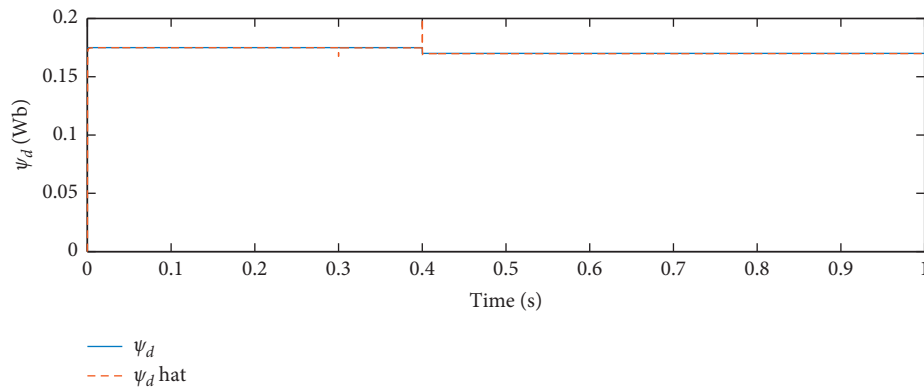
## 5. Simulation Analysis

The parameters of the PMSM used in simulation are shown in Table 1. Meanwhile, the initial value of the observer is set to 0.

The load torque disturbance changes from 0 Nm to 20 Nm at 0.05 s. The inductance disturbance changes from 0.0085 H to 0.0105 H at 0.3 s. Amplitude demagnetization changes from 0.175 Wb to 0.17 Wb at 0.4 s.

The parameters of the observer module are as follows:

$$\begin{aligned}
G &= \begin{bmatrix} 10 & 0 \\ 0 & 100 \end{bmatrix}, \\
k &= \begin{bmatrix} 40000 & 0 \\ 0 & 1000 \end{bmatrix}, \\
\Gamma &= \begin{bmatrix} 67 & \\ & 180 \end{bmatrix}.
\end{aligned} \tag{25}$$

FIGURE 2: Simulation waveforms of  $i_d$ ,  $\hat{i}_d$ ,  $i_q$ , and  $\hat{i}_q$ .FIGURE 3: Simulation waveforms of  $\psi_{rd}$  and  $\hat{\psi}_{rd}$ .

As is shown in Figure 2, when the PMSM is loaded at 0.05 s, the current  $i_q$  jumps from the initial value 0 A to 19 A. But when the inductance changes at 0.3 s,  $i_q$  is almost not affected. When an amplitude demagnetization fault occurs at 0.4 s,  $i_q$  increases slightly. We can conclude that only the loading makes  $i_q$  increase by a large margin, the demagnetization fault has little effect on  $i_q$ , and the inductance parameter variation of the PMSM basically has nothing to do with  $i_q$ . We use  $i_d=0$  control algorithm, so the current  $i_d$  always remains at 0 A.  $i_d$  shakes only when the load torque disturbance occurs, and then it quickly returns to 0 A.

As is shown in Figure 3,  $\hat{\psi}_{rd}$  is not affected when the PMSM is loaded at 0.05 s and it shakes when the inductance disturbance occurs at 0.3 s. When an amplitude demagnetization occurs at 0.4 s,  $\psi_{rd}$  decreases from 0.175 Wb to 0.170 Wb and  $\hat{\psi}_{rd}$  shakes and then quickly keeps up with  $\psi_{rd}$ .

Matlab simulation results verify the feasibility and effectiveness of the theoretical method.

## 6. Conclusion

During the operation of the PMSM, it is affected by disturbances and demagnetization fault. The inductance is one of the important disturbances for the PMSM, so an adaptive sliding-mode observer is proposed to realize the amplitude demagnetization fault robust detection method with inductance disturbance for the PMSM in this paper.

Firstly, a mathematical model of the demagnetization fault of the PMSM in the d-q coordinate is established. Then, an adaptive control estimation algorithm is designed to realize the amplitude demagnetization fault detection of the permanent-magnet flux-linkage, while the sliding-mode control strategy overcomes the inductance disturbance. Finally, the Matlab simulation results show the effectiveness of the adaptive sliding-mode observer.

## Data Availability

There do not exist supporting data regarding this manuscript.

## Conflicts of Interest

The authors declare that they have no conflicts of interest.

## References

- [1] G. H. B. Foo, X. Zhang, and D. M. Vilathgamuwa, "A sensor fault detection and isolation method in interior permanent-magnet synchronous motor drives based on an extended Kalman filter," *IEEE Transactions on Industrial Electronics*, vol. 60, no. 8, pp. 3485–3495, 2013.
- [2] S. Chakraborty, E. Keller, A. Ray, and J. Mayer, "Detection and estimation of demagnetization faults in permanent magnet synchronous motors," *Electric Power Systems Research*, vol. 96, pp. 225–236, 2013.

- [3] J. Mao, *Unifying Electrical Engineering and Electronics Engineering*, Springer, Berlin, Germany, 2013.
- [4] W. Zhao, A. Yang, J. Ji, Q. Chen, and J. Zhu, "Modified flux linkage observer for sensorless direct thrust force control of linear vernier permanent magnet motor," *IEEE Transactions on Power Electronics*, vol. 34, no. 8, pp. 7800–7811, 2019.
- [5] H. Su, J. Zhang, and X. Chen, "A stochastic sampling mechanism for time-varying formation of multiagent systems with multiple leaders and communication delays," *IEEE Transactions on Neural Networks and Learning Systems*, vol. 30, no. 12, pp. 3699–3707, 2019.
- [6] C. Zhang, M. Zhang, J. He et al., "Demagnetization faults robust detection method based on an adaptive sliding mode observer for PMSM," *Journal of Advanced Computational Intelligence and Intelligent Informatics*, vol. 20, no. 7, pp. 1127–1134, 2016.
- [7] Y. Shu and Z. Kong, "Adaptive sliding mode variable structure control for a new hyper chaos system," *Journal of Chongqing University of Technology (Natural Science)*, vol. 24, no. 11, pp. 109–112, 2010, in Chinese.
- [8] C. Xu, H. Su, C. Liu, and G. Zhang, "Robust adaptive synchronization of complex network with bounded disturbances," *Advances in Difference Equations*, vol. 2019, no. 1, p. 483, 2019.
- [9] C. Xu, Y. Zhao, B. Qin, and H. Zhang, "Adaptive synchronization of coupled harmonic oscillators under switching topology," *Journal of the Franklin Institute*, vol. 356, no. 2, pp. 1067–1087, 2019.
- [10] R. Kandiban and R. Arulmozhiyal, "Design of adaptive fuzzy PID controller for speed control of BLDC motor," *International Journal of Soft Computing and Engineering*, vol. 2, no. 1, pp. 386–391, 2012.
- [11] M. A. M. Cheema, J. E. Fletcher, M. Farshadnia, D. Xiao, and M. F. Rahman, "Combined speed and direct thrust force control of linear permanent-magnet synchronous motors with sensorless speed estimation using a sliding-mode control with integral action," *IEEE Transactions on Industrial Electronics*, vol. 64, no. 5, pp. 3489–3501, 2017.
- [12] P. Xi, Y. Deng, Z. Wang, and H. Li, "Speed adaptive sliding mode control with an extended state observer for permanent magnet synchronous motor," *Mathematical Problems in Engineering*, vol. 2018, Article ID 6405923, 13 pages, 2018.
- [13] B. Du, S. Han, C. Zhang et al., "Sensorless control of interior permanent magnet synchronous motor based on active disturbance rejection controller," *Transactions of China Electrotechnical Society*, vol. 32, no. 3, pp. 105–112, 2017, in Chinese.
- [14] X. Zhang and Z. Li, "Sliding-mode observer-based mechanical parameter estimation for permanent magnet synchronous motor," *IEEE Transactions on Power Electronics*, vol. 31, no. 8, pp. 5732–5745, 2016.
- [15] C. Elmas and O. Ustun, "A hybrid controller for the speed control of a permanent magnet synchronous motor drive," *Control Engineering Practice*, vol. 16, no. 3, pp. 260–270, 2008.
- [16] A. Hosseini, R. Trabelsi, M. Mimouni et al., "Sensorless backstepping control for a five-phase permanent magnet synchronous motor drive based on sliding mode observer," *Lecture Notes in Electrical Engineering*, pp. 251–261, Springer, Berlin, Germany, 2016.
- [17] M. Geethu and P. Kunjumon, "Sensorless adaptive PID speed control for permanent magnet synchronous motor drives," in *Proceedings of the 2016 International Conference on Emerging Technological Trends*, IEEE, Kollam, India, October 2016.
- [18] A. T. Nguyen, M. S. Rafiq, H. H. Choi, and J.-W. Jung, "A model reference adaptive control based speed controller for a surface-mounted permanent magnet synchronous motor drive," *IEEE Transactions on Industrial Electronics*, vol. 65, no. 12, pp. 9399–9409, 2018.
- [19] M. Qutubuddin and N. Yadaiah, "A new intelligent adaptive mechanism for sensorless control of permanent magnet synchronous motor drive," *Biologically Inspired Cognitive Architectures*, vol. 24, pp. 47–58, 2018.
- [20] J. Liu, H. Li, and Y. Deng, "Current adaptive sliding mode control based on disturbance observer for permanent magnet synchronous motor," *Optics and Precision Engineering*, vol. 25, no. 5, pp. 1229–1241, 2017.
- [21] W. Xu, Y. Jiang, C. Mu, and F. Blaabjerg, "Improved nonlinear flux observer-based second-order SOIFO for PMSM sensorless control," *IEEE Transactions on Power Electronics*, vol. 34, no. 1, pp. 565–579, 2019.
- [22] C. Zhang, G. Wu, J. He, and K. Zhao, "Sliding observer-based demagnetisation fault-tolerant control in permanent magnet synchronous motors," *The Journal of Engineering*, vol. 2017, no. 6, pp. 175–183, 2017.
- [23] H. Zhu and Z. Zhao, "Direct control of bearingless permanent magnet slice motor based on novel flux linkage observer," *Proceedings of the CSEE*, vol. 38, no. 14, pp. 4242–4251, 2018.
- [24] G. Huang, Y. Luo, C. Zhang, and K. Zhao, "Online demagnetization detection of permanent magnet synchronous traction motor based on extended flux linkage," *Journal of the China Railway Society*, vol. 38, no. 2, pp. 48–55, 2016, in Chinese.
- [25] H. Jin and J. Huang, "Adaptive flux estimation and parameters identification of induction motors based on model reference approach," *Transactions of China Electrotechnical Society*, vol. 21, no. 1, pp. 65–69, 2006, in Chinese.

## Research Article

# On Zero Left Prime Factorizations for Matrices over Unique Factorization Domains

Jinwang Liu , Tao Wu , Dongmei Li , and Jiancheng Guan 

School of Mathematics and Computing Science, Hunan University of Science and Technology, Xiangtan, Hunan 410081, China

Correspondence should be addressed to Jiancheng Guan; [jiancheng\\_guan@aliyun.com](mailto:jiancheng_guan@aliyun.com)

Received 17 February 2020; Accepted 26 March 2020; Published 22 April 2020

Guest Editor: Hou-Sheng Su

Copyright © 2020 Jinwang Liu et al. This is an open access article distributed under the Creative Commons Attribution License, which permits unrestricted use, distribution, and reproduction in any medium, provided the original work is properly cited.

In this paper, zero prime factorizations for matrices over a unique factorization domain are studied. We prove that zero prime factorizations for a class of matrices exist. Also, we give an algorithm to directly compute zero left prime factorizations for this class of matrices.

## 1. Introduction

Multidimensional linear systems theory has a wide range of applications in circuits, systems, control of networked systems, signal processing, and other areas (see, e.g., [1, 2]). Multivariate polynomial matrix theory is a well-established tool for these systems, since many problems in the analysis and synthesis of control systems can be well solved using multivariate polynomial matrix techniques [1–3].

In recent years,  $n$ -D polynomial matrix factorizations have been widely studied [4–10]. In [11, 12], the zero left prime factorization problem was raised. This problem has been solved in [4–6]. The minor left prime factorization problem has been solved in [7, 10]. In the algorithms given in [7, 10], a fitting ideal of some module over the multivariate ( $n$ -D) polynomial ring needs to be computed. It is a little complicated.

It is well known that a multivariate polynomial ring over a field is a unique factorization domain. Then, the following problem is interesting.

**Problem 1.** How to decide if a matrix with full row rank over a unique factorization domain has a zero left prime factorization?

In this paper, we will give a partial solution to this problem.

## 2. Preliminaries

Let  $R$  be a unique factorization domain. The set of all  $l \times m$  matrices with entries from  $R$  is denoted by  $R^{l \times m}$ . Let

$F \in R^{l \times m}$  ( $l < m$ ). We denote the greatest common divisor of all  $l \times l$  minors of  $F$  by  $d(F)$ . Let  $C \in R^{l \times l}$  be a submatrix of  $F$ . By deleting  $C$  from  $F$ , we get a submatrix of  $F$ . This submatrix is denoted by  $F \setminus C$ .

Let  $C \in R^{m \times m}$ .  $\text{adj}(C)$  denotes the adjoint matrix of  $C$ .  $\text{acof}_{ij}(C)$  denotes the  $i, j$ th algebraic cofactor of  $C$ .

**Definition 1.** Let  $F \in R^{l \times m}$  ( $l < m$ ), and let  $C \in R^{l \times l}$  be a submatrix of  $F$ . A minor of  $F$  consisting of  $l - 1$  columns from  $C$  and one column from  $F \setminus C$  is said to be a related minor of  $C$ .

The following definition is from the multidimensional systems theory [13].

**Definition 2.** Let  $F \in R^{l \times m}$  be of full row rank. Then,  $F$  is said to be zero left prime (ZLP) if the  $l \times l$  minors of  $F$  generate the unit ideal  $R$ . Suppose  $F$  has a factorization  $F = CF_1$ , where  $C \in R^{l \times l}$  and  $F_1 \in R^{l \times m}$ . If  $F_1$  is ZLP, then this factorization is said to be a zero left prime factorization.

## 3. Main Results

First, we need a lemma.

**Lemma 1.** Let  $F = (C, \bar{C}) \in R^{l \times m}$  ( $l < m$ ), where  $C \in R^{l \times l}$  and  $\bar{C} \in R^{l \times (m-l)}$ . Then, the elements of  $\text{adj} C \cdot \bar{C}$  are just all related minors of  $C$  (up to a sign).

*Proof.* Let  $C = (c_{ij})_{l \times l}$  and  $\bar{C} = (\bar{c}_{ij})_{l \times (m-l)}$ . Let  $\text{adj} C \cdot \bar{C} = (b_{ij})_{l \times (m-l)}$ . Then,

$$\begin{aligned} b_{ij} &= \text{acof}_{1i}(C)\bar{c}_{1j} + \cdots + \text{acof}_{li}(C)\bar{c}_{lj} \\ &= \det \begin{pmatrix} c_{11} & \cdots & c_{1i-1} & \bar{c}_{1j} & c_{1i+1} & \cdots & c_{1l} \\ \vdots & & \vdots & \vdots & \vdots & & \vdots \\ c_{l1} & \cdots & c_{li-1} & \bar{c}_{lj} & c_{li+1} & \cdots & c_{ll} \end{pmatrix}, \end{aligned} \quad (1)$$

by Laplace Theorem. Thus,  $b_{ij}$  is a related minor of  $C$  (up to a sign). It is clear that they are just all related minors of  $C$  (up to a sign).

Now, we prove the main theorem of this paper.  $\square$

**Theorem 1.** *Let  $F \in R^{l \times m}$  ( $l < m$ ). If there exists an  $l \times l$  submatrix  $C$  of  $F$  such that  $\det C$  is a common factor of all related minors of  $C$ , then there exists  $F_1 \in R^{l \times m}$  such that  $F = CF_1$  and  $F_1$  is ZLP; i.e.,  $F$  has a ZLP factorization.*

*Proof.* We can change the order of the columns of  $F$  such that the submatrix  $C$  consists of the left  $l$  columns of  $F$ . Thus, there exists an invertible matrix  $Q \in R^{m \times m}$  such that  $FQ = (C, \bar{C})$ , where  $C \in R^{l \times l}$  and  $\bar{C} \in R^{l \times (m-l)}$ . Since  $\det C$  is a common factor of all related minors of  $C$ , by Lemma 1, we have  $C^{-1}\bar{C} = \text{adj} C \cdot \bar{C} / \det C \in R^{l \times (m-l)}$ . Let

$$Q_1 = \begin{pmatrix} I_l & -C^{-1}\bar{C} \\ 0 & I_{m-l} \end{pmatrix}. \quad (2)$$

Then,  $Q_1 \in R^{m \times m}$ . We have

$$\begin{aligned} FQ_1 &= (C, \bar{C})Q_1 \\ &= (C, \bar{C}) \begin{pmatrix} I_l & -C^{-1}\bar{C} \\ 0 & I_{m-l} \end{pmatrix} \\ &= (C, O). \end{aligned} \quad (3)$$

Then,

$$\begin{aligned} F &= (C, O)Q_1^{-1}Q^{-1} \text{ (by (3))} \\ &= C(I_l, O)Q_1^{-1}Q^{-1}. \end{aligned} \quad (4)$$

Let  $F_1 = (I_l, O)Q_1^{-1}Q^{-1} \in R^{l \times m}$ . Then,  $F = CF_1$ . Since  $F_1$  consists of the upper  $l$  rows of invertible matrix  $Q_1^{-1}Q^{-1}$ , we have  $F_1$  is ZLP.  $\square$

**Corollary 1.** *Let  $F \in R^{l \times m}$  ( $l < m$ ). If there exists an  $l \times l$  submatrix  $C$  of  $F$  such that  $\det C$  is a common factor of all related minors of  $C$ , then  $\det C = d(F)$ .*

*Proof.* Clearly,  $d(F) | \det C$ . By Theorem 1, there exists  $F_1 \in R^{l \times m}$  such that  $F = CF_1$ . By Cauchy–Binet formula, we have  $\det C | d(F)$ . Therefore,  $\det C = d(F)$ .  $\square$

**Corollary 2.** *Let  $F \in R^{l \times m}$  ( $l < m$ ). If there exists an  $l \times l$  submatrix  $C$  of  $F$  such that  $\det C$  is a common factor of all related minors of  $C$ , then  $F$  is equivalent to  $(C, O)$ .*

*Proof.* By Theorem 1, there exists  $F_1 \in R^{l \times m}$  such that  $F = CF_1$  and  $F_1$  is ZLP. By Quillen–Suslin theorem, there exists

$F_2 \in R^{(m-l) \times m}$  such that  $(F_1^T, F_2^T)^T$  is an invertible matrix. Since  $F = CF_1 = (C, O)(F_1^T, F_2^T)^T$ , we have  $F$  being equivalent to  $(C, O)$ .

Now, let  $F \in R^{l \times m}$  ( $l < m$ ). Suppose there exists an  $l \times l$  submatrix  $C$  of  $F$  such that  $\det C = d(F)$ . We can give an algorithm to directly compute the ZLP factorization of  $F$ .  $\square$

*Algorithm 1*

- (i) Compute all  $l \times l$  minors of  $F$  and  $d(F)$ .
- (ii) Find an  $l \times l$  submatrix  $C$  of  $F$  such that  $\det C = d(F)$ .
- (iii) Compute invertible matrix  $Q$  such that  $FQ = (C, \bar{C})$ .
- (iv) Let  $Q_1 = \begin{pmatrix} I_l & -C^{-1}\bar{C} \\ 0 & I_{m-l} \end{pmatrix}$  and  $F_1 = (I_l, O)Q_1^{-1}Q^{-1}$ .  
Then,  $F = CF_1$ .

Now, we give an example to illustrate this algorithm.

*Example 1.* Let  $R = \mathbb{Z}[x, y]$ , and let

$$F = \begin{pmatrix} 6x^2y + 2xy & 2x & 2xy \\ 6x^2y^2 + 6x^2y + 2xy^2 + 5xy & 2xy + 2x & 2xy^2 + 2xy + y \end{pmatrix}. \quad (5)$$

Then,  $d(F) = 2xy$ . Let

$$C = \begin{pmatrix} 2x & 2xy \\ 2xy + 2x & 2xy^2 + 2xy + y \end{pmatrix}. \quad (6)$$

Then,  $C$  is a  $2 \times 2$  submatrix of  $F$  and  $\det C = d(F)$ . Let

$$Q = \begin{pmatrix} 0 & 0 & 1 \\ 1 & 0 & 0 \\ 0 & 1 & 0 \end{pmatrix}. \quad (7)$$

Then,  $FQ = (C, \bar{C})$ , where

$$\bar{C} = \begin{pmatrix} 6x^2y + 2xy \\ 6x^2y^2 + 6x^2y + 2xy^2 + 5xy \end{pmatrix}. \quad (8)$$

Thus,  $-C^{-1}\bar{C} = \begin{pmatrix} -y \\ -3x \end{pmatrix}$ . Let

$$Q_1 = \begin{pmatrix} 1 & 0 & -y \\ 0 & 1 & -3x \\ 0 & 0 & 1 \end{pmatrix}. \quad (9)$$

Then,

$$Q_1^{-1}Q^{-1} = \begin{pmatrix} y & 1 & 0 \\ 3x & 0 & 1 \\ 1 & 0 & 0 \end{pmatrix}. \quad (10)$$

Let

$$F_1 = \begin{pmatrix} y & 1 & 0 \\ 3x & 0 & 1 \end{pmatrix}. \quad (11)$$

Then,  $F = CF_1$ .

## Data Availability

No data were used to support this study.

## Conflicts of Interest

The authors declare that there are no conflicts of interest regarding the publication of this article.

## Acknowledgments

This paper was supported by the National Science Foundation of China (11971161 and 11871207).

## References

- [1] N. K. Bose, *Applied Multidimensional Systems Theory*, Van Nostrand Reinhold, New York, NY, USA, 1982.
- [2] N. K. Bose, B. Buchberger, and J. P. Guiver, *Multidimensional Systems Theory and Applications*, Kluwer, Dordrecht, The Netherlands, 2003.
- [3] O. Bachelier and T. Cluzeau, "Digression on the equivalence between linear 2D discrete repetitive processes and roesser models," in *Proceedings of the Digression on the Equivalence Between Linear 2D Discrete Repetitive Processes and Roesser Models*, pp. 1–6, Zielona Gora, Poland, September 2017.
- [4] J. F. Pommaret, "Solving bose conjecture on linear multidimensional systems," in *Proceedings of the 2001 European Control Conference (ECC)*, pp. 1853–1855, Porto, Portugal, September 2001.
- [5] V. Srinivas, "A generalized Serre problem," *Journal of Algebra*, vol. 278, no. 2, pp. 621–627, 2004.
- [6] M. Wang and D. Feng, "On lin-bose problem," *Linear Algebra and Its Applications*, vol. 390, pp. 279–285, 2004.
- [7] M. Wang and C. P. Kwong, "On multivariate polynomial matrix factorization problems," *Mathematics of Control, Signals, and Systems*, vol. 17, no. 4, pp. 297–311, 2005.
- [8] M. Wang, "On factor prime factorizations for  $n$ -D polynomial matrices," *IEEE Transactions on Circuits and Systems I: Regular Papers*, vol. 54, no. 6, pp. 1398–1405, 2007.
- [9] J. Liu and M. Wang, "Further remarks on multivariate polynomial matrix factorizations," *Linear Algebra and its Applications*, vol. 465, pp. 204–213, 2015.
- [10] J. Guan, W. Li, and B. Ouyang, "On minor prime factorizations for multivariate polynomial matrices," *Multidimensional Systems and Signal Processing*, vol. 30, no. 1, pp. 493–502, 2019.
- [11] Z. Lin, "Notes on  $n$ -D polynomial matrix factorization," *Multidimensional Systems and Signal Processing*, vol. 10, no. 4, pp. 379–393, 1999.
- [12] Z. Lin and N. K. Bose, "A generalization of Serre's conjecture and some related issues," *Linear Algebra and its Applications*, vol. 338, no. 1–3, pp. 125–138, 2001.
- [13] D. C. Youla and G. Gnani, "Notes on  $n$ -dimensional system theory," *IEEE Transactions on Circuits and Systems*, vol. 26, no. 2, pp. 105–111, 1979.

## Research Article

# On Serre Reduction of Multidimensional Systems

Dongmei Li , Jinwang Liu, and Licui Zheng 

Department of Mathematics and Computational Sciences, Hunan University of Science and Technology, Xiangtan 411201, China

Correspondence should be addressed to Dongmei Li; [dml@hnust.edu.cn](mailto:dml@hnust.edu.cn)

Received 17 February 2020; Accepted 17 March 2020; Published 11 April 2020

Guest Editor: Hou-Sheng Su

Copyright © 2020 Dongmei Li et al. This is an open access article distributed under the Creative Commons Attribution License, which permits unrestricted use, distribution, and reproduction in any medium, provided the original work is properly cited.

Serre reduction of a system plays a key role in the theory of Multidimensional systems, which has a close connection with Serre reduction of polynomial matrices. In this paper, we investigate the Serre reduction problem for two kinds of  $nD$  polynomial matrices. Some new necessary and sufficient conditions about reducing these matrices to their Smith normal forms are obtained. These conditions can be easily checked by existing Gröbner basis algorithms of polynomial ideals.

## 1. Introduction

Multidimensional ( $nD$ ) systems arise naturally in several fields of control, circuits, signals, and network synthesis (see [1–5]). Serre reduction problem aims at simplifying  $nD$  systems to some equivalent forms with fewer equations in fewer unknowns, and rewriting these systems such that the key information on them [6], which does not show obviously in the original forms, can be derived from the new equivalent forms more easily. In general, this involves Serre reduction of multivariate ( $nD$ ) polynomial matrices to some simple equivalent forms, especially their Smith normal forms. Serre reduction can help to investigate the structural of  $nD$  polynomial matrices, which has wide applications in image, complex networked system, and other areas (see [6–11]).

In the theory of  $nD$  systems, the Serre reduction for a polynomial matrix to its Smith normal form plays a critical role. It preserves relevant system properties from the system theory point of view. The reduced matrix has good properties and corresponds to a system which consists of much less equations in unknowns than its original form. For single variable polynomial matrices, the problem for reducing the matrix to its Smith normal form has been well solved. Frost and Storey presented an example for 2D polynomial matrices which cannot be reduced to its Smith normal form [12]. For  $nD$  ( $n \geq 2$ ) case, since this reduction problem is equivalent to a highly difficult problem, the isomorphism of two finitely presented modules, the criteria determining

whether arbitrary  $nD$  polynomial matrix can be Serre reduced to its Smith normal form has not been presented so far. The reduction for several special classes of polynomial matrices to their Smith normal forms has been investigated. For the polynomial ring  $K[x_1, x_2]$ , Lee and Zak [13] presented a necessary condition for a class of 2D polynomial matrices on reducing them to the Smith normal forms. Lin et al. [14] proposed a sufficient and necessary condition, the existence of a special polynomial vector, under which a kind of  $nD$  polynomial matrices can be reduced to the Smith normal forms. Lin et al. [14] generalized this result to the case when  $K[x_1, x_2, \dots, x_n]$ ,  $n \geq 3$ . Furthermore, they showed that a class of  $l \times l$   $nD$  polynomial matrices  $P$  can be reduced to its Smith normal form  $\text{diag}(I_{l-1}, d)$  for  $\det P = x_1 - f(x_2, \dots, x_n) \triangleq d$ . Boudellioua [15] gave some similar conditions using module theoretic approach. Li et al. [16] proposed a sufficient and necessary condition under which  $P$  can be reduced to its Smith normal form  $\text{diag}(I_{l-1}, d^q)$  for  $P \in K^{l \times l}[x_1, x_2, \dots, x_n]$  and  $\det P = d^q$ ,  $d = x_1 - f(x_2, \dots, x_n)$ .

The results that we mentioned above mainly study polynomial matrices whose reduced matrices correspond to systems which contains only one equation in one unknown with form  $\text{diag}(I_{l-1}, \det F(z))$ , where  $F(z)$  is the polynomial matrix corresponds to the given  $nD$  system. In practical applications, the reduced matrix corresponds to a given system which is a more general form with more than one equation in unknowns, such as,  $\text{diag}(I_r, dI_{l-r})$ . In this



paper, we will investigate these systems and the reduced matrices. The following questions are considered.

*Problem 1.* Let  $F(z) \in K^{l \times l}[z]$  and  $\det F(z) = d^r = (z_1 - f(z_2, \dots, z_n))^r$ , where  $r$  is a positive integer. When is  $F(z)$  reduced to its Smith normal form  $\text{diag}(I_{l-r}, dI_r)$ ?

*Problem 2.* Let  $F(z) \in K^{l \times m}[z]$  ( $l \leq m$ ) has full rank and  $d_r(F) = d^q = (z_1 - f(z_2, \dots, z_n))^q$ , where  $d_r(F)$  is the greatest common divisor (g.c.d.) of all the  $r \times r$  minors of  $F(z)$  and  $q$  is a positive integer. Is there a tractable criterion for  $F(z)$  to be reduced to its Smith normal form?

This paper is organized as follows. We present some basic preliminary knowledge and main results for reducing several kinds of matrices to their Smith normal forms in Section 2. An example is established to illustrate our results and the constructive computational method in Section 3.

## 2. Preliminaries and Results

In the following,  $K[z] = K[z_1, \dots, z_n]$  denotes the polynomial ring in  $n$  variables  $z_1, \dots, z_n$  with coefficients in the field  $K$ ,  $\bar{K}$  denotes the algebraic closed field of  $K$ ,  $K^{l \times m}[z]$  denotes the set of  $l \times m$  matrices with entries in  $K[z]$ ,  $0_{r \times t}$  denotes the  $r \times t$  zero matrix, and  $I_r$  denotes the  $r \times r$  identity matrix. The argument  $(z)$  is omitted whenever its omission does not cause confusion, for example, we denote  $F(z)$  by  $F$  for simplicity.

For  $F(z) \in K^{l \times m}[z]$ , we use  $d_i(F)$  to denote the greatest common divisor of all the  $i \times i$  ( $i = 1, \dots, l$ ) minors of  $F(z)$ .

*Definition 1* (see [17]). Suppose  $F(z) \in K^{l \times m}[z]$  be of full row (column) rank, we say  $F(z)$  is zero left prime (zero right prime) if all the  $l \times l$  ( $m \times m$ ) minors of  $F(z)$  have no common zero or generate the unit ideal  $K[z]$ .

If  $F(z)$  is a zero left prime (zero right prime) matrix, we simply say that  $F(z)$  is ZLP (ZRP). By Quillen–Suslin theorem [18], we see that  $F(z)$  is ZLP iff there exists an  $m \times m$  invertible matrix  $N(z) \in K[z]$  such that  $F(z) \cdot N(z) = (E_l \ 0_{l \times (m-l)})$ . Quillen–Suslin theorem states that finite generated projective  $K[z]$ -module is free, and it is equivalent to saying that any ZLP (ZRP) matrix on  $K[z]$  can be completed to an invertible (unimodular) square matrix.

*Definition 2* (see [17]). Let  $F(z) \in K^{l \times m}[z]$ ,  $l \leq m$ , the Smith normal form of  $F(z)$  is defined as

$$S = \left( \text{diag}\{\Phi_i\} \ 0_{l \times (m-l)} \right), \quad (1)$$

where

$$\Phi_i = \begin{cases} \frac{d_i}{d_{i-1}}, & 1 \leq i \leq r, \\ 0, & r < i \leq m, \end{cases} \quad (2)$$

$r$  is the rank of  $F(z)$ ,  $d_0 \equiv 1$ ,  $d_i$  is the g.c.d. of the  $i \times i$  minors of  $F$ , and  $\Phi_i$  satisfies the divisibility property:

$$\Phi_1 \mid \Phi_2 \mid \dots \mid \Phi_r. \quad (3)$$

*Definition 3* (see [17]). Let  $T_1(z)$  and  $T_2(z)$  be two matrices in  $K^{l \times m}[z]$ , then  $T_1(z)$  and  $T_2(z)$  are said to be equivalent (or  $T_1(z)$  can be reduced to  $T_2(z)$  if there exist two invertible (unimodular) matrices  $M(z)$  and  $N(z)$  such that  $T_2(z) = M(z) \cdot T_1(z) \cdot N(z)$ ).

First, we give the following several well-known results about the factorization of  $n$ D polynomial matrices [10, 17, 19, 20].

**Lemma 1** (see Hilbert zeros Theorem [17, 20]). Suppose  $f_1(z), f_2(z), \dots, f_s(z) \in K[z]$ , then  $f_1(z), f_2(z), \dots, f_s(z)$  have no common zero in  $\bar{K}^n$  if and only if the ideal generated by  $f_1(z), f_2(z), \dots, f_s(z)$  is the unit ideal  $K[z]$ .

**Lemma 2** (see [19]). Suppose  $F(z) \in K^{l \times m}[z]$  is of full column rank and the reduced minors of  $F(z)$  generate  $K[z]$ , then  $F(z)$  admits a zero prime factorization  $F(z) = F_0(z) \cdot G_0(z)$  with  $F_0(z) \in K^{l \times m}[z]$ ,  $G_0(z) \in K^{m \times m}[z]$ , and  $\det G_0(z) = d_m(F)$ , and  $F_0(z)$  is a ZRP matrix.

*Remark 1.* Suppose  $F(z) \in K^{l \times m}[z]$  has full row rank and the  $l \times l$  reduced minors of  $F(z)$  generate  $K[z]$ , then  $F(z)$  admits the factorization as  $F(z) = G_0(z) \cdot F_0(z)$  with  $G_0(z) \in K[z]^{l \times l}$ ,  $F_0(z) \in K^{l \times m}[z]$ , and  $\det G_0(z) = d_l(F)$ . Hence,  $F_0(z)$  is a ZLP matrix.

**Lemma 3** (see [17, 20]). Suppose  $F(z) \in K^{l \times m}[z]$  has normal rank  $r$ , if the  $r \times r$  reduced minors of  $F$  generate  $K[z]$ , then there exists a ZLP matrix  $H(z) \in K^{(l-r) \times l}[z]$  such that  $H(z)F(z) = 0_{(l-r) \times m}$ .

**Lemma 4** (see [17]). Let  $g(z) \in K[z] = K[z_1, z_2, \dots, z_n]$  and  $f(z) \in K[z_2, \dots, z_n]$ . Suppose that  $g(f, z_2, \dots, z_n) = 0$ , then  $z_1 - f(z_2, \dots, z_n)$  is a divisor of  $g(z)$ .

In what follows, for a polynomial matrix  $F(z)$ , we use  $F \begin{pmatrix} i_1 & i_2 & \dots & i_s \\ j_1 & j_2 & \dots & j_t \end{pmatrix}$  to denote an  $s \times t$  submatrix of  $F(z)$  constituted by the  $i_1, \dots, i_s$  rows and  $j_1, \dots, j_t$  columns of  $F(z)$ .

**Lemma 5.** Suppose  $F(z) = F_1(z)F_2(z)$  with  $F(z), F_1(z), F_2(z) \in K^{l \times m}[z]$ . If all the  $k \times k$  minors of  $F(z)$  have no common zero, for some  $k$  ( $k \leq l$ ), then all the  $k \times k$  minors of  $F_i(z)$  ( $i = 1, 2$ ) have no common zero.

*Proof.* For any  $k \leq l$ , since

$$F \begin{pmatrix} i_1 & i_2 & \dots & i_k \\ j_1 & j_2 & \dots & j_k \end{pmatrix} = F_1 \begin{pmatrix} i_1 & i_2 & \dots & i_k \\ 1 & 2 & \dots & l \end{pmatrix} \cdot F_2 \begin{pmatrix} 1 & 2 & \dots & l \\ j_1 & j_2 & \dots & j_k \end{pmatrix}, \quad (4)$$

according to Cauchy–Binet formula, we obtain

$$\det F \begin{pmatrix} i_1 & i_2 & \cdots & i_k \\ j_1 & j_2 & \cdots & j_k \end{pmatrix} = \sum g_i \cdot h_i, \quad (5)$$

where  $g_i$  and  $h_i$  are  $k \times k$  minors of  $F_1(z)$  and  $F_2(z)$ , respectively. Suppose that all the  $k \times k$  minors of  $F_i(z)$  have a common zero point  $a_0$ . So, the  $k \times k$  minors of  $F(z)$  have a common zero point  $a_0$ . This contradicts the assumption. Therefore, all the  $k \times k$  minors of  $F_i(z)$  ( $i = 1, 2$ ) have no common zero.  $\square$

**Lemma 6.** Suppose  $A(z), B(z) \in K^{l \times m}[z]$  and  $A(z)$  can be reduced to  $B(z)$ , then  $d_k(A) = d_k(B)$  for  $k = 1, 2, \dots, \alpha$ ,  $\alpha = \min\{l, m\}$ .

*Proof.* Since  $A$  can be reduced to  $B$ , by Definition 3, there are invertible matrices  $U$  and  $V$  such that  $A = UB$ . Setting  $C = UB$ , according to Cauchy–Binet formula, we have that

$$\det C \begin{pmatrix} i_1 & i_2 & \cdots & i_k \\ j_1 & j_2 & \cdots & j_k \end{pmatrix} = \sum f_i g_j, \quad (6)$$

where  $f_i$  is a  $k \times k$  minors of  $U$ ,  $g_j$  is a  $k \times k$  minors of  $B$ , and so  $d_k(B) | d_k(C)$ . Note that  $B = U^{-1}C$ , similar to the procedure above, we have that  $d_k(C) | d_k(B)$ . Hence,  $d_k(C) = d_k(B)$ .

In the following, we denote  $z_1 - f(z_2, \dots, z_n)$  by  $d$  and  $d_l(F(z))$  by  $d(F)$  simply. We can obtain the following result, which gives a positive answer to Problem 1.  $\square$

**Theorem 1.** Suppose  $F(z) \in K^{l \times l}[z]$  has a full row rank and  $\det F(z) = d^r$ , where  $d = z_1 - f(z_2, \dots, z_n)$ ,  $r$  is a positive integer. If all the  $(l-r) \times (l-r)$  minors of  $F(z)$  have no common zero and  $d | d_{l-r+1}(F)$ , then  $F(z)$  can be reduced to its Smith form:

$$D(z) = \begin{pmatrix} 1 & & & & & \\ & \ddots & & & & \\ & & 1 & & & \\ & & & d & & \\ & & & & \ddots & \\ & & & & & d \end{pmatrix}, \quad (7)$$

with  $\det D(z) = d^r$ .

*Proof.* We first prove that  $\text{rank } F(f(z_2, \dots, z_n), z_2, \dots, z_n)$  is  $l-r$ . Since  $d | d_{l-r+1}(F)$ , it follows that  $\text{rank}(F(f(z_2, \dots, z_n), z_2, \dots, z_n)) \leq l-r$ . Because  $(l-r) \times (l-r)$  minors of  $F(z)$  have no common zero, then  $d \nmid d_r(F)$ . Combined with Lemma 5, we obtain that  $d_r(F(f(z_2, \dots, z_n), z_2, \dots, z_n)) \neq 0$ , and  $\text{rank}(F(f(z_2, \dots, z_n), z_2, \dots, z_n)) = l-r$ . Let  $b_1(z_1, z_2, \dots, z_n), \dots, b_q(z_1, z_2, \dots, z_n), c_1(z_2, \dots, z_n), \dots, c_q(z_2, \dots, z_n)$  be the  $(l-r) \times (l-r)$  minors of  $F(z_1, z_2, \dots, z_n)$  and  $F(f(z_2, \dots, z_n), z_2, \dots, z_n)$ , respectively. It is straightforward that  $c_i(z_2, \dots, z_n)$  is a divisor of  $b_i(f(z_2, \dots, z_n))$  ( $i = 1, \dots, q$ ). Since  $b_1(z), \dots, b_q(z)$  have no common zero, then  $b_1(f(z_2, \dots, z_n), z_2, \dots, z_n), \dots, b_q(f(z_2, \dots, z_n), z_2, \dots, z_n))$  also have no common zero. So,

$c_1(z_2, \dots, z_n), \dots, c_q(z_2, \dots, z_n)$  also have no common zero, i.e., the  $(l-r) \times (l-r)$  minors of  $F(f(z_2, \dots, z_n), z_2, \dots, z_n)$  have no common zero.

We then show that  $F(z)$  can be reduced to its Smith normal form. According to Lemma 3, there exists a ZLP polynomial matrix  $H \in K^{(r) \times l}[z]$  which satisfies  $H \cdot F(f(z_2, \dots, z_n)) = 0_{(r) \times m}$ . By Quillen–Suslin Theorem, we can complete  $H$  into an  $l \times l$  unimodular matrix  $V(z_2, \dots, z_n)$ , that is,  $H$  is the last  $r$  rows of  $V(z_2, \dots, z_n)$ . We have that the last  $r$  rows of the matrix  $V \cdot F(f(z_2, \dots, z_n))$  are the zero polynomials. According to Lemma 4, there is the common divisor  $d$  in the last  $r$  rows of  $V \cdot F(z_1, z_2, \dots, z_n)$ , i.e.,

$$V \cdot F = \begin{pmatrix} 1 & & & & & \\ & \ddots & & & & \\ & & 1 & & & \\ & & & d & & \\ & & & & \ddots & \\ & & & & & d \end{pmatrix} \begin{pmatrix} g_{11} & \cdots & g_{1l} \\ \vdots & \ddots & \vdots \\ g_{r1} & \cdots & g_{rl} \\ g_{(r+1)1} & \cdots & g_{(r+1)l} \\ \vdots & \ddots & \vdots \\ g_{l1} & \cdots & g_{ll} \end{pmatrix}, \quad (8)$$

where  $g_{ij} \in K[z]$ . Setting  $D(z) = \text{diag}(1, \dots, 1, d, \dots, d)$ , then  $\det D(z) = d^r$ . Combining with  $d \nmid d_{l-r}(F)$ ,  $d | d_{l-r+1}(F)$ , and  $\det F(z) = d^r$ , we obtain that the Smith normal form of  $F(z)$  is  $D(z)$ . Let

$$G = \begin{pmatrix} g_{11} & \cdots & g_{1l} \\ \vdots & \ddots & \vdots \\ g_{r1} & \cdots & g_{rm} \\ g_{(r+1)1} & \cdots & g_{(r+1)l} \\ \vdots & \ddots & \vdots \\ g_{l1} & \cdots & g_{ll} \end{pmatrix}, \quad (9)$$

Then,  $\det G = 1$  and  $F = V^{-1}DG$ . Note that  $U$  and  $G$  are unimodular matrices, so  $F(z)$  can be reduced to its Smith normal form  $D(z)$ .

Denote

$$D(z) = \begin{pmatrix} I_{l-r} & \\ & dI_r \end{pmatrix}. \quad (10)$$

In order to investigate Problem 2, we consider the following simple case first.  $\square$

**Theorem 2.** Suppose  $F(z) \in K^{l \times m}[z]$  ( $l \leq m$ ) has full row rank with  $d_l(F) = d^r$ , where  $r$  is a positive integer. If all the  $(l-r) \times (l-r)$  minors of  $F(z)$  have no common zero and  $d | d_{l-r+1}(F)$ , then  $F(z)$  can be reduced to its Smith normal form.

*Proof.* Since all the  $(l-r) \times (l-r)$  minors of  $F(z)$  have no common zero, by Lemma 1, then all the  $(l-r) \times (l-r)$  minors of  $F(z)$  generate  $K[z]$ . Combined with  $d | d_{r+1}(F)$ , we have that the Smith normal form of  $F(z)$  is the matrix:

$$P(z) = (D(z) \quad 0_{l \times (m-l)}). \quad (11)$$

According to Remark 1, there exist  $G_0(z) \in K^{l \times l}[z]$  with  $\det G_0(z) = d^r$ ,  $F_0(z) \in K^{l \times m}$  such that  $F(z) = G_0(z) \cdot F_0(z)$ , and  $F_0(z)$  is ZLP. Combining with Lemma 5, we have that the  $(l-r) \times (l-r)$  minors of  $G_0(z)$  have no common zero and  $d \mid d_{l-r+1}(G_0)$ . From Theorem 1, there exist two  $l \times l$  unimodular polynomial matrices  $U(z)$  and  $V(z)$  which satisfy  $G_0(z) = U(z) \cdot D(z) \cdot V(z)$ . It is straightforward that  $V(z) \cdot F_0(z)$  is also ZLP. According to Quillen–Suslin theorem, there is an invertible matrix  $Q(z) \in K^{m \times m}[z]$  such that  $V(z) \cdot F_0(z) \cdot Q(z) = (I_l \quad 0_{l \times (m-l)})$ . Hence,

$$\begin{aligned} F(z) \cdot Q(z) &= G_0(z) \cdot F_0(z) \cdot Q(z) = U(z) \cdot D(z) \cdot V(z) \\ &\quad \cdot F_0(z) \cdot Q(z) \\ &= U(z) \cdot D(z) \cdot (I_l \quad 0_{l \times (m-l)}) = U(z) \cdot P(z). \end{aligned} \quad (12)$$

Thus,  $F(z)$  can be reduced to its Smith normal form  $P(z)$ .  $\square$

**Lemma 7.** Suppose  $V(z) \in K^{l \times l}[z_2, \dots, z_n]$  is a unimodular matrix. If all the  $(l-r) \times (l-r)$  minors of  $D^s(z) \cdot V(z) \cdot D(z)$  have no common zero, then the matrix  $D^s(z) \cdot V(z) \cdot D(z)$  can be reduced to the matrix  $D^{s+1}(z)$ .

*Proof.* Setting  $F(z) = D^s(z) \cdot V(z) \cdot D(z)$  and

$$V_1 = \begin{pmatrix} P_1 & P_2 \\ P_3 & P_4 \end{pmatrix}, \quad (13)$$

where  $P_1 \in K^{(l-r) \times (l-r)}[z_2, \dots, z_n]$ ,  $P_2 \in K^{(l-r) \times r}[z_2, \dots, z_n]$ ,  $P_3 \in K^{r \times (l-r)}[z_2, \dots, z_n]$ , and  $P_4 \in K^{r \times r}[z_2, \dots, z_n]$ , we obtain that

$$F(z) = \begin{pmatrix} I_{l-r} & \\ & d^s I_r \end{pmatrix} \begin{pmatrix} P_1 & P_2 \\ P_3 & P_4 \end{pmatrix} \begin{pmatrix} I_{l-r} & \\ & d I_r \end{pmatrix}. \quad (14)$$

Note that  $P_1$  is ZLP (since  $U(z)$  an invertible matrix), and according to Quillen–Suslin theorem, there exists an invertible matrix  $Q_{11} \in K^{(l-r) \times (l-r)}[z_2, \dots, z_n]$  such that  $P_1 \cdot Q_{11} = I_{l-r}$ . Setting

$$Q_1 \triangleq \begin{pmatrix} Q_{11} & \\ & I_r \end{pmatrix}, \quad (15)$$

$$P_3 \cdot Q_{11} \triangleq P_{31},$$

we partition  $P_2$  and  $P_{31}$  as

$$P_2 = \begin{pmatrix} \alpha_1 \\ \vdots \\ \alpha_m \end{pmatrix}, \quad (16)$$

$$P_{31} = (\beta_1 \quad \dots \quad \beta_m),$$

where  $\alpha_1, \dots, \alpha_m \in K^{1 \times r}[z_2, \dots, z_n]$  and  $\beta_1, \dots, \beta_m \in K^{r \times 1}[z_2, \dots, z_n]$ .

We obtain that

$$\begin{aligned} F(z) &= \begin{pmatrix} I_{l-r} & \\ & d^s I_r \end{pmatrix} \cdot \begin{pmatrix} P_1 & dP_2 \\ P_3 & dP_4 \end{pmatrix} \cdot Q_1 \cdot Q_1^{-1} \\ &= \begin{pmatrix} I_{l-r} & \\ & d^s I_r \end{pmatrix} \cdot \begin{pmatrix} P_1 & dP_2 \\ P_3 & dP_4 \end{pmatrix} \cdot \begin{pmatrix} Q_{11} & \\ & I_r \end{pmatrix} \cdot Q_1^{-1} \\ &= \begin{pmatrix} I_{l-r} & \\ & d^s I_r \end{pmatrix} \cdot \begin{pmatrix} I_{l-r} & dP_2 \\ P_{31} & dP_4 \end{pmatrix} \cdot Q_1^{-1} \\ &= \begin{pmatrix} 1 & & & d\alpha_1 \\ & \ddots & & \dots \\ & & 1 & d\alpha_{l-r} \\ d^s \beta_1 & \dots & d^s \beta_{l-r} & d^{s+1} P_4 \end{pmatrix} \cdot Q_1^{-1}. \end{aligned} \quad (17)$$

Setting

$$\begin{aligned} Q_2 &= \begin{pmatrix} 1 & & & 0_{(l-r) \times r} \\ & \ddots & & \\ & & 1 & \\ -d^s \beta_1 & \dots & -d^s \beta_{l-r} & I_r \end{pmatrix}, \\ Q_3 &= \begin{pmatrix} 1 & & -d\alpha_1 \\ & \ddots & \vdots \\ & & 1 & -d\alpha_{l-r} \\ 0_{(l-m) \times (l-r)} & & & I_r \end{pmatrix}, \end{aligned} \quad (18)$$

we have that

$$\begin{aligned} Q_2 \cdot F(z) &= \begin{pmatrix} 1 & & d\alpha_1 \\ & \ddots & \dots \\ & & 1 & d\alpha_{l-r} \\ 0_{r \times (l-r)} & & & d^{s+1} P_4 \end{pmatrix} \cdot Q_3 \cdot Q_3^{-1} \cdot Q_1^{-1} \\ &= \begin{pmatrix} I_{l-r} & \\ & d^{s+1} P_4 \end{pmatrix} \cdot Q_3^{-1} \cdot Q_1^{-1}. \end{aligned} \quad (19)$$

Since  $P_4$  is ZLP, according to Quillen–Suslin theorem, there exists an invertible matrix  $Q_{51} \in K^{r \times r}[z_2, \dots, z_n]$  such that  $P_4 \cdot Q_{51} = I_r$ . Setting

$$Q_5 \triangleq \begin{pmatrix} I_{l-r} & \\ & Q_{51} \end{pmatrix}, \quad (20)$$

we see that

$$\begin{aligned} F(z) &= Q_2^{-1} \begin{pmatrix} I_{l-r} & \\ & d^{s+1} P_4 \end{pmatrix} \begin{pmatrix} I_{l-r} & \\ & Q_{51} \end{pmatrix} Q_5^{-1} Q_3^{-1} Q_1^{-1} \\ &= Q_2^{-1} \cdot \begin{pmatrix} I_{l-r} & \\ & d^{s+1} I_r \end{pmatrix} Q_5^{-1} Q_3^{-1} Q_1^{-1}. \end{aligned} \quad (21)$$

Obviously,  $Q_2^{-1}$  and  $Q_5^{-1} Q_3^{-1} Q_1^{-1}$  are invertible. So,  $F(z)$  can be reduced to

$$D^{s+1}(z) \triangleq \begin{pmatrix} I_{l-r} & \\ & d^{s+1} I_r \end{pmatrix}. \quad (22)$$

$\square$

**Theorem 3.** Suppose  $F(z) \in K^{l \times l}[z]$  with  $\det F(z) = d^q$ . If all the  $(l-r) \times (l-r)$  minors of  $F(z)$  have no common zero and  $d^{q/r} \mid d_{l-r+1}(F)$ , where  $q, q/r$  are positive integers. Then,  $F(z)$  can be reduced to its Smith normal form:

$$D^{q/r}(z) = \begin{pmatrix} I_{l-r} & \\ & d^{q/r} I_r \end{pmatrix}. \quad (23)$$

*Proof.* When  $q/r = 1$ , by Theorem 1, the conclusion is correct.

When  $q/r \geq 2$ , since  $d \mid d_{l-r+1}(F)$ , it follows that  $\text{rank}(F(f(z_2, \dots, z_n), z_2, \dots, z_n)) \leq l-r$ . All the  $(l-r) \times (l-r)$  minors of  $F(z)$  have no common zero, and doing the same as that of the proof of Theorem 1, we obtain that  $\text{rank}(F(f(z_2, \dots, z_n), z_2, \dots, z_n)) = l-r$  and

$$V_1(z) \cdot F(z) = \begin{pmatrix} I_{l-r} & 0_{l-r,r} \\ 0_{r,l-r} & dI_r \end{pmatrix} \cdot F_1(z), \quad (24)$$

where  $V_1(z) \in K^{l \times l}[z]$  is a unimodular matrix and  $F_1(z) \in K^{l \times l}[z]$ . Hence,

$$F(z) = V_1^{-1}(z) \cdot D(z) \cdot F_1(z). \quad (25)$$

We know that  $\det F_1(z) = d^{q-r}(z)$  from the equation above. According to Lemma 5, all the  $(l-r) \times (l-r)$  minors of  $F_1(z)$  have also no common zero. If  $(q/r) \geq 2$ , combined with  $r$  is a positive integer, then  $q-r \geq 2$ ; imitating the procedure above, we obtain that

$$F_1(z) = V_2^{-1}(z) \cdot D(z) \cdot F_2(z). \quad (26)$$

Then,

$$F(z) = V_1^{-1} \cdot D(z) \cdot V_2^{-1}(z) \cdot D(z) \cdot F_2(z). \quad (27)$$

Using Lemma 5 again, all the  $(l-r) \times (l-r)$  minors of  $D(z) \cdot V_2^{-1}(z) \cdot D(z)$  also have no common zero. Combined with Lemma 7, two invertible matrices  $N_1(z), U_1(z) \in K^{l \times l}[z]$  exist and satisfy  $D(z) \cdot V_2^{-1}(z) \cdot D(z) = N_1(z) \cdot D^2(z) \cdot U_1(z)$ . Therefore,

$$F(z) = V_1^{-1} \cdot N_1(z) \cdot D^2(z) \cdot U_1(z) \cdot F_2(z). \quad (28)$$

Note that  $\det F(z) = d^q$  and  $\det D^2(z) = d^{2r}$ , then  $\det U_1(z) \cdot F_2(z) = d^{q-2r}$ . Furthermore, from Lemma 5, we see that the  $(l-r) \times (l-r)$  minors of  $U_1(z) \cdot F_2(z)$  also have no common zero.

If  $(q/r) \geq 3$ , repeating the previous process, we obtain that

$$F(z) = V_1^{-1}(z) \cdot N_1(z) \dots N_{(q/r)-1}(z) \cdot D^{q/r}(z) \cdot U_{(q/r)-1}(z) \cdot F_{q/r}(z). \quad (29)$$

Note that  $\det F(z) = d^q$  and  $\det D^{q/r}(z) = d^q$ , we see  $\det(U_{(q/r)-1}(z) \cdot F_{q/r}(z)) = 1$ . Hence,  $V_1^{-1}(z) \cdot N_1(z) \dots N_{(q/r)-1}(z)$  and  $U_{(q/r)-1}(z) \cdot F_{q/r}(z)$  are invertible matrices. So,  $F(z)$  can be reduced to its Smith normal form  $D^{q/r}(z)$ .  $\square$

**Theorem 4.** Suppose  $F(z) \in K^{l \times m}[z]$  ( $l \leq m$ ) has full row rank with  $d_1(F) = d^q$  and  $d^{q/r} \mid d_{l-r+1}(F)$ , where  $q$  and  $q/r$  are

positive integers. Then,  $F(z)$  can be reduced to its Smith normal form if and only if all the  $(l-r) \times (l-r)$  minors of  $F(z)$  have no common zero.

*Proof (sufficiency).* Since all the  $(l-r) \times (l-r)$  minors of  $F(z)$  have no common zero and  $d^{q/r} \mid d_{l-r+1}(F)$ , then the Smith normal form of  $F(z)$  is

$$P(z) = \begin{pmatrix} D^{q/r}(z) & \\ & 0_{l \times (m-l)} \end{pmatrix}. \quad (30)$$

According to Remark 1, there exist  $G_0(z) \in K^{l \times l}[z]$  with  $\det G_0(z) = d^r$ ,  $F_0(z) \in K^{l \times m}$  satisfy  $F(z) = G_0(z) \cdot F_0(z)$ , and  $F_0(z)$  is ZLP. Combining with Lemma 5, we have that the  $(l-r) \times (l-r)$  minors of  $G_0(z)$  have no common zero and  $d \mid d_{l-r+1}(G_0)$ . From Theorem 3, there are invertible matrices  $U(z), V(z) \in K^{l \times l}[z]$  which satisfy  $G_0(z) = V(z) \cdot D^{q/r}(z) \cdot U(z)$ . It is straightforward that  $U(z) \cdot F_0(z)$  is also a ZLP matrix. From Quillen–Suslin theorem, we have that there is an invertible matrix  $Q(z) \in K^{m \times m}[z]$  which satisfy  $U(z) \cdot F_0(z) \cdot Q(z) = \begin{pmatrix} I_l & \\ & 0_{l \times (m-l)} \end{pmatrix}$ . Hence,

$$\begin{aligned} F(z) \cdot Q(z) &= G_0(z) \cdot F_0(z) \cdot Q(z) = V(z) \cdot D^{q/r}(z) \cdot U(z) \\ &\quad \cdot F_0(z) \cdot Q(z) \\ &= V(z) \cdot D^{q/r}(z) \cdot \begin{pmatrix} I_l & \\ & 0_{l \times (m-l)} \end{pmatrix} = U(z) \cdot P(z). \end{aligned} \quad (31)$$

So,  $F(z)$  can be reduced to its Smith normal form  $P(z)$ .  $\square$

*Necessity.* Assume  $P(z)$  is the Smith normal form of  $F(z)$ . It is obvious that all the  $(l-r) \times (l-r)$  minors of  $P(z)$  have no common zero and  $d^{q/r} \mid d_{l-r+1}(P)$ . Since  $F(z)$  can be reduced to  $P(z)$ , by Lemmas 5 and 6, we have that all the  $(l-r) \times (l-r)$  minors of  $F(z)$  have no common zero and  $d^{q/r} \mid d_{l-r+1}(F)$ .

*Remark 2.* Let  $f_1(z), \dots, f_s(z)$  be some nonzero polynomials in  $K[z]$ ; by Lemma 1, we know a necessary and sufficient condition of  $f_1(z), f_2(z), \dots, f_s(z)$  have no common zero.  $K[z]$  is the reduced Gröbner basis of the ideal  $I$ , which is generated by  $f_1(z), \dots, f_s(z)$ , and contains a unit of  $K$ . By Theorems 1–4, we can check whether such a kind of  $nD$  polynomial matrices can be reduced to its Smith normal form by using the existing Gröbner basis algorithms. So, the conditions of Theorems 1–4 can be verified easily.

### 3. An Example

In this section, we present an example to explain our method on how to reduce the polynomial matrix we considered to its Smith normal form.

*Example 1.* We consider the following 3D polynomial matrix:

$$F(z) = \begin{pmatrix} 1 + z_3 & 1 - z_3^2 - z_3 & z_1 z_3 - z_2^2 \\ -z_1^2 + 2z_1 z_2^2 + z_2^4 z_3 & z_1^2 z_3 - 2z_1 z_2^2 z_3 - z_2^4 z_3^2 + z_2^4 & z_1 z_2^4 z_3 - 2z_1 z_2^4 + z_1^2 z_2^2 \\ -2z_1^2 + 4z_1 z_2^2 - 2z_2^4 & 2z_1^2 z_3 - 4z_1 z_2^2 z_3 + 2z_2^4 z_3 & z_1^2 - 2z_1^2 z_2^4 - 2z_1 z_2^4 - 2z_1 z_2^2 + 2z_2^6 + z_2^4 \end{pmatrix}, \quad (32)$$

with  $\det F(z) = (z_1 - z_2^2)^4$ . Then, we will prove that  $F(z)$  can be reduced to its Smith normal form.

*Step 1.* By computing,  $d_2(F) = (z_1 - z_2^2)^2$  and the reduced Gröbner basis of the ideal, which is generated by the  $1 \times 1$  minors of  $F(z)$ , is  $\{1\}$ . Combined with Remark 2 and Lemma 1, we have that the  $1 \times 1$  minors of  $F(z)$  have no common zero. Let  $d = z_1 - z_2^2$ , and then according to Theorem 3, we have that  $F(z)$  is can be reduced to its Smith normal form:

$$P(z) = \begin{pmatrix} 1 & & \\ & d^2 & \\ & & d^2 \end{pmatrix}, \quad (33)$$

where  $d = z_1 - z_2^2$ .

*Step 2.* Substituting  $f(z_2, z_3) = z_2^2$  for  $z_1$  in  $F(z)$ , we have

$$F(z_2^2, z_2, z_3) = \begin{pmatrix} 1 + z_3 & 1 - z_3^2 - z_3 & z_2^2 z_3 - z_2^2 \\ z_2^4 + z_2^4 z_3 & z_2^4 - z_2^4 z_3^2 - z_2^4 z_3 & z_2^6 z_3 - z_2^6 \\ 0 & 0 & 0 \end{pmatrix}. \quad (34)$$

Then, we construct the following invertible matrix:

$$U_1(z_2, z_3) = \begin{pmatrix} 1 & 0 & 0 \\ -z_2^4 & 1 & 0 \\ 0 & 0 & 1 \end{pmatrix}, \quad (35)$$

such that

$$U_1(z_2, z_3) \cdot F(z_2^2, z_2, z_3) = \begin{pmatrix} 1 + z_3 & 1 - z_3 - z_3^2 & z_2^2 z_3 - z_2^2 \\ 0 & 0 & 0 \\ 0 & 0 & 0 \end{pmatrix}. \quad (36)$$

Computing by singular,

$$U_1(z_2, z_3) \cdot F(z_1, z_2, z_3) = \begin{pmatrix} 1 & & \\ & d & \\ & & d \end{pmatrix} \cdot \begin{pmatrix} 1 + z_3 & 1 - z_3 - z_3^2 & z_1 z_3 - z_2^2 \\ -z_1 + z_2^2 & z_1 z_3 - z_2^2 z_3 & z_1 z_2^2 - z_2^4 \\ -2z_1 + 2z_2^2 & 2z_1 z_3 - 2z_2^2 z_3 & z_1 + 2z_1 z_2^2 - 2z_2^4 - z_2^2 \end{pmatrix}. \quad (37)$$

*Step 3.* Suppose

$$F_1 = \begin{pmatrix} 1 + z_3 & 1 - z_3 - z_3^2 & z_1 z_3 - z_2^2 \\ -z_1 + z_2^2 & z_1 z_3 - z_2^2 z_3 & z_1 z_2^2 - z_2^4 \\ -2z_1 + 2z_2^2 & 2z_1 z_3 - 2z_2^2 z_3 & z_1 + 2z_1 z_2^2 - 2z_2^4 - z_2^2 \end{pmatrix}, \quad (38)$$

repeating Step 2 to  $F_1$ , we have

$$U_2 = \begin{pmatrix} 1 & 0 & 0 \\ 0 & 1 & 0 \\ 0 & -2 & 1 \end{pmatrix}. \quad (39)$$

Hence,

$$U_2 \cdot F_1 = \begin{pmatrix} 1 & & \\ & d & \\ & & d \end{pmatrix} \cdot \begin{pmatrix} 1 + z_3 & 1 - z_3 - z_3^2 & z_1 z_3 - z_2^2 \\ -1 & z_3 & z_2^2 \\ 0 & 0 & 1 \end{pmatrix}. \quad (40)$$

*Step 4.* Let

$$F_2 = \begin{pmatrix} 1 + z_3 & 1 - z_3^2 - z_3 & z_1 z_3 - z_2^2 \\ -1 & z_3 & z_2^2 \\ 0 & 0 & 1 \end{pmatrix}, \quad (41)$$

we check easily that  $F_2$  is an invertible matrix.

*Step 5.* By Lemma 7, we obtain

$$\begin{aligned}
\begin{pmatrix} 1 & \\ & d \\ & & d \end{pmatrix} \cdot U_2^{-1} \cdot \begin{pmatrix} 1 & \\ & d \\ & & d \end{pmatrix} &= U_2^{-1} \cdot U_2 \cdot \begin{pmatrix} 1 & \\ & d \\ & & d \end{pmatrix} \cdot U_2^{-1} \cdot \begin{pmatrix} 1 & \\ & d \\ & & d \end{pmatrix} \\
&= U_2^{-1} \cdot \begin{pmatrix} 1 & 0 & 0 \\ 0 & 1 & 0 \\ 0 & -2 & 1 \end{pmatrix} \cdot \begin{pmatrix} 1 & \\ & d \\ & & d \end{pmatrix} \cdot \begin{pmatrix} 1 & 0 & 0 \\ 0 & 1 & 0 \\ 0 & 2 & 1 \end{pmatrix} \cdot \begin{pmatrix} 1 & \\ & d \\ & & d \end{pmatrix} \\
&= U_2^{-1} \cdot \begin{pmatrix} 1 & 0 & 0 \\ 0 & d & 0 \\ 0 & -2d & d \end{pmatrix} \cdot \begin{pmatrix} 1 & 0 & 0 \\ 0 & 1 & 0 \\ 0 & 2 & 1 \end{pmatrix} \cdot \begin{pmatrix} 1 & \\ & d \\ & & d \end{pmatrix} \\
&= U_2^{-1} \cdot \begin{pmatrix} 1 & \\ & d^2 \\ & & d^2 \end{pmatrix}.
\end{aligned} \tag{42}$$

Hence,

$$\begin{aligned}
F(z) &= U_1^{-1} \cdot \begin{pmatrix} 1 & \\ & d \\ & & d \end{pmatrix} \cdot F_1 \\
&= U_1^{-1} \begin{pmatrix} 1 & \\ & d \\ & & d \end{pmatrix} \cdot U_2^{-1} \cdot F_2 \\
&= U_1^{-1} \cdot U_2^{-1} \cdot \begin{pmatrix} 1 & \\ & d^2 \\ & & d^2 \end{pmatrix} \cdot F_2.
\end{aligned} \tag{43}$$

Thus,

$$F(z) = U(z) \cdot \begin{pmatrix} 1 & \\ & d^2 \\ & & d^2 \end{pmatrix} \cdot V(z), \tag{44}$$

where  $U(z) = U_1^{-1} \cdot U_2^{-1}$  and  $V(z) = F_2$  are invertible matrices.

#### 4. Conclusions

In this paper, we have investigated the Serre reduction problem for two classes of multivariate polynomial matrices  $F(z)$  with the g.c.d. of maximal order minors as  $(z_1 - f(z_2, \dots, z_n))^q$ . We have obtained some tractable sufficient and necessary conditions under which such kinds of matrices can be reduced to their Smith forms. These conditions can be checked by using the existing Gröbner basis algorithms to the associated minors of the given matrix. We also give an example to illustrate our method. All of these could provide useful information for reducing  $nD$  systems.

#### Data Availability

The data used to support the findings of this study are included within the article.

#### Conflicts of Interest

The authors declare that there are no conflicts of interest regarding the publication of this paper.

#### Acknowledgments

This research was supported by the National Natural Science Foundation of China (11871207 and 11971161).

#### References

- [1] E. Antoniou and S. Vologianidis, "On the reduction of 2-D polynomial system into first order equivalent models," *Multidimensional Systems and Signal Processing*, vol. 31, no. 1, 2020.
- [2] H. Su, J. Zhang, and X. Chen, "A stochastic sampling mechanism for time-varying formation of multiagent systems with multiple leaders and communication delays," *IEEE Transactions on Neural Networks and Learning Systems*, vol. 30, no. 12, pp. 3699–3707, 2019.
- [3] O. Bachelier and T. Cluzeau, "Digression on the equivalence between linear 2d discrete repetitive processes and roesser models," in *Proceedings of the 2017 10th International Workshop on Multidimensional (nD) Systems (nDS)*, pp. 1–6, Zielona Gora, Poland, September 2017.
- [4] N. Bose, *Applied Multidimensional Systems Theory*, Van Nostrand Reinhold, Newyork, NY, USA, 1982.
- [5] N. Bose, B. Buchberger, and J. Guiver, *Multidimensional Systems Theory and Applications*, Kluwer, Dordrecht, The Netherlands, 2003.
- [6] M. S. Boudelloua and A. Quadrat, "Serre's reduction of linear functional systems," *Mathematics in Computer Science*, vol. 4, no. 2-3, pp. 289–312, 2010.
- [7] H. Su, Y. Ye, Y. Qiu, Y. Cao, and M. Z. Q. Chen, "Semi-global output consensus for discrete-time switching networked systems subject to input saturation and external disturbances," *IEEE Transactions on Cybernetics*, vol. 49, no. 11, pp. 3934–3945, 2019.
- [8] C. Xu, Y. Zhao, B. Qin, and H. Zhang, "Adaptive synchronization of coupled harmonic oscillators under switching topology," *Journal of the Franklin Institute*, vol. 356, no. 2, pp. 1067–1087, 2019.

- [9] A. Quadrat, "An introduction to constructive algebraic analysis and its applications," *Les cours du CIRM*, vol. 1, no. 2, pp. 281–471, 2010.
- [10] J. Liu, D. Li, and L. Zheng, "The Lin-Bose problem," *IEEE Transactions on Circuits and Systems II: Express Briefs*, vol. 61, no. 1, pp. 41–43, 2014.
- [11] C. Xu, H. Su, C. Liu, and G. Zhang, "Robust adaptive synchronization of complex network with bounded disturbances," *Advances in Difference Equations*, vol. 2019, no. 1, 2019.
- [12] M. G. Frost and C. Storey, "Equivalence of matrices over  $R[s, z]$ : a counter-example," *International Journal of Control*, vol. 34, no. 6, pp. 1225–1226, 1981.
- [13] E. Lee and S. Zak, "Smith normal form over  $R[z_1, z_2]$ ," *IEEE Transactions on Automatic Control*, vol. 28, no. 1, pp. 115–118, 1983.
- [14] Z. Lin, M. S. Boudelloua, and L. Xu, "On the equivalence and factorization of multivariate polynomial matrices," in *Proceedings of the 2006 IEEE International Symposium on Circuits and Systems*, pp. 4911–4914, Island of Kos, Greece, May 2006.
- [15] M. S. Boudelloua, "Further results on the equivalence to Smith form of multivariate polynomial matrices," *Control and Cybernetics*, vol. 42, no. 2, pp. 543–551, 2013.
- [16] D. Li, J. Liu, and L. Zheng, "On the equivalence of multivariate polynomial matrices," *Multidimensional Systems and Signal Processing*, vol. 28, no. 1, pp. 225–235, 2017.
- [17] D. Li, J. Liu, and D. Chu, "The Smith form of a multivariate polynomial matrix over an arbitrary coefficient field," *Linear and Multilinear Algebra*, pp. 1–14, 2020.
- [18] D. Quillen, "Projective modules over polynomial rings," *Inventiones Mathematicae*, vol. 36, no. 1, pp. 167–171, 1976.
- [19] M. Wang and D. Feng, "On Lin-Bose problem," *Linear Algebra and Its Applications*, vol. 390, pp. 279–285, 2004.
- [20] J. Liu, D. Li, and L. Zheng, "Factorization for n-D polynomial matrices over an arbitrary coefficient field," *Journal of Systems Science and Complexity*, vol. 33, no. 1, pp. 196–210, 2020.

## Research Article

# Improved Feature Learning: A Maximum-Average-Out Deep Neural Network for the Game Go

Xiali Li <sup>1</sup>, Zhengyu Lv <sup>1</sup>, Bo Liu <sup>1</sup>, Licheng Wu,<sup>1</sup> and Zheng Wang<sup>2</sup>

<sup>1</sup>*School of Information Engineering, Minzu University of China, Beijing 100081, China*

<sup>2</sup>*Department of Management, Taiyuan Normal University, Shanxi 030619, China*

Correspondence should be addressed to Xiali Li; [xiaer\\_li@163.com](mailto:xiaer_li@163.com)

Received 30 January 2020; Revised 5 March 2020; Accepted 16 March 2020; Published 9 April 2020

Guest Editor: Michael Z. Q. Chen

Copyright © 2020 Xiali Li et al. This is an open access article distributed under the Creative Commons Attribution License, which permits unrestricted use, distribution, and reproduction in any medium, provided the original work is properly cited.

Computer game-playing programs based on deep reinforcement learning have surpassed the performance of even the best human players. However, the huge analysis space of such neural networks and their numerous parameters require extensive computing power. Hence, in this study, we aimed to increase the network learning efficiency by modifying the neural network structure, which should reduce the number of learning iterations and the required computing power. A convolutional neural network with a maximum-average-out (MAO) unit structure based on piecewise function thinking is proposed, through which features can be effectively learned and the expression ability of hidden layer features can be enhanced. To verify the performance of the MAO structure, we compared it with the ResNet18 network by applying them both to the framework of AlphaGo Zero, which was developed for playing the game Go. The two network structures were trained from scratch using a low-cost server environment. MAO unit won eight out of ten games against the ResNet18 network. The superior performance of the MAO unit compared with the ResNet18 network is significant for the further development of game algorithms that require less computing power than those currently in use.

## 1. Introduction

Deep learning and reinforcement learning are increasingly being used in developing algorithms for playing various games such as backgammon, Atari, Shogi, chess, Go, StarCraft, Texas poker, and mahjong, where the artificial intelligence (AI) program applying the algorithms has reached or even surpassed the performance level of top human players. However, large-scale deep neural networks consume a lot of computing power in game search processes and training of the network, so huge amounts of computing power are required to run these programs.

Tesauro et al. first used temporal difference (TD) reinforcement learning algorithms [1, 2] and backpropagation neural networks [3] to achieve superhuman performance levels in backgammon, demonstrating that deep learning can be effectively combined with reinforcement learning algorithms. Various game programs, including the AlphaGo [4] series, AlphaGo Zero [5], Alpha Zero [6], Alpha Star [7],

Libratus [8], Pluribus [9], AI Suphx [10], and ELF Go [11] all use deep neural networks (DNNs) as their prediction model. These programs have beaten human players, thereby demonstrating the application prospects of deep convolution neural networks (CNNs) in the gaming field. However, such networks have many parameters, resulting in high computing requirements and slow training processes. Often, the game problems are solved using a distributed cluster or even a dedicated chip, such as a tensor processing unit. For small games like the Atari series games, including Atari using DQN (Deep Q Network) [12], C51 (51-atom agent) [13], QR-DQN (Distributional Reinforcement Learning with Quantile Regression) [14], HER (Hindsight Experience Replay) [15], TD3 (Twin Delayed Deep Deterministic) [16], DDPG (Deep Deterministic Policy Gradient) [17], SAC (Soft Actor-Critic) [18], A2C/A3C (Asynchronous Actor-Critic, Asynchronous Advantage Actor-Critic) [19, 20], TRPO (Trust Region Policy Optimization) [21], and PPO (Proximal Policy Optimization) [22], the end-to-end learning mode is



achieved using a DNN to learn from video inputs. In game research, most studies focus on the efficiency of the reinforcement learning algorithm itself but neglect the problems of neural network adaptation, selection, and design in the deep reinforcement learning algorithm. To achieve a powerful machine learning solution on a personal computer and enable the deep reinforcement learning algorithm to be extended to equipment with low computing power for fast training, we need a method that can achieve high performance with reduced computing power consumption.

In order to improve the performance of DNN [23–26] in the deep reinforcement learning algorithm, this paper presents a method to improve the learning speed and reduce the required parameters by optimizing the network structure. We propose a convolution layer-based network structure that reduces the overall computational cost by reducing the number of iterations executed with a higher rate of learning the signature graph on the network. The network structure uses a maximum-average-output (MAO) layer instead of a partial convolution layer in 17 layers of CNN. By randomly selecting the input channels during the training process, different convolution cores have the opportunity to learn different features and have better generalization ability and learning efficiency.

First, this study provides another way to optimize the deep convolution neural network. The output of this layer is based on the principle of the piecewise function [23]. It has different ideas in improving the deep convolution neural network from the improvement of ELM [25, 26]. In this paper, approaching the nonlinear function by piecewise linear function, the MAO layer has less computing power than some convolution layers using activation functions such as tanh or sigmoid functions and has better fitting performance than those using the ReLU activation function. In addition, MAO reduces computation latency by learning more features at each level to reduce the number of required layers. The network model is based on a full convolution network and therefore has fewer parameters, which allows it to run and train on a graphics processor with less memory than traditional programs.

Second, this study verifies that improving the learning efficiency of the network can also help to enhance the efficiency of the learning algorithm. The deep reinforcement learning model mentioned in this article uses the same reinforcement learning algorithm as AlphaGo Zero. By comparing the structure of ResNet18 [24] and MAO network used in the benchmark control group, we directly compare the learning effect of MAO and ResNet18 networks when they have the same affiliation trained in the game.

## 2. Maximum-Average-Out Deep Neural Network

The reinforcement learning method used in this study was a DQN. The general neural network needs a large quantity of data to support learning features through the DNN. Deep reinforcement learning needs significant search space and calculation time to generate a sufficient number of samples and requires multiple iterations to learn the corresponding

features. The MAO layer helps the convolution layer learn different feature maps by randomly dropping out [27] some feature maps during training, thus improving the efficiency of the convolution layer learning features. This principle is similar to that of the dense layer in the Maxout network [23]. By increasing the number of neurons in a single layer to increase the number of feature maps, a segmented function is formed to improve the learning efficiency of the feature map in this layer. The number of learning features within each training neural network is increased by selecting the feature map output with the maximum average value of these feature maps. The results calculated by the convolution layer in the structure can play a more significant role in the convolution layer than can be accomplished using the Maxout function directly. This makes the network learning more robust, indirectly reducing the neural network learning time and therefore reducing the total reinforcement learning time.

*2.1. Structure of Maximum-Average-Out Unit.* The MAO unit input port is a dropout-controlled channel selector where the input is  $n$  feature maps. The input selector is only working in the training stage, while the prediction step is in the all-pass state. The input data are  $M_0$ , which is an  $l \times m \times n$  tensor. The channel mask in training is randomly generated by a dropout function. The mask  $V_{1 \times 1 \times n}$  is a  $1 \times 1 \times n$  tensor, while in prediction it is a tensor of  $V_{1 \times 1 \times n}$  for all elements. The selection of the  $d$ -th channel in the selected feature map  $M_0$  is calculated using the following formula, and the symbol “:” represents the whole dimension of the referenced tensor:

$$M_1(:, :, d) = M_0(:, :, d) \times V(:, :, d). \quad (1)$$

The selected feature map  $M_1$  is calculated with a size of  $l \times m \times n$  in the convolution layer where the depth of  $M_1$  is  $k$  and the size of the convolution kernel  $C_k$  is  $3 \times 3 \times k$ . The feature map  $M_2$  is obtained using

$$M_2 = M_1 * C_k, \quad (2)$$

where the size of  $M_2$  is  $(l-2) \times (m-2) \times n$ . The average vector  $V_{\text{avg}}$  of the  $d$ -th channel is calculated using

$$V_{\text{avg}}(1, 1, d) = \text{avg}(M_2(:, :, d)). \quad (3)$$

The size of  $V_{\text{avg}}$  is  $1 \times 1 \times k$ , and the maximum value  $v_{\text{max}}$  of the average vector  $V_{\text{avg}}$  is calculated using

$$v_{\text{max}} = \max(V_{\text{avg}}(1, 1, k)). \quad (4)$$

The selection mask vector  $V_{\text{select}}$  is given by

$$V_{\text{select}}(1, 1, d) = V_{\text{avg}}(1, 1, d) \geq v_{\text{max}} ? 1 : 0. \quad (5)$$

Through the selection mask vector, the feature map with the maximum average value is selected for

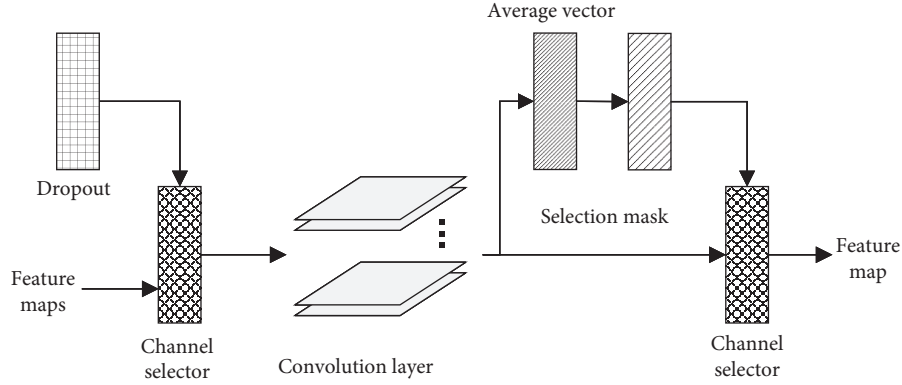


FIGURE 1: MAO unit.

output. The calculation is then divided into the following 2 steps:

- (i) Select the feature map  $M_2$  so that  $M_3$  can be obtained by using the selection mask  $V_{\text{select}}$ , as shown in 6. The elements in the selected feature map are unchanged, while the elements in the unselected feature map are assigned values of 0.

$$M_3(:, :, d) = M_2(:, :, d) \times V_{\text{select}}(1, 1, d). \quad (6)$$

- (ii)  $M_3$  merges its channels by adding the feature maps (see (7)), where  $M_{\text{out}}$  represents the feature maps selected by the segmented function.

$$M_{\text{out}}(:, :) = \sum_d M_3(:, :, d). \quad (7)$$

A schematic diagram of the MAO unit of any given channel is shown in Figure 1. The channel selector is a  $1 \times 1 \times n$  convolution layer, which is input into the channel selector from the upper-level feature map. During training, a group of selection vectors is generated by a dropout function and then input into the convolution to control the input of different feature maps. During prediction, however, the channel selector controlled by a dropout function will allow a feature map to pass through. The convolution layer of depth  $k$  is selected from the channel. There is no activation function in this layer for the feature input to the selector. By calculating the average value of each feature map, up to a vector of length  $k$ , the channel with the maximum average value is selected to output the feature map.

This structure is improved on the basis of convolution layer, referring to the construction idea of Maxout [23], and using dropout to select feature map in the training stage. This structure makes the convolution layer reduce the similarity between convolution kernels when learning features so as to improve the utilization of convolution kernels and increase the number of convolution layer learning features in this structure.

The MAO layer is composed of multiple channels, each of which contains multiple MAO units, as shown in Figure 2. Its use is similar to the convolution layer using rectified linear unit (ReLU).

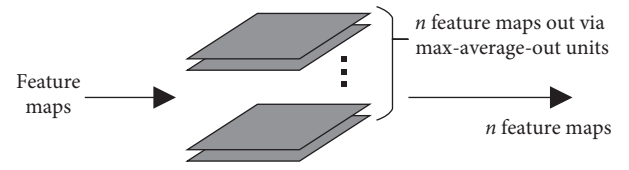


FIGURE 2: MAO layer.

**2.2. Overall Network Structure.** The overall structure of the network is a full CNN with 19 layers. In this network, the MAO block (Figure 3) is composed of a MAO layer and mlpconv [23] layers. A mlpconv layer is a 2-layer CNN that is abbreviated by multilayer perceptron convolution. To ensure fewer parameters after using MAO layer, we combined MAO layer with 2 mlpconv blocks to form a MAO block. By using this structure, whole networks can be deepened, yielding superior generalization abilities and the capacity to learn more features, primarily by MAO layers. The convolution kernel size was  $3 \times 3$ , and the activation function was ReLU.

In this paper, the input of the MAO network (Figure 4) is a state feature map represented by a  $19 \times 19 \times 3$  tensor, which is input through the first mlpconv block [23] with a hidden layer width of 80 and then transferred to the middle MAO block. There are two common MAO blocks in the middle of the network, one policy and one value piece, followed by the output layer consisting of a MAO layer and GAP (global average pooling) layer. A MAO block with a width of 40 was used along with four groups of MAO layers. The MAO layer of the output layer is a group of outputs, and the width of the strategy portion is 362. After the GAP calculation, a vector  $p$  with a length of 362 is calculated, and the width of the board value estimation portion is 1. After the GAP, the output becomes a scalar value, and tanh is added as its activation function to output the scalar  $v$ . Using the full CNN, the generalization ability is ensured with fewer parameters, and the training speed and computational power can be reduced compared to other methods.

### 3. Results

In this study, programs using either the MAO or ResNet18 networks, combined with the AlphaGo Zero reinforcement learning algorithm, were developed and their training time

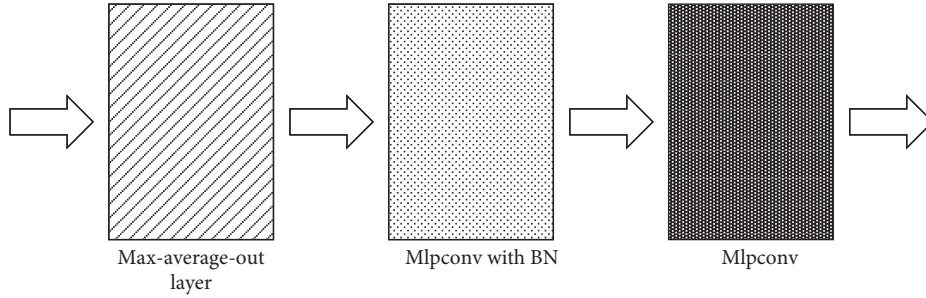


FIGURE 3: MAO block.

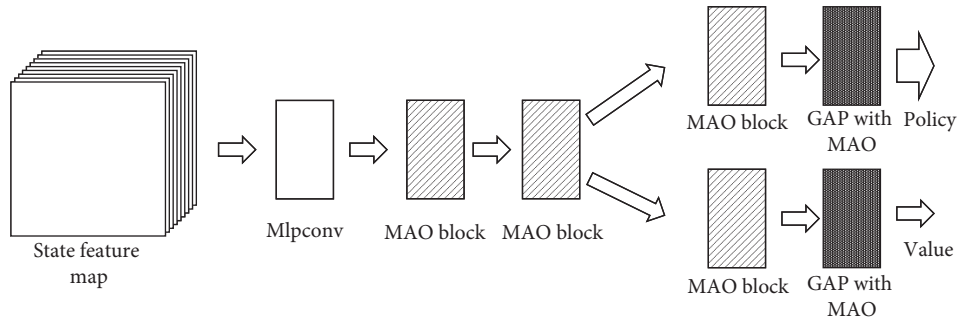


FIGURE 4: MAO network.

and parameters were compared using the experimental conditions shown in Table 1. The programs using the MAO and ResNet18 networks are henceforth referred to as the MAO program and the ResNet18 program, respectively.

In order to reduce the work caused by debugging superparameters and make comparison with ResNet18, the learning rate and minibatch in this paper adopt the parameters mentioned in paper [23, 24] and make fine adjustment within a reasonable range, that is, learning rate = 0.001 and minibatch = 128.

After seven days of training, the ResNet18 and MAO networks had learned from scratch through 60 games of self-play. Although the training time was limited, the results for the MAO program self-play still showed strong attributes. For example, in 10 games against the ResNet18 program, the MAO program took the opposing stones first. The networks were then pitted against each other in 10 games of Go, with the results shown in Table 2. Note that, in Table 2, the label “+Resign” indicates that the player won by resignation of the opponent. ResNet18 and MAO network models in deep reinforcement learning (DRL) verified a distinct effect in playing Go, so that faster DNN learning corresponded with faster DRL learning.

Because of its high learning efficiency, our MAO neural network learned more features than the ResNet18 network while utilizing fewer parameters, as evidenced by the total byte usage of 2 MB and 500 MB, respectively. Therefore, our network is expected to show higher reinforcement learning efficiency than the ResNet18 network. In the ten games played between the two different programs, the eyes which are important shape for Go game between the winner and loser was only 0.5 to 11.5. However, the MAO program won 8 games, while the ResNet18 program won only 2 games.

TABLE 1: Computer configuration.

Toolkit package	CNTK 2.7
Runtime	.Net 4.7.2
OS	Windows 10
CPU	AMD 2700X@4.0 GHz
RAM	32 GB
GPU	RTX2070
Threads used	16
Development environment	Visual studio 2017 community
Communicate environment	GTP + sabaki v0.43.3
Optimization function	Stochastic gradient descent (SGD)
Learning rate	0.001
Minibatch	128
Epoch	10

TABLE 2: Test results.

Comparison	Black side	White side	Result
1	MAO	ResNet18	B + resign
2	ResNet18	MAO	W + resign
3	MAO	ResNet18	B + resign
4	ResNet18	MAO	W + resign
5	MAO	ResNet18	W + resign
6	ResNet18	MAO	W + resign
7	MAO	ResNet18	B + resign
8	ResNet18	MAO	W + resign
9	MAO	ResNet18	B + resign
10	ResNet18	MAO	B + resign

This indicates that the program learned the rules and game patterns more quickly using the MAO network.

Figure 5 shows snapshots of Go boards during some sample games. Specifically, Figure 5(a) shows 2 stones,

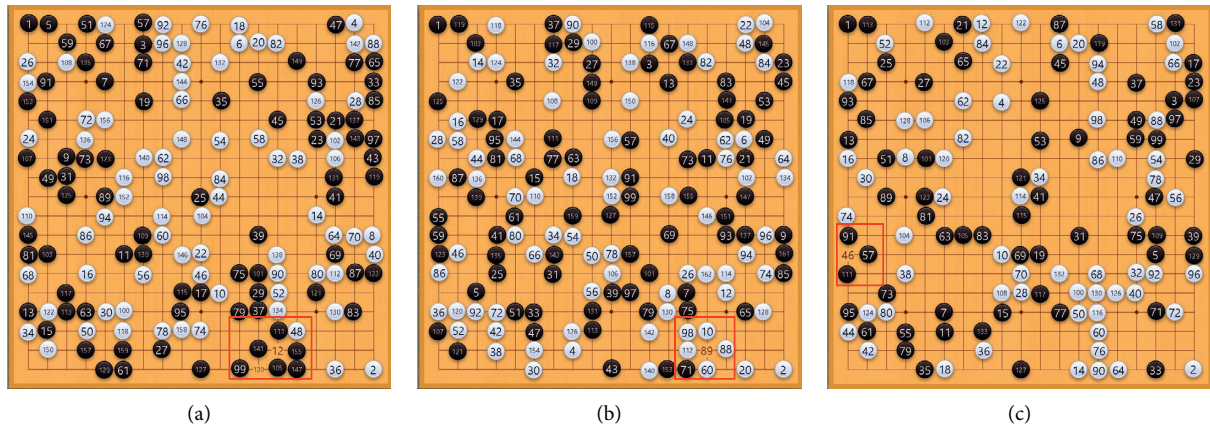


FIGURE 5: Go boards during games between programs using the ResNet18 and MAO algorithms. In this figure, the numbers on the stones indicate the steps that each player plays and red boxes highlight the stones, represented by a number without a stone present, taken by the opponent in the enclosed area. (a) MAO (B) vs. Resnet18 (W), (b) Resnet18 (B) vs. MAO (W), and (c) Resnet18 (B) vs. MAO (W).

indicated by the red box, being taken by the black pieces, which in this case was the MAO program. Figure 5(b) shows one stone, indicated by the red box, being taken by the white player, which in this case was the MAO program. Contrarily, Figure 5(c) shows one stone, indicated by the red box, being taken by the black side, which in this case is the ResNet18 program. Figure 5 clearly demonstrates that the more efficient MAO program can learn the value of eating the opposing pieces more quickly than the ResNet18 program could, and it had a relatively high probability for using similar moves to force the opponent to resign in the middle of the game (winning by resignation). In addition, the MAO program seemed to apply the concept of occupying the board in the Go game more effectively than the ResNet18 program did and thus put more pressure on its opponent. This indicates that the neural network can learn to play for superior board status early in the game. From these results, we can conclude that deep reinforcement learning can be improved by pruning the search algorithm and state space or by using better expert knowledge to guide the early training and achieve rapid improvement in game-play performance. Furthermore, learning more features in a shorter time implies that the program can learn to prune the search algorithm and state space faster and thus generate knowledge to guide moves in subsequent rounds of self-play.

Figure 5(a) shows two stones (red box) taken by the black side when MAO (B) vs. ResNet18 (W) is playing chess, Figure 5(b) shows one stone (red box) taken by the white side when ResNet18 (B) vs. MAO (W) is playing chess, and Figure 5(c) shows one stone (red box) taken by the black side when ResNet18 (B) vs. MAO (W) is playing chess. As shown in Figure 5, the more efficient MAO can learn the value of eating more quickly than ResNet18, and it has a relatively high probability to use this similar move to make the opponent give up in the middle stage (relatively more purposeful), and it can learn better the concept of land occupation in go game and put pressure on the opponent.

## 4. Conclusion

This study explores the possibility of improving DNN structures to increase the efficiency of deep reinforcement learning for application in Go programs. Through the comparative experiments presented in this paper, this is shown to be a feasible and effective scheme for speeding up the deep reinforcement learning algorithm by improving the DNN. Moreover, the MAO network proposed in this paper also demonstrates its ability to improve the feature learning efficiency by controlling the channel input of the convolution layer during the training process. This work further shows that the improvement of the learning efficiency of deep reinforcement learning algorithms can be achieved by pruning the search space and improving the learning efficiency of the neural network. Notably, the latter is easier to achieve than the former. In the future, we intend to continue to perform experiments and obtain more data to further verify the superior performance of the proposed network, by applying this proposed network structure to image processing and other fields to verify and demonstrate its generalizability. On the other hand, we will consider to use multiagent [28, 29] constructure to implement and improve the efficiency of the proposed MAO network.

## Data Availability

Data are available via the e-mail lzywindy@163.com.

## Conflicts of Interest

The authors declare that they have no conflicts of interest.

## Acknowledgments

This study was funded by the National Natural Science Foundation of China (61873291 and 61773416) and the MUC 111 Project.

## References

- [1] R. S. Sutton, "Learning to predict by the methods of temporal differences," *Machine Learning*, vol. 3, no. 1, pp. 9–44, 1988.
- [2] G. Tesauro, *Practical Issues in Temporal Difference Learning*, Springer, vol. 8, pp. 257–277, Berlin, Germany, Berlin, Germany, 1992.
- [3] G. Tesauro, "Td-gammon, a self-teaching backgammon program, achieves master-level play," *Neural Computation*, vol. 6, no. 2, pp. 215–219, 1994.
- [4] D. Silver, A. Huang, C. J. Maddison et al., "Mastering the game of go with deep neural networks and tree search," *Nature*, vol. 529, no. 7587, pp. 484–489, 2016.
- [5] D. Silver, J. Schrittwieser, K. Simonyan et al., "Mastering the game of go without human knowledge," *Nature*, vol. 550, no. 7676, pp. 354–359, 2017.
- [6] D. Silver, T. Hubert, J. Schrittwieser et al., "A general reinforcement learning algorithm that masters chess, shogi, and go through self-play," *Science*, vol. 362, no. 6419, pp. 1140–1144, 2018.
- [7] V. Zambaldi, D. Raposo, S. Adam et al., "Relational deep reinforcement learning," 2018, <http://arxiv.org/abs/1806.01830>.
- [8] N. Brown and T. Sandholm, "Safe and nested subgame solving for imperfect-information games," in *Advances in Neural Information Processing Systems*, pp. 689–699, MIT Press, Cambridge, MA, USA, 2017.
- [9] N. Brown and T. Sandholm, "Superhuman ai for heads-up no-limit poker: Libratus beats top professionals," *Science*, vol. 359, no. 6374, pp. 418–424, 2018.
- [10] msra, <https://www.msra.cn/zh-cn/news/features/mahjong-ai-suphx>, 2019.
- [11] Y. Tian, Q. Gong, W. Shang, Y. Wu, and C. Lawrence Zitnick, "Elf: an extensive, lightweight and flexible research platform for real-time strategy games," in *Advances in Neural Information Processing Systems*, pp. 2659–2669, MIT Press, Cambridge, MA, USA, 2017.
- [12] V. Mnih, K. Kavukcuoglu, D. Silver et al., "Playing atari with deep reinforcement learning. computer science," 2013, <http://arxiv.org/abs/1312.5602>.
- [13] M. G. Bellemare, W. Dabney, and R. Munos, "A distributional perspective on reinforcement learning," in *Proceedings of the 34th International Conference on Machine Learning*, vol. 70, pp. 449–458, Sydney, Australia, August 2017.
- [14] W. Dabney, M. Rowland, M. G. Bellemare, and R. Munos, "Distributional reinforcement learning with quantile regression," in *Proceedings of the Thirty-Second AAAI Conference on Artificial Intelligence*, New Orleans, LA, USA, February 2018.
- [15] M. Andrychowicz, W. Filip, A. Ray et al., "Hindsight experience replay," in *Advances in Neural Information Processing Systems*, pp. 5048–5058, MIT Press, Cambridge, MA, USA, 2017.
- [16] F. Scott, Herke van Hoof, and D. Meger, "Addressing function approximation error in actor-critic methods," 2018, <http://arxiv.org/abs/1802.09477>.
- [17] T. P. Lillicrap, J. J. Hunt, P. Alexander et al., "Continuous control with deep reinforcement learning," 2015, <http://arxiv.org/abs/1509.02971>.
- [18] T. Haarnoja, A. Zhou, P. Abbeel, and S. Levine, "Soft actor-critic: off-policy maximum entropy deep reinforcement learning with a stochastic actor," 2018, <http://arxiv.org/abs/1801.01290>.
- [19] M. Babaeizadeh, I. Frosio, T. Stephen, J. Clemons, and J. Kautz, "Reinforcement learning through asynchronous advantage actor-critic on a gpu," 2016, <http://arxiv.org/abs/1611.06256>.
- [20] V. Mnih, A. P. Badia, M. Mirza et al., "Asynchronous methods for deep reinforcement learning," in *Proceedings of the International Conference on Machine Learning*, pp. 1928–1937, New York, NY, USA, February 2016.
- [21] John Schulman, S. Levine, P. Abbeel, M. Jordan, and P. Moritz, "Trust region policy optimization," in *Proceedings of the International Conference on Machine Learning*, pp. 1889–1897, Lille, France, February 2015.
- [22] John Schulman, W. Filip, P. Dhariwal, A. Radford, and O. Klimov, "Proximal policy optimization algorithms," 2017, <http://arxiv.org/abs/1707.06347>.
- [23] M. Lin, Q. Chen, and S. Yan, "Network in network," 2013, <http://arxiv.org/abs/1312.4400>.
- [24] K. He, X. Zhang, S. Ren, and J. Sun, "Deep residual learning for image recognition," in *Proceedings of the IEEE Conference on Computer Vision and Pattern Recognition*, pp. 770–778, Las Vegas, NV, USA, December 2016.
- [25] X. Luo, J. Sun, L. Wang et al., "Short-term wind speed forecasting via stacked extreme learning machine with generalized correntropy," *IEEE Transactions on Industrial Informatics*, vol. 14, no. 11, pp. 4963–4971, 2018.
- [26] X. Luo, Y. Li, W. Wang, X. Ban, J.-H. Wang, and W. Zhao, "A robust multilayer extreme learning machine using kernel risk-sensitive loss criterion," *International Journal of Machine Learning and Cybernetics*, vol. 11, no. 1, pp. 197–216, 2020.
- [27] P. Baldi and P. Sadowski, "The dropout learning algorithm," *Artificial Intelligence*, vol. 210, pp. 78–122, 2014.
- [28] B. Liu, N. Xu, H. Su, L. Wu, and J. Bai, "On the observability of leader-based multiagent systems with fixed topology," *Complexity*, vol. 2019, Article ID 9487574, 10 pages, 2019.
- [29] H. Su, J. Zhang, and X. Chen, "A stochastic sampling mechanism for time-varying formation of multiagent systems with multiple leaders and communication delays," *IEEE Transactions on Neural Networks and Learning Systems*, vol. 30, no. 12, pp. 3699–3707, 2019.